THE ENERGY SPECTRUM OF ULTRA HIGH ENERGY COSMIC RAYS MEASURED BY THE HIGH RESOLUTION FLY'S EYE OBSERVATORY IN STEREOSCOPIC MODE

by

William F. Hanlon

A dissertation submitted to the faculty of
The University of Utah
in partial fulfillment of the requirements for the degree of

Doctor of Philosophy

Department of Physics

The University of Utah

December 2008

THE UNIVERSITY OF UTAH GRADUATE SCHOOL

SUPERVISORY COMMITTEE APPROVAL

of a dissertation submitted by

William F. Hanlon

This dissertation has been read by each member of the following supervisory committee and by majority vote has been found to be satisfactory.

	Chair: Wayne Springer
	Ben Bromley
	David Keida
	Thomas Richmond
	Orest Symko

THE UNIVERSITY OF UTAH GRADUATE SCHOOL

FINAL READING APPROVAL

To the Graduate Council of the University of Utah:

I have read the dissertation of William F. Hanlon in its final form and have found that (1) its format, citations, and bibliographic style are consistent and acceptable; (2) its illustrative materials including figures, tables, and charts are in place; and (3) the final manuscript is satisfactory to the Supervisory Committee and is ready for submission to The Graduate School.

Date

Wayne Springer
Chair, Supervisory Committee

Approved for the Major Department

David Keida
Chair/Dean

Approved for the Graduate Council

David S. Chapman
Dean of The Graduate School

ABSTRACT

The High Resolution Fly's Eye cosmic ray observatory is designed to observe cosmic rays entering the Earth's atmosphere with energies above 10^{18} eV. These ultra high energy cosmic rays produce a cascade of many particles called an extended air shower. Charged particles from the air shower deposit energy in the atmosphere, which acts as a calorimeter, causing atmospheric N_2 excitation which results in the production of copious amounts of ultraviolet light. This ultraviolet light is collected by the HiRes detector to determine the shape of the shower and ultimately the energy of the cosmic ray which caused it. The air fluorescence method utilized by the HiRes detector to observe and reconstruct extended air showers is described in detail. The energy, arrival direction, and composition of cosmic rays entering the atmosphere can be measured using this method.

The construction and operation of the HiRes observatory, as well as the calibration procedures are also explained. Detailed simulations of extended air showers in the atmosphere, as well as modeling of the detector's response under varying operating conditions are described. The method of processing raw cosmic ray data to the final analysis stage is also reported.

HiRes utilizes a superior method of observing showers by combining two detectors to view showers in stereoscopic mode. The energy spectrum of ultra high energy cosmic rays measured using the HiRes detector in stereoscopic mode is described. Energies from 10^{18} eV and above are measured. Several different models are fit to the reconstructed spectrum. Well known features of the cosmic ray spectrum, including the ankle and the Greisen-Zatsepin-Kuz'min (GZK) suppression are observed. The ankle is found to be at 18.55 ± 0.04 (stat)$^{+0.07}_{-0.02}$ (sys) $\log_{10}$(eV) and the GZK suppression at 19.76 ± 0.04 (stat)$^{+0.01}_{-0.16}$ (sys) $\log_{10}$(eV). The spectral indices are also measured and found to be 3.31 ± 0.03 (stat)$^{+0.03}_{-0.06}$ (sys) below the

ankle, 2.84 ± 0.04 (stat)$^{+0.01}_{-0.02}$ (sys) between the ankle and the GZK suppression, and 6.8 ± 1.5 (stat)$^{+0.0}_{-1.4}$ (sys) above the GZK suppression. The measured number of events above $10^{19.76}$ eV is compared to an expected number of events, assuming no GZK suppression. The significance of the GZK suppression is measured in this way to be 3.7 standard deviations.

CONTENTS

LIST OF FIGURES

LIST OF TABLES

ACKNOWLEDGEMENTS

I would like to thank Wayne Springer for his insightful, invaluable, and patient assistance, John Matthews for his kind and generous support, and Charlie Jui for helping me enter the Doctoral program here at the University of Utah. I could not have taken on this Herculean task without the benefit of their help. I'd also like to thank Konstantin Belov for his encouragement and interest in my work and for suggesting the use of the adaptive sieve algorithm.

The staff members of the HiRes group need to be recognized, for without their tireless technical and administrative efforts this experiment would not have succeeded. I therefore thank Mike Cassidy, Gary McDonough, Frank Misak, Jeremy Smith, and Stan Thomas for their hard work that went into making HiRes run. Thanks are also extended to those members of collaborating institutions that contributed to the running of this experiment.

This work was supported by US NSF grants PHY-9100221, PHY-9321949, PHY-9322298, PHY-9904048, PHY-9974537, PHY-0073057, PHY-0098826, PHY-0140688, PHY-0245428, PHY-0305516, PHY-0307098, PHY-0649681, and PHY-0703893, and by the DOE grant FG03-92ER40732. The cooperation of Colonels E. Fischer, G. Harter, and G. Olsen, the US Army, and the Dugway Proving Ground staff is greatly appreciated. An allocation of computer time from the Center for High Performance Computing at the University of Utah is gratefully acknowledged. The computational resources for this project have been provided by the National Institutes of Health (Grant # NCRR 1 S10 RR17214-01) on the Arches Metacluster, administered by the University of Utah Center for High Performance Computing.

CHAPTER 1

INTRODUCTION

1.1 Ultra High Energy Cosmic Ray Physics

In Chapter 2, a brief history of cosmic ray physics is given. A description of ultra high energy cosmic ray physics is provided. Interesting details of the spectrum are examined. The astrophysical phenomena that are studied via observation of cosmic rays are also described here. The potential sources as well as the physics of propagation through space are discussed. Finally, the physics of extensive air showers and the air fluorescence method are described.

1.2 Description of the HiRes Detector

The High Resolution Fly's Eye Detector, also called HiRes, is a cosmic ray observatory with two detectors, HiRes1 and HiRes2. Each detector is similarly constructed with large light gathering mirrors and "cameras" that scan the sky for cosmic ray air showers. In addition to the detectors, there are artificial light sources used for calibration and monitoring of the atmosphere described in Chapter 3. Details about the optical apparatus used to "see" the showers are explained. Procedures for nightly operation of the detector as well as the amount of operation time accumulated over the period covered in this work is presented. Finally, calibration procedures are described.

1.3 Analysis

Chapter 4 studies the different tools and techniques used to understand the operation of the detector through Monte Carlo simulation and processing of the raw data collected in the field to the final analysis stage. The details of how the Monte Carlo simulates air showers are described. The Monte Carlo simulation must

accurately reflect the actual detector as closely as possible, so the information used to make that happen is also described. The different stages of analysis that convert the real raw data, which contain noise, artificial light sources, and cosmic ray air showers, to a final product with only well reconstructed cosmic ray candidates are presented.

1.4 Results

Chapter 5 provides the results of the analysis of approximately six years of stereo data collection. Distributions of interesting physical observables relating to air showers are shown. A comparison of data with the Monte Carlo simulation of the detector shows that the Monte Carlo accurately represents the data and the nightly conditions under which they are collected. Resolution studies are performed on the Monte Carlo data to verify that the reconstruction is valid and to estimate the resolution with which data can be reconstructed. Details about how the aperture is calculated and also the spectrum are provided and the final spectrum is shown. Error analysis of systematic uncertainties is discussed. A discussion of the validity of the GZK suppression with the data model is given and the significance of the measurement of the suppression as seen by the HiRes detector is also provided.

1.5 Conclusions

In Chapter 6 a summary of the results is given. Data analysis tasks that could further improve the measurement are discussed as well.

CHAPTER 2

ULTRA HIGH ENERGY COSMIC RAY PHYSICS

The study of cosmic rays is a rich field of research that has contributed to many important discoveries in particle physics and astrophysics. There are still many unanswered questions in the field, some of which are sure to greatly impact our understanding of the universe when finally resolved. Cosmic rays are a natural, ubiquitous form of extraterrestrial radiation, contributing about 27 mrem, or only 7.5 % of the total U.S. average radiation exposure per person per year of 360 mrem [22]. In addition to the astrophysical phenomena being studied, cosmic rays contribute or are theorized to contribute to many important terrestrial phenomena. Cloud formation and global climate effects have been linked to solar modulation of galactic cosmic rays [57]. Cosmic rays have also been theorized as contributing to the cause of lightning [25]. Radiocarbon dating is possible only because of the constant cosmic ray flux creating new carbon-14 isotopes in the Earth's upper atmosphere via the reaction

$$n + {}^{14}_{7}N \rightarrow {}^{14}_{6}C + p \tag{2.1}$$

The half-life of carbon-14 is 5730 years and any trace amounts present in the formation of the earth would have vanished long ago without this reaction continually occurring.

In this chapter, a brief history of cosmic rays physics is presented. The physics of production and transport of ultra high energy cosmic rays is examined, as well as the techniques used to observe them. The properties of the atmosphere important to cosmic ray detection and light production and propagation in the air are also discussed.

2.1 History

Cosmic ray physics plays an important role not only in astrophysics, but also in elementary particle physics. At the end of the nineteenth century, Maxwell's theory of electromagnetism was still being experimentally tested. The conduction of electrical currents in low pressure gas tubes was a particularly fertile area of experimentation. The identification of *cathode rays* as electrons was soon followed by the identification of ionizing radiation called α-particles, β-particles, and γ-rays.

To further study ionizing radiation, the gold-leaf electroscope was designed. The electroscope consists of a closed container in which a vertical insulated metal strip with a strip of gold leaf is attached to the top. The bottom of the gold leaf is free to swing upward. When an electric charge is applied to the metals, a similar charge in both causes the gold leaf to move away from the vertical position due to coulomb repulsion. Ionizing radiation causes the leaf to discharge a leakage current, whereby the leaf will move back towards the vertical metal strip. The rate at which the gold leaf falls back towards the vertical can be used to determine the amount of ionizing radiation present.

At the beginning of the 20th century when electroscopes were taken to dark locations away from natural sources of radiation, the movement of the electroscope puzzled physicists. C.T.R. Wilson took an electroscope underground into a railway tunnel and observed no falloff in the rate of ionization [41]. Rutherford later proved that ionization due to naturally occurring radiation underground or contaminating the materials of the electroscope was the cause. In 1910, Wulf took an electroscope up the Eiffel Tower and discovered a decrease in the ionization rate that was much less than was expected had the source been purely terrestrial [41]. The small decrease in ionization implied that a radiation source travelling through the atmosphere may have been present.

In 1912, Hess made balloon flights with electroscopes to 5 km and in 1914, Kolhörster made flights to 9 km. They were startled to find that above 1.5 km above sea level, the ionization rate increased with altitude, indicating an extraterrestrial source of the ionizing radiation [41]. Hess was also able to determine that the source

of the radiation was much more energetic than known terrestrial sources such as radium. In 1925, Millikan dubbed the extraterrestrial radiation *cosmic rays*. In 1929, Skobeltsyn observed tracks in a cloud chamber designed to observe β-rays that did not curve at all in the presence of a magnetic field, indicating energies in excess of 15 MeV. Photos of these tracks are the first taken of cosmic rays. In the same year, Bothe and Kolhörster employed the newly invented Geiger-Müller detector to detect the passage of individual cosmic rays. The Geiger counter allowed for very fast response time to identify the time of cosmic ray events accurately, but suffered from background contamination. Bothe and Kolhörster advanced cosmic ray physics by implementing coincidence counting, a technique still employed today. By placing dense absorbers between photographic plates, they found that the mass absorption coefficient matched that of atmospheric attenuation. They were also interested in discovering whether cosmic rays were charged or neutral radiation. They determined via the coincidence method that the cosmic rays were charged particles and their energies were about 10^9 - 10^{10} eV [41].

From the 1930s until the early 1950s, cosmic rays provided particles energetic enough to probe the nucleus. Cosmic rays were the primary method of discovering new particles until physicists developed sufficiently powerful accelerators around 1953. Using improved cloud chambers and Geiger counters as coincidence triggers, positrons were observed by their similar tracks to electrons, but bending in opposite directions to electrons in magnetic fields. This provided evidence to Dirac's relativistic field equations predicting the existence of an antiparticle counterpart to the electron.

In 1936, Anderson and Neddermeyer announced the discovery of a deeply penetrating particle with mass between an electron and proton. This particle was dubbed a mesotron and was at first theorized to be the particle predicted by Yukawa that binds neutrons and protons in the atomic nucleus. It was soon realized though that these muons, as they are now called, interacted too weakly with nuclei to be the Yukawa particle.

In 1939, Pierre Auger discovered extensive air showers. These large showers of

charged particles resulted from a single high energy cosmic ray interacting with an air molecule in the upper atmosphere, causing a cascade of lower energy particles. Using Geiger counters separated over long distances (up to a few hundred meters), Auger and his collaborators determined that they were observing the secondary particles produced by a primary cosmic ray with energies around 10^{15} eV and containing 10^6 particles [9].

In 1947, kaons and lambdas were discovered by taking the cloud chambers aloft in high altitude balloon experiments, and at observatories located in the Pyrenees in France and the White Mountains in California [41].

Nuclear emulsions were developed that could track the passage of subatomic particles and in 1947, the pion predicted by Yukawa eleven years earlier was observed by Powell, Lattes, and Occhialini. In 1952 and 1953, the Ξ^- and Σ particles were also observed by studying cosmic ray tracks in bubble and cloud chambers. At this time, accelerators became the progenitor of new particle discoveries.

Two groups independently theorized that there is an upper bound to the cosmic ray spectrum, at which energy a sudden and dramatic drop in the flux occurs. In two separate papers published in 1966, Kenneth Greisen of Cornell University and G. T. Zatsepin and V. A. Kuz'min of the USSR Academy of Sciences predicted that this change in the spectrum would occur at around 6×10^{19} eV [24, 59]. This feature in the spectrum would come to be called the *GZK cutoff*, named after Greisen, Zatsepin, and Kuz'min.

In 1967, Kenneth Greisen led a group of physicists that wished to study the extensive air showers first observed by Auger. Greisen realized that the large number of charged particles in the air shower would excite nitrogen molecules as they travelled through the atmosphere and be visible on the ground by the ultraviolet emissions of the de-excited N_2 molecules. This way of observing air showers is called the *air fluorescence* technique [21]. Although the Cornell detector was not sensitive enough to observe air showers using this method, other experiments soon followed with success.

The University of Utah deployed an air fluorescence detector in 1976 at Volcano

Ranch, New Mexico. It overlooked the MIT Volcano Ranch Ground Array built by Linsley and Scarsi, which had reported the detection of an air shower with an enormous primary particle energy of 1×10^{20} eV in 1961. The Utah air fluorescence detector successfully observed EAS via the air fluorescence technique. In 1981, the success of the Volcano Ranch air fluorescence detector was followed up by an improved design built at the U.S. Army Dugway Proving Grounds in Utah. The experiment was called the Fly's Eye since the hexagonal photomultiplier tubes that collected the light from the air showers resembled the compound eye of a fly when packed into a cluster. The first site, dubbed Fly's Eye I, consisted of 67 spherical mirrors 1.5 m in diameter focusing onto clusters of 12 or 14 phototubes. Each phototube observed a 5° cone of sky, providing 2π steradian solid angle coverage. A second site called Fly's Eye II was deployed in 1986 located 3.4 km away. The two sites acted in conjunction to provided stereo observation of air showers with energies in excess of 10^{17} eV. The Fly's Eye experiment reported observing an air shower with primary particle energy of 3.2×10^{20} eV in 1991 [16]. The Fly's Eye experiment ceased operations in 1992.

In 1993, a prototype of an improved Fly's Eye design was tested at the Fly's Eye I site. This new version was called the High Resolution Fly's Eye and was operated as a prototype detector until 1996. During this period, hybrid observations were made using the HiRes prototype to observe showers via air fluorescence and the CASA-MIA ground array located at Fly's Eye II.

The HiRes experiment began collecting data in May 1997 at the HiRes1 site atop Little Granite Mountain. Monocular data collection was performed while the HiRes2 site was being built 12.6 km away on Camel's Back Ridge. Stereo data collection using HiRes1 and HiRes2 to simultaneously observe showers began in December 1999. The HiRes experiment collected data for about 6.5 years, ending operations in April 2006.

2.2 Physics

The study of ultra high energy cosmic rays will help provide answers to important and long-standing questions about astrophysical processes still not completely understood nearly a century after the discovery of cosmic rays. The areas of study most salient to modern cosmic ray research fall into three broad categories: spectrum, chemical composition, and anisotropy.

2.2.1 Spectrum

Figure 2.1 shows the cosmic ray spectrum as measured by various experiments. The most prominent feature is the relative stability of the flux over an enormous range of energies. Empirically it can be seen that the cosmic ray flux roughly follows a power law distribution which goes as

$$N(E)dE \propto E^{-\gamma}dE \tag{2.2}$$

where γ is called the *spectral index* of the flux. The dashed line in the figure is drawn for $\gamma = 3$. Close inspection shows that from 10^{11} eV to between 10^{15} and 10^{16} eV, the flux moves away from this line with increasing energy, indicating the spectral index is less than 3. In this region, γ is found to be ~ 2.7. Beyond this region, the spectrum steepens with $\gamma \sim 3.2$, until around 6×10^{18} eV where it flattens again to $\gamma \sim 2.5$. At around 6×10^{19} eV, the spectrum drops again. This feature of the spectrum called the "GZK cutoff" is a theorized upper limit to the cosmic ray flux, beyond which there is a very abrupt turnoff in the spectrum. This feature of the spectrum is very important to the study of cosmic rays and will be discussed further in later sections. The features of the spectrum have colorful names to identify them. The kink around 10^{15} eV is known as the *knee*. The second kink at around 6×10^{18} eV is called the *ankle*. Figure 2.2 shows a close up of the ultra high energy region, where the structure of the ankle can be better seen.

Another feature of Figures 2.1 and 2.2 is the event rates. At 10^{11} eV, 1 particle per m^2 can be observed every second. In the region of the knee, the event rate drops to 1 particle per m^2 per year. At the ankle, the event rate is lower still,

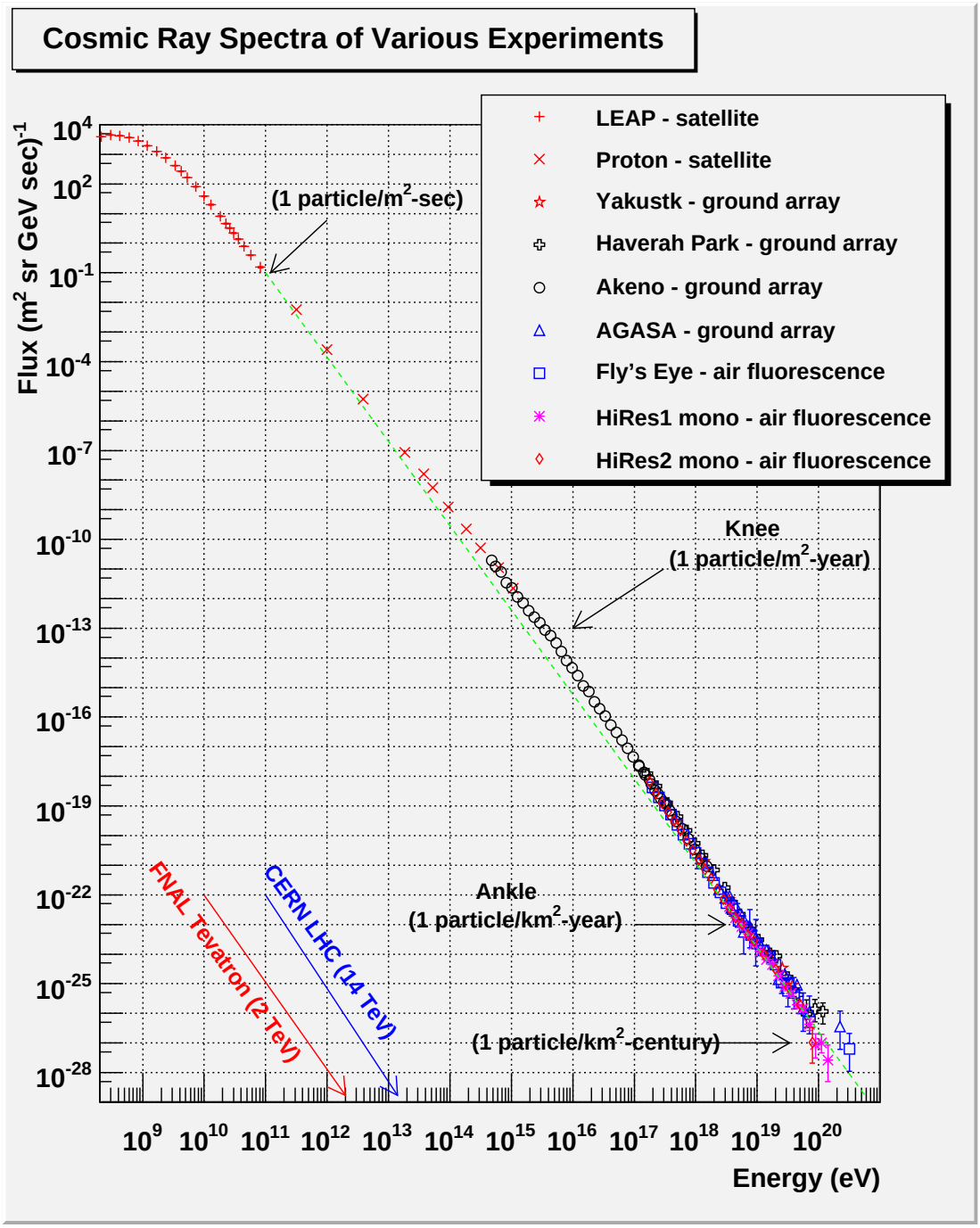

Figure 2.1. The flux of cosmic rays over eleven decades of energy. Note that the spectrum is remarkably stable of such an enormous range of energies. The HiRes experiment is measuring the spectrum beginning around 10^{18} eV and above. The dashed line shows a E^{-3} spectrum.

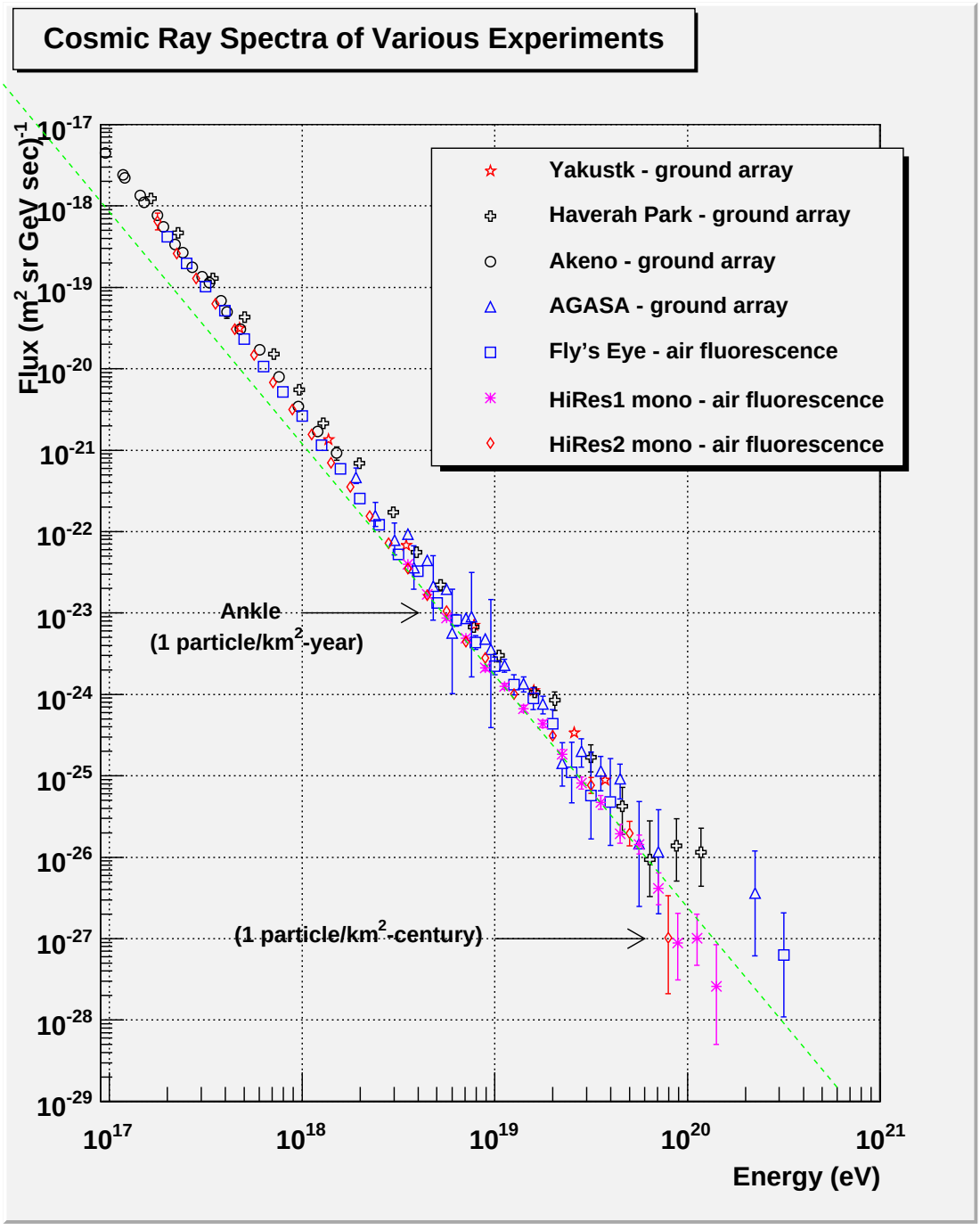

Figure 2.2. A zoom in on the cosmic ray spectrum in the region of interest for HiRes. At the highest energies the flux of cosmic rays is only about 1 particle per km^2 per century.

around 1 particle per km^2 per year. Finally, around 10^{20} eV, the event rate drops to 1 particle per km^2 per century!

The legend in the figures shows a trend in the method of detecting cosmic rays among the different energy ranges. At the lowest energies shown, satellite-based experiments are used to directly observe the passage of the cosmic ray particles. Direct measurement of low energy cosmic rays are done using balloons or satellites carrying calorimeters, emulsion stacks, or transition radiation detectors.

As the energy range being studied increases and the flux drops, the method of observation must account for the low event rates. Consequently, direct observation is no longer possible to collect enough events for a sufficiently reliable statistical sample. Indirect measurements are then made in which the cosmic ray primary particle is not directly observed, but instead, the particles produced in its interaction with air molecules in the atmosphere are detected. Indirect observations are made by measuring the density and arrival times of electrons and muons at the ground produced in the EAS or by scintillation light produced in the atmosphere as the charged particles excite nitrogen molecules.

The energy, arrival direction, and composition must then be inferred through reconstruction methods appropriate to the detector. In the energy region around the knee, ground-based arrays which measure the charged particle flux at the ground of the air shower caused by the cosmic ray are used to make observations. The size of the ground arrays can be as large as several hundred km^2 for the observatories that measure the highest energy cosmic rays. In the region of ultra high energy, air fluorescence detectors which have large apertures ($\sim 10^4$ km^2 steradians at 10^{20} eV) capable of collecting the light from very distant air showers are used to view the most energetic events. Hybrid detectors such as Telescope Array and the Pierre Auger experiment also exist, which combine the air fluorescence and the ground array techniques to observe very large energy showers.

A third striking feature is that cosmic rays with such enormous energies even exist. At the present time, it is not known what source or process is responsible for accelerating cosmic rays into the ultra high energy regime, although there are many

competing models. The highest energy terrestrial accelerators can boost particles to $\sqrt{s} = 10^{13}$ eV (LHC at CERN), a full seven decades of energy short of the highest energy cosmic ray observed. To put things into more familiar terms, the SLAC LINAC is a 3 km long linear accelerator that can boost electrons to 50 GeV. Its average acceleration gradient is 17 MeV/m (this is also the same gradient proposed for the International Linear Collider). To accelerate a cosmic ray to 10^{20} eV with this gradient, the LINAC would need to be extended to $\sim 6 \times 10^9$ km, which is about the distance from the Earth to Pluto. Or using 12 V car batteries to accelerate a proton to such high energies would require 8×10^{18} of them connected in series. As one can see, this is a very exciting and mysterious puzzle to be solved.

2.2.2 Composition

Determining the species of particle or nucleus that is observed by a cosmic ray detector is important to understanding the astrophysical processes that produced them. The composition of cosmic rays includes essentially all elements in the periodic table. Figure 2.3 shows the relative abundances of the elements in the solar system and cosmic rays produced in the galaxy. Over all energies, approximately 87% are protons, 12% helium, and 1% heavier elements [50]. In the region of 10^{12} eV to 10^{15} eV, the composition changes to about 50 % protons, 25 % helium, 13 % CNO, and 13 % iron [51].

The relative abundances of cosmic rays is very similar to the average abundances of stellar material found in the galaxy. In the distribution of elements found in the solar system, there is an overabundance of light nuclei such as lithium, beryllium, and boron and an underabundance of hydrogen and helium compared to galactic abundances. One way to understand the composition of cosmic rays is to assume that the relative abundances match the average galactic composition and that heavy nuclei spallate into lighter nuclei as they propagate through interstellar space. The elemental and isotopic abundances of cosmic rays are important to understanding nucleosynthesis models of stars, the evolution of stars and the origins of galactic cosmic rays. The relative abundance of radioactive isotopes can help determine the

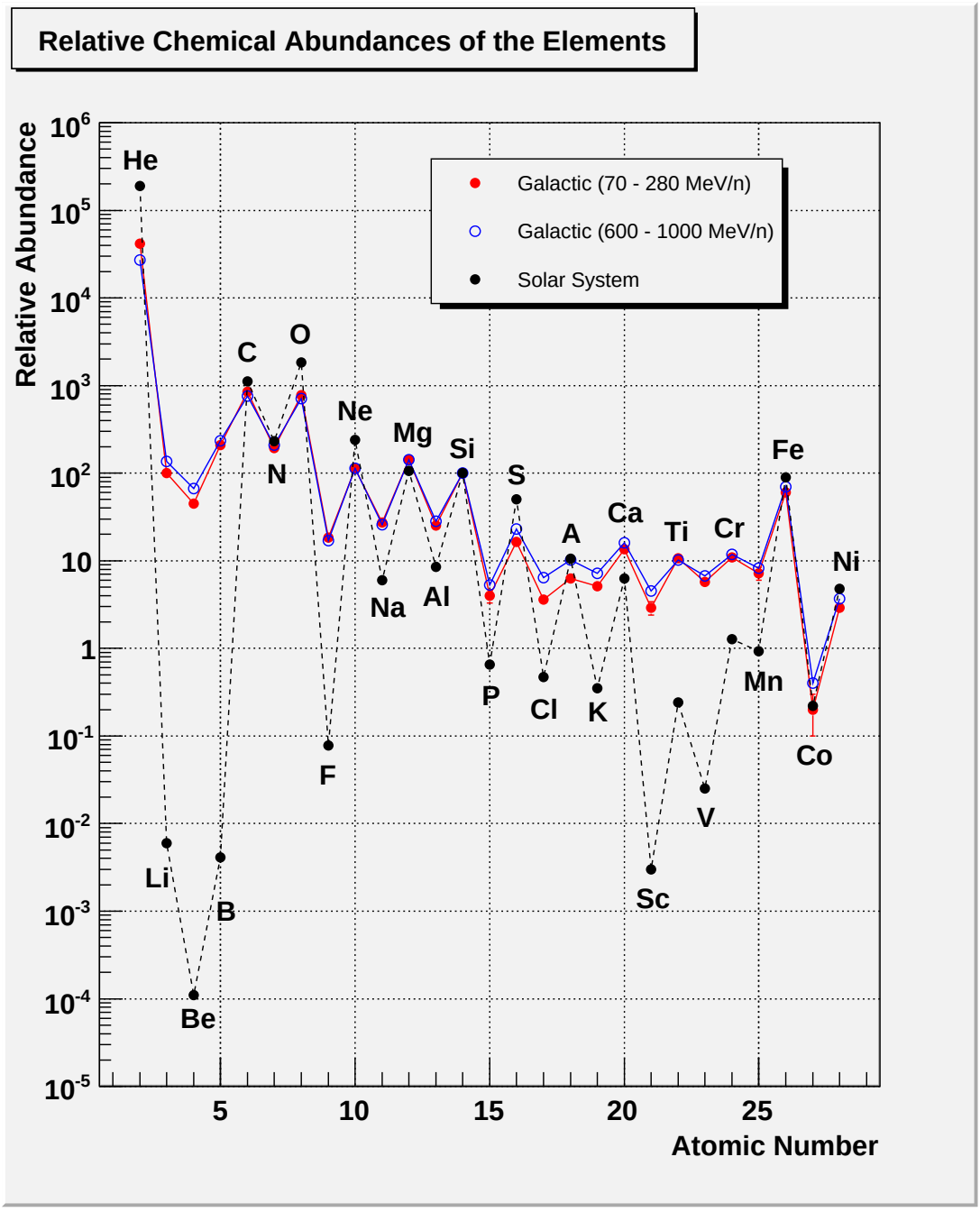

Figure 2.3. The relative chemical abundances of cosmic rays measured at the Earth compared to galactic and solar system abundances. All abundances are normalized relative to silicon. Data from [50].

distance to the objects that created them.

At low energies, where the flux is larger, the composition can be directly measured. At higher energies, the composition must be inferred by observing the properties of the extended air showers. HiRes models ultra high energy cosmic rays by assuming proton and iron nuclei primaries. Iron induced air showers interact more quickly in the atmosphere than proton showers and therefore, the shower maximum size develops earlier. By measuring the shower maximum size, also called $x_{\max}$, of many showers and by comparing it to simulations of hadronic interaction models, the composition of showers as a function of energy can be found. HiRes composition studies have shown that the composition of showers above 10^{17} eV increases in mass with increasing energy [8].

2.2.3 Anisotropy

A measurement of the arrival directions can help identify from which region of the sky cosmic rays come. If a correlation of a large number of very high energy cosmic rays is made to a particular point in the sky, astronomers can search for source candidates. This is especially important in the ultra high energy regime, since no one yet knows for certain what processes are responsible for accelerating cosmic rays to such high energies.

Galactic and interstellar magnetic fields complicate matters by bending the trajectory of charged particles as they travel through space - so much so that for low energy cosmic rays ($< 10^{17}$ eV), it may not be possible to find their source. Ultra high energy particle trajectories are bent less due to their very high rigidity, so a search for their sources are more likely to yield success. The AGASA experiment has reported seeing a 4.5σ excess of cosmic rays within 20° of the galactic center and a 3.9σ excess within 20° of the Cygnus region for energies between 10^{18} to $10^{18.4}$ eV [26]. The Fly's Eye experiment also reported an excess of events in the direction of the galactic plane for energies between 2×10^{17} and 3.2×10^{18} eV [17]. The topic of ultra high energy anisotropy is still an important and active part of the field since no definitive answers have yet to be provided about the sources of these most energetic particles. The Pierre Auger Observatory has reported observing a

correlation of ultra high energy cosmic ray arrival directions and the locations of relatively nearby active galactic nuclei (AGN) [4].

2.2.4 Sources and Propagation

To unravel the mystery of ultra high energy cosmic rays, the sources that can accelerate them to such large energies must be identified. The size of the acceleration regions as well as the distance to the sources are very important in not only gaining greater understanding of astrophysical phenomena, but also in answering the question of whether the GZK cutoff is valid.

2.2.4.1 Sources

There are two general models of proposed ultra high energy cosmic rays: bottom-up and top-down. The bottom-up model envisions particles being created with relatively low energies in currently known sources such as supernovae, active galactic nuclei, or pulsars, and being accelerated to ultra high energies through extended regions of space via the Lorentz force. Top-down models theorize the existence of super heavy X particles, such as super heavy dark matter or topological defects such as magnetic monopoles, cosmic strings, or domain walls. Due to their large rest mass, the decay of these X particles produce more familiar forms of matter with ultra high energies.

Bottom-up acceleration scenarios include a one time acceleration in very high electromagnetic fields. These large field densities occur near compact objects such as neutron stars or accretion disks of black holes. This acceleration method does not lend itself to solving the problem of the smooth power law distribution of the spectrum over such an extended energy range. A second scenario is a diffusive, stochastic shock acceleration model, where magnetized plasma clouds distributed throughout large regions of space are encountered by charged particles. This is also known as Fermi acceleration. This type of acceleration model does provide a power law spectrum, though. The distance and time between successive accelerations does imply very long acceleration times until a particle can reach ultra high energies. Between acceleration shocks, competing energy loss mechanisms

must also be overcome.

Figure 2.4 shows the size and magnetic field strengths of astrophysical objects required to boost protons and iron nuclei to 10^{20} eV, first shown by Hillas [29]. Hillas has shown that the maximum energy of a particle with charge Ze within a given acceleration region of size R is

$$E_{\max} \approx \beta Z \left(\frac{B}{1\mu\mathrm{G}}\right)\left(\frac{R}{1\mathrm{kpc}}\right) 10^{18}\mathrm{eV} \tag{2.3}$$

where β is the acceleration efficiency and B is the magnetic field strength [14]. In the figure, astrophysical objects below the line do not have a sufficient combination of size and magnetic field strength to accelerate particles to ultra high energies.

Top-down decays produce quarks and leptons. The quarks quickly hadronize, producing jets, and massive unstable leptons also decay, causing a cascade of energetic photons, neutrinos, and light leptons. This cascade of particles also includes a small number of protons and neutrons. The protons and neutrons ejected from the X particle decay may become an ultra high energy particle.

2.2.4.2 Propagation

In 1965, the 2.73 K cosmic microwave background (CMB) was first observed by Penzias and Wilson [46]. It was quickly realized in 1966 by Griesen [24] and Kuz'min and Zatsepin [59] that a sea of isotropic and homogeneous photons filling interstellar space would interact with high energy particles travelling long distances. In the laboratory frame, a 2.73 K photon is expected to have energy $E_\gamma \approx kT = 2.4 \times 10^{-4}$ eV. In the rest frame of an ultra high energy proton though, this photon becomes a 145 MeV gamma ray, which is sufficient energy to produce a pion. Although other reactions may cause an ultra high energy proton to lose energy when interacting with CMB photons, pion photoproduction is the most important at the highest energies of the cosmic ray spectrum. To estimate where the GZK cutoff should occur, we can determine the minimum proton energy required to produce a pion with CMB photon.

Some ways in which UHE charged particles and nuclei can lose energy in space are pair production and pion production described by the reactions

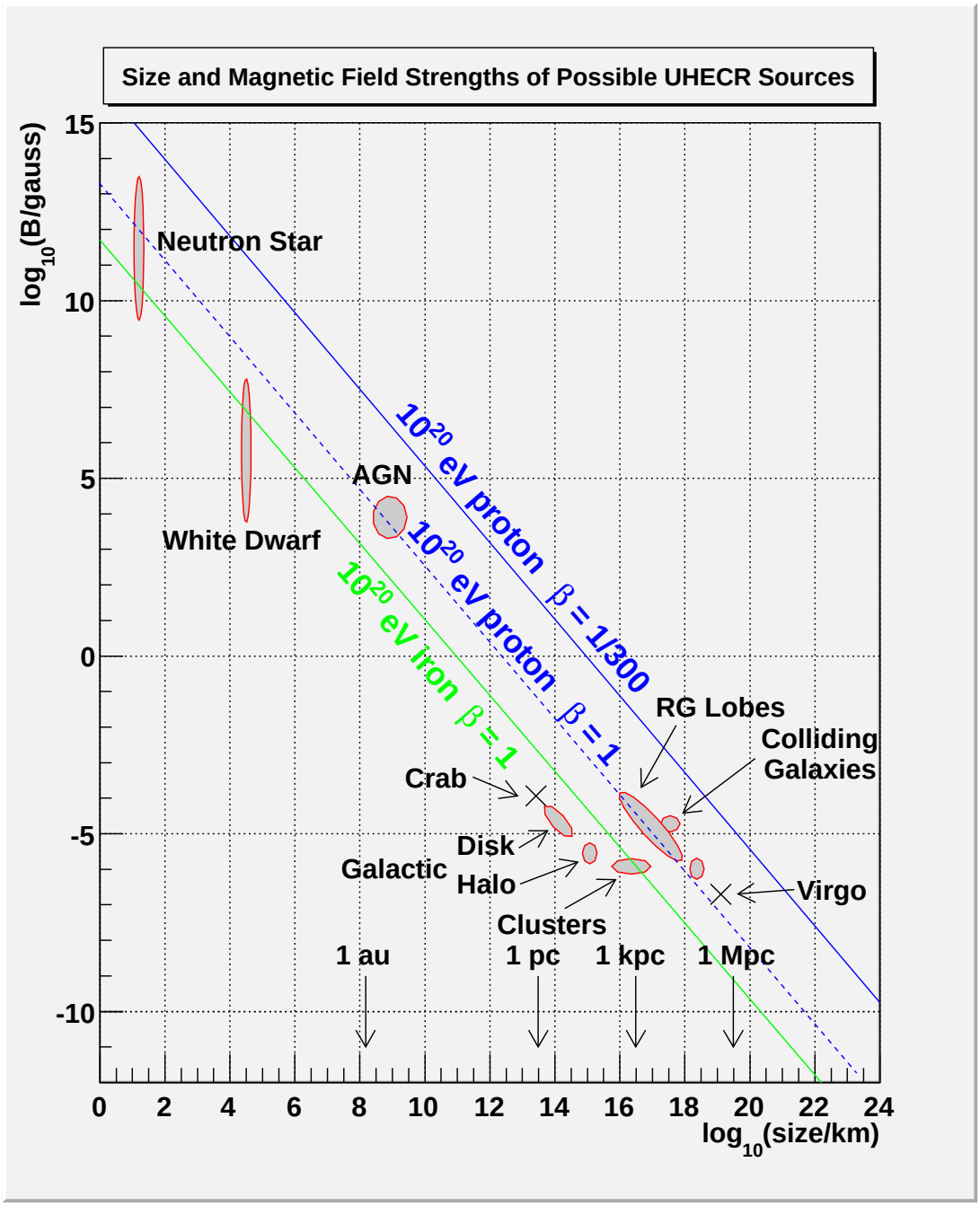

Figure 2.4. Size and magnetic field strengths of possible sources of ultra high energy cosmic rays. Objects below the diagonal lines do not have a sufficient combination of the two to accelerate protons or iron nuclei to ultra high energies [14]. The velocity of the shock wave or efficiency of the acceleration mechanism is represented by β.

$$p + \gamma \rightarrow p + e^+ + e^- \tag{2.4}$$

$$p + \gamma \rightarrow \pi + N \tag{2.5}$$

where p is a high energy proton and γ is a 2.73 K CMB photon.

The specific reaction we will examine is

$$p + \gamma \rightarrow p + \pi^0 \tag{2.6}$$

where a proton interacts with a CMB photon to produce a π^0. The initial reaction can be written as

$$(p_p + p_\gamma)^2 = \left(\frac{E_p}{c} + \frac{E_\gamma}{c}\right)^2 - (\vec{p_p} + \vec{p_\gamma}) \cdot (\vec{p_p} + \vec{p_\gamma}) \tag{2.7}$$

$$= \frac{E_p^2}{c^2} + \frac{E_\gamma^2}{c^2} + 2\frac{E_p E_\gamma}{c^2} - \vec{p_p}^{\,2} - \vec{p_\gamma}^{\,2} - 2\vec{p_p} \cdot \vec{p_\gamma} \tag{2.8}$$

$$= m_p^2 c^2 + 2\frac{E_p E_\gamma}{c^2} - 2\vec{p_p} \cdot \vec{p_\gamma} \tag{2.9}$$

where p_p is the 4-momentum, E_p is the energy, m_p is the mass, and $\vec{p_p}$ is the three-dimensional momentum of the proton in the initial state in the laboratory frame, and similarly for the incoming photon. Rewriting the final term of equation 2.9 by expanding the dot product, we find

$$(p_p + p_\gamma)^2 = m_p^2 c^2 + 2\frac{E_p E_\gamma}{c^2} - 2|\vec{p_p}||\vec{p_\gamma}| \cos\theta \tag{2.10}$$

$$= m_p^2 c^2 + 2\frac{E_p E_\gamma}{c^2} - 2\frac{E_p E_\gamma}{c^2} \cos\theta \tag{2.11}$$

$$= m_p^2 c^2 + 2\frac{E_p E_\gamma}{c^2}(1 - \cos\theta) \tag{2.12}$$

where we've exploited the fact that $\beta_\gamma = 1$ and $\beta_p \approx 1$, since the proton's energy is in the ultra-relativistic regime. To find the threshold energy of the reaction, we choose $\cos\theta = -1$. This represents a head-on collision and provides the maximum energy transfer to the proton. In this case then, we find in the laboratory frame for the initial collision

$$(p_p + p_\gamma)^2 = m_p^2 c^2 + 4\frac{E_p E_\gamma}{c^2} \tag{2.13}$$

Because $(p_p + p_\gamma)^2$ is a Lorentz invariant, we may equate equation 2.13 with the invariant mass of the final reaction state, in which a proton and pion are produced.

This is done in the center of mass frame of the final reaction where $\sqrt{s} = m_p + m_{\pi^0}$. Writing this equation out

$$m_p^2 c^2 + 4\frac{E_p E_\gamma}{c^2} = (m_p + m_{\pi^0})^2 c^2 \tag{2.14}$$

Solving this equation for E_p gives us

$$E_p = \frac{\left(m_{\pi^0}^2 + 2m_p m_{\pi^0}\right) c^4}{4E_\gamma} \tag{2.15}$$

The CMB is found to agree remarkably well with that theorized by a black body at 2.73 K. Therefore, the energy of the CMB photons is described by a Planck spectrum. Figure 2.5 shows the expected CMB photon density in space using a Planck spectrum. Although a thermal photon at 2.73 K would be expected to have an average energy $E \sim kT = 2.4 \times 10^{-4}$ eV, the mean of the Plank distribution shown in the figure is at 6.4×10^{-4} eV. Using the mean of the black body spectrum and using equation 2.15, we find the photopion production threshold to be 1.1×10^{20} eV.

As Figure 2.5 shows there is a high frequency tail to the Planck distribution which may cause photopion production for lower energy protons. The γp cross section is shown in Figure 2.6. As can be seen in the figure, the interaction cross section rises rapidly above the pion production threshold, peaking at about 550 mb at 1232 MeV which corresponds to the Δ nuclear resonance. The excitation of the Δ resonance is an energetically favorable state in which the $J = 1/2$ nucleon becomes a $J = 3/2$ state. The bumps and wiggles at higher energies represent similar nuclear resonances. The Δ state can be achieved by a 2.5×10^{20} eV proton colliding with a 6.4×10^{-4} eV CMB photon.

By examining the γp cross section we can also estimate the expected mean interaction length of an ultra high energy proton travelling through space. The mean free path for collisions is $\lambda_{\text{coll}} = (n_\gamma \sigma)^{-1}$, where n_γ is the CMB photon density and σ is the cross section. Integrating the distribution in Figure 2.5 yields a photon density of $n_\gamma = 412$ photons/cm^3. An examination of Figure 2.6 reveals the average cross section is about 0.12 mb. Calculating the mean free path, one

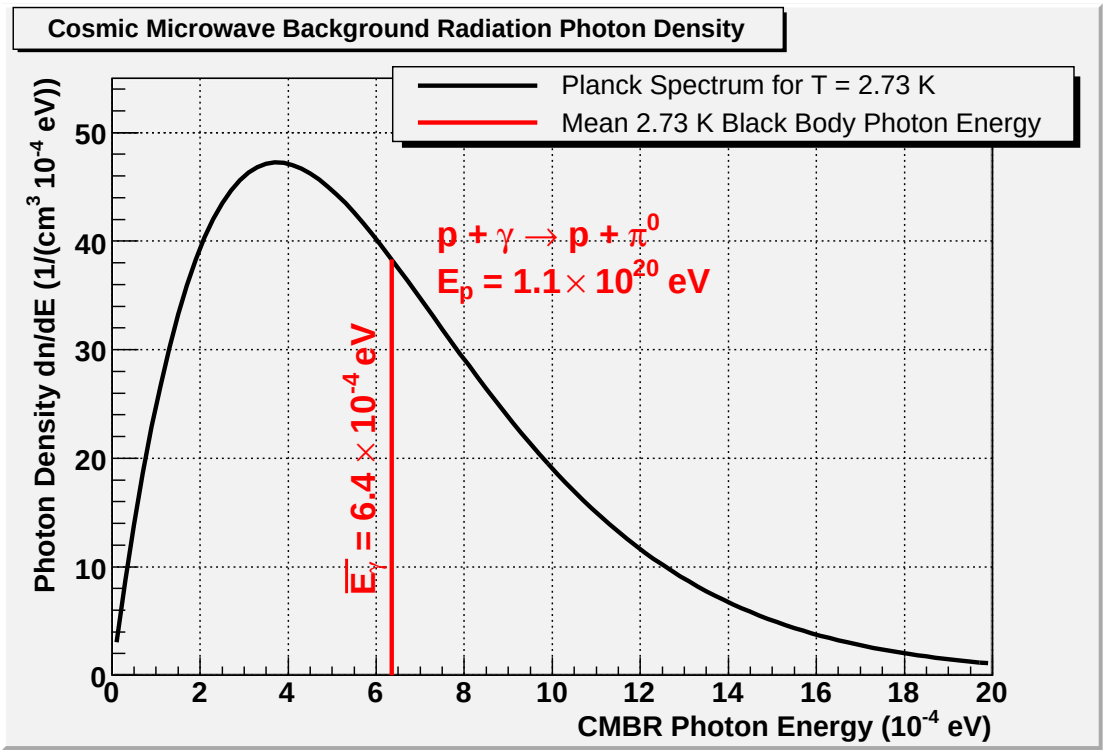

Figure 2.5. The cosmic microwave background radiation photon density and proton energies corresponding to the photopion production threshold. The total density over all photon energies is 412 photons/cm^3. The mean of the distribution is 6.4×10^{-4} eV with a corresponding photopion production threshold of 1.1×10^{20} eV. The GZK cutoff is considered to be at $E_p \approx 6 \times 10^{19} = 10^{19.78}$ eV though due to the assumed distribution of sources and the affect of several competing energy loss mechanisms. For a proton with 6×10^{19} eV energy, a CMB photon with 11.3×10^{-4} eV has enough energy to produce a π^0.

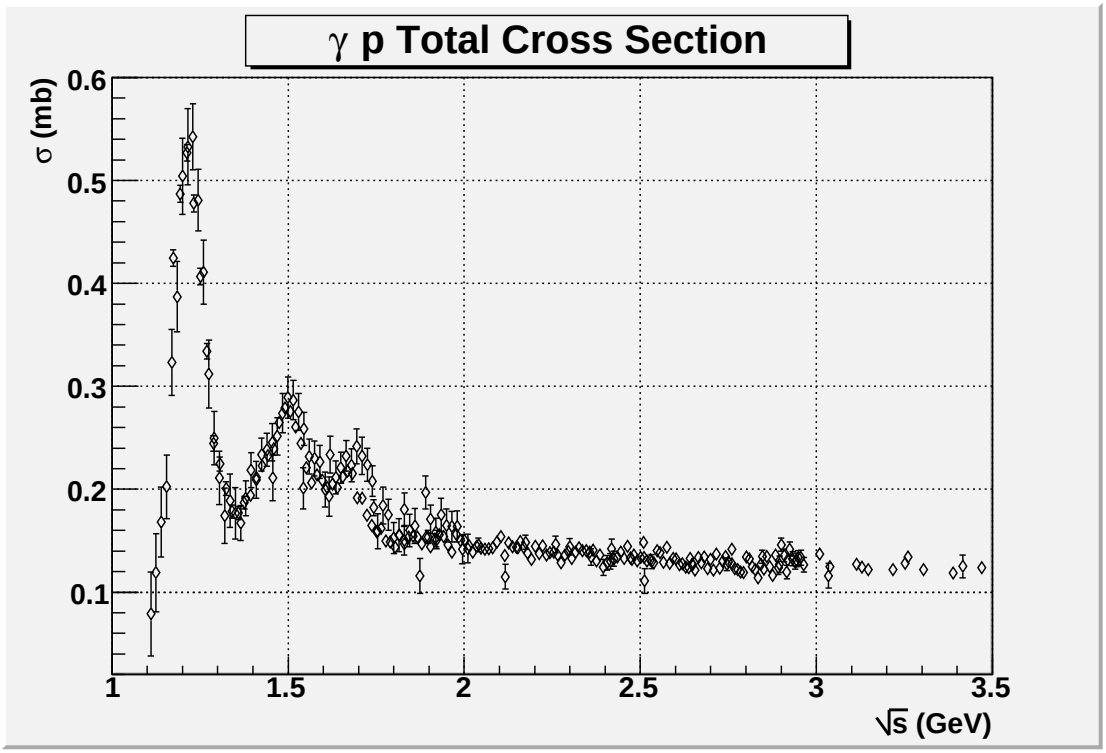

Figure 2.6. The total γp interaction cross section. The photopion production mechanism is responsible for most of the energy loss of ultra high energy protons interacting with CMB photons. The displayed cross section starts with the π^0 production threshold at $\sqrt{s} = 1.078$ GeV. Note the subsequent rapid increase in cross section up to $\sqrt{s} = 1.232$ GeV which corresponds with the Δ resonance. Data from [7].

finds $\lambda_{\text{coll}} = 2 \times 10^{24}$ cm. The more relevant measure, though, is the distance scale for energy loss, $\lambda_{\text{attn}} = (\kappa n_\gamma \sigma)^{-1}$, where κ is the mean energy loss, or inelasticity, per interaction. At the pion production threshold, the inelasticity is about 0.13 and rises to an average of 0.22 at the Δ resonance, and it continues to increase for higher proton energies due to the production of more pions and imparting more kinetic energy to the secondary particles [24, 55]. Using $\kappa = 0.22$, we find $\lambda_{\text{attn}} = 9.2 \times 10^{24}$ cm. Table 2.1 shows some relevant cosmic distances to compare to λ_{attn}.

This distance corresponds to a characteristic time $\tau = 3.1 \times 10^{14}$ seconds. The age of the universe is 13.7×10^9 years $= 4.3 \times 10^{17}$ seconds, so τ is several orders of magnitude smaller than the lifetime of the universe; therefore, it is unlikely that protons with energies greater than the GZK cutoff are solely the result of processes related to the birth of the universe. Any super GZK particles observed today must have been produced in the relative recent past.

Altogether, the most important energy loss mechanisms for protons with energies greater than 10^{18} eV are redshift, pair production, and photopion production. Redshift energy loss is essentially constant over energies $> 10^{18}$ eV and is the dominant cause of energy loss between $10^{18} < E_p < 3 \times 10^{18}$ eV. Pair production dominates between $3 \times 10^{18} < E_p < 4.8 \times 10^{19}$ eV. Finally, photopion production rises rapidly and becomes the dominant energy loss mechanism for $E_p > 4.8 \times 10^{19}$ eV [12]. Nuclei can also lose energy due to photodisintegration, whereby nucleons are liberated from the nucleus by interaction with CMB photons. The combined effect of these energy losses is to move the accepted value of the GZK cutoff to be at 5.8×10^{19} eV. Berezinsky and Grigor'eva define $E_{1/2}$ which is the energy at which a power law extrapolation of the integral spectrum exceeds twice the flux calculated by accounting for the aforementioned energy losses [12].

The effect of the GZK cutoff on the spectrum then is dependent on the distance to sources with sufficient energy to accelerate particles to energies around 10^{20} eV. This search for anisotropy is being conducted by UHE cosmic ray observatories around the world by recording the arrival direction of ultra high energy events and

Table 2.1. Table of cosmological distances.

Object/Location/Distance	dist (cm)	dist (pc)
Alpha Centauri (Closest star)	4.1×10^{18}	1.338
V4641 Sgr (Closest black hole)	1.5×10^{21}	0.5×10^{3}
Galactic center	2.5×10^{22}	8×10^{3}
Large Magellanic Cloud	1.5×10^{23}	50×10^{3}
Diameter of the galaxy	2.2×10^{23}	70×10^{3}
$\lambda_{\rm coll}$ ($E_p = 1.1 \times 10^{20}$ eV)	2.0×10^{24}	648×10^{3}
Andromeda Galaxy	2.5×10^{24}	800×10^{3}
Diameter of local group	9.2×10^{24}	3×10^{6}
$\lambda_{\rm attn}$ ($E_p = 1.1 \times 10^{20}$ eV)	9.2×10^{24}	3×10^{6}
Centaurus A (Closest AGN)	1.3×10^{25}	4×10^{6}
Leo Minor (Closest galaxy cluster)	2.2×10^{25}	7×10^{6}
Diameter of Virgo supercluster	9.3×10^{25}	30×10^{6}
Hydra-Centarus (closest supercluster)	1.9×10^{26}	60×10^{6}
Mkn 421 (closest BL Lac)	3.4×10^{26}	110×10^{6}
3C 273 (closest quasar)	2.4×10^{27}	766×10^{6}

searching for clustering of events and correlations with suspected sources such as AGNs.

2.2.5 Extensive Air Showers

Because of the extremely low flux in the regime of ultra high energy cosmic rays, direct detection is not realistically possible. An indirect measurement method must then be applied. As a very high energy cosmic ray enters the earth's atmosphere, it quickly interacts with a nitrogen or oxygen atom, exchanging some of its kinetic energy in an inelastic collision and initiating a chain reaction of particle production processes that result in an *extended air shower*. This EAS is a pancake shaped mass of particles several hundred meters wide and about 10 m thick that propagate through the atmosphere towards the ground at about the speed of light. It is the reaction products of the EAS that can be observed to infer the properties of the primary particle that produced it.

As Figure 2.7 shows, a hadronic shower can be thought of as containing three components: an electromagnetic component, a hadronic core, and a muon component.

In the figure, a proton is the primary particle which collides with an air molecule. The inelastic collision results in a variety of secondary particles such as pions, kaons, neutrons, and protons. The secondary nucleons and charged pions which have energy above about 1 GeV continue this process of nuclear collision, creating more hadronic secondary particles. The neutral pions have very short lifetimes, 8.4×10^{-17} seconds, and decay into two gamma rays, each of which initiates an electromagnetic cascade. Many charged pions decay before another hadronic interaction into muons. Muons are weakly interacting and lose energy only through ionization. Low energy (soft) muons will decay in flight into electrons, positrons, and muon neutrinos. Relativistic muons with $\gamma > 20$ may actually reach the surface of the earth before decaying due to time dilation. If a nucleus heavier than a proton initiates the air shower, it quickly breaks up upon its first interaction, and the resulting shower may be considered a superposition of several smaller energy hadronic showers, each feeding its own electromagnetic cascade and hadronic core.

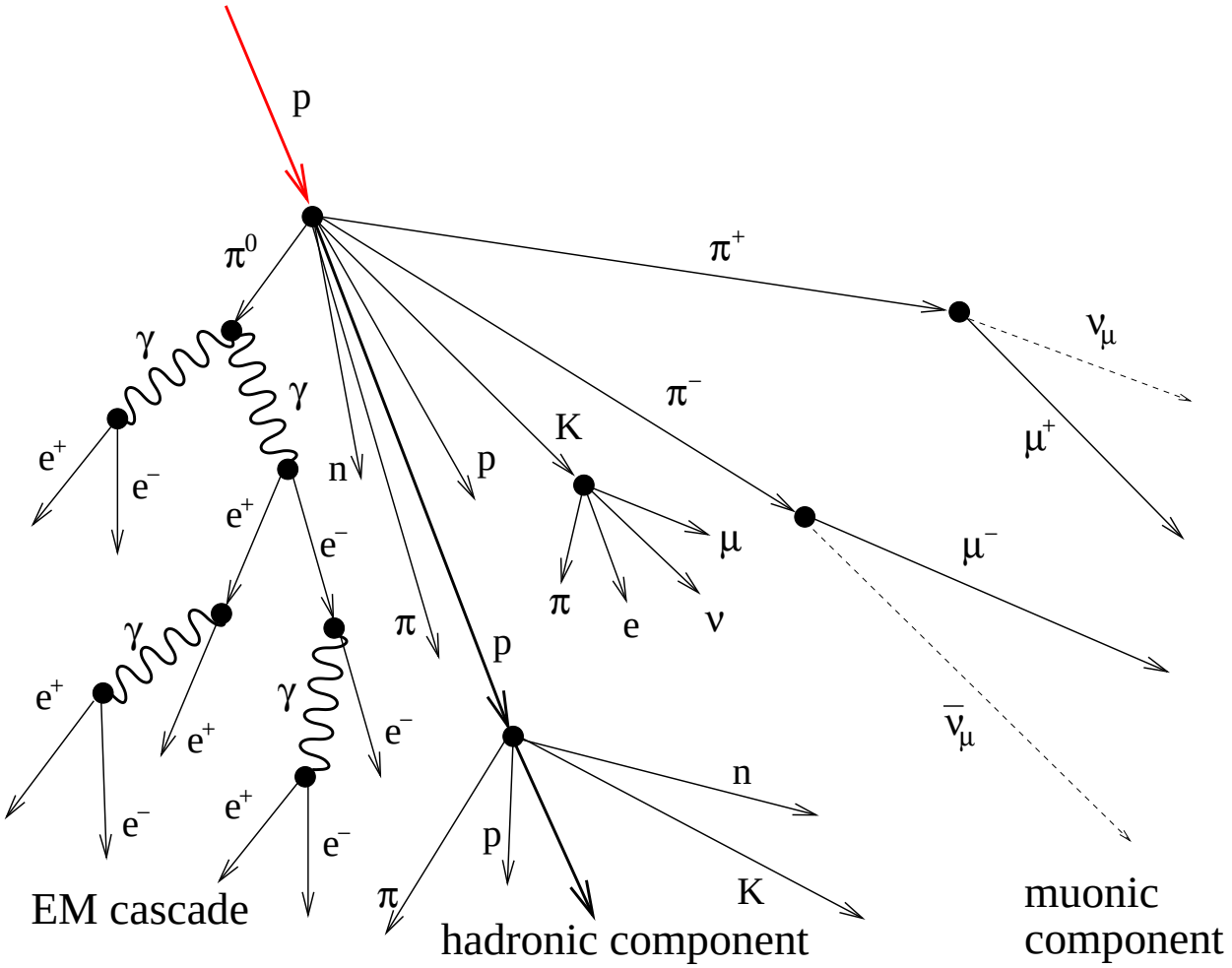

Figure 2.7. Anatomy of an extended air shower. In this figure a proton initiates the air shower, but any hadronic primary would create a similar chain reaction of particle production. The electromagnetic component is composed of electrons and photons that create fluorescence light observed by detectors like HiRes, the hadronic component is the core of the shower, and the muonic component is weakly interacting and can be detected by ground arrays.

The electromagnetic cascade is the largest component of the EAS and most important to air fluorescence detectors like HiRes. A high energy photon initiates the cascade by pair production of an electron and a positron. Each lepton then creates a gamma ray via bremsstrahlung; the gamma rays then pair produce, which creates another electron/positron pair; and so forth. In a hadronic shower additional gamma rays are created by the decay of neutral pions. A simple way to understand the gross properties of an EAS is to use a simple branching model, as shown in Figure 2.8. In the limit of ultra high energies, the radiation lengths for pair production and bremsstrahlung are nearly the same [41]. We can then define an interaction length, λ, over which distance one of these reactions takes place. At each vertex, separated by the distance λ, an interaction takes place and each particle carries away half the energy of the particle that created it. If the gamma ray, which initiated the cascade starts with energy E_0, pair produces an electron and positron, each lepton carries away energy $E_0/2$. Each one of these secondary particles radiates a photon due to bremsstrahlung, and it and the newly created gamma rays carry away energy $E_0/4$. As can be seen then, at each interaction length, the average particle energy is halved and the number of particles in the cascade doubles. At a depth x, the number of interactions (branchings) is $n = x/\lambda$ and the number of particles in the shower is

$$N(x) = 2^n = 2^{x/\lambda} \tag{2.16}$$

The energy per particle can be expressed as a function of x and parameter λ as

$$E(x) = E_0/2^{x/\lambda} \tag{2.17}$$

Particle production continues until the energy per particle drops below the threshold energy at which it can create new particles via bremsstrahlung and pair production. This energy is called the critical energy, E_c. An accepted value of E_c is 81 MeV/c^2 [54]. Below energy E_c, $N(x)$ begins to decrease. This point in the shower is called $x_{\max}$ or the shower maximum. Therefore,

$$N(x_{\max}) = N_{\max} = \frac{E_0}{E_c} \tag{2.18}$$

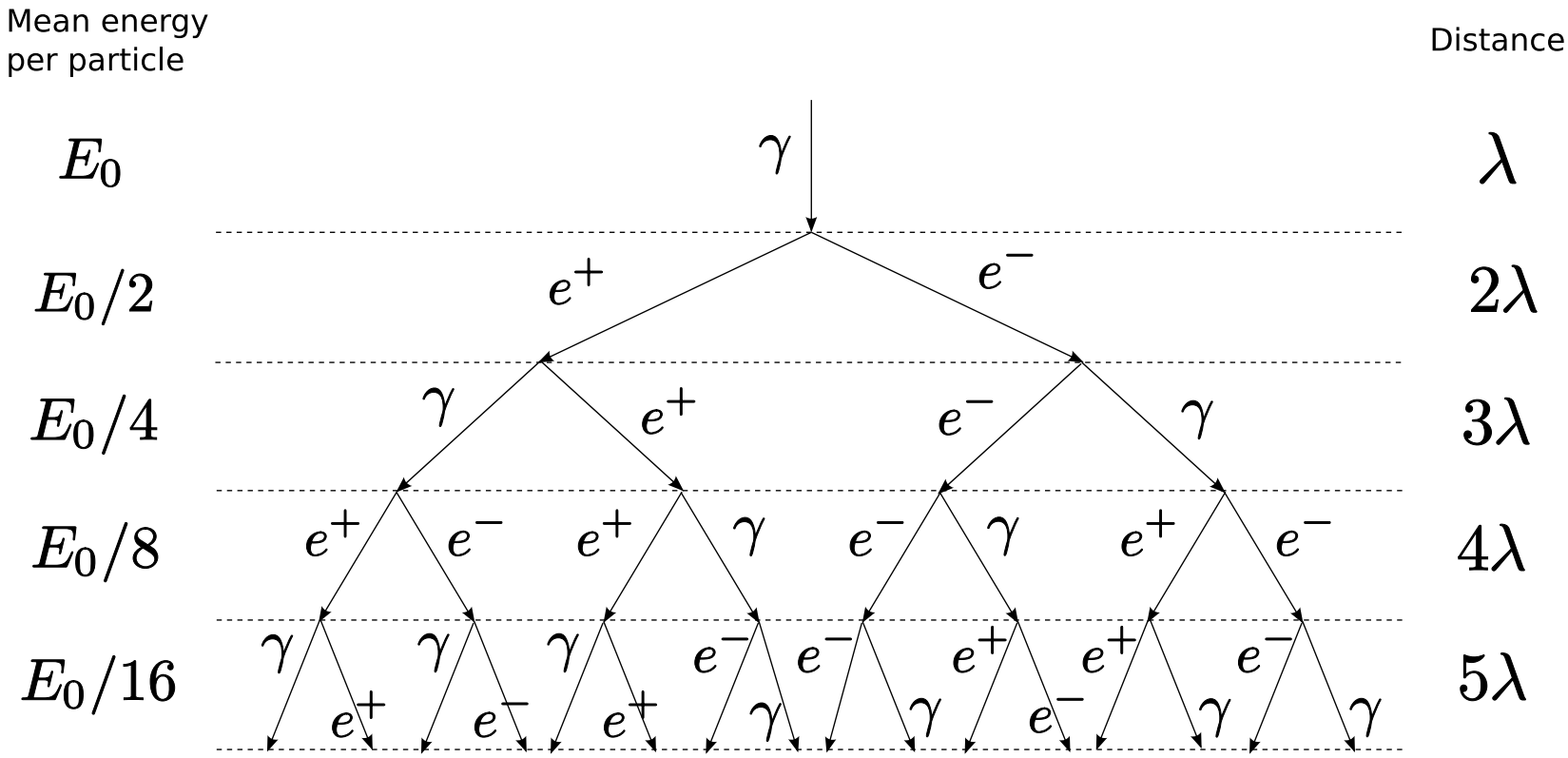

Figure 2.8. The simple branching model of an electromagnetic cascade. Photons pair produce and e^+ and e^- bremsstrahlung until the average energy per particle falls below the critical energy for further particle production. Each each interaction length λ the average particle per energy is halved and the number of particles is doubled.

Substituting equation 2.16 into equation 2.18, we find the following relation between $x_{\max}$ and the primary particle energy

$$x_{\max} = \lambda \frac{\ln(E_0/E_c)}{\ln 2} \tag{2.19}$$

It can be seen that $N_{\max} \propto E_0$ and $x_{\max} \propto \ln(E_0)$.

If the EAS is initiated by a nucleus, the principle of superposition may be called into play. The resulting shower may be considered to be a superposition of A subshowers, each driven by one of the A nucleons in the primary. The primary energy, E_0, is divided equally among each nucleon in this model and it can be shown

$$x_{\max} \propto \lambda \frac{E_o}{AE_c} \tag{2.20}$$

This result suggests that the nuclear species of the primary particle initiating an EAS can be determined by observing the longitudinal development of the shower.

2.2.5.1 Air Fluorescence Method

As the charged particles travel through the atmosphere, they ionize the nitrogen in the atmosphere. The nitrogen fluorescence yield spectrum is wavelength dependent and a detailed analysis of the physics of the excitation and de-excitation of nitrogen by cosmic rays is presented in [21]. Most fluorescence light is emitted between 300 and 400 nm, with three strong peaks in the spectrum at 337, 357, and 391 nm. The transmission of the atmosphere is good in this range of wavelengths, with a vertical attenuation length of about 15 km [51].

Ionizing particles in the atmosphere excite N_2 molecules, which remain in an excited state for typically 10 to 50 nsec before relaxing and emitting a photon in the UV wavelengths. It has been determined that for altitudes from the ground up to 60 km, the fluorescence spectrum is composed almost entirely of excitation of the molecular N_2 second positive band system (2P) and the N_2^+ ion first negative band system (1N) [21]. Between 300 and 400 nm, the fluorescence yield is slightly temperature-dependent and pressure-dependent and its energy dependence is proportional to electron energy loss rate (dE/dx). A 1.4 MeV electron produces about 3.25 photons/meter emitted isotropically and the yield increases for increasing

electron energy [38]. A typical 1 EeV shower will produce about 10^9 electrons at $N_{\max}$, so a large number of UV photons are expected to be produced in a shower, even for fluorescence efficiencies below 1 %.

Air fluorescence detectors observe the fluorescence light generated by the EAS. They use optical imaging systems in a camera-like fashion to capture the fluorescence photons of the shower. The imaging systems act as a "camera," using a mirror to increase the light collection efficiency and focusing the image onto an array of photomultiplier tubes (PMTs). Each PMT in the array has a pixel size of some solid angle of the sky which it views. The PMTs generate an electronic image of light sweeping across them describing the development of the shower in space and time, which can be recorded and analyzed to determine the properties that characterize each shower on an event by event basis.

Air fluorescence detectors have the advantage of observing the development of a large portion of the shower. A perfectly constructed detector could observe the shower from first interaction high in the atmosphere, watch it grow in size to $N_{\max}$, then decay as the energy is dissipated in the lower atmosphere. In reality, due to physical and financial restraints, no fluorescence detector can observe all showers so well, but observation of part of the shower's development, especially being able to observe $N_{\max}$, provides an abundance of physical information about the primary particle which initiated the shower.

A shower can be parameterized into a functional form which describes the number of particles at any given depth using the parameters $N_{\max}$, $x_{\max}$, x_0, and λ. This functional form, called the *Gaisser-Hillas shower profile*, was first developed by T. K. Gaisser and A. M. Hillas to analytically describe extended air showers [23]. The shower profile using this model is given by

$$N(x) = N_{\max}\left(\frac{x - x_0}{x_{\max} - x_0}\right)^{(x_{\max}-x_0)/\lambda} \exp\left(\frac{x_{\max} - x}{\lambda}\right) \tag{2.21}$$

where $N(x)$ is the number of particles at depth x in units of g/cm^2, $N_{\max}$ is the maximum number of particles in the shower at depth $x_{\max}$. x_o and λ have been referred to as the depth of first interaction and the characteristic proton interaction

length in air showers, but it has been shown that x_0 is physically meaningless, often taking on negative values, and λ, usually fixed to 70 g/cm^2, is not the proton interaction length but a fitting parameter dependent on the mass and energy of the primary particle [53].

A second method of parameterization called *Gaussian-in-age* may also be used. It uses three parameters to describe an air shower profile and is written as

$$N(s) = N_{\max} \exp\left(-\frac{1}{2}\left(\frac{s-1}{\sigma_s}\right)^2\right) \tag{2.22}$$

where s is the *shower age* and σ_s is the width of the shower profile. The shower age describes the point of development of the shower taking the value $s = 0$ at first interaction, $s = 1$ at $N_{\max}$, and going to $s = 3$ in the limit of ever increasing depth. Using this parameterization, the shower profile is symmetric about age $s = 1$ and is relieved of some problems of correlation between parameters present in the Gaisser-Hillas formula. All work presented in this study use the Gaussian-in-age parameterization. More information about shower parameterization and how it is used in HiRes analysis to determine the properties of observed air showers is described in section 4.3.

Since real fluorescence detectors do not always observe the entire shower profile, the light information gathered by the detector must be divided into discrete bins of flux, along with the atmospheric depth of each bin. The light bins are then subjected to one of the fitting methods described above to determine the parameters needed to describe the shower for the model in question. The energy of the primary particle can then be determined via a calorimetric measurement, i.e., integrating the entire fitted shower profile weighted with the expected atmospheric energy deposit of the electromagnetic cascade at all depths. As discussed in section 2.2.2, determination of $x_{\max}$ may be used to infer the composition of the primary particle. Information about the direction of the shower track can provide a position in space from which the shower came, aiding in the study of cosmic ray anisotropy.

Air fluorescence detectors suffer from the extreme sensitivity to light needed to most efficiently collect the faint UV light of air showers that often come from

40 km or more away. Therefore, they only run during moonless night hours during which the signal-to-noise ratio is high. The amount of possible data collection time a detector may have over a given period is called the *duty cycle*, and in the case of fluorescence detectors is around 10 %. An additional complication for fluorescence detectors is the variability of the atmosphere which acts as an enormous calorimeter. Clouds and haze can interfere with the ability to observe some or all of the air shower profile, causing gaps in the profile or even scattering light in a way to ruin the profile altogether. The number of particles at any given point in the shower is measured as a function of atmospheric depth, which is dependent on knowing the density and temperature profile of the atmosphere from the observation level to high in the atmosphere.

2.2.5.2 Ground Arrays

A ground array is a second method used to observe extended air showers. They use charged particle detectors located at ground level to measure the spatial and temporal distribution of these particles as they pass through. Since the muonic and electromagnetic components of the air shower surround the hadronic core, the lateral distribution of the shower is used to determine the core's location. Ground arrays must cover very large areas and have many individual detectors to observe ultra high energy air showers, but can run during daylight and bad weather, providing them with the capability to reach a 100 % duty cycle. Because ground arrays sample the shower only at ground level, they can not observe the entire development of the shower, including $x_{\max}$.

2.3 The Atmosphere

The atmosphere is the calorimeter that an air shower dumps its energy into. By observing the light produced by air molecules releasing this energy in the form of UV photons, the air fluorescence technique is possible. The two properties of the atmosphere most important to observing cosmic ray air showers are those that affect shower development and shower observation.

2.3.1 Light Production

Light detected by air fluorescence detectors is produced by two processes. Scintillation light is produced by N_2 excitation by the electromagnetic component of the shower. Čerenkov light is produced by relativistic particles in the shower.

Scintillation light is the ultraviolet light emitted by atmospheric N_2 excitation. Scintillation light production is discussed in detail in section 4.7.

Čerenkov light is produced by particles exceeding the velocity of light in the medium through which it is travelling. For cosmic rays secondaries in the atmosphere, this relation can be expressed as a minimum energy threshold that is dependent on the height, since the index of refraction is dependent on atmospheric density. This relation can be written as

$$v(h) = c/n(h) \tag{2.23}$$

where $v(h)$ is the speed of light in the atmosphere at height h, c is the speed of light in vacuum, and $n(h)$ is the index of refraction. The minimum energy at which Čerenkov light is produced is

$$E_{\min} = \frac{0.511}{\sqrt{2\delta}} \tag{2.24}$$

where $\delta = 1 - n$ and the result $E_{\min}$ is expressed in MeV. There is a maximum emission angle as well defined by $\cos(\theta_{\max}) = 1/n$. The number of Čerenkov photons created per particle per meter is

$$\frac{dN_p}{dl} = 4\pi\alpha \left(1 - \left(\frac{E_{\min}}{E}\right)^2\right) \int \frac{\delta}{\lambda^2} d\lambda \tag{2.25}$$

where α is the fine structure constant and E is the energy of the particle. Note that the $1/\lambda^2$ factor causes most of the Čerenkov light to be found in the short wavelength (UV) part of the spectrum.

The total amount of Čerenkov light produced by all particles at depth x is

$$\frac{dN(x)}{dl} = \int_{E_{\min}}^{\infty} N_e(x) f(E, x) \frac{dN_p}{dl} dE \tag{2.26}$$

where $N_e(x)$ is the number of charged particles, and $f(E, x)$ is the distribution of electron energies. The angular distribution of Čerenkov light is

$$\frac{d^2 N_\gamma}{dl d\Omega} = \frac{dN_\gamma}{dl} \frac{\exp(-\theta/\theta_0)}{2\pi \sin\theta} \tag{2.27}$$

where $\theta_0 = 0.83 E_{\min}^{-0.67}$.

2.3.2 Light Propagation

Both scintillation and Čerenkov light are attenuated by scattering and absorption in the atmosphere. We consider Rayleigh (molecular) scattering, Mie (aerosol) scattering, and ozone scattering, which are used in the simulation of light propagation by the HiRes Monte Carlo and reconstruction code.

2.3.2.1 Rayleigh Scattering

Rayleigh scattering is the light scattering process that dominates when the size of the scatterer is much smaller that the wavelength of light. It is the scattering process of the molecular component of the atmosphere. The amount of light scattering per unit distance is

$$\frac{dN}{dl} = -\rho \frac{N}{x_R} \left(\frac{400}{\lambda} \right)^4 \tag{2.28}$$

where ρ is the atmospheric density, x_R is the mean free path for scattering at $\lambda = 400$ nm, and λ is the wavelength of the light being scattered expressed in units of nanometers [51]. The angular distribution is

$$\frac{d^2N}{dl d\Omega} = \frac{dN}{dl} \frac{3}{16\pi} (1 + \cos^2 \theta) \tag{2.29}$$

The transmission coefficient for Rayleigh scattering from a point in the sky located a distance Δx from a receiver is

$$T_R = \exp \left(-\frac{\Delta x}{x_R} \left[\frac{400}{\lambda} \right]^4 \right) \tag{2.30}$$

where λ is expressed in nanometers. The $1/\lambda^4$ factor causes the strongest scattering in the shortest wavelengths.

2.3.2.2 Aerosol Scattering

Mie scattering is the scattering process which dominates when the size of the scatterer is about the same or larger than the wavelength of light. For this reason, it is also referred to as aerosol scattering. Aerosols are the nonmolecular component of

the atmosphere such as dust, dirt, and other impurities larger than an air molecule. Therefore, unlike Rayleigh scattering, aerosol scattering can change over time since it is dependent upon the temporally and spatially variable distribution of aerosols. It is not strongly wavelength dependent and scatters strongly in the forward direction. Mie scattering is a complicated process, so we use a simplified model instead. The density of aerosol scatterers is assumed to decrease exponentially as a function of height with a characteristic distance, H_{M}, called the scale height. A horizontal attenuation length measured near the ground, L_{M}, is also used.

The amount of light scattered per unit distance is

$$\frac{dN}{dl} = -\frac{N}{L_{\mathrm{M}}}\rho(h) \tag{2.31}$$

where h is the vertical height above the ground and the mixing layer height h_{M} is defined as

$$\rho(h) = \begin{cases} 1 & h \leq h_{\mathrm{M}} \\ \exp(-\frac{h-h_{\mathrm{M}}}{H_{\mathrm{M}}}) & h > h_{\mathrm{M}} \end{cases} \tag{2.32}$$

As the equation 2.32 shows, the mixing layer defines the height at which an exponential decline in the density of aerosols begins. For all work presented here, the mixing layer is always set to 0.

The angular distribution of light is

$$\frac{d^2N}{dld\Omega} = \frac{dN}{dl}\varphi(\theta) \tag{2.33}$$

where $\varphi(\theta)$ is the aerosol phase function. Different aerosol models may implement different $\varphi(\theta)$. The use of phase functions in HiRes analysis is described in section 4.6.5.1. The transmission of Mie scattering between a scatterer at vertical height h_1 and a receiver at height h_2 is

$$T_{\mathrm{M}} = \exp\left(\frac{H_{\mathrm{M}}}{(h2-h1)L_{\mathrm{M}}}(e^{-h_1/H_{\mathrm{M}}} - e^{-h_2/H_{\mathrm{M}}})\right) \tag{2.34}$$

2.3.2.3 Ozone Scattering

Ozone is a UV light absorber which is also considered for data analysis. The amount of light scattered per unit distance by ozone at a height h above the ground is

$$\frac{dN}{dl} = -NA_{O_3}(\lambda)\rho_{O_3}(h) \tag{2.35}$$

where $A_{O_3}(\lambda)$ is the wavelength dependent ozone attenuation coefficient and $\rho_{O_3}(h)$ is the ozone density. The transmission of ozone scattering over a slant depth of x between the scatterer and the receiver is

$$T_{O_3} = \exp(-xA_{O_3}) \tag{2.36}$$

Figure 2.9 shows the wavelength dependence of the attenuation coefficient and the altitude dependence of the ozone pressure. The data shown are based on the USAF Handbook of Geophysics and Space Environment.

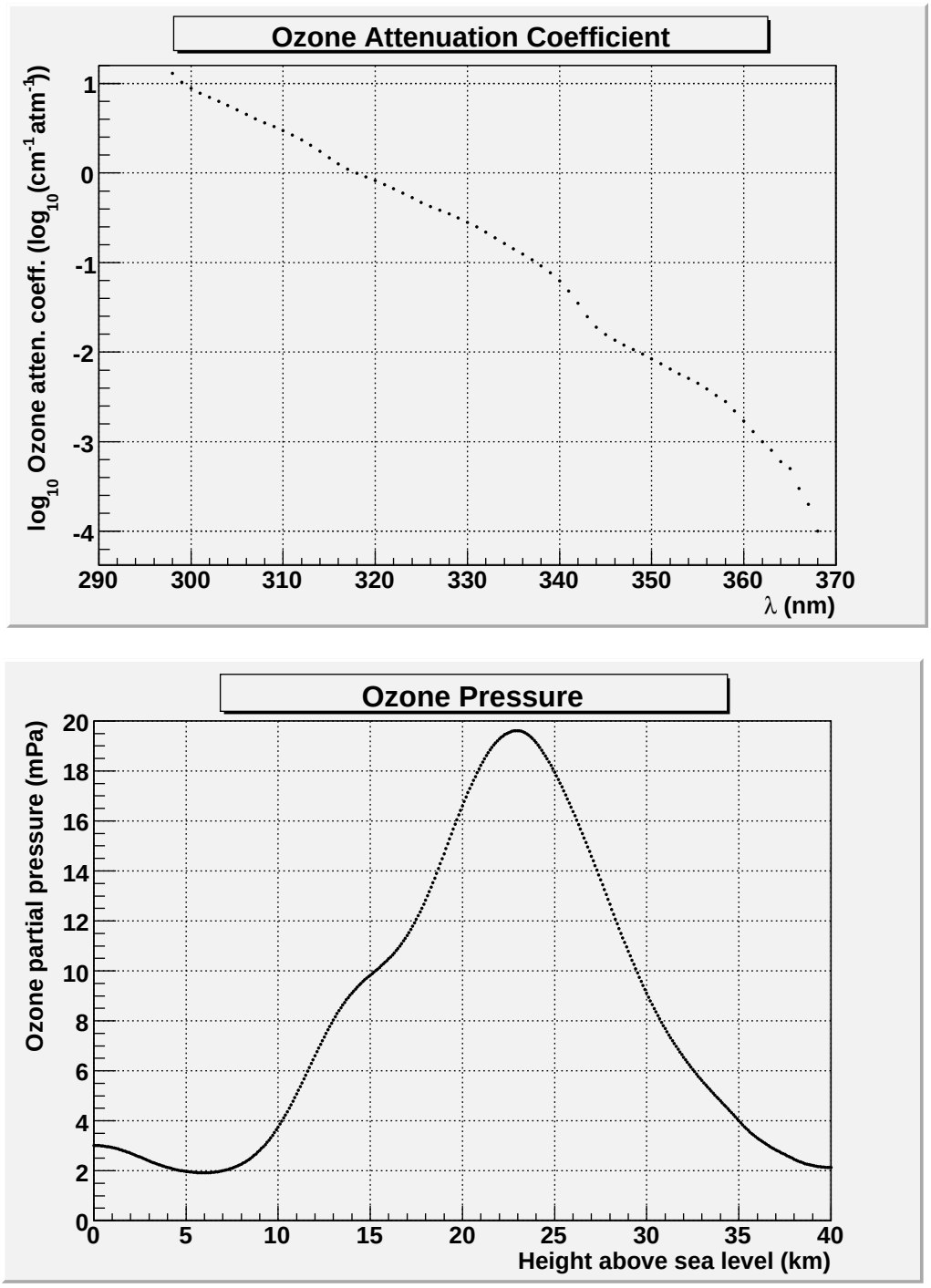

Figure 2.9. The ozone attenuation coefficient and density. Note the strong wavelength dependence of the ozone attenuation coefficient.

CHAPTER 3

DESCRIPTION OF THE HIRES DETECTOR

The important equipment that comprises the HiRes experiment is described here as well as the data collection procedures. Calibration of the detector is important for accurate measurement of shower parameters and the calibration procedures are described here as well.

3.1 Equipment

The HiRes experiment is compromised of two observatories and a multitude of artificial light sources used for calibration and testing. The observatories, HiRes1 and HiRes2, are each made up of a set of rings of spherical mirrors, photomultiplier tube clusters, and electronics racks, that scan the sky for cosmic ray air shower tracks. A mirror ring covers approximately 14° in elevation and nearly the full 360° azimuthal range. HiRes1 contains one ring of 21 mirrors covering from 3° to 17° in elevation. HiRes2 contains two rings of mirrors. Ring 1 covers 3° to 17°, while ring 2 covers 17° to 30° in elevation. Each mirror has an electronics rack that controls its operation and communication with a central facility where all mirror data is collected.

Figure 3.1 shows two mirrors housed in a mirror building. The cloverleaf segments are visible, as well as the cluster boxes and the electronics rack that controls the mirrors.

Figure 3.2 is a close up view of an actual cluster box at HiRes2. The protective UV filter is lowered and the mirror is visible in the reflection. The cluster box is arranged in a tightly packed hexagonal array of 16 rows and 16 columns. The small gaps between the tubes are visible here as well.

Figure 3.1. Two mirrors at HiRes2. The segmented cloverleaf construction is clearly visible here. In front of each mirror is a photomultiplier tube cluster box. The electronics rack which controls both mirrors is visible to the right of the mirrors. The protective door is raised here and can be seen in the lowered state on the building to the right. These are ring 1 mirrors that view from 3° to 17° in elevation.

Figure 3.2. A HiRes2 cluster box with the UV filter lowered. The cluster contains 256 photomultiplier tubes arranged in a tightly packed hexagonal array of 16 rows and 16 columns. On the left the YAG laser fiber for this mirror can be seen. Half of the mirror is seen reflected on the cluster box.

Each site also has a YAG calibration laser that is used nightly to determine phototube calibration by measuring the response to the laser light fed to each mirror via fiber optic lines. A steerable laser is also found at each site. The steerable lasers are used to measure the atmospheric response to laser shots of various polarizations, energies, and geometries.

Between the sites is an array of vertical xenon flashers. These flashers are radio controlled and periodically emit light easily distinguished as upward going tracks into the sky. The flashers are fixed in location and always seen by the same mirrors, and are therefore a useful measure of the atmosphere as well.

Most equipment is located in Utah's Great Salt Lake Desert on the U.S. Army Dugway Proving Grounds, approximately 100 km southwest of Salt Lake City. This location is ideal for the relatively dry air and low amount of light pollution. In addition, the local terrain provides for placement of the detector on small mountains above the desert floor. This puts the detectors above any ground level haze and dust that lies close to the surface. The only piece of equipment not located on Dugway Proving Grounds is a YAG laser stationed at the town of Terra, about 12 km from the Dugway main gate.

Table 3.1 shows the locations of the important pieces of HiRes equipment. HiRes uses a Cartesian coordinate system, called the HiRes universal coordinate system, which defines the origin as the central timing facility's GPS antenna at HiRes1. The latitude, longitude, and height above sea level, as well as the HiRes universal coordinates of each major piece of equipment is listed in the table.

3.1.1 HiRes1

The HiRes1 detector is one of two observatories that make up the HiRes experiment. It is located on Little Granite Mountain on the Dugway Proving Grounds. Twenty-one mirrors are stationed to cover almost the full azimuthal range in a single ring configuration which covers elevation angles from 3° to 17°. Figure 3.3 shows the physical placement and pointing directions of the mirrors. Figure 3.4 shows the elevation angles covered by each of the mirrors.

Although the mirror numbers range from 1 to 22, there are only 21 or 20 mirrors

Table 3.1. The surveyed locations of the major pieces of HiRes equipment. Latitude, longitude and height are measured using WGS84 geodetic datum. The x, y, and z coordinates are distances measured from the from the HiRes coordinate origin, which is defined as the central timing GPS antenna at HiRes1. d_1 and d_2 are the distances from HiRes1 and HiRes2 respectively. All distances are measured in meters.

	Latitude	Longitude	Height	x	y	z	d_1	d_2
HiRes1	40.195 209	-112.835 724	1576.29	0.00	0.00	0.00	0.00	12627.70
HiRes2	40.132 072	-112.958 968	1535.40	-10506.27	-7005.29	-53.92	12627.70	0.00
HR1SLS	40.195 219	-112.835 474	1574.78	21.30	1.10	-1.51	21.38	12610.58
HR2SLS	40.131 485	-112.958 719	1553.34	-10485.20	-7070.56	-34.82	12646.48	71.21
Vertical Flasher 1km N	40.138 805	-112.950 878	1337.00	-9815.40	-6258.20	-249.48	11643.43	1036.19
Vertical Flasher 2km N	40.145 453	-112.942 966	1324.00	-9140.08	-5520.69	-260.83	10681.16	2028.13
Vertical Flasher 4km N	40.158 749	-112.927 138	1324.00	-7789.59	-4045.50	-258.00	8781.25	4022.73
Vertical Flasher 8km N	40.185 334	-112.895 464	1329.00	-5088.60	-1095.20	-249.23	5211.09	8019.88
Vertical Flasher 10km N	40.198 623	-112.879 616	1346.00	-3738.01	380.00	-231.28	3764.39	10019.15
Vertical Flasher 1km S	40.136 910	-112.948 825	1333.00	-9640.59	-6468.90	-253.43	11612.57	1037.75
Vertical Flasher 2km S	40.141 633	-112.938 836	1325.00	-8788.59	-5945.29	-259.72	10613.82	2028.89
Vertical Flasher 4km S	40.151 077	-112.918 856	1327.00	-7084.59	-4898.20	-254.79	8616.77	4023.44
Vertical Flasher 8km S	40.169 956	-112.878 879	1331.00	-3676.70	-2803.90	-246.79	4630.43	8020.72
Vertical Flasher 10km S	40.179 390	-112.858 882	1339.00	-1972.70	-1756.70	-237.74	2652.18	10020.14
Intersite Flasher	40.221 663	-112.816 131	1443.29	1668.00	2935.00	-134.00	3378.52	15717.14
Terra Laser	40.303 573	-112.629 774	1507.68	17512.60	12056.25	-104.80	21261.59	33888.08

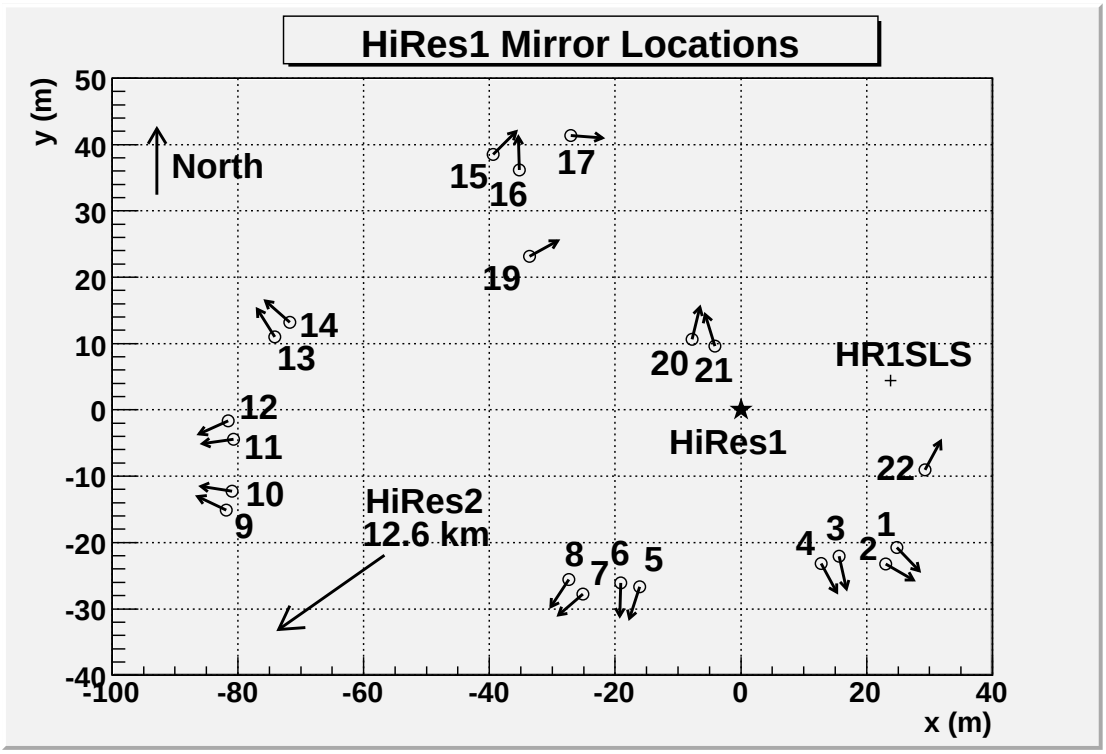

Figure 3.3. The location and pointing directions of the mirrors at HiRes1. All distances are measured in meters. The coordinate system origin is the HiRes1 central timing GPS antenna located on the central facility where operators run the detector. HiRes2 is located 12.6 km to the southwest.

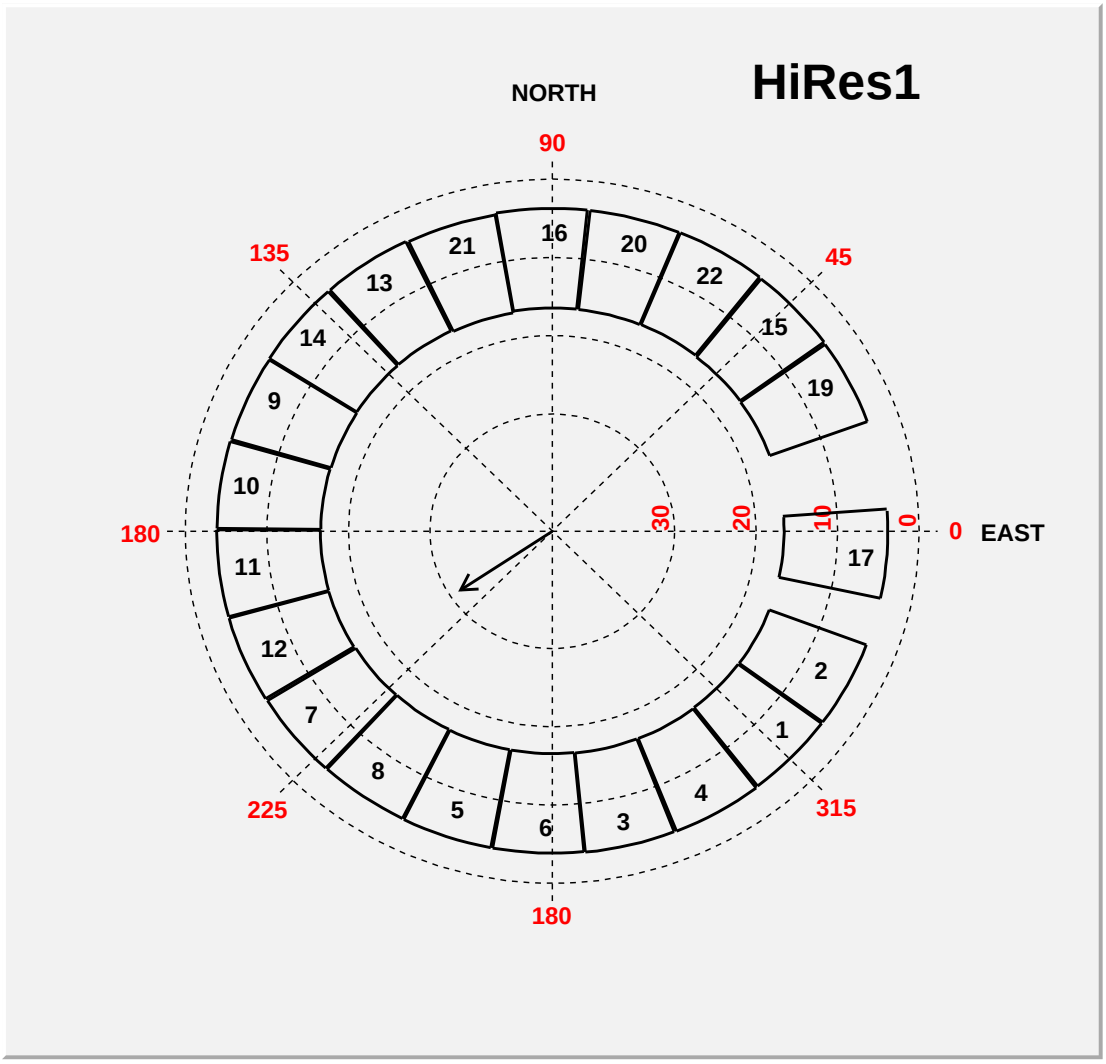

Figure 3.4. Sky map showing the angular coverage of mirrors at HiRes1. The theta angle measures elevation from the ground. The gap counterclockwise from mirror 17 is the space for mirror 18, which was never deployed. The gap clockwise from mirror 17 part of the sky not covered by the detector. The arrow in the center points in the direction of HiRes2.

used for stereo data analysis, depending on the date in question. Mirror 18 was never deployed and its assigned location in the sky map is adjacent counterclockwise to mirror 17. From the period of 1 December, 1999 (start of stereo operations) to 25 September, 2001, mirror 17 was in place and took data. On 25 September, 2001, the HiRes detector was taken offline due to a heightened security posture at Dugway. Mirror 17 was removed from HiRes1 during this period. When data collection resumed on 2 May, 2002, only 20 mirrors were present from that time to the end of data collecting operations. In late 2005, two additional mirrors, numbered 24 and 25, were placed at HiRes1 pointed higher in the sky in a ring 2 configuration looking towards HiRes2. These mirrors were used to test a mobile deployment scheme for HiRes mirrors and electronics. These two mirrors are not used for stereo data analysis.

The genesis of the High Resolution Fly's Eye detector followed from the success of the University of Utah Fly's Eye detector that ran from 1981 to 1992 at a site about 3 km northwest of Little Granite Mountain. The HiRes design improved on the original Fly's Eye experiment by implementing a finer pixel size (i.e., phototubes with 1° cone field of view), larger fixed mirrors, and improved electronics. A prototype detector was constructed at the original Fly's Eye site using 14 mirrors in five rings that viewed from 3° to 60° in elevation. The operation of the prototype revealed that for the highest energy events, which develop deeper in the atmosphere, a preferred configuration to optimize the detection of these events would be one that can search in a larger azimuthal range. In 1997, the prototype mirrors were moved to Little Granite Mountain.

HiRes monocular data collection began in May, 1997 with 14 mirrors. These initial 14 mirrors utilized the so-called revision 3 (rev3) electronics. Additional mirrors were added until the final mirror was installed in March, 1998. These newer mirrors utilized improved electronics referred to as revision 4 (rev4). Further information about the electronics is provided in section 3.1.1.1.

The HiRes1 detector consists of 12 mirror buildings, a central facility, a steerable laser building, and a calibration YAG laser building. Each mirror building houses

one or two mirrors and associated electronics. To prevent damage to the mirrors from weather, dust, and direct sunlight, each building has a roll-up type garage door which is lowered whenever data collection is not taking place. Placed in front of each mirror is a curtain that is used to protect mirrors from direct sunlight in the event of door failure. An electromagnet holds the curtain in place. If there is a power failure at the site or if a light sensor detects a preset amount of light, the power to the electromagnet is cut off and the curtain drops in front of the mirror.

The central facility is where the operations of the detector are controlled. It houses the central timing rack, the data acquisition computer (DACQ), GPS receiver, and equipment for communication with the internet and local area network. Each mirror communicates with the central timing crate and the DACQ via 10BASE2 ethernet. The DACQ is a standard 386 type computer running Linux, which runs the user interface that controls operation of the detector.

Each detector unit is made up of a mirror, a photomultiplier tube cluster, and an electronics rack. The spherical mirror is a passive device that only collects light and focuses it onto the plane of the photomultiplier tube cluster. The cluster box has dimensions of 71.12 cm x 63.50 cm x 35.56 cm and houses 256 photomultiplier tubes packed in a tight hexagonal array of 16 rows and 16 columns. A narrow bandpass UV filter is placed in front of the tube cluster to protect the tubes from dust and reject light not in the UV range of the spectrum. The back of each photomultiplier tube has connections for low voltage power, high voltage, and an output signal. The typical operating high voltage is around 1000 V, but varies for each tube due to gain balancing.

The electronics rack houses a VME crate, a high voltage power supply, low voltage power supplies, a high voltage zener board and pegboard (Figure 3.5(a)), and fans to cool the electronics. The low voltage power supplies convert the 115 VAC single phase input power to +12, -12, and +5 VDC for the VME electronics and the preamplifiers in the photomultiplier tubes. The high voltage supply provides voltage of about 1000 VDC distributed through a zener board which acts as a voltage divider providing the HV in 20 VDC steps to a backplane. The pegboard

is used to select the HV to individual tubes by selecting which stepped down HV line to use. The pegboard is used to control the amount of high voltage on a tube-by-tube basis. This is an important consideration in gain balancing of a cluster. The high voltage supply is only turned on during dark conditions when data is to be collected. Control of the high voltage is protected through several sets of interlocks to prevent damage to the tubes by exposure to excessive light. Often when referring to a "mirror," this includes the collective unit of mirror, electronics rack, and cluster.

3.1.1.1 HiRes1 Electronics

The brain of each mirror is contained in the VME crate, each of which contains a CPU (Figure 3.5(b)), 16 ommatidial boards (OMB) (Figure 3.5(c)), a garbage board (Figure 3.5(d)), a programmable pulse generator (PPG) board (Figure 3.5(e)), and a trigger board (Figure 3.5(f)).

The CPU board houses a Motorola 68030 processor and controls the operation and communications of all electronics with the DACQ and central timing. The garbage board controls remote operation of the building door, monitors temperatures, and performs other diagnostic routines. The PPG board generates signals sent to the PMT preamps to test the low voltage response of all PMTs. This is done as a diagnostic test each night before data collection to determine if any tubes are malfunctioning.

The ommatidial boards perform secondary amplification of PMT output signals, signal integration, and analog-to-digital conversion. Each ommatidial board controls a 4×4 subcluster of tubes. During normal operation, a tube generates a signal from some combination of sky noise, ambient electronic noise, or light from a UV source. This signal is amplified by the preamps contained in the PMT electronics and sent to its host ommatidial board. The signal is sent through a low-pass filter and discriminator to determine if a tube trigger has occurred. If the signal level is above the threshold value, a tube trigger is initiated and the signal is processed further. The ommatidial board performs signal shaping and integration via filters and amplifiers along one or two possible signal channels (channel A or

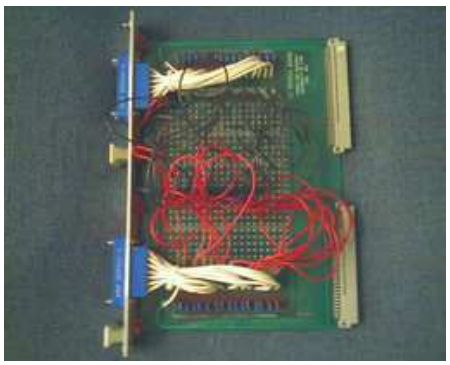

(a) HiRes1 peg board

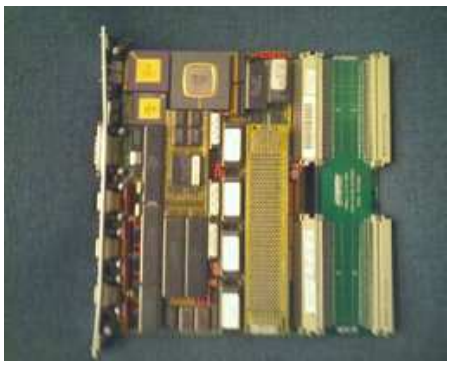

(b) HiRes1 VME CPU board

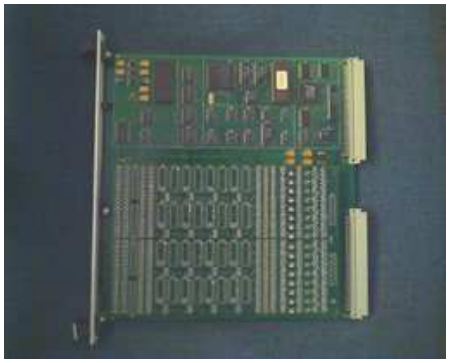

(c) HiRes1 rev4 ommatidial board

(d) HiRes1 garbage board

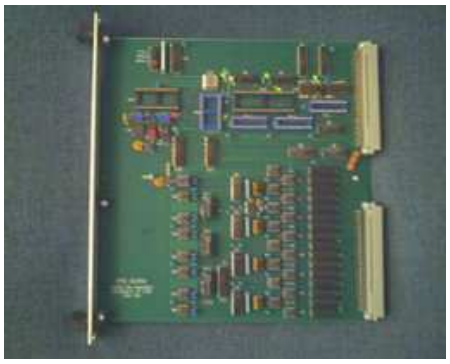

(e) HiRes1 PPG board

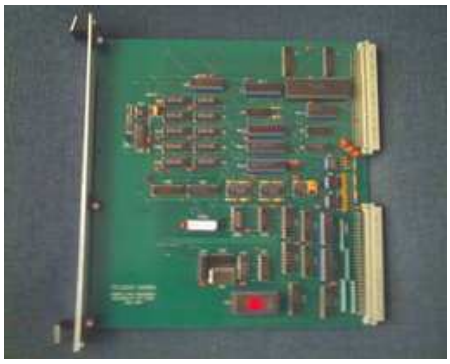

(f) HiRes1 trigger board

Figure 3.5. Circuit board modules used in HiRes1 electronics.

B). A signal delay is used to ensure the entire pulse is collected before further processing. A 5.6 μsec integration gate is used to collect the tube signal before digitization, followed by a 25 μsec holdoff time, during which further triggers are inhibited for the tube. The signal is digitized via the ADC, and a check is performed to see if a subcluster trigger has occurred. A subcluster trigger occurs if three of the 16 tubes in the subcluster trigger and there is at least one adjacent pair of triggered tubes. If a subcluster has triggered, the mirror trigger board checks for a mirror level trigger condition. A mirror trigger occurs when three of the 16 subclusters trigger and at least one pair is adjacent.

When a mirror level trigger is initiated, an additional 25 μsec holdoff time is imposed to allow for any other tubes that follow behind in time from early triggering tubes. This is done to prevent tracks from being cutoff early in the subcluster. The CPU sends a packet to the central timing computer requesting a GPS timestamp. The GPS time is sent back to the CPU and the mirror is prohibited from further triggering for 8 msec. During this 8 msec window, also called dead time, the CPU reads out the QDC, TDC, and thresholds of the triggered tubes and sends the data back to the DACQ in the form of an EVENT packet over the ethernet link. This type of electronics is also called "sample and hold," since when an event occurs, only a single measure of the charge on each tube is taken.

The difference between rev3 and rev4 electronics is contained in the ommatidial boards. When a tube signal is received, rev4 boards utilize two processing channels: A and B. Channel A uses a 100 nsec low-pass filter, a 600 nsec delay line, and an integrator with 1.2 μsec integration window. Channel B uses a 375 nsec low-pass filter, a 1600 nsec delay line, and a 5.6 μsec integrator. Either channel may satisfy the condition for a tube trigger, but in data processing, only the channel B information is utilized for analysis. Also, thresholds of the different channels are independently set. Rev3 boards use only one processing channel identical to the rev4 channel B. Finally, rev3 boards use a 12-bit ADC and rev4 boards use a 16 bit ADC, giving them a larger dynamic range. Figures 3.6 and 3.7 show block diagrams of the HiRes1 electronics.

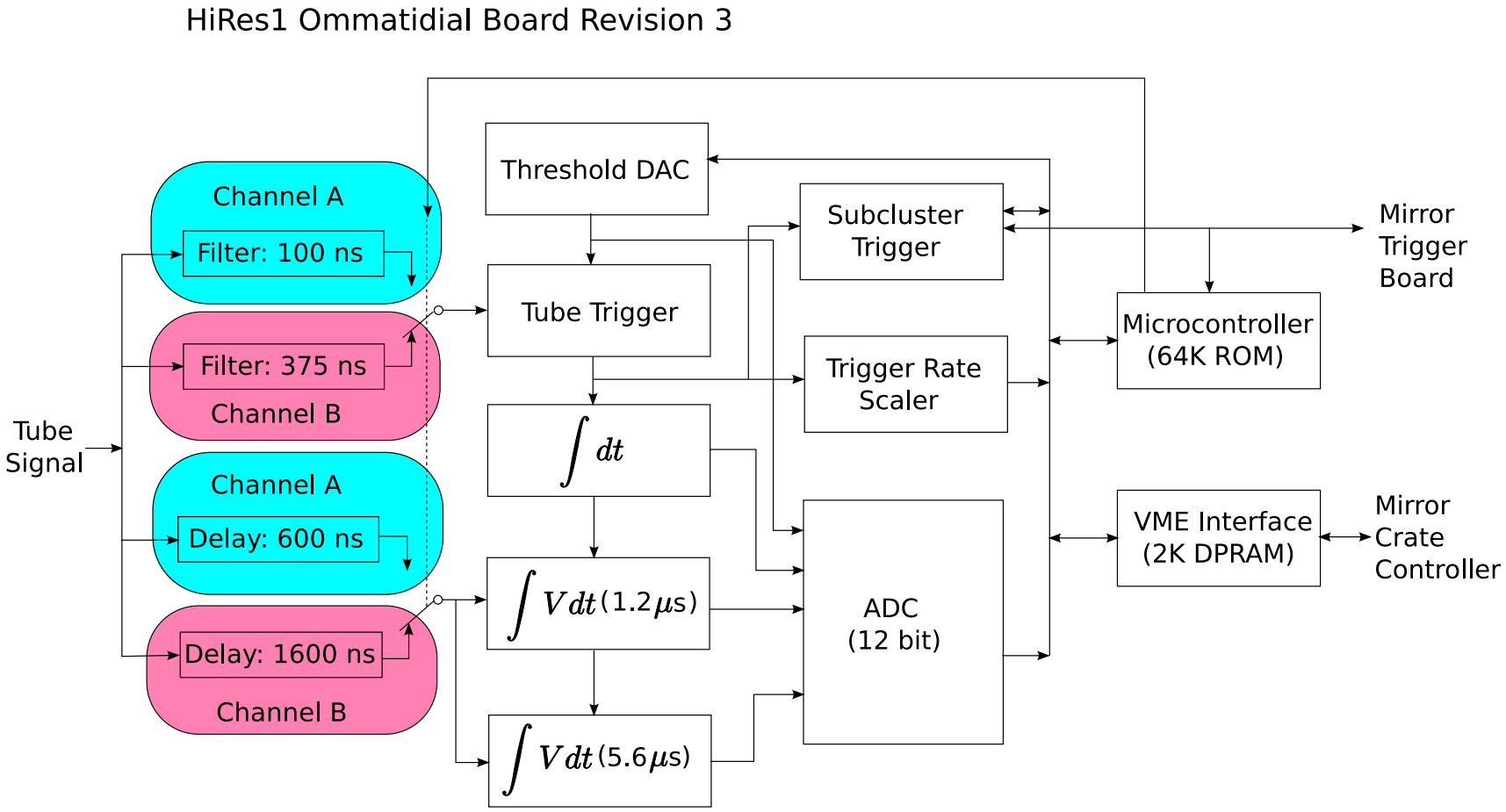

Figure 3.6. Block diagram of the rev3 electronics used in HiRes1 ommatidial boards. This type of electronics is used in mirrors 1 - 14. Rev3 electronics have a software selectable processing channel A, but only channel B is used.

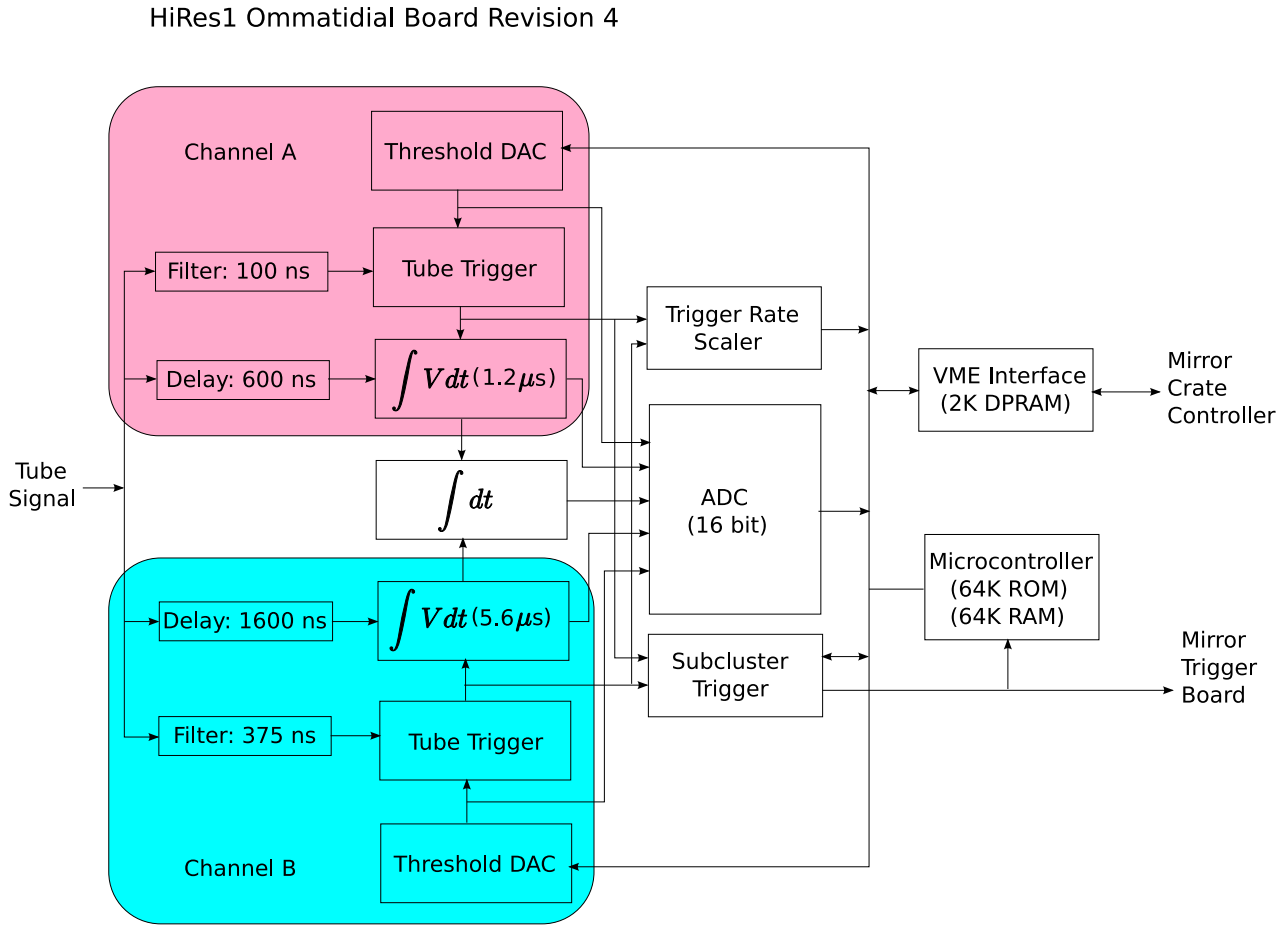

Figure 3.7. Block diagram of the rev4 electronics used in HiRes1 ommatidial boards. This type of electronics is used in mirrors 15 - 22. Rev4 mirrors may trigger on channel A or B, but only signal processed by channel B are used in data analysis.

Mirrors trigger at a constant rate while viewing the sky even under quiescent conditions due to sky noise and electronic noise. Each mirror triggers at about 0.5 - 2 Hz. The trigger rate of each tube is continuously adjusted via a threshold DAC. This trigger rate is selected to optimize the sensitivity of each mirror to true cosmic ray events and reduce the amount of mirror dead time. Tube thresholds are varied to maintain a mirror countrate of 200 Hz, where the countrate counts the number of individual tube triggers.

3.1.2 HiRes2

The HiRes2 detector is located on Camel's Bank Ridge, 12.6 km southwest of the HiRes1 detector. Forty-two mirrors are housed in 21 buildings covering nearly the full azimuthal range. HiRes2 employs two rings of mirrors. Ring 1 has 21 mirrors that view along the same elevation angles as HiRes1: 3° to 17°. Ring 2 has 21 mirrors that view from 17° to 31° in elevation. The mirror and cluster design is identical to HiRes1: 5.08 m^2 spherical mirrors in a four leaf clover segment construction focusing onto a cluster box of 256 photomultiplier tubes arranged in 16 rows and 16 columns. The electronics design varies significantly from HiRes1, though, by utilizing flash analog to digital conversion (FADC) electronics to continuously sample the signal in a tube even during an event trigger. Unlike the sample and hold electronics at HiRes1, this allows the development in time of cosmic ray air showers to be viewed as the light spot from the shower sweeps across the face of the cluster. This method also provides for a better way of binning the shower data, called time binning.

HiRes2 also employs a YAG calibration laser used for nightly calibration. A steerable laser (HR2SLS) similar to the one at HiRes1 is also located at this site. Figure 3.8 shows the physical placement and pointing directions of the mirrors and Figure 3.9 shows the elevation angles viewed by each of the mirrors.

Figure 3.10 shows the HiRes2 communications path. The central facility of HiRes2 houses the central host computer which controls the operations of the detector. The central host computer is made up of a VME CPU, a GPS receiver, a VLink module, and two clock modules. The VME CPU is the brain of the detector

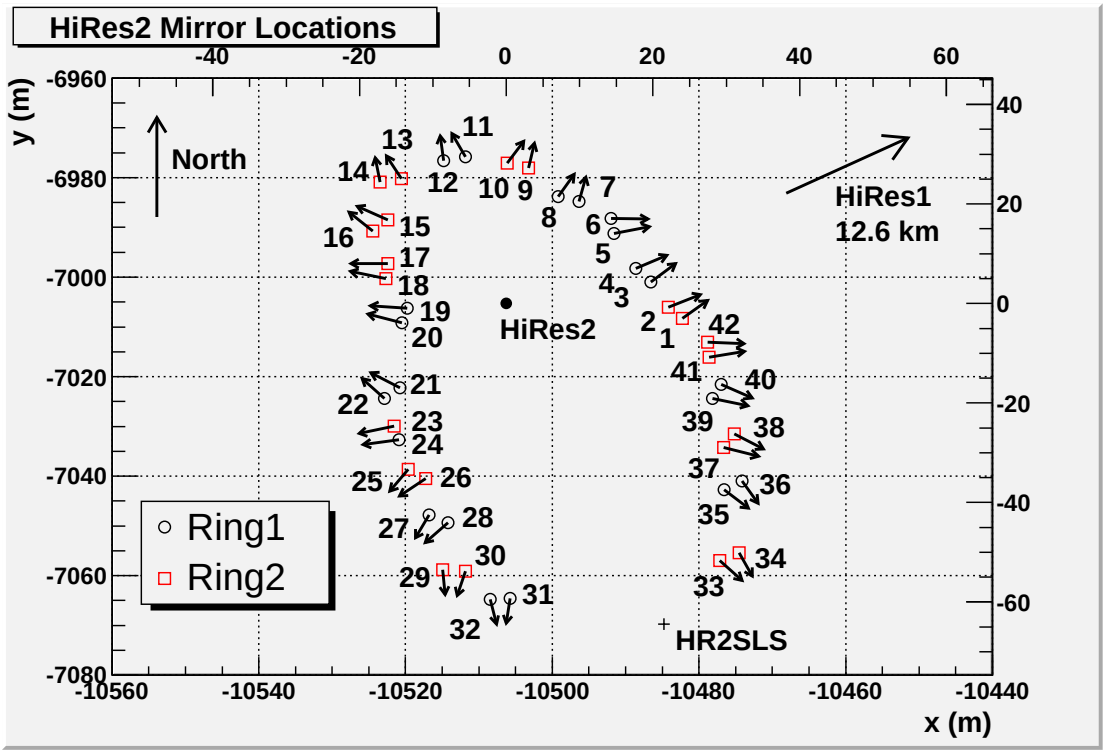

Figure 3.8. The location and pointing directions of the mirrors at HiRes2. All distances are measured in meters. The bottom and left axes label positions in HiRes1 global coordinate system and the top and right axes label positions in HiRes2 local coordinates. HiRes1 is located 12.6 km to the northeast. Ring 1 mirrors have an elevation angle of about 10° and ring 2 mirrors have an elevation angle of about 24°.

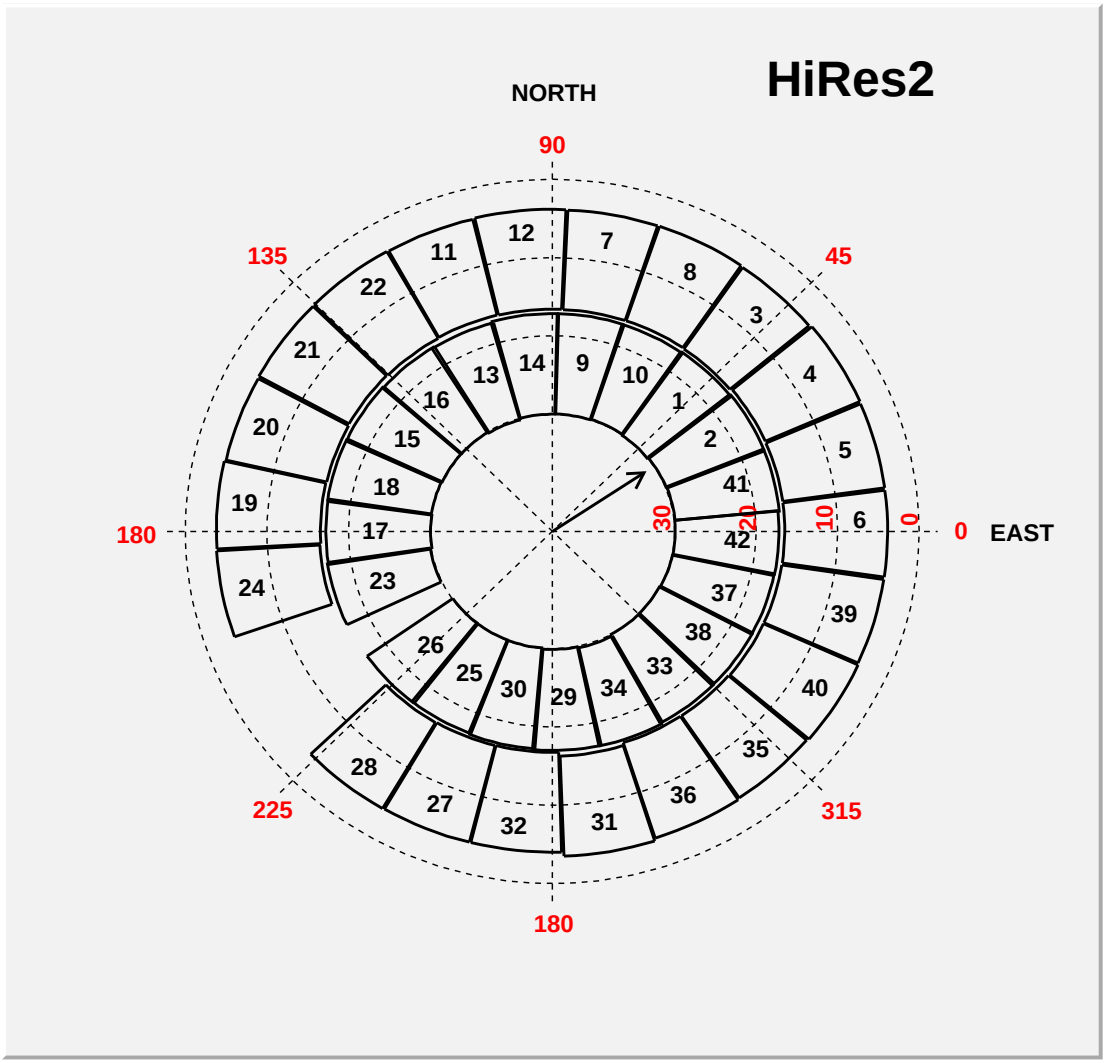

Figure 3.9. Sky map showing the angular coverage of mirrors at HiRes2. The theta angle measures elevation from the ground. The outer band of mirrors constitute ring 1 and the inner band are ring 2. The gaps on the southwest side are parts of the sky not viewed by the detector. The arrow in the center points in the direction of HiRes1.

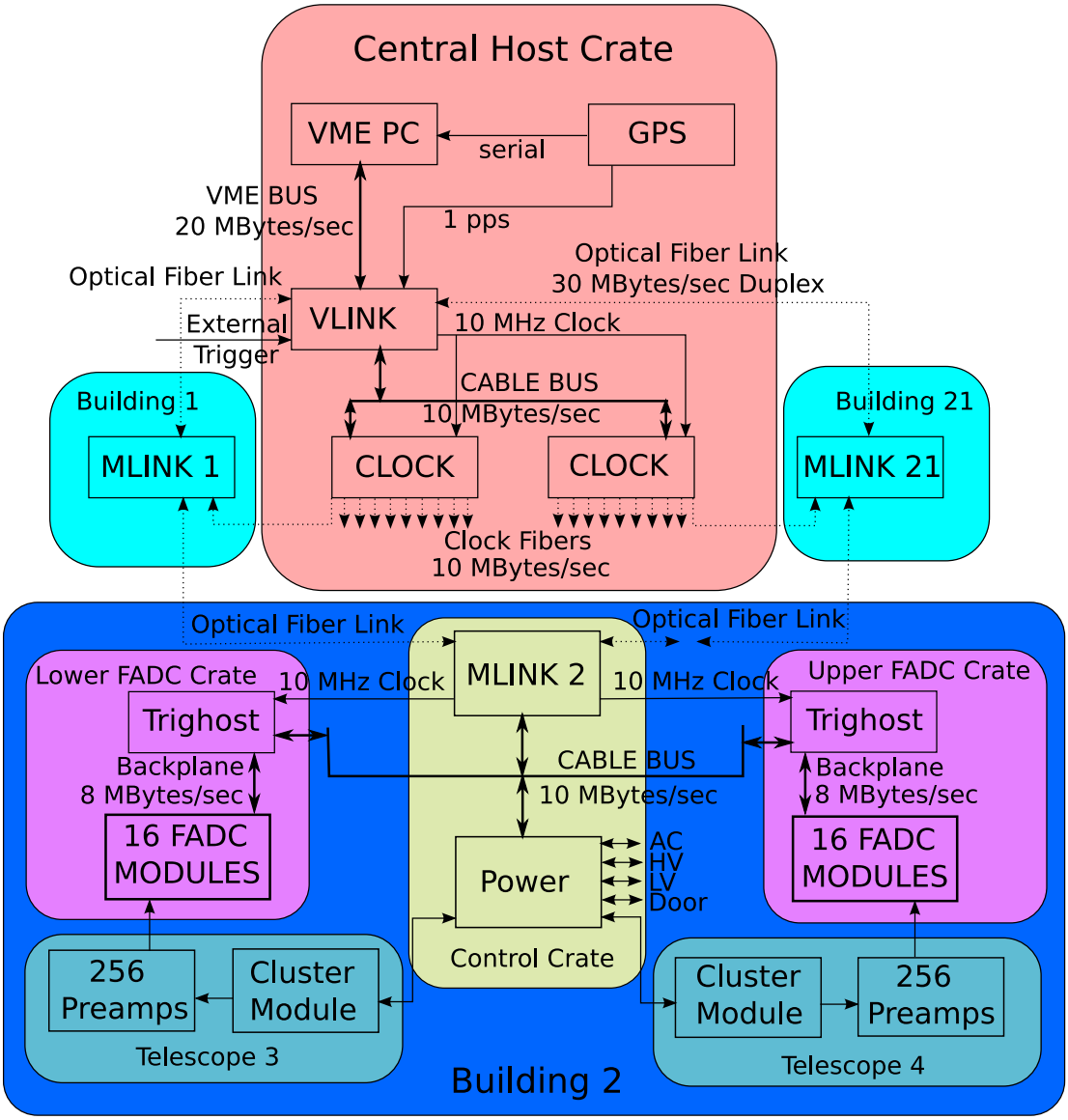

Figure 3.10. Block diagram of the communications at HiRes2. The central host crate is located in the central facility where operators control operation of the detector. Two fiber optic rings provide communications with the mirror buildings. A telescope is a mirror and phototube cluster that scans the sky for cosmic ray tracks, where the FADC modules digitize and process the analog tube signals.

facilitating command and control communications between the rest of the site's hardware and the operators. It also acts as the DACQ, receiving data from mirrors and storing them to disk. The GPS receiver provides accurate time necessary for event reconstruction and particularly important for identifying stereo coincidence with HiRes1 events. The VLink module provides communications with the mirrors via two independent optical fiber rings. Each ring is connected in a serial fashion between mirrors. A break in the ring prevents further communications beyond that point, but the ring running in the opposite direction can still be used to communicate with all mirrors. The VLink also communicates and with two clock modules which deliver a 10 MHz clock signal to all buildings via independent equal length optical fibers.

3.1.2.1 HiRes2 Electronics

Each building houses two mirrors, two phototube clusters, and one electronics rack. The electronics rack contains the hardware to control both mirrors and communicate with the central host. Each rack contains two FADC crates, a power board, a mirror link (MLink) module, two low voltage power supplies, a high voltage power supply, and fans and heat exchangers for cooling of the rack. The MLink module (Figure 3.11(a)) controls communications via the optical fiber with the central VLink. The power board (Figure 3.11(b)) controls the application of low voltage AC and DC power, high voltage to the cluster, and controls remote operation of the doors. Each PMT cluster contains its own programmable pulse generator module to allow test pulses to test the preamps of each of the PMTs in the cluster.

Each FADC crate processes analog differential input signals from the phototube cluster by processing, digitizing, and analyzing them online for potential cosmic ray tracks. Each crate contains one Trighost module and sixteen FADC modules .

The Trighost (Figure 3.11(c)) is the host module for the mirror, and facilitates all backplane communications with the FADC modules, as well as being the trigger processor. A set of four programmable logic devices (PLDs) and a digital signal processor (DSP) scan vertical and horizontal sums of tube signals to determine the

trigger state of the mirror.

The MLink module carries out communications with neighboring mirror buildings to complete a bidirectional fiber optic link. Each one also communicates directly with two Trighost modules and a power module.

Each FADC module contains twenty analog processing subassemblies, a digital signal processor, and a programmable logic device. Figure 3.11(d) shows a single FADC module. One of the analog subassemblies has been removed and can be seen on the left of the board. Normally, a copper shield covers the subassemblies to protect them from electronic noise; it has been removed in the photo. On the far upper right corner the DSP and just below it, the PLD can be seen.

A FADC module processes a vertical column of 16 PMTs, as well as two analog sums: a vertical projection of the column it is responsible for and a horizontal projection made up of a single row of tubes formed by a cable bus which also connects all FADC modules. Each sum is digitized twice: once with lower gain to allow for greater dynamic range and recovery of signals which saturate the high gain channels, and once with a longer filter time to allow the generation of triggers by comparison with adjustable threshold levels. Each FADC module then processes 20 signal channels and a mirror is responsible for 320 processing channels. The differential analog output signals from the PMTs are fed to a FADC board by two 25-pin connectors at the top and bottom on the front of the module. Between these connectors runs a 50-pin flat cable bus for horizontal analog sums. Each analog channel is processed by a subassembly on the FADC module with variable gain and offset (pedestal) via dual 12 bit DACs. The digital section of the FADC module samples and digitizes the analog channels every 100 ns (10 MHz clock rate) via 8 bit ADCs, storing them in a ring buffer, called M1, and delayed by 820 μsec. The long buffer time allows time to form triggers based on data communicated from different mirrors as well as trigger logic onboard the local Trighost module. The deep buffering in combination with parallel processing by the onboard DSPs theoretically allow zero dead time mirror readout for triggered events.

Trigger channels are formed from the vertical and horizontal sums by using 6

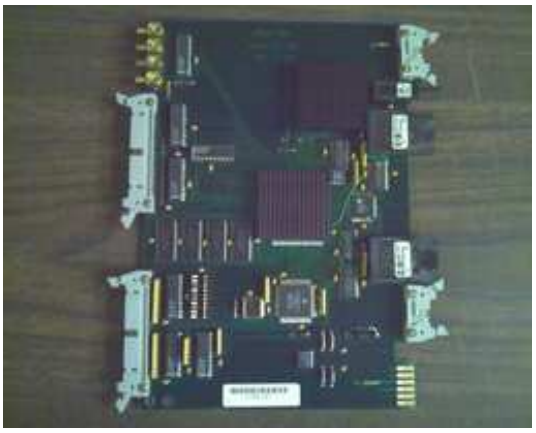

(a) HiRes2 MLink board

(b) HiRes2 power board

(c) HiRes2 Trighost board

(d) HiRes2 FADC board

Figure 3.11. Circuit board modules used in HiRes2 electronics.

bit counters to broaden the pulse widths. This is done by incrementing the counter if a signal is above a set threshold and decrementing it if the signal is below, always protecting against overflow and underflow. If a counter and either of its nearest neighbors is nonzero, this represents an overlap in the broadened pulse width. A coincidence in the broadened pulses and the OR of the undoubled pulses constitute a twofold coincidence. Repeating the process among neighboring channels constitutes a threefold coincidence in space and time. If two or more threefold coincidences are found, followed by 5 μsec without a coincidence or 102.4 μsec total trigger time, a primary trigger is formed. The trigger causes the Trighost DSP to read out the times of the first and last coincidence and the coincidence pattern, which is stored in a local trigger queue and also sent to neighboring mirrors, to alert them of a possible event trigger and subsequent readout of their M1 buffers.

A confirming scan follows in which 16 bit DSPs housed on the FADC modules scan the event buffer for high gain channels that are above predetermined thresholds. These channels are reported back to the Trighost module which performs a pattern recognition scan on those channels. The result of this pattern checking is to either initiate an event trigger or to reject it and to communicate the decision to the neighboring mirrors that were initially notified of a possible event. If an event trigger is confirmed, the mirror initiates a readout scan, reading out the times and channel information stored in the M1 ring buffer.

The details of the trigger logic changed several times over the course of running HiRes2, defining trigger epochs. There are seven trigger epochs and are shown in Table 3.2.

Gains and pedestals are controlled by 12 bit DACs. The pedestals are set by servoing the DACs until an optimum setting of 10 FADC counts is achieved. Throughout the night, snapshots, readouts of all signal channels without a trigger, of the night sky are taken. The setting of the pedestal DACs are then set so that the minimum signal in the presence of sky noise is 10 FADC counts. The setting of the pedestal DACs, therefore, are changing continuously throughout the night depending on what a tube is seeing. For instance, a bright star may come into

Table 3.2. The different trigger algorithms in use at HiRes2. Data provided by [35].

Epoch	Start Date	Stop Date	Version	Description
1	01 Dec 1999	04 Jan 2000	1	DSP confirming scan shows at least 6 hits above threshold.
2	05 Jan 2000	31 Aug 2000	2	New version of Trighost code. Looks for at least 4 hits in 6x6 subcluster.
3	01 Sep 2000	14 Mar 2001	3.1	Mirror trigger for one cluster with > 3 adjacent hits. If there are at least 3 three-fold coincidences in the primary trigger, mark adjacent triggers with the ID of the primary mirror.
4	15 Mar 2001	21 Sep 2001	3.2	Adjacent mirror trigger version. Activates trigger if there are 2 three-folds in either view with number of tubes > 10. Prescale changes from 64 to 128 and secondary trigger accepts every 64th and 128th event regardless.
5	09 May 2002	27 May 2003	4	Number of hits > 3 in a cluster. No same time clusters allowed of any size.
6	28 May 2003	31 Jan 2004	5	Confirming threshold lowered, but servoed according to average trigger DAC in the mirror.
7	01 Feb 2004	03 Apr 2006	6	Number of hits > 2 in a cluster confirming thresholds midway between versions 4 and 5. Servoed according to variances in each channel. Readout thresholds servoed as in version 5.

the field of view of a tube, requiring the DACs to compensate for the light source. Gain DACs are set by using the RXF calibration to set an optimum of 1 FADC count per $N_{\rm pe}$. This procedure is done by offline analysis after a RXF run. The gain settings of all tubes are determined and stored in a file, the contents of which are loaded into the central host and distributed to each mirror when starting the detector. Unlike HiRes1, gain balancing is done not by adjusting high voltages, but instead through the DACs. Further details about the electronics used at HiRes2 can be found in [20].

Figure 3.12 shows an example of a cosmic ray air shower observed by HiRes2. The digitization of the light converted to FADC counts for all tubes that viewed the shower is shown in Figures 3.12(a) and 3.12(b). The digitized waveforms clearly show a light source (the peaks in the distribution) that progress in time across the different tubes. To either side of the peak is the readout of the tube for about $\pm$60 ns before and after the shower moved across the tube. Figure 3.12(c) shows the mirrors that observed the shower and the circles represent tubes that triggered during the event. The relative size of each circle indicates the amount of light collected by the tube.

3.1.3 Detector Optics

As the name of the experiment implies, "seeing" light is important to our observation of cosmic ray air showers. Two passive and one active device constitute the "eyes" of the detector: the mirror, the UV filter, and the photomultiplier tube. As an EAS develops in the atmosphere, a small amount of UV light (about 4 photons per meter of track length) from de-excited N_2 molecules is transmitted isotropically. A large collecting surface is used to gather this light and reflect it through a UV filter onto a plane of PMTs.

The relative sizes, positions, and shapes of the detector optics is important to understanding how light sources are imaged and consequently measured. This is done by ray tracing in the simulation and reconstruction software. When EAS light is simulated by the Monte Carlo or the effective area of a bin is calculated, the position of the light source relative to the viewing mirror is used to determine what

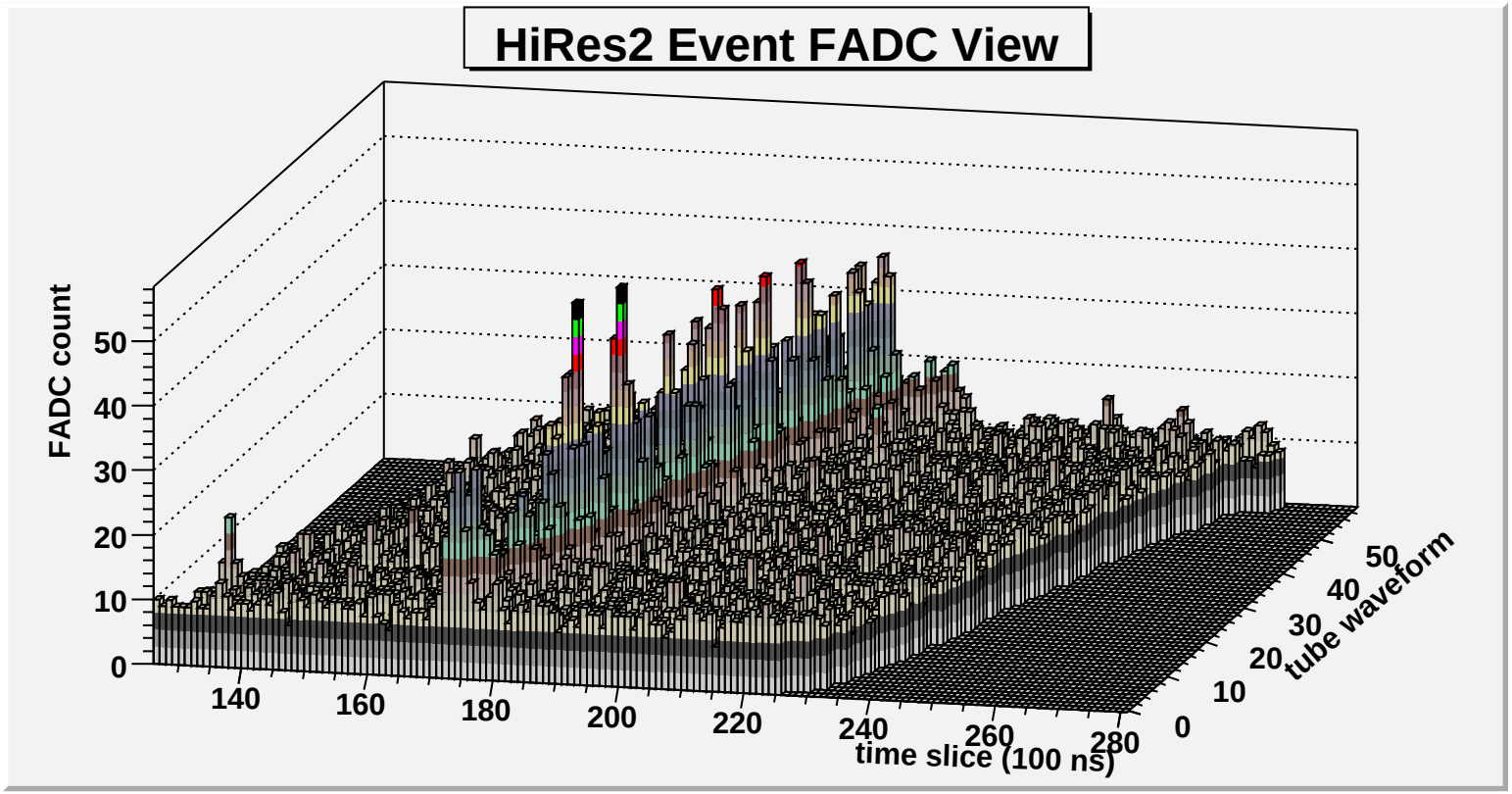

(a) FADC waveform lego plot.

Figure 3.12. The FADC waveforms of a cosmic ray air shower. In each bin is the number of 8 bit FADC counts for each 100 ns time slice for each tube that viewed the shower. Note that noise tubes are excluded from the FADC display. This is a three mirror event and all three mirrors are shown in the FADC view. The tubes waveforms are ordered in time and the pedestal level of about 10 FADC counts is clearly seen in the lego plot. The peak signal count is about 50 FADC counts which corresponds to 150 $N_{\rm pe}$ after gain conversion. By observing the centroid of the FADC distribution it can be seen that the shower took about 5000 ns to sweep across the cluster. This shower is about 1 EeV, with $R_{\rm p} = 7$ km.

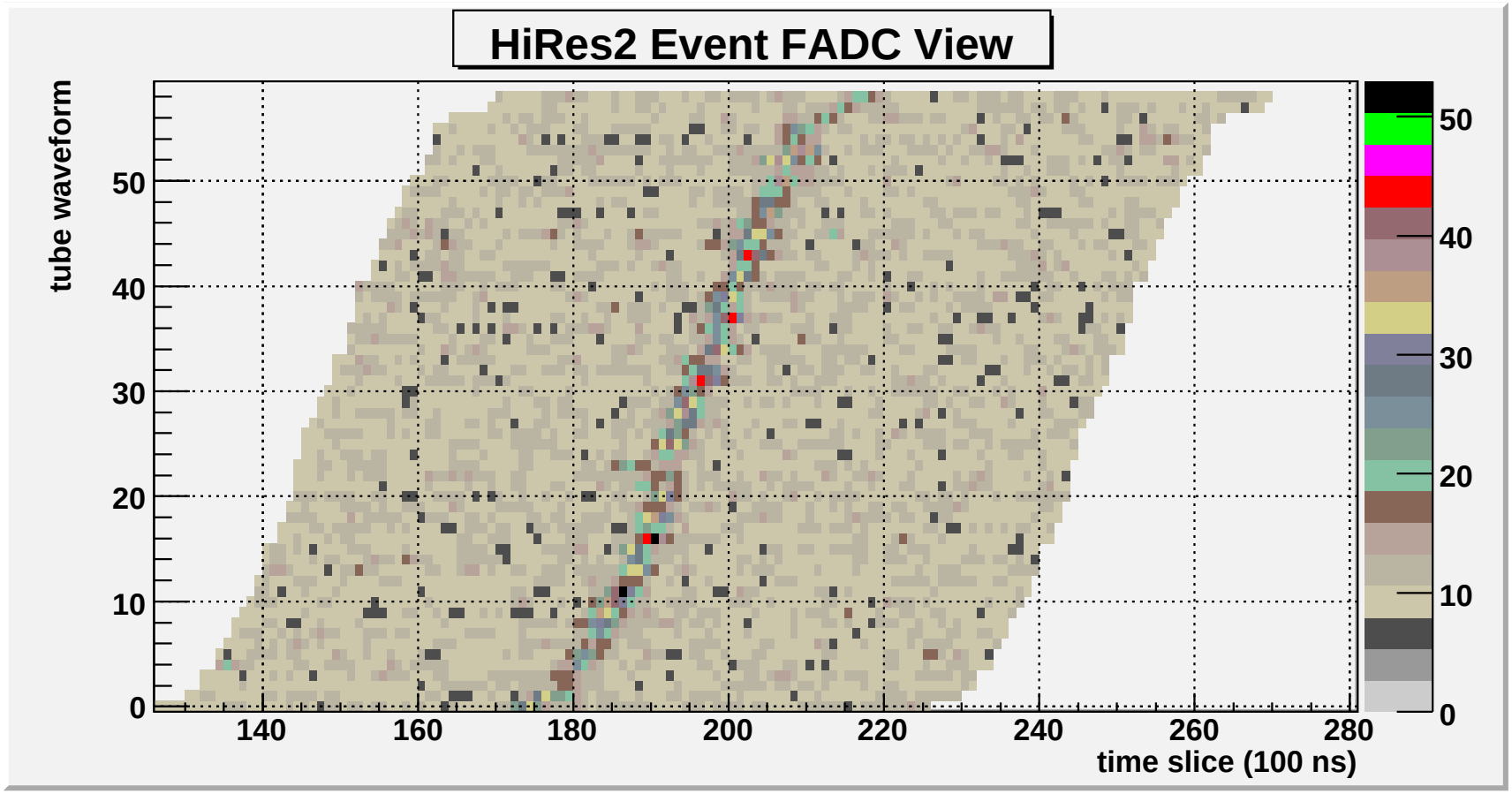

(b) FADC waveform projection.

Figure 3.12. continued.

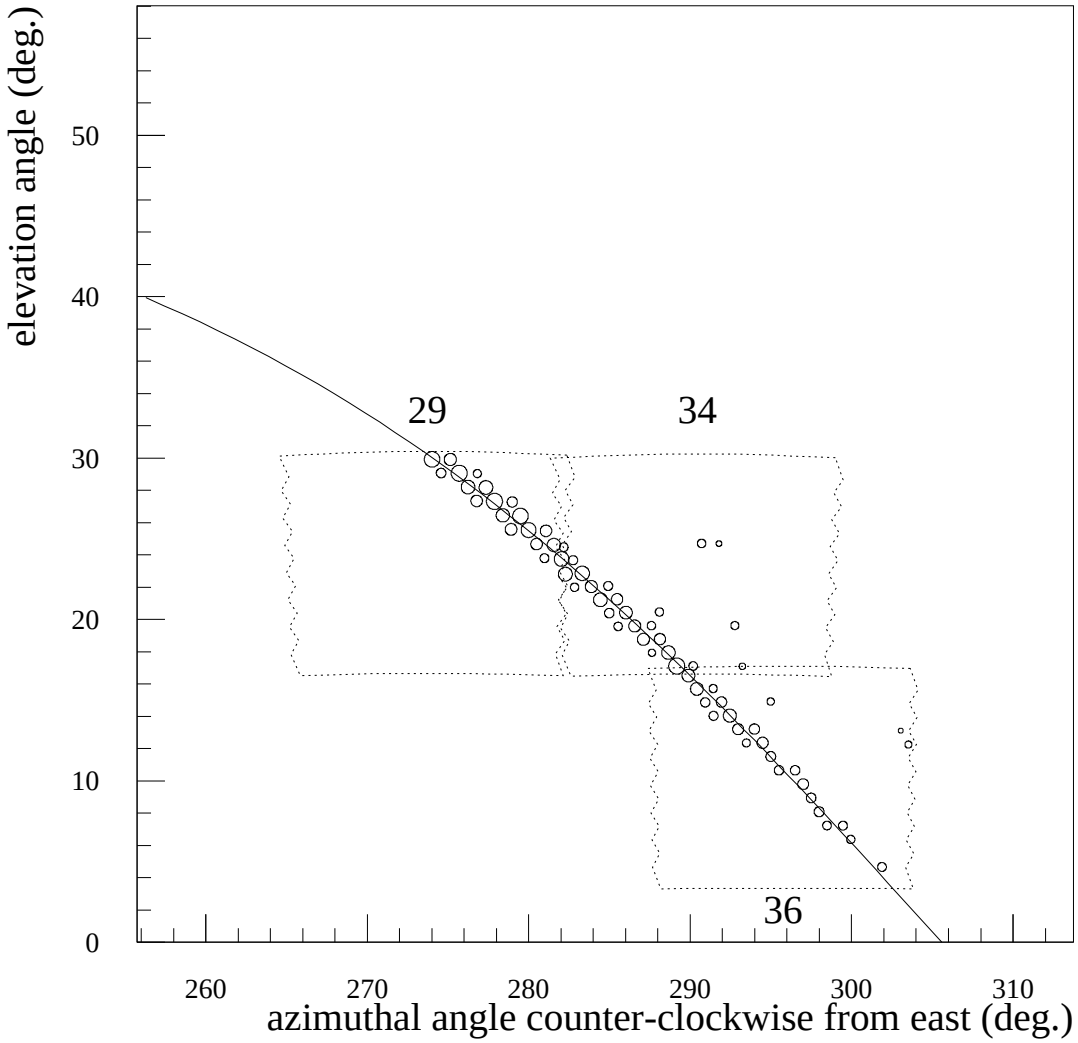

(c) Event display

Figure 3.12. continued.

part of the mirror and cluster see the source. The spot size, cracks between the mirror, and the sensitivity of the tubes are taken into consideration to determine the detector's response to the light. The constants used to describe the detector optics shown in Table 3.3.

The passage of light through the atmosphere, reflecting off the mirror, and passing through the UV filter all cause attenuation and must be understood well for proper calibration of the detector and absolute measurement of the energy of an EAS. Transmission effects due to the atmosphere are explained in section 2.3. Here the role of the detector as it pertains to transmission effects is examined.

3.1.3.1 Mirror

The HiRes mirrors are spherical mirrors with a 4.74 m radius of curvature and total surface area of 5.08 m^2 constructed from four cloverleaf segments (see Figure 3.1). Each mirror faces out towards the sky and reflects the collected light onto a cluster box of 256 photomultiplier tubes approximately 2.30 m away. Protecting the tubes is a narrow bandpass UV optical filter which allows the transmission of light between 300 and 400 nm. Due to obscuration of the cluster box and gaps between the tubes, the total *effective* area of the mirror is approximately 3.8 m^2. The effective area is an important consideration when calculating bin flux and is discussed further in section 4.8.8.1.

A single mirror and cluster observes approximately 16° in azimuth and 14° in zenith angle. At HiRes, the elevation angle determines which "ring" a mirror inhabits. Mirrors that view the sky with a central elevation angle of about 10° are ring 1 mirrors and those with a central elevation angle of about 24° are ring 2 mirrors.

Mirror reflectivity is wavelength dependent and varies from mirror to mirror. Over time dust settles on the mirrors and can cause further attenuation. The Monte Carlo and reconstruction code considers two epochs of mirror reflectivity: the period preceding 9 April 2004 and the period after. On 2 April 2004 a mirror washing was performed and the reflectivities of the mirrors were measured before and after the cleaning.

Table 3.3. Constants that describe HiRes mirror optics.

Radius of curvature	186.61 inches
Mirror - cluster distance	90.51 inches
Diameter of center button	2.00 inches
Pre-slumped diameter of mirror segment	50.00 inches
Width of PMT cluster	28.00 inches
Height of PMT cluster	25.00 inches
Thickness of PMT cluster	14.00 inches
Measured spot size at center of curvature	0.30 inches
Radius of the unmasked part of the mirror	100.00 inches
PMT flat-to-flat distance	1.645 inches

The reflectivity of mirror n can be expressed as

$$\begin{aligned} R_n(\lambda) &= \beta_n f(\lambda) \\ &= \beta_n(-326.1 + 2.631\lambda - 0.5816\lambda^2 + 0.4316\lambda^3) \end{aligned} \tag{3.1}$$

where β_n is a mirror dependent normalization and $f(\lambda)$ is the wavelength dependence. This equation is used for HiRes1 and HiRes2 mirrors for the pre and post-washing epochs. The normalization β_n measures the relative change in reflectivity between the washing periods.

Figure 3.13 shows the normalizations of all mirrors at both sites (β_n) and the total measured mirror reflectivities (R_n). Notice that the mirror reflectivities after the washing are higher than the prewashing period as expected.

Two methods of measuring the mirror reflectivity are utilized. One method to measure the reflectivities utilizes a reflectometer, which contains a UV light source and a spectrometer. The reflectometer is calibrated to a standard reference mirror then taken to each mirror where it is placed on the mirror at multiple points on each mirror segment. Utilizing this method, the reflectometer measures the mirror's response to the light source and is compared to the reference mirror the determine the absolute reflectivity.

A simple way of performing the reflectivity measurement is to use the RXF mounted on a stand placed at about the same distance as the cluster and illuminating the entire mirror. The phototube cluster of each mirror then acts as the light measuring device. The RXF is placed at several different locations relative to the cluster (above, below, left, and right) to uniformly illuminate the cluster. The mirror reflectivities shown in Figure 3.13 are a result of this measurement and are used in this analysis.

3.1.3.2 Ultraviolet Filter

The UV filter is a narrow band pass filter made of glass and used to restrict the light reflected from the mirror and impinging on the cluster face to between 300 and 400 nm. This is done to improve the signal to noise ratio of an already small signal. In Figure 3.2 the lowered UV filter can be seen at the bottom. Figure 3.14

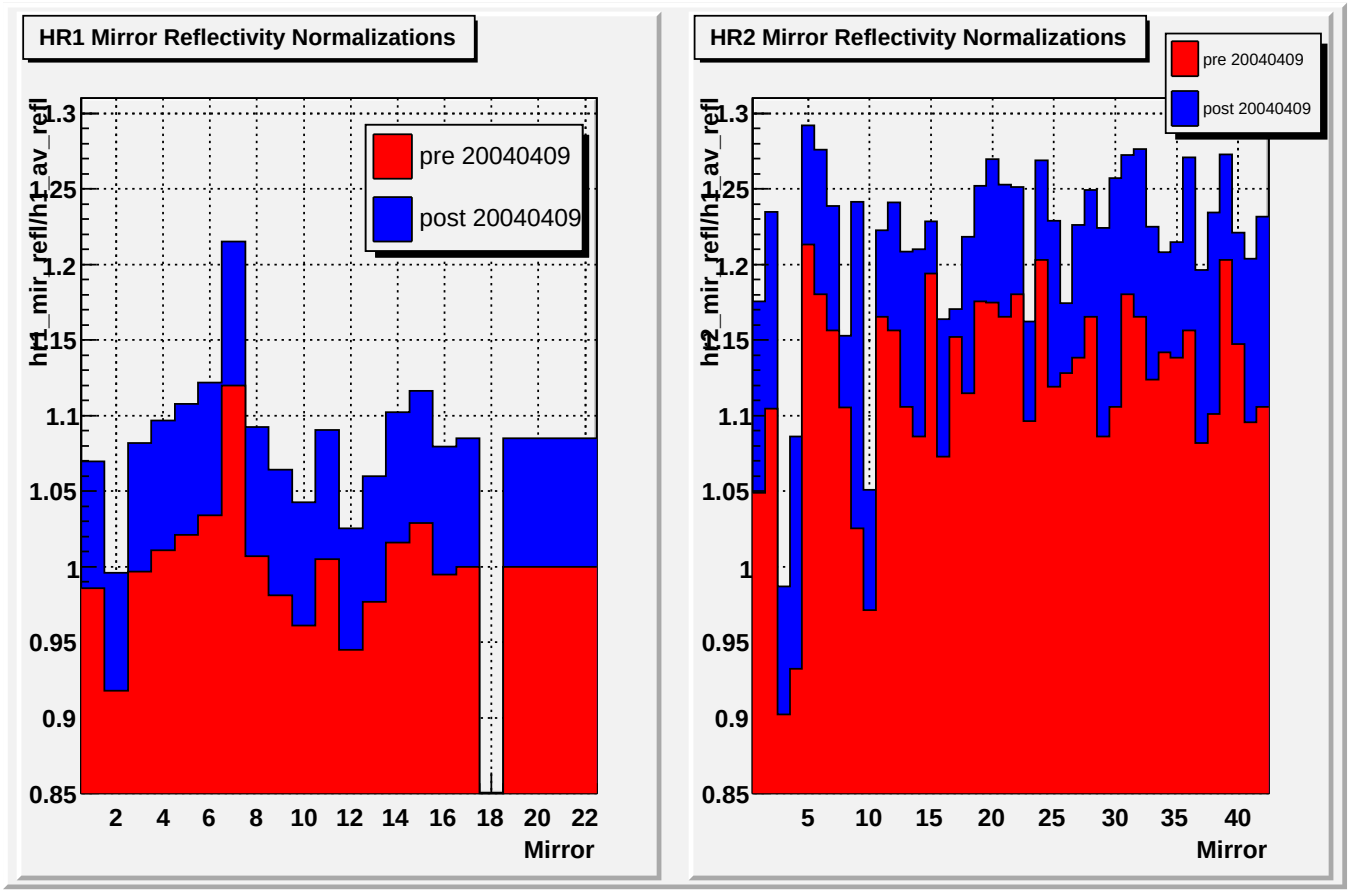

(a) Mirror reflectivity normalizations.

Figure 3.13. The normalizations, β_n, and the wavelength dependent mirror reflectivities, R_n, of all mirrors at HiRes1 and HiRes2. The two epochs used by the Monte Carlo and in reconstruction are shown: the period before a washing of the mirrors on 4 September 2004 and the period after.

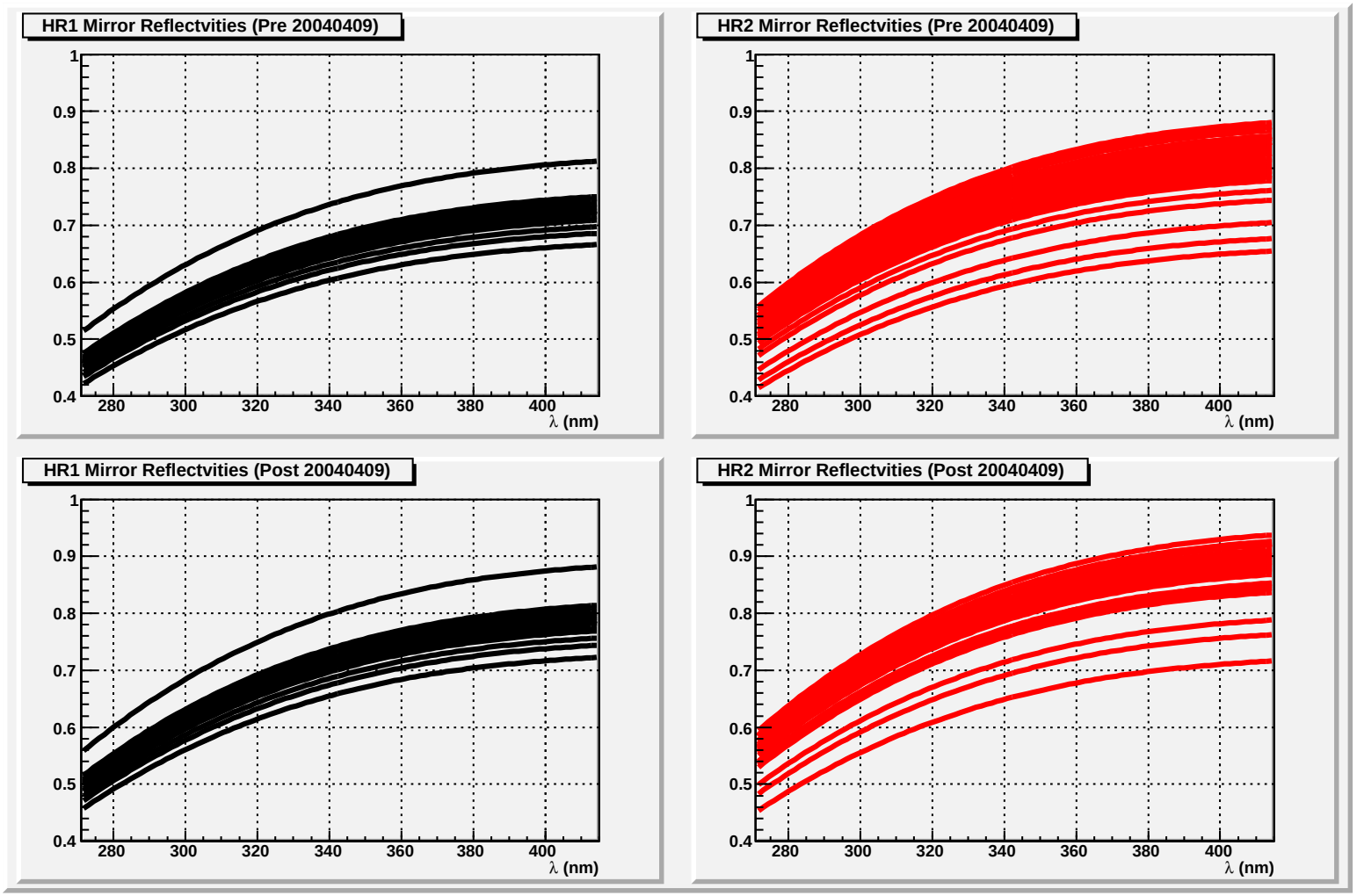

(b) Mirror reflectivities

Figure 3.13. continued.

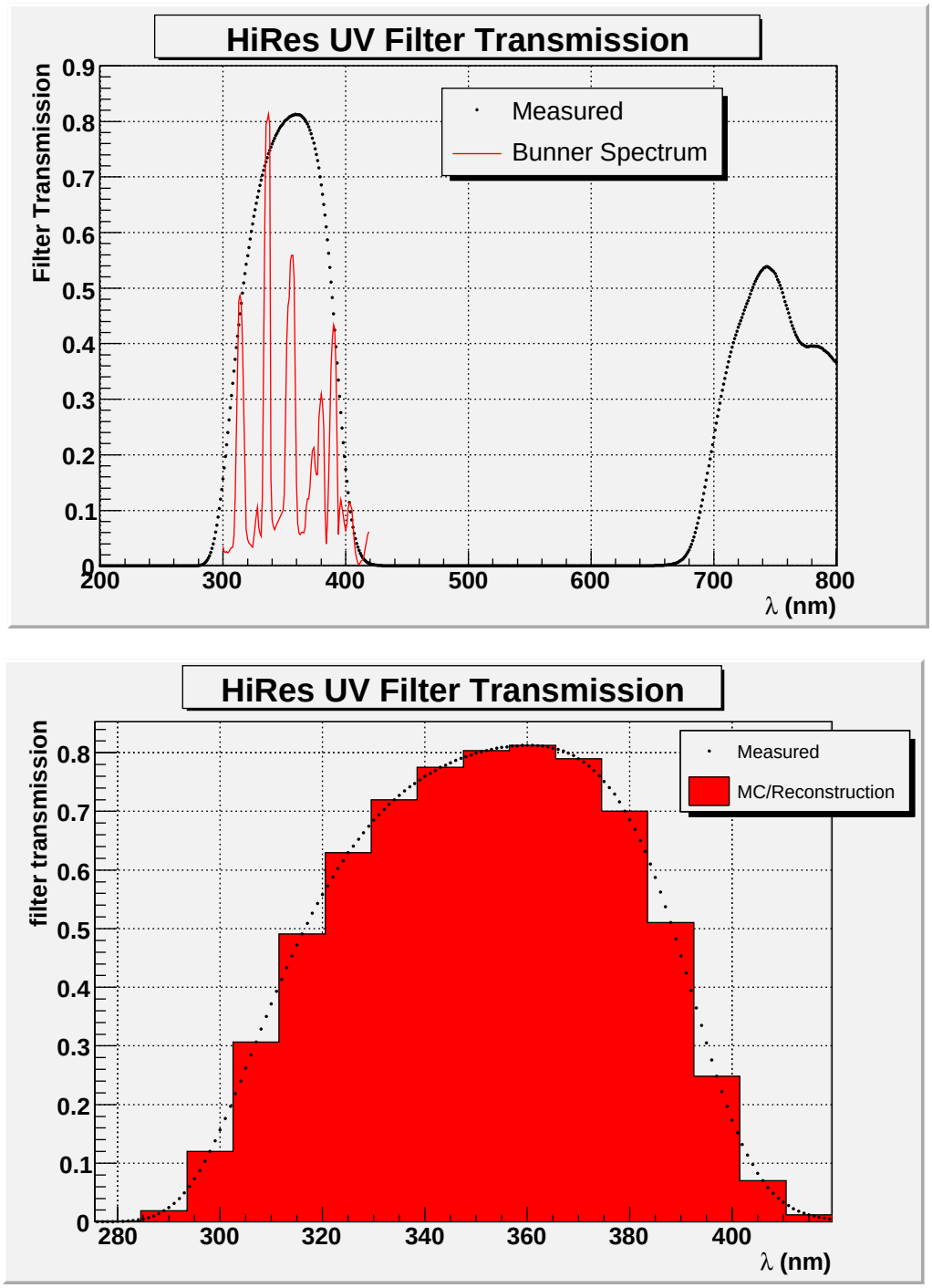

Figure 3.14. UV filter transmission as measured for different wavelengths. The top figure shows the measured transmission over all wavelengths tested. The Bunner fluorescence spectrum is drawn as well to see where the peaks in the N_2 excitation spectrum lie. The bottom plot shows the measured transmission as well as the binned transmission used by the Monte Carlo and reconstruction code.

shows the measured filter transmission as well as the binned transmission that is used in the Monte Carlo and reconstruction code.

Each filter has dimensions 71.88 cm x 62.23 cm and completely covers the face of the cluster box and all PMTs. The thickness of each piece of filter glass varies according to the specific chemical composition and manufacturing process used from about 2.5 mm to 5 mm. The requirement placed upon the manufacturer and polisher is that the transmission coefficient be uniform over the entire surface of the glass. The filter is held in place by a door that can swing down to allow access to the front of the PMT cluster. The chemical composition of the filters is proprietary and the manufacturing formula is held by Kopp Glass, Inc. in Pittsburgh, PA.

3.1.3.3 Photomultiplier Tube

Each photomultiplier tube has a pixel size of about a 1° cone. Connections for low voltage power, high voltage, and signal lines are made through the back and the light sensitive photocathode is at the front facing towards the UV filter and mirror. Two types of tubes are in use: Phillips XP3062/FL and EMI 9974KAFL. The flat-to-flat distance (2 × the inradius) of all tubes is 4.2 cm and all have similar quantum efficiencies. Figure 3.15 shows a picture of a PMT alongside one that has the preamplifier and electrical connector at the back exposed.

Figures 3.16 and 3.17 show the circuit diagrams of the PMT preamplifiers that deliver the PMT signal to the ommatidial boards. Two different input lines allow for signals from the PMT or a PPG test signal. The transimpedance amplifier acts as a current-to-voltage converter which feeds the differential driver. The output is a differential signal which is then delivered to the ommatidial boards via twisted pair cables.

The expected number of photoelectrons ejected from the photocathode for each photon to hit it is called the quantum efficiency. It is wavelength dependent and the quantum efficiency of the tubes is shown in Figure 3.18. The figure shows the QE over a much wider band of the EM spectrum than is needed by HiRes. The Bunner nitrogen UV fluorescence spectrum scaled in arbitrary units is also plotted to show the part of the QE curve we are most interested in. The simulation and

Figure 3.15. A HiRes photomultiplier tube. Each tube views about 1° cone of the sky. The disassembled tube on the left shows the small circuit board that contains the preamplifiers. The hexagonal shape of the tube face can be clearly seen here.

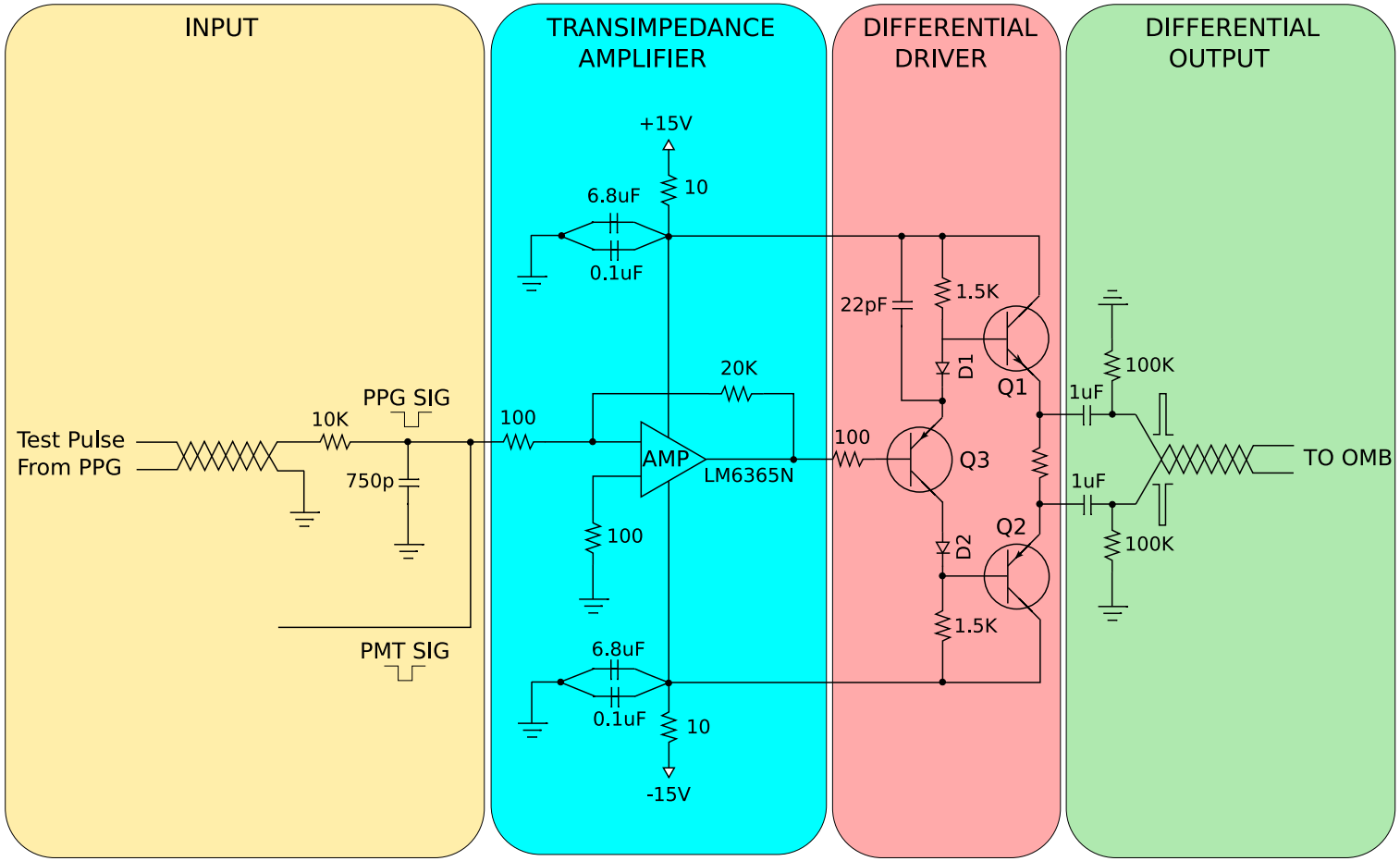

Figure 3.16. The Rev3 preamplifier circuit diagram. Four stages convert the input signal to a differential output signal to be fed to the ommatidial boards.

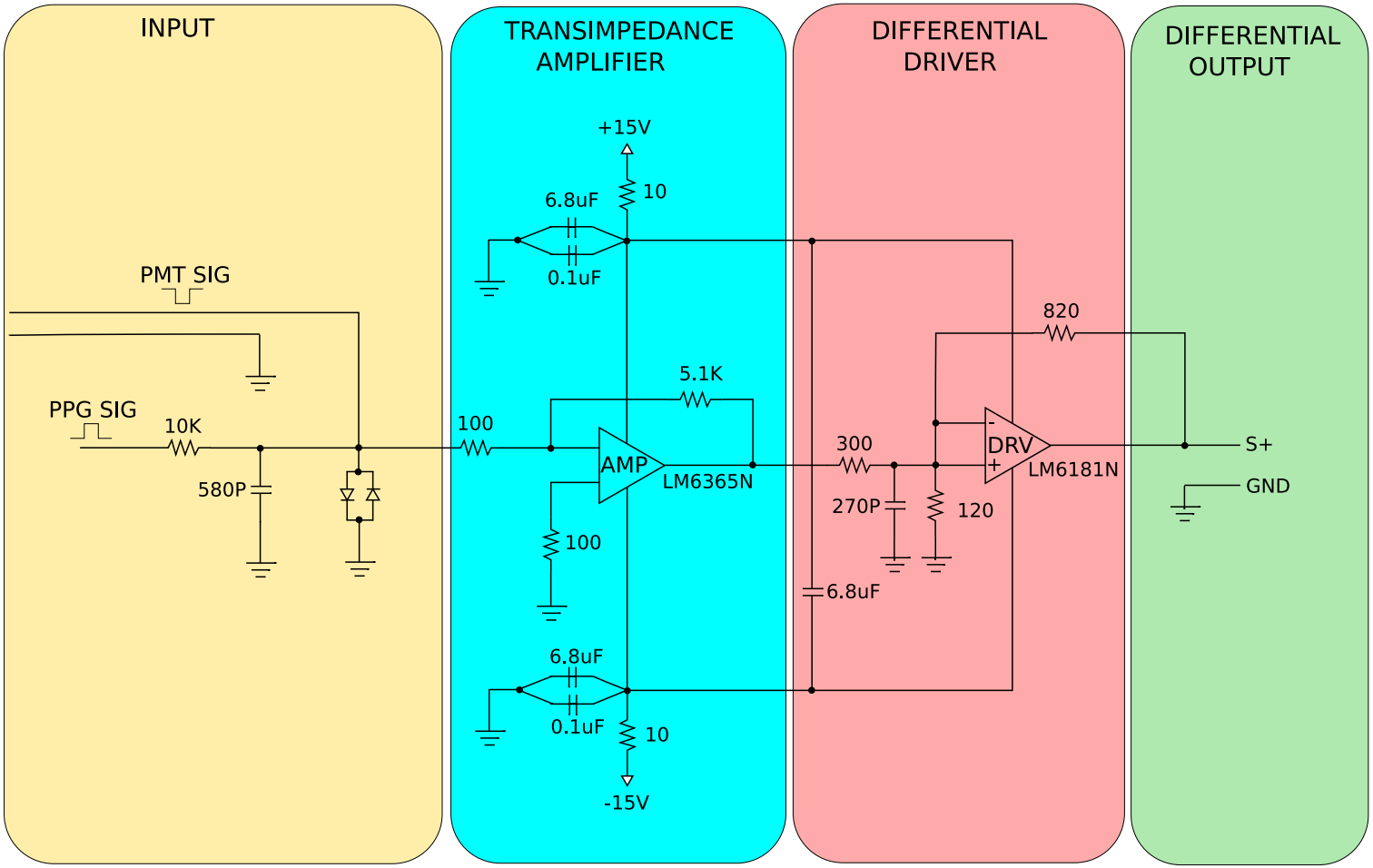

Figure 3.17. The Rev4 preamplifier circuit diagram. It is similar to the rev3 preamp except that the driver stage has been replaced with an op-amp.

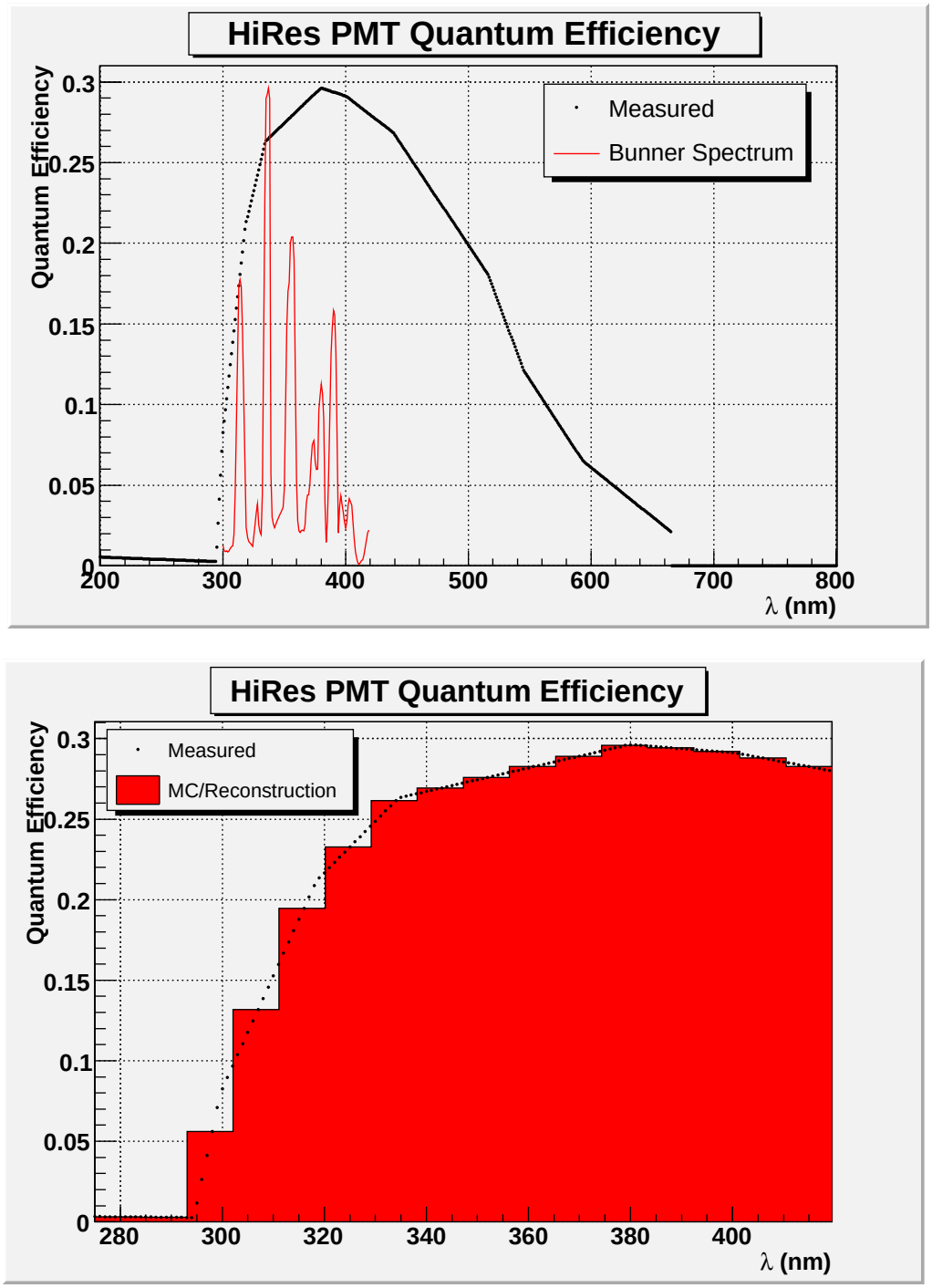

Figure 3.18. The quantum efficiency of HiRes PMTs as measured for different wavelengths. The top figure shows the measured QE over all wavelengths tested. The Bunner fluorescence spectrum is drawn as well to see where the peaks in the N_2 excitation spectrum lie. The bottom plot shows the measured QE as well as the binned QE used by the Monte Carlo and reconstruction code.

reconstruction software use only the part of the spectrum between 271 nm and 415 nm and the QE in this range is shown as well.

The sensitivity of the PMTs is also measured and shown in Figure 3.19. The figure labels the tubes as "HiRes1" and "HiRes2", since HiRes2 only uses Phillips PMTs, the "HiRes2" response is same as for a Phillips tube. Rev3 mirrors use the EMI tubes and rev4 use Phillips as well. The tube response accounts for the size of the active area of the photocathode as well as the collection efficiency of the dynode chain. The tube profiles shown in the figure are used by the ray tracing routines in the reconstruction code.

3.1.4 YAG laser

Each detector has its own frequency-tripled Nd:YAG (neodymium-doped yttrium aluminum garnet) calibration laser, which illuminates all tubes at 355 nm. It fires 8 mJ pulses 6 nsec in duration down optical fibers to each mirror. The energy of each shot is monitored by placing a beam splitter before the fiber bundles, where 1 % of the energy is directed to a radiometer. A set of filter wheels is used to attenuate the light to different levels to measure the response to varying energy levels [31].

Each mirror and cluster unit has three optical fibers, two on either side of the cluster box, and one positioned at the center of the mirror. Two types of shots are performed during firing, one fires the laser through the fiber at the mirror center and directly illuminates the cluster, another fires the laser through the pair on the cluster box, which reflects off the mirror before illuminating the cluster. This allows tracking of mirror reflectivity by doing a differential analysis of the two types of shots.

The operation of the YAG lasers is different between the two detectors. At HiRes1 two YAG runs are done before data collection starts. The first run is done with the doors closed and is called a *yag* part. The second run is done with the doors open and is called a *yag-open* part. Sky noise levels can also be estimated by examining the difference between the closed and open door shots. Then during data collection the YAG laser is not fired again. Once data collection ceases the

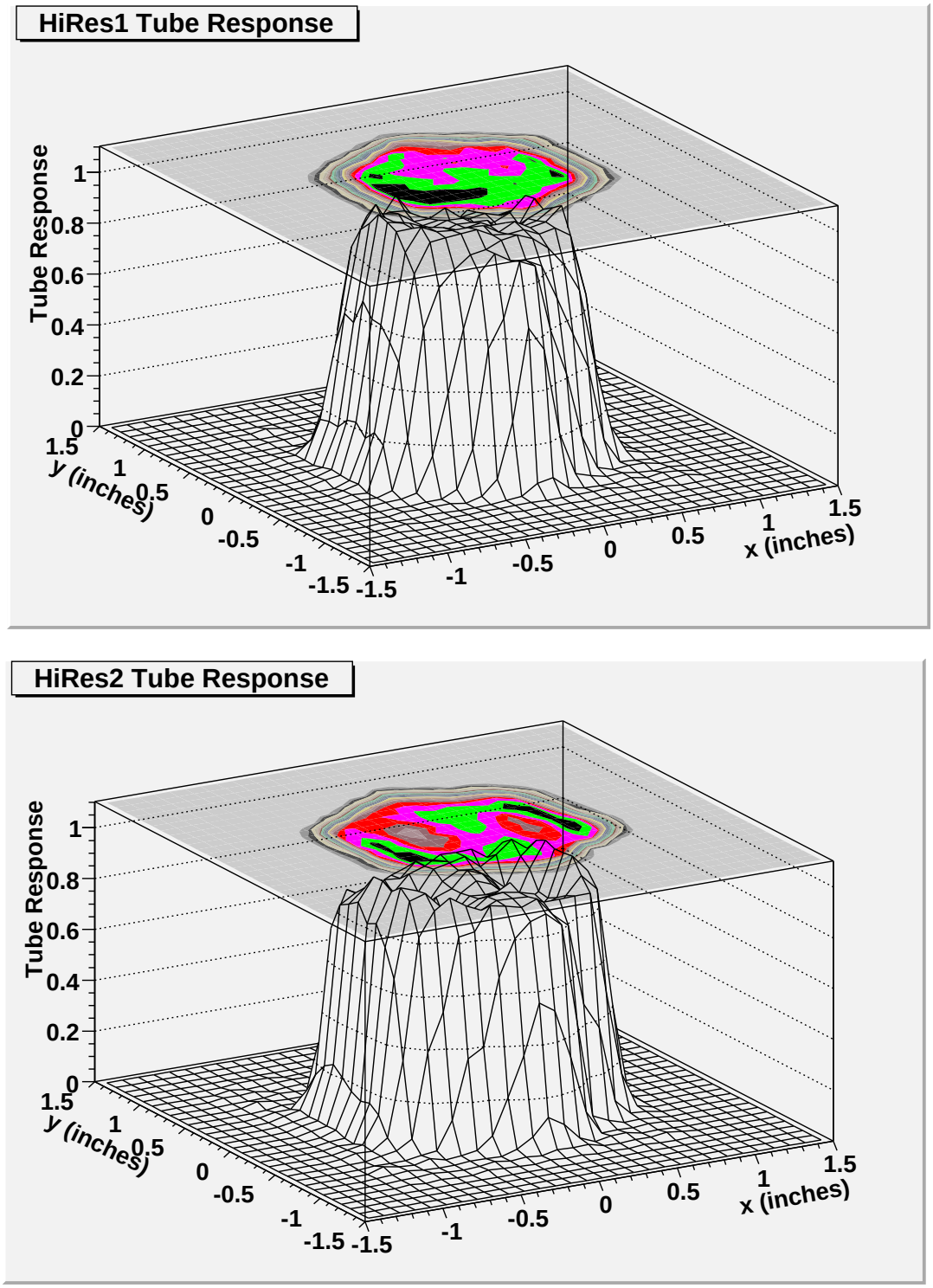

Figure 3.19. The tube response profile of HiRes1 and HiRes2 tubes. Note that the hexagonal shape of the tube is clearly seen in the projection. HiRes2 tubes have a 10 % larger acceptance than HiRes1 tubes as can be seen in the figure.

yag and yag_open shots are performed again. At HiRes2 YAG shots are done before the start of the run and at the end of the run with doors closed. During running with the doors open the YAG laser periodically fires throughout the night.

The YAG laser is used to determine the gain of all tubes for each night. This is done by determining the relative gain of each tube on each night with respect to the last RXF calibration. The implementation of the YAG laser in the calibration databases is described in section 4.6.5.4.

3.1.5 Steerable Laser

Each detector has its own Nd:YAG steerable laser used to probe the atmosphere around the detector. The laser located at HiRes1 is called HR1SLS and the laser at HiRes2 is called HR2SLS. Each laser is equipped with dichroic optics to produce a beam at 355 nm. This wavelength is chosen because it is close to the 357 nm peak in the N_2 fluorescence spectrum. Each laser fires at a maximum of 50 mJ (HR1SLS) or 7 mJ (HR2SLS) with a pulse duration of about 7 nsec.

Each shot's energy is monitored by passing the beam out of the laser into a beam splitter which samples 1 % of the energy by passing it to a calibrated photodiode and measured by a radiometer. The beam then passes through a quarter wave plate to produce a circularly polarized beam. Rayleigh scattering of light is polarization dependent and rotating of the laser head to different positions would produce different orientations of linearly polarized light without this precaution. The beam then passes through a computer controlled set of filter wheels containing attenuating filters to allow a range of energies to be sent to the sky. A second filter wheel contains more quarter wave plates to allow linearly polarized light if desired.

A dichroic mirror directs the beam up a beam pipe to a second mirror, which is controlled by a set of computer controlled stepping motors to allow firing in any azimuthal direction and a wide range of elevation angles.

The lasers use GPS timing to fire at a set millisecond offset so that those events can be easily extracted from the data stream. Each laser fires at a four Hz rate, with 111 msec offset for HR1SLS and a 222 msec offset for HiRes2. The details of the construction of the lasers are discussed further in [30, 32].

Throughout the night the lasers fire a series of patterns at different azimuths and elevation angles. The different shot patterns are also symmetric about the north and south of each detector. This can give a measure of the uniformity of the atmosphere surrounding the detector. As the laser fires the energy, time, geometry, and filter wheel settings are recorded by the same computer controlling the laser.

A sample of some of the HR2SLS shots as seen by HiRes1 is shown in Figure 3.20. Figure 3.20(a) is a low elevation shot fired to the south of HiRes1. Figure 3.20(b) and Figure 3.20(c) may look similar, but are fired at very different elevation angles. The shot in Figure 3.20(b) is fired at HiRes1 and passes just above it, while the shot in Figure 3.20(c) is a vertical shot aimed directly towards the zenith. Figure 3.20(d) shows a laser shot passing over HiRes1 similar to that seen in Figure 3.20(b), except passing to the north of the detector. The scattering distances from the beam to the detector are very different for each shot and probe different atmospheric optical thicknesses. Shots seen at HiRes2 are similarly fired in azimuth and elevation.

3.1.6 Vertical Flasher

Light sources that can be used to probe the atmosphere for optical clarity and relative calibration are placed between the two detectors. Ten xenon "flashers" are placed at a distance of 1 km, 2 km, 4 km, 8 km, and 10 km from HiRes2, five along a north leg and five along a south leg (Figure 3.21). The xenon flash bulb provides a stable light source with $\sim \pm 5\,\%$ shot to shot stability that can be observed by both detectors in stereo mode.

Each flasher unit is designed to operate in all weather conditions in the field with power provided only with batteries and solar panels. Each flasher unit is enclosed in cylindrical metal tubes with a Pyrex window facing up towards the zenith. A xenon flash bulb is provided with about 1800 V through a battery, DC-to-DC converter, and step up transformer. The flash bulb faces down towards a mirror which redirects the light beam vertically up into the sky. Each pulse lasts about 1 μsec in duration and provides about 10^{-4} joules of energy to the sky. A waterproof box protects the electronics and batteries. A solar panel is used to recharge the batteries during the day, providing enough charge to ensure the system will operate

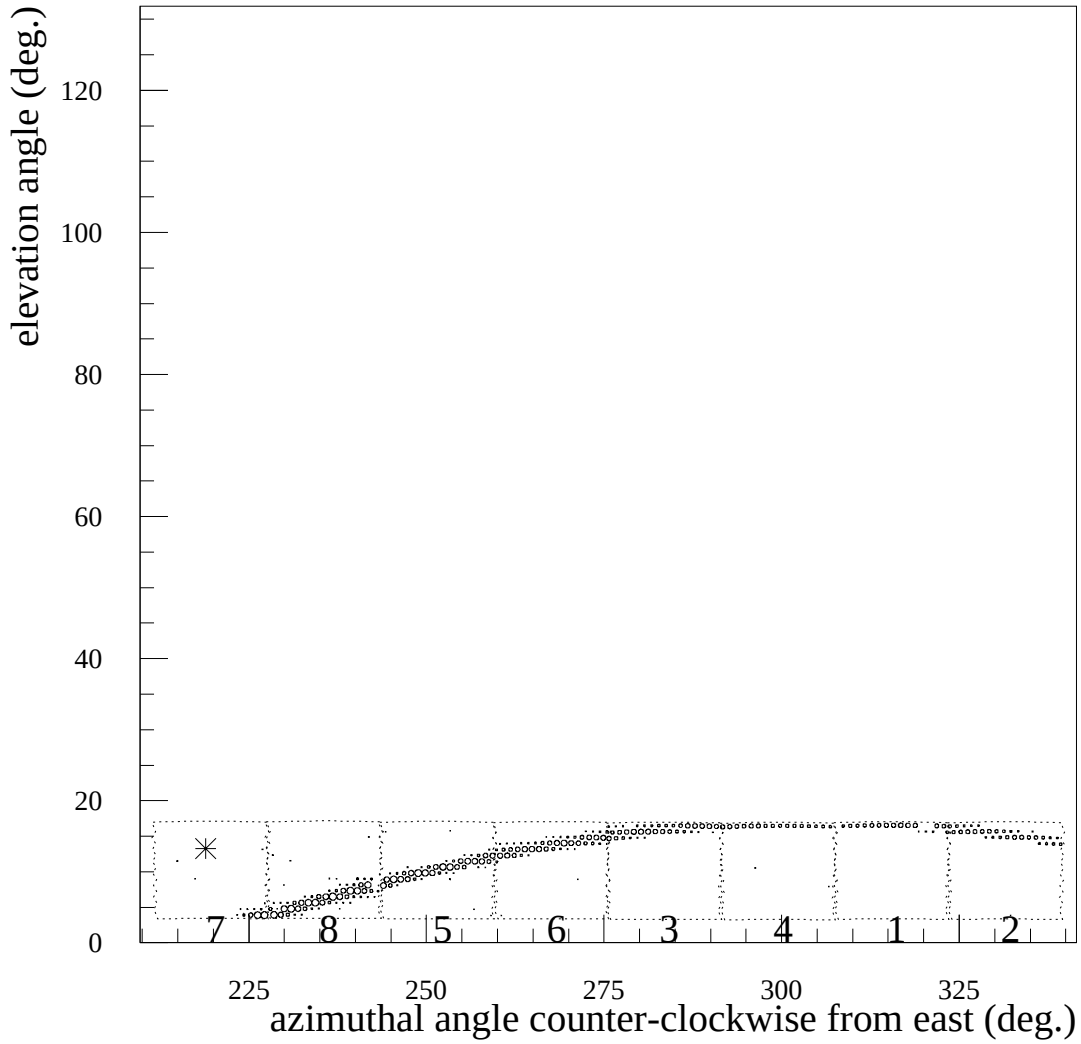

(a) Azi = 4°, Elev = 5°

Figure 3.20. Various HR2SLS shots as seen at HiRes1. Some shots are taken at the same geometry but with the filter wheels in various positions, giving different polarizations and sky energies. Shots are also done a symmetric manner north and south of the detector.

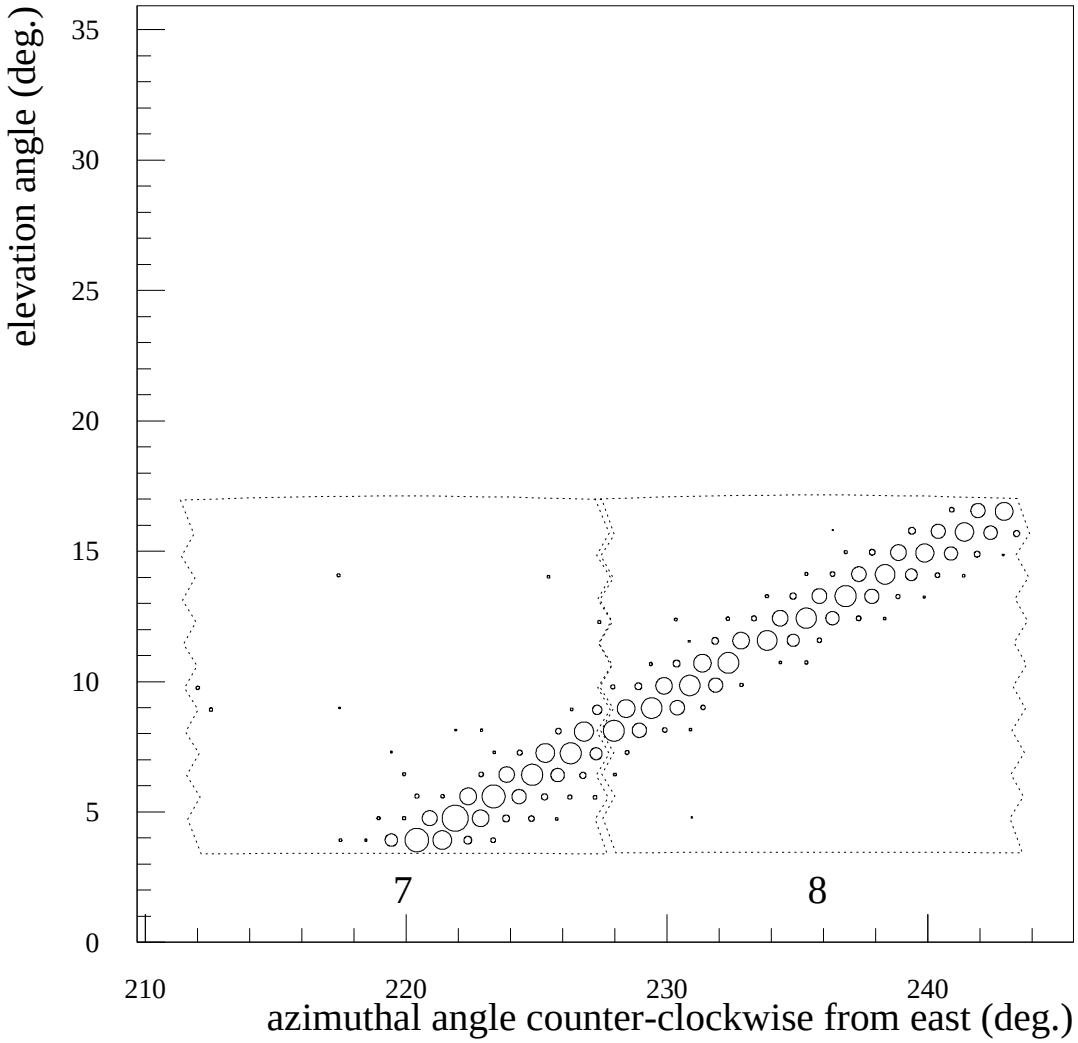

(b) Azi = 32°, Elev = 0.6°

Figure 3.20. continued.

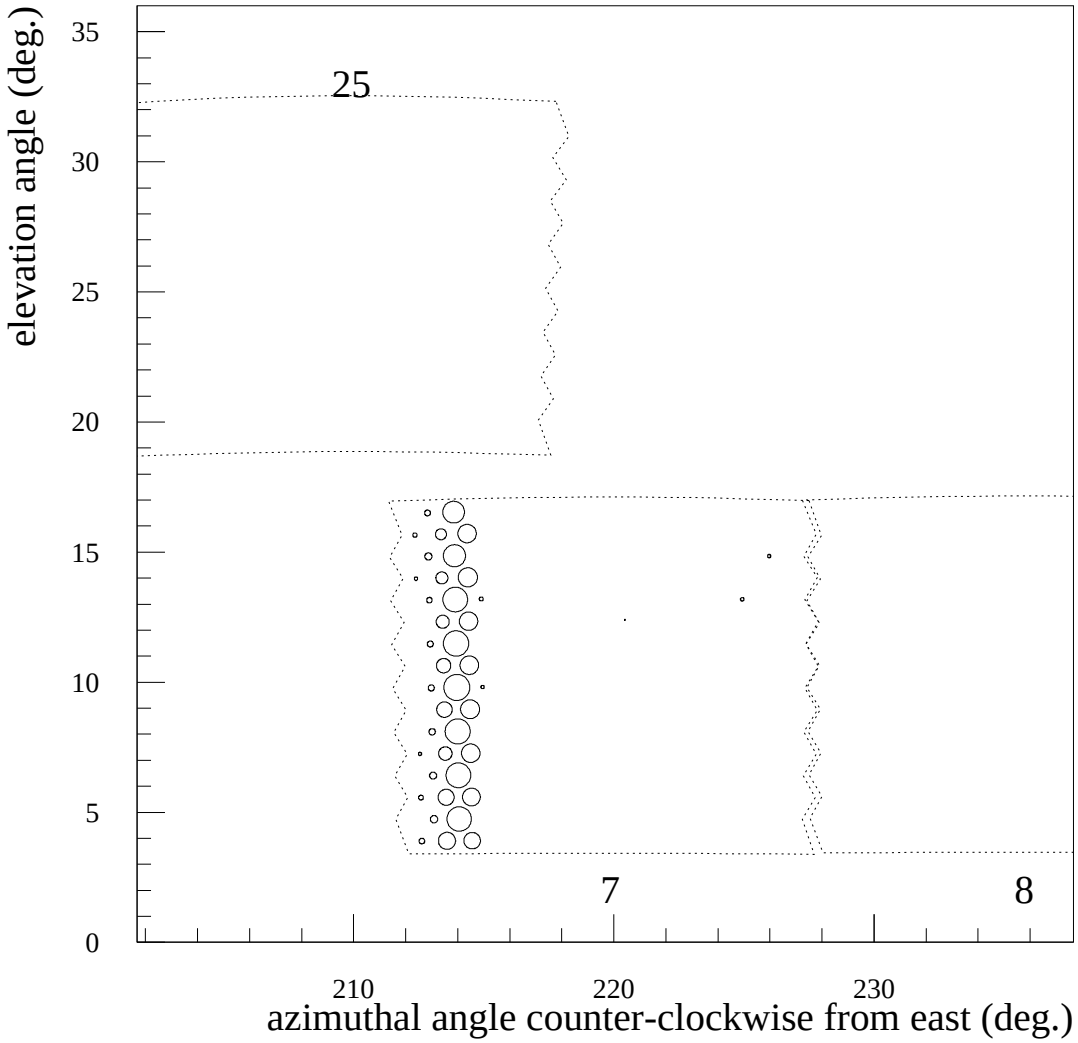

(c) Azi = 34°, Elev = 90°

Figure 3.20. continued.

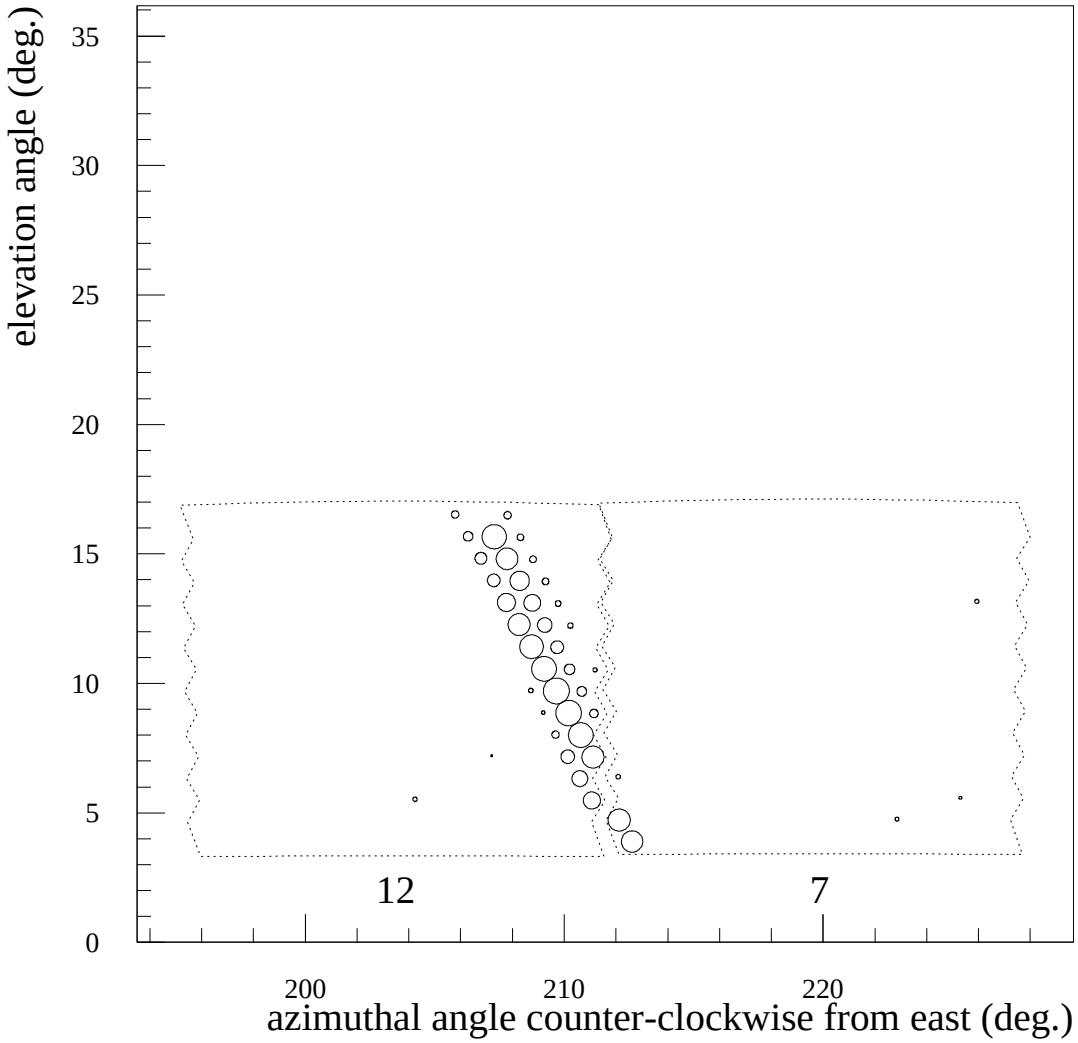

(d) Azi = 36°, Elev = 0.6°

Figure 3.20. continued.

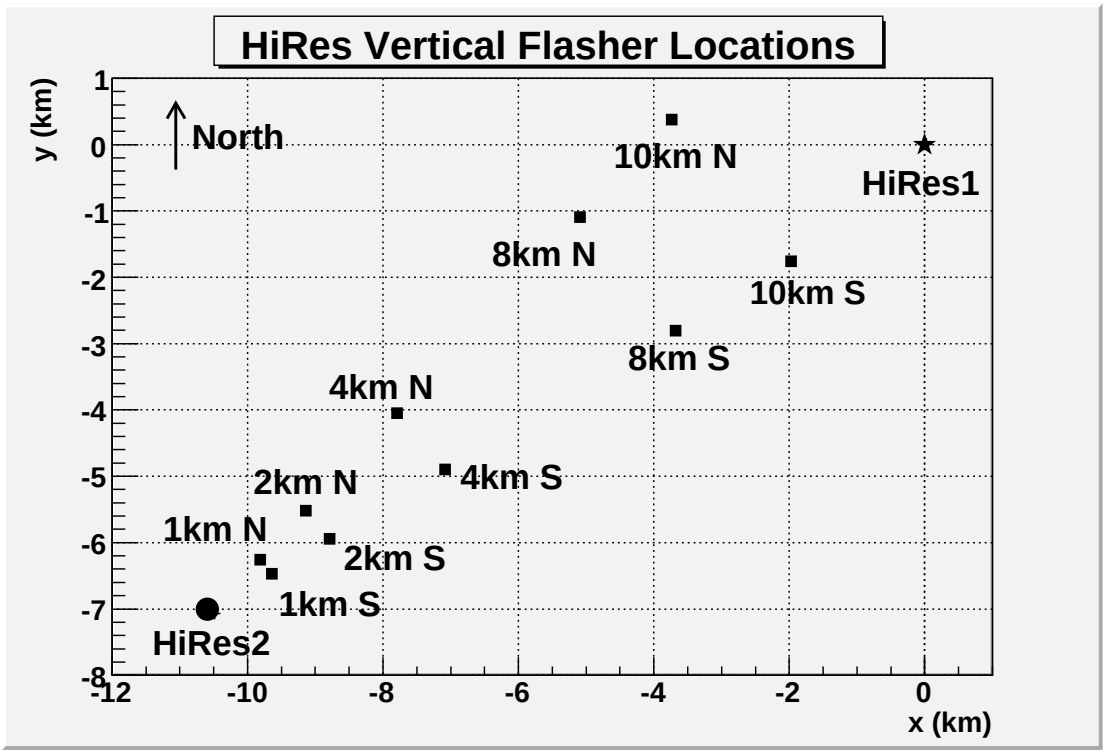

Figure 3.21. The location of the vertical flasher array. Each flasher is designated by its distance from HiRes2 and whether it lies on the north or south leg. All south leg flashers appear in HiRes1 mirror 7 and HiRes2 mirrors 2 and 4. The north leg 1 km, 2 km, 4 km, 8 km, and 10 km flashers are seen in HiRes1 mirrors 7, 12, 11, or 10 and HiRes2 mirrors 1 and 3.

even during the longest winter nights ($\sim$ 12 hours).

The flasher assemblies use heaters to evaporate dew and melt snow off of the windows during times of high humidity and after snowfall. Each unit is operated via radio control by a computer which runs software which schedules the firing of the individual flashers. A one way link from the control computer uses a dual-tone multifrequency generator to communicate with an individual flasher to tell it when to activate and deactivate heaters and when to fire. The computer records all commands as well as the times they are sent. The firing pattern is to alternate each second firing of one of a pair of flashers at a given distance, then to pause 20 seconds while the window heaters are turned on for 10 seconds, then to repeat the pattern with another pair. The cycle is completed in 200 seconds and is repeated every 600 seconds.

An additional feature of the flasher array is to act as a GPS clock. Rarely, problems with GPS timing have been missed by operators during data collection. If even one detector loses GPS timing, stereo event matching is hindered since a time window is used to determine stereo coincidence. The flasher control computer has its own GPS timing and is programmed to instruct the flashers to flash a set number of times at the top of each hour (called "bongs"). If a detector's GPS timing is off by a constant or near constant offset, as is often the case when there is a problem, by matching the reported time of the bongs, stereo timing can be corrected.

Figure 3.22 shows the stereo detection of two of the 10 flashers. In addition to making measurements of optical clarity the flashers can also detect low clouds. Figure 3.23 shows a flasher beam hitting a cloud. A complete description of the flasher units is found in [58].

3.1.7 Intersite Flasher

An inclined xenon flasher is located at the old Fly's Eye II site and is called the intersite flasher. Eleven mirrors at HiRes1 (Figure 3.24(a)) and four mirrors at HiRes2 (Figure 3.24(b)) can see the flasher when it is operable and weather conditions are good, providing a wide range of scattering angles with which to probe

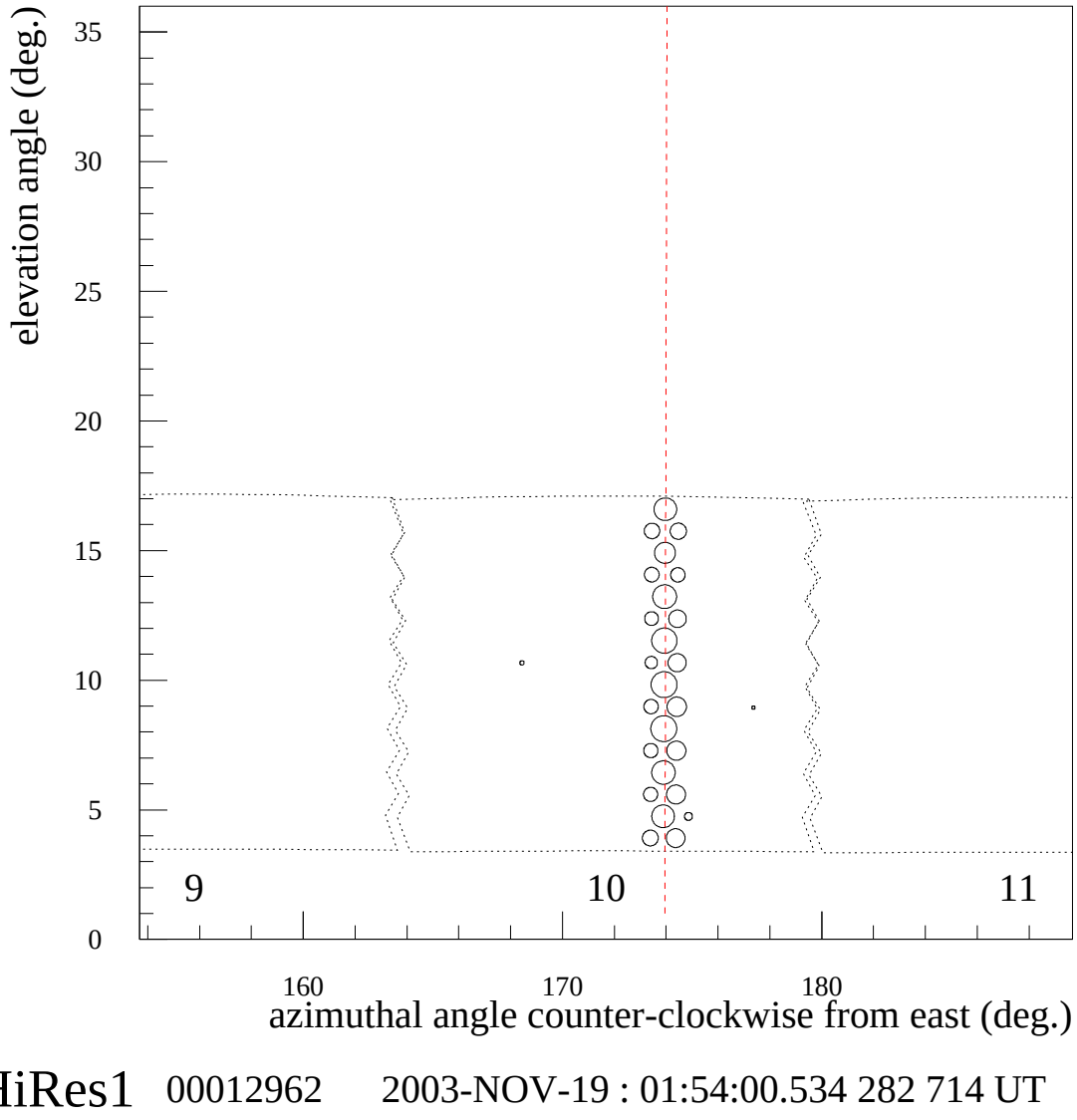

(a) 10 km North Flasher - HiRes1

Figure 3.22. Two vertical flasher shots as seen at HiRes1 and HiRes2. Notice that the 10 km track is thicker than the 4 km track in HiRes1 and vice versa for HiRes2. This is because the 10 km flasher is closer to HiRes1 and the 4 km flasher is closer to HiRes2.

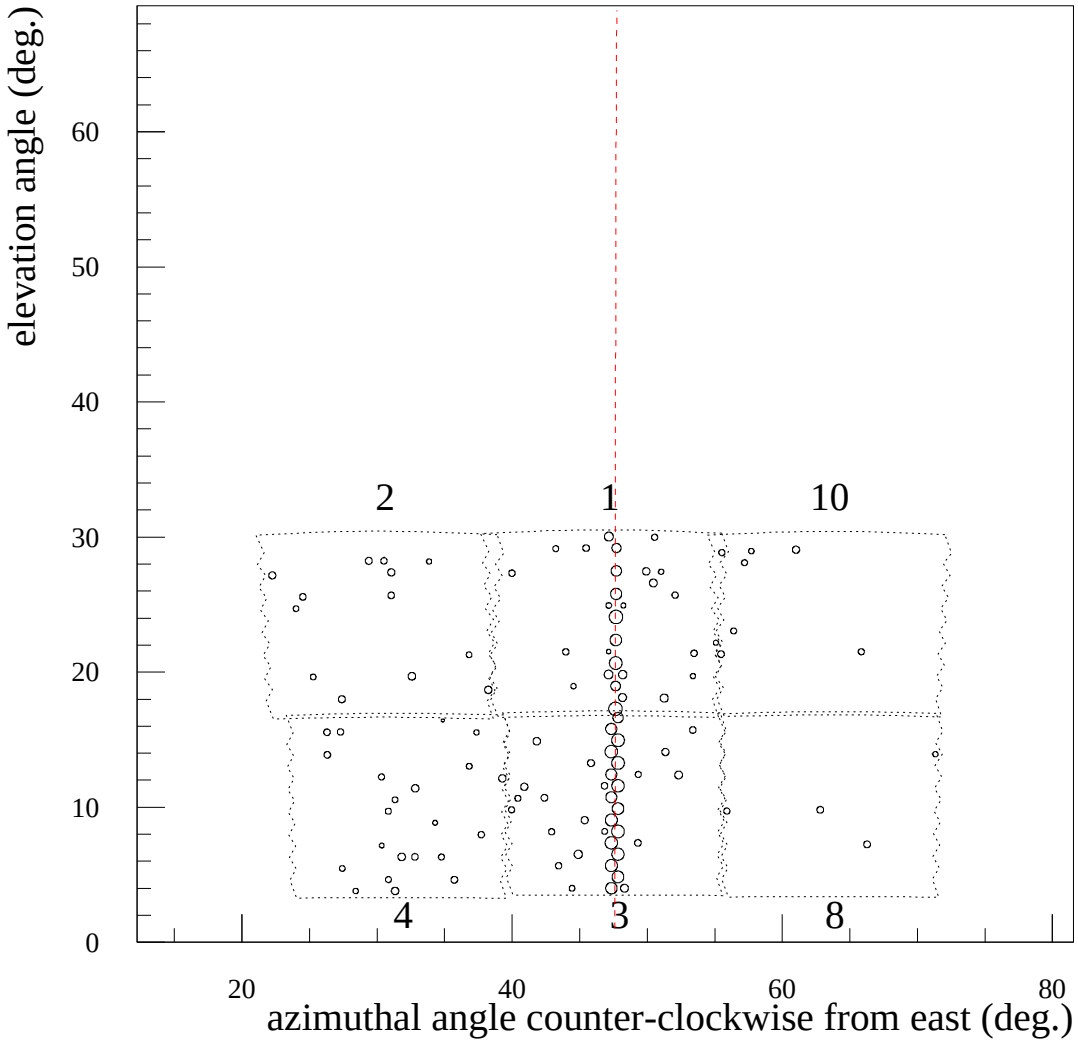

(b) 10 km North Flasher - HiRes2

Figure 3.22. continued.

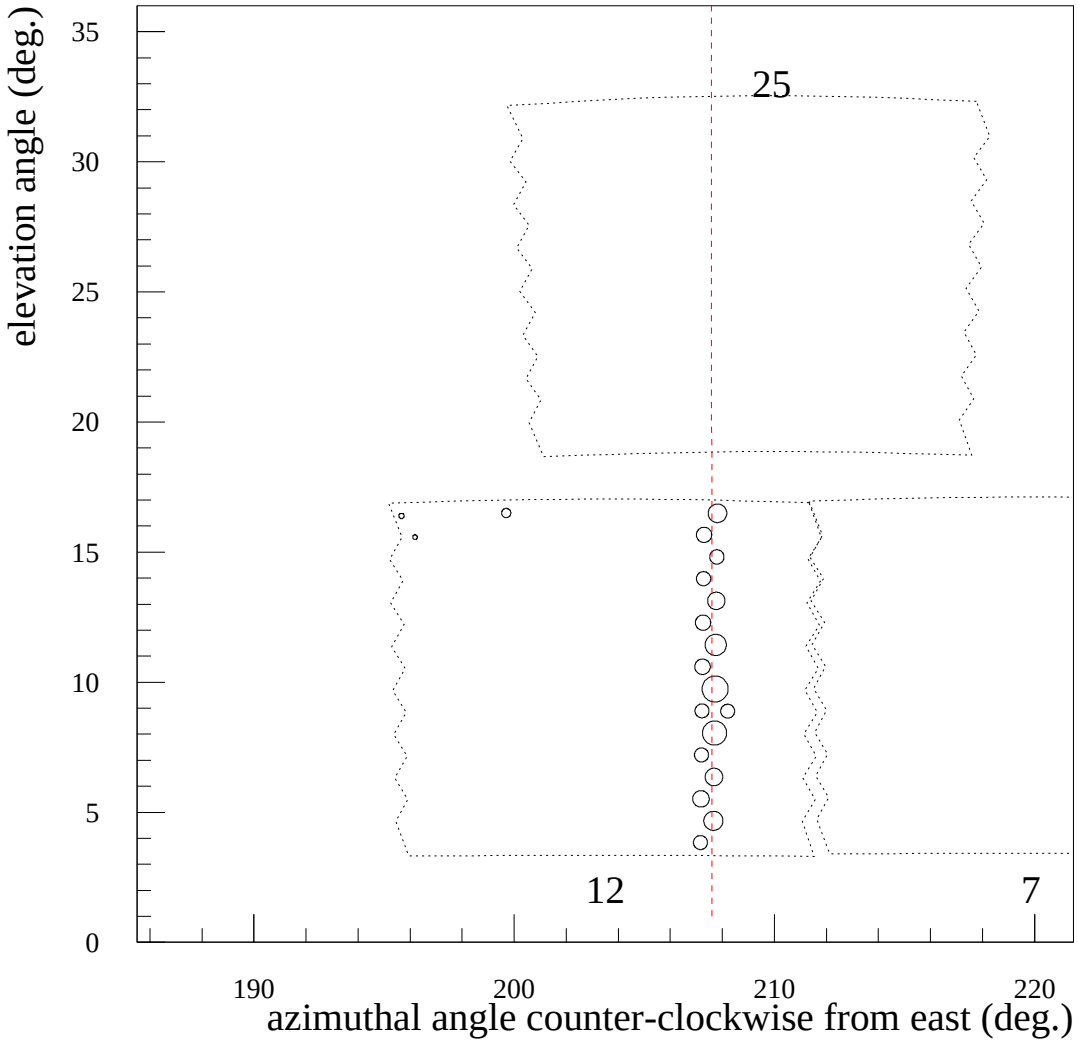

(c) 4 km North Flasher - HiRes1

Figure 3.22. continued.

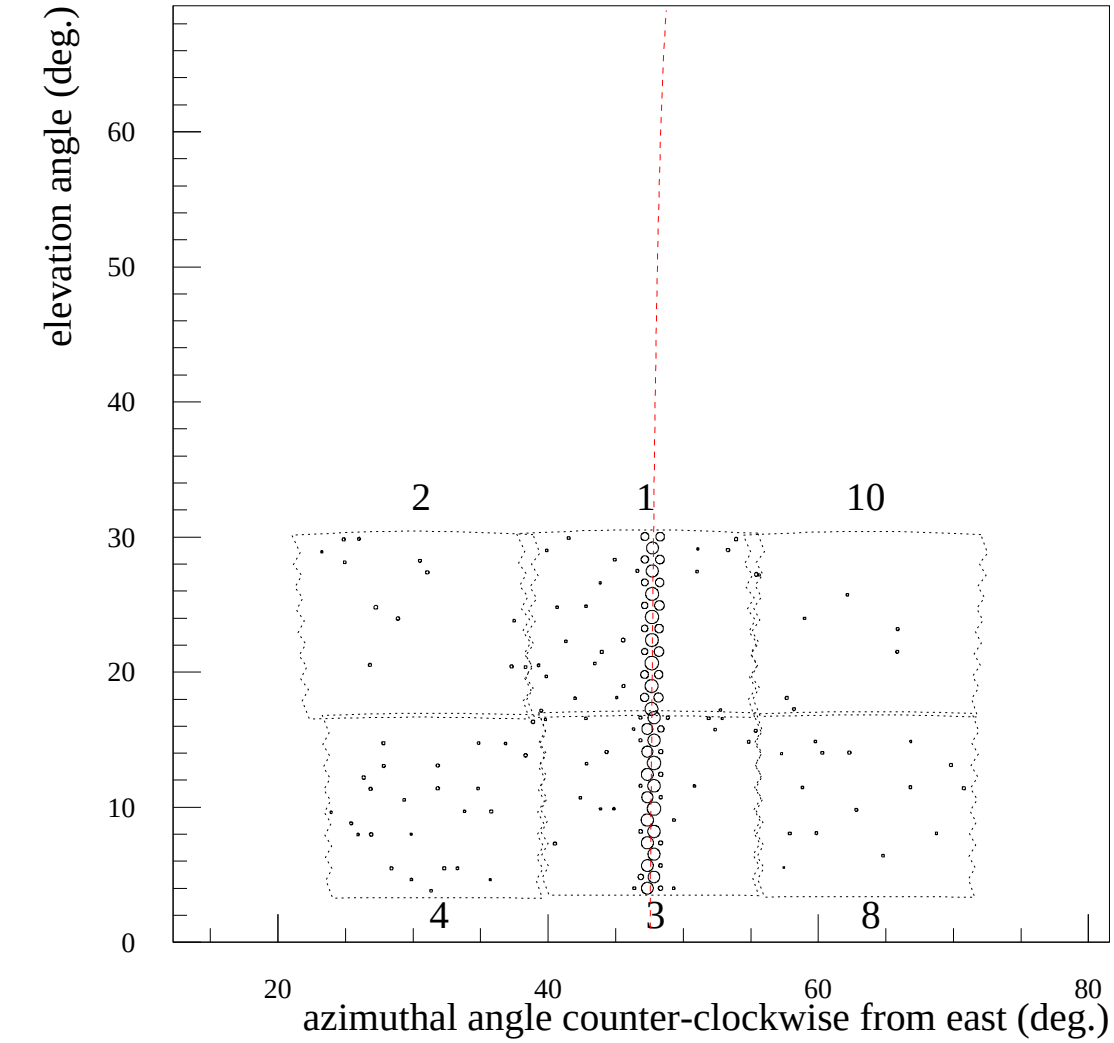

(d) 4 km South Flasher - HiRes2

Figure 3.22. continued.

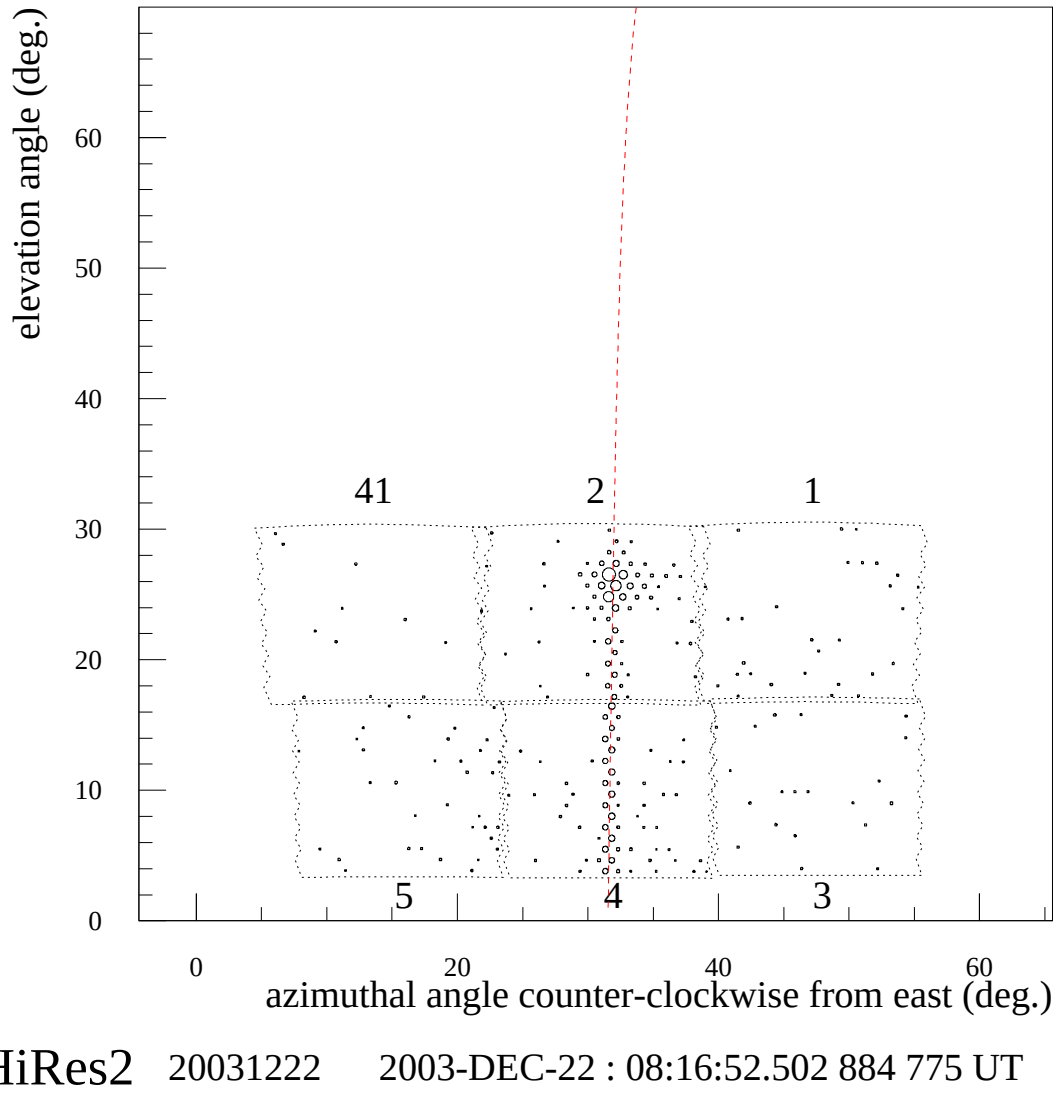

Figure 3.23. The 4 km south vertical flasher as seen by HiRes2 hitting a cloud. The mushroom feature at the top of the track is indicative of the flasher beam hitting a cloud. This cloud was only 2 km above ground level.

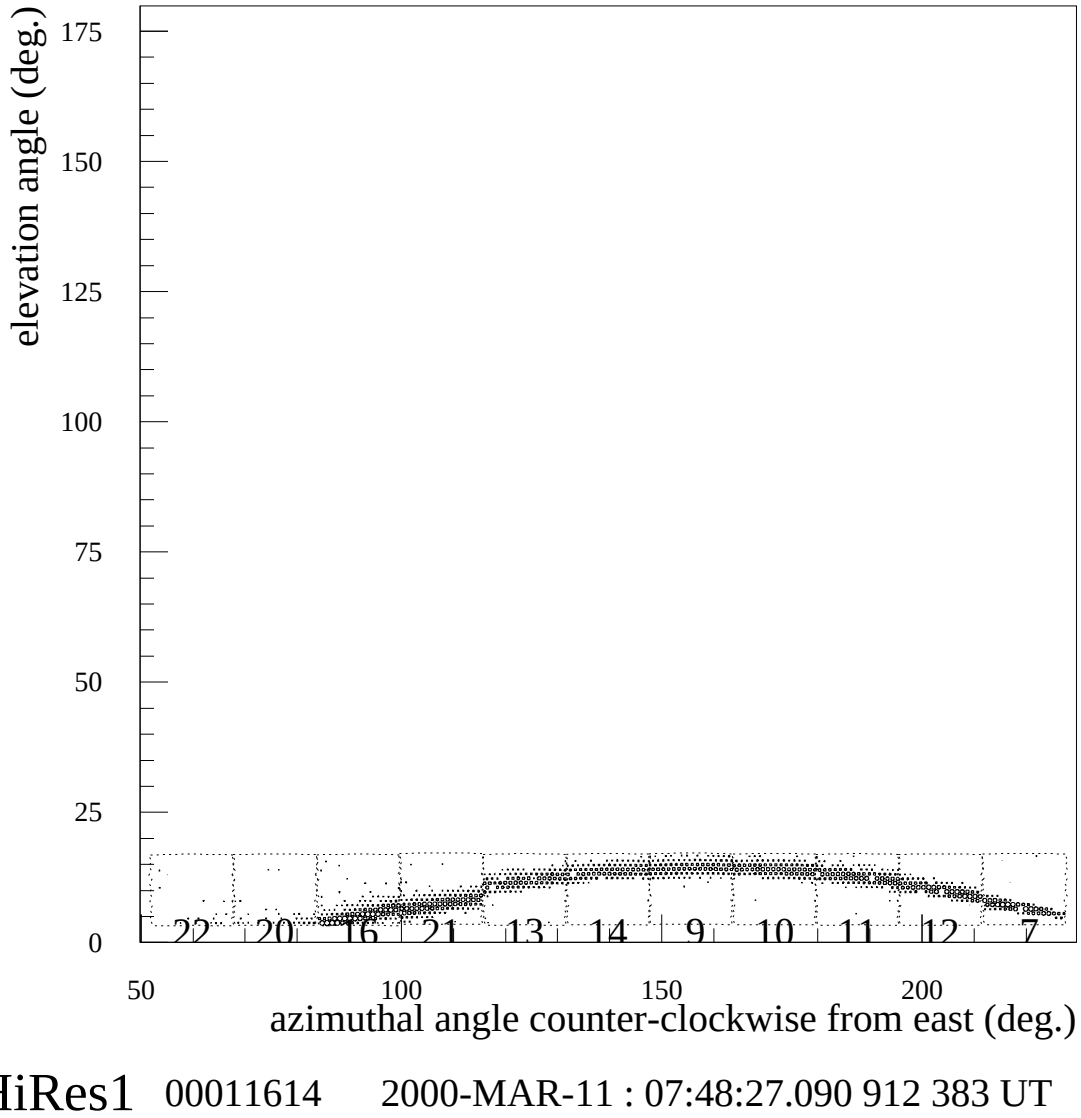

(a) Intersite flasher seen at HiRes1.

Figure 3.24. The intersite flasher as seen by HiRes1 and HiRes2. The flasher is located about 3 km northeast of HiRes1. It's track starts in HiRes1 mirror 20 and travels southwest to mirror 7. At HiRes2 The track begins in mirror 4.

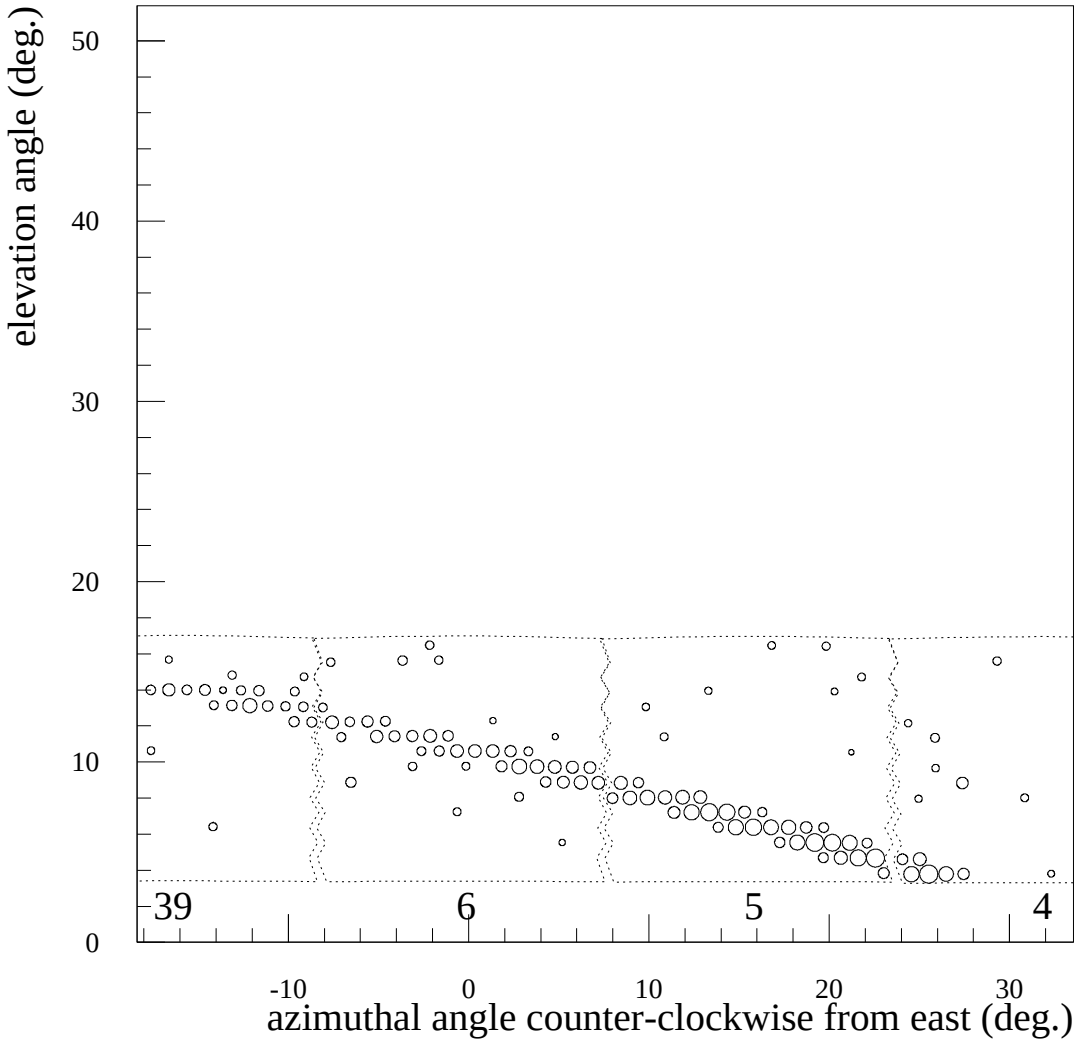

(b) Intersite flasher seen at HiRes2.

Figure 3.24. continued.

the atmosphere. It is an automated system with its own computer dedicated to determining when to start firing on each night and requires no operator intervention except when it malfunctions. The operation of the intersite flasher is sporadic at times and is not always present in the stereo data. Long periods of data collection exist where the intersite flasher was inoperable.

3.1.8 Vertical Laser

A vertical Nd:YAG laser very similar to those used elsewhere in the HiRes experiment is located 21 km (34 km) northeast of HiRes1 (HiRes2) in the town of Terra, just outside the Dugway Proving Grounds.

This laser is designed to test the high energy stereo aperture of the detectors under varying weather conditions. It fires shots with energy between 1 and 5 mJ to simulate light production of showers with energies between 6×10^{19} and 10^{20} eV. It is found that the detectors easily see the laser at this distance under weather conditions that are found to be worse than those accepted for normal analysis. The reconstruction efficiency is about 60 % for a shot simulating a 40 EeV shower and rapidly reaches 100 % at around 60 EeV, which is the GZK cutoff energy. This tells us that the aperture of the HiRes experiment does indeed have the capability of seeing super-GZK air showers out to 30 km away. Figure 3.25 shows the Terra laser as observed from HiRes1 and HiRes2. As the figure shows, this distant laser is easily seen by the detectors.

3.2 Data Collection

3.2.1 Run Procedures

3.2.1.1 HiRes1

HiRes1 operations begin with a site inspection to ensure that there is no damage to any of the mirrors or buildings. All curtains are checked to make sure that they did not drop since the end of the previous run. The DACQ program is started and power is applied to all electronics racks. A PPG test is performed, in which a series a programmable pulses is sent to each tube's preamplifier to verify their proper operation. A diagnostic routine is run to verify the GPS time between the DACQ

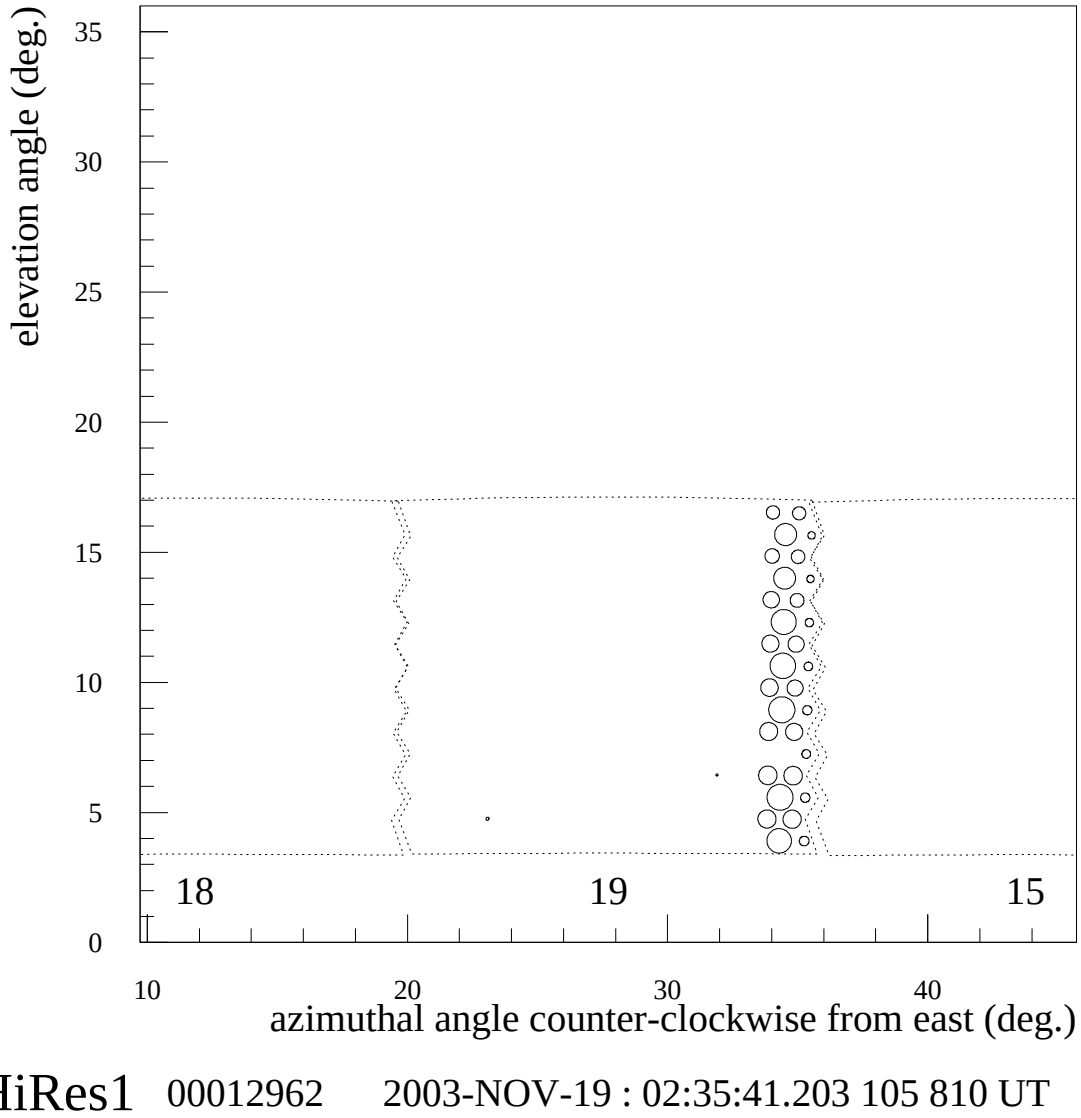

(a) The Terra vertical laser seen at HiRes1.

Figure 3.25. The vertical laser located at Terra. This laser is 34 km from HiRes2 and 21 km from HiRes1 and is seen very well. It fires shots with energies to simulate the light production of super-GZK air showers.

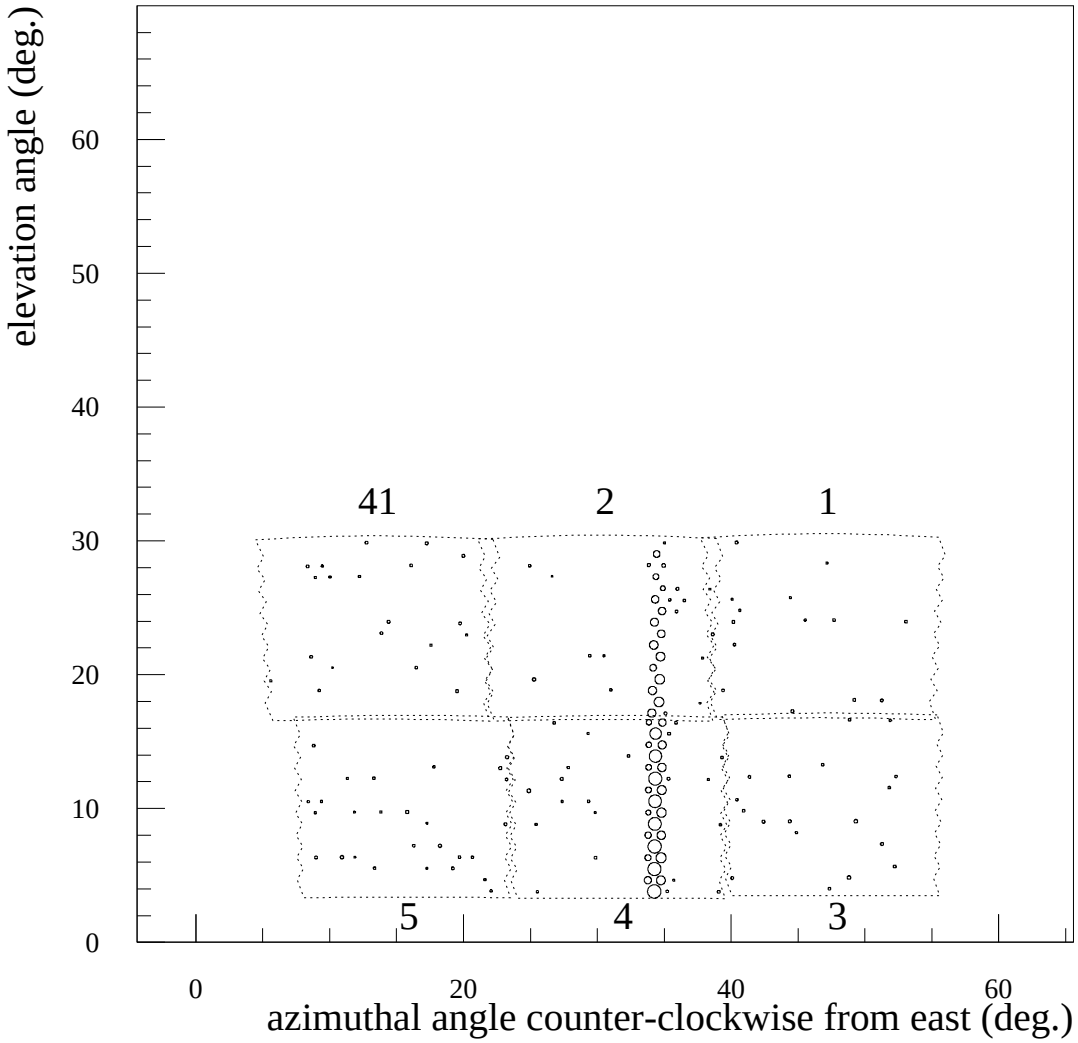

(b) The Terra vertical laser seen at HiRes2.

Figure 3.25. continued.

and central timing, ensure that all mirrors are online, check low voltage readbacks, tube countrates, perform snapshots to test for dead tubes, verify pedestals are being properly set, set and read back thresholds, and check TDCs by performing a holdoff delay test. A calibration routine is then performed to do calibration of all QDCs and TDCs. A series of test charges and times are sent to the electronics and the digitized values are read back. These values are used to determine the QDC gain and TDC calibration for each tube on a nightly basis.

When within 30 minutes of the scheduled run start, the high voltage is turned on and the calibration YAG laser is warmed up. After the high voltage has stabilized for several minutes, a series of snapshots are taken with the door closed (called a *noise* part). When snapshots are completed, the calibration YAG laser is fired 100 times on each mirror. This is done through two sets of fibers for each mirror. One set is mounted on the cluster. When the laser fires, the light is transmitted through the fiber optic cable, onto the mirror and is reflected onto the cluster. The second set of fibers is mounted at the center of the mirror. This fiber directly illuminates the cluster without any mirror reflection. The purpose of this test is to allow a measurement of the mirror reflectivity by looking at the difference in light between the two sets of shots.

About 5 minutes before the scheduled run start, the doors are opened and another series of snapshots are taken (called a *noise_open* part). The noisiness of a tube can be measured by examining its response to door closed noise, where there is no sky noise, and door open noise where potential light sources may be present in the field of view. Another series of YAG laser shots is also performed with the doors open (called a yag_open part).

At the scheduled run start time, the detector is started, but not permitted to trigger yet. The mirrors are allowed to stabilize their thresholds for about 5 minutes until the average countrate of each mirror is about 200 Hz. When thresholds and countrates have stabilized the detector is permitted and triggers are enabled. At this point, the detector is collecting cosmic ray data and said to be operating in monocular mode.

During the start up procedure, the artificial light sources are also powered up and prepared. There is an array of vertical flashers, a steerable laser at each site, an intersite flasher, and a vertical laser located at Terra. The intersite flasher and vertical laser are completely automated and do not require operator intervention. The other sources require an operator to get them started.

During data collection, the thresholds and count rates of all mirrors are monitored by the operator. The artificial light sources are also observed to ensure that they are operating and that the weather is good enough for them to be seen. Regular excursions outside, no less than once per hour, are made to investigate the weather and enter a weather code into the DACQ. The weather code is a seven-digit code that indicates the quadrants of the sky that have cloud coverage, the amount of cloud coverage directly overhead, the optical thickness of the overhead clouds, and if there is any haze in the air. This code can be subjective and depends on the operators regularly checking the sky and allowing proper time for their eyes to adjust to low light levels outdoors.

If any mirror malfunctions, the operators make whatever repairs are necessary to get it running again. If it cannot be repaired, it is removed from the current night's run and experts are sent notice that maintenance is required as soon as possible.

At the end of the run, the reverse procedure is performed: yag_open, noise_open, doors closed, noise, yag, calib, and diag. All equipment is then powered down until the next evening of running.

3.2.1.2 HiRes2

HiRes2 run procedures are similar to HiRes1. The site is first checked for any physical problems with mirrors or doors. The DACQ and the central host computers are then started. Power to all electronics racks is turned on and communications between the central VLink and the MLink modules in each building are established. A series of snapshots are taken and PPG tests are performed. At around 30 minutes prior to the run the high voltage is applied and the calibration YAG laser is fired and each mirror's response is recorded. A few minutes before run start, the doors

are opened and the detector is started in monocular mode. When both HiRes1 and HiRes2 are concurrently running the detector is said to be collecting data in stereo mode.

Prior to 25 September 2001, HiRes1 and HiRes2 were each manned by their own set of operators. The Dugway Proving Grounds entered into a heightened security status during at this time and operators were restricted from getting to the sites. Data collection was ceased until 2 May 2002, when an arrangement was made with the Army to allow certain personnel to access the sites. Because of the restrictive nature of the agreement, qualified operators were in short supply, so HiRes1 was set up to be run remotely and operators only manned HiRes2. An additional duty of HiRes2 runners then became to physically verify all mirrors and buildings were in operating condition before a night's run and to perform any maintenance that remote HiRes1 runners requested to fix any malfunctioning equipment.

3.2.2 Running Time

Because HiRes is a fluorescence detector it has a lower duty cycle than a ground array. This is because the detector is sensitive to bright light sources and requires a sky clear of obscurations such as clouds or fog. Therefore, the detector only runs during clear, moonless evenings. The detector is run only if three or more hours of dark time where the moon is not visible is available. This means that the HiRes detector is run for about 2 weeks of every month, with the run lasting about three hours starting around the time of the last quarter Moon, peaking during the new moon to about 12 hours in the winter or five hours in the summer, then tapering back down to 3 hours around the first quarter moon. Figure 3.26 shows an example of the seasonal variation of runtimes, as well as actual runtimes in monocular modes and stereo.

The maximum duty cycle of a fluorescence detector is then limited to about 16 % per year. During periods of inclement weather the night's run is paused, shutting the doors if rain, snow, lightning, or high winds are expected. Also maintenance actions may delay or even cause cancellation of a run. All of these factors limit the expected duty cycle to about 10 % per year. HiRes accumulated 3460 hours of

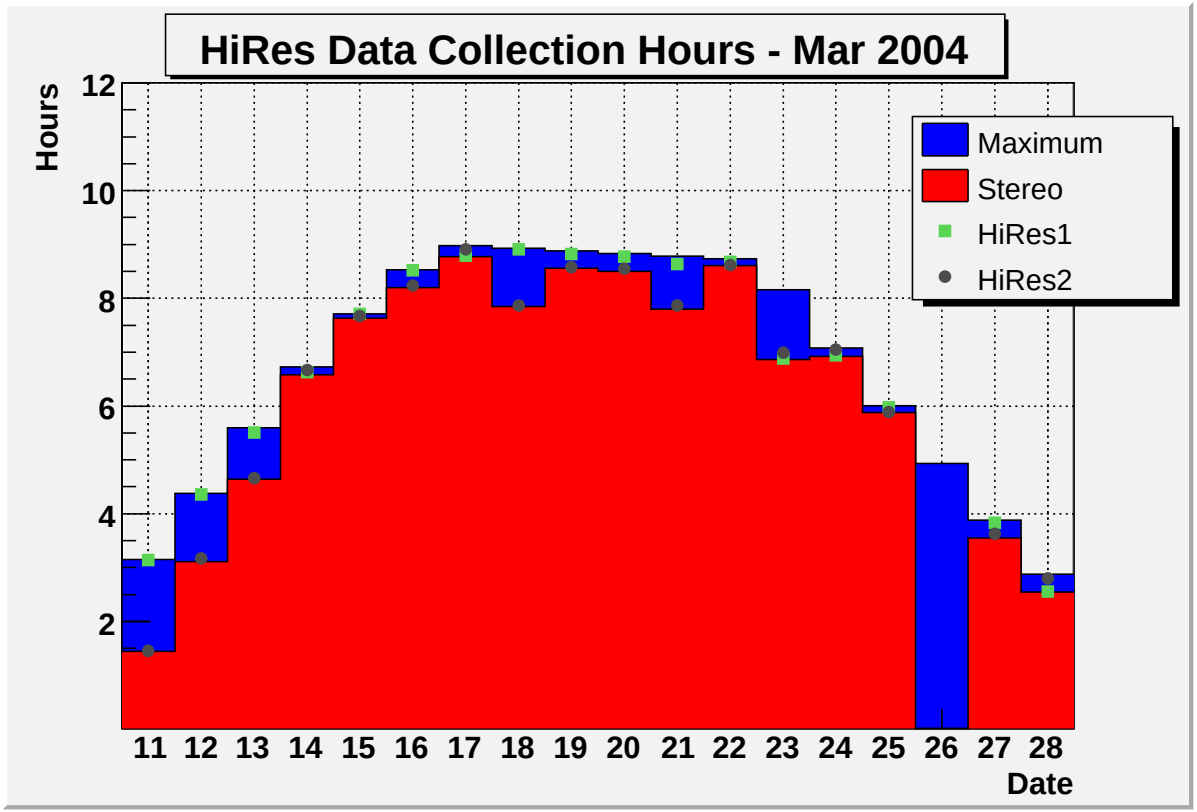

(a) Spring run (#54)

Figure 3.26. Seasonal variation of run times. HiRes can only collect data during clean moonless evenings, therefore the amount of run time varies on each night. For four seasonal runs the maximum running time is shown, as well as the actual amount of data collection time for each detector in monocular mode and in stereo. Some nights little or no data was collected due to poor weather. The four missing days in the December were due to base restrictions imposed by the Army. Two missing days in June were lost due to bad weather. On 12 June, the HiRes2 central link was down so the detector did not run.

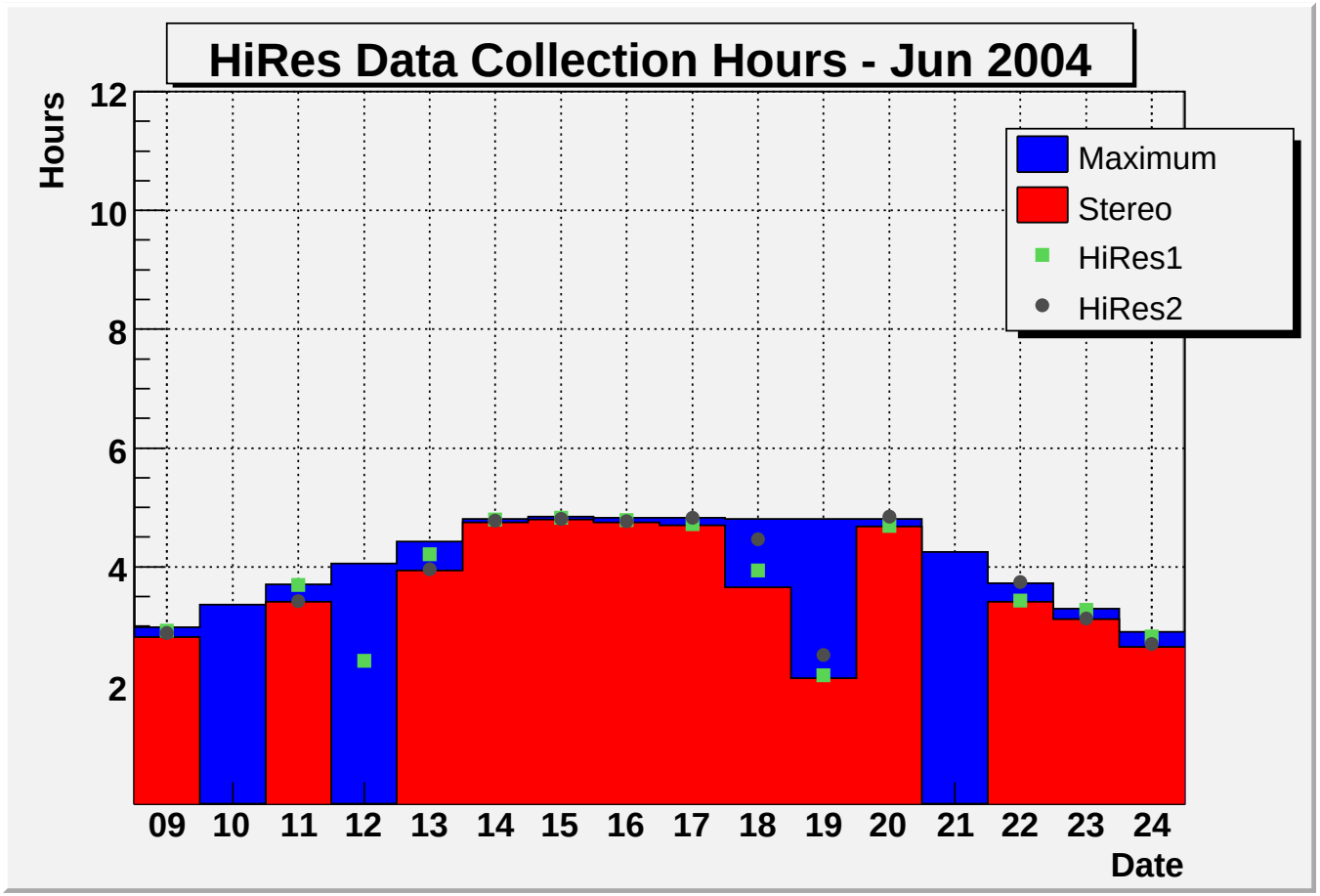

(b) Summer run (#57)

Figure 3.26. continued.

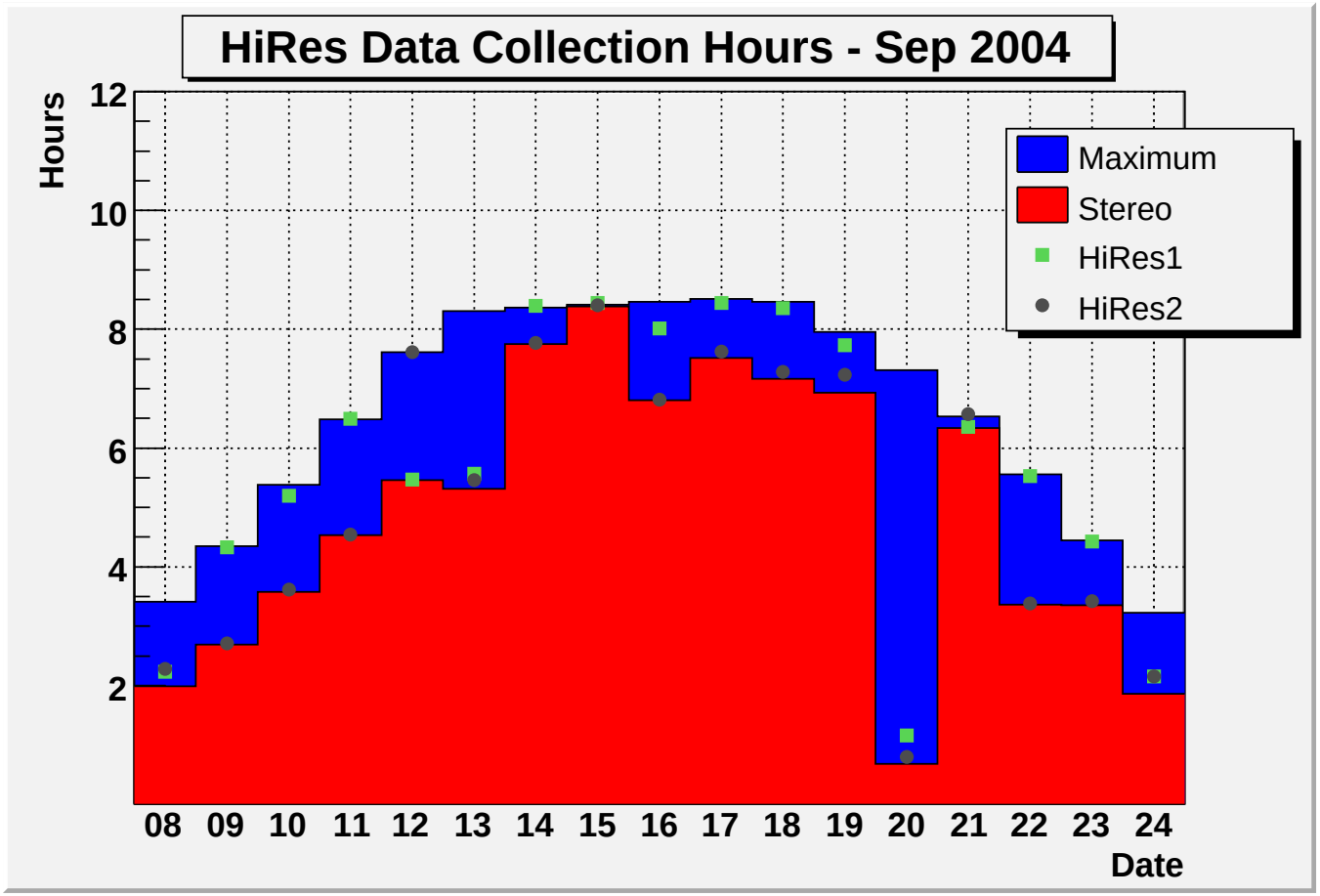

(c) Fall run (#60)

Figure 3.26. continued.

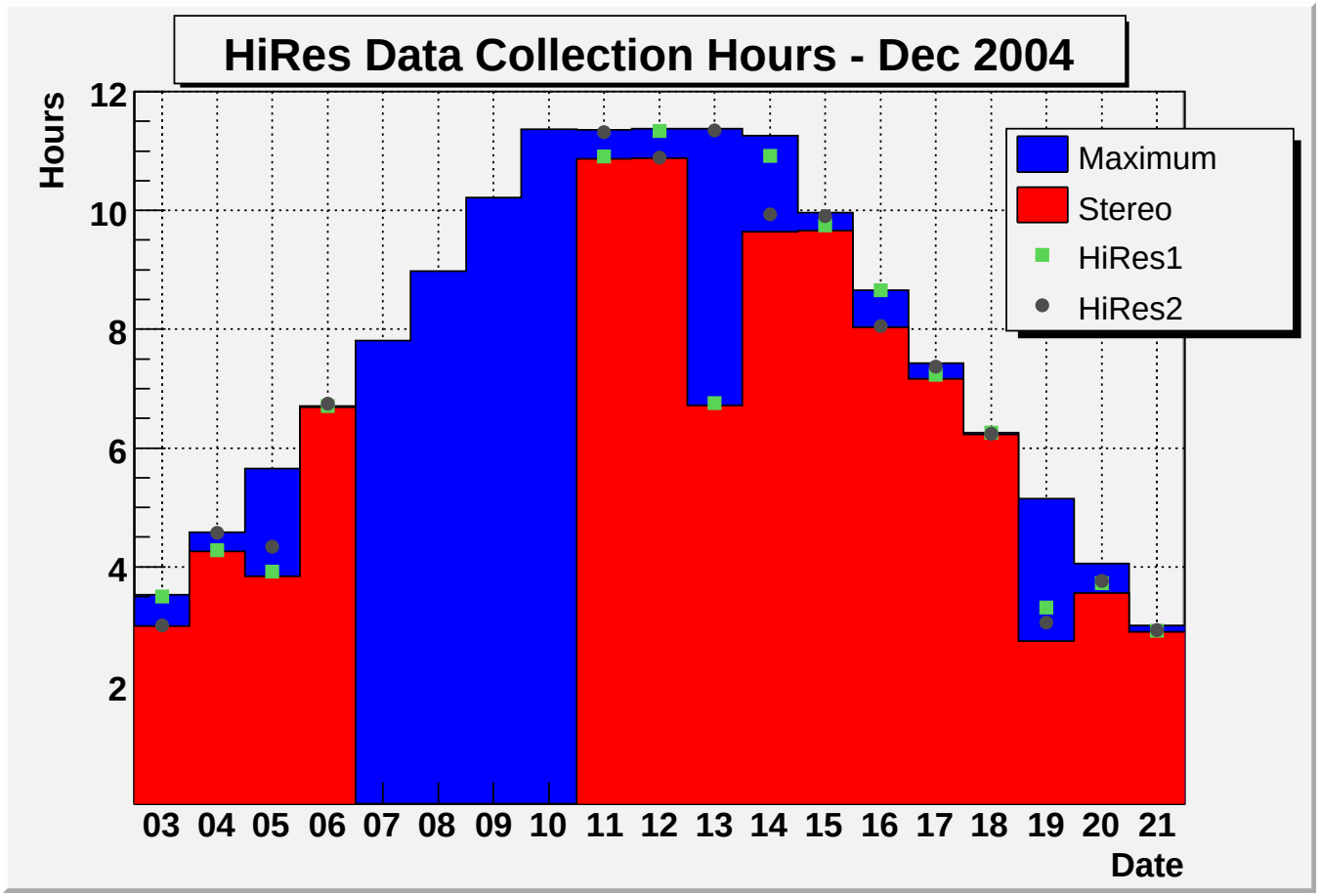

(d) Winter run (#63)

Figure 3.26. continued.

stereo data over 6 years of operations, resulting in a 7 % duty cycle. Poor weather and Army base restrictions were the main factors in cutting the runtime. A yearly accounting of the amount of stereo hours collected is shown in Table 3.4.

Because the HiRes detectors are located on an Army facility, there are periods when sensitive tests are being conducted by the military or the base is on a heightened security posture and operators are restricted from base. Some of the longest periods of restriction are shown in Table 3.5.

During the period of 1 May 2002 to 17 September 2003, the 3 hour minimum rule was extended to a 5 hour minimum rule, so this also reduced the number of stereo hours that were possible to collect. The 5 hour rule is assumed in all plots that consider the maximum number of stereo hours available unless otherwise stated.

This work encompasses the period of stereo data collection beginning 1 December 1999 and ending 11 November 2005. There were 74 stereo data collection runs during this time. Over this period the maximum possible stereo time was 8507.29 hours and 3460.08 hours of stereo data were actually collected. Figure 3.27 shows the maximum and actual stereo data collected. Each bin represents a single run. Figure 3.28 shows the *integrated* runtime over this period. As will be explained in section 5.4.1 the runtime (also called ontime) is an important consideration in determining the stereo exposure and ultimately the cosmic ray ultra high energy spectrum.

3.2.3 Cloud Monitoring

Two dedicated cloud monitoring systems are in use at HiRes1. Each system uses the same type of infrared sensor which detects infrared light in the 5.5 - 20 μm range. The differential temperature between the IR sensor which is in thermal equilibrium with a preselected patch of sky and the housing unit is measured. Since clouds are warmer than the clear sky, a differential increase in temperature indicates a cloud is in the field of view.

A fixed system is in use which consists of an array of 11 infrared sensors that each view $30^\circ \times 30^\circ$ patches of sky. Each sensor is fixed in place and the sensor does

Table 3.4. Yearly breakdown of maximum possible hours to run the HiRes detector in stereo mode, and the actual hours that were collected.

Year	Maximum Hours	Actual Stereo Hours	Efficiency	Duty Cycle
1999	183.53	38.06	0.21	0.05
2000	1494.38	503.75	0.34	0.06
2001	1402.07	357.34	0.25	0.04
2002	1416.07	366.55	0.26	0.04
2003	1455.37	800.74	0.55	0.09
2004	1355.65	743.94	0.55	0.08
2005	1200.22	649.70	0.54	0.09
total	8507.29	3460.08	0.41	0.07

Table 3.5. Periods of extended restriction from the HiRes detectors. Data was not collecting during these periods.

Start Date	End Date	Run Days Lost
05 May, 2000	01 August, 2000	39
14 June, 2001	26 June, 2001	13
13 August, 2001	28 August, 2001	16
26 September, 2001	01 May, 2002	137
06 December, 2004	09 December, 2004	4
08 June, 2005	18 June, 2005	5

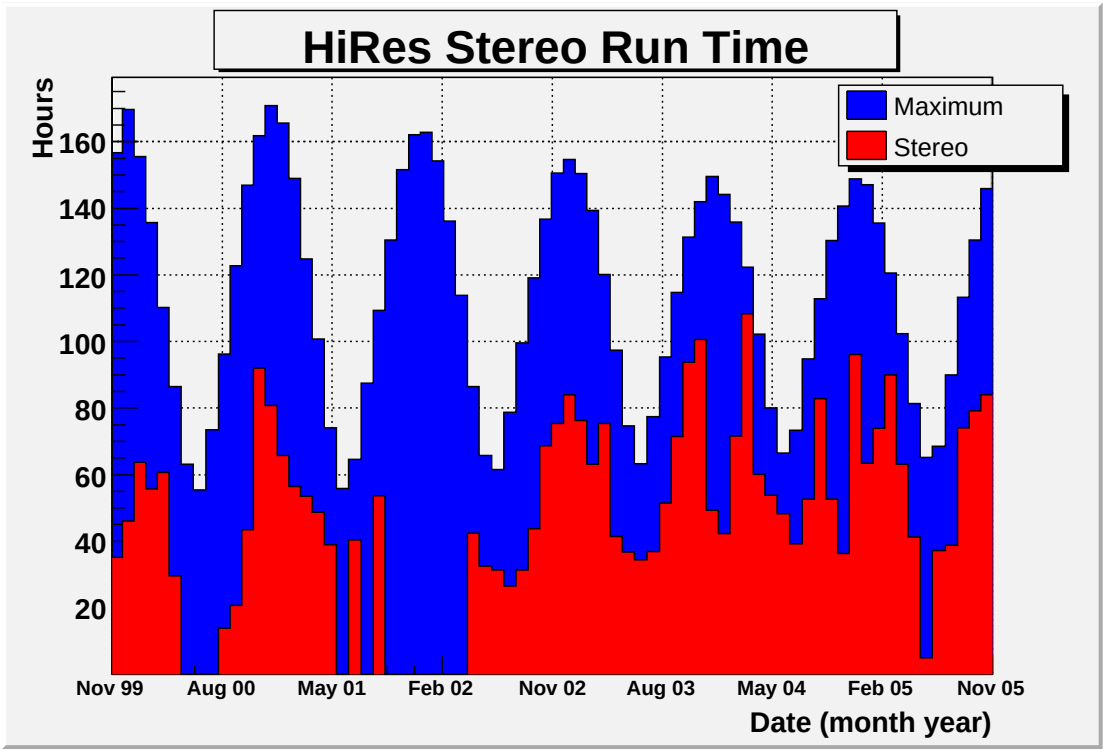

Figure 3.27. The maximum run time and actual stereo collection time for all runs from 1 December, 1999 to 11 November, 2005 (runs #1 to #74). The gaps in stereo collection time are due to Army base restrictions preventing operators from getting to the sites. Poor weather and inoperable equipment are the prime reasons for loss of stereo data during other times.

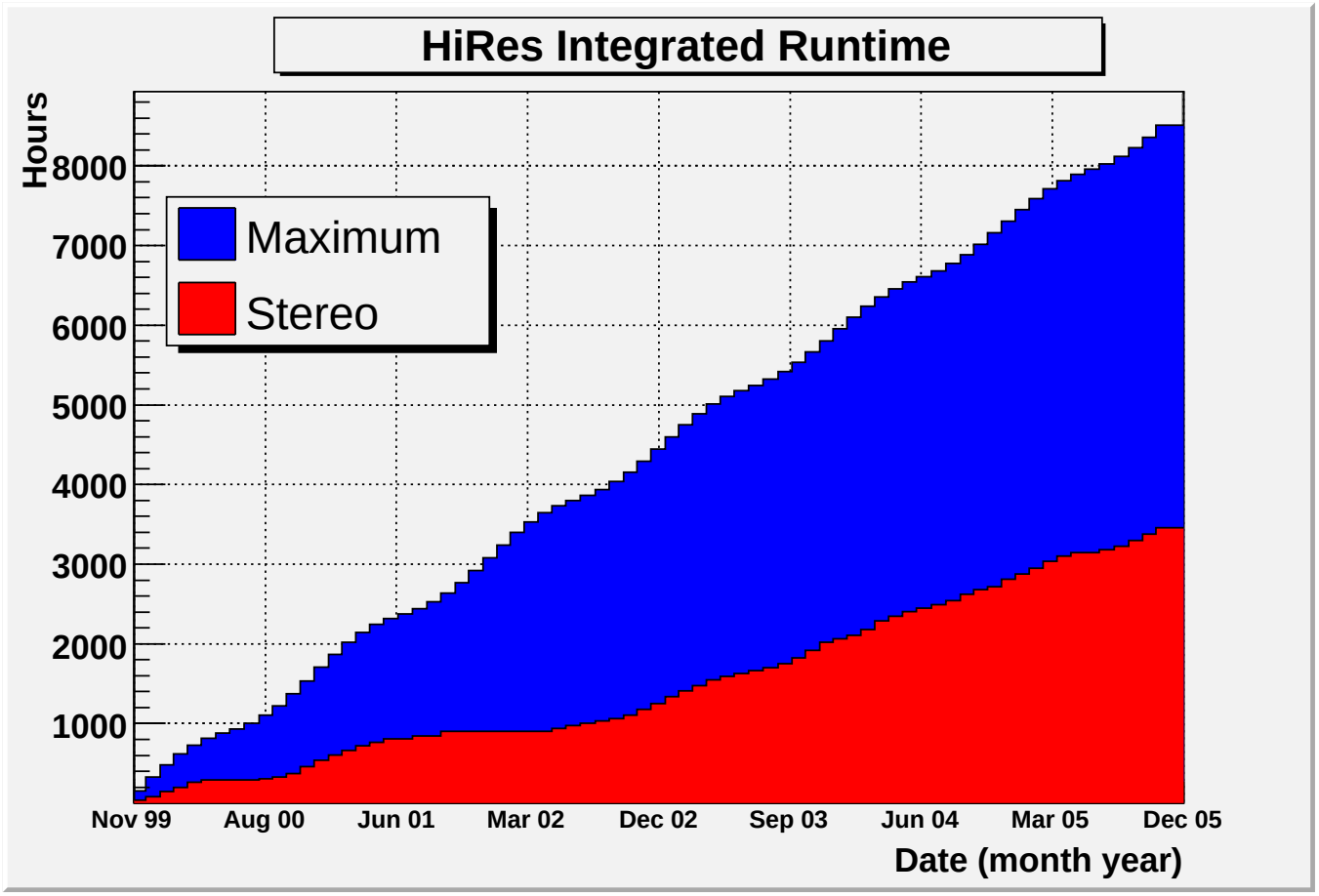

Figure 3.28. The integrated stereo running time. The maximum possible runtime includes periods when operators were restricted from Dugway. This can be seen in the integrated stereo runtime in the flat period between September, 2001 and May, 2002. A minimum 5 hour running rule was in use from May, 2002 to October, 2003 and this is accounted for in the maximum runtime curve.

not move. The IR sensors are housed in aluminum tubes which act as collimators and attached to different cluster stands each pointing in a different direction around the site. The temperatures are read out periodically by the electronics crate of the mirror to which the sensor is attached and so is available through the normal data stream.

A second system uses an infrared camera mounted on a motorized head with a small field of view (3°). The camera is pointed in all azimuthal directions and takes temperature readings of the sky. There are 3000 independent 3° patches of sky scanned with the sensor, which has an integration time of about 0.2 seconds. Each entire scan of the sky takes about 12 minutes. This system has its own dedicated computer control and DACQ. At the beginning of each night's run, operators activate the camera via the DACQ and shut it down at the end of the night. The scanning cloud monitor is less robust than the fixed monitoring system because of mechanical problems. The pan and tilt platform that the camera is attached to has cables that inevitably rub against the platform and break the conductors. So there are many periods when this camera was not fully functional.

The details of the construction of the cloud monitor and images of some clouds that enter the field of view of HiRes1 are found in [45]. Yulia Fedorova performed an analysis using the fixed detectors, described in [33].

Operators are tasked with stepping outside of the central facility no less than once per hour to examine the weather and the optical quality of the night sky. When clouds are present operators must make a decision to shut down the detector if the amount of cloud coverage is too low or too thick (no stars visible through the cloud layer). The steerable lasers, intersite flasher, and the vertical flasher array can also be used to verify that clouds are present in the sky. Figure 3.23 shows a vertical flasher hitting a cloud and Figure 3.29 shows the HiRes2 steerable laser also hitting a cloud.

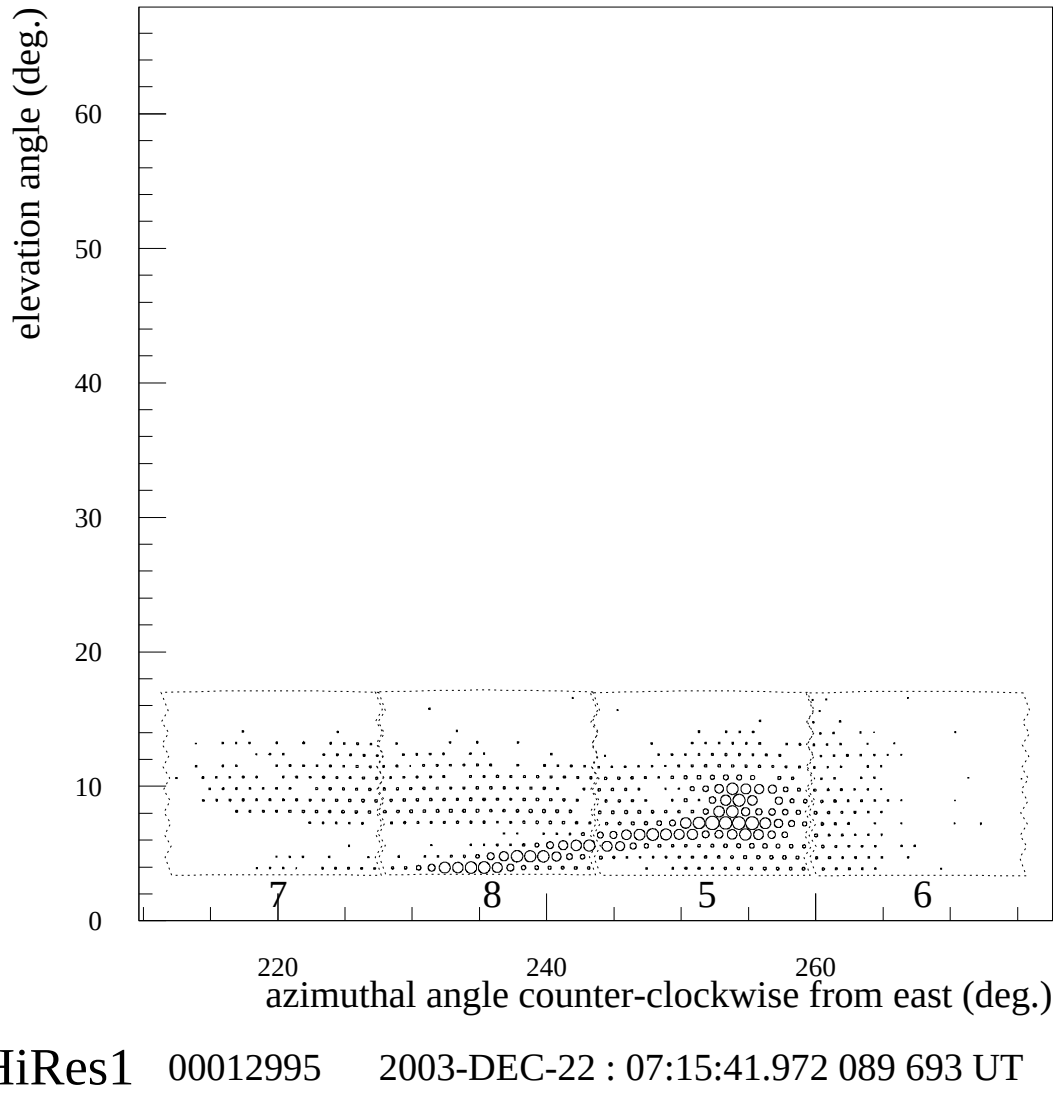

Figure 3.29. A HR2SLS laser shot viewed by HiRes1 that hits a cloud. The mushrooming at the right end of the track indicates scattering in the cloud and the wide dispersal to the left and above the main track is the light reflecting of the cloud.

3.3 Calibration

In addition to normal data collection operations, special runs are made to perform calibration of the detectors. Several types of calibration are performed in an attempt to make an absolute calibration. Each run night prior to and after data collection, a series of calibration procedures are performed that allow us to determine the relative calibration of the detector. By using a standard reference light source, we can anchor the nightly relative calibrations to a well measured light source for the absolute calibration.

Each tube was tested at a phototube calibration facility before being put in place in the field. National Institute of Standards and Technology (NIST) calibrated photodiodes were used to determine the gain and sensitivity of PMTs by illuminating a photodiode with at 325 nm He-Cd laser beam passed through an UV filter. The calibrated photodiode determined the amount of light transmitted from the laser through the filter glass. The tubes were then placed on a translation table and illuminated by the laser beam with a 1 mm spot size. The gain of the phototubes can be expressed as

$$G \propto \mathrm{e}^{\alpha} V^{\beta} \tag{3.2}$$

where V is the voltage applied to the tube, and α and β are constants. The laser beam was used to measure α and β at seven points on each tube. The tube response measured by this process for a typical tube is shown in Figure 3.19. Tubes that had nonuniform response or poor sensitivity were rejected and not placed in the detector. The voltages needed to obtain a given gain were also determined and grouped together with similar tubes to make gain balancing at the detector easier by using the HV zener board and peg board to set high voltages at HiRes1. At HiRes2, gains are set through software by the gain DACs as explained in section 3.1.2.1.

3.3.1 Roving Xenon Flasher

The roving xenon flasher (RXF) is used in the field to occasionally monitor each tube's sensitivity to allow a continual monitoring of their gains. The RXF is a standard candle that can be moved from mirror to mirror in the field and checked

in the laboratory as well. The pulse-to-pulse variation is small (about 0.3 %) and the stability of a night's calibration efforts is about 2 % [37].

During a calibration run when normal data collection is not being performed, the RXF is placed in the center of each mirror using a rod so that it is the same distance from each cluster box. It is then fired at the cluster for some period of time. Longer periods provide better calibration, but the procedure is time consuming when calibrating 21 or 42 mirrors in one night. A typical illumination period is 3 minutes. After the RXF calibration is completed the flasher is brought back to the laboratory and tested against NIST calibrated photodiodes to determine its absolute output. By knowing the number of photons produced by the RXF for each flash, the conversion to number of QDC or FADC counts in each tube can be determined to find their gains. The mean yield of the RXF has been measured to be 12,000 photons per tube flash.

Another method of determining the light flux on a tube is through photoelectron statistics, where the absolute output of the RXF is not needed to determine the N_{pe} in a tube for each RXF flash. Using this method the mean N_{pe} is found from the measured pulse area of each tube.

The statistical parent distribution of photoelectrons, φ, in a single tube over many measurements can be related to the mean and uncertainty of the charge distribution

$$\mu_{\mathrm{QDC}} = G \cdot \varphi \tag{3.3}$$

$$\sigma_{\mathrm{QDC}} = G\sqrt{\alpha\varphi} \tag{3.4}$$

where μ_{QDC} is the mean of the tube's charge distribution, σ_{QDC} is the standard deviation, G is the tube gain, φ is the mean number of photoelectrons of the parent distribution, and α is the excess noise factor. α is the part of the tube signal that is not due to the RXF light and is caused by ambient electronic noise in the tube.

As with any statistical parent distribution the true mean and standard deviation can not be known, only estimated by taking many measurements. In the limit of a

very large number of measurements, the parent distribution can be estimated very well. We estimate φ and its uncertainty using

$$N_{\mathrm{pe}} = \frac{n-3}{n-1}\alpha\frac{\bar{Q}^2}{S^2} - \frac{\alpha}{n},\ n > 3 \tag{3.5}$$

$$\sigma^2_{N_{\mathrm{pe}}} = \frac{2}{n-5}\varphi^2\left[1 + 2(n-2)\left(\frac{\alpha}{n\varphi}\right) + (n-2)\left(\frac{\alpha}{n\varphi}\right)^2\right],\ n > 5 \tag{3.6}$$

where N_{pe} is the estimate for φ, $\sigma^2_{N_{\mathrm{pe}}}$ is the standard deviation, n is the number of measurements (i.e., the number of RXF flashes), $\bar{Q}$ and S are the mean and standard deviation of the charge distribution. For large n the N_{pe} count and standard deviation can be expressed as

$$N_{\mathrm{pe}} \approx \alpha\frac{\bar{Q}^2}{S^2},\ n \gg 3 \tag{3.7}$$

$$\sigma_{N_{\mathrm{pe}}} \approx \frac{2}{n-5}\varphi^2,\ n \gg 5 \tag{3.8}$$

We replace $\bar{Q}$ with μ_{QDC} and S with σ_{QDC} in equation 3.7 to obtain the more familiar form of

$$\mu_{\mathrm{pe}} = \alpha\frac{\bar{Q}^2}{S^2} \tag{3.9}$$

where we now see that we can measure the N_{pe} in a tube by only measuring the mean and width of the charge distribution in a tube [37]. Figure 3.30 shows the measured charge distribution for a single tube during one RXF run. Figure 3.31 shows the gain fit for a single tube during a night when the RXF was fired at varying intensity.

The procedure to determine the excess noise factor, α, for FADC based electronics is described, a similar procedure for sample and hold electronics is also be utilized. α is measured by using a test cluster of 256 PMTs in the lab. The gain of each tube is set to deliver one FADC count for a single photon. Single photon calibration is done using a pulsed LED and neutral density filters to reduce the photon yield down to about one per pulse. The gain of each tube is measured for different voltages, which allow the single photoelectron peak to be clearly seen above pedestal in the pulse width distribution of the PMT's response. The gain of each tube is then determined for the nominal operating voltage of 1050 volts DC,

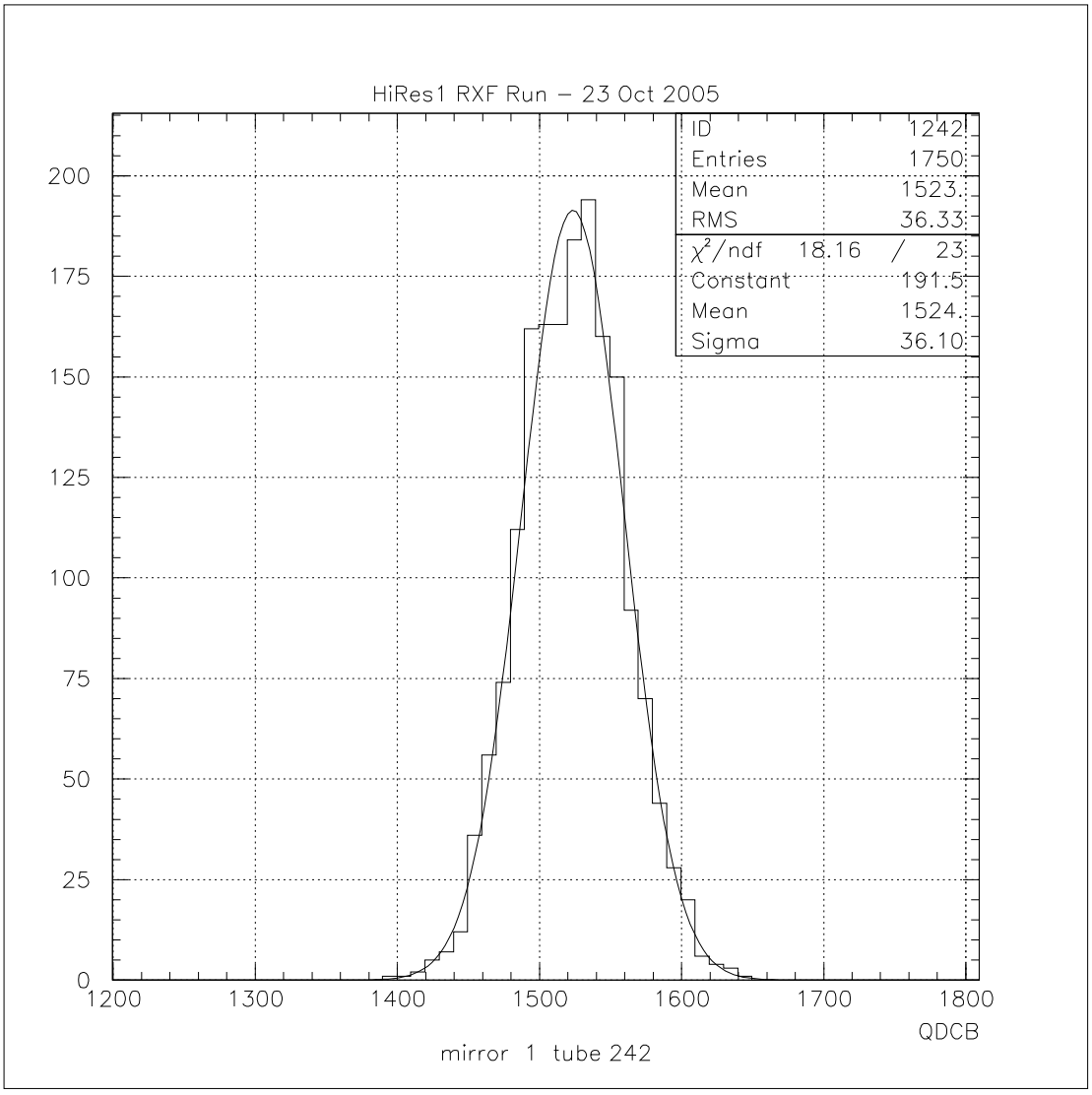

Figure 3.30. The measured channel B QDC charge distribution of HiRes1 mirror 1 for the RXF calibration done on 23 October 2005. This was a long run (20 minutes per mirror) to improve statistics, one reading was taken for each RXF flash which fired at ~ 1.5 Hz.

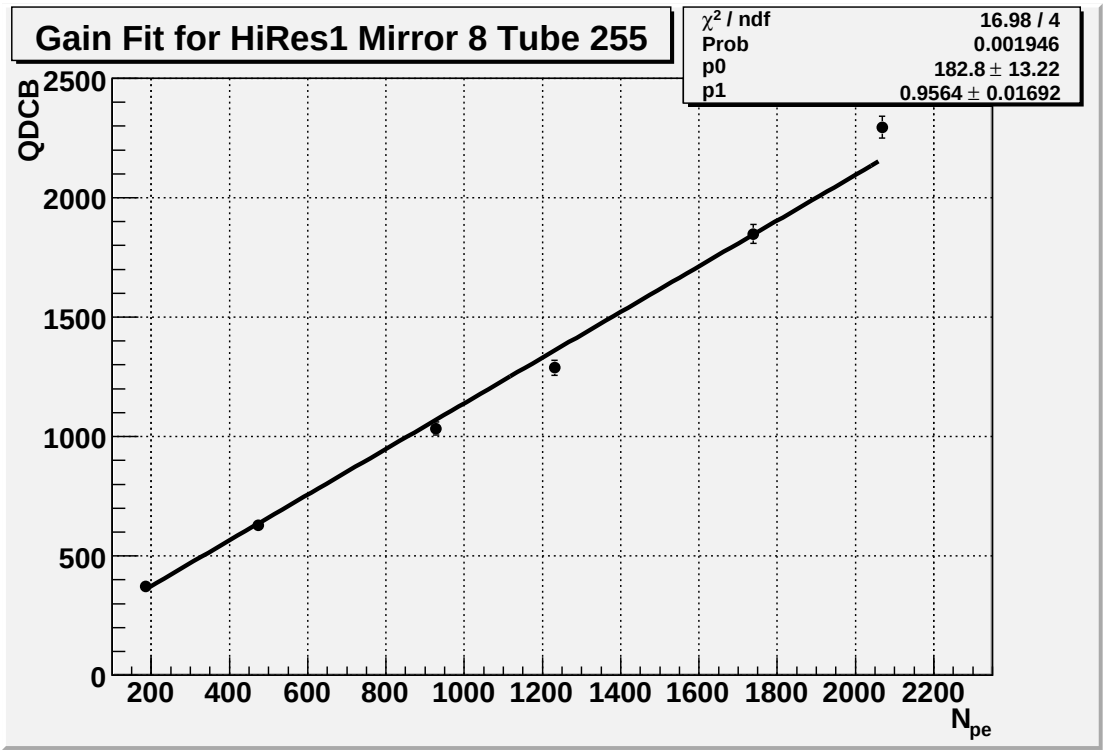

Figure 3.31. The gain fit for a single PMT. On 7 December 2000 RXF shots were fired at a single mirror using several neutral density filters to attenuate the RXF flux. These are not pedestal subtracted QDCs, so the y-intercept is not 0. The slope represents the gain of the tube.

at which a single photon produces one FADC count. Using equation 3.4 we can write the PMT gain as

$$G = \frac{\sigma^2_{\mathrm{QDC}}}{\mu_{\mathrm{QDC}}} \frac{1}{\alpha} \tag{3.10}$$

By observing the mean and width of the charge distribution of all 256 tubes in the test cluster, along with the measured gain, α can be determined. α is measured to be 1.35 for HiRes2 tubes and 1.5 for HiRes1 tubes [6].

Once a RXF calibration is complete, the gains of all tubes are known. A RXF run requires that no data be taken though and takes several hours and several people to complete. Therefore RXF calibrations are only done periodically. To maintain the calibration of the detector on a nightly basis the YAG laser is fired on all mirrors at the start and end of a real data collection night. The YAG laser is also fired in the same way on the night of the RXF run, to determine the response of all tubes relative to the YAG laser, and to tie that response to that evening's RXF calibration. Calibration epochs can be defined by examining the RXF runs used to calibrate the detectors.

A database of the gains for all tubes for every night of running has been created and is used in processing the data and Monte Carlo. Figure 3.32 shows the average nightly gain for all mirrors at both HiRes1 and HiRes2 over the entire period of data collection. Implementation of the RXF data in the processing routines is discussed further in section 4.6.5.4.

3.3.2 Roving Laser

A nitrogen laser that is able to be driven in the desert around the detectors is employed occasionally. This laser is called the roving laser, or ROVSLS, and emits light at 337 nm. This is a manpower and time intensive exercise that can be done while normal data collection operations take place. The N_2 laser is driven to sites selected for their distance to different mirrors and fired vertically. Before each series of shots a radiometer and attenuating filter is placed directly in front of the beam and the laser is fired for some large number of shots to get a good measurement of the laser energy. Then the filter and radiometer are removed and shots are fired

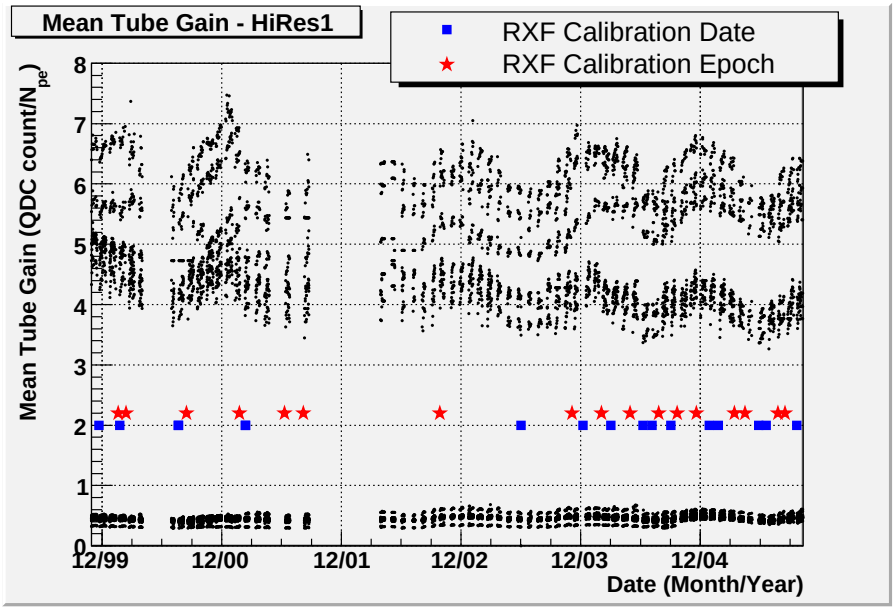

(a) HiRes1

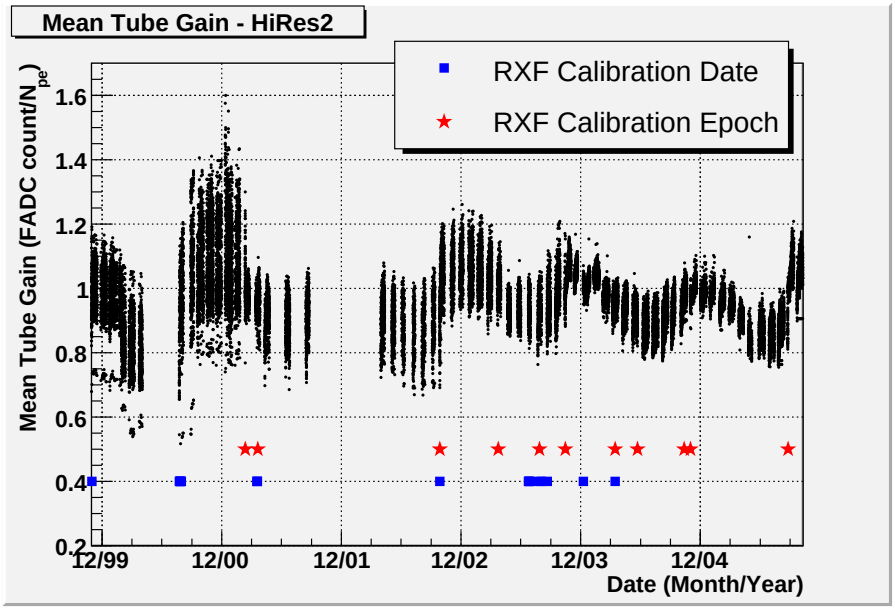

(b) HiRes2

Figure 3.32. The average tube gain for all active HiRes1 (top) and HiRes2 (bottom) mirrors over the period of stereo data collection. The squares denote nights when RXF calibrations were done but not used in the gain database and the stars denote nights of RXF calibrations that were used in the gain database. Note the difference between HiRes1 rev3 (bottom) and rev4 (top) gains. Rev4 electronics have a greater dynamic range and therefore have higher gains.

into the sky. When the shots at a location are complete another series of shots is fired and measured with the radiometer to verify the stability of the laser's energy.

Most ROVSLS runs take the laser to be observed by every mirror at both detectors. This requires about 40 or more different locations where to laser must be driven, set up, energy measured, fired and recorded by the detector, then packed up and moved to the next site. These efforts are done to determine the absolute end-to-end calibration of the detector. For these ROVSLS runs the laser is placed at about 4 km from the mirror observing it, since at this distance the response of the detector is not sensitive to atmospheric conditions that are not purely molecular [58]. Because of security and safety restrictions as well as terrain limitations in traveling around the Dugway Proving Grounds though, the laser can not always be placed at this optimum distance.

CHAPTER 4

ANALYSIS

In this chapter the tools and methods used to analyze and understand data collected from cosmic ray air showers are detailed. An air shower simulation package, CORSIKA, is used to study how air showers are formed in the atmosphere. Using CORSIKA several studies are performed to understand how air showers deposit their energy in the atmosphere, which theoretical model best parameterizes them, and how much energy is lost to processes that cannot be detected by the air fluorescence method. The simulation that accounts for the physics of air showers and response of the HiRes detector, utilizes the Monte Carlo method for shower generation and is described as well. The methods used to process simulated and real cosmic ray data are described also.

4.1 CORSIKA Shower Simulation Package

Understanding how air showers develop in the atmosphere is important to our understanding of how to measure their properties. The CORSIKA (**CO**smic **R**ay **SI**mulations for **KA**skade) shower simulation package is an air shower Monte Carlo program designed to allow detailed study of the properties of extensive air showers with energies up to 10^{20} eV. It allows for the use of several different, well studied hadronic interaction drivers (e.g., DPMJET, neXus, QGSJet, SIBYLL, VENUS, etc.), and different electromagnetic interaction drivers (e.g., EGS4 or NKG derived particle density) [28]. All models (hadronic and electromagnetic) suffer from having to be extrapolated to the highest EAS energies and rapidity ranges, since these energies cannot be produced in the laboratory and beam collider experiments cannot detect particles with low transverse momenta.

For all work done in this analysis the QGSJet (**Q**uark **G**luon **S**tring model with **JET**s) hadronic and the EGS4 (**E**lectron **G**amma **S**hower system version 4) electromagnetic interaction models are used.

4.1.1 QGSJet

The QGSJet driver simulates hadronic interactions where the center of mass energy is greater than 12 GeV. If a hadronic secondary particle falls below this level, CORSIKA uses GHEISHA or the ISOBAR model to track it. For this analysis, GHEISHA is used for the low energy hadronic interactions.

QGSJet utilizes the Gribov-Regge theory which theorizes that high energy hadron-hadron scattering as a Pomeron exchange process. The topological expansion of QCD represents a Pomeron as a cylinder of gluons and quarks loops. Under the Pomeron model, particle production in inelastic collisions is done by cutting the Pomerons and forming strings. QGSJet simulates hadronic interactions by supercritical Pomeron exchange of the soft hadronic interactions. For the highest energy interactions, minijets are also simulated [28].

4.1.2 EGS4

EGS4 was developed at SLAC to simulate electromagnetic cascades in various geometries and energies up to a few thousand GeV. Its popularity grew beyond the confines of SLAC and was used by other experimental groups as well and therefore became a well understood and trusted simulation package. It has been adopted for use in CORSIKA for treatment of the electromagnetic component of air showers. EGS4 can simulate the transport of electrons and photons in any element or compound by providing cross section tables for elements 1 through 100 via its PEGS4 package. EGS4 directly simulates many physics processes including bremsstrahlung production, positron annihilation in flight and at rest, Molière multiple scattering, Møller and Bhaba scattering, Compton scattering, and pair production as well as others. A complete description of the EGS4 code system can be found in [44].

4.2 CORSIKA Shower Library

The shower libraries used by the Monte Carlo are generated by the CORSIKA air shower simulation package using the QGSJET hadronic model driver and EGS4 electromagnetic transport system. Several hundred showers for most 0.1 $\log_{10}(E/\mathrm{eV})$ energy bins between 10^{17} and $10^{20.5}$ eV were generated and are stored in the library. Table 4.1 shows the number of showers generated for each energy bin for iron and proton primaries. For all of the work done for the energy spectrum CORSIKA version 6.003 and QGSJet01 are used.

Showers with energies between the energy bins shown in Table 4.1 can be provided to the Monte Carlo by interpolating shower parameters between the energy bins. The change in N_{max} as a function of energy for CORSIKA showers was measured to determine the interpolation scale factor for each species of primary in the shower library. When a shower with an energy that is not equal to one of the energy bins in the library is requested, it is scaled by this factor. All relevant shower parameters, including x_{max}, σ_{s}, and τ_0, are accordingly scaled to any energy desired within the minimum and maximum energies contained in the shower library.

The shower library consists of many ASCII text files containing the raw CORSIKA shower profiles for showers generated at the energies listed in Table 4.1. The contents of each file are:

1. A header describing the primary particle type, primary particle energy, zenith angle of the shower axis, and thinning weight.
2. 205 slant depths in g/cm^2 at which each shower is sampled.
3. The remainder of the file contains shower profiles providing the number of charged particles at each sampled depth. Each profile entry contains:
   a. x_{max} of the shower.
   b. Smoothed N_{max}.
   c. Unsmoothed N_{max}.
   d. 205 measurements of the number of charged particles.

All showers are generated with zenith angle of 45° and sampled at 5 g/cm^2 vertical

Table 4.1. Number of CORSIKA/QGSJet showers in the hires_soft shower library by primary energy in eV.

$\log_{10}(E)$	proton	iron	$\log_{10}(E)$	proton	iron
17.0	792	800	18.8	500	0
17.1	500	0	18.9	500	0
17.2	500	0	19.0	850	800
17.3	500	0	19.1	500	0
17.4	500	0	19.2	500	0
17.5	800	603	19.3	500	0
17.6	500	0	19.4	500	0
17.7	800	773	19.5	1768	1760
17.8	500	0	19.6	500	0
17.9	500	0	19.7	699	800
18.0	800	800	19.8	398	0
18.1	500	0	19.9	680	0
18.2	0	0	20.0	920	800
18.3	1000	0	20.1	480	0
18.4	500	0	20.2	0	0
18.5	1580	2000	20.3	340	0
18.6	500	0	20.4	280	0
18.7	873	800	20.5	286	740
			total	21846	10676

depths, therefore the sampled slant depths are in steps of $5\sqrt{2} = 7.07$ g/cm^2, from 0 g/cm^2 (top of the atmosphere) to 1450 g/cm^2, providing 205 sampling points. Each shower is subjected to a smoothing procedure to reduce fluctuations caused by thinning, noticeable only for the low energy showers. The $x_{\max}$ and $N_{\max}$ of each shower are determined by interpolation of the smoothed shower profile. The unsmoothed $N_{\max}$ is stored as well.

When the Monte Carlo requests a shower in the subroutine hr_shower, it first calls a subroutine called bkv_corsika_init to initialize the shower library interface by loading in the number of showers available for each energy bin and then randomly selecting a shower from the energy bin closest to the requested primary particle energy and storing it in memory. The subroutine uses an empirically measured elongation rate to interpolate and scale the shower on the fly to the desired energy and returns the measured parameters that characterize the shower: $N_{\max}$, $x_{\max}$, $\sigma_{\rm s}$, τ_0. Another subroutine, bkv_shower, is called by the user to return the number of shower particles at any requested depth. When bkv_corsika_init is called again a new shower is loaded into memory. Further details about the Monte Carlo routines are given in section 4.6.

As discussed in section 4.4, there is an inherit energy loss in CORSIKA showers due to the energy threshold that limits how low a particle can be tracked. To correct for the artificial energy loss, the shower energy provided by the shower library can be understood as

$$\begin{aligned} E_2 &= E_1 + 0.11 E_0 \\ &= \left(1 + 0.11 \frac{E_0}{E_1}\right) E_1 \end{aligned} \tag{4.1}$$

where E_0 is the known energy of the primary particle, E_1 is the energy of the shower as it is stored in the shower library (i.e., the energy of the shower with artificial energy losses due to the CORSIKA threshold cuts), and E_2 is the energy of the shower corrected for artificial energy losses imposed by CORSIKA, but lacking the electromagnetic fraction correction. So E_2 is the *expected* energy of a shower that is returned from the shower library. If it is integrated using equation 4.14, it will

still fall short of the primary particle energy by a factor precisely equal to the missing energy of the electromagnetic fraction. To find the ratio of E_0/E_1 over 200000 showers were integrated to find E_1. This was done by using each shower in the shower library exactly once and sampling all primary particle energies from 10^{17} eV to $10^{20.5}$ eV in steps of 0.01 $\log_{10}(E/\text{eV})$. This forced the interpolation of showers as well as using the "raw" shower profiles stored in the library. Figure 4.1 shows the ratio of E_1/E_0 for the showers in this energy range. The result is energy dependent but the dependence is small, so the mean of E_1/E_0 was fitted to a constant and found to be 0.7433. This sets the correction factor of $1 + 0.11E_0/E_1$ in equation 4.1 to be 1.1480.

The shower library routine bkv_corsika_init is modified to scale the number of shower particles and $N_{\max}$ by multiplying these values by 1.1480 to correct for the artificial losses imposed by the CORSIKA energy threshold cuts. Figure 4.2 shows the effect of the correction for a single shower. The upper shower profile has been subjected to the correction in equation 4.1. If it were integrated for the energy, it would return E_2. The lower profile is the "raw" shower profile as it is stored in the shower library and if integrated would give E_1. E_0 for this shower is 10^{18} eV.

The result of this correction is tested on all showers in the library and shown in Figure 4.3. The energy pull of $(E_1' - E_0)/E_0$ is shown in the distribution on the left and the energy pull of $(E_2' - E_0)/E_0$ is shown on the right, where E_1' and E_2' have the same meaning as in equation 4.1, but are corrected for electromagnetic fraction missing energy. The expected value of the pull should be 0, indicating that the integrated shower energy returns the energy of the primary particle. This is only true for the distribution on the right which is corrected for the CORSIKA threshold cuts using equation 4.1.

In section 4.5 it will be seen that some of the dE/dx used in different analyses are approximately 10% higher than what is currently used. The analyses that use inflated dE/dx do not correct showers for the energy lost due to the CORSIKA threshold cut and instead compensate for the lost energy by using a large value of α. Although the proper energy for a shower is returned when integrated, this

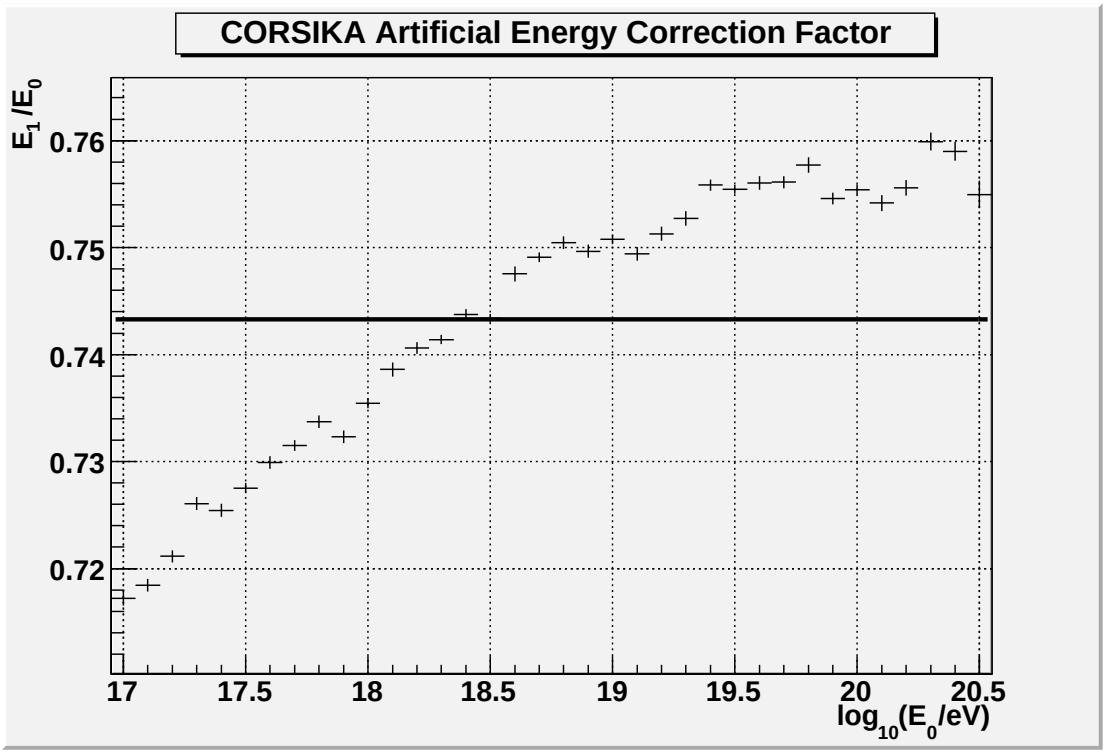

Figure 4.1. The ratio of the raw CORSIKA shower energy to the primary particle energy of many showers read from the shower library. The solid line is the fit to a constant and its value is 0.7433.

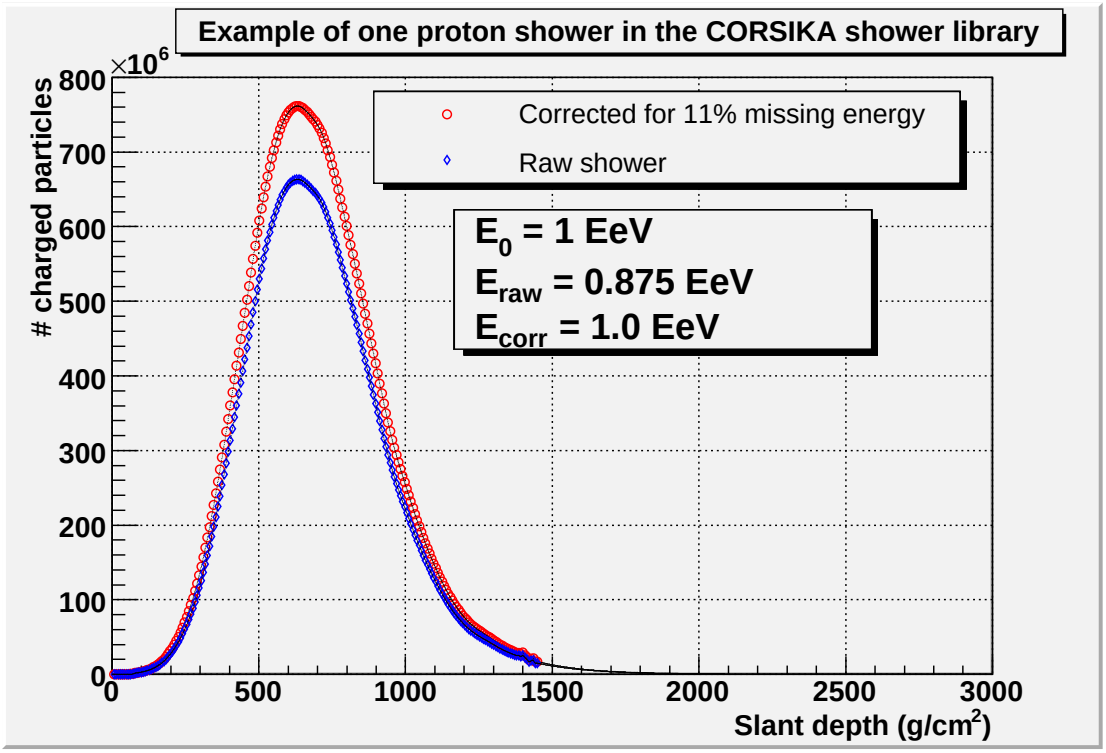

Figure 4.2. Example of one proton shower in the CORSIKA shower library. This is the first shower in the 10^{18} eV shower file. The lower profile is the raw shower as directly read out of the file. As discussed in section 4.4, this profile suffers from the 11% missing energy caused by the CORSIKA threshold cuts. The upper profile has been corrected for the missing 11% energy. The markers indicate the number of charged particles for the 205 points sampled in 7.07 g/cm^2 steps contained in the shower library. The "lines" overlaid on the markers are actually interpolated *points* sampled at 1 g/cm^2 steps. Notice that the interpolated points are well behaved and follow along as expected with the discrete points read out of the shower library.

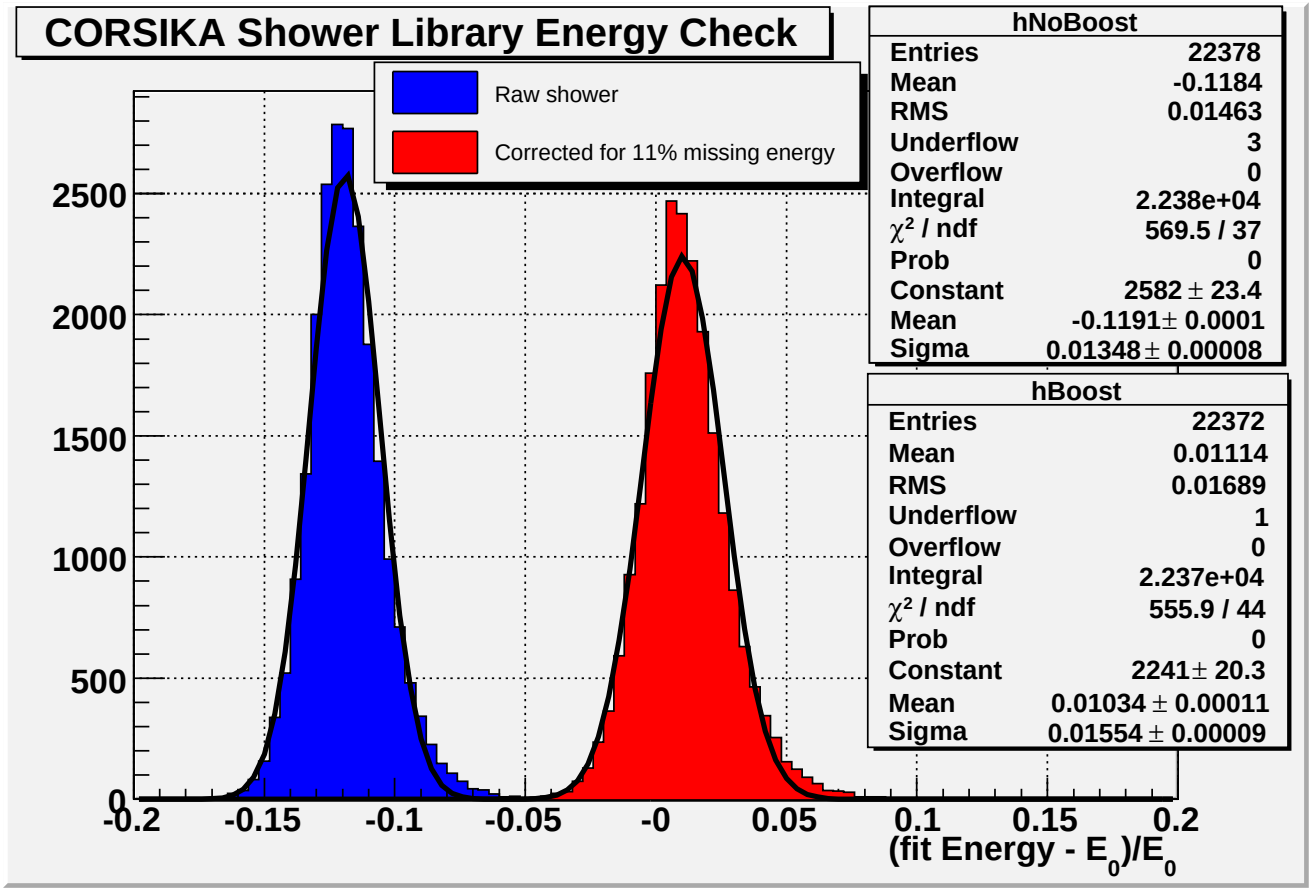

Figure 4.3. The energy pull of the proton induced showers in the CORSIKA shower library. The effect of the 11% artificial energy loss is shown by the difference in the means between the two distributions. For each shower the profile was read out from the library and fitted to a Gaussian-in-age function to determine the shower parameters. The energy of each shower was computed using equation 4.14 and compared to the energy of the primary particle, giving the pull. It can be seen that if the 11% correction is not made, the energy of the showers is wrong by that amount.

approach is flawed. By not properly correcting the CORSIKA showers for lost electrons, the Monte Carlo trigger and aperture can be affected since less light is attributed to a shower.

To ensure that the "boosting" procedure described above does not adversely affect the showers that are extracted from the library, all proton showers were subjected to the procedure and fitted using the Gaussian-in-age functional form. The showers in the library can be considered perfectly measured showers over almost the entire profile. Each observation point was assigned an error of $\sqrt{wN}$, where w is the CORSIKA thinning weight used in generation of the library (10^6) and N is the number of shower particles at the observed depth. The "pull" of each shower parameter was determined by creating distributions of the difference of fitted parameters and measured parameters as returned by bkv_corsika_init. Figure 4.4 shows that the bias between fitting and measuring $N_{\max}$ is small, around 1%. Additionally practically no change is discerned between unboosted and boosted showers.

Figure 4.5 shows a similar result for $x_{\max}$ in that no change occurs from the boosting procedure. It is worth noting though that there is a bias in the Gaussian-in-age fitting of the CORSIKA showers. Both boosted and unboosted showers have a -11 g/cm^2 shift in the difference between fitted and measured $x_{\max}$. Figure 4.6 shows that $\sigma_{\rm s}$ is also stable under the boosting procedure and the bias in this parameter between fitting and measuring is very small.

Figure 4.7 shows the distribution of measured $N_{\max}$ obtained from the shower library for all energies in steps of $0.01\log_{10}(E/\mathrm{eV})$. Note that only the values of $N_{\max}$ in the energy bins shown in Table 4.1 are not scaled by interpolation. All other energy bins though have their $N_{\max}$ scaled. Figure 4.8 shows the elongation rate of the CORSIKA showers. The same procedure of requesting showers in all energy bins $0.01\log_{10}(E/\mathrm{eV})$ wide was used to examine the range of $x_{\max}$ returned by the shower library routines. Figure 4.9 shows the measured $\sigma_{\rm s}$ as a function of energy for all CORSIKA proton showers in the library.

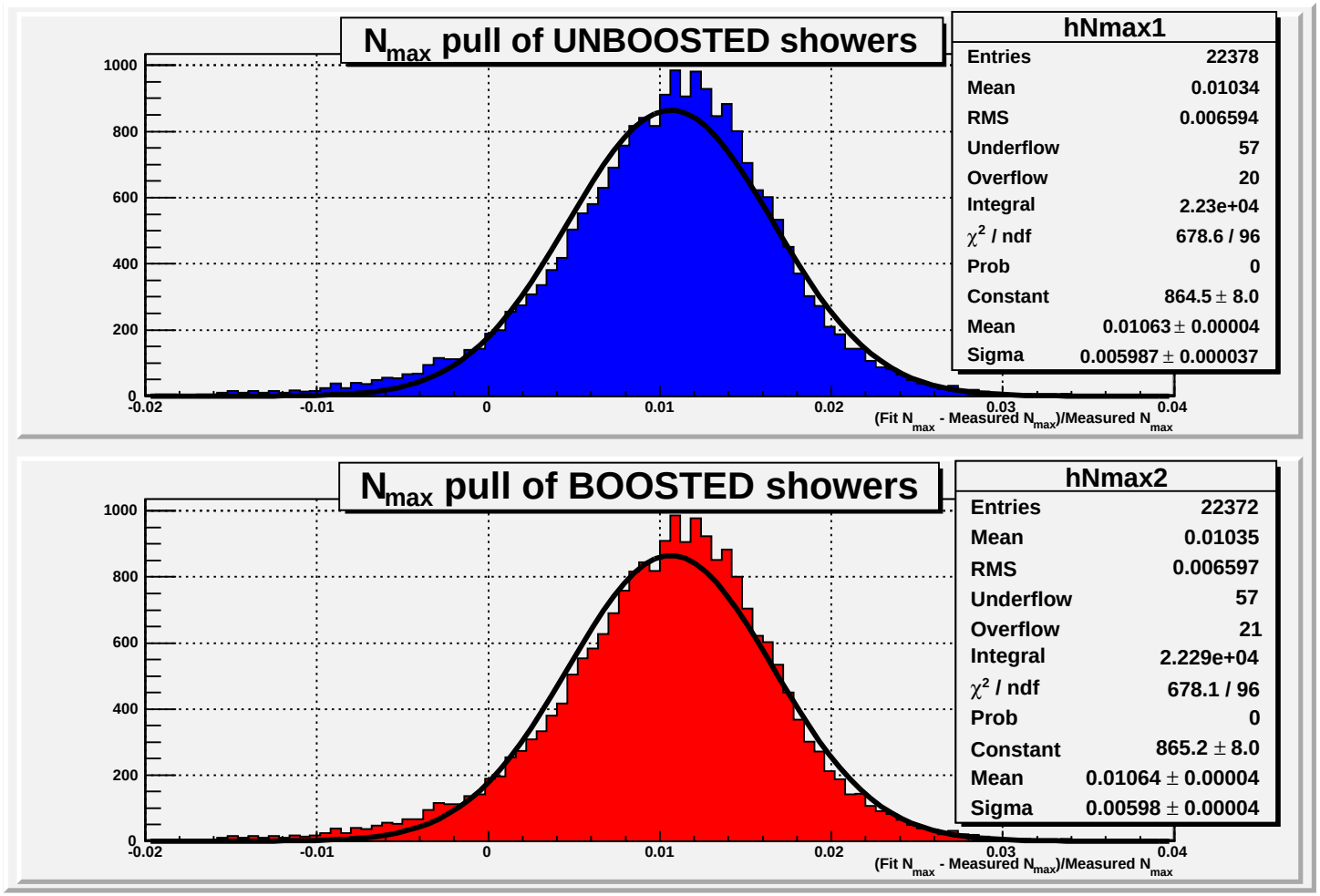

Figure 4.4. The $N_{\max}$ pull distribution of the shower library. Note that showers corrected by increasing the number of shower particles does not change the pull of fitted $N_{\max}$ to measured $N_{\max}$. This is for all proton showers contained in the library.

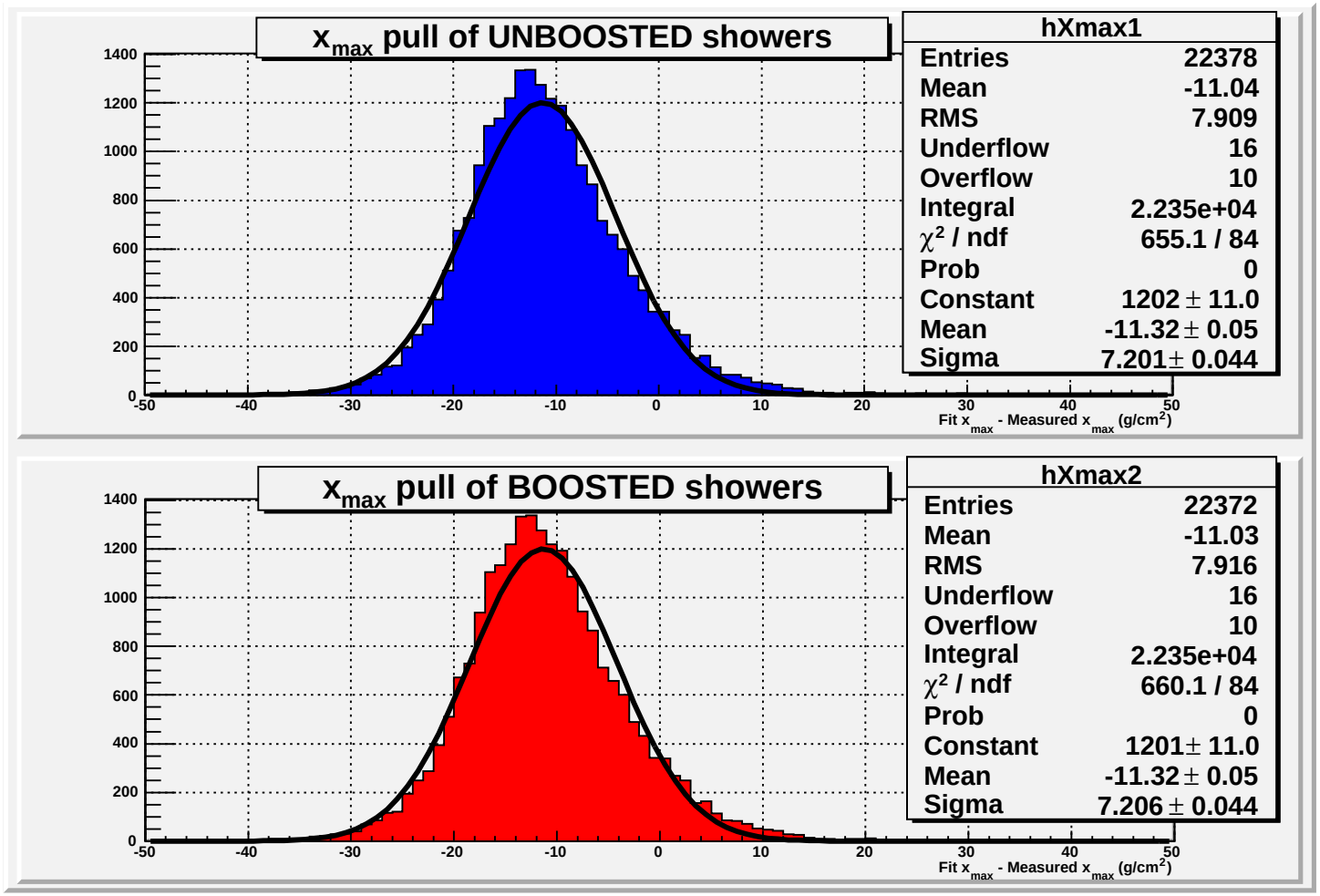

Figure 4.5. The $x_{\max}$ pull distribution of the shower library. Note that showers corrected by increasing the number of shower particles does not change the pull of fitted $x_{\max}$ to measured $x_{\max}$. This is for all proton showers contained in the library.

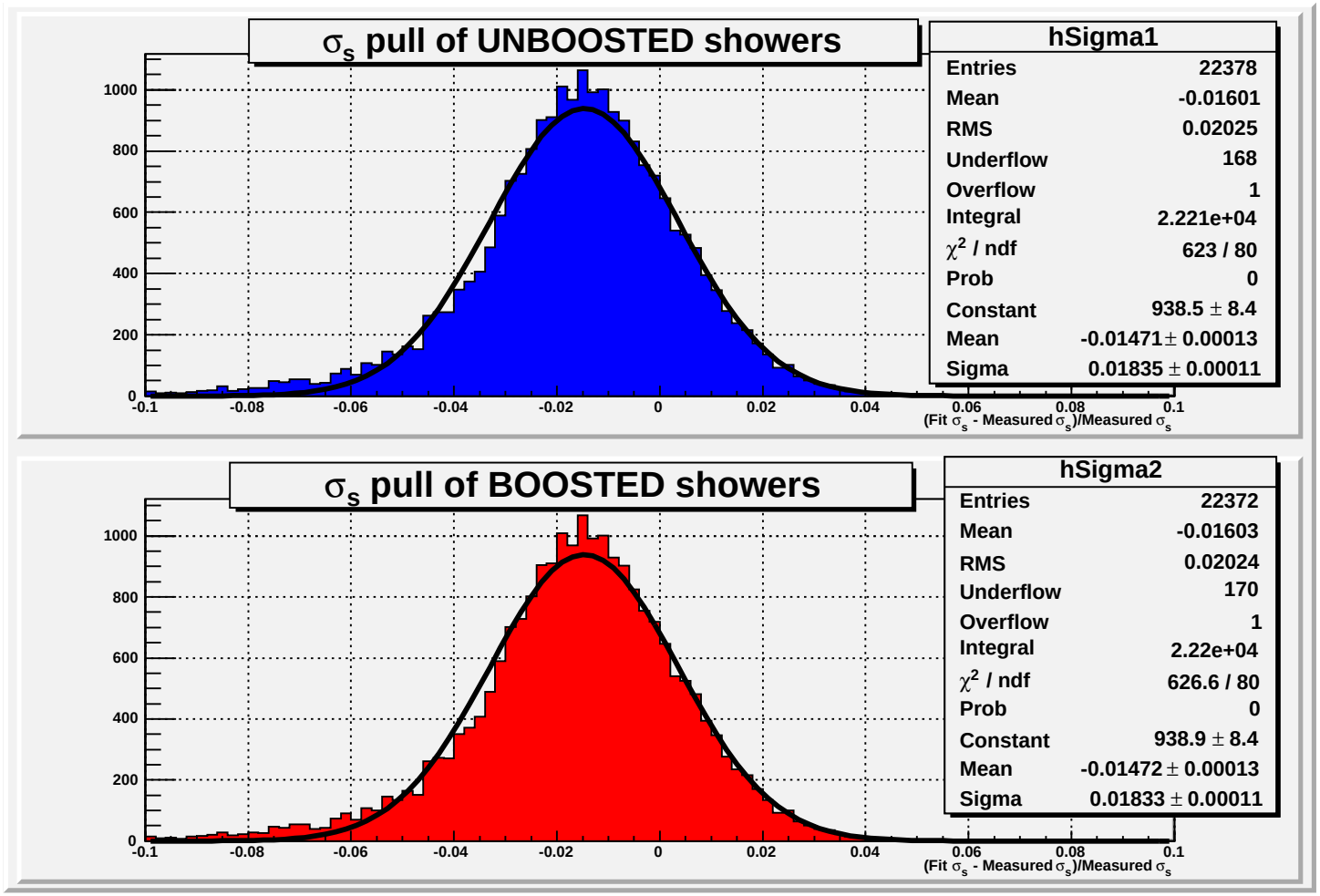

Figure 4.6. The σ_s pull distribution of the shower library. Note that showers corrected by increasing the number of shower particles does not change the pull of fitted σ_s to measured σ_s. This is for all proton showers contained in the library.

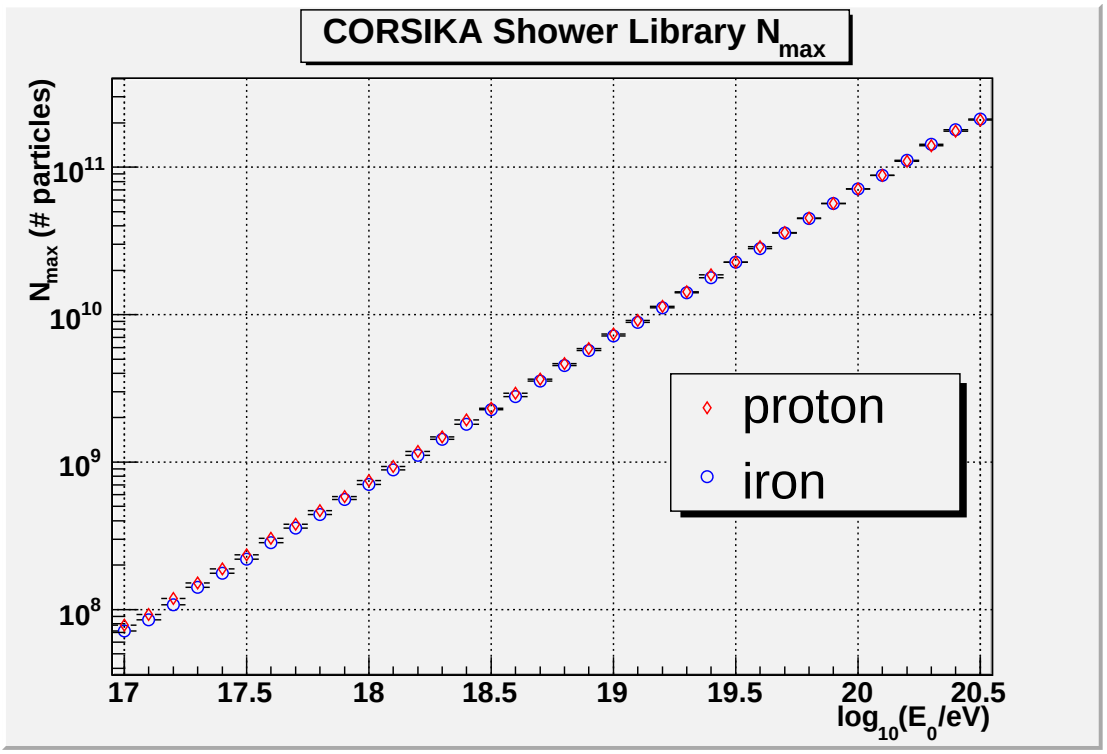

Figure 4.7. The measured $N_{\max}$ of the proton and iron showers contained in the CORSIKA shower library used by the Monte Carlo. Because of the large number of shower particles in each bin, errors are extremely small.

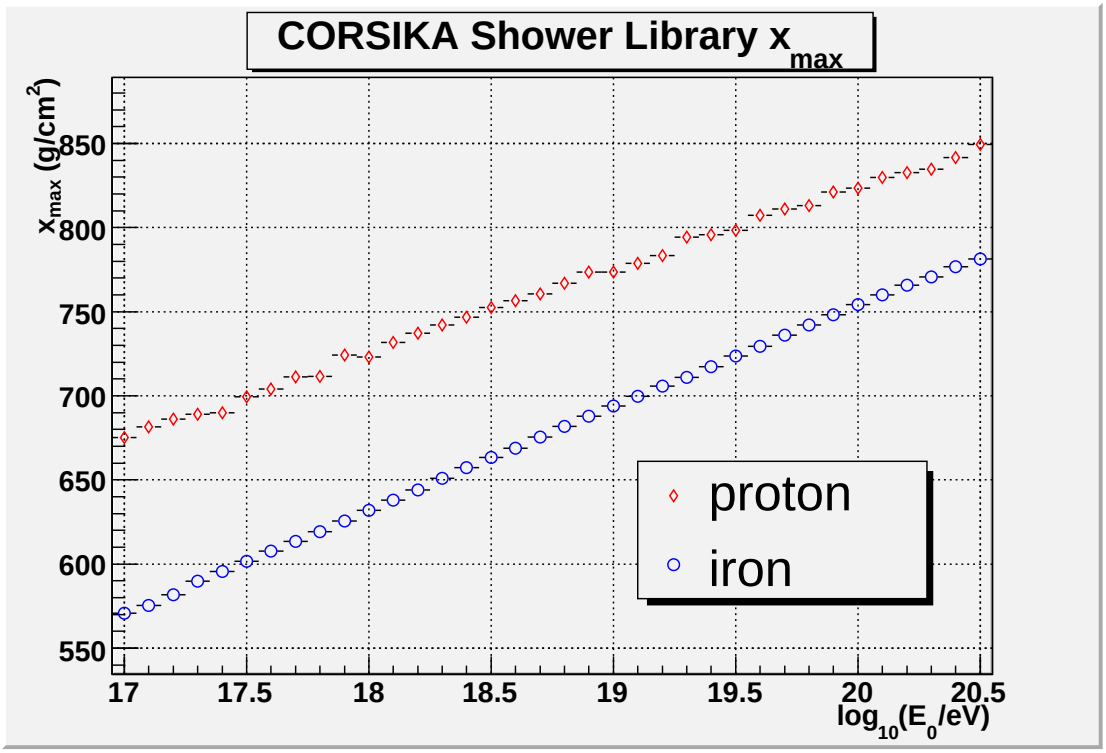

Figure 4.8. The measured $x_{\max}$ of the proton and iron showers contained in the CORSIKA shower library used by the Monte Carlo. This is the "natural" elongation rate of the showers generated by CORSIKA. A fit to the proton and iron distributions finds the elongation rate to be 49.5 $(\mathrm{g/cm^2})/\log_{10}(E_0/\mathrm{eV})$ and 60.9 $(\mathrm{g/cm^2})/\log_{10}(E_0/\mathrm{eV})$ respectively.

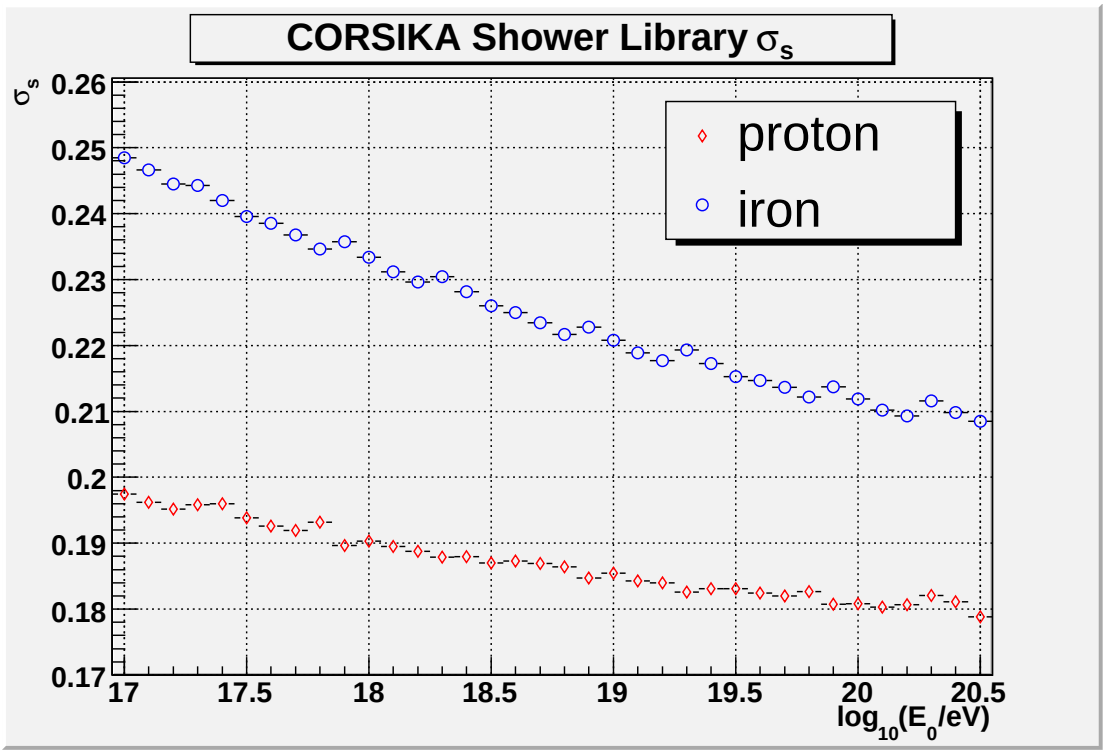

Figure 4.9. The measured σ_s of the proton showers contained in the CORSIKA shower library used by the Monte Carlo.

4.3 Shower Parameterization

The great benefit of the fluorescence method of observing showers is that the development of a shower is measured over a large range of depths as opposed to one single measurement taken by ground arrays. Some parts of a shower may not be visible to a fluorescence detector though due to atmospheric anomalies or detector acceptance. For this reason the charged particle profile as a function of depth of a shower is fit to a functional form to allow extrapolation of the profile to parts of the shower not directly measured. Additionally, as equation 4.14 shows, the energy measurement of a shower requires integration to infinity, or in practice to very large depths where the shower may even have entered the ground. Two parametric equations are available to describe showers: Gaisser-Hillas and Gaussian-in-age.

The Gaisser-Hillas function is expressed as

$$N(x) = N_{\max}\left(\frac{x - x_0}{x_{\max} - x_o}\right)^{(x_{\max}-x_0)/\lambda} \exp\left(\frac{x_{\max} - x}{\lambda}\right) \tag{4.2}$$

where $N_{\max}$ is the number of charged particles at shower maximum, x_0 is the depth of first interaction, $x_{\max}$ is the depth of shower maximum, and λ is a scale constant, also referred to as the proton interaction length for air showers, and is set to 70 g/cm^2. It has been shown that the parameters of this function are correlated and x_0 is actually physically meaningless since fitting allows it to take on negative values. Another disadvantage of using x_0 is that it is not observed. It has also been shown that $N_{\max}$ and λ are correlated and that λ is dependent on the primary mass and energy [53].

A simpler functional form is utilized that exploits the symmetry of a shower profile when plotted as a function of shower age

$$s(x) = \frac{3x}{x + 2x_{\max}} \tag{4.3}$$

where s is the age of the shower at a given depth x. Using this definition $s = 0$ at the start of shower development, $s = 1$ at shower maximum, and $s \to 3$ as $x \to \infty$. Following the prescription of applying the Gaussian-in-age profile as detailed in [53], the point of first interaction, also denoted by x_0, is here implicitly set to 0. As

stated previously, x_0 can not be measured experimentally by the HiRes detector. In section 4.4, when using CORSIKA to determine the energy loss of electrons in an air shower, a modified form of equation 4.3 is used to determine the *pseudoage* of a shower. The pseudoage is used only for the determination of dE/dx through the CORSIKA study. All shower profile fitting in the reconstruction uses the definition of age given by equation 4.3.

The Gaussian-in-age profile is expressed as

$$N(s) = N_{\max} \exp\left(-\frac{1}{2}\left(\frac{s-1}{\sigma_{\rm s}}\right)^2\right) \tag{4.4}$$

where $\sigma_{\rm s}$ is a parameter that measures the shower width. Utilizing equation 4.3, equation 4.4 can be recast in terms of shower depth resulting in

$$N(x) = N_{\max} \exp\left(-\frac{2}{\sigma_{\rm s}^2}\left(\frac{x-x_{\max}}{x+2x_{\max}}\right)^2\right) \tag{4.5}$$

Notice that equation 4.4 is independent of the shower starting point x_0 and is a function of three parameters instead of four, thereby simplifying the shower profile model. Figure 4.10 shows equations 4.4 and 4.5 plotted for a shower with average $\sigma_{\rm s}$ and $x_{\max}$. As previously noted that shower is symmetric when plotted as a function of shower age.

The average shower profile of data, CORSIKA proton showers, and CORSIKA iron showers is shown in Figure 4.11. The data points are fitted using both the Gaisser-Hillas and the Gaussian-in-age functions. Both describe the shower profile well and very little deviation can be seen between the two fitting methods in the figure. Nevertheless, the lack of correlation between parameters and the simpler functional form of the Gaussian-in-age equation is preferred and used in this analysis for all shower fitting.

A potential problem with both fitting methods is that they fail to fit showers well in the tails far from $x_{\max}$. The difference between the number of shower particles produced by CORSIKA and the number predicted by the Gaisser-Hillas and Gaussian-in-age profiles has been shown to deviate significantly in the tails of the profile, thereby requiring a cut on shower age or relative size of shower at a

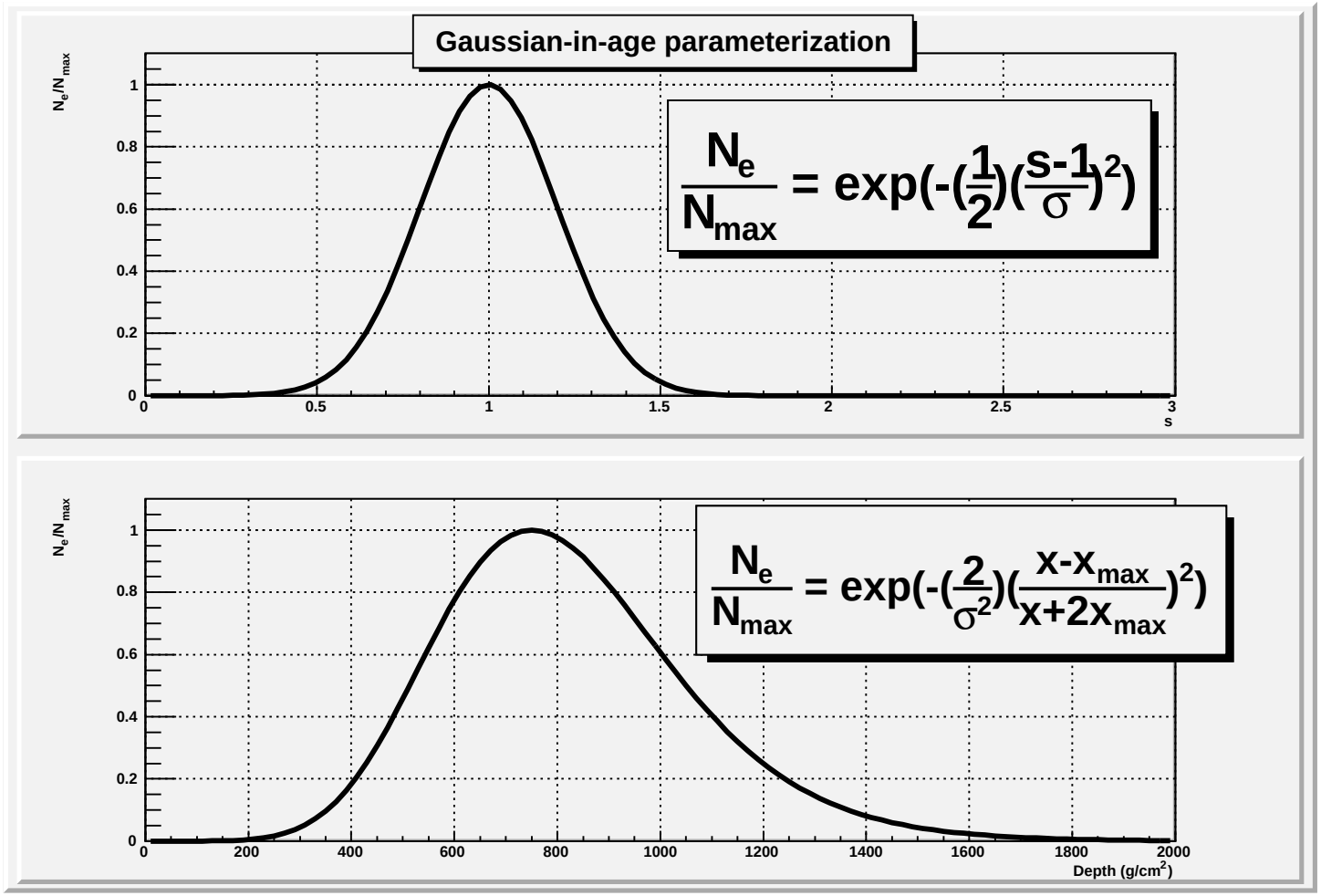

Figure 4.10. The functional form of the Gaussian-in-age shower profile. The top figure is plotted as a function of shower age and it can be seen that the shower profile is symmetric. The bottom figure is plotted as a function of shower depth by using equation 4.5. It can be seen that the shower is not symmetric about $x_{\max}$ when plotted in this way. σ_s of 0.2 and $x_{\max}$ of 750 g/cm^2 are used.

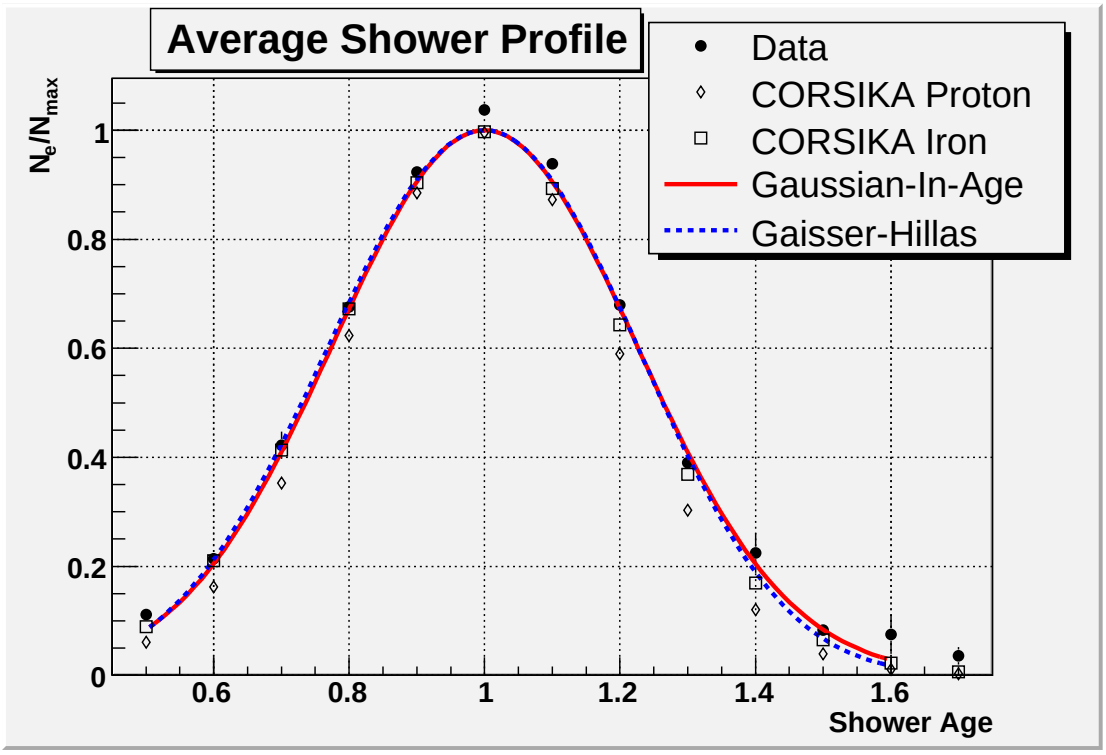

Figure 4.11. The average profile of showers and comparison of Gaussian-in-age and Gaisser-Hillas fits to the data. The data points are the average of all showers examined in this analysis. The contents of the CORSIKA shower library are also shown. Note that the profile has been normalized to shower $N_{\max}$.

given depth to best fit showers [53]. The difference between CORSIKA generated shower sizes and the sizes predicted by both parametric equations are shown in Figure 4.12. Several thousand Monte Carlo showers from the 80/20 mix set with energies between 10^{18} and $10^{18.01}$ are shown. It can be seen that the Gaussian-in-age prediction is more stable to lower shower ages. The range of ages where the predictions agree well is in accord with what is observed by the HiRes observatory. The solution to fitting showers accurately is to use only shower observation points that are measured to contain some fraction of $N_{\max}$ particles. The recommended fraction is 1% of $N_{\max}$ by C. Song [53].

4.4 Energy Loss

The energy loss, dE/dx, of charged particles as they pass through the atmosphere is of great importance to our understanding of the energy of cosmic ray induced air showers. We use dE/dx in two ways: to determine the scintillation yield of electrons in the shower and to determine the calorimetric energy deposited by the electrons into the atmosphere.

Our understanding of dE/dx is derived from the CORSIKA shower simulation package [27], which bases its implementation of electron energy loss on the EGS4 electron transport simulation [44]. The energy loss study that was done for this work closely followed the same procedure as described in [54].

The air fluorescence method of observing showers determines the energy of the primary particle by integrating the energy deposit over the shower profile,

$$E_{\mathrm{cal}} = \frac{E_{\mathrm{c}}}{X_0} \int_0^{\infty} N_{\mathrm{e}}(x) dx \tag{4.6}$$

where E_{cal} is the calorimetric energy of the primary particle, E_{c} is the electron critical energy in air, X_0 is the electron radiation length in air, and $N_{\mathrm{e}}(x)$ is the number of electrons at depth x.

There is a definitional problem with E_{c} though as shown by the the Particle Data Group [7]. Some define the electron critical energy as the energy at which the bremsstrahlung and ionization loss rates are equal [13], while others define it to be the energy at which ionization loss per radiation length and the electron energy

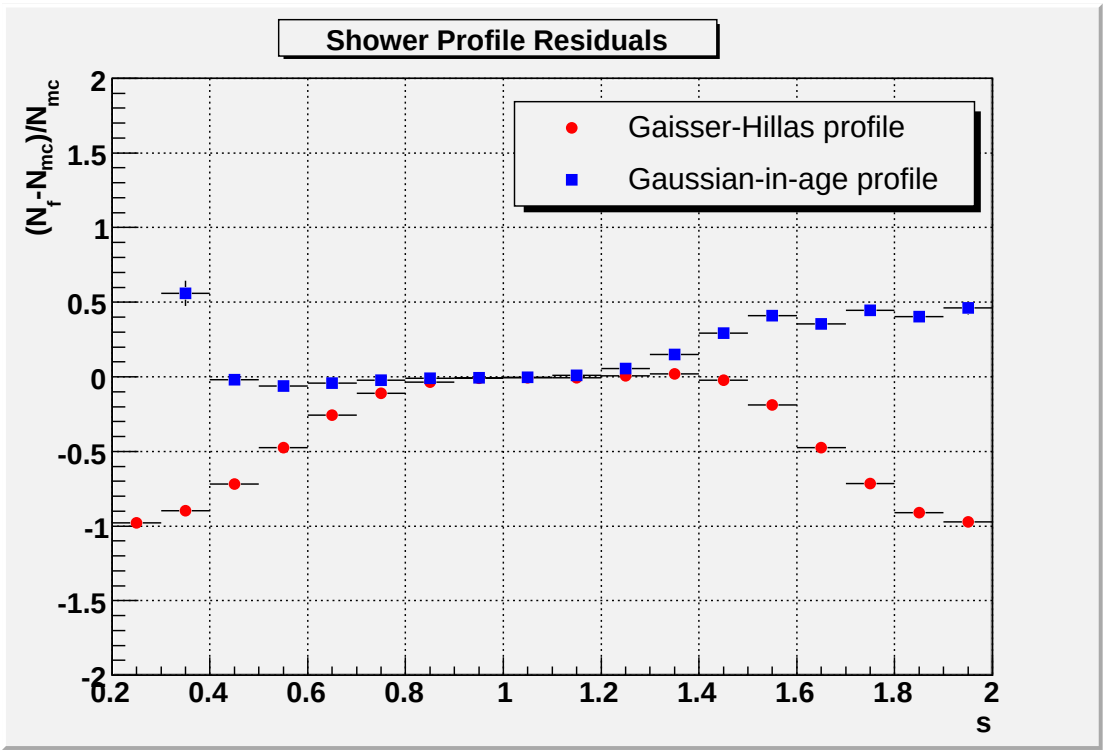

Figure 4.12. The residuals of CORSIKA generated Monte Carlo showers and the shower size predicted by the Gaisser-Hillas and Gaussian-in-age profiles. This is for a small subset of proton and iron showers mixed in 80/20 proportion and limited to primary energies between 10^{18} and $10^{18.01}$.

are equal [48]. Figure 4.13 shows the energy loss for electrons travelling through copper and the difference between the two definitions.

Since our simulation of air showers is used to understand the operation of the detector, we also use it to resolve this definitional problem and instead define the energy of a primary cosmic ray as

$$E_{\mathrm{cal}} = \int_0^\infty \alpha(x) N_{\mathrm{e}}(x) dx \tag{4.7}$$

where $\alpha(x)$ is the mean ionization loss rate for depth x. It is hoped that $\alpha(x)$ is approximately equal to E_{c}/X_0 that was used in previous experiments and it will be shown that is indeed true.

To determine the mean ionization loss rate, 100 CORSIKA showers were generated with 10^{18} eV proton primaries and 45° zenith angle. To decrease computation time, CORSIKA has a thinning option, which was selected for this simulation. Since the computation time scales proportionally to the primary particle energy, thinning is used to select a small subset of secondary particles to follow through the atmosphere [28]. When thinning is turned on, all secondary particles with energy below a chosen fraction, $\epsilon_{\mathrm{th}} = E/E_0$, of the primary energy, E_0, are submitted to the thinning algorithm. When secondary particles are created during particle interactions, if the sum of the energy of those particles falls below the thinning energy, one of the secondaries is chosen at random to be placed on the particle stack and followed, while all others are discarded. The probability to be chosen is weighted by the energy of the secondary particle

$$p_i = E_i / \sum_j E_j \tag{4.8}$$

where p_i is the probability assigned to secondary particle i, E_i is its energy, and $\sum_j E_j$ is the total energy of all secondary particles. The chosen secondary is then weighted by $1/p_i$ during any subsequent transport to conserve energy.

For this study ϵ_{th} was chosen to be 10^{-5}, which is one order of magnitude lower than the CORSIKA default of 10^{-4}, allowing us to track particles down to lower energies before they are exposed to the thinning procedure. Fluctuations in the

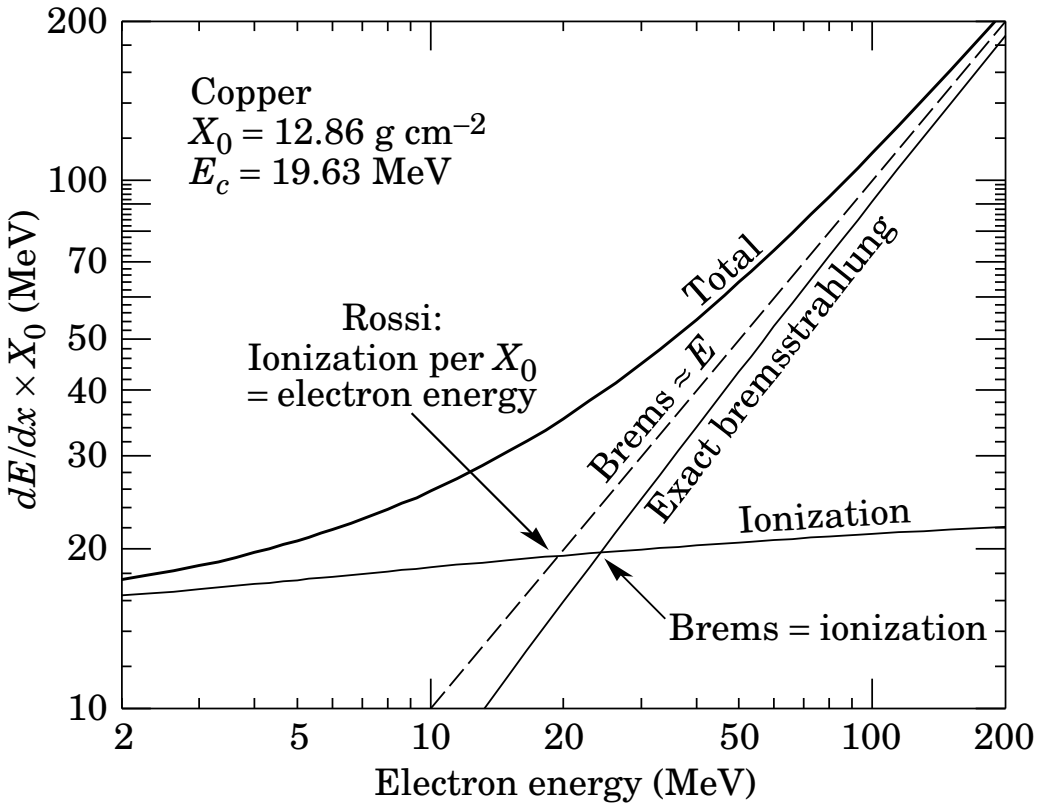

Figure 4.13. The electron critical energy E_c and the two definitions attributed to Rossi [48] and Berger and Seltzer [13]. This plot provided by the Particle Data Group [7].

shower profile can be seen for low energy ($\sim 10^{17}$ eV) showers if $\epsilon_{\rm th}$ is set higher, so care must be taken in the trade off between computational speed and accurate shower simulation.

CORSIKA follows particles down to a user-defined cutoff energy, after which no further interactions are simulated, and the remaining kinetic energy is deposited into the atmosphere. For the CORSIKA runs done to study dE/dx, the energy threshold cuts were chosen to be 300 MeV, 300 MeV, 100 keV, and 100 keV for hadrons, muons, electrons, and photons respectively. These threshold cuts were chosen to strike a balance between allowing tracking of particles to a sufficiently low energy and decreasing computation time during shower generation.

The calorimetric energy of an air shower in the atmosphere is approximately

$$E_{\rm cal} \approx \int_{\epsilon}^{\infty} \Delta E(k)\eta_{\rm e}(k)dk \tag{4.9}$$

where $\eta(k)$ is the differential energy spectrum of electrons with kinetic energy k and $\Delta E(k)$ is the ionization energy loss in the atmosphere. Because of the CORSIKA imposed energy threshold cuts the lower limit of the integral is not 0, but instead ϵ, which makes this an approximate calorimetric measurement.

The electron energy spectrum can be expanded by using the energy spectrum of the electrons at various depths along the shower

$$\eta_{\rm e}(k) = \int_{0}^{\infty} N_{\rm e}(x)n_{\rm e}(k,x)\frac{dx}{\Delta x(k)} \tag{4.10}$$

where $N_{\rm e}$ is the total number of electrons at depth x, $n_{\rm e}(k,x)$ is the normalized electron energy spectrum as functions of kinetic energy and depth, and $\Delta x(k)$ is the mean free path of electrons. Replacing $\eta_{\rm e}(k)$ in equation 4.9 with equation 4.10 we can rewrite it as

$$E_{\rm cal} \approx \int_{0}^{\infty} N_{\rm e}(x)\left(\int_{\epsilon}^{\infty}\frac{\Delta E}{\Delta x}(k)n_{\rm e}(k,x)dk\right)dx \tag{4.11}$$

Since we parametrize showers using the Gaussian-in-age functional form, we will recast the parenthesised term in equation 4.11 as a function of k and s, where s is the pseudoage of the shower, defined as

$$s(x) = \frac{3(x-x_0)}{(x-x_0)+2(x_{\rm max}-x_0)} \tag{4.12}$$

In this equation x_0 is the depth of first interaction of the primary with an air molecule and $x_{\max}$ is the depth at which the shower reaches its maximum size. Pseudoage is used for this CORSIKA study because x_o is known. For data reconstruction x_0 is not observed and the shower age is defined by equation 4.3.

The mean ionization energy loss is now written as

$$\alpha(s) = \int_{\epsilon}^{\infty} \frac{\Delta E}{\Delta x}(k)\tilde{n}_{\mathrm{e}}(k,s)dk \tag{4.13}$$

where $\tilde{n}_{\mathrm{e}}(k,s)$ is now a function of kinetic energy and age. Combining equations 4.11 and 4.13 we get

$$E_{\mathrm{cal}} \approx \int_{0}^{\infty} \alpha(s(x))N_{\mathrm{e}}(x)dx \tag{4.14}$$

which is approximately the desired result of equation 4.7. It will be shown that the threshold energy ϵ in the approximation of the calorimetric energy, equation 4.14, will require a correction to get the correct energy of the primary particle. This procedure is described in section 4.5.

Equation 4.13 is a convolution of two functions, $\Delta E/\Delta x$, the ionization energy loss of electrons and $\tilde{n}_{\mathrm{e}}$ the normalized electron energy spectrum. The energy loss function used is data provided by the NIST ESTAR database. This database contains the energy loss data for many different particles through different media. For determination of $\alpha(s)$, the electron collision stopping power in dry air was used (see Figure 4.14). The NIST ESTAR dE/dx data uses a combination of measured data and theoretical calculations to provide the energy loss of electrons over a large range of energies. It uses the scattering theory of Bethe and Sternheimer density corrections in its calculation of ionization energy loss [43].

The electron energy distribution is provided by a version of CORSIKA, modified by this author and written to histogram the age of the shower and the energy of electrons during each transport step. Figure 4.15 shows the energy distribution of electrons for 100 proton induced showers. Figure 4.16 shows the distribution at $s = 1$ and the photon distribution as well.

To perform the integral in equation 4.13 the CORSIKA electron distributions in Figure 4.15 are divided into slices along the age axis and the convoluted with the

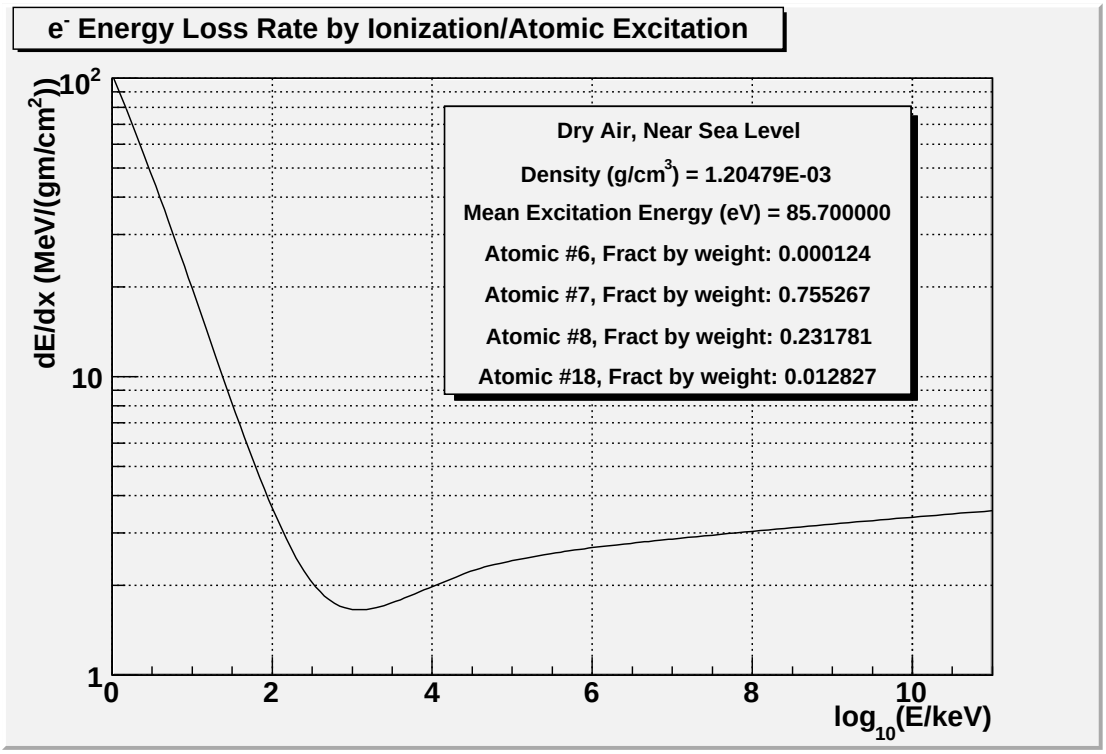

Figure 4.14. The electron energy loss rate due to ionization used to find $\alpha(s)$. This is the $\Delta E/\Delta x$ function in equation 4.13.

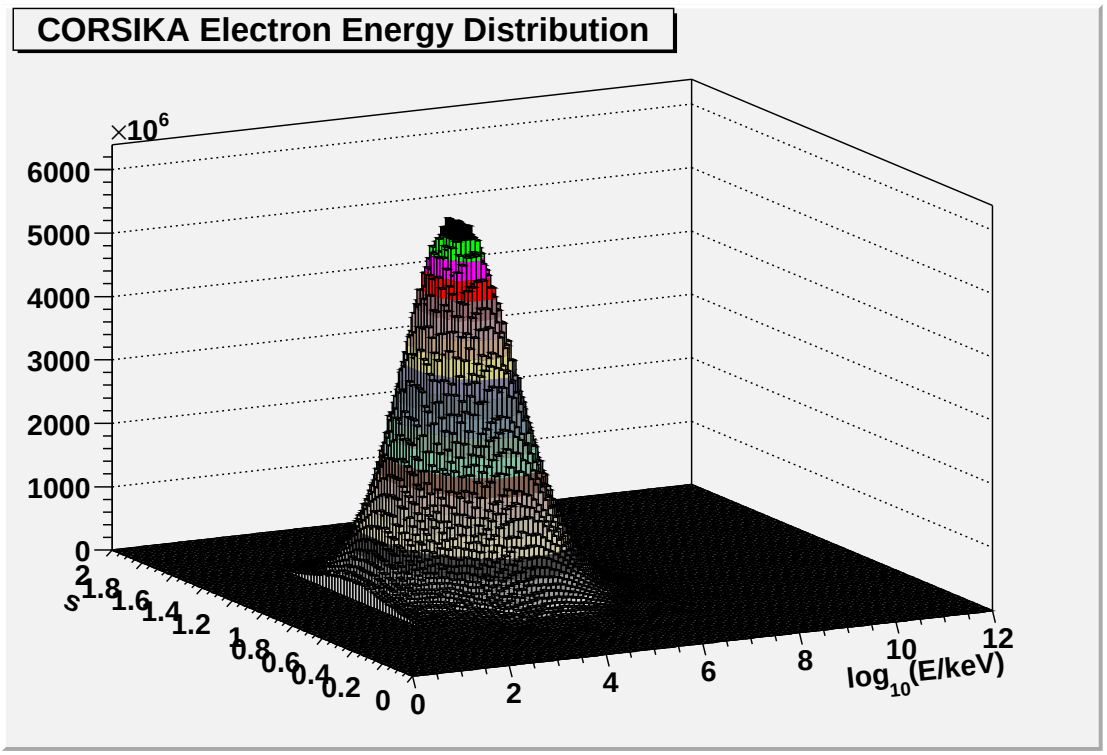

Figure 4.15. The electron distribution as function of shower age and kinetic energy. This is the $\tilde{n}_{\mathrm{e}}(k, s)$ function in equation 4.13. This distribution was produced by 100 proton primaries with energy of 10^{18} eV and zenith angle of 45°.

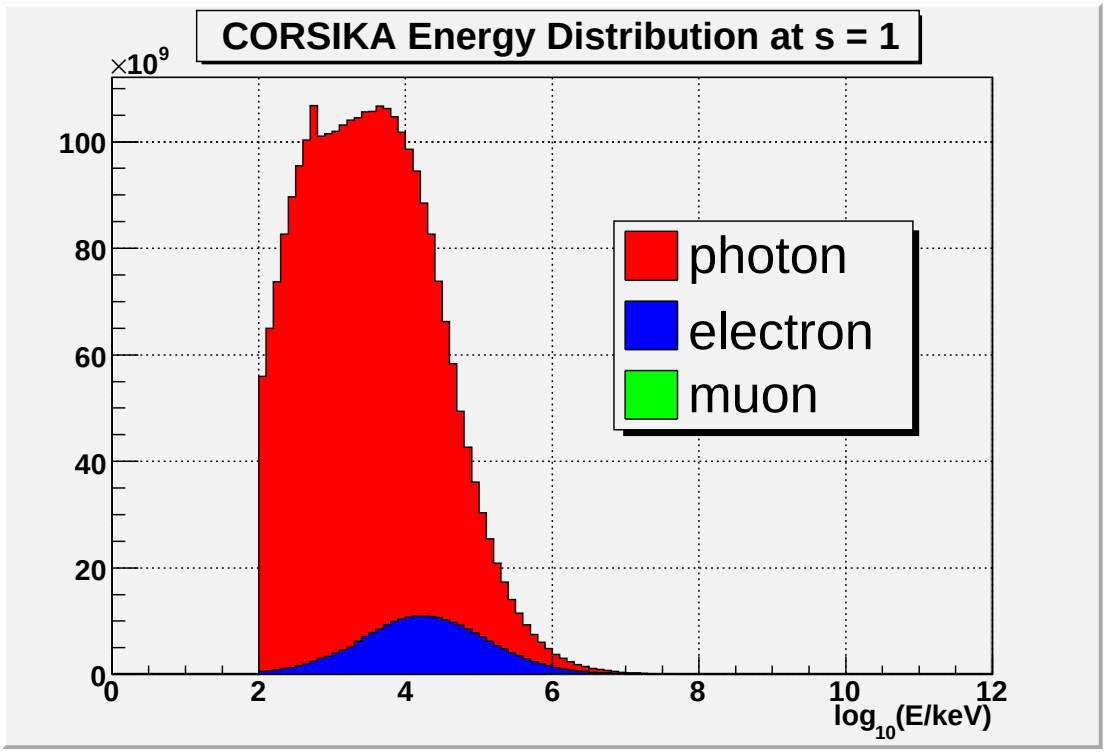

Figure 4.16. Energy distribution of CORSIKA photons and electrons at $x_{\max}$. The electron distribution is a slice along the age axis ($s = 1$) from Figure 4.15. Notice that the muonic component is negligible at this stage of the shower. This distribution was produced by 100 proton primaries with energy of 10^{18} eV and zenith angle of 45°.

NIST ESTAR dE/dx (Figure 4.14) and integrated over kinetic energy. The result is shown in Figure 4.17. The figure shows the result of the previous study performed by Song, et al. and the current results agree well. The weighted mean of this study is indicated by the solid line and has the value of 2.21 MeV/(g/cm^2). This is similar to the mean value of 2.18 MeV/(g/cm^2) used in the Fly's Eye experiment [10].

The $\alpha(s)$ curve is fitted with a decaying exponential function of the form $A + Be^{Cx}$. The fitted parameters are found to be $A = 2.014$, $B = 0.434$, and $C = -1.108$. This function is now used by the Monte Carlo and reconstruction to determine the energy scintillation light yield and the energy deposit of showers in the atmosphere.

The question may be asked as to why another source is used for dE/dx instead of the dE/dx that is implicitly used by CORSIKA? The EGS4 electron transport routines also impose threshold cuts on particles that it moves through media, utilizing the PEGS4 stopping power data bundled with the EGS4 package. For use in CORSIKA, PEGS4 provides five tables of dE/dx for dry air at a fixed temperature and pressure. Each table has a minimum threshold energy of 50 keV, 150 keV, 400 keV, 1 MeV, or 3 MeV. When a threshold cut is set by the user in the CORSIKA data file, CORSIKA automatically selects the file with the next lowest threshold cut value supported by the PEGS4 data. For instance, if an electron threshold cut of 60 keV is requested, CORSIKA will actually use the 50 keV cut file to determine the energy deposit for electrons above 60 keV, since that is the value supported by the PEGS4 data. Note that CORSIKA still respects the 60 keV cut in this case by not following electrons that fall below this energy threshold.

EGS4 handles two cases of electron transport energy loss, discrete and continuous. In the case of discrete energy loss, particles above the cutoff energy are produced and transported. Continuous energy loss is the result of secondary particles that have energies below the threshold cuts. In this case, the energy deposited by the electron contains an average radiative (i.e., bremsstrahlung) loss as well as the desired ionization loss. The EGS4 manual states the energy loss as

$$-\left(\frac{dE}{dx}\right)_{\text{continuous}} = -\left(\frac{dE}{dx}\right)_{\text{bremsstrahlung}} - \left(\frac{dE}{dx}\right)_{\text{sub-cutoff}} \tag{4.15}$$

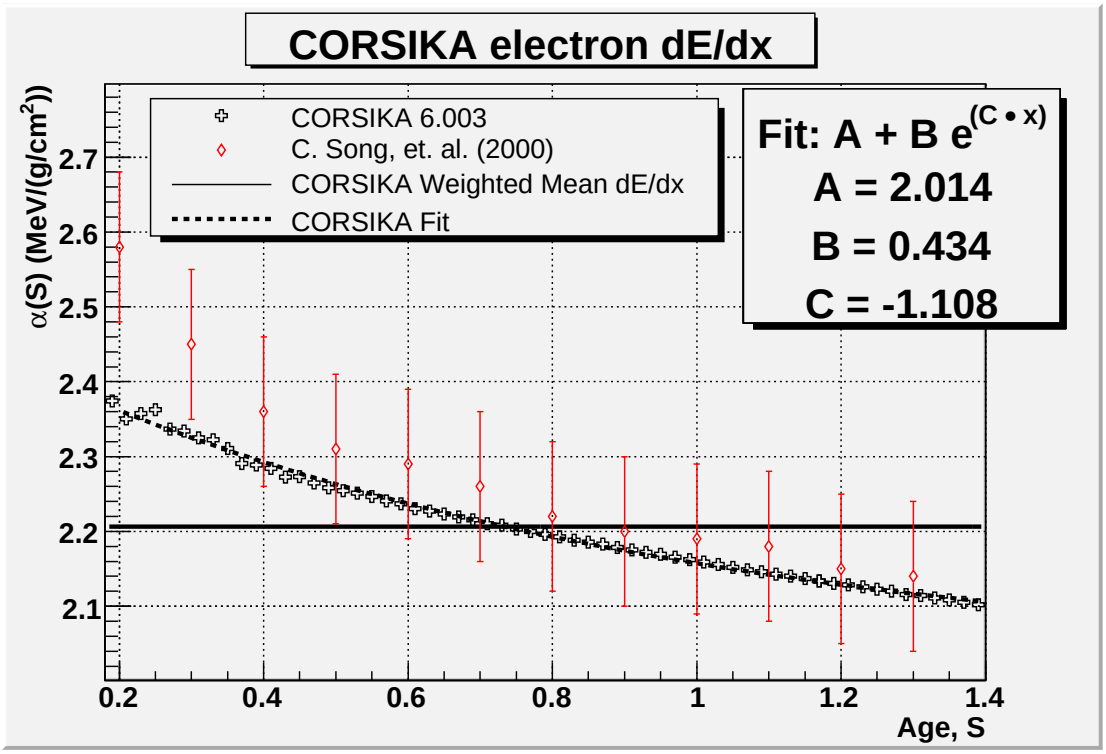

Figure 4.17. Electron energy loss of high energy air showers through the atmosphere as determined by a study of CORSIKA. The result of Song, et al. [54] is shown as a comparison to a previous similar study. The weighted mean is the mean of the CORSIKA 6.003 data.

where $\left(\frac{dE}{dx}\right)_{\text{continuous}}$ is the total continuous energy loss, $\left(\frac{dE}{dx}\right)_{\text{bremsstrahlung}}$ is the energy loss of soft bremsstrahlung photons, and $\left(\frac{dE}{dx}\right)_{\text{sub-cutoff}}$ is the ionization energy loss of the electrons that fall below the threshold cut.

Figure 4.18 shows the effect of directly extracting the dE/dx information from CORSIKA. Using different electron threshold cuts, it can be seen that the dE/dx curves contain more radiative energy losses as the threshold cut is raised. Since we are interested in only the ionization losses, we cannot use this data. Note that as the threshold cut is taken to its lowest allowed value (the value used for the dE/dx study), it approaches the NIST ESTAR dE/dx.

By separating the sources of the two functions under the integral in equation 4.13, the unwanted average bremsstrahlung radiative loss is decoupled from the ionization energy loss that is desired. To test the validity of the α measurement and since equation 4.6 is strictly true for purely electromagnetic showers, CORSIKA γ-ray initiated showers are generated then integrated using equation 4.14. It is found that the CORSIKA showers do not give back the energy of the primary particle as expected. The reason is that electrons that fall below the artificial 100 keV threshold cut carry away some of the energy. A detailed study of this loss, described in [54] and verified for a smaller subset of energies by me, shows that the CORSIKA energy cut causes an 11% energy discrepancy for γ-ray initiated showers. Therefore for all further studies involving CORSIKA showers, the energy scale is boosted by adding 11% of the primary particle's energy to the shower being studied.

4.5 Electromagnetic Fraction

Section 4.4 describes the procedure to determine the energy of γ-ray induced showers. To determine the energy of hadronic showers, additional energy losses must be accounted for. There are components of hadronic showers that cause "missing energy" that is not observed by a fluorescence detector, e.g., nuclear excitation, high energy muons, and neutrinos, that divert energy from nitrogen fluorescence. The ratio of calorimetric energy to total energy of the primary

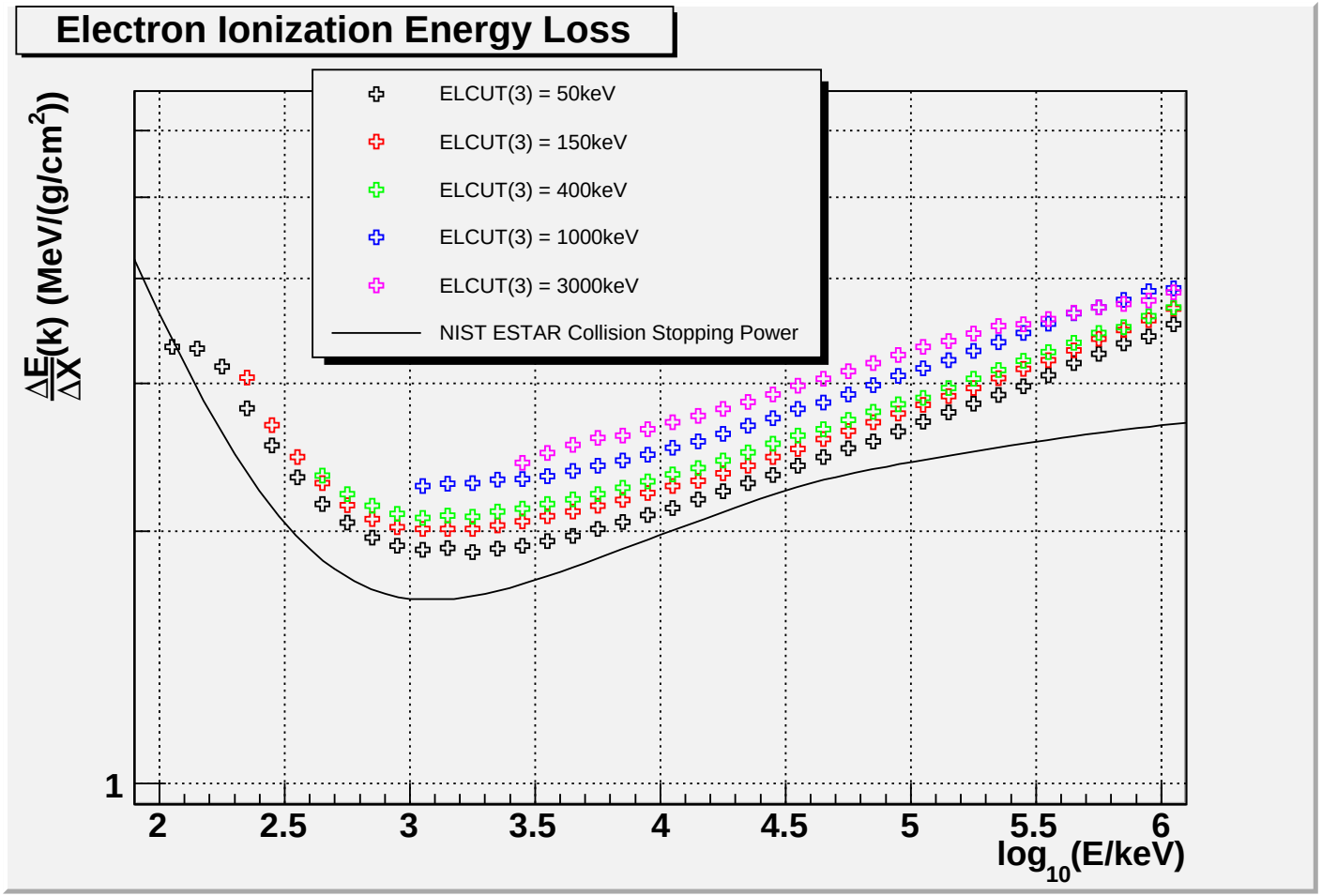

Figure 4.18. The effect of EGS4 continuous energy loss to the dE/dx curve. EGS4 contains an undesired radiative energy loss component in addition to the ionization loss that is averaged into the total energy loss of electrons that fall below threshold cuts.

particle is called the electromagnetic fraction. It is energy dependent and can be parameterized as a function of calorimetric energy

Previous experiments such as the Fly's Eye used an estimate of missing energy based on an analysis of Linsley [40]. The Fly's Eye experiment parameterized the results of Linsley's study as [10]

$$\frac{E_{\rm cal}}{E_o} \cong 0.99 - 0.0782 E_0^{-0.175} \tag{4.16}$$

where $E_{\rm cal}$ is the calorimetric energy of equation 4.6 and E_0 is the energy of the primary particle. It was estimated that this electromagnetic fraction parameterization was valid from 10^{15} eV to 10^{20} eV.

To determine the missing energy for our showers we again turn to CORSIKA. There are over 32000 proton and iron induced showers stored in the shower library that is used by the Monte Carlo to generate showers at arbitrary energies. Each shower is used to determine the electromagnetic fraction by integrating the shower profile using equation 4.14 and α shown in Figure 4.17 and extrapolating the shower to very large depths ($4 \times x_{\rm max}$). As explained previously 11% of the primary particle energy is then added to this result to compensate for the artificial energy lost due to CORSIKA cuts. The ratio of calorimetric energy to primary energy is then plotted as a function of calorimetric energy and fitted to the functional form

$$\frac{E_{\rm cal}}{E_0} = A + B \cdot (E_{\rm cal})^C \tag{4.17}$$

Figure 4.19 shows the resultant fits for pure proton induced showers, pure iron induced showers, and two different mixes of the two. The figure also shows the parameterization of Linsley (equation 4.16) as well as the result from Song, et al. The 50/50 weighting is shown for historical purposes since previous measurements of the energy spectrum used this weighting. The energy spectrum done for this work uses the 80/20 proton/iron mix.

Table 4.2 shows parameterizations of the electromagnetic fraction used in recent works. These analyses used an average dE/dx that did not vary with shower age and a 50%/50% proton/iron mix. The last three rows show the results of the analysis

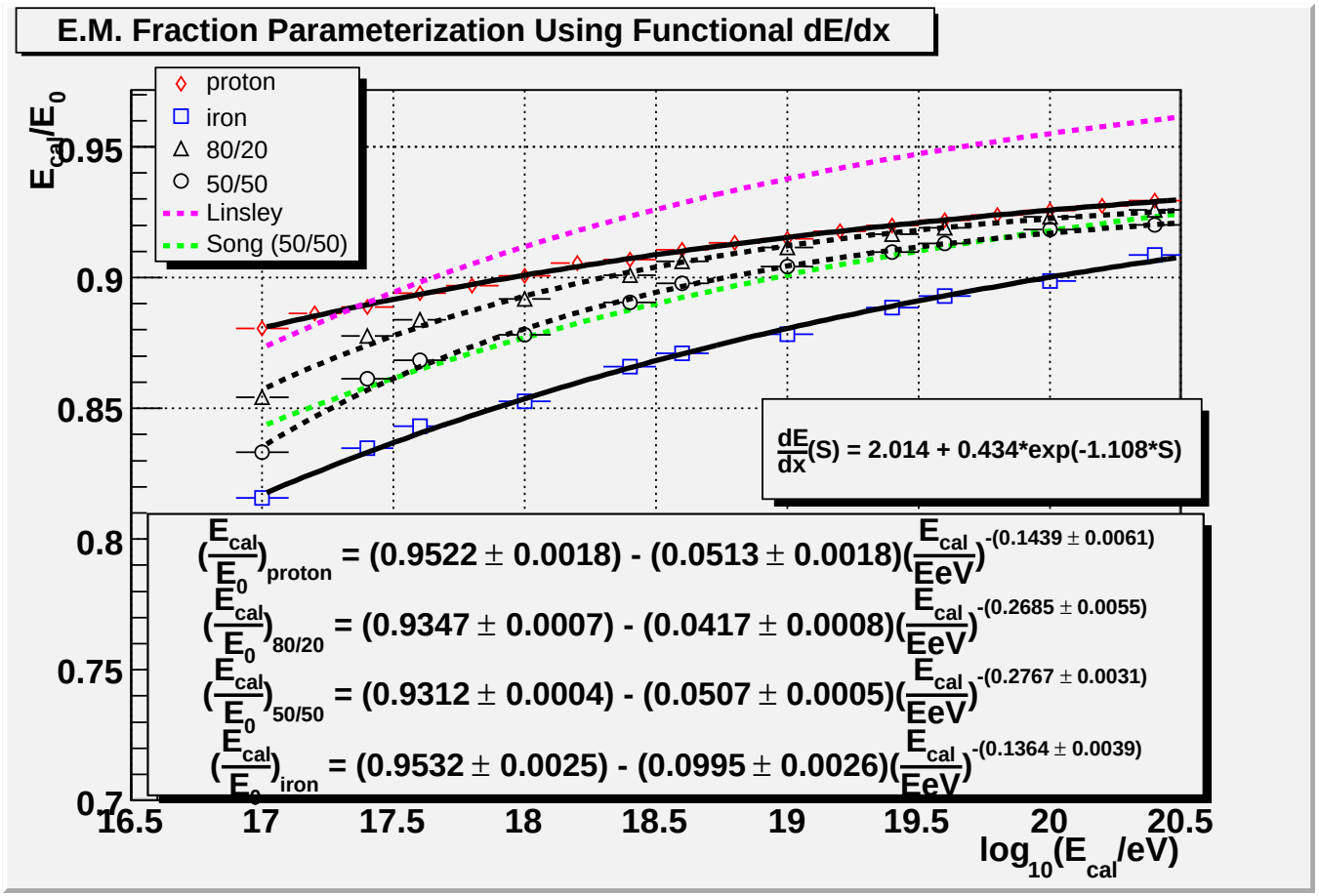

Figure 4.19. The parameterization of missing energy of hadronic showers. The 21846 proton and 10676 iron showers contained in the shower library were used to determine these values. The 11% missing energy due to CORSIKA threshold cuts is already added into the showers. The only energy missing in this plot is due to real physical phenomena (e.g., nuclear excitation, hard muons, neutrinos, etc.).

Table 4.2. Recent parameterizations of electromagnetic fraction missing energy correction using the form $E_{\rm cal}/E_0 = A + B \cdot (E_{\rm cal})^C$. dE/dx is in units of MeV/(g/cm^2).

Name	Date	dE/dx	A	B	C
Abu-Zayyad [5]	2000	2.18	0.8660	-0.0720	-0.1490
Song, et al. [54]	2000	2.19	0.9590	-0.0820	-0.1500
Reil [47]	2002	2.38	0.9437	-0.0963	-0.1260
Belov [11]	2005	2.44	0.9469	-0.0969	-0.1260
Hanlon (50/50)	2007	2.19	0.9483	-0.0540	-0.2510
Hanlon (50/50)	2007	-	0.9312	-0.0507	-0.2767
Hanlon (80/20)	2007	-	0.9347	-0.0417	-0.2685

described here, one with the method of an average dE/dx of 2.19 MeV/(g/cm^2) and two with the functional dE/dx shown in Figure 4.17 with indicated mix ratio.

Notice that some analyses use dE/dx values approximately 10% larger than what is currently found. These analyses use an inflated value of dE/dx to compensate for the energy lost due to the CORSIKA threshold cuts and do not correct the shower library for artificial missing energy. This was discussed in detail in section 4.1.

4.6 Monte Carlo Simulation

The aperture of this experiment is a measure of the detector's acceptance of events that are viewed in a given solid angle over a given surface area. The HiRes aperture is energy dependent since with varying energy an EAS produces differing amounts of light. For example a high energy EAS that produces a larger amount of scintillation light can be seen from a further distance than a lower energy one. Variations in atmospheric clarity, either localized (e.g., a single cloud) or global anomalies (e.g., uniform haze filling the entire fiducial volume) may also diminish the detector's ability to view showers. Because of the low rate of incidence of the most energetic showers we rely heavily on an accurate simulation of the experimental apparatus to determine our estimated efficiency in reconstructing showers. Using this simulation we can generate as many artificial showers as we desire to attain large enough statistics, particularly at the highest energies, to increase our confidence in the aperture measurement. The importance of the aperture to the spectrum measurement will be discussed in greater detail in section 5.4.1.

The Monte Carlo also allows us to *understand* our detector under conditions that we explicitly control. This is of paramount importance in an experiment as complex as this. For example changes in the electronics, specific atmospheric conditions, detector response, or inoperative mirrors can be studied to understand how it affects our ability to collect and properly analyze data under varying circumstances. The many "adjustable knobs" that go into any single event must be understood with the greatest degree of accuracy for us to have confidence in the final measurement

of the spectrum. The efficacy of the reconstruction routines can therefore be tested by resolution studies and data/Monte Carlo comparisons. Both of these subjects are explored further in sections 5.2 and 5.3.

The HiRes Monte Carlo, also referred to as mc_stereo, is written to provide this accurate simulation. The Monte Carlo simulates the geometry of the detector, atmospherics, electronics response, trigger logic, and operating conditions of the detector in a *time-dependent* manner. This time-dependent simulation greatly improves the estimate of the aperture by recreating operating conditions such as atmospheric clarity, the actual stereo live time during a given hour, removing mirrors that were inoperative, and using the same tube gains and pedestals. Using this method, the temporally relative variations in the atmosphere, differing stereo ontimes, and dead mirrors are automatically accounted for and do not require independent systematic analyses of each of these effects to try and determine the impact on the aperture.

A Monte Carlo run requires the user to input the date for which stereo data is to be simulated. Before generating air showers various databases that record the operating conditions of the detector during that night are read in and are used to further improve the simulation by simulating the actual running conditions of the detector during that time. If no stereo data were collected on a given night, then standard values are used for calculations that depend on database information. The databases used by the Monte Carlo are discussed in detail in section 4.6.5.

Broadly, the Monte Carlo performs four high level functions for each shower generated with many individual subroutines called upon to perform each function. First, initialization of required constants is performed (section 4.6.1), second, a shower is "generated" by simulating the light produced by a high energy primary particle or nuclei and the light propagated to the detector (section 4.6.2), third, the response of the detector is mimicked by the electronics generation function (section 4.6.3), and finally the event data are written to an output DST file using the same data format as real data. Figure 4.20 summarizes the procedure to generate a simulated shower.

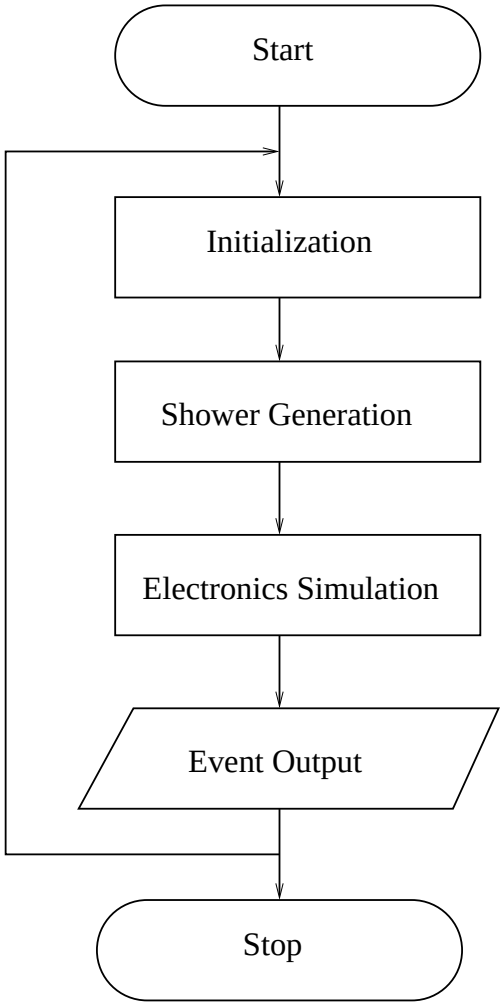

Figure 4.20. Logical overview of the major functional components of the HiRes stereo Monte Carlo program. All four functions are executed for a fully reconstructed stereo event. Some events may not be reconstructed by the electronics simulation if it is generated as shower that would not be seen by the detector or is a poor event in a similar manner.

4.6.1 Initialization

The initialization routines are used to control how the Monte Carlo will run by setting various parameters such as the date for which data are to be simulated, the primary species to throw, which hadronic model to use, and what primary energies will be allowed. They also load in the various databases that contain the information about the actual running conditions for the given night, read in the geometry of the detector, and set measured parameters such as tube quantum efficiencies, UV filter transmissions, and mirror reflectivities. Figure 4.21 summarizes the most important functions of the initialization block.

The initialization block begins by reading in the user provided data file which specifies important operating limits of the Monte Carlo. The user specifies the date for which Monte Carlo will simulate a data collecting night. Also the ranges of allowed zenith (θ), azimuth (ϕ), shower (γ) angles, and pseudodistances ($R_{\rm p}$) are specified (see Figures 4.22 and 4.23). The allowed range of energies, spectral index, hadronic model, and primary species are set here as well. Table 4.3 shows the parameter limits used for this work. For all Monte Carlo runs the primary species ID is either 14 (for proton) or 5626 (for iron), the spectral index is set to 0 indicating that a split spectrum input is desired, and the model is set to 3 to use the QGSJet hadronic interaction model provided through CORSIKA generated showers. Two different primary species are chosen for shower generation, either proton or iron, and the results of the two different Monte Carlo files are mixed in a proportion of 80% proton and 20% iron to simulate what is believed to be the composition mix of real air showers. The mixing procedure is detailed further in section 4.6.4. After the parameter limits are read in, different subroutines open the output DST, load in the geometry of the detector, set constants such as mirror reflectivities and UV filter transmissions (Figure 3.14).

The hourly ontime database is read in to determine the number of hours the detector operated for that night. This database contains hourly entries for the number of seconds the detector ran in stereo mode and the status of each mirror at HiRes1 and HiRes2 (on or off). The number of events thrown for each hour

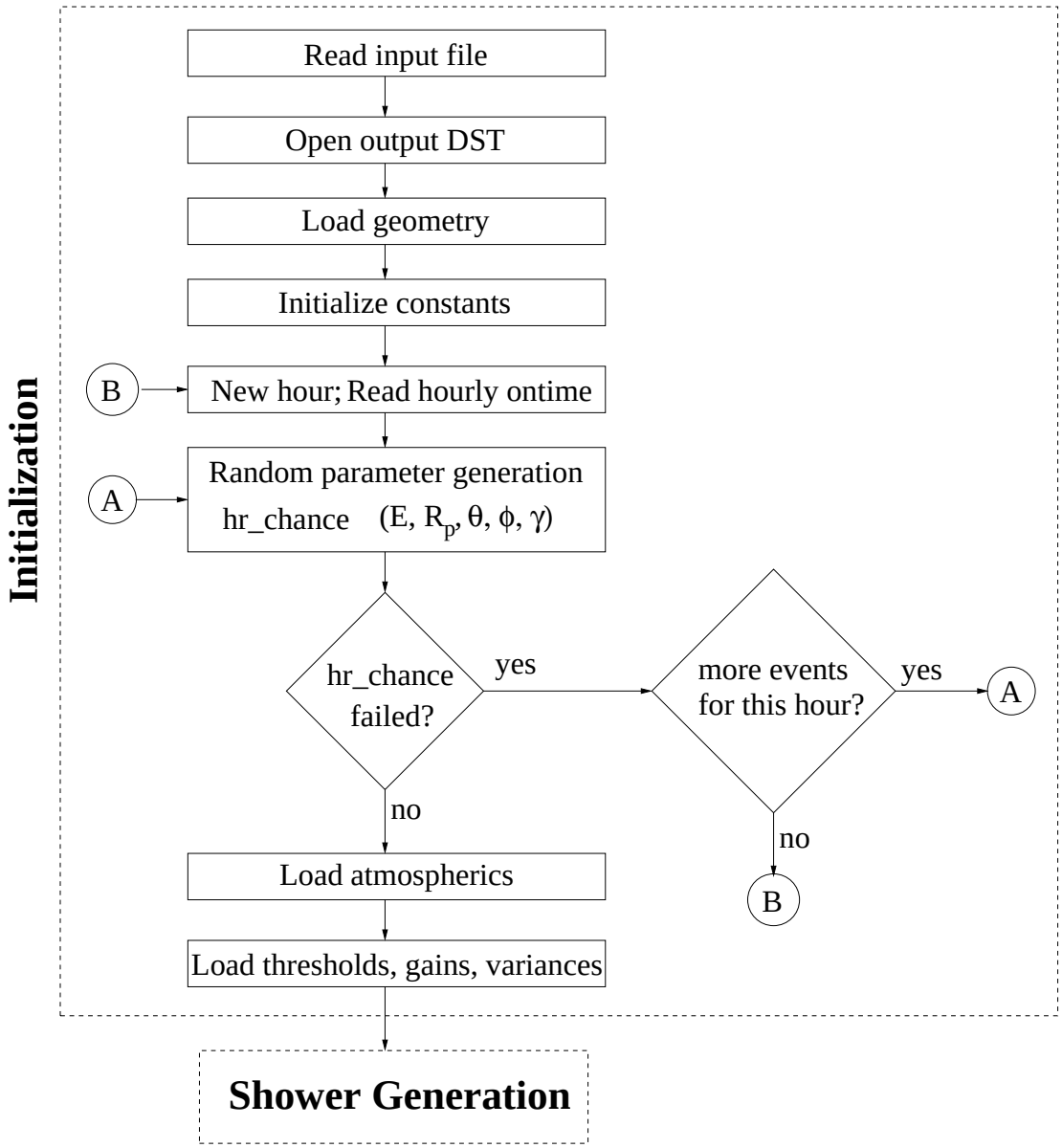

Figure 4.21. Block diagram showing the major functional responsibilities of the initialization function of mc_stereo.

Table 4.3. Parameter limits used for event generation in mc_stereo for this study.

Parameter	Minimum	Maximum	units
Zenith Angle (θ)	0.00	89.99	degrees
Azimuth Angle (ϕ)	0.00	360.00	degrees
Plane Angle (γ)	0.00	360.00	degrees
Pseudodistance ($R_{\rm p}$)	0.00	75.00	km
Energy	2.0×10^{17}	1.0×10^{21}	eV

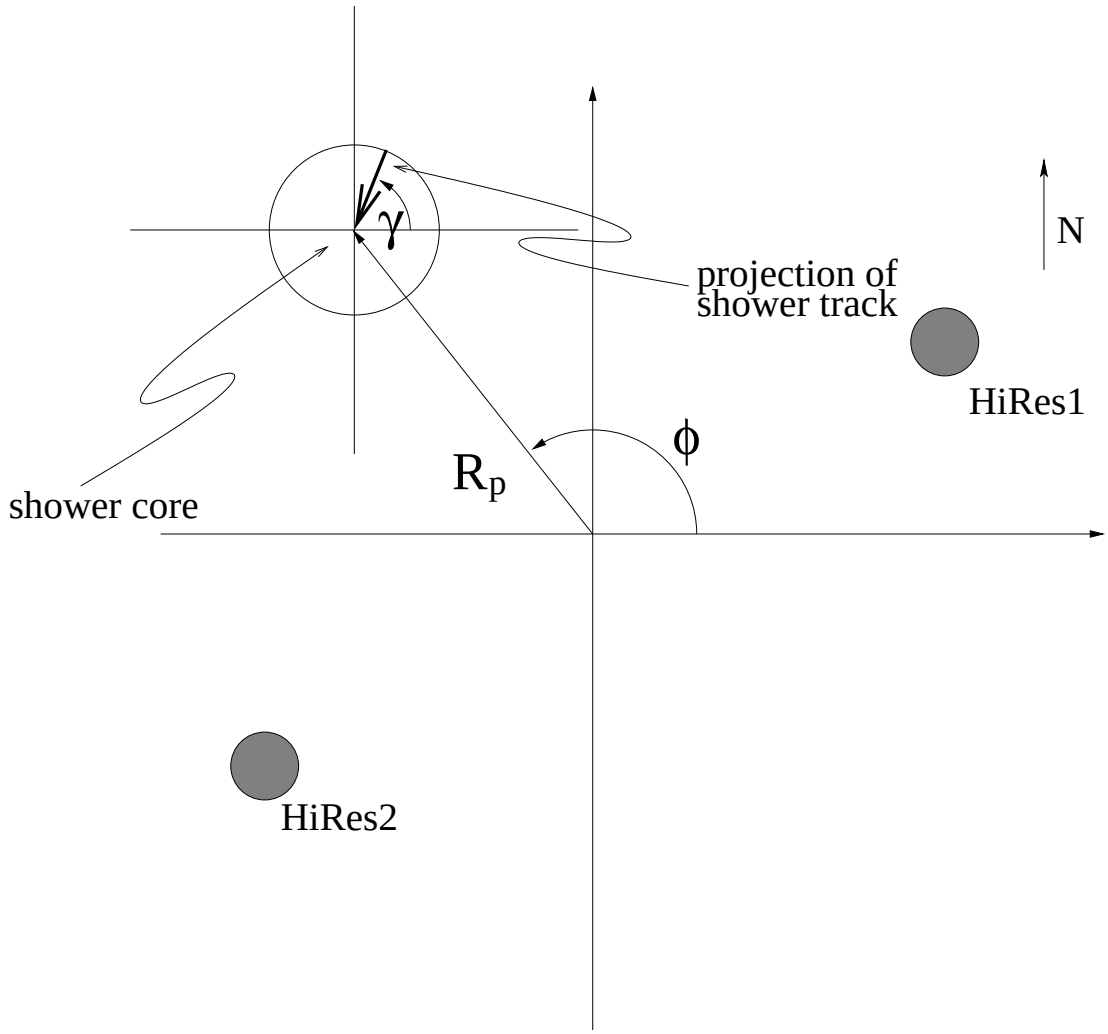

Figure 4.22. Geometric parameters thrown by mc_stereo during shower initialization. This is an overhead projection with the shower track "flattened." The zenith angle $\theta = 0°$ points directly out of the page and has a radius of 0 in the projection. The azimuth angle ϕ and the shower angle γ naturally lie in the plane of the page. The pseudo-distance, $R_{\rm p}$, is projected into the page and would only naturally lie in it for a vertical shower ($\theta = 0°$).

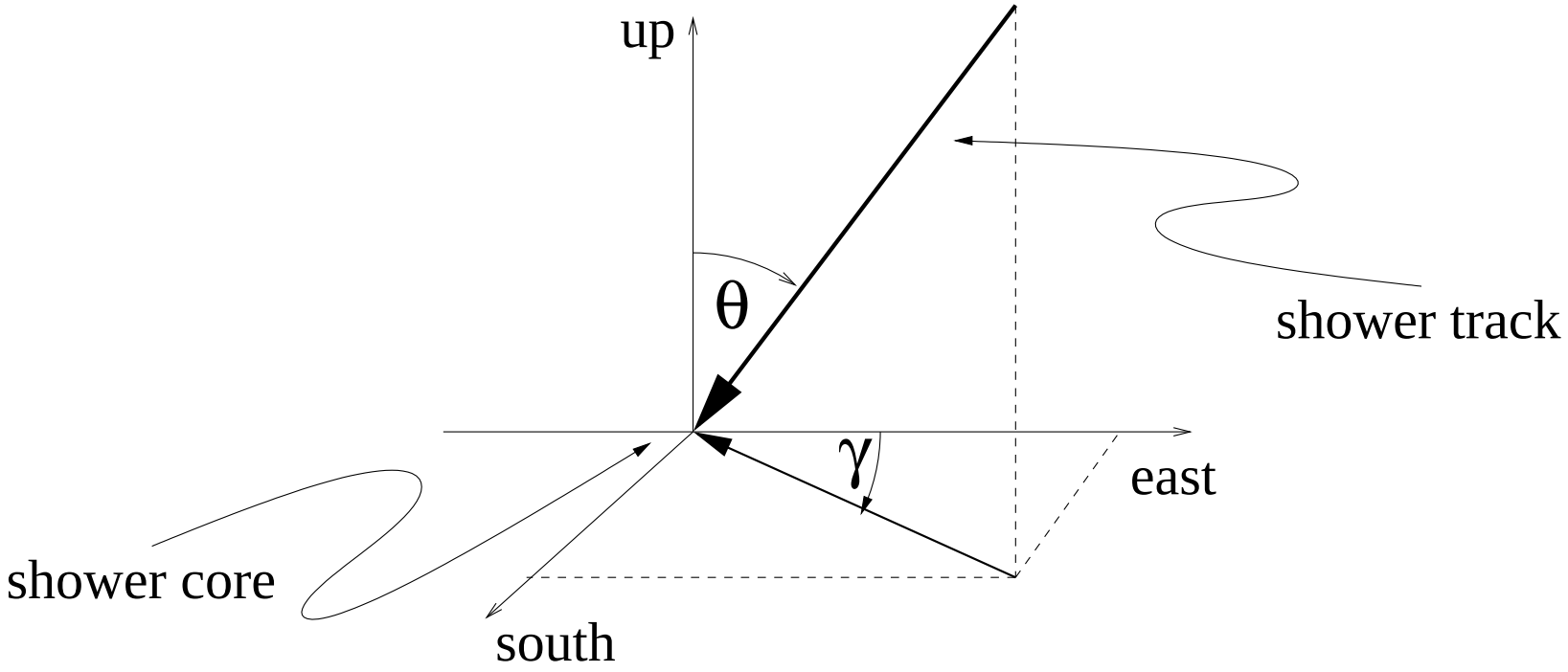

Figure 4.23. Geometric parameters thrown by mc_stereo during shower initialization. This is a three dimensional view of the shower track and the shower core showing the zenith angle θ points in the direction normal to the surface of the earth and the shower angle γ is the local azimuthal angle found by projecting the shower track onto the earth's surface.

is determined by normalizing the number of trials requested in the input data file by the fraction of stereo ontime. This method ensures that the relative number of events thrown and reconstructed is in the same proportion as that seen in the real data under normal operating conditions.

The main random parameter generating subroutine, hr_chance, is then called. It generates six parameters that are needed to characterize a shower: energy, pseudodistance ($R_{\rm p}$), depth of first interaction (τ_0), zenith angle (θ), azimuth angle (ϕ), and the plane angle (γ). All thrown values except τ_0 are bounded by the limits provided by the user in the input data file. Figures 4.22 and 4.23 show how the geometric parameters are placed relative to the detector.

The energy generated by hr_chance can be chosen from different input spectra: Fly's Eye, fixed index, or split spectrum. The Fly's Eye spectrum is the measured spectrum described in [15]. Fixed index spectrum is one with a constant falling spectral index. For this study the split spectrum mode is used. The split spectrum falls as E^{-3} for energies below $10^{18.5}$ eV and $E^{-1.5}$ for energies above the break. This broken spectrum is used to reduce the computational time required to generate a large data set with sufficient statistics at the highest energies. When used during analysis care must be taken that the events above the break are reweighted (or more specifically deweighted) to ensure that those events are not overrepresented in the sample population. Figure 4.24 shows how this spectrum compares to the Fly's Spectrum.

To further reduce computational time, the pseudodistance is subjected to an energy dependent cut. By observing the trigger rate of the detector it can be shown that for a shower of a given energy there is a limit as to how far away it can be seen. The pseudodistance cut shown in Figure 4.25 is therefore applied to each event. If the randomly generated $R_{\rm p}$ and energy fall above the maximum $R_{\rm p}$ as shown in Figure 4.25 the event fails hr_chance and no attempt at shower generation and electronics simulation is made.

Atmospheric information for the current hour is loaded and utilized as well at this stage. Horizontal attenuation length, vertical scale height, and mixing layer

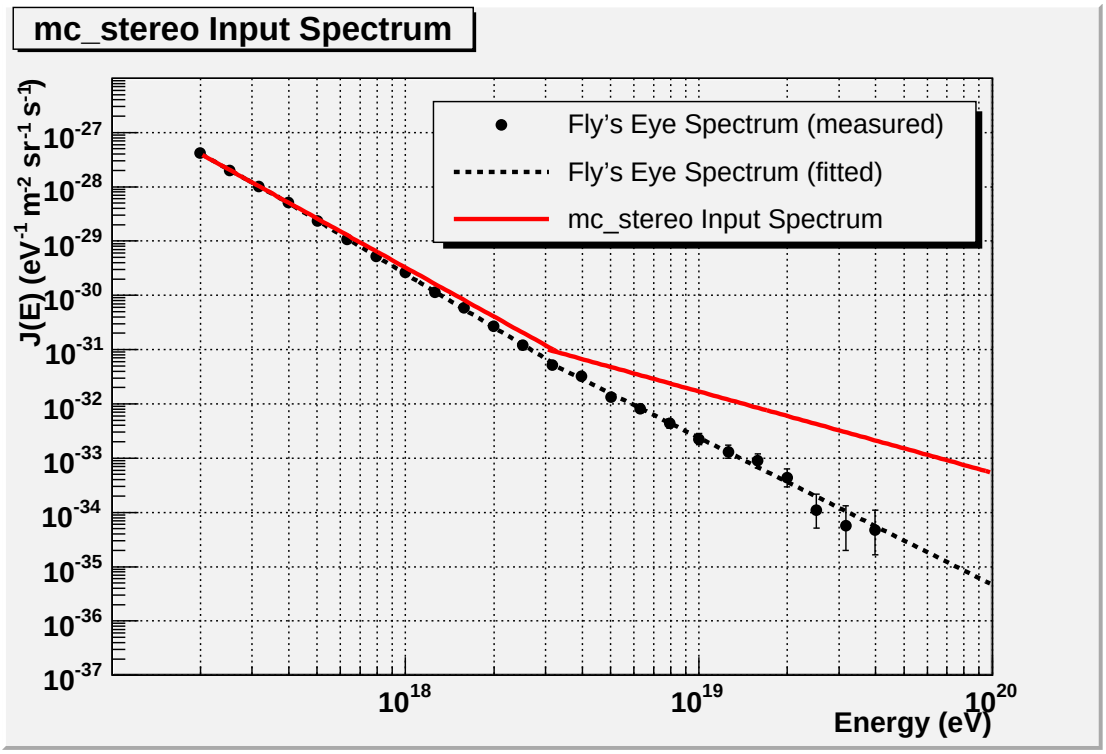

Figure 4.24. The input spectrum used by the Monte Carlo for this analysis. It is a simple split spectrum that falls as E^{-3} for energies below $10^{18.5}$ eV and $E^{-1.5}$ for energies above the break. For comparison the Fly's Eye spectrum is also shown [15]. The input split spectrum was normalized so that the it had the same flux as the Fly's Eye spectrum at 2×10^{17} eV. The change in spectral index of the input spectrum requires deweighting of events with energies above $10^{18.5}$ for proper analysis.

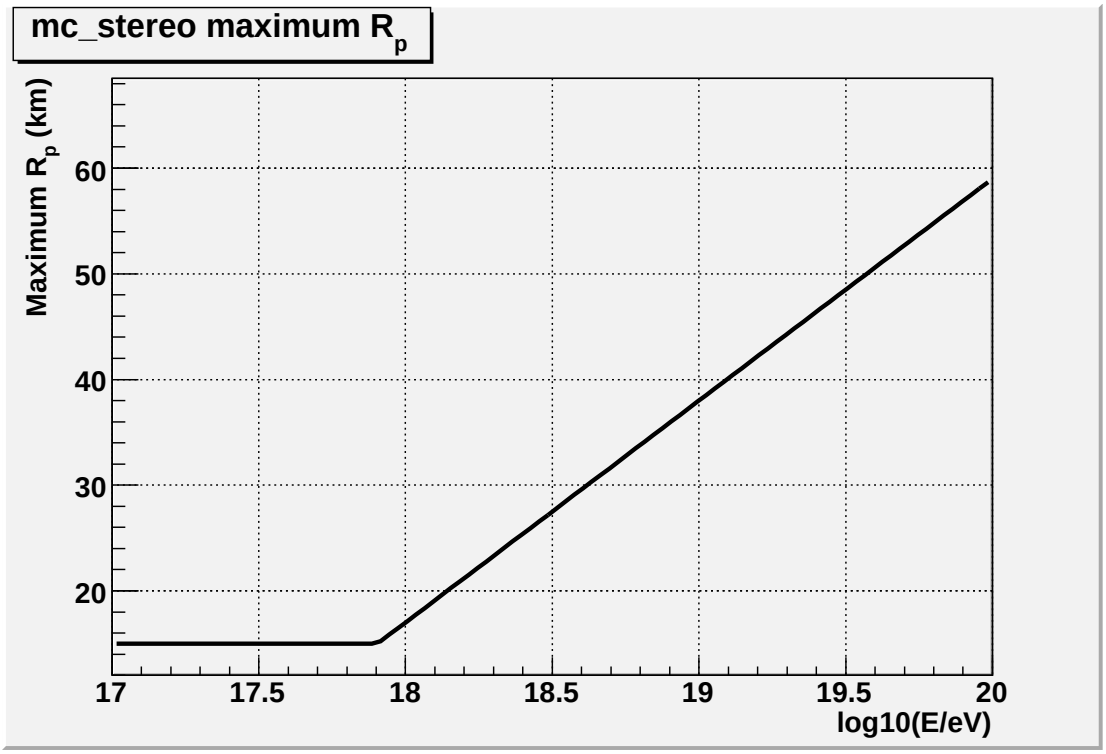

Figure 4.25. The maximum pseudodistance ($R_{\rm p}$) function used by mc_stereo. For each event an energy and a $R_{\rm p}$ value are generated. If the $R_{\rm p}$ value exceeds the maximum $R_{\rm p}$ for the given energy as shown in the plot, then the event fails to be fully reconstructed as it is assumed to be too far away to trigger the detector.

height are read in from a database generated from atmospheric measurements made by the steerable laser at HiRes2.

More time-dependent databases are read in and initialized for the current hour. The HiRes2 variances, ADC gains, pedestals, and trigger DAC settings are read in. A gain correction that ties the energy scale of the Monte Carlo to the measured energy scale of the detectors is also set. HiRes1 thresholds are set as well. All of this information is stored in a DST bank to be written out with the event.

4.6.2 Shower Generation

The functional steps of the shower generation block are summarized in Figure 4.26. Shower generation is sped up by using a library of showers generated by an air shower simulation package. For this study, the shower library is derived from the CORSIKA air shower simulation using the QGSJet hadronic model. The subroutine shw_init is called with the randomly generated shower energy provided by hr_chance and returns a shower from the shower library. The details of the shower library are discussed further in section 4.2. The shw_init subroutine returns the depth of shower maximum ($x_{\max}$), the number of particles at shower maximum ($N_{\max}$), the shower width parameter (σ_s), the depth of first interaction (τ_0) and loads the scaled shower into memory. When the Monte Carlo needs to know the number of shower particles at an arbitrary depth, the subroutine hr_shower uses the stored shower to determine the answer.

Next, additional geometric quantities of the shower are computed in hr_shwpln where the pseudodistance and the plane normal vector relative to each eye is calculated. The shower is then divided into segments in hr_newtrack. Useful information about the shower such as number of shower particles, depth, time, height, and angular size at each segment is calculated as well as the minimum and maximum angles at which the shower is seen at each eye.

The most important subroutine of the shower generation procedure is hr_newlight. This subroutine first calculates the number of Čerenkov photons that accumulate along the shower track from the point of first interaction to the first depth seen by the detector. Then for each shower segment seen by the detector (calculated in

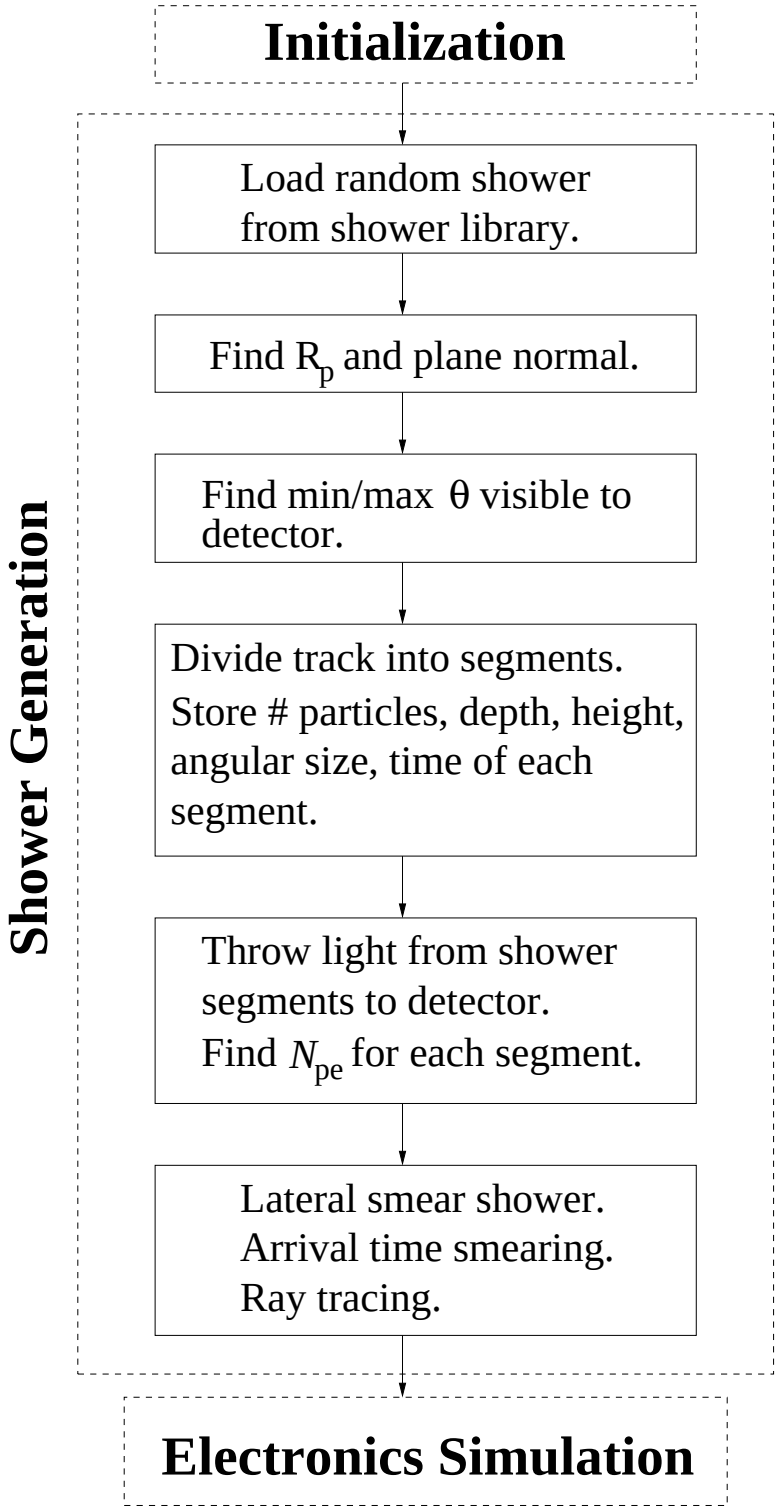

Figure 4.26. Block diagram showing the major functional responsibilities of the shower generation function of mc_stereo

hr_newtrack) it calculates the N_{pe} that would measured in the detector from the shower.

The light from the shower is broken up into four components: scintillation light, direct Čerenkov light, Rayleigh scattered Čerenkov light, and aerosol scattered Čerenkov light. Additionally each component of light is broken up into sixteen bins nine nanometers wide in wavelength, where the contribution from each wavelength is stored, since attenuation among the different UV wavelengths is not uniform for the Mie, ozone, and Rayleigh scattering cross sections (see Figure 4.27).

The shower's Čerenkov beam from the point of first interaction to the first viewed shower segment is computed. Then for each segment the following actions are performed:

1. The Čerenkov beam is updated with the amount of Čerenkov light produced in the current segment and atmospheric attenuation along the track segment is applied to the beam.
2. Counters that hold the amount of light from each of the four components that are seen by the detector are initialized to zero.
3. The flux of scintillation light generated in the current segment and seen by the detector is calculated using the shower age and number of particles. The scintillation efficiency used by the Monte Carlo is shown in Figure 4.28.
4. The scintillation light is scaled as a function of dE/dx. The necessity of scintillation scaling and the energy loss is discussed further in sections 4.4 and 4.7.
5. The flux of direct Čerenkov light scattered to the detector is calculated.
6. The flux of Rayleigh scattered Čerenkov light seen by the detector is calculated.
7. The aerosol scattering transmission factor from the shower track to the detector is calculated.
8. The Rayleigh and ozone scattering transmission factor from the shower track to the detector is calculated.

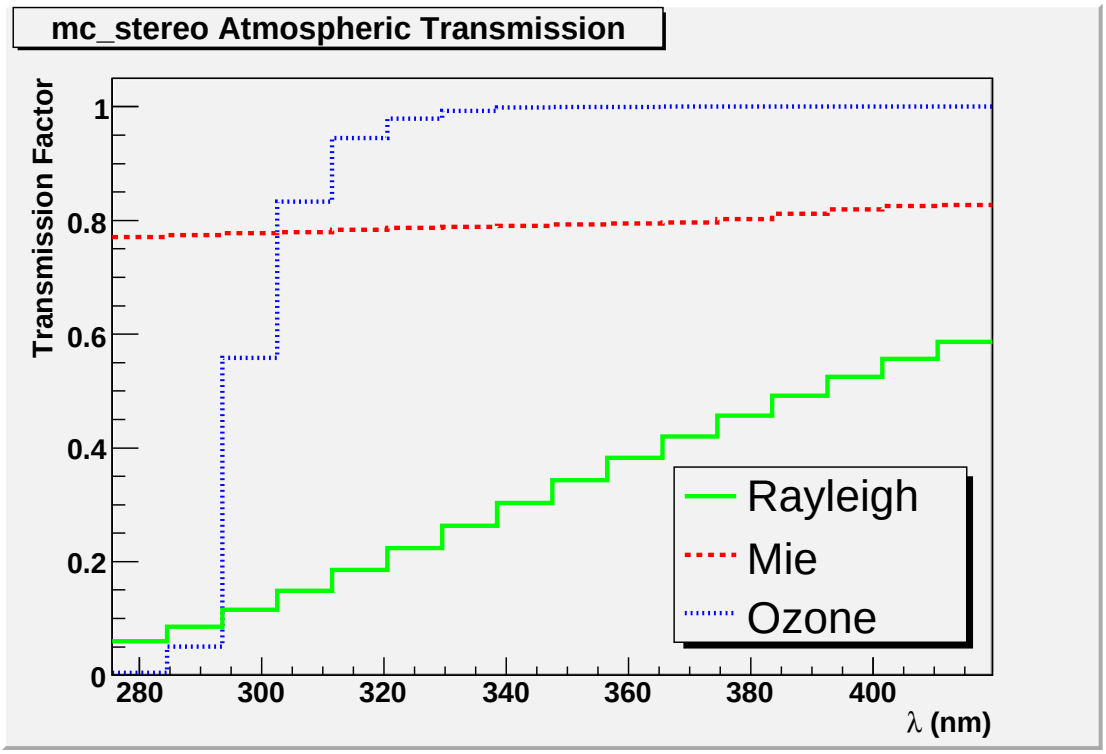

Figure 4.27. The wavelength dependence of the Mie, ozone, and Rayleigh atmospheric transmission factors of UV light as implemented by mc_stereo. This is the transmission factor applied to a light source at an altitude of 3.8 km and zenith angle of 79°, an average geometry of high energy events seen by HiRes.

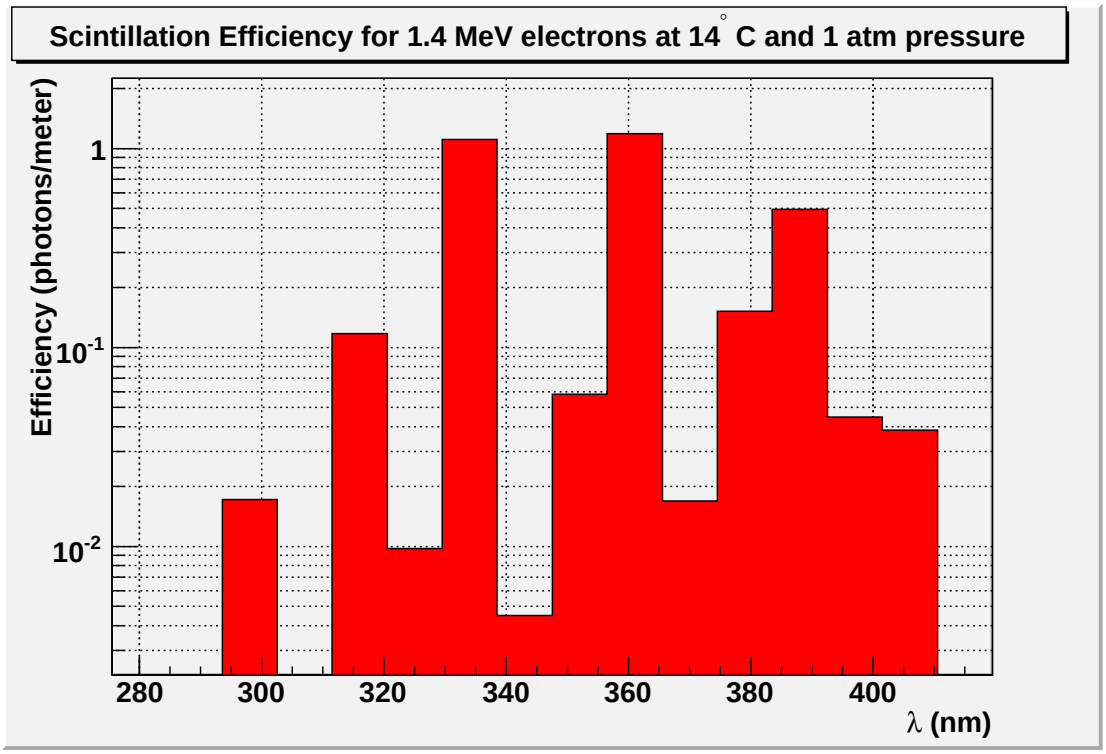

Figure 4.28. The scintillation efficiency of 1.4 MeV electrons as implemented by mc_stereo (scin2p.f). The integral of this plot is 3.25 photons/meter as measured in [38].

9. The flux of all light components among the sixteen wavelength bins is accumulated and stored. Atmospheric attenuation from the previous steps is applied as well.

Figure 4.29 summarizes the steps performed by the hr_newlight subroutine.

At the end of hr_newlight, we know the number of photoelectrons produced by each segment of the shower that would fall into a 5.084 m^2 mirror with reflectivity normalized to that of HiRes1 mirror 17. The final mirror reflectivity correction will be applied during ray tracing in the hr_pe_times procedure which follows.

The hr_pe_times subroutine finishes the shower generation block by implementing the Nishimura-Kamata-Greisen (NKG) function [39] to simulate the lateral width of the shower, determining which detector elements actually view the shower, ray tracing the shower and applying the final mirror reflectivity correction, and assigning arrival times to the shower light at the detector.

4.6.3 Electronics Simulation

The Monte Carlo must try to faithfully imitate the electronic response of the detector to a light source, this involves converting the $N_{\rm pe}$ in a tube to a discrete signal profile and digitizing as the electronics at each site do.

The FADC electronics of HiRes2 is simulated first by the hr_electronics_fadc subroutine. The noise tubes are added to the list of tubes that detected the shower using a Poisson distribution. The row and column sums are calculated and a check is made to see if each mirror triggered. Tubes in mirrors that trigger have their $N_{\rm pe}$ converted to analog signal profile (voltage vs. time) and then digitized with a 10 MHz sampling rate. The simulated data is then saved in the same format as real data in the FRAW, FTRG1, and FPHO1 DST banks.

There are corrections made to the Monte Carlo that must be accounted for to properly reconstructed the simulated data. The gains provided by the gain database are lacking the excess noise factor, α, but are added in during the electronics simulation of both HiRes1 and HiRes2. Figure 4.30 shows that effect of the α gain correction. The figure shows the FPHO1 $N_{\rm pe}$ as a function of the thrown $N_{\rm pe}$

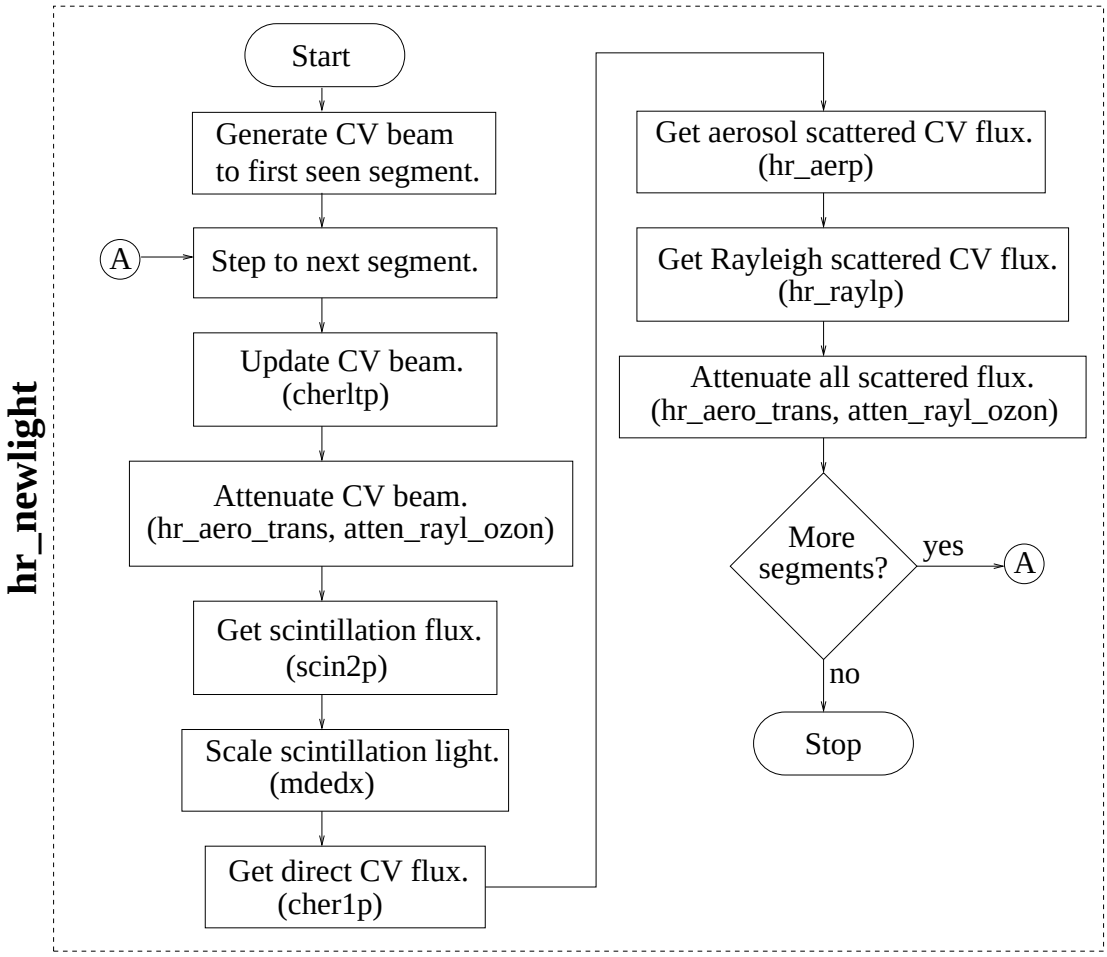

Figure 4.29. Functional block diagram of the hr_newlight subroutine. It determines the $N_{\rm pe}$ measured by a mirror 5.084 $\rm m^2$ with mirror reflectivity normalized to HiRes1 mirror 17 for each shower segment. All quantum efficiency and UV filter corrections are applied as well.

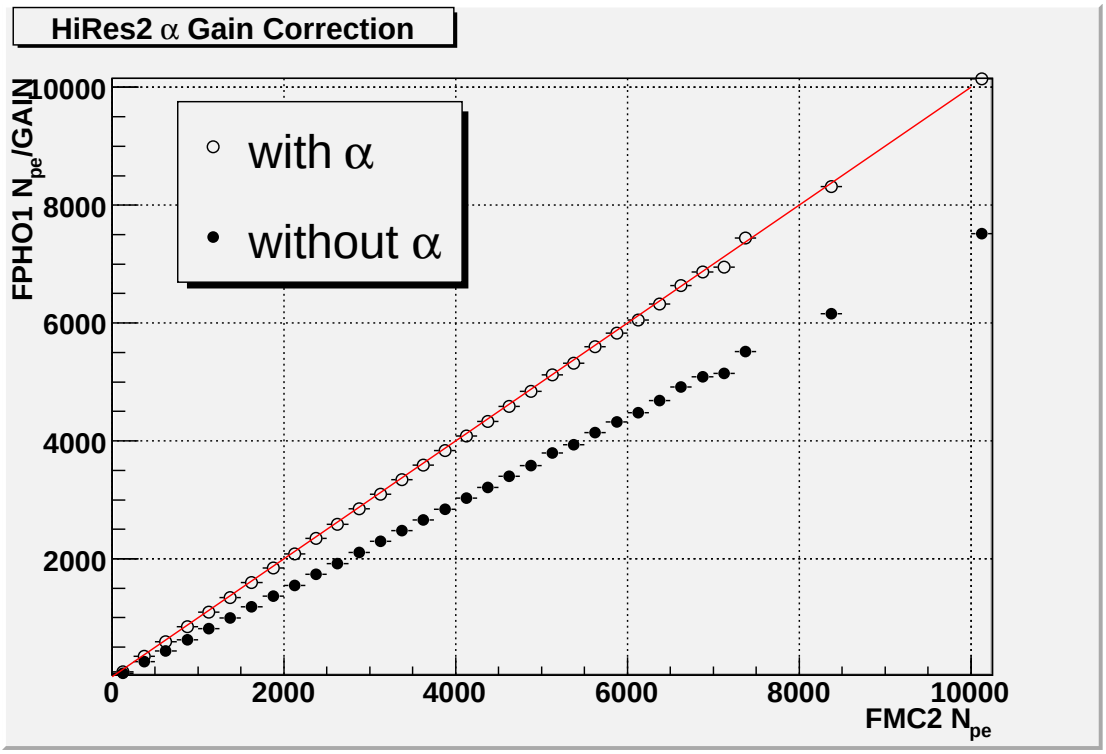

Figure 4.30. A comparison of the mc_stereo output FPHO1 $N_{\rm pe}$ to the thrown $N_{\rm pe}$ using the gain correction factor with and without α. The line shows 1-to-1 correspondence that is expected and it is only attained when α is applied to the gains for each tube. The HiRes2 value for α is 1.35.

stored in the FMC2 bank. The FMC2 value is the value we expect to get back when we try to reconstruct the amount of light seen in a tube. By applying the gain to the FPHO1 $N_{\rm pe}$ without the additional α correction, Figure 4.30 clearly shows that the light in the tube is underestimated. By normalizing the gain by α we get back the expected light, as seen by the 1-to-1 correspondence in the figure. Figure 4.31 shows the same correction is needed for HiRes1 tubes.

The sample and hold electronics of HiRes1 is imitated using similar steps. Noise tubes are added assuming Poisson fluctuations, tube signals are generated by taking the $N_{\rm pe}$ and converting to an analog signal profile and digitizing it. Finally the event trigger algorithm is applied to see which mirrors trigger for the event. The HRAW1 DST bank is filled the data just a real event.

A 10% correction is made to rev3 tubes to account for normalization in the gain database. Since the gain database is normalized to rev4 tubes and these tubes have a 10% higher integrated quantum efficiency, a factor of 1.1 must be applied to rev3 tubes to match what the Monte Carlo "threw" for the tube [19]. Figure 4.32 shows the effect. The figure shows for one month's worth of Monte Carlo data, the HRAW1 $N_{\rm pe}$ stored by mc_stereo as a function of the thrown $N_{\rm pe}$ stored in the FMC1 bank. The HRAW1 value is the value processed by the simulated electronics with all applied gains, mirror reflectivity, and quantum efficiency applied to it. The FMC1 value is the $N_{\rm pe}$ we expect to get back when reconstructing the signal for a tube. Note that rev3 and rev4 have different slopes. A fit was done for each and the slope of the rev4 line is 1.0 and the slope of the rev3 line is 1.1, showing that indeed and additional 10% is applied to the rev3 $N_{\rm pe}$.

The final step of a Monte Carlo event is to store the FRAW1, FTRG1, FPHO1, and HRAW1 banks into a DST and write the event to disk. Additionally information about the true values generated by the Monte Carlo in creation of the event is stored as well in the FMC1 and FMC2 banks. This allows us to perform resolution studies for example to determine if we can accurately reconstruct events.

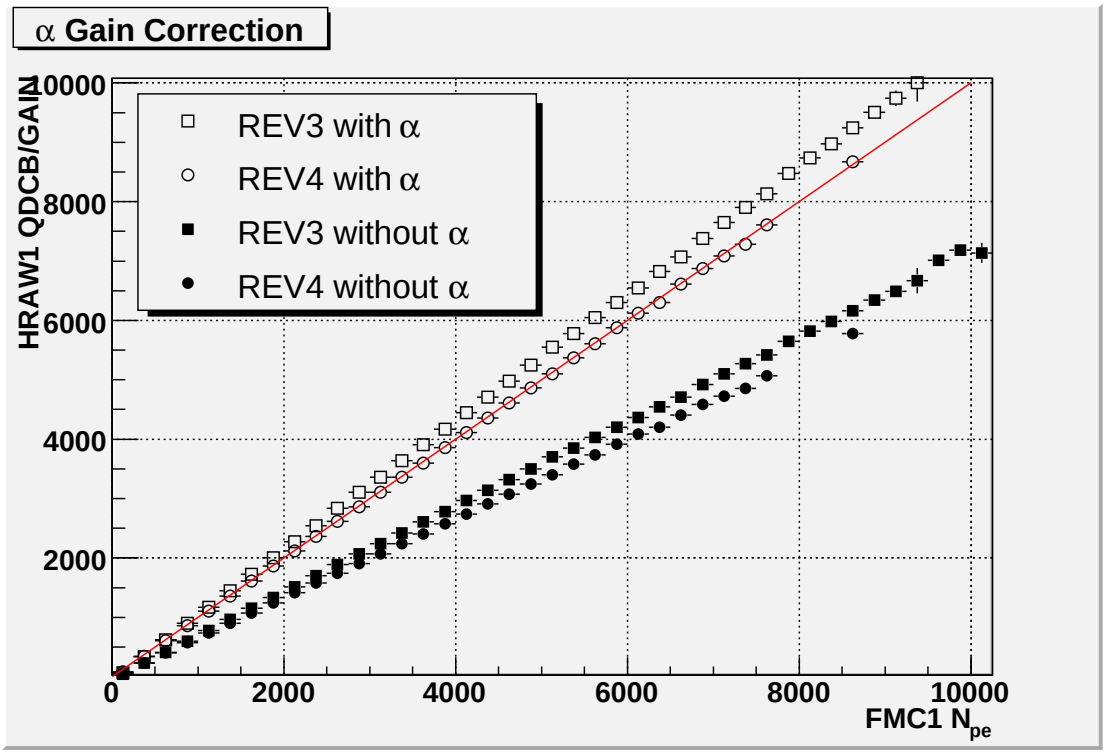

Figure 4.31. A comparison of the mc_stereo output HRAW1 $N_{\rm pe}$ to the thrown $N_{\rm pe}$ using the gain correction factor with and without α. The line shows 1-to-1 correspondence that is expected and it is only attained when α is applied to the gains for each tube. The HiRes1 value for α is 1.5. The 10% difference between rev3 and rev4 tubes can be see here as well.

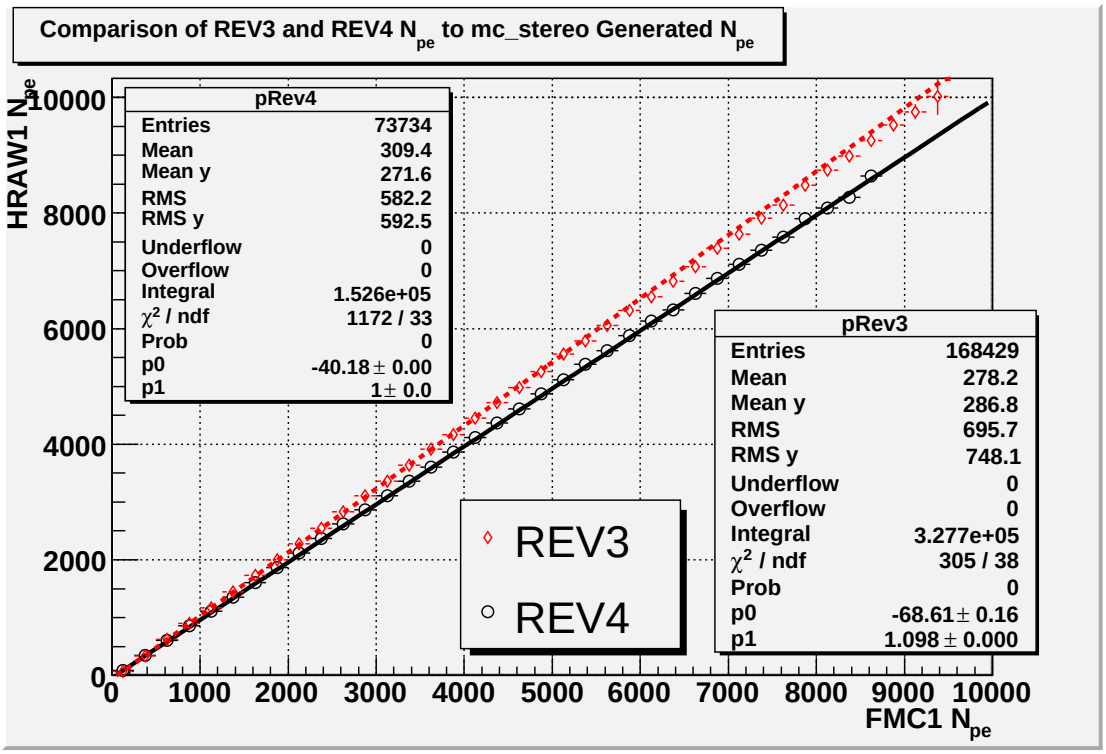

Figure 4.32. Rev3 tubes have an additional 10% added to the HRAW1 $N_{\rm pe}$ to correct for smaller tube acceptance. For one months worth of simulated data the HRAW1 $N_{\rm pe}$ was plotted versus the thrown FMC1 $N_{\rm pe}$ value and a linear fit was done. The slope of the line for rev3 tubes is 1.098 and for rev4 tubes is 1.000, clearly showing the 10% correction done by the Monte Carlo on rev3 tubes only.

4.6.4 Time Scrambling and Composition Mixing

The Monte Carlo allows only one primary species to be thrown during a run, so we need a way to simulate the measured composition of cosmic primaries to have good agreement with the collected data. The measured composition is 80% proton and 20% iron [2], so a Monte Carlo set of each primary species was generated and mixed together in this same proportion. Therefore a separate offline mixing routine was written that scans all of the events in proton and iron Monte Carlo DSTs for each day. For each proton event a uniformly distributed random number between 0 and 1 is thrown, if the value of the random number is less than or equal to 0.8 then the proton event is kept, otherwise it is ignored. A similar procedure is done with iron events where an event is kept if the random value is 0.2 or less. The combined proton and iron Monte Carlo is then time scrambled.

A problem with the Monte Carlo generation is the time of each event. Although it references a database of stereo ontime for each hour, events are thrown with simulated FRAW1 timestamps 10 milliseconds apart starting at the top of a given hour. This causes all events for a given hour on typical night to start at second 0 and end several seconds later. Whereas the real event times are of course spread out much more widely in time. This compression of event times in the simulated data could cause an entire nights worth of events to be rejected when temporally dependent cuts (e.g., weather cuts) are applied.

So a second post Monte Carlo generation routine, takes each event and scrambles the simulated FRAW1 and HRAW1 timestamps to fall within the actual time during which the detector operated in stereo collection mode. Additionally thrown events that do not have any time stamp at all associated with them, for example events that fail the R_{p} cut and do not trigger any mirrors, are time scrambled for the aperture calculation, since the same temporal cuts need to be applied to these events as well for proper accounting of the detector's efficiency.

4.6.5 Databases

To make the Monte Carlo simulation as realistic as possible, we wish to simulate the conditions under which the detector also ran. Therefore for each night that

real data was collected, we store information about the running conditions of the detector and store them into databases which are then used for a simulated night's data. For example, if the detector only ran for 30 minutes during the first hour of running, the Monte Carlo should only generate events for thirty minutes worth of simulated running time. If in the following hour the detector ran for the fill 60 minutes, then the Monte Carlo again mimics this number of events. This ensures the relative event rate under the dynamic conditions of the detector is maintained and ensures that our aperture calculation is correct. The databases that the Monte Carlo uses are atmospheric, radiosonde, HiRes1 thresholds, HiRes1 and HiRes2 gains, HiRes2 variances, and hourly ontime. Many of these databases are used in reconstruction as well.

4.6.5.1 Atmospheric Database

The atmospheric database provides information about the optical clarity of the atmosphere on an hourly basis and is fully described in [49]. It provides measurements of the vertical aerosol optical depth (VAOD), horizontal extinction length (HAL), and scale height, as well as other information. It uses HR2SLS laser shots as reconstructed by HiRes1 to measure the transmission of the atmosphere surrounding the detector from heights of several hundred meters to six kilometers.

Using a modified version of the shower reconstruction code, eleven different HR2SLS geometry configurations shown in Table 4.4 are used. The laser shots are then reconstructed and fitted for laser energy, polarization, aerosol horizontal attenuation length, aerosol mixing layer height, and aerosol scale height. The aerosol and Rayleigh phase functions used to determine the aerosol scattering parameters is the same used by the Monte Carlo and reconstruction shown in Figure 4.33.

The atmospheric database is an ASCII file found in the hires_soft constants repository. The format of the file is shown in Table 4.5 for one chosen hour. Each column corresponds to a laser geometry shown in Table 4.4. Up to fourteen geometries are stored for each hour, in this example only the six actually measured are shown. Each column contains the following information:

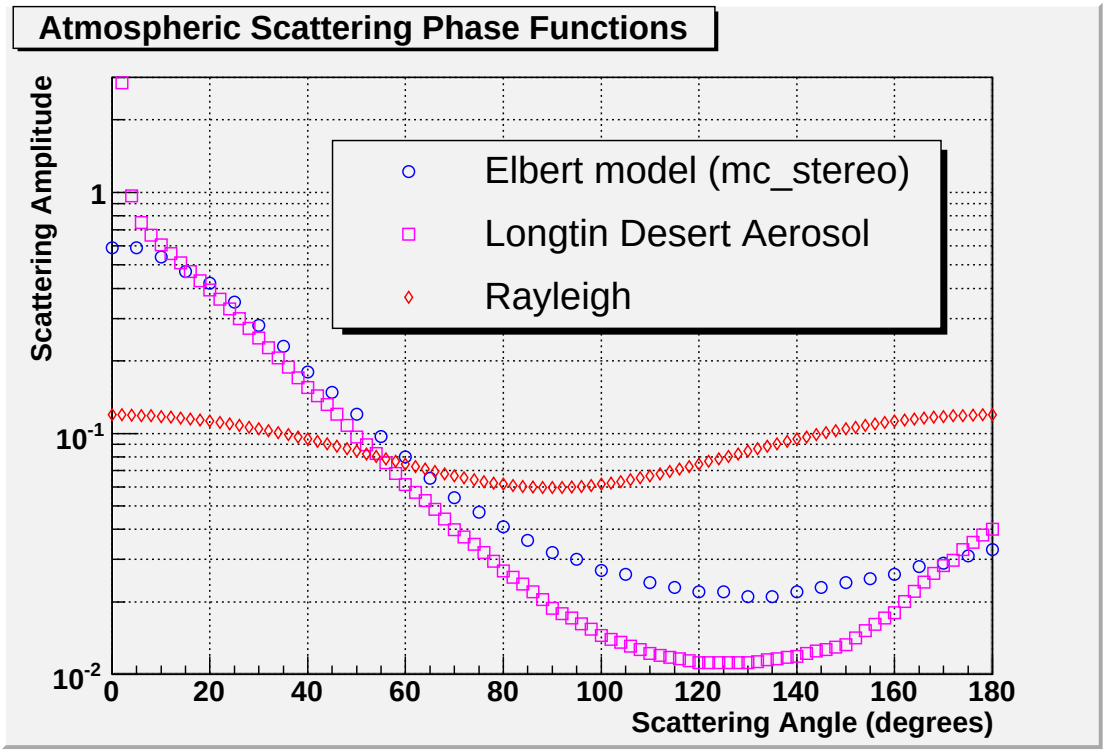

Figure 4.33. Aerosol scattering phase function used by mc_stereo (aero_phase.inc). This function was determined by Jerry Elbert assuming an a^{-4} aerosol distribution, where a is the aerosol particle size. The Longtin desert aerosol measurement and the Rayleigh scattering phase function are shown for comparison. All phase functions are normalized to unity over 4π solid angle.

Table 4.4. HR2SLS geometries used measure the atmospheric parameters supplied by the atmospheric database. Phi and the elevation angles are the angles of the laser track axis, zlow and zhigh are the minimum and maximum heights for which measurements were used for fitting, and scattering angle is range of scattering angles between the laser track and the detector.

lgeom	phi (deg)	elevation (deg)	zlow (km)	zhigh (km)	scattering angle (deg)
1	49	4	0.45	1.4	36 - 160
2	64	5	0.63	2.0	66 - 154
3	79	10	0.72	3.7	66 - 144
4	94	10	0.66	5.4	81 - 157
5	109	10	1.29	5.2	111 -155
6	319	10	1.08	4.2	106 - 150
7	334	10	1.04	6.0	91 - 159
8	349	10	1.08	6.6	77 - 153
9	4	5	0.57	2.0	61 - 155
10	19	4	0.40	1.7	31 - 165
11	34	90	0.63	3.8	94 - 106

Table 4.5. Format of the atmospheric database used to determine vertical aerosol optical depth, horizontal extinction length, and vertical scale height. This is the entry for the six measured geometries on the night of 27 December 1999, hour 3 UTC.

lsr	:	1	1	1	1	1	1
lshots	:	14	15	15	13	15	15
al	:	24.2	29.6	40.1	29.1	41.0	9.6
ha	:	0.5	1.0	1.1	0.8	1.1	0.2
hm	:	0.0	0.0	0.0	0.0	0.0	0.0
vaod	:	0.0221	0.0319	0.0268	0.0265	0.0260	0.0186
ene	:	5.59	5.40	12.47	11.78	5.04	5.32
t4	:	0.731	0.662	0.717	0.698	0.724	0.764
rms	:	0.009	0.012	0.025	0.012	0.009	0.011
t10	:	0.879	0.831	0.856	0.857	0.860	0.898
t16	:	0.922	0.889	0.906	0.907	0.909	0.934
t23	:	0.944	0.920	0.933	0.934	0.935	0.953
t30	:	0.956	0.937	0.947	0.948	0.949	0.963
phi	:	78.6	93.9	109.1	319.7	334.9	349.7
elev	:	10.1	10.1	10.2	10.1	9.9	10.0

1.	lsr	Indicates if the measurement for this geometry is available.
2.	lshots	Number of laser shots used to obtain mean values.
3.	al	Mean aerosol horizontal attenuation length (km).
4.	ha	Mean aerosol scale height (km).
5.	hm	Mean aerosol mixing layer (km).
6.	vaod	Mean vertical aerosol optical depth.
7.	ene	Laser energy used for fitting (mJ).
8.	t4	Mean aerosol transmission - 4° elevation, 30 km distance.
9.	rms	RMS on aerosol transmission (t4 geometry) from lshots.
10.	t10	Mean aerosol transmission - 10° elevation, 30 km.
11.	t16	Mean aerosol transmission - 16° elevation, 30 km.
12.	t23	Mean aerosol transmission - 23° elevation, 30 km.
13.	t30	Mean aerosol transmission - 30° elevation, 30 km.
14.	phi	Phi angle of laser for this geometry (degrees).
15.	theta	Theta angle of laser for this geometry (degrees).

Figure 4.34 shows the aerosol horizontal attenuation length over the entire period of good weather stereo operations covered by this work. The mean of the distribution is found to be 38.58 km. Figure 4.35 shows the scale height of the atmosphere over the same period and the mean is found to be 2.26 km. The vertical aerosol optical depth is shown in Figure 4.36. Air shower measurements are most sensitive to observations through large optical depths over small elevation angles, so the transmission for 4° elevation laser shots is shown in Figure 4.37.

4.6.5.2 Radiosonde Database

The radiosonde database contains pressure and temperature measurements obtained from radiosonde balloons launched from the Salt Lake City International Airport. Twice daily, at 00:00 and 12:00 UTC, radiosonde balloons are launched and record the temperature, pressure, humidity, wind speed and wind direction at many depths upon its ascent. The information from the 12:00 UTC flight is processed into tables containing height, atmospheric depth, pressure, and density and is useful for

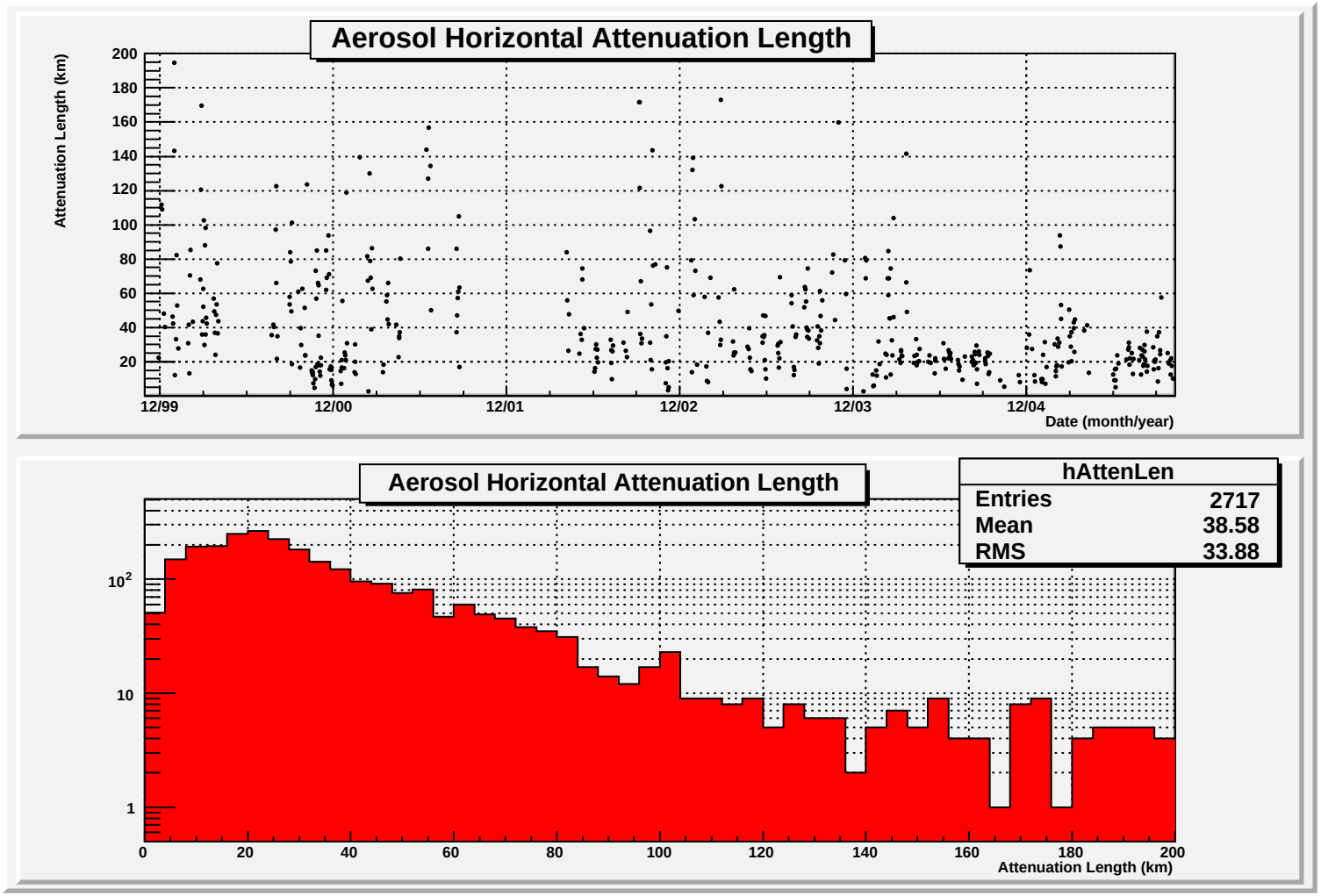

Figure 4.34. The aerosol horizontal attenuation length for all good weather stereo hours of operation.

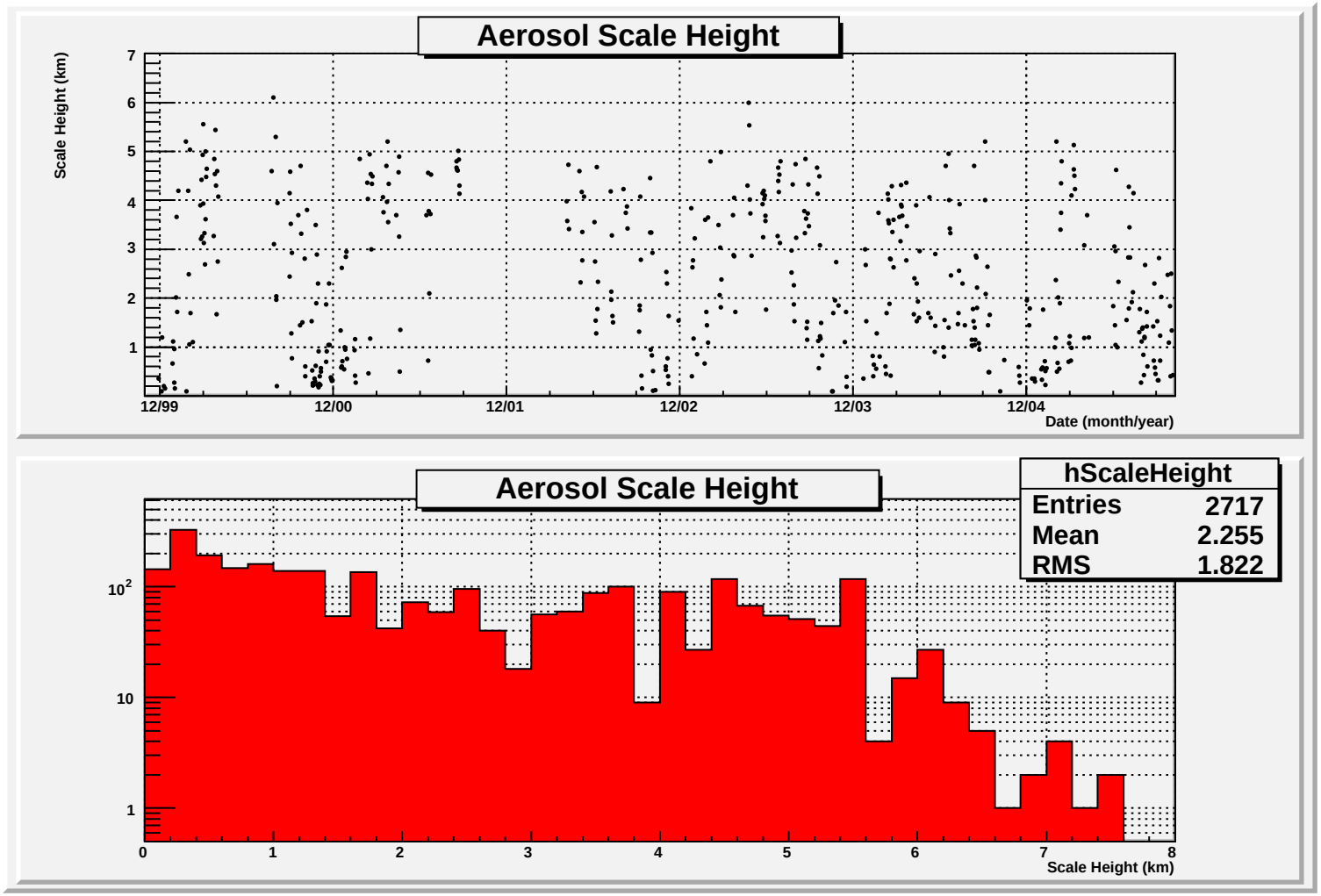

Figure 4.35. The aerosol vertical scale height for all good weather stereo hours of operation.

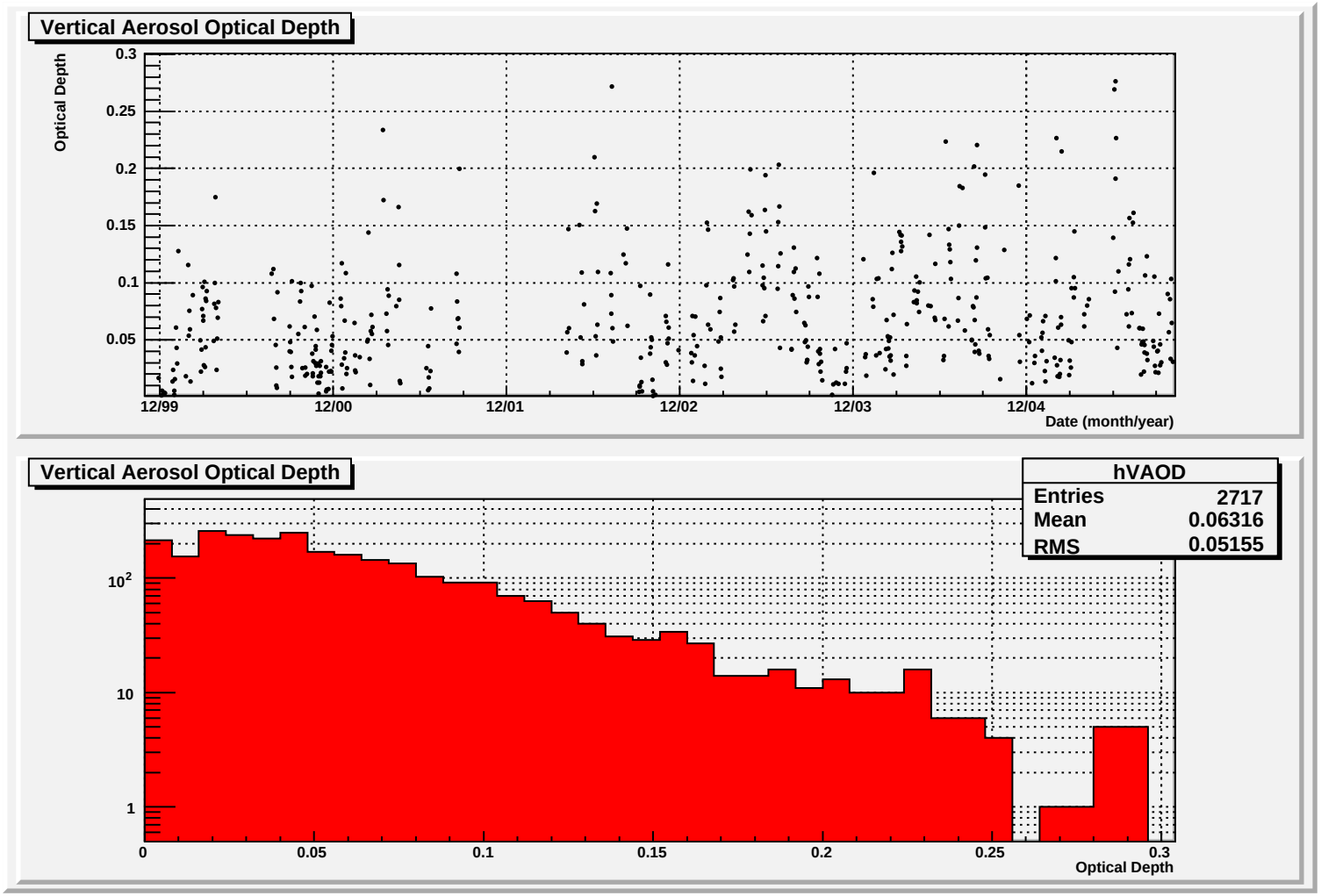

Figure 4.36. The vertical aerosol optical depth for all good weather stereo hours of operation.

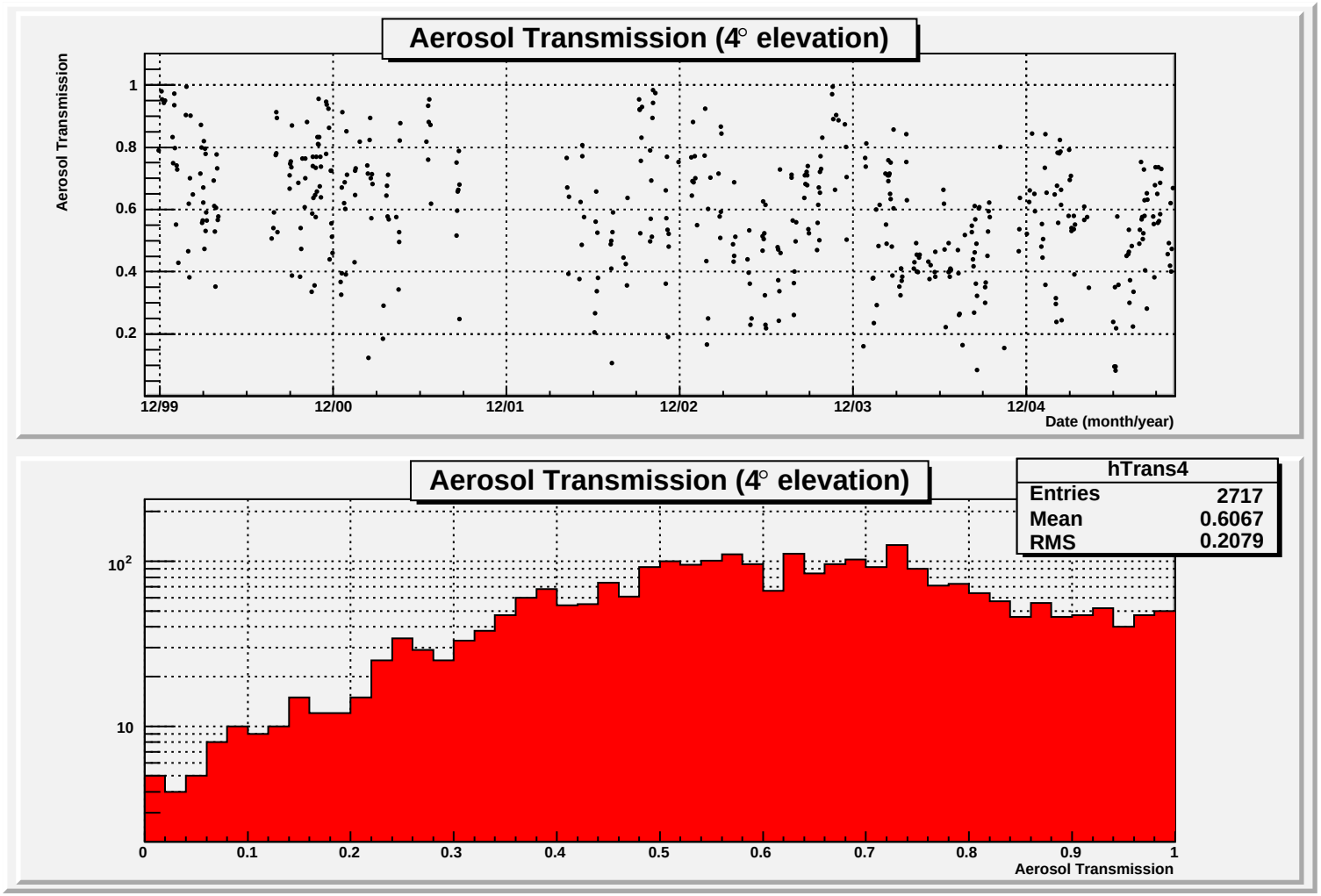

Figure 4.37. The aerosol transmission for all good weather stereo hours of operation. This is the transmission measured by laser shots with 4° elevation angle. Air shower measurements are most sensitive to observations through large optical depths.

our experiment to determine the slant depth of showers. Temperature and density readings are also used to determine the amount of ozone and molecular scattering.

The format of the file is shown in Table 4.6. Each row corresponds to readings taken at a given depth. The contents of each row are: measurement type, height in meters, temperature in Kelvin, vertical depth in g/cm^2, and density in g/cm^3. The measurement type is one of four types:

0: Header denoting the date and time of the recording
4: A mandatory level measurement
5: A significant level measurement
9: A surface level measurement

A mandatory level measurement is a measurement taken at specific pressure levels as dictated by international standard. A significant level measurement is one where abrupt changes in temperature are recorded and a surface level measurement is the measurement taken upon launching at the surface of the earth [34].

Figures 4.38, 4.39, and 4.40 show the average temperature, density and vertical depth profiles obtained from the radiosonde data over the period of HiRes stereo operations. The 1976 U.S. standard atmosphere model [42] is shown as a comparison to the actual atmosphere measured by radiosonde data. The plots measure altitude from sea level. For reference, the height of HiRes sites is approximately 1.5 km above sea level and vertical depth of 860 g/cm^2.

4.6.5.3 HiRes1 Threshold Database

The HiRes1 threshold database contains hourly averages of the thresholds and countrates for each mirror of the sample and hold electronics. Currently only the thresholds are used by the Monte Carlo. Each file contains a month's worth of data. The file format is as follows:

1. Day, hour, mirror.
2. 256 mean thresholds. (QDC counts)
3. 256 number of threshold measurements.

Table 4.6. Format of the radiosonde database used to determine atmospheric density and temperature as a function of height. This is the entry for the night of 01 December 1999, hour 12 UTC.

9	1288	285.35	867.00	0.001057
4	1451	285.75	850.00	0.001035
4	3041	272.45	700.00	0.000894
5	4568	259.05	575.00	0.000772
5	5026	255.05	541.00	0.000738
4	5610	251.05	500.00	0.000693
5	5788	251.25	488.00	0.000676
4	7230	242.05	400.00	0.000575
5	8314	231.85	342.00	0.000513
4	9200	226.05	300.00	0.000462
5	9910	219.85	269.00	0.000426
4	10380	218.45	250.00	0.000398
4	11810	217.85	200.00	0.000319
5	12445	217.85	181.00	0.000289
5	13543	212.65	152.00	0.000249
4	13630	213.85	150.00	0.000244
5	14977	215.45	121.00	0.000195
5	15880	220.45	105.00	0.000166
4	16200	218.85	100.00	0.000159
5	16297	219.85	98.50	0.000156
5	16591	220.65	94.10	0.000148
5	17867	212.25	76.90	0.000126
4	18450	215.45	70.00	0.000113
4	20570	215.45	50.00	0.000081
4	23790	214.45	30.00	0.000049
4	26340	214.45	20.00	0.000032
5	27248	214.25	17.30	0.000028
5	29151	218.45	12.80	0.000020
4	30750	218.25	10.00	0.000016
5	32241	214.85	7.90	0.000013

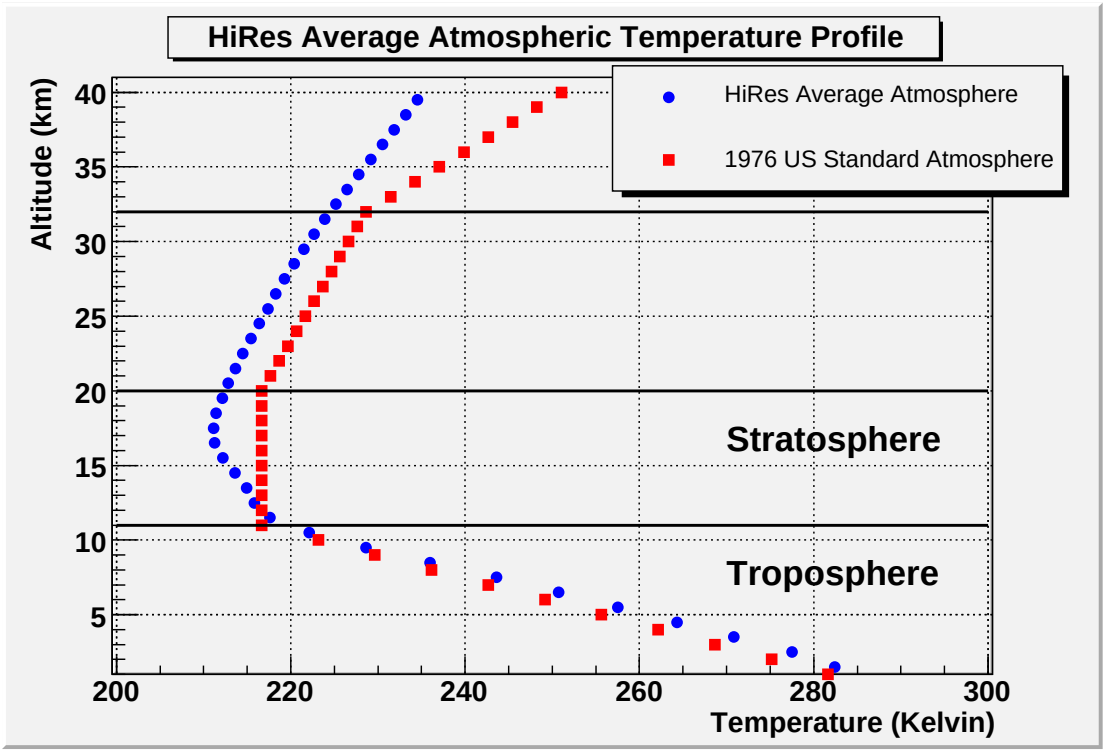

Figure 4.38. The average temperature profile of the HiRes atmosphere. The profile is derived from radiosonde balloon data launched from the Salt Lake City International Airport. The average profile for all hours of stereo operation is plotted here. The 1976 U.S. standard atmosphere is shown for comparison. Altitude is measured from sea level. The height of the HiRes2 detector is 1.5 km in this plot.

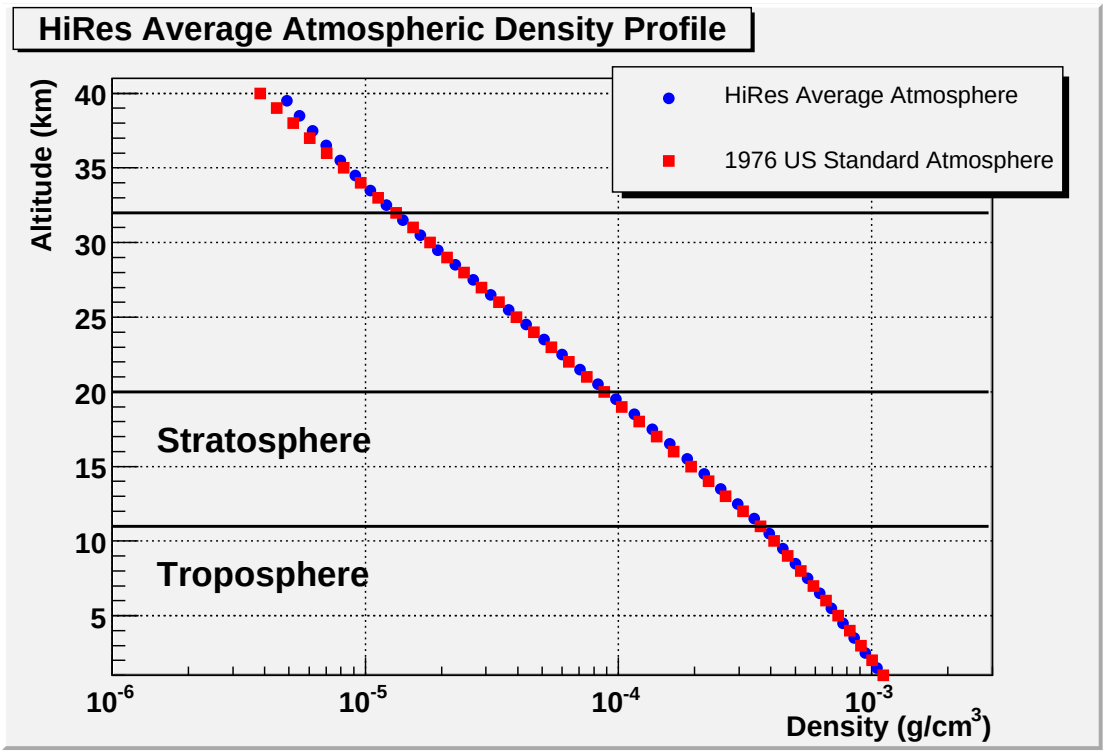

Figure 4.39. The average density profile of the HiRes atmosphere. The profile is derived from radiosonde balloon data launched from the Salt Lake City International Airport. The average profile for all hours of stereo operation is plotted here. The 1976 U.S. standard atmosphere is shown for comparison. Altitude is measured from sea level. The height of the HiRes2 detector is 1.5 km in this plot.

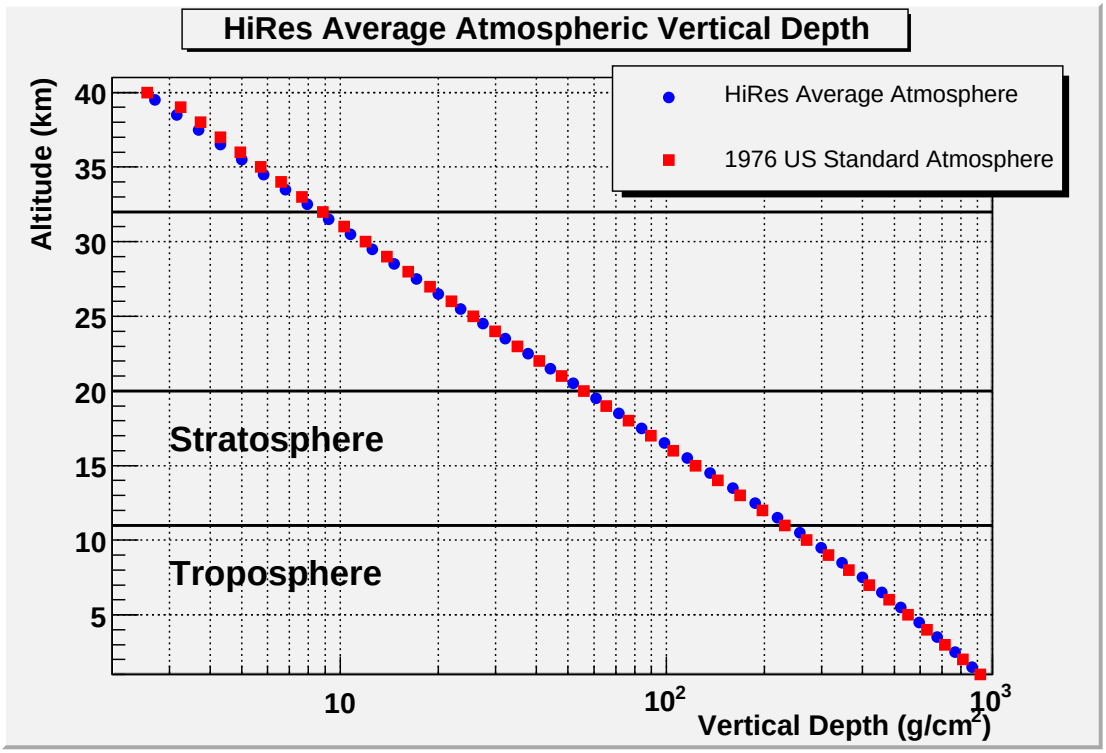

Figure 4.40. The average atmospheric depth of the HiRes atmosphere. The profile is derived from radiosonde balloon data launched from the Salt Lake City International Airport. The average profile for all hours of stereo operation is plotted here. The 1976 U.S. standard atmosphere is shown for comparison. Altitude is measured from sea level. The height of the HiRes2 detector is 1.5 km in this plot and the depth is approximately 860 g/cm^2.

4. 256 mean countrates.
5. 256 number of countrate measurements.

For each mirror the mean threshold and countrate of each tube is stored. The thresholds and countrates are reported by each mirror at HiRes1 every minute, so up to 60 measurements could be contained in the average. The thresholds are used by the Monte Carlo to accurately simulate the noise level in each tube and they also affect the trigger for each mirror.

4.6.5.4 Gain Database

The gain database is used to simulate the response of each individual tube at Hires1 and HiRes2 ((21 HiRes1 mirrors + 42 HiRes2 mirrors) × 256 tubes/mirror = 16128 tubes total). Periodically (several times a year) a roving xenon flasher (RXF) calibration is performed. Since the RXF has a stable known light flux we can use it as the basis for the absolute calibration of each tube. On these calibration nights, the calibration YAG laser is also used to illuminate all tubes before and after the RXF calibration is performed. The energy of the YAG laser is measured by a radiometer and so its shot-by-shot energy is known. We can determine the relative calibration of the YAG laser to the RXF on the night of calibration to determine each tube's gain or the expected QDCB value per N_{pe}.

Before a night of actual data taking, the YAG laser is fired as well. We can then determine the absolute gain of each tube by using the nightly YAG laser shots and "anchoring" them to the RXF standard candle shots taken on the RXF calibration night. The gain for a given tube then can be expressed as

$$G = G_{\mathrm{YAG}}(\mathrm{mon})\frac{G_{\mathrm{RXF}}(\mathrm{calib})}{G_{\mathrm{YAG}}(\mathrm{calib})} \tag{4.18}$$

where $G_{\mathrm{RXF}}(\mathrm{calib})$ is the gain of the tube as measured by the YAG laser found during the night of the RXF calibration, $G_{\mathrm{YAG}}(\mathrm{calib})$ is the gain of the tube as measured by the RXF found during the night of the RXF calibration, and $G_{\mathrm{YAG}}(\mathrm{mon})$ is the tube gain as measured by the current night's YAG laser calibration relative to $G_{\mathrm{RXF}}(\mathrm{calib})$.

Figure 3.32(a) shows the QDC gains for *all* active HiRes1 mirrors over the entire period of stereo data taking used in this study (mirror 17 was taken out of service after the September 2001 shutdown and is not shown). The rev4 electronics QDCs have a larger dynamic range and therefore have higher gains as seen in the figure. Figure 3.32(b) shows the FADC gains for *all* 42 HiRes2 mirrors over the same period of time. Figures 4.41 and 4.42 show the information available for a single mirror at each site for one night. Although TDC gains and pedestals are available in the database, only the QDC gains are currently used. The Monte Carlo uses an assumed pedestal of 257.166 QDC counts, but the pedestals in the database are used for reconstruction of real data. The HiRes2 gain database only provides FADC gains, which are used in the Monte Carlo and for data reconstruction.

The HiRes1 gain database is a collection of ASCII text files. Each file contains 22 entries (one for each mirror) in the following format:

1. Header consisting of year, month, day, mirror, RXF calibration day, RXF gain on the calibration day, YAG gain on the calibration day, YAG gain on the current day, corrected YAG gain on the current day.
2. 256 QDCB gains. (QDC counts/$N_{\rm pe}$)
3. 256 QDCB gain flags.
4. 256 days from which calibration for the tube is derived.
5. 256 QDCB pedestals. (QDC counts)
6. 256 QDCB pedestal flags.
7. 256 TDC pedestals. (TDC counts)
8. 256 TDC gains. (TDC counts/μsec)
9. 256 TDC flags.

The values of RXF gain and YAG gain in the header are averages for the mirror. The flags are used to indicate the quality of the measurement. For instance the gain flags can indicate that there was a problem with the current day's YAG calibration and that another day's YAG calibration is used for the tube. In that instance, the date of the YAG calibration would be recorded in the list of 256 calibration days.

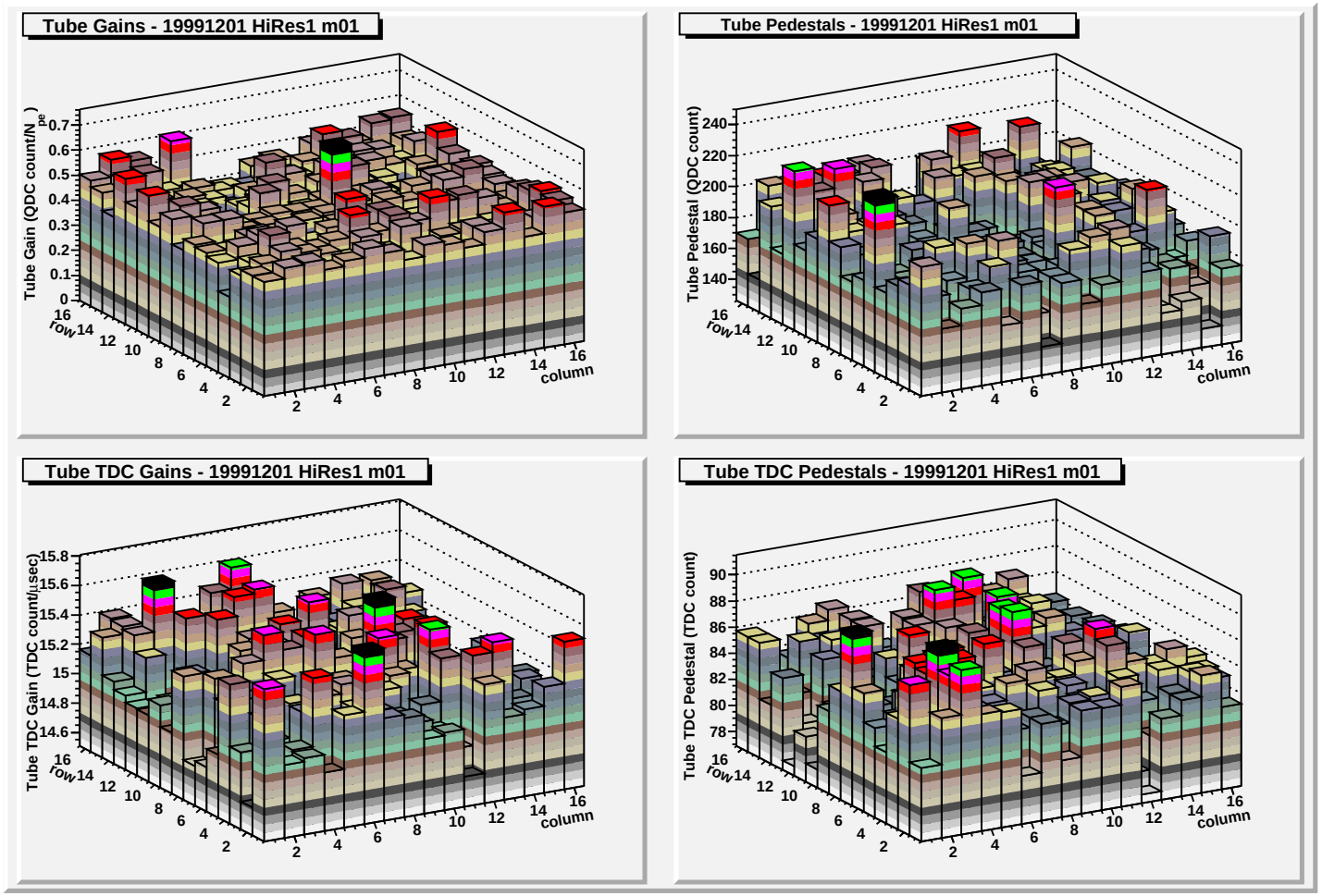

Figure 4.41. The QDC gains, QDC pedestals, TDC gains, and TDC pedestals of all 256 tubes of HiRes1 mirror 1 on the night of 1 December 1999. Additional information such as status flags and dates of calibration are also available for each tube.

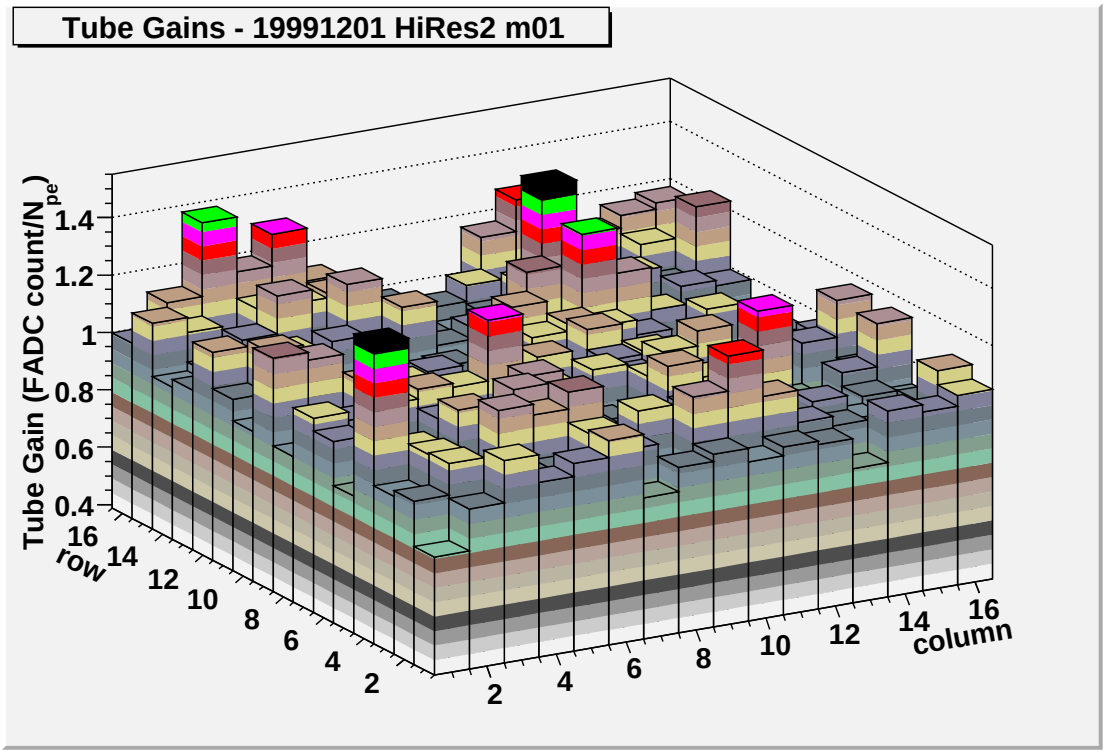

Figure 4.42. The FADC gains of all 256 tubes of HiRes2 mirror 1 on the night of 1 December 1999. Additional information such as status flags and dates of calibration are also available for each tube.

The HiRes2 gain database is similar, but describes FADC gains. It does not contain items 5 - 9 that are recorded for HiRes1.

4.6.5.5 HiRes2 Variance Database

The HiRes2 variance database contains the 16 average trigger DAC settings for both horizontal and vertical trigger sums and the FADC count variances for all 256 tubes of each mirror at Hires2 for each hour of stereo data collection. The database is used to properly simulate the trigger and signal noise of the FADC electronics. Table 4.7 shows the table entry for one mirror on hour 2 UTC of 1 December 1999. It consists of

1. Number of hours in the file.
2. Day, hour, ontime in seconds for the current hour.
3. Mirror number.
4. Vertical column trigger DAC settings.
5. Horizontal row trigger DAC settings.
6. 256 variance measurements of the high gain channels.
7. 16 variance measurements of the column trigger channels.
8. 16 variance measurements of the column low gain channels.
9. 16 variance measurements of the row trigger channels.
10. 16 variance measurements of the row low gain channels.

4.6.5.6 Ontime Database

The hourly ontime database is used by the Monte Carlo to properly generate the relative number of events seen by the detector each hour and to disable mirrors in the simulation that were inoperative during actual running conditions. This is an important consideration for the aperture calculation and the impact of missing mirrors is explored further in section 5.4.1.

Each row summarize the status of both detectors for a given hour. The contents of each row are

1. Date in YYYYMMDD format.

Table 4.7. Format of the HiRes2 variance database. It contains the hourly average trigger DAC setting and variances for each mirror. This is the entry for mirror 1 on hour 2 of 1 December 1999.

```
  98  !  number of hours in database
19991201  2 1320  ! day  hour  sec_alive
 1  ! mir  trigger dacs and variances
 1100 1100 1100 1100 1100 1100 1100 1100 1100 1100 1100 1100 1100 1100 1100 1100 ! V TRIG DACS
 1100 1100 1100 1100 1100 1100 1100 1100 1100 1100 1100 1100 1100 1100 1100 1100 ! H TRIG DACS
  4.2  4.2  4.1  3.5  3.7  3.6  3.5  0.0  3.6  3.3  4.6  3.9  4.4  3.9  3.6  4.2 ! var -- chs   1 to  16
  3.3  3.5  4.4  3.8  3.3  4.2  4.7  3.3  4.1  4.1  3.5  3.9  3.1  3.9  4.4  4.3 ! var -- chs  17 to  32
  3.5  3.5  3.4  3.4  3.2  3.5  3.9  3.5  3.4  3.8  3.6  4.4  3.7  3.9  4.8  6.5 ! var -- chs  33 to  48
  4.5  3.9  0.0  4.0  3.6  3.7  4.0  3.4  3.6  3.7  4.1  4.1  3.4  3.8  4.5  4.9 ! var -- chs  49 to  64
  3.8  3.6  4.1  3.2  4.0  3.8  3.2  4.1  3.5  4.1  4.1  3.8  4.0  3.8  4.4  4.7 ! var -- chs  65 to  80
  3.9  4.2  4.4  3.7  4.2  3.6  3.4  3.6  3.5  3.8  3.9  3.6  3.3  3.6  4.1  4.6 ! var -- chs  81 to  96
  3.6  3.9  3.4  3.7  3.9  3.3  3.5  4.2  3.6  3.5  3.7  3.6  4.0  4.1  5.3  4.1 ! var -- chs  97 to 112
  3.4  3.5  3.7  3.9  4.2  3.9  3.8  4.0  3.7  4.2  4.7  3.6  4.0  3.8  4.2  5.2 ! var -- chs 113 to 128
  3.5  3.4  3.9  2.7  3.6  3.7  3.8  4.2  3.5  3.7  3.3  3.7  4.1  4.1  3.5  3.6 ! var -- chs 129 to 144
  3.4  3.6  3.9  3.0  3.4  3.4  3.6  3.2  3.8  3.8  3.4  3.3  3.5  4.4  4.1  4.0 ! var -- chs 145 to 160
  3.3  3.7  3.4  3.5  3.6  3.4  3.6  3.5  3.3  3.5  3.5  3.7  4.2  3.5  4.3  3.6 ! var -- chs 161 to 176
  3.5  3.9  3.8  3.8  3.8  3.5  3.9  3.3  3.8  3.7  4.0  4.1  4.2  4.0  4.0  4.0 ! var -- chs 177 to 192
  4.0  3.5  3.8  3.8  4.1  3.3  3.4  3.7  3.4  3.7  3.8  3.2  4.2  3.7  3.9  3.6 ! var -- chs 193 to 208
  3.7  3.8  3.5  3.7  4.0  4.5  3.6  3.7  4.1  3.9  4.0  4.0  3.6  4.4  4.1  3.5 ! var -- chs 209 to 224
  3.7  3.8  3.4  3.3  3.3  3.8  3.0  3.6  3.1  3.6  3.4  3.3  3.3  3.7  3.7  3.6 ! var -- chs 225 to 240
  3.4  3.8  3.4  4.0  3.8  3.8  3.4  3.9  3.6  3.7  3.4  3.4  3.9  3.7  3.4  3.8 ! var -- chs 241 to 256
 13.5 13.7 12.6 11.7 13.7 12.9 12.3 13.0 12.6 13.5 14.9 14.1 13.4 13.7 15.3 15.9 ! var -- chs 257 to 272
  0.8  0.8  0.8  0.7  0.9  0.8  0.7  0.9  0.7  0.8  0.8  0.8  0.8  0.8  0.9  0.9 ! var -- chs 273 to 288
 13.4 14.5 14.5 14.5 14.0 13.7 13.6 13.9 13.3 12.9 13.2 13.8 13.5 15.1 12.5 17.4 ! var -- chs 289 to 304
  0.8  0.8  1.0  0.8  0.9  0.8  0.8  0.9  0.8  0.8  0.8  0.8  0.9  0.9  0.8  0.8 ! var -- chs 305 to 320
```

2. UTC Hour.
3. Ontime seconds for HiRes1 mono operation.
4. Ontime seconds for HiRes2 mono operation.
5. Ontime seconds for stereo operation.
6. HiRes1 mirror status consisting of 22 status bits.
7. HiRes2 mirror status consisting of 42 status bits.

Table 4.8 shows the entry for 12 January 2000. Hour seven indicates that HiRes1 ran for almost the full hour, but HiRes2 did not run at all, therefore the ontime of HiRes2 and the stereo ontime are both 0 for this hour. The first 22 status bits indicate that all active mirrors at HiRes1 ran. Mirror 18 which never ran at HiRes1 is marked with the 0 status bit. Since HiRes2 did not run during this hour all mirrors there are marked with the 0 status bit. Hour 9 shows that HiRes1 again ran the full hour, while HiRes2 ran only partially for the hour and now there was some stereo ontime recorded. In this hour mirror 17 at HiRes1 was dropped from running, as indicated by the 0 bit and at HiRes2 all mirrors expect mirror 1 were running. Since mirror 1 points in the direction of HiRes1, this missing mirror can greatly affect the stereo aperture. For all Monte Carlo events simulated for this hour, any light falling on HiRes2 mirror 1 is effectively ignored, since that mirror did not actually run.

4.7 Fluorescence Yield

As electrons from an air shower travel through the atmosphere they excite nitrogen molecules in the air. The subsequent relaxation and emission of fluorescence light is how the HiRes detector measures the properties of the shower. The air fluorescence yield must be understood to relate the amount of measured light to size of the shower at any given depth. The light is proportional to the size of the shower and is weakly dependent on temperature and pressure. The measurement of fluorescence yield used in this analysis is based on the work of Kakimoto, et al [38]. Figure 4.43 shows the fluorescence spectrum used in the reconstruction as well as a comparison to previous measurements.

Table 4.8. Sample entry from the hourly ontime database. Each row summarizes for an hour the number of seconds each detector ran, the number of seconds ran in stereo, and a binary code indicating whether a mirror was operative. This example has been truncated by showing the status of only five mirrors at HiRes2. The actual database entry has 37 more status bits for the remaining mirrors.

DATE	HOUR	H1ON	H2ON	STEREO	1	2	3	4	5	6	7	8	9	0	1	2	3	4	5	6	7	8	9	0	1	2	1	2	3	4	5
20000112	7	3294	0	0	1	1	1	1	1	1	1	1	1	1	1	1	1	1	1	1	1	0	1	1	1	1	0	0	0	0	0
20000112	8	3590	556	465	1	1	1	1	1	1	1	1	1	1	1	1	1	1	1	1	1	0	1	1	1	1	0	1	1	1	1
20000112	9	3600	1978	1556	1	1	1	1	1	1	1	1	1	1	1	1	1	1	1	1	1	0	0	1	1	1	0	1	1	1	1
20000112	10	3591	930	911	1	1	1	1	1	1	1	1	1	1	1	1	1	1	1	1	1	0	0	1	1	1	0	1	1	1	1
20000112	11	3591	1753	1677	1	1	1	1	1	1	1	1	1	1	1	1	1	1	1	1	1	0	0	1	1	1	0	1	1	1	1
20000112	12	3600	3279	3277	1	1	1	1	1	1	1	1	1	1	1	1	1	1	1	1	1	0	0	1	1	1	0	1	1	1	1
20000112	13	97	723	96	1	1	1	1	1	1	1	1	1	1	1	1	1	1	1	1	1	0	0	1	1	1	0	1	1	1	1

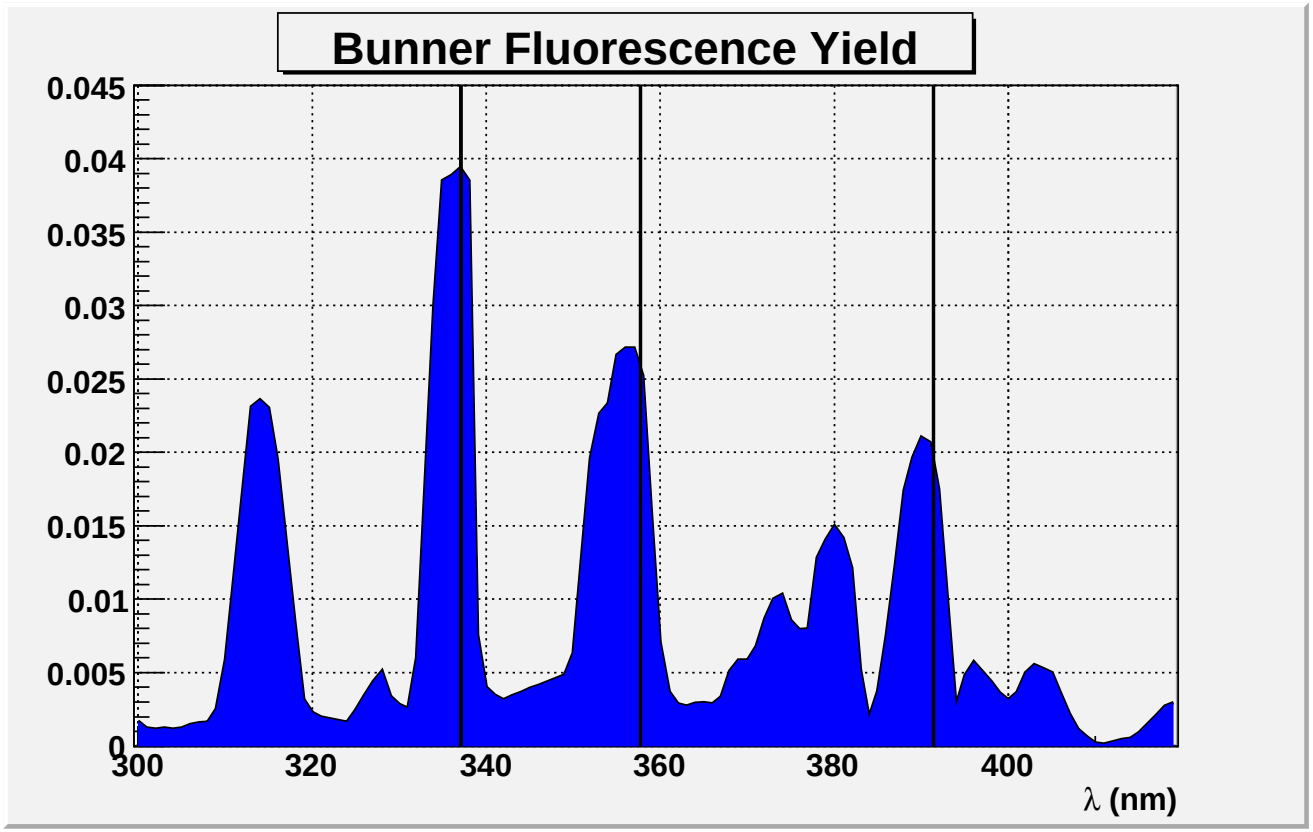

(a) Bunner fluorescence yield.

Figure 4.43. Comparison of different fluorescence yield measurements. The Bunner [21] spectrum was used in older reconstruction code. The other two figures show the the Kakimoto, et al. measurement that is currently used [38]. The second figure shows the Kakimoto measurement binned in a continuous manner as done for the Bunner plot. The third plot shows the Kakimoto measurement as it is implemented in the analysis code using 16 bins 9 nm wide. The three solid lines indicate the wavelengths measured by the Kakimoto experiment.

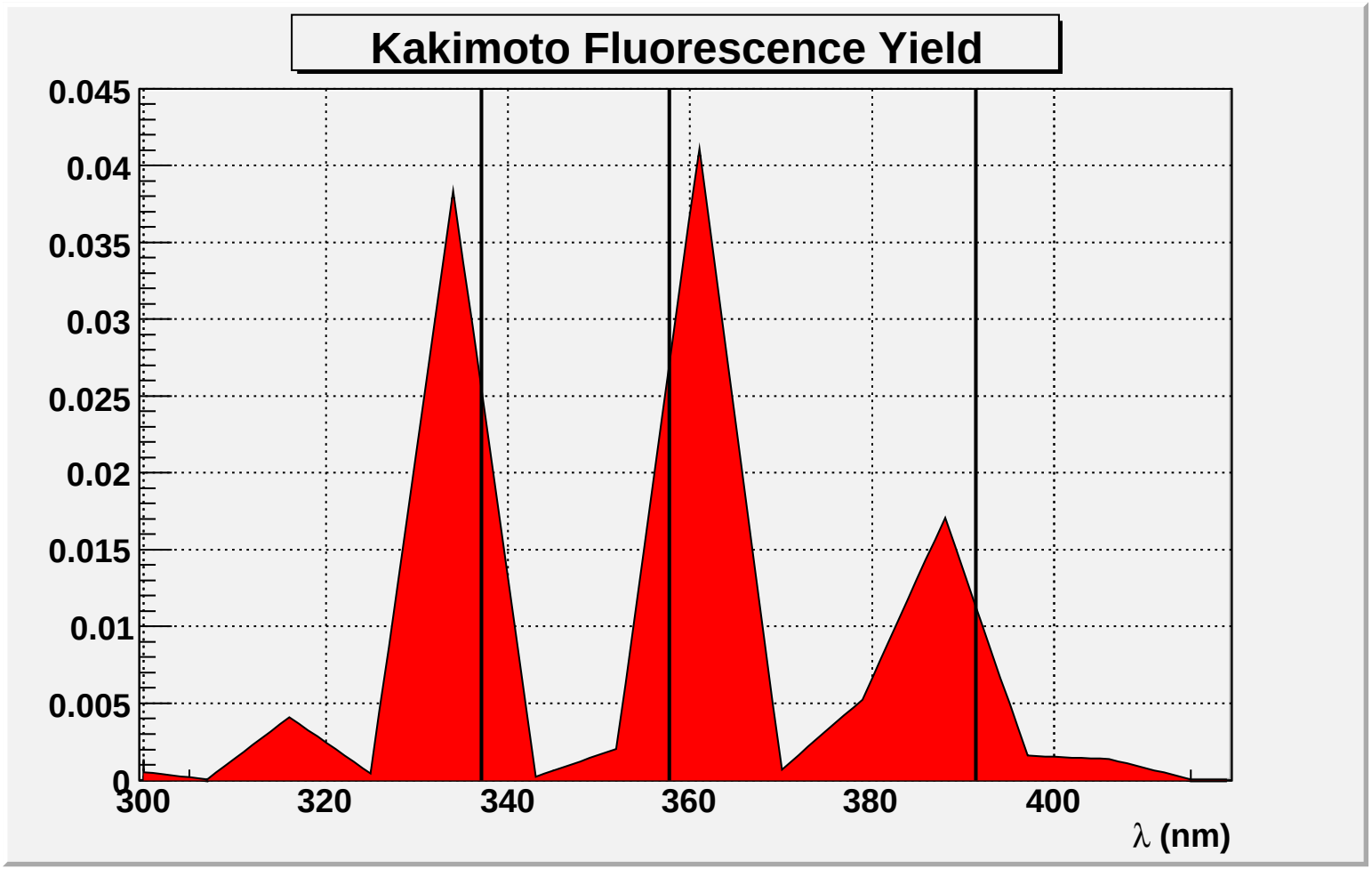

(b) Kakimoto fluorescence yield.

Figure 4.43. continued.

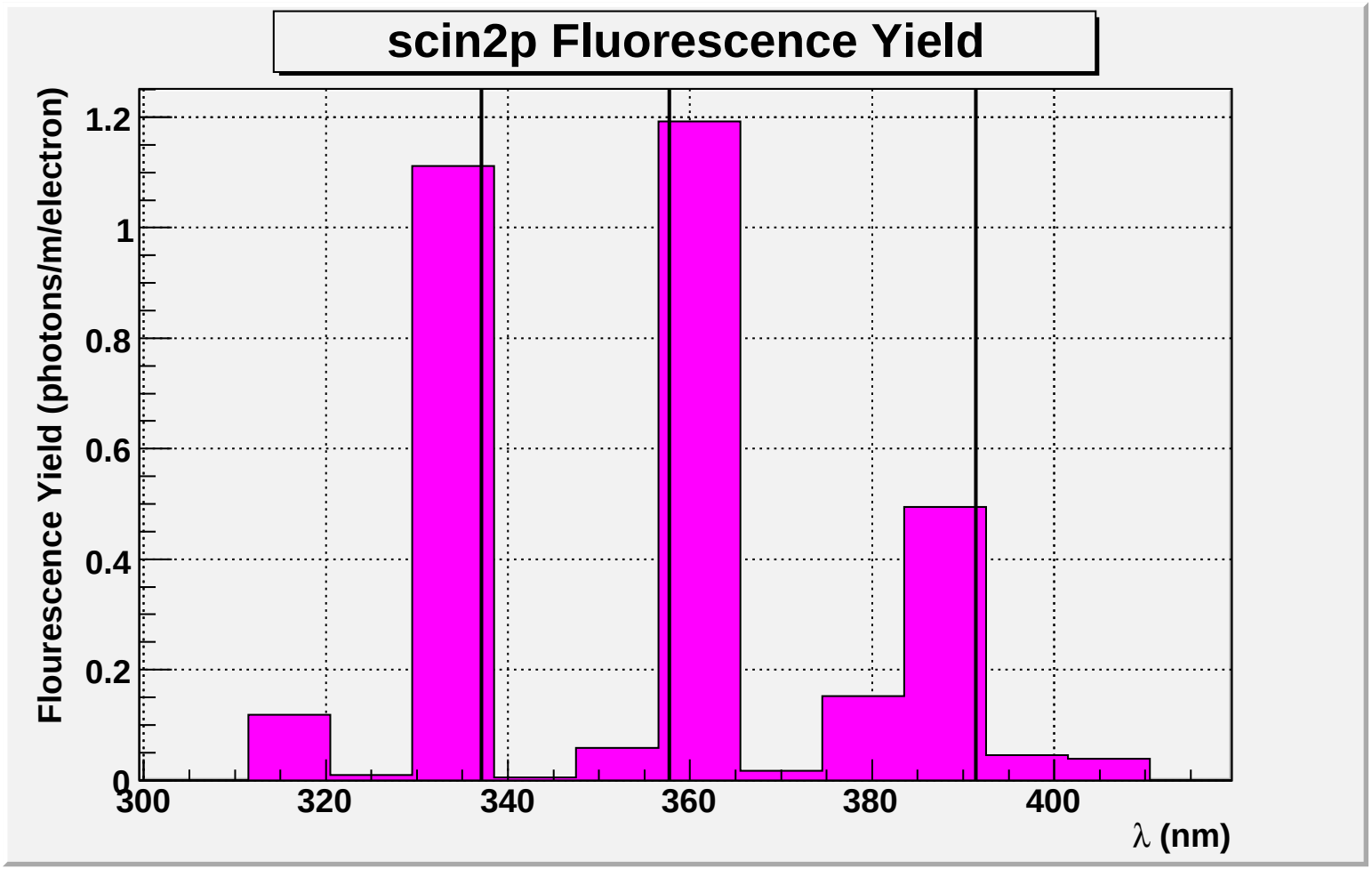

(c) Monte Carlo scin2p fluorescence yield

Figure 4.43. continued.

The Kakimoto experiment used different electron sources at four different energies to measure the fluorescence yield at three UV wavelengths, 337.1 nm, 357.7 nm, and 391.4 nm. A strontium source was used for the 1.4 MeV measurement and an electron synchrotron was used for measurements at 300, 650, and 1000 MeV. Figure 4.44 shows the Kakimoto data and the it can be seen that the fluorescence yield is proportional to the energy loss of the electrons in air.

The fluorescence yield is described by

$$Y = \frac{\left(\frac{dE}{dx}\right)}{\left(\frac{dE}{dx}\right)_{1.4\mathrm{MeV}}} f(\rho, T) \tag{4.19}$$

where dE/dx is the energy loss, $(dE/dx)_{1.4\mathrm{MeV}}$ is the energy loss for a 1.4 MeV electron measured to be 1.668 MeV-cm^2/g, and $f(\rho, T)$ is a function of atmospheric density and pressure. The implemented form for $f(\rho, T)$ used by the analysis code utilizes the 16 bin wavelength dependence. Equations 4.20 and 4.21 show the formulae used to calculate $dE/dx \cdot f(\rho, T)$ of equation 4.19.

$$N_i^{\mathrm{scin}} = \frac{\eta_i^{\mathrm{scin}} a_1 \rho}{N_{\mathrm{total}}^{\mathrm{scin}} f_1 (1 + \sqrt{T}\rho b_1)} \tag{4.20}$$

$$N_{13}^{\mathrm{scin}} = \frac{a_2 \rho}{f_2 (1 + \sqrt{T}\rho b_2)} \tag{4.21}$$

where N_i^{scin} is the number of scintillation photons for wavelength bin i, η_i^{scin} is the fluorescence yield efficiency, ρ is the density, T is the temperature, $N_{\mathrm{total}}^{\mathrm{scin}}$ is the total fluorescence yield over all wavelength bins for a 1.4 MeV electron and a_1, b_1, f_1, a_2, b_2, and f_2 are constants. Equation 4.20 is used for all the wavelength bins except bin 13 where equation 4.21 is used to determine the yield. Note these equations are the fluorescence yield for each ionizing particle in the shower.

Fluorescence yield is used to estimate the amount of scintillation light produced for some small segment of track. When the Monte Carlo or reconstruction routines simulate a shower, the shower track is divided into many small segments so that the properties of the atmosphere and shower may be considered constant. Equation 4.19 is then used to determine the amount of scintillation light for each ionizing particle in the segment. Multiplying the known number of shower particles by the yield

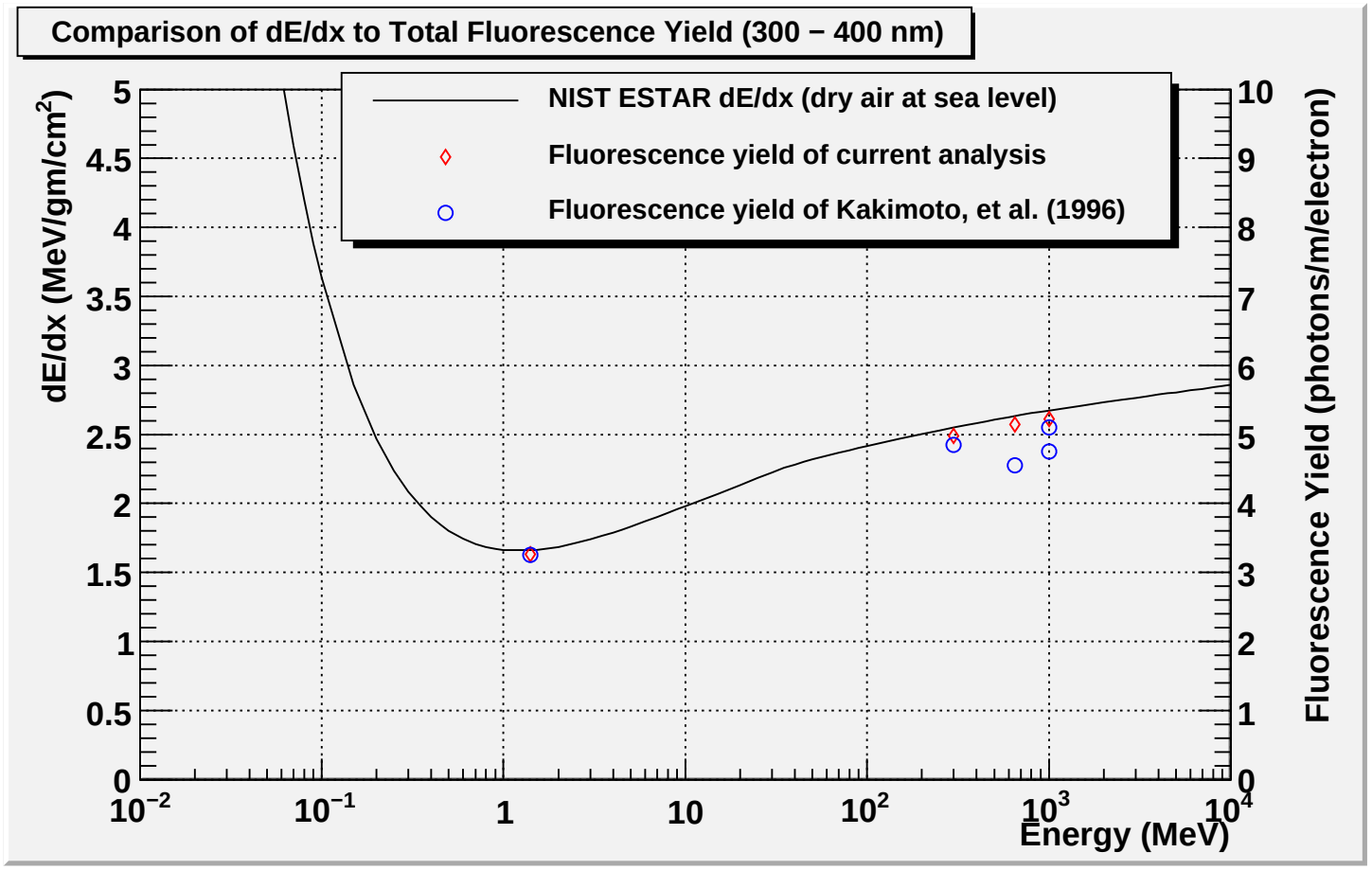

Figure 4.44. Comparison of dE/dx to the total fluorescence yield as measured by Kakimoto, et al. and implemented in the reconstruction code. The circles show the *measured* points of the Kakimoto experiment and the diamonds show the *calculated* fluorescence yield used in the reconstruction.

then gives the amount of scintillation light produced by the shower for the track segment.

4.8 Data Reconstruction

4.8.1 DSTs and Banks

HiRes data are processed into DSTs (**D**ata **S**ummary **T**ape). The name is a historical holdover from times when data was actually more likely to be stored on magnetic tape media. Now disks are cheap enough and have large enough capacities that all HiRes DSTs are actually files stored on disk. For purposes of long term storage, DSTs may, of course, be stored on tape, but it would not be efficient to use them for real data processing where speed and ease of use is desired.

The HiRes DST data storage system is a flexible, modular, extensible framework for storing and processing large amounts of data using minimal storage space. A DST file is superior to an ASCII text file because all data is tightly packed to reduce storage space. To verify data integrity DST files are written as 32 kilobyte blocks of data, with each block containing a 4 byte cyclic redundancy check (CRC) checksum. As DST blocks are written to a file, a CRC is performed and the checksum stored with the block. When the file is subsequently read out for analysis, each block is checked again by computing a checksum value and compared to the checksum stored with the block. If the two do not match, the file has been corrupted and an error is reported to the operator.

A DST file is used to store a collection of DST banks. A bank is a logical analysis unit, which is used to describe some process or measurement. Each bank is made up of one or more bank elements that contain information that is used to characterize the bank.

An example of a bank is the HRAW1 bank, in which is stored the information for an event as measured by the HiRes1 detector. A DST file that contains stereo event data would have one HRAW1 bank entry for each event stored in the file. Some of the important elements of this bank are:

HRAW1 Bank contents:

JDAY	Mean truncated Julian day.
JSEC	Seconds into Julian day.
MSEC	Milliseconds of Julian day.
NMIR	Number of mirrors in this event.
NTUBE	Number of tubes in this event.

Arrays of mirror information. One entry for each of NMIR mirrors.

MIR	Mirror number (1-22).
MIRTIME_NS	Time of mirror holdoff in nanoseconds.

Arrays of tube information. One entry for each of NTUBE tubes.

TUBEMIR	Mirror number (1-22).
TUBE	Tube number (1-256).
QDCB	Digitized channel B charge integral.
TDC	Digitized tube trigger to holdoff time.
THB	Trigger threshold in mV for channel B.
PRXF	Number of photons.

Two special banks are the START and STOP banks which are used to define events. Typically a cosmic ray event will have many banks that are used in the analysis. In addition to signal information from the tubes that observe the events, information such as the distance, direction, angle, and energy of the shower will all be stored in separate banks. The START and STOP banks are used to logically demarcate the contents of a single cosmic ray event. Typically when referring to an event, when speaking in the context of the data file, this is meant to signify the contents of all DST banks stored within a START and STOP bank.

Currently there are 150 DST banks available for use in the hires_soft analysis software. Only 17 of them actually used in the analysis of stereo data. A brief description of the contents of each bank used in stereo analysis is provided below.

4.8.2 Analysis Banks

A stereo event is built from several processes that begin with monocular measurements from each site and are finally combined to do stereo measurements. As events are processed, the banks that were generated by preceding processes are kept in the event, even if a different bank's information supersedes another. This is done to allow verification of calculations performed by the different processes. Therefore each stereo event has banks that contain monocular information from HiRes1 and HiRes2, as well stereo banks. The most important analysis banks used for stereo analysis are shown in Table 4.9.

A standard naming scheme for banks is used for most banks. If a bank name begins with "H" or ends in "1", then it is usually a HiRes1 mono data bank. If it begins with "F" or ends in "2", it is usually a HiRes2 mono data bank. Stereo data bank names sometimes begin with the letter "S", but this convention is not rigorously imposed.

4.8.2.1 HiRes1 Analysis Banks

The HRAW1 bank is used to store the signal and timing information of all tubes that observe an event. Only the data from mirrors and tubes that trigger are stored in the bank. The most important information is the channel B QDC count which, when adjusted for gain and pedestal, provide the N_{pe} collected by each tube as light from an air shower sweeps across it.

The HBAR bank is meant to be an improved version of the HRAW1 bank. It stores the tube signal information, but also stores more detailed information about the calibration used to determine tube N_{pe}, such as quantum efficiency, 1st and 2nd order gain corrections, UV filter transmission coefficients, and mirror reflectivity. This bank is no longer used and instead the gain databases are used to provide calibration of the HRAW1 bank.

The pass2 process stores information about the calculations made in determining if the event is the result of random noise in the PASS2 bank. It contains the PLOG element, which is the measurement of whether the event is noise or a real event, the RVEC element, which is the magnitude of the Rayleigh vector, and the UPWARD

Table 4.9. A list of banks used in the stereo analysis of cosmic ray data. Many other banks are available in the analysis software, but only these few are used for the stereo analysis.

Information provided	Banks	When filled
Tube signal, timing	HRAW1, HBAR, FRAW1, FPHO1	pass0, pass1
HiRes2 mirror state	FTRG1	pass0, pass1
Noise filter	PASS2, FPASS2	pass2
Track data	PASS3, FPASS3	pass3
Shower-detector plane	HPLN1, FLPN1, SPLN1, SPLN2	pass3, pass5
Track geometry	HCTIM	pass4
Track profile	HCBIN, TIMBIN	pass4, pass5
Shower fit	SHWA,SHWB	pass5
Monte Carlo data	HRMCPROC, FMC1, FMC2	Monte Carlo

element to indicate if the track is upward or downward going. The information from this bank is used to determine if an event is caused by random noise or an upward going event caused by an artificial light source such as a laser or vertical flasher.

The pass3 process stores information about the plane fitting calculation in the PASS3 bank. Data such as the track length, the lateral angular width, the inverse angular speed in microseconds per degree, and tubes which are part of the cosmic ray track are stored in this bank. This information is used to determine if a track is too short, too "fat" or too close to be well reconstructed.

The HPLN1 bank stores the plane normal vector of the shower-detector plane for an event that was determined by the pass3 plane fitting routine. The pass3 plane fit is performed only using the information from HiRes1, so it is a monocular measurement of the shower-detector plane. A list of tubes that actually lie on the shower detector plane is also stored in this bank, to differentiate from noise tubes that are off the plane.

The SPLN1 bank is an analog of the HPLN1 bank, but the plane normal vector stored here is calculated using a improved fitting method and error estimation. The SPLN1 bank is filled during the pass5 process and provides the plane normal vector for all subsequent analysis when it becomes available in the data stream.

4.8.2.2 HiRes2 Analysis Banks

The FRAW1 bank stores the signal and timing information for each triggered tube of a HiRes2 event. For each triggered tube 100 measurements of the FADC count are recorded. Each measurement is a digitized value ranging from hexadecimal 00 - FF and the period of the measurements is 100 ns. The time of the mirror trigger is recorded as well as the time of each tube trigger relative to the mirror trigger. There are 320 channels of data that may be stored in the FRAW1 bank. Channels 1 - 256 correspond to the high gain measurements of the 256 phototubes in the cluster. Channels 257 - 272 correspond to the trigger channel column sums. Channels 273 - 288 measure the digitized readings of the low gain column sums. Channels 289 - 304 and channels 305 - 320 record the trigger channel row sums and

low gain channel row sums, respectively.

The FPHO1 bank is a simplified measure of the tube signal and is similar to the HRAW1 bank. It uses the high gain channel information of FRAW1 by integrating the time slices and performing a pedestal subtraction to compute $N_{\rm pe}$ count for each tube. The time of each tube trigger is stored as well.

The FTRG1 bank records detailed information about the state of a mirror during an event. It can provide the row and column pattern of trigger codes as well as information about the status of various mirror parameters during an event.

The FPASS2, FPASS3, FPLN1, SPLN2 are all direct analogs of the similarly named HiRes1 banks. They contain information about the noise filter and shower-detector plane relative to mono measurements made using the HiRes2 data.

4.8.2.3 Stereo Analysis Banks

The HCTIM bank contains the measured geometry of the track. Information such as $R_{\rm p}$, the core vector, the track vector, the shower zenith angle, the shower azimuth angle, and the psi angle are stored here. Each value is measured relative to each site, so for example there are two core vectors stored in the bank.

The shower profile is divided into angular bins and stored in the HCBIN bank. Each bin's pointing direction, signal in units of $N_{\rm pe}/{\rm m}^2/{\rm degree}$, and effective area correction factor are recorded. The bins are calculated using geometry and not timing information. This is the only binning method available for HiRes1.

The rapid sampling in time of air showers using the FADC electronics at HiRes2 allows for time binning. Time bins are stored in the TIMBIN bank and contains information similar to the HCBIN bank. A new improved version of angular binning was created and it is also stored here.

The SHWA and SHWB banks store the shower fit information. The measurements of energy, $x_{\rm max}$, $N_{\rm max}$, and $\sigma_{\rm s}$ are stored in this bank. The breakdown of the different light components and the number of calculated charged particles is also stored for each bin that is used to produce a shower fit. Each bank holds three different fits. The first fit is a fit done using HiRes1 mono bin information, the second fit is done using HiRes2 mono bin information, and the third fit is done

using bins combined from both sites, also called a global fit. The details of the information stored in the SHWA and SHWB banks is detailed in section 4.8.8.2.

4.8.2.4 Monte Carlo Banks

The Monte Carlo has a few banks that store information about the values generated for each event. Using the information in these banks, the validity of the reconstruction can be verified by comparing reconstructed parameters to thrown parameters.

The FMC1 and FMC2 banks store the information about which mirrors and tubes observed a shower, the signals and times of tube and mirror hits, the shower geometry relative to each site, as well as the parameters needed to characterize the thrown shower. Each simulated event contains one of these banks for each detector that triggers. For example an event may be observed by HiRes1 but too far away to be seen by HiRes2. The event will then have a FMC1 bank, but will not have a FMC2 bank.

The HRMCPROC bank stores information about the both detectors that is required to properly simulate them before any events are generated. All tube pedestals, gains, DAC settings, and simulated sky noise levels are recorded here. Information from the input data file specifying the ranges of energies and shower angles allowed are also stored. Since some of this information changes for each hour (data from the hourly databases for example) it is generated for each hour of data that is simulated.

4.8.3 Pass0

4.8.3.1 HiRes1 pass0

During HiRes1 data collection the time order of packets generated by the mirrors is not necessarily the same order in which they are written into the data file written by the DAQ computer. A standard Ethernet network ran over 10BASE2 cable connects all mirror electronics with the DAQ. Since Ethernet is a shared broadcast transmission medium, Ethernet packet collisions may cause the time order in which packets are received by the DAQ to be different from the order in which they were

generated in the crates.

Pass0 is an offline process that is ran after data collection to create events by performing mirror matching. Mirror matching is done by using a time window of 100 microseconds and searching for coincident mirror triggers that fall within that window. If no other mirrors are found to have triggered within the time window then a single mirror event is written to the pass0 output DST file. If other mirrors triggered within the time window, then a multi-mirror event is written to the output DST file.

4.8.3.2 HiRes2 pass0

The pass0 process for HiRes2 data is simplified in that events are built online by communication between the TRIGHOST modules of mirrors that observe an event and the central host crate. When a mirror triggers, it alerts neighboring mirrors to begin a mirror store window, creating an event. The data from all participating mirrors are then sent to the DAQ system for storage on disk in a FPKT1 raw data file. Pass0 then for HiRes2 FPKT1 files consists of converting the raw data format to a DST formatted file.

4.8.4 Pass1

4.8.4.1 HiRes1 Pass1

HiRes1 pass1 applies calibration from RXF runs to convert raw QDC counts to N_{pe} (HBAR NPE) and photons (HRAW1 PRXF) measured by each triggered tube in a event. TDC calibrations performed during the nightly calibration routine are also used to assign times to tube triggers. The event data is stored in HRAW1 and HBAR banks.

Pass1 is run on each pass0 data file. The process also needs two noise-closed files to determine pedestals, two calib files for TDC calibration, and RXF files to determine the QDC calibration. Each night at least two noise-closed files are generated, one before the run and one after the run and similarly for calib files. It is not uncommon for more than two of these types of files to be generated if the operator is running tests or running again after repairing mirrors that didn't run

correctly the first time. A special routine is used to chose the best noise-closed file and calib file by checking the times of the file generation and the start and stop times of the actual data taking. For example if multiple calib files are created before the actual data taking begins, the last one that occurs before data collection is used as the first file. The one that occurs last after data collection is chosen as the second file. The RXF calibration file used is the one from the last RXF run.

Note that since the gain database described in section 4.6.5.4 has become available, that method of QDC calibration is used. TDC calibration still relies upon use of the nightly calib files though. For all HiRes1 signal information used in this work, the HRAW1 bank is used by calibrating the QDCB count for each tube using the gain database. The HBAR bank, which holds similar information, has been deprecated since the introduction of the gain database.

4.8.4.2 HiRes2 Pass1

HiRes2 pass1 packs the data from the pass0 file into FRAW1 and FPHO1 banks that contain the timing and signal information for all tube hits in triggered events. Calibration is done by analyzing the DAC settings and performing a gain balancing routine which attempts to set the gain to one photoelectron per FADC count. The N_{pe} count for each tube then is found by integrating the number of photoelectrons over the 100 time slices taken for each tube and using an average quantum efficiency. The FRAW1 bank contains the FADC counts for all time slices for each triggered tube. This information is integrated and corrected for pedestal to fill the FPHO1 bank which contains the number of pedestal subtracted N_{pe} for each tube.

4.8.4.3 Stereo Pass1

Stereo data files are then created by using a 200 microsecond time window within which to look for coincident event triggers between both sites. If an event is found to have triggered at both sites within this time window a stereo event is written to a stereo pass1 file. All subsequent passes described henceforth will operate on stereo data files. The stereo matching of events therefore relies upon the proper operation of the GPS clocks at both sites to accurately reconstruct stereo events. When there

are problems with the GPS clock at either site other methods of syncing up the time can be used such as using vertical flashers or steerable lasers. All subsequent processing steps described henceforth will only operate on stereo data.

Figure 4.45 shows the number of pass1 events collected by HiRes1, HiRes2, and in stereo. Since pass1 events are not filtered, and no weather cuts have been applied to this plot, this is equivalent to the total number of events collected by the HiRes detector. HiRes1 in mono mode has collected 147 million events, about three times the number collected by HiRes2 in mono mode. The number stereo events is only about 3% of the total number of HiRes1 events and 8% of the HiRes2 events. Therefore the requirement of stereo coincidence is seen to be an effective (passive) noise filter.

By normalizing each bin's event count by the detector ontime, the event rate can be seen. Figure 4.46 shows the event rate of both sites in monocular mode as well as in stereo. The stereo event rate of 0.3 events/second is much lower than the monocular rate at either site.

4.8.5 Pass2

In the data, most tube hits are noise or triggered by artificial light sources such as planes, bright stars, or lasers. As Figure 4.45 shows, a good number of noise events are implicitly cut by the requirement of stereo coincidence. Mono events which are not coincident in time between both detectors are then effectively cut during the pass1 stereo processing. Pass2 is a filter used to explicitly cut noise events that cause mirror triggers using a Rayleigh filter.

The Rayleigh noise filter is derived from the random walk problem in two dimensions, where each triggered tube in an event represents a unit step. Each step is assigned a direction based on the tube's placement on the cluster and a vector is formed. For true noise, which is randomly distributed in time and space, we use the Rayleigh distribution as the probability density function [52]

$$f(r;s) = \frac{r}{s^2} \exp\left(-\frac{r^2}{2s^2}\right) \tag{4.22}$$

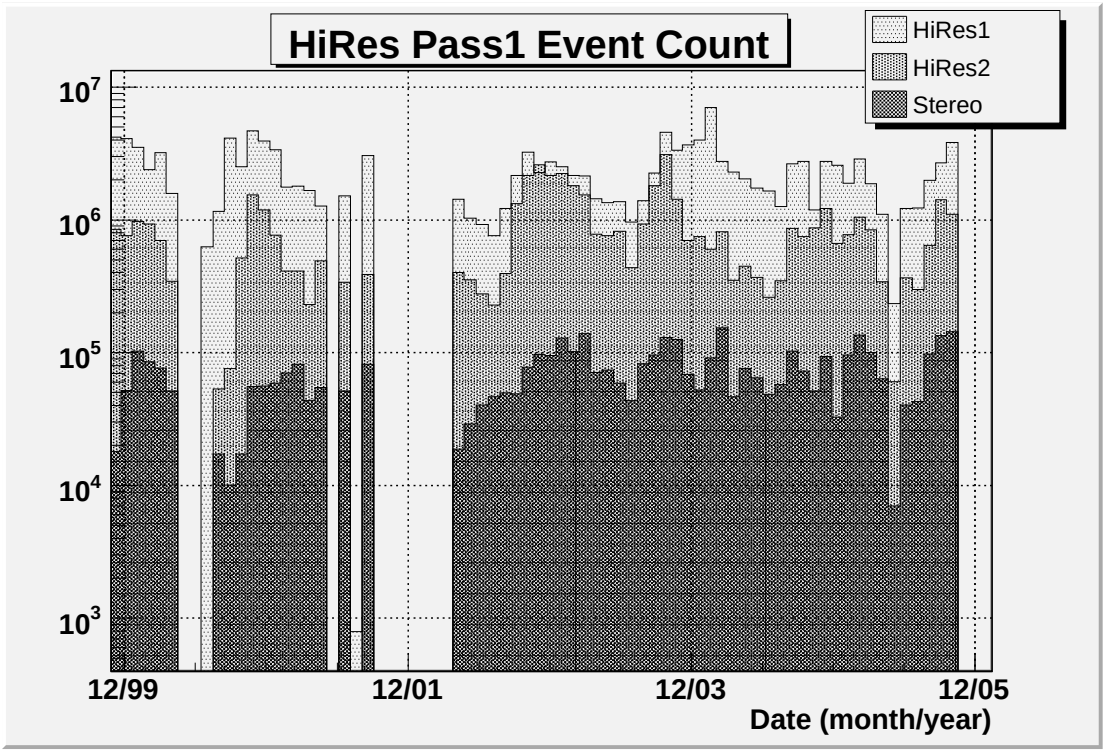

Figure 4.45. The number of events collected by HiRes over the period of this work. Each bin contains one data collection run. The gaps represent times when data collection was halted. There are no weather cuts in this plot. The total number of events collected by HiRes1, HiRes2 and in stereo is 147.1 million, 52.5 million, and 4.4 million, respectively.

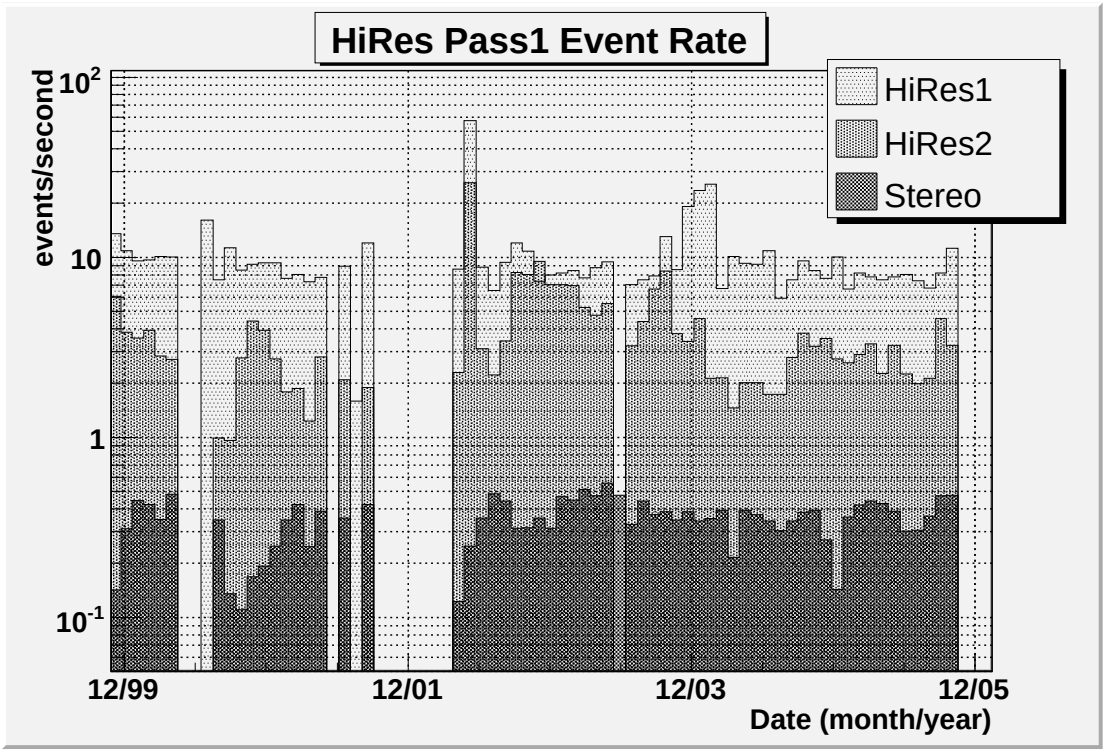

Figure 4.46. The event rate of the HiRes detectors over the period of this work. Each bin contains one data collection run. The gaps represent times when data collection was halted. There are no weather cuts in this plot. The average event rate of HiRes1, HiRes2 and in stereo is 8.39, 2.80, and 0.31 events per second, respectively.

where r is resultant vector after n steps and $s^2 = n/2$. The probability that resultant vector magnitude of length r will exceed a distance R is

$$P(r > R) = \int_R^\infty f(r)dr = \exp\left(-\frac{R^2}{n}\right) \tag{4.23}$$

The pass2 routine implements the Rayleigh filter by summing unit vectors where each unit step is a neighboring tube triggered in time order. As each tube is added, a resultant vector is formed whose length, r, is used to determine the probability that the triggered tubes are the result of random noise. Pass1 requires that $P \leq 0.01$ to be accepted as a real event. An additional requirement is there be at least three adjacent neighboring tubes that form a "track". The resultant vector also indicates the direction of the track, in particular whether the track is upward-going or downward-going. The filter rejects events with a Rayleigh vector within 10° of horizontal, tagging these as upward travelling events. The resultant probability of the event being noise is stored in the data stream as $-\log_{10}(P(r))$ also referred to as $P_{\log}$. A $P_{\log}$ value of 2 then corresponds to a 1% probability that the event is noise. Events with $P_{\log} < 2$ are considered noise. This cut is not applied until the pass5 stage though. Only events that are considered upward going are cut in pass2.

Figure 4.47 shows an event that was rejected by the pass2 noise filter. Notice that not all tubes which collected light are added into the Rayleigh vector since they are not part of a nearest neighbor pair. Also notice that the unit step marked 8 is very far from the cluster of tubes at the bottom of the mirror. This step is still added as part of the Rayleigh vector even though it is physically far from the cluster which would more likely be considered a true event. The large arrow shows the resultant Rayleigh vector found to have a magnitude of 2.70 and angle of 260°. Although this is classified as a downward-going event, the calculation of equation 4.23 is 0.4 indicating that the event is noise.

Figure 4.48 shows the noise probability for all post pass2 events that are not upward-going. Since only events with a noise probability of less than 1% are considered cosmic ray candidates, the figure shows that the vast majority ($\sim 80\%$) are noise triggers.

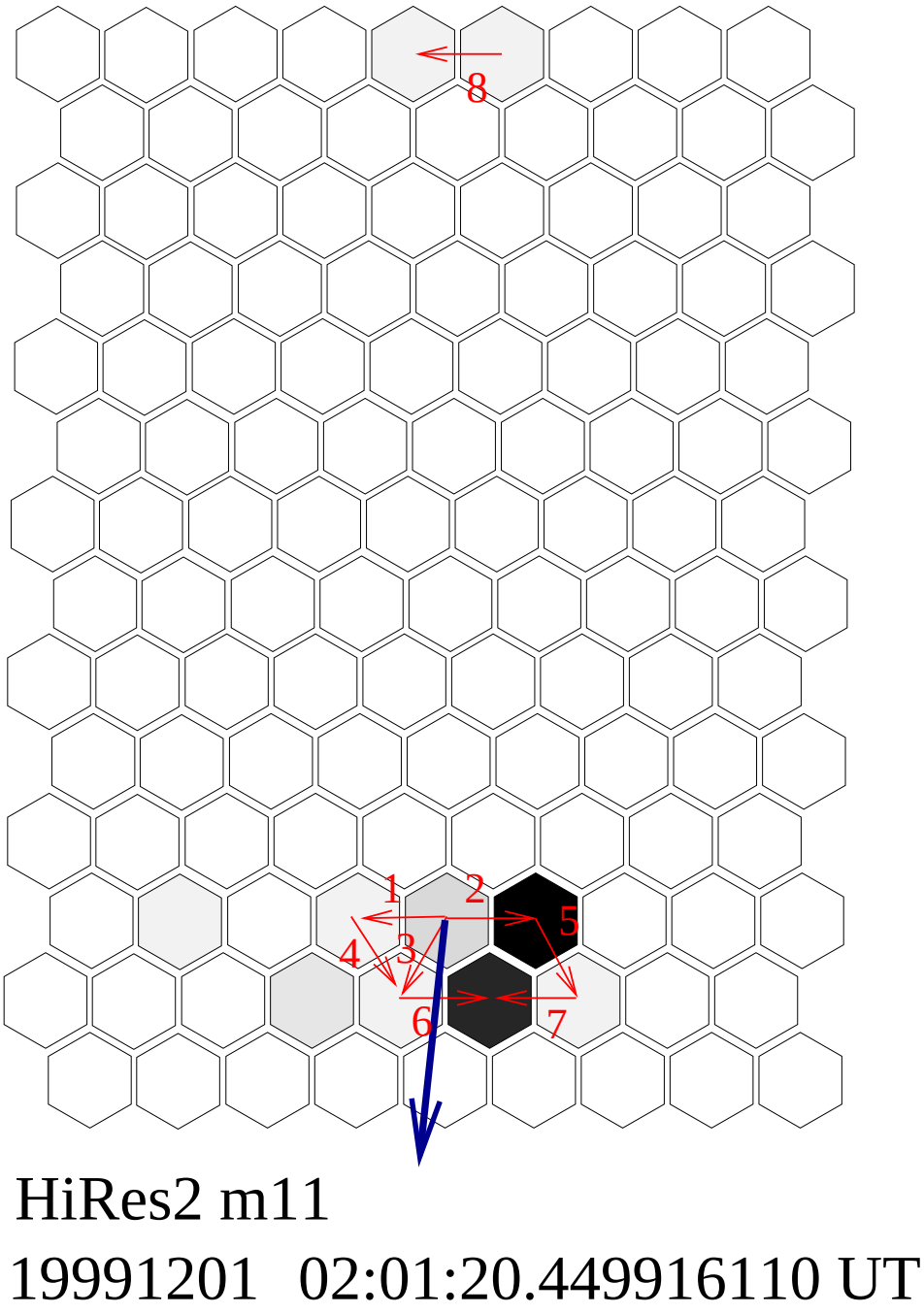

Figure 4.47. Example of an event rejected by the pass2 noise filter. The number arrows indicate the time order direction of each step taken between neighboring pairs of tubes that recorded a "hit". The darker colored tubes recorded more light than lighter colored tubes. The thick dark arrow is the resultant Rayleigh vector found by summing the individual unit steps. The $P_{\log}$ value for this event is 0.4 indicating that it is a noise event.

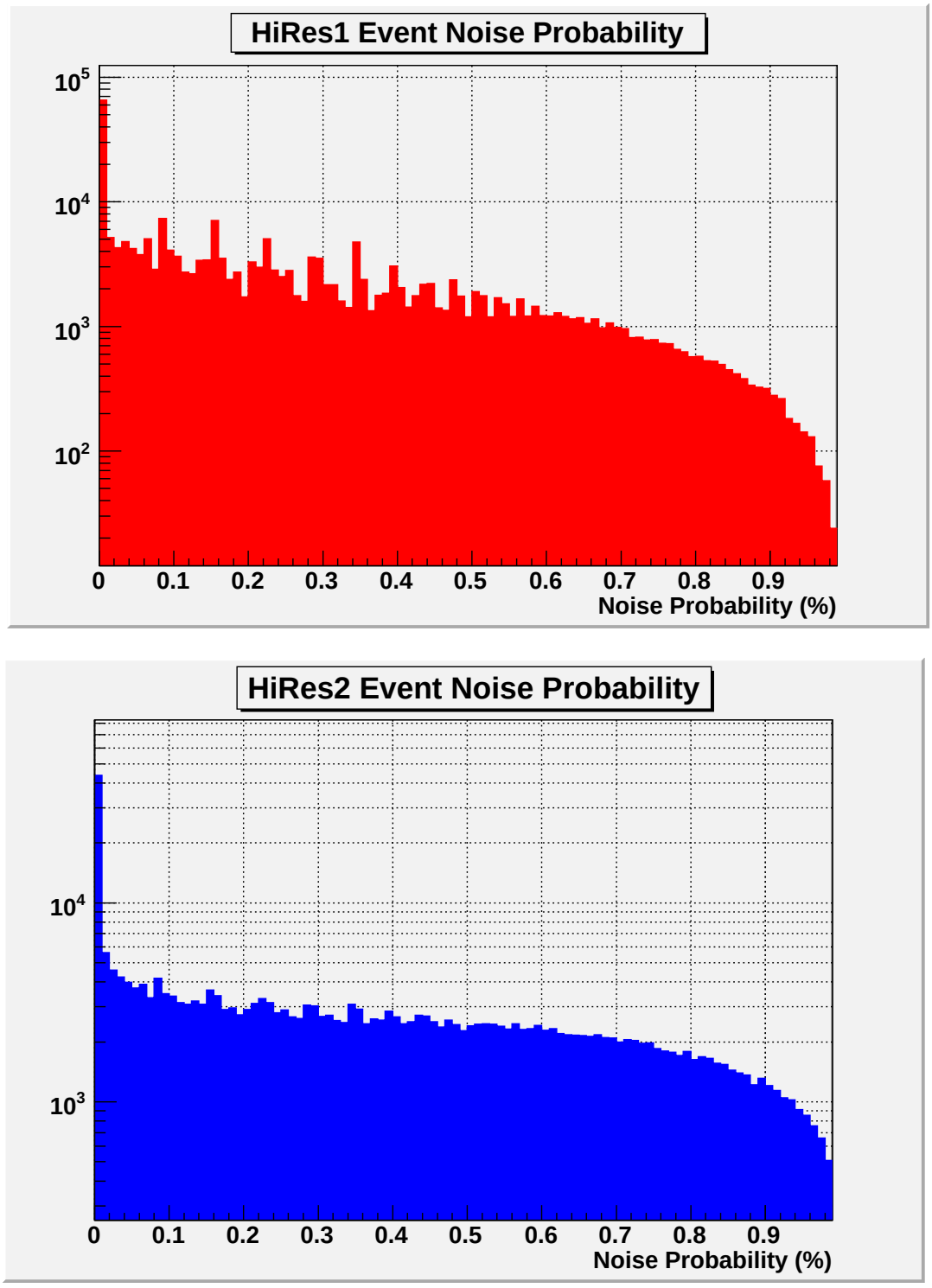

Figure 4.48. Probability that an event is noise as determined by the random walk problem. This plot shows $P(r)$ for all events that are not found to be upward-going events. Only events with a noise probability of 1% or less are considered as cosmic ray candidates.

4.8.6 Pass3

As a shower develops in the atmosphere, light is propagated to photomultiplier tubes in the HiRes detectors, and appears as an arc along a great circle on the celestial sphere (see Figure 4.49). Given a ray along this arc and a ray along the pointing direction of one of the tubes to observe the shower, a plane can be formed. The *shower-detector plane* is formed by using all tubes that observe a shower and performing an amplitude weighted fit to determine the shower-detector plane normal vector. If the tube pointing directions are projected onto a unit sphere, the shower detector plane appears as a line on the surface of the sphere, corresponding approximately to the lateral centroid of the charged particle distribution along any transverse slice.

The amplitude weighted fit is done by first searching for clusters of tubes that could possibly comprise a true event. Under the reasonable assumption that tubes contained in an air shower event are closely correlated spatially and temporally, a tube is added to a cluster if it is closer than 1.2 degrees and has a trigger time within 2 microseconds of any other tube already in the cluster. To form a cluster at least two tubes must satisfy these requirements. Any tube not part of a cluster is then rejected as noise. Then the Rayleigh filter is again applied to the proposed cluster of tubes to ensure that at least one pair of tubes has been found to satisfy the nearest neighbor requirements of the pass2 filter. Finally the cluster of tubes is used to minimize the function

$$\chi^2 = \sum_{i=1}^{N} \frac{(\hat{n} \cdot \hat{n_i})^2 \cdot S_i}{\sigma_i^2} \tag{4.24}$$

where $\hat{n_i}$ is the pointing direction vector of tube i, S_i is the tube signal in $N_{\rm pe}$, σ_i is the uncertainty, and $\hat{n}$ is the shower-detector plane normal vector. σ_i is assigned an uncertainty of 1 degree, the approximate angular width of a tube.

After the plane of the shower is determined, observables shown in figure 4.50 can be calculated such as "good" tubes (which are tubes that are part of the shower-detector plane found in the amplitude weighted fit), photons per good tube, track length (measured in degrees), and inverse angular speed (measured in

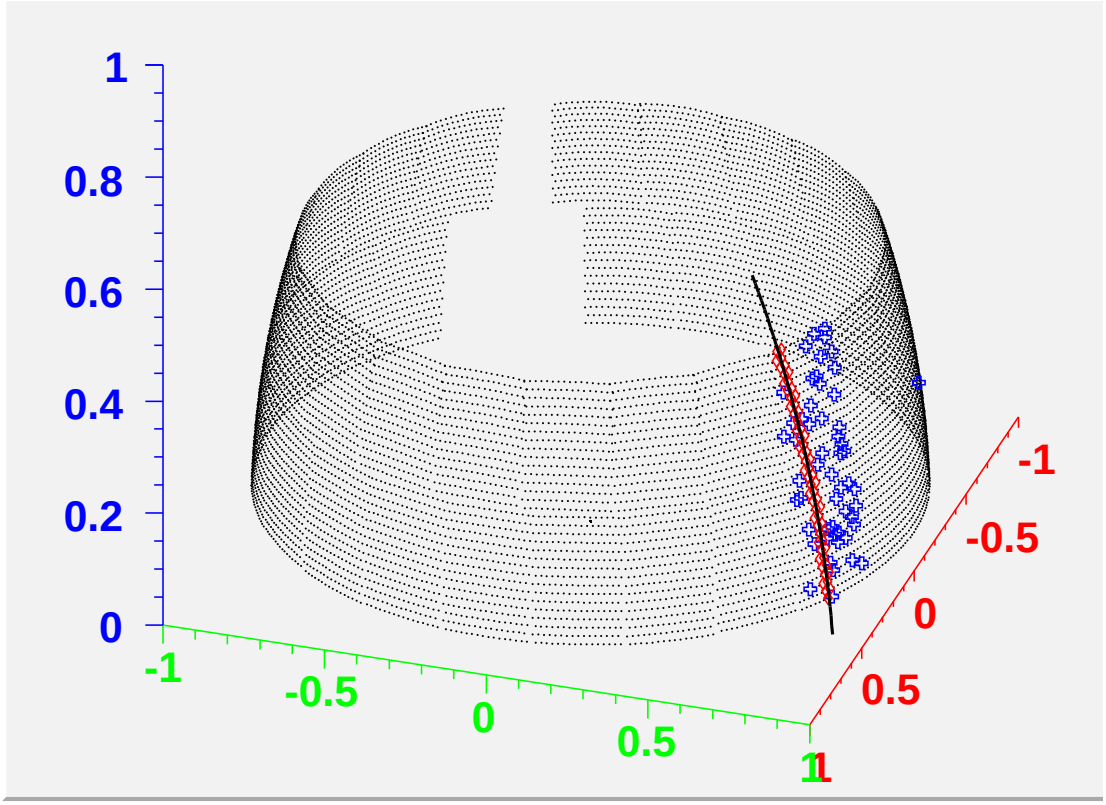

Figure 4.49. A shower track viewed by one of the HiRes detectors appears as an arc on the celestial sphere, which can be normalized to a unit sphere. Here a shower track observed by HiRes2 is projected onto the unit sphere. Each dot represents a tube center (10752 tubes total), the plus (+) markers are tubes that triggered but are not part of the shower-detector plane (noise tubes), and the diamonds are tubes that are part of the shower-detector plane. The solid line is the shower track projected onto the sphere.

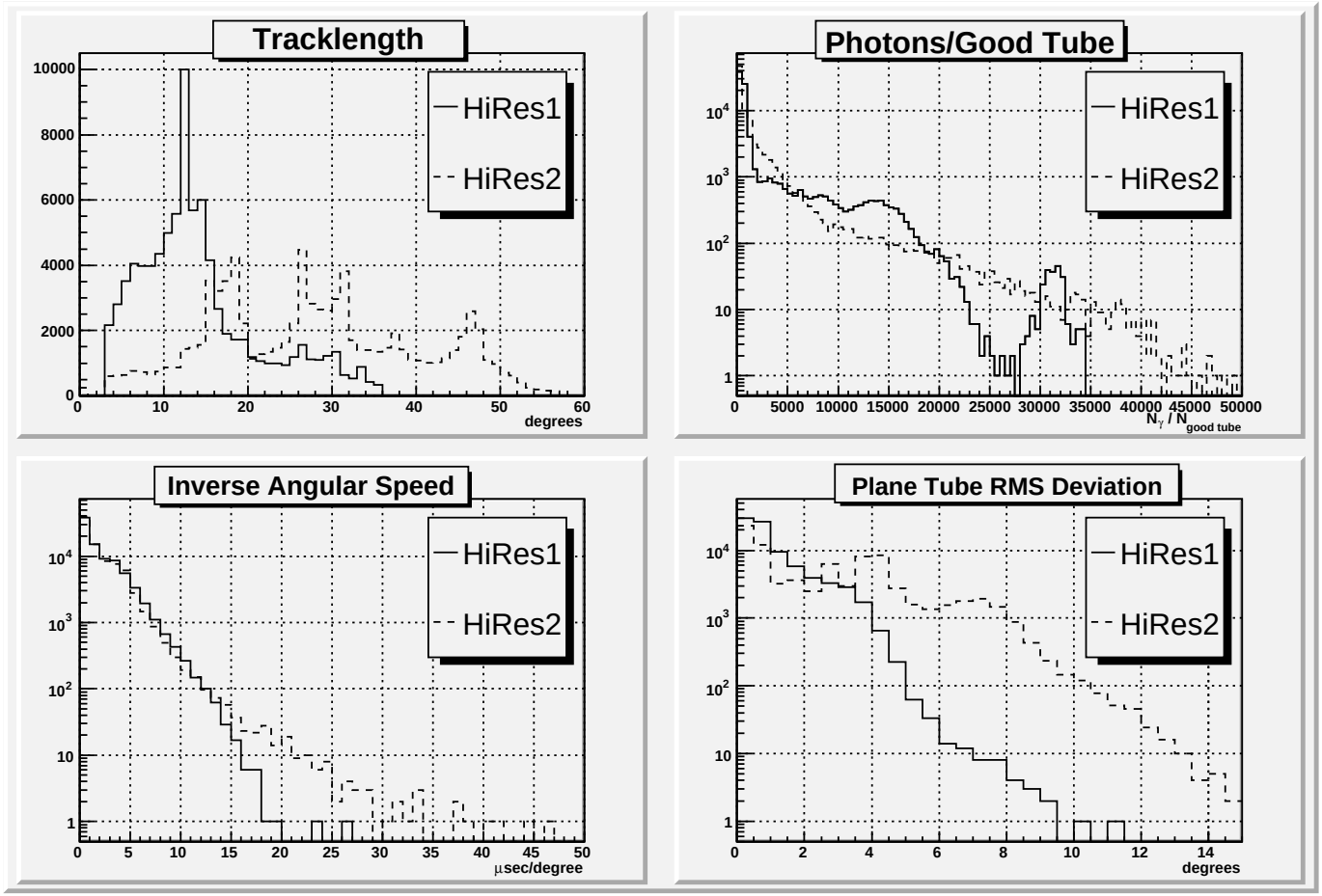

Figure 4.50. Observables calculated in pass3. These are the distributions for all data events that survive pass3 cuts. Pass3 is a stereo process so the values for both HiRes1 and Hires2 for each event are displayed. Downstream processes in pass5 will make cuts on these observables to select quality events.

microseconds/degree). In addition to rejecting events that fail the fitting routine, for lack of sufficient number of nearest neighbor pairs for instance, these observables may also used to cut events. At the pass3 stage the criteria for rejection are

1. HiRes1 tracklength $> 36^\circ$ or HiRes2 tracklength $> 57^\circ$.
2. The shorter of the two tracklengths $< 3^\circ$ or the longer of the two tracklengths $< 6^\circ$.

4.8.7 Pass4

Pass4 completes the calculation of the geometry of the shower, by determining the impact parameter, R_p, the shower angle with the horizontal plane, ψ, and the location of the shower core (the point of impact with the ground). Figure 4.51 shows the geometry of the shower-detector plane. In the figure tube i with elevation angle χ_i observes a segment of the shower track. The distance to any part of the track can be found once R_p and ψ are known. Two methods are available to determine the shower geometry, using a time fit or intersection of two planes. The time fit method is used for a monocular analysis of a shower profile. A problem with the time fit is that although the shower-detector plane may be well determined by a monocular observation, the angle of the shower within the plane, ψ, is more difficult to accurately measure. In this analysis, the power of stereo observation allows us to increase the accuracy of the shower geometry by using the shower-detector planes reconstructed at both sites. The intersection of the planes defines the shower axis. Utilizing the fact that the shower axis, the plane normal vector, and R_p for a given site are all orthogonal, R_p, ψ, and the shower core can be determined.

4.8.7.1 Time Fit

The shower axis angle and the impact parameter can be found using the time information of the tubes found to be part of the shower-detector plane. As Figure 4.51 shows the time t_0 is the time when the shower is at a distance R_p from the detector. We can define the time at which the shower is seen by other tubes relative to t_0 by utilizing the shower geometry shown in the figure. The time t_i is then

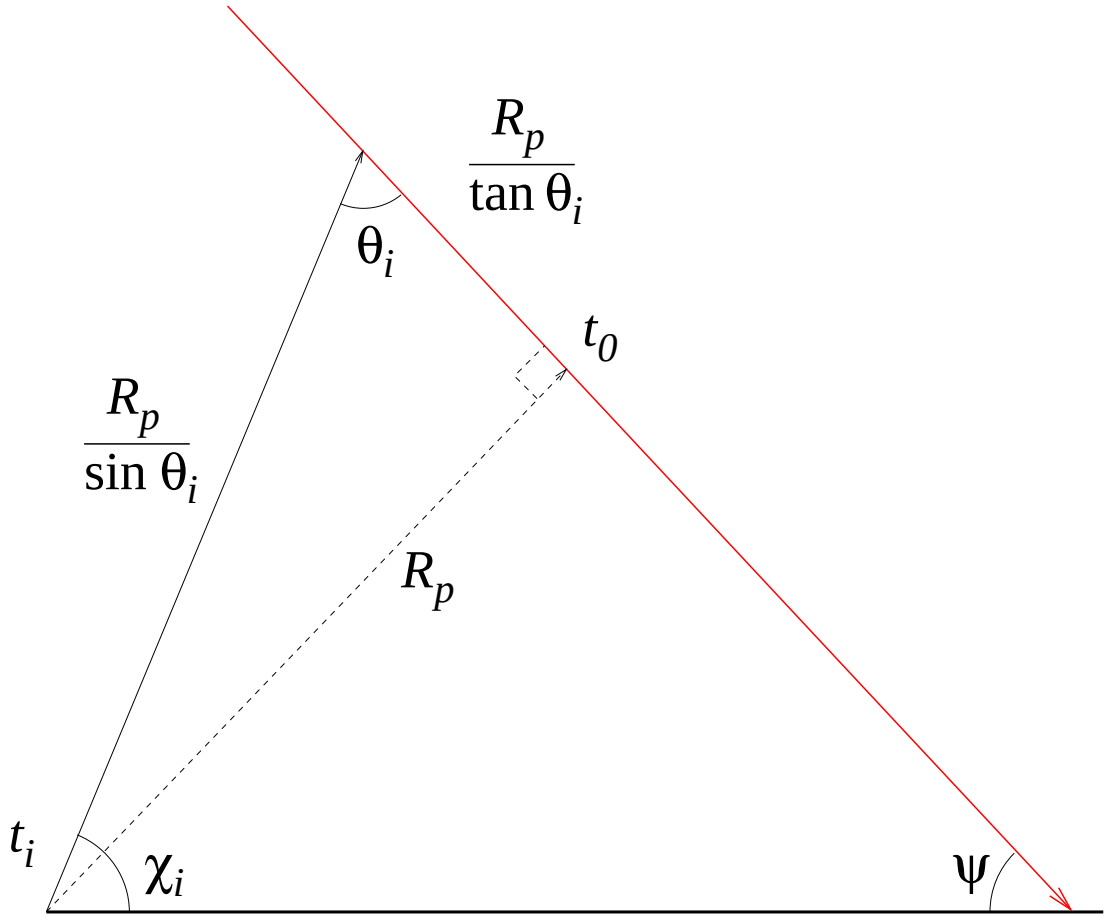

Figure 4.51. The track geometry in the shower-detector plane. The angle χ_i is the elevation angle of tube i and is known.

$$\begin{aligned} t_i &= t_0 - \frac{R_{\rm p}}{c\tan(\theta_i)} + \frac{R_{\rm p}}{c\sin(\theta_i)} \\ &= t_0 + \frac{R_{\rm p}}{c}\tan\left(\frac{\pi-\psi-\chi_i}{2}\right) \end{aligned} \tag{4.25}$$

where we've utilized the relation $\theta_i = \pi - \psi - \chi_i$. A three parameter fit to minimize the χ^2 function

$$\chi^2_{\rm time} = \sum_{i=1}^{N} \frac{1}{\sigma^2}\left\{t_i - \left(t_o + \frac{R_{\rm p}}{c}\tan\left(\frac{\pi-\psi-\chi_i}{2}\right)\right)\right\}^2 \tag{4.26}$$

is used to find the best solution for t_0, $R_{\rm p}$, and ψ.

4.8.7.2 Stereo Plane Intersection

This work uses the stereo observation of showers to make a better determination of the shower track. Each site has a shower-detector plane as determined by an amplitude weighted fit as described in section 4.8.6. The intersection of the two planes defines the shower axis. Once the shower detector plane and the shower axis are known, the cross product of the two provides $R_{\rm p}$. Figure 4.52 shows the geometry of crossed planes. The various geometric observables can be obtained utilizing the relations in equations 4.27 through 4.31

$$\frac{\hat{n}_1 \times \hat{n}_2}{|\hat{n}_1 \times \hat{n}_2|} = \hat{t} \tag{4.27}$$

$$\hat{t} \times \hat{n}_1 = \hat{R}_{\rm p,1} \tag{4.28}$$

$$(\vec{R}_{\rm p,1} - \vec{f}_r) \cdot \hat{n}_2 = 0 \tag{4.29}$$

$$\hat{t} \times \hat{n}_2 = \hat{R}_{\rm p,2} \tag{4.30}$$

$$(\vec{R}_{\rm p,2} + \vec{f}_r) \cdot \hat{n}_1 = 0 \tag{4.31}$$

where $\hat{n}_1$ is the HiRes1 unit plane normal vector, $\hat{t}$ is the track unit vector, $\hat{R}_{\rm p,1}$ is the HiRes1 $R_{\rm p}$ vector, and $\vec{f}_r$ is the vector from HiRes1 to HiRes2. The vectors specific to HiRes2 are similarly labeled.

The core vector relative to each site, as well as the azimuth and elevation angle of the shower can be found by the relationships

$$\vec{c}_1 = \vec{R}_{\rm p,1} - \frac{R^z_{\rm p,1}}{t_z}\hat{t} \tag{4.32}$$

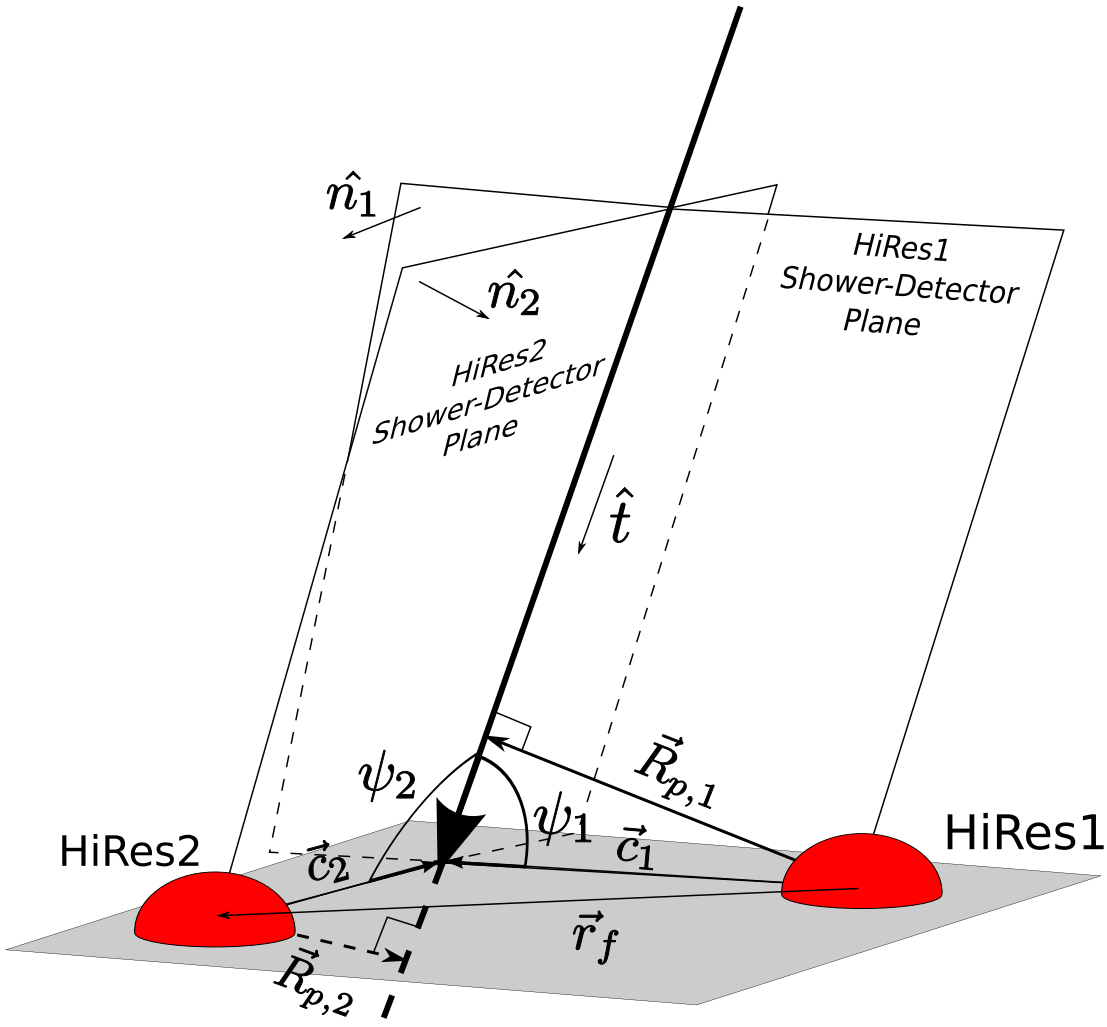

Figure 4.52. Using the stereo geometry of two crossed planes to locate the shower track. Once a shower detector plane at both sites is determined, the intersection of the planes defines the shower axis. The shower axis, the plane normal, and $R_{\rm p}$ are orthogonal vectors, allowing us to determine $R_{\rm p}$ given the other two vectors. Additional geometric information such as the shower core location is easily determined as well.

$$\vec{c}_2 = \vec{R}_{\mathrm{p},2} - \frac{R^z_{\mathrm{p},2}}{t_z}\hat{t} \quad (4.33)$$

$$\theta = \arccos(-t_z) \quad (4.34)$$

$$\phi = \arctan(-\frac{t_y}{t_x}) \quad (4.35)$$

where t_x, t_y, t_z are the x, y, and z components of the track vector t, and c_1 and c_2 are the HiRes1 and HiRes2 core vectors.

Figure 4.53 shows the core locations of all pass4 events. Figure 4.54 shows the important geometric shower observables calculated in the pass4 processing stage. The pseudodistance, R_{p}, and the angle of the shower with the horizontal in the shower-detector plane, ψ, are measured relative to each site and so may differ between HiRes1 and HiRes2 for each event. The zenith angle of the shower, θ, and the azimuth angle of the shower, ϕ, are found by projecting the shower track onto the horizontal plane. They should both agree between HiRes1 and HiRes2 measurements and the figure shows that they do. The mean difference between the HiRes1 and HiRes2 measurements are less than one degree for both.

After the shower geometry is determined, HCBIN angular bins are filled for HiRes1 and HiRes2. HCBIN angular bins have been made obsolete through the use of an improved binning routine named BinTrack. BinTrack angular bins are calculated in the pass5 procedure and are stored in the TIMBIN bank. A discussion of the angular and time binning techniques are found in section 4.8.8.1.

Table 4.10 shows the number of events that enter each stage of the processing and how many survive cuts to go on to the next stage.

4.8.8 Pass5

Pass5 is the final processing stage for stereo data. It performs binning of shower profiles and profile fitting to determine the parameters that characterize a shower. Once the shower parameters are determined the profile can be integrated to determine the energy of the primary particle that initiated the air shower.

The shower-detector planes are first refitted to do an improved estimate of the errors. The SPLN1 and SPLN2 banks are then filled using the improved planes.

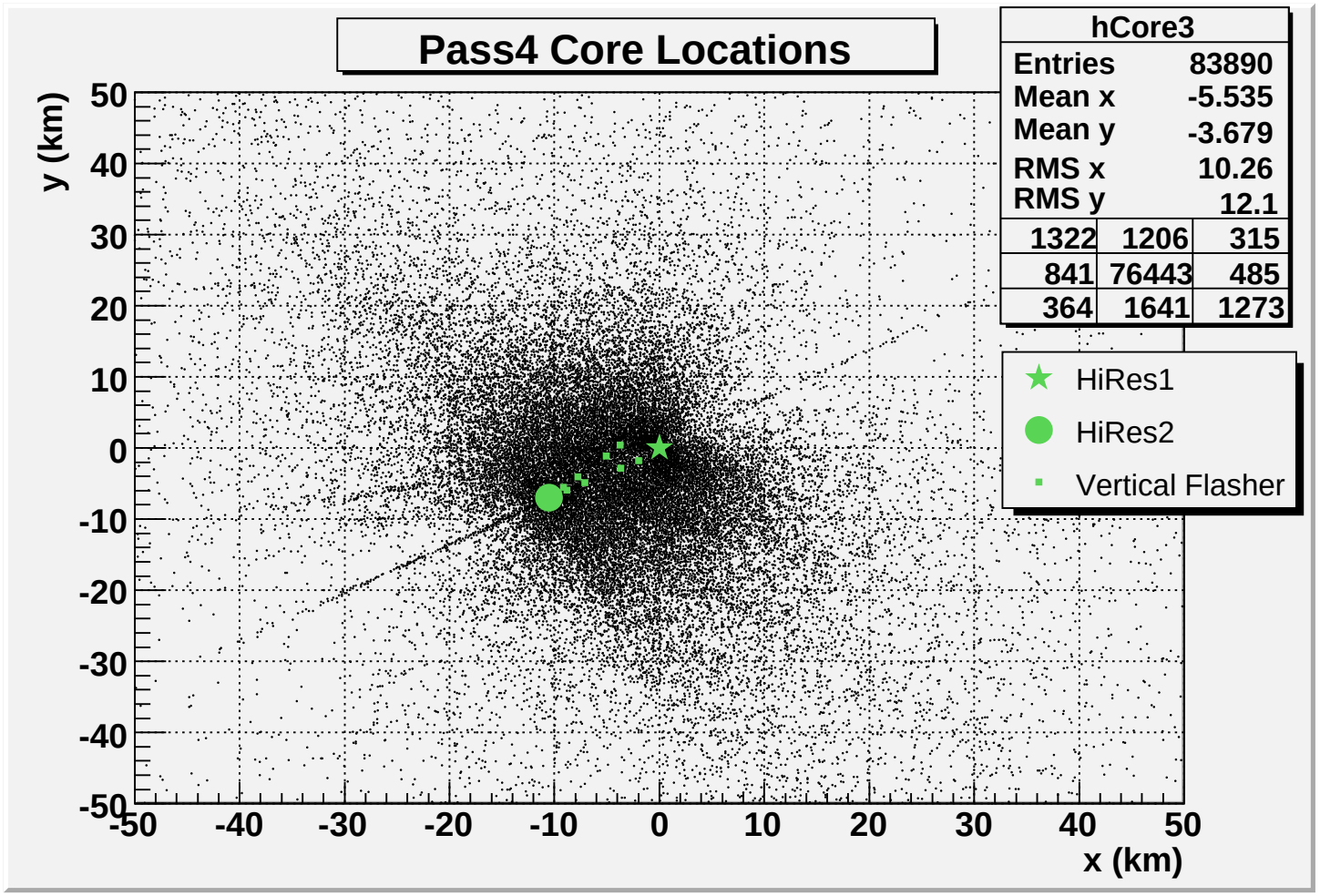

Figure 4.53. The core location of all pass4 events. HiRes1 is the origin of the coordinate system and HiRes2 is located 12.6 km to the southwest.

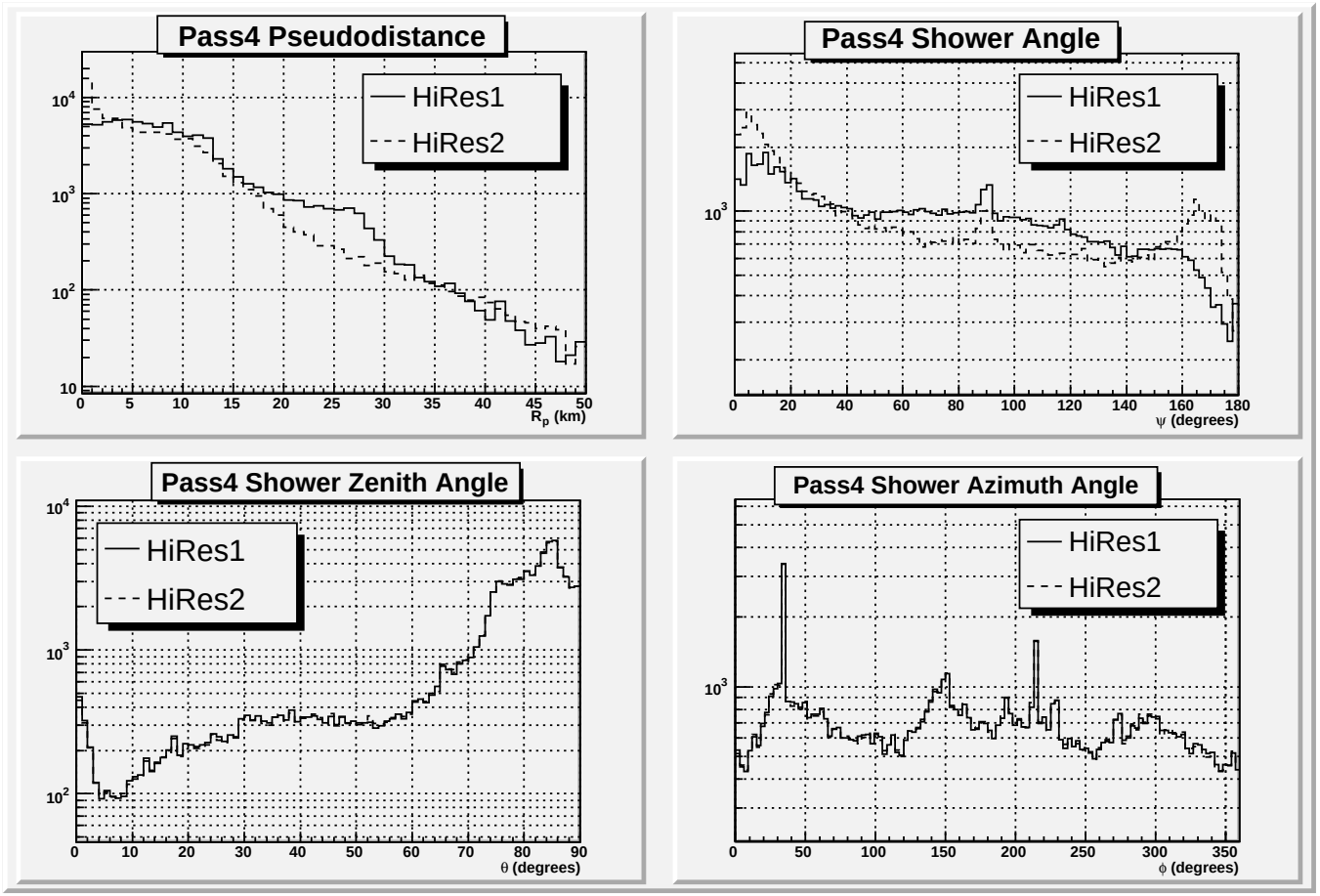

Figure 4.54. Information about shower geometry calculated in pass4. All events that survive to pass4 are shown here. Notice that the shower zenith angle and azimuth angle distributions are nearly identical as is expected, since HiRes1 and HiRes2 should both agree on these values. $R_{\rm p}$ and ψ are calculated relative to each site though and will not necessarily be the same for each shower.

Table 4.10. The number of events surviving the processing chain to the end of the pass4 processing stage.

Stage	# cut	# out	% cut	% remaining
HiRes1 pass1	0	136,099,385	0	
HiRes2 pass1	0	50,685,473	0	
Stereo pass1	0	2,658,769	0	100.0
pass2	2,358,479	300,290	88.7	11.3
pass3	215,539	84,751	71.8	3.2
pass4	861	83,890	1.0	3.2

Then the shower geometry is recalculated and the HCTIM bank is refilled using the improved plane estimates.

4.8.8.1 Binning Methods

The shower is then binned using two different methods: time binning and angular binning. Binning is a way of taking the continuous light distribution across the cluster and breaking it up into discrete points that can be used to fit the shower profile. Each bin measures the light flux that falls across some number of tubes (a bin may contain more than one tube, even more than one mirror) in units of $N_{\rm pe}/{\rm m}^2/{\rm degree}$. The signals of all tubes contained in a bin are summed to obtain the $N_{\rm pe}$ count and the length of track observed by the bin is measured in degrees. The mirrors that observe the shower act as light collectors which determine the total light flux to impinge upon a cluster. The area of HiRes mirrors is 5.08 $\rm m^2$. In addition to the size of the mirror other factors influence the acceptance of photons on the cluster such as dead space between the tubes, the active region of each tube's photocathode, and geometric affects of focusing the light from a semi-spherical mirror unto the flat plane of the cluster box. Ray tracing is performed to determine the correction needed in the flux calculation, called the *effective* area, which is always less than the full area of the mirror.

Angular binning uses the geometry of the track and detector to distribute the total light collected from a shower (see Figure 4.55). This method of binning is appropriate for the sample and hold electronics at HiRes1, where only the total integrated light profile is available. Time binning takes snapshots of the shower as it moves across the detector. This method is only available at HiRes2 where the FADC electronics system records the shower information at a 100 MHz rate. Angular binning may also be performed at HiRes2 by integrating the time profile of light in each tube and treating it in a similar fashion to HiRes1 tube signals.

Figure 4.56 shows an event at HiRes2 where angular and time bins have be constructed from a shower's light profile. Typically time binning provides a finer sampling of the shower profile as the figure shows.

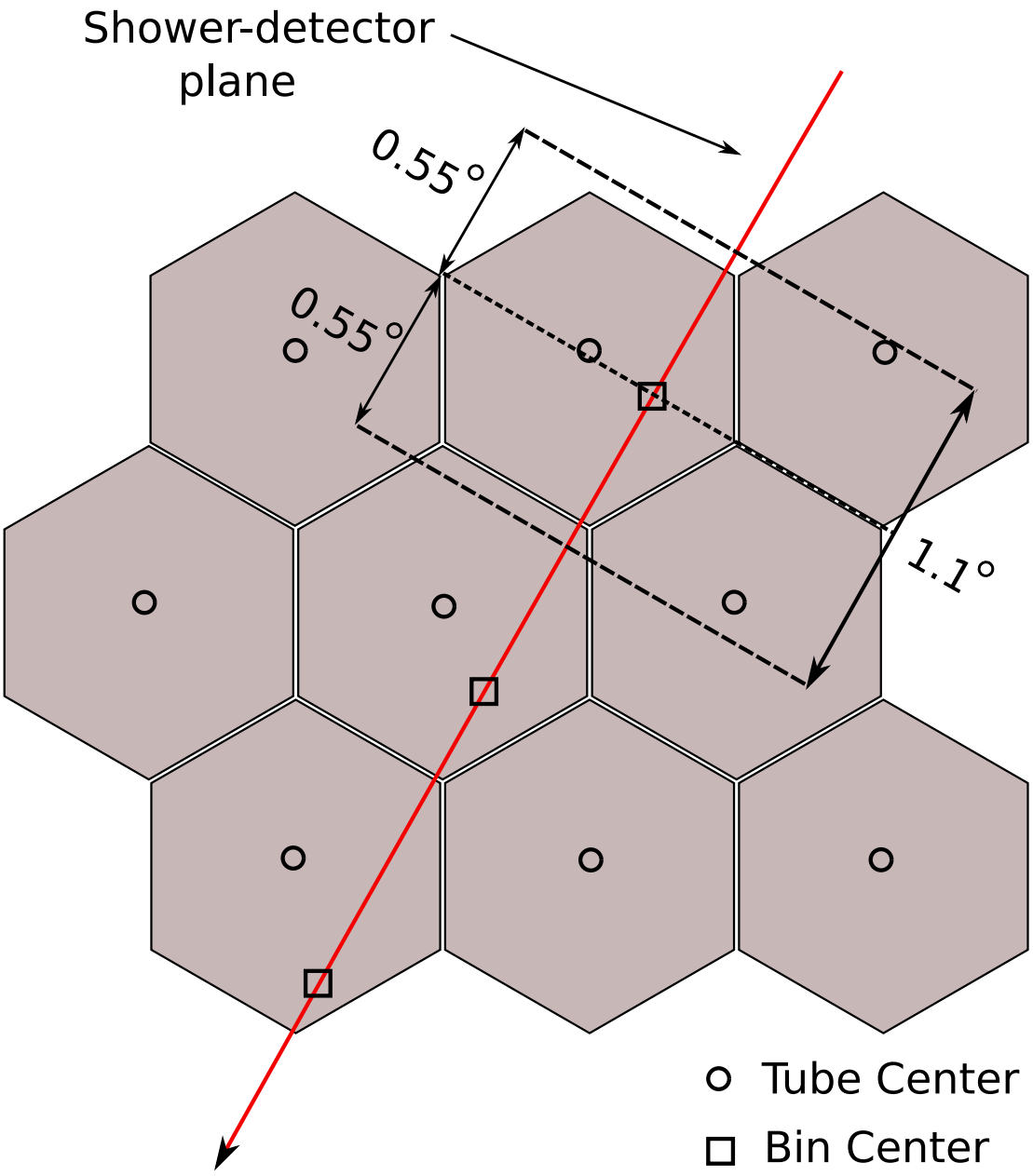

Figure 4.55. Relative sizes of tubes and angular bins on a cluster. BinTrack creates angular bins that are 1.1° degrees wide along a track in the shower-detector plane. Ray tracing is used to determine the acceptance of each bin that depends on the location of the track on the cluster as well as gaps between tubes.

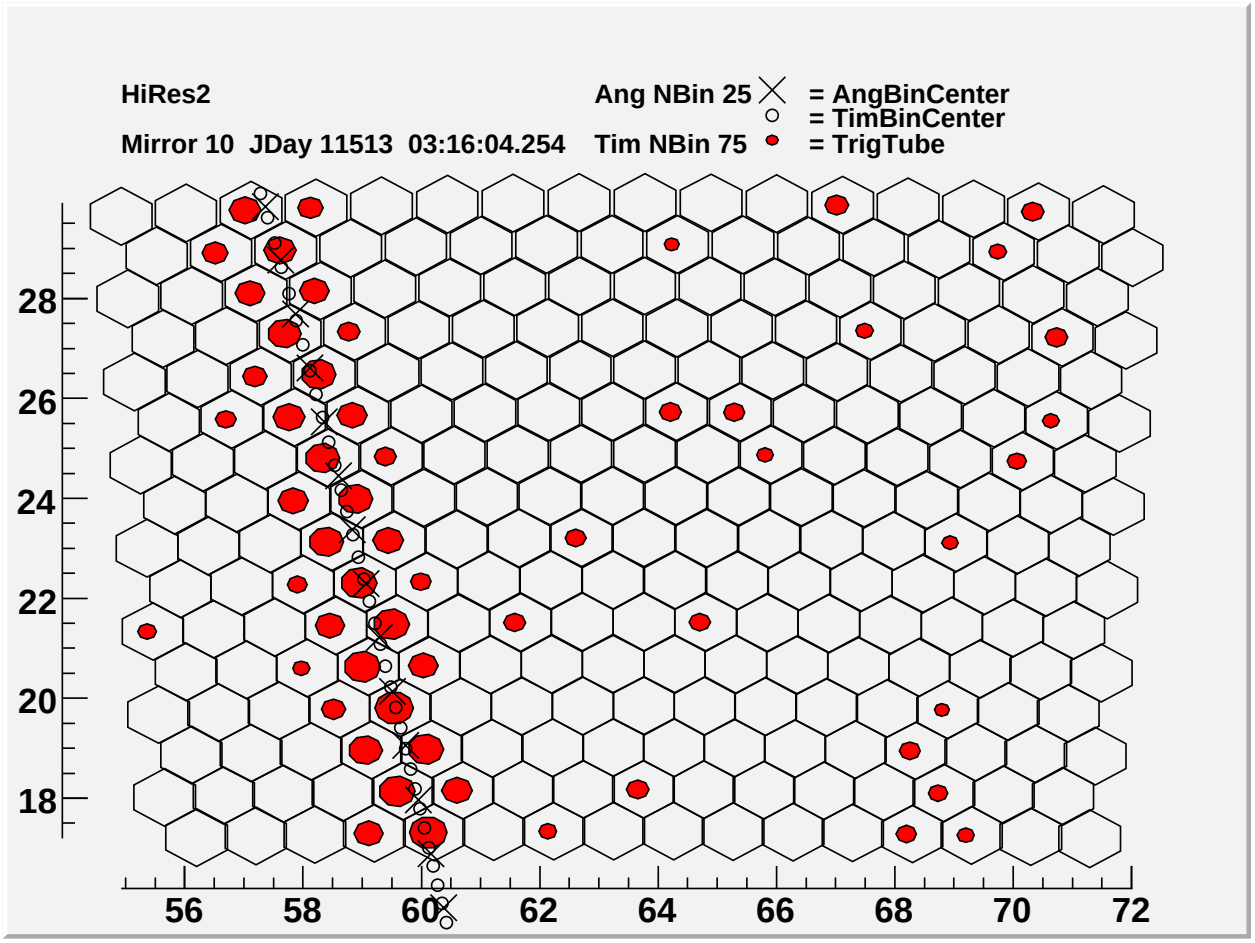

Figure 4.56. Example of angular binning and time binning for a single event. Note that there are many more time bins than angular bins, giving more sampling points of the shower. For this event, the angular width of the angular bins are 1.1° and vary for each time bin. Each time bin is 0.6 μsec wide.

Angular bins are determined using the BinTrack routine. Seven steps are performed to create these angular bins:

1. Read in shower geometry (shower-detector plane, core location, R_p, shower direction).
2. Project triggered, in-plane tube centers onto the shower-detector plane.
3. Find the topmost pointing tube and mark the top bin center.
4. Step down the shower-detector plane in 1.1° intervals marking successive bin centers.
5. Sort tubes into bins, possibly splitting tubes among different bins by assigning weighting factors to the tubes.
6. Trace rays coming from an angular range of 3.1° (±1° past bin boundary) over each bin to find the effective light collecting area of the detector for the light coming into the bin.
7. Compute the bin flux and error in photoelectrons/m^2/degree and store in the TIMBIN bank.

The binning procedure described here is designed to run after PASS4 in the processing chain, so shower geometry is available in the HCTIM, SPLN1, and SPLN2 banks. In addition, noise tubes which are greater than 3σ off of the shower-detector plane or which have bad timing are flagged in the SPLN banks. Only those tubes that pass the SPLN cuts are included in the binning procedure.

More bins are defined by then stepping down the shower track in 1.1° increments. Once all bins have been defined, the set of triggered, in-plane tubes that observed the shower are sorted into bins. Tubes that straddle bin boundaries must be included in multiple bins with an associated fraction of the tube contained within the bin. This fraction is used to weight the tube's contribution to the bin signal. As Figure 4.57 shows a 1° diameter circular approximation is used to describe each tube. If a tube's center as projected onto the shower-detector plane lies within $\Delta\theta/2 - r/2 = 0.05°$ of a bin center, it is considered wholly within the bin (i.e., the tube fraction is 1). If a tube's center lies greater than 0.05° but less than 1.05° of a

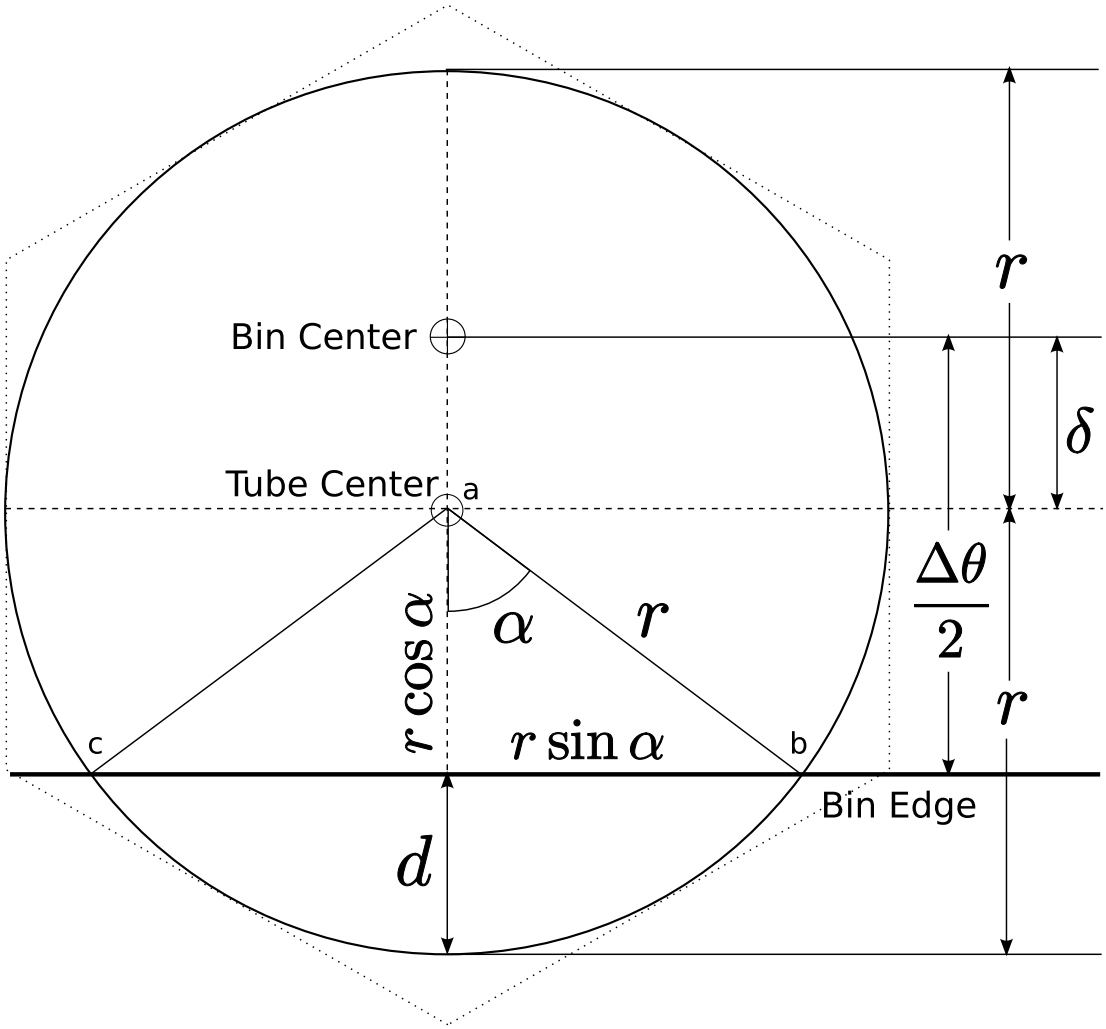

Figure 4.57. The characteristic geometry of an angular bin. The hexagonal tube shape is approximated by a 1° circle (2 × the inradius of a hexagonal HiRes phototube). The angular size of the bin ($\Delta\theta$) is 1.1°. Using this approximation the $N_{\rm pe}$ measured by a tube can be fractionated among bins. If a tube crosses bin boundaries, as shown here, the fraction of the tube contained in the bin is used to weight the tube's $N_{\rm pe}$ contribution to the bin.

bin center, it is considered partially in the bin and a fraction describing how much of the tube is contained is determined by the following formula

$$f = 1 - \frac{1}{\pi}[\cos^{-1}(\Delta\theta - 2\delta) - (\Delta\theta - 2\delta)\sin(\cos^{-1}(\Delta\theta - 2\delta))] \tag{4.36}$$

where δ is the angular distance between the tube center and the bin center in degrees. If a tube's center lies greater than $\Delta\theta/2 + r/2 = 1.05°$ from a bin center, it is not included in the bin.

To determine the fraction of a tube contained in a bin we need to calculate the ratio of the area of the circular segment *abc* (A_1) to the area of the circle (A_0). The angular difference between the tube center and bin center is easily found since we know the pointing directions of the tube and the bin center, $\hat{t}$ and $\hat{b}$. In this case then

$$\delta = \cos^{-1}(\hat{t} \cdot \hat{b}) \tag{4.37}$$

Using units of angular distance it can be seen from the figure that

$$\cos\alpha = \frac{r - d}{r} \tag{4.38}$$

The area of the circular segment *abc* can be found by taking the area of the circular sector *abc* and removing the area of the triangle *abc*. The area of the circular sector is $r^2\alpha$ and the area of the triangle is $2((r/2) \cdot \sin\alpha \cdot r\cos\alpha) = r^2 \sin\alpha\cos\alpha$. The area of the circular segment (A_1) is then $r^2(\theta - \sin\alpha\cos\alpha)$. We now need to express α in terms of $\Delta\theta$ and δ. The distance from the bin edge (chord *bc*) to the edge of the circle (arc *bc*) is

$$d = \delta + r - \frac{\Delta\theta}{2} \tag{4.39}$$

Using $r = 1/2$ we find

$$\frac{r - d}{r} = \Delta\theta - 2\delta \tag{4.40}$$

Using equation 4.40 we can now write the area of the segment as

$$A_1 = \frac{1}{4}\left(\cos^{-1}(\Delta\theta - 2\delta) - (\Delta\theta - 2\delta)\sin\left(\cos(\Delta\theta - 2\delta)\right)\right) \tag{4.41}$$

Since the area of circle is $\pi/4$ so we can now write the fraction of the tube contained in the bin as

$$f = 1 - \frac{A_1}{A_0} = 1 - \frac{1}{\pi}\left(\cos^{-1}(\Delta\theta - 2\delta) - (\Delta\theta - 2\delta)\sin\left(\cos(\Delta\theta - 2\delta)\right)\right) \qquad (4.42)$$

which is the same as equation 4.36. Figure 4.58 shows the distribution of tube fractions for all tubes reconstructed on a typical day. The bin size is slightly larger than the angular size of a bin, so the tube fraction most commonly seen is $f = 1$.

After all tubes have been assigned to bins, the effective light collecting area of the detector associated with each bin is found by sweeping 1000 rays across each. Along the line of the shower track the number of rays that hit the photocathode of triggered tubes in the bin are counted. Rays hitting untriggered tubes are not counted as contributing to effective area. We start the ray tracing sweep one degree above and continue to one degree below the bin boundary to ensure complete coverage. The ray tracing procedure may also calculate the effective area for a shower that has lateral extent as well as for line sources by using the NKG function. Note that dead tubes are accounted for in a passive manner since they did not contribute to the signal in the bin and they also reduce the effective area of the bin.

The ray tracing procedure is done by throwing 1000 rays starting 1 degree above the bin boundary down and stepping down along the shower-detector plane to 1 degree below the bin boundary, for a total angular coverage of 3.1 degrees. When the shower lateral function is taken into account, at each step down the NKG function is used to move laterally off the shower-detector plane before throwing the ray. The ray tracing incorporates the effects of the spherical mirror focusing the spot onto the cluster plane, the distance between the mirror surface and the cluster, the relative position of the light source to the mirror surface, the dimensions of the cluster box, the tube profile response and quantum efficiency.

The result of each thrown ray can be a tube hit, a bin hit, a cluster hit, or no hit. No hit occurs when the ray fails to register on the photocathode of one of the tubes in the bin that observed the shower (it must be a "good" tube on the

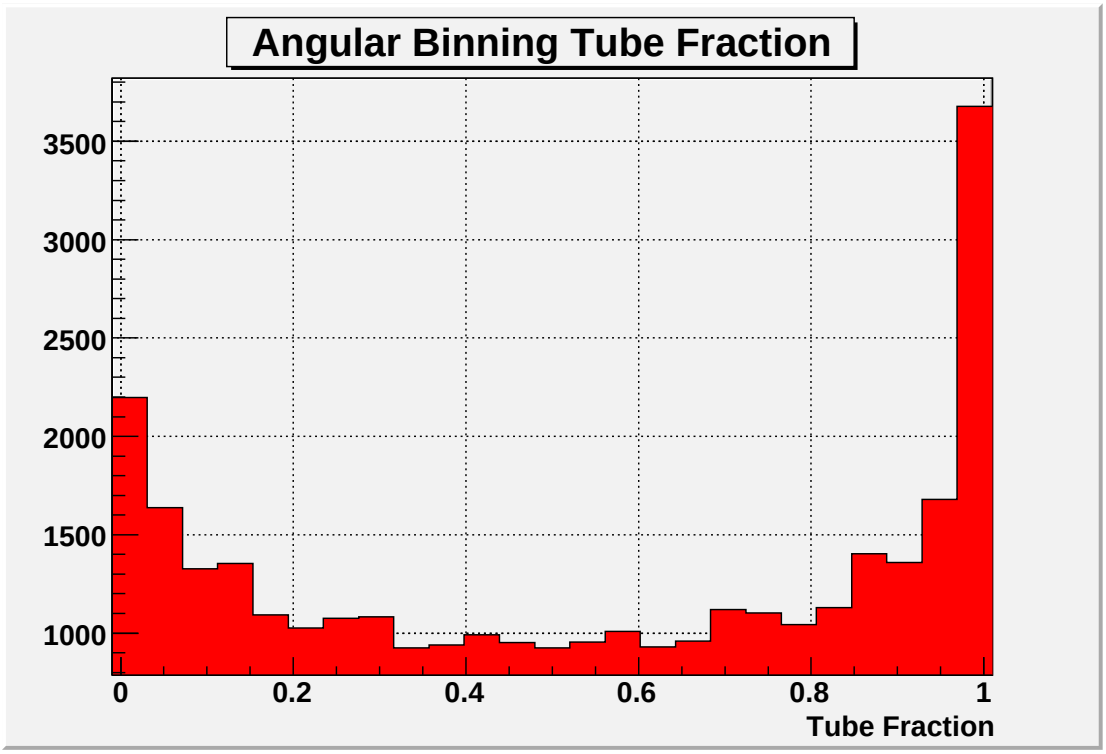

Figure 4.58. Distribution of tube fractions for all reconstructed events for a typical day.

shower-detector plane). No hit may mean that the ray fell outside of the bounds of the bin, landed on a crack, hit the photocathode but failed to register due to tube sensitivity, or even hit the side of the cluster box. A tube hit is a ray that hits a good tube in the bin and registers as a hit on the photocathode. A bin hit is a ray that lands in the boundaries of the bin, and does not need to land on the photocathode of a good tube. A cluster hit is a ray that lands on the face of the cluster, but does not need to land in the bin boundaries or even hit a good tube. Note that using this definition a tube hit is automatically a bin hit and a cluster hit as well, but a bin hit is not necessarily a tube hit. The effective area, $A_{\rm eff}$, is then computed as

$$A_{\rm eff} = \frac{N_{\rm tube}}{N_{\rm bin}} \frac{N_{\rm cluster}}{N_{\rm thrown}} A_{\rm mir} \tag{4.43}$$

where $N_{\rm tube}$ is the number of tube hits, $N_{\rm bin}$ is the number of bin hits, $N_{\rm cluster}$ is the number of cluster hits, $N_{\rm thrown}$ is the number of rays thrown, and $A_{\rm mir}$ is the area of the mirror, 5.084 m^2. For bins that have triggered tubes from multiple mirrors, the ray tracing procedure is repeated for each mirror and the effective areas are summed.

The uncertainty of the effective area calculation is

$$\sigma^2_{A_{\rm eff}} = \sum_i^{N_{\rm mir}} \left(\frac{1}{A^i_{\rm eff} N_{\rm thrown}/A_{\rm mir}} \right)^2 \tag{4.44}$$

where $A^i_{\rm eff}$ is the total effective area of mirror i, found by summing the effective areas of all bins for that mirror.

Figure 4.59 shows the distribution of effective areas found using this technique. The effective area of HiRes2 bins is found to be around 10% larger than HiRes1, which is in good agreement with what is expected. The 10% increase in effective area is due to the larger photocathode of the HiRes2 tubes.

The final step in the binning procedure is to sum the signals of all the tubes contained in the bin, weighting them appropriately using the fraction found in the previous step. For HiRes1, weighted light flux for an angular bin, $\phi_{\rm bin}$, is determined by

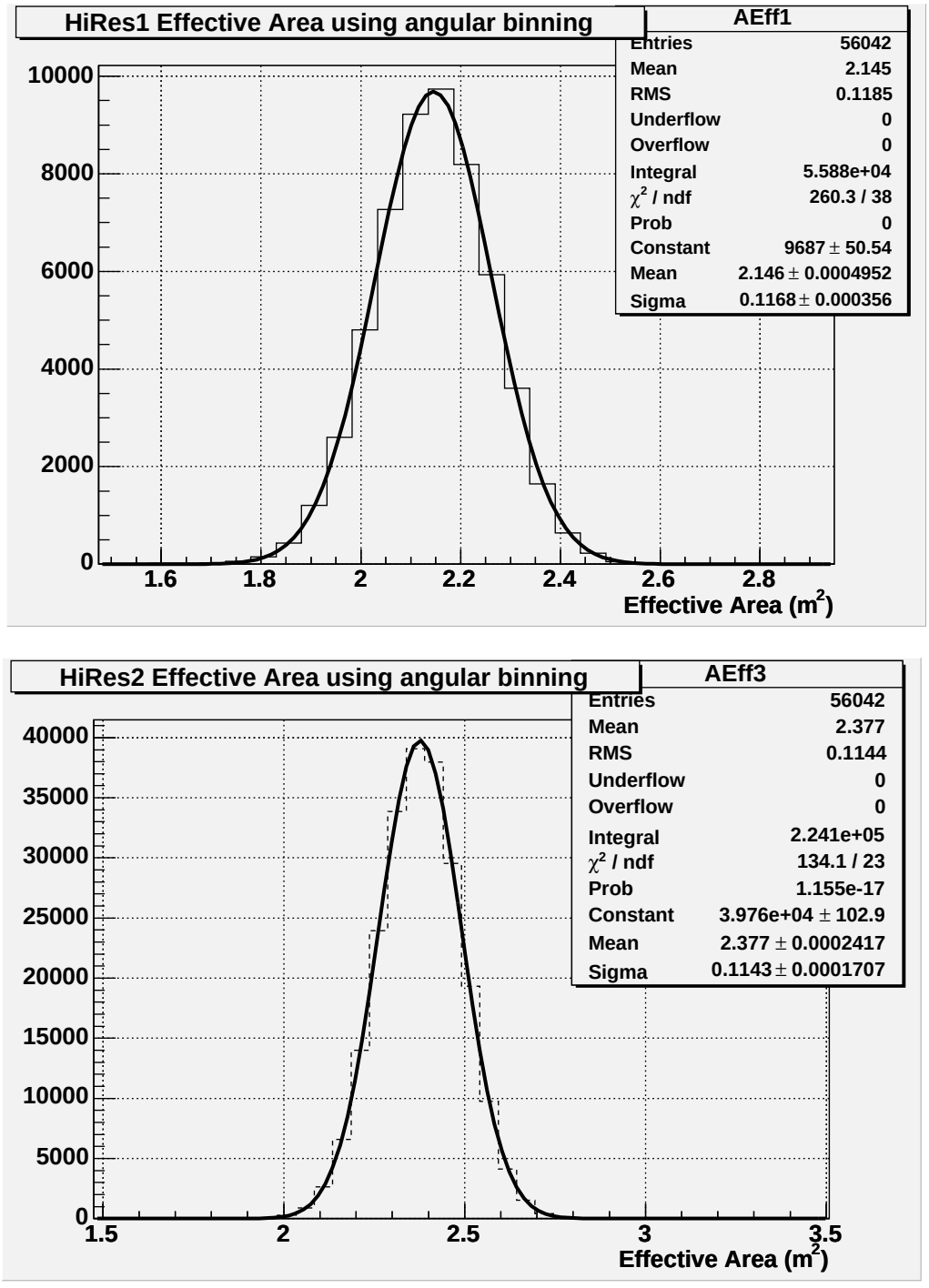

Figure 4.59. Effective area of bins at HiRes1 and HiRes2 using 1.5° bins. The total area of a mirror is 5.084 m^2. It is seen here that for 1.5° bins, the average effective area is 2.15 m^2 for HiRes1 and 2.38 m^2 for HiRes2. The difference is due to the larger size of the photocathode of HiRes2 tubes and the quantum efficiency effects.

$$\phi_{\rm bin} = \frac{1}{A_{\rm eff} \cdot \Delta\theta} \sum_{i=1}^{N_{\rm tube}} f_i \cdot N_\gamma^i \cdot \eta_{355} \tag{4.45}$$

where $N_{\rm tube}$ is the number of tubes contained in the bin, f_i is the fraction of the ith tube, N_γ^i is the number of photons, and η_{355} is the quantum efficiency measured at 355 nm (0.2781 $N_{\rm pe}$/photon). The weighted number of photoelectrons in the bin is then normalized by $A_{\rm eff}$, the effective area associated with the bin, and $\Delta\theta$, the bin angular size, to give us bin flux. Note that this light flux is measured flux at the front of the cluster face, after mirror reflection and UV filter transmission affects have occurred.

The uncertainty assigned to each bin is determined using the standard error propagation formula

$$\sigma_{\phi_i}^2 = \phi_i^2 \left[\left(\frac{\sigma_{\Delta\theta}}{\Delta\theta} \right)^2 + \left(\frac{\sigma_{A_{\rm eff}}}{A_{\rm eff}} \right)^2 + \left(\frac{\sigma_{N_{\rm pe}}}{N_{\rm pe}} \right)^2 \right] \tag{4.46}$$

where we consider only error contributions from $N_{\rm pe}$, the bin size, and the effective area. The error on bin size is estimated from the relative error between tube pointing directions on the cluster. The distance between adjacent tubes (i.e., cracks) is about 40 mm and the estimated variance from tube to tube is about 1 mm. Each tube views about 1 degree of sky therefore the uncertainty in tube pointing direction, and bin boundaries, is about 1/40 degree. This uncertainty applies at each bin boundary, so the total relative error is $\sqrt{2}/40$ degrees. Working out the flux uncertainty it is found to be

$$\sigma_{\phi_i}^2 = \phi_i^2 \left[\left(\frac{\sqrt{2}}{40\Delta\theta} \right)^2 + \left(\frac{\sigma_{A_{\rm eff}}}{A_{\rm eff}} \right)^2 + \left(\frac{\sum_j f_j^2 N_\gamma^j \eta_{355}}{\left(\sum_j f_j N_\gamma^j \eta_{355} \right)^2} \right)^2 \right] \tag{4.47}$$

The summation over j is over the tubes contained in the bin i.

HiRes2 tube flux is also similarly determined using the FPHO1 bank, which provides tube signal information intended to simulate the sample and hold electronics of HiRes1. In this case, relative quantum efficiency is corrected by FADC software during data taking, so we do not make this correction in our binning procedure.

Time binning is done exclusively for HiRes2 events. Time binning uses the FADC fast readout of the shower as it develops across individual tubes. The angular

and time width of time bins changes for each event. The time width is found by taking the total crossing time of the shower across the cluster and normalizing by the track length. For a given event, the time width of each time bin is the same, but the angular width may vary. Once the bins have been determined, ray tracing and the flux are treated similarly to the angular binning procedure described above.

4.8.8.2 SHWFIT

The final stage of data processing is the *shwfit* program that fits shower profiles to determine the $x_{\max}$, $N_{\max}$, $\sigma_{\rm s}$ parameters and integrates the profiles to determine the energies of the showers. Shwfit fills two banks, SHWA and SHWB, to allow for multiple attempts at fitting a shower using different ways of binning the shower. Table 4.11 shows which profiles are fit and stored in the SHWA and SHWB banks.

A fit is deemed "mono" if only one site's bins are used to make up the shower profile to be fitted and "global" if both site's bins are used. In all cases though the geometry of the shower has been determined using stereo geometry as described in section 4.8.6. The SHWA global fit is a hybrid in the sense that the shower profile is built using time binning at HiRes2 and angular binning at HiRes1 since time binning is not possible using the sample and hold electronics there. Figure 4.60 gives an overview of the major functional steps performed by shwfit.

Shwfit was written to be completely synchronous with the geometry, light production, and mirror reflectivity routines used by the Monte Carlo. In this way the same constants, dE/dx, phase functions, atmospherics, etc. are completely consistent with the detector simulations. Since most Monte Carlo routines are written in FORTRAN 77 and shwfit is written in C, this compatibility is attained by using C wrappers to the identical FORTRAN routines used by the Monte Carlo.

Shwfit begins by opening the input DST with events to analyze. The detector geometry is loaded and the atmospheric database is initialized. Additional constants used by the Monte Carlo FORTRAN routines are also initialized as well.

Next the profile loop is entered. This loop is performed for each of the six profiles that needs to fitted. ShwfitInit zeros out the structure that holds the current profile being processed. If the profile is a mono profile, the profile bins, shower geometry,

Table 4.11. The different profiles that are stored in the SHWA and SHWB banks.

Fit	Type	Profile Source
SHWA1	Mono	HR1 HCBIN angular bins
SHWA2	Mono	HR2 TIMBIN time bins
SHWA3	Global	HR1 BinTrack angular bins, HR2 TIMBIN time bins
SHWB1	Mono	HR1 BinTrack angular bins
SHWB2	Mono	HR2 BinTrack angular bins
SHWB3	Global	HR1 and HR2 BinTrack angular bins

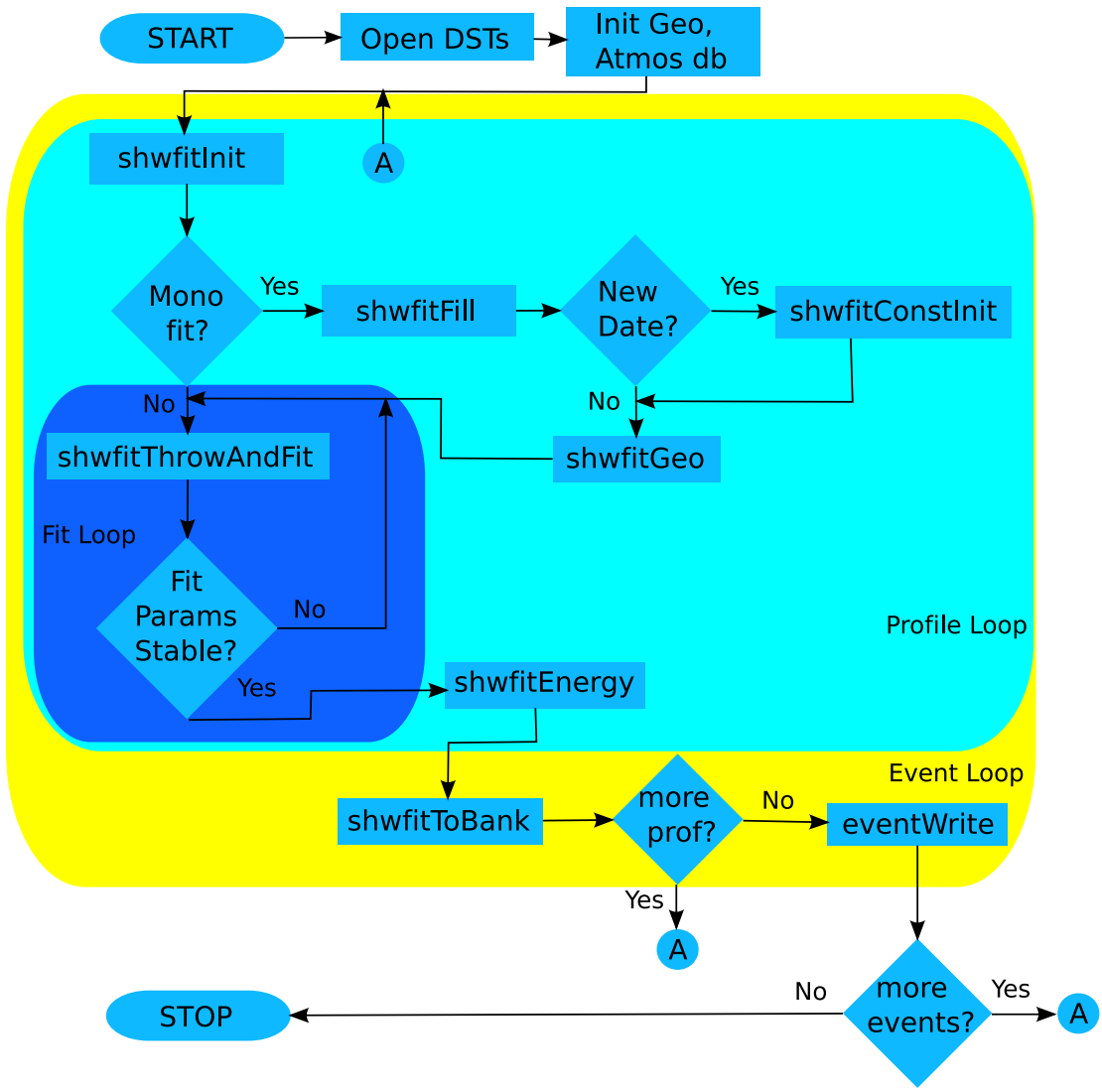

Figure 4.60. Functional block diagram of the shwfit routine. There are six different profiles that are fitted for each event, four mono profiles and two global profiles. Each profile uses different methods of binning the light collected by the detectors.

time of the event, and atmospherics are loaded into memory by shwfitFill. If a new date is encountered for this loop, shwfitConstInit loads in various constants needed by the processing routines. Of particular importance is the mirror reflectivity which varies by date. ShwfitGeo is used to determine various properties of the shower for each bin such as distance from the detector to the shower, slant depth, atmospheric density, and slant depth from the previous bin.

ShwfitThrowAndFit generates a shower in a manner identical to that described in section 4.6.2 and then fits the shower using the adaptive sieve algorithm. This throwing and fitting loop is done several times until the shower parameters stabilize. For the first entry into the fitting loop a default set of shower parameters is used in the shower generation, subsequent shower generation and fitting is done using the shower parameters found from the previous fitting attempt. If the fit fails for any reason, then the parameters from the last good fit attempt are saved and the routine exits. The looping over throwing and fitting showers is attempted for a maximum of five times. In most cases, the shower parameters stabilize in less then three fitting attempts.

Two important routines are called from shwfitThrowAndFit: shwfitThrowShower and shwfitDoFit. ShwfitThrowShower is the light generation routine that takes as its input some parameters that describe a shower profile and the information about the shower that was loaded into memory by the preceding routines. It then generates a shower in a manner nearly identical to the hr_newlight. For each bin it determines the *propagator*, p, which describes the expected scintillation $N_{\rm pe}$ per number of charged particles in the shower viewed in a bin. The light flux is termed "expected" because it is the flux as determined by the simulation taking into account the assumed shower profile fed to the routine, distance to the shower, the atmospheric conditions, mirror reflectivities, dE/dx, and quantum efficiencies. The propagator is then used to convert the *measured* light flux into the number of shower particles in the field of view of the bin by

$$N_{\rm ch} = \frac{\phi\Delta\theta - (\varphi_{\rm rayl} + \varphi_{\rm aero} + \varphi_{\rm direct})}{p} \tag{4.48}$$

where ϕ is the measured light flux in $N_{\rm pe}/{\rm m}^2/{\rm degree}$, $\Delta\theta$ is the bin angular size,

φ_{rayl} is the Rayleigh scattered Čerenkov light flux in N_{pe}/m^2, φ_{aero} is the aerosol scattered Čerenkov flux, φ_{direct} is the direct Čerenkov flux, and p is the propagator.

The structure of the propagator for a part of a shower at depth x_i is

$$p(x_i) = \sum_{j=1}^{16} S(x_i, \lambda_j) A_1(x_i, \lambda_j) A_2(x_i, \lambda_j) A_3(x_i, \lambda_j) \tag{4.49}$$

where $S(x_i, \lambda_j)$ is the scintillation component of light in $N_{\text{pe}}/\text{m}^2/\text{charged particles}$, $A_1(x_i, \lambda_j)$ is the aerosol transmission from the shower to the detector, $A_2(x_i, \lambda_j)$ is the Rayleigh transmission, and $A_3(x_i, \lambda_j)$ applies effects of mirror reflectivity, overall tube response, and a photometric scale factor that relates the Monte Carlo simulation to an absolute energy scale measured in the field using roving laser shots. The summation is performed over 16 wavelength bins from 280 nm to 415 nm. The structure of S can be written as

$$S(x_i, \lambda_j) = \zeta Y(\tau(x_i), \rho(x_i), \lambda_j) \eta(\lambda_j) T(\lambda_j) \alpha(x_i) \tag{4.50}$$

where Y is the scintillation efficiency at temperature τ and atmospheric density ρ, η is the quantum efficiency (section 3.1.3.3), T is the UV filter transmission (section 3.1.3.2), α is dE/dx (section 4.4), and ζ is a constant factor not dependent on depth or wavelength. A_1 and A_2 are exponential functions described in section 2.3. A_3 can be written as

$$A_3(\lambda_j) = f(\lambda_j) G_1 G_2 \tag{4.51}$$

where $f(\lambda_j)$ is the wavelength dependent part of mirror reflectivity described in section 3.1.3.1, G_1 is the Monte Carlo photometric scale correction, and G_2 is a scale factor applied for proper photomultiplier tube response. G_1 and G_2 are not wavelength dependent.

We can now rewrite equation 4.48 using the expanded form of the propagator

$$N_{\text{ch}}(x_i) = \frac{\tilde{\phi}(x_i)}{\sum_{j=1}^{16} \zeta Y(\tau(x_i), \rho(x_i), \lambda_j) \eta(\lambda_j) T(\lambda_j) \alpha(x_i) A_1(x_i, \lambda_j) A_2(x_i, \lambda_j) f(\lambda_j) G_1 G_2} \tag{4.52}$$

where $\tilde{\phi}(x_i) = \phi \Delta\theta - (\varphi_{\text{rayl}} + \varphi_{\text{aero}} + \varphi_{\text{direct}})$ is the Čerenkov corrected bin signal.

Once the number of shower particles for each bin is determined a fit is done to find the best set of shower parameters that describe the shower. This is done by the shwfitDoFit routine which utilizes a truncated χ^2 method called the adaptive sieve algorithm devised by Martin Block and described fully in section 4.8.8.3 and [18]. Figure 4.61 shows the functional steps performed by the shwfitDoFit routine as well as the steps performed by the adaptive sieve algorithm.

If any parameters of the fit need to be fixed this is done first during the initialization of the routine which sets up the Minuit fitter. The fitting engine used for all minimizations is the Minuit fitting package developed at CERN. It is robust, well tested, and is flexible. It provides for different minimization strategies (Nelder-Mead simplex method or Davidon-Fletcher-Powell variable-metric algorithm), computes function gradients on the fly, and provides several different methods of parameter error estimation. All fitting done in shwfitDoFit uses the MINIMIZE directive which instructs Minuit to begin fitting with the MIGRAD fitting strategy (Davidon-Fletcher-Powell variable metric approach) and to switch to the SIMPLEX strategy if MIGRAD fails to obtain an acceptable result. The MIGRAD fitting method utilizes a variable-metric method with an inexact line search. It also checks for positive-definiteness of the covariance matrix and corrects for non-positive-definite results [36].

Minuit also provides a method to fix parameters. The shwfitThrowAndFit routine checks all fit results to see if the parameter σ_{s} is less than 0.141 or greater then 0.299. During development of the fitting routine it was found that if a fit is returned with σ_{s} beyond these limits, the fitting routine has "bumped" up against the limits in parameter space of physically realizable showers. To save these showers from being rejected, the σ_{s} parameter is fixed to the average value of 0.209 and then refitted as a two parameter fit, where x_{max} and N_{max} are still allowed to vary. The Minuit manual also suggests that fitting be performed with no parameter limits. It was found that many showers were fitted in unphysical regions of parameter space though. In the case of using no limits on the fits, the profile constraint of fixing the σ_s parameter was very useful in finding those showers and refitting them, thereby

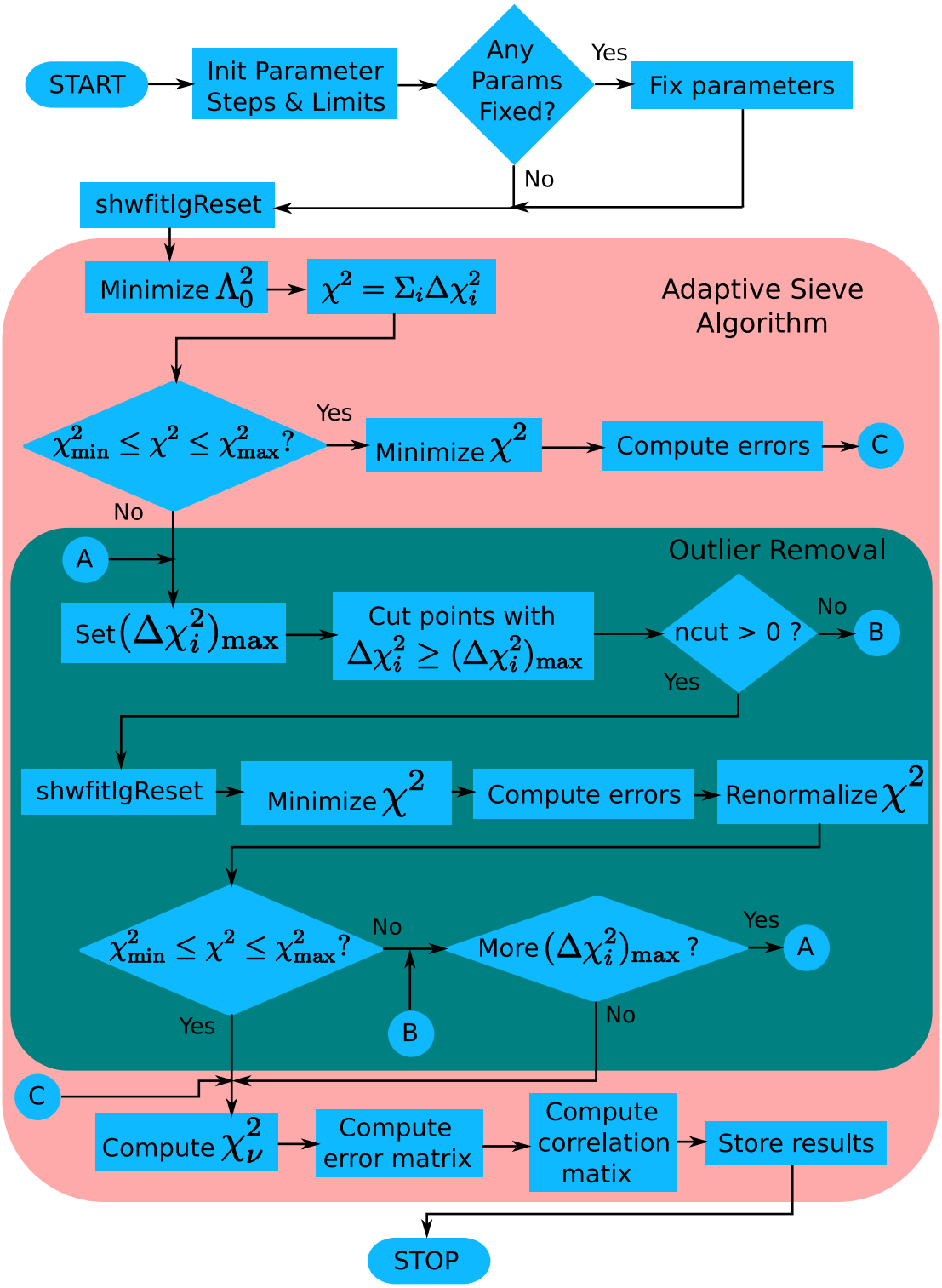

Figure 4.61. Functional block diagram of the shwfit fitting routine. The adaptive sieve algorithm is used to cut outliers that have large residuals. The Minuit fitter is the fitting engine that performs minimizations of the Λ_0^2 and χ^2 functions.

saving many showers from being rejected.

Each bin is assigned a quality code, that indicates if the bin is considered "good" or not. The shwfitGeo routine may mark a bin as bad if its viewing angle to the shower is found to fall to close to the shower track thereby exposing it to too much direct Čerenkov light for example. In the shwfitThrowShower routine, if a bin is found to have more Čerenkov light than scintillation light, then it is marked bad. The fitting routines may mark bins as bad if they exceed the maximum residual being used in the outlier removal loop of the adaptive sieve algorithm. The shwfitIgReset routine sets the bin codes for the fitting loop.

The Λ_0^2 function is minimized and if found to be acceptable, a standard χ^2 fit is done and the routine exits. If the Λ_0^2 fit is not satisfactory, the outlier removal loop is then executed. The outlier removal loop first looks for data points with $\Delta\chi_i^2(x_i; x_{\max}, N_{\max}, \sigma_s)_{\max}$ greater than 9. Then a χ^2 fit is done on the truncated data set. If the resultant χ^2 value is acceptable, then the renormalization factor is calculated and the loop exits. Otherwise a smaller $\Delta\chi_i^2(x_i; x_{\max}, N_{\max}, \sigma_s)_{\max}$ is chosen and the χ^2 fit is attempted again. Four $\Delta\chi_i^2(x_i; x_{\max}, N_{\max}, \sigma_s)_{\max}$ are used: 9, 6, 4, and 2. If after the four attempts in the outlier removal loop, the χ^2 is not acceptable, the fitting is considered a failure and appropriate codes are set so that the event is flagged. After the outlier removal loop is completed, the parameter errors are computed using the MINOS error estimator, which gives improved error estimates by taking into account parameter correlations and nonlinearities in the fitting model.

Once the fit loop is completed the energy of the shower is calculated. Using the fitted parameters of the shower, the profile of the shower can be found for any depth using an appropriate model. The Gaussian-in-age model is used here (equation 4.4). The shower is integrated from a depth of 0 g/cm^2 to $4 \times x_{\max}$ in 1000 steps. At each step the shower age is determined using equation 4.12 and the number of shower particles is found using equation 4.4. dE/dx is then found using the parameterization described in section 4.4. This integral gives the electromagnetic energy component of the shower. A missing energy correction is then

also applied using the 80/20 proton/iron parameterization described in section 4.5. This routine also calculates the observed "deposited" energy. Observed deposited energy measures the amount of energy actually seen by the HiRes detector. It is found using only the bins that are considered good by the fitting routine. The dE/dx and missing energy fraction conversion are applied the same way for this calculation.

Calculation of the shower energy is an integral expressed as

$$E = \int_0^\infty \alpha(s(x)) N_{\rm ch}(x; N_{\rm max}, x_{\rm max}, \sigma_{\rm s}) dx \tag{4.53}$$

where $\alpha(s(x))$ is the dE/dx function shown in Figure 4.17 evaluated at depth x and $N_{\rm ch}(x; N_{\rm max}, x_{\rm max}, \sigma_{\rm s})$ is the number of charged particles at that depth. In implementing the integral in equation 4.53, it becomes a sum using Simpson's rule

$$E = \sum_{i=1}^{1000} \alpha(s(x_i)) N_{\rm ch}(x_i; N_{\rm max}, x_{\rm max}, \sigma_{\rm s}) \Delta x_i \tag{4.54}$$

where the summation is done in 1000 equally spaced depths from $x = 0$ to $x = 4x_{\rm max}$, which is sufficiently deep enough into the shower to approximate an integration to infinity. $N_{\rm ch}(x_i; N_{\rm max}, x_{\rm max}, \sigma_{\rm s})$ is known at any depth since it uses the Gaussian-in-age functional form of the shower using the parameters $N_{\rm max}$, $x_{\rm max}$, and $\sigma_{\rm s}$ found when fitting the shower profile.

The influence of various factors that affect the calculation of shower energy can be seen by replacing $N_{\rm ch}$ with the expression 4.52. Making this substitution

$$E = \sum_i \alpha(s(x_i)) N_{\rm ch}(x_i) \Delta x_i \tag{4.55}$$

becomes

$$E = \sum_i \frac{\alpha(s(x_i)) \tilde{\phi}(x_i) \Delta x_i}{\sum_{j=1}^{16} \zeta Y(\tau(x_i), \rho(x_i), \lambda_j) \eta(\lambda_j) T(\lambda_j) \alpha(x_i) A_1(x_i, \lambda_j) A_2(x_i, \lambda_j) f(\lambda_j) G_1 G_2} \tag{4.56}$$

The use of the propagator allows evaluation of errors for individual sources of uncertainty (e.g., quantum efficiency, UV filter transmission, aerosol transmission, etc.).

Once the energy is determined the appropriate bank is filled. When all profiles have been fitted and their energies calculated, the event is written to the output DST for storage onto disk.

Figure 4.62 shows an example of an event. The figure shows the shower profile as number of charged particles as a function of slant depth. Since this is a global event, the information from HiRes1 and HiRes2 are both displayed. The fit to the shower is shown as well (the solid black line). The figure also shows the mirrors and tubes from each detector that observed the event. The panel on the right shows the measured and reconstructed data of the event.

4.8.8.3 Adaptive Sieve Algorithm

The adaptive sieve algorithm [18] is designed to fit "real world" data where the measured data points are only approximately Gaussian and, due to experimental error, often are contaminated by outliers. The sieve endeavors to remove only those data points that are truly far from the parent distribution, while keeping those that best describe it. The steps taken by the algorithm are

1. Make a fit of all data points by minimizing the *Lorentzian* function, Λ_0^2, where $\Lambda_0^2(\boldsymbol{x};\boldsymbol{\alpha}) \equiv \sum_i \ln\left(1+\gamma\Delta\chi_i^2(x_i;\boldsymbol{\alpha})\right)$. Here $\Delta\chi_i^2(x_i;\boldsymbol{\alpha}) = ((y_i - y(x_i;\boldsymbol{\alpha}))/\sigma_i)^2$, $y(x_i;\boldsymbol{\alpha})$ is the theoretical value at x_i, σ_i is the experimental error, and $\boldsymbol{\alpha} = \{\alpha_1,\ldots,\alpha_M\}$ is the M-dimensional parameter space of the fit. The parameter γ is an empirically measured constant set to 0.179. The choice of this value and its physical significance is explained in further detail below.

2. Calculate χ^2 using the Lorentzian minimized set of data points by $\chi^2 = \sum_i \Delta\chi_i^2(x_i;\boldsymbol{\alpha})$.

3. If the χ^2 from step 2 is satisfactory then perform a standard χ^2 fit, with all data points and exit the algorithm.

4. Using the Λ_0^2 fit as the initial estimator for the theoretical distribution, evaluate $\Delta\chi_i^2(x_i;\boldsymbol{\alpha})$ for all experimental data points.

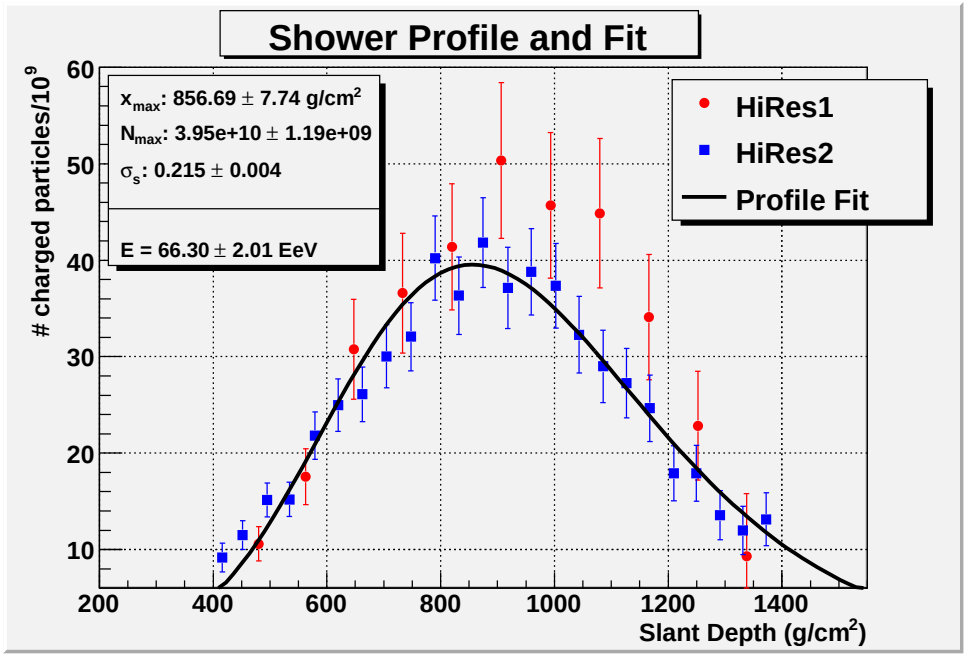

(a) Shower profile

Date	19 Nov 2003
Time	06:35:31.263
RA	22h 6m 38.4s
Dec	26.53°
$N_{\max}$	$(3.96 \pm 0.12) \times 10^{10}$ particles
$x_{\max}$	856.69 ± 7.74 gm/cm^2
σ_s	0.215 ± 0.004
Energy	66.30 ± 2.01 EeV
Energy Deposit	62.04 ± 1.88 EeV
Fit χ^2	1.14
HiRes1 R_p	15.17 km
HiRes2 R_p	20.16 km
HiRes1 ψ	142.42°
HiRes2 ψ	120.51°
HiRes1 Core x	-20.40 km
HiRes1 Core y	14.32 km
HiRes2 Core x	-9.79 km
HiRes2 Core y	21.25 km
Shower θ	60.15°
Shower ϕ	169.12°

Figure 4.62. Example of a cosmic ray event viewed in stereo, reconstructed, and fit using SHWFIT. This is a global fit which uses the information of both detectors simultaneously to create a shower profile for fitting. In this case the SHWA3 fit is used which combines HiRes2 time bins with HiRes1 angular bins in creating the shower profile. Information about the geometry of the event and the reconstructed parameters is provided in the box to the right.

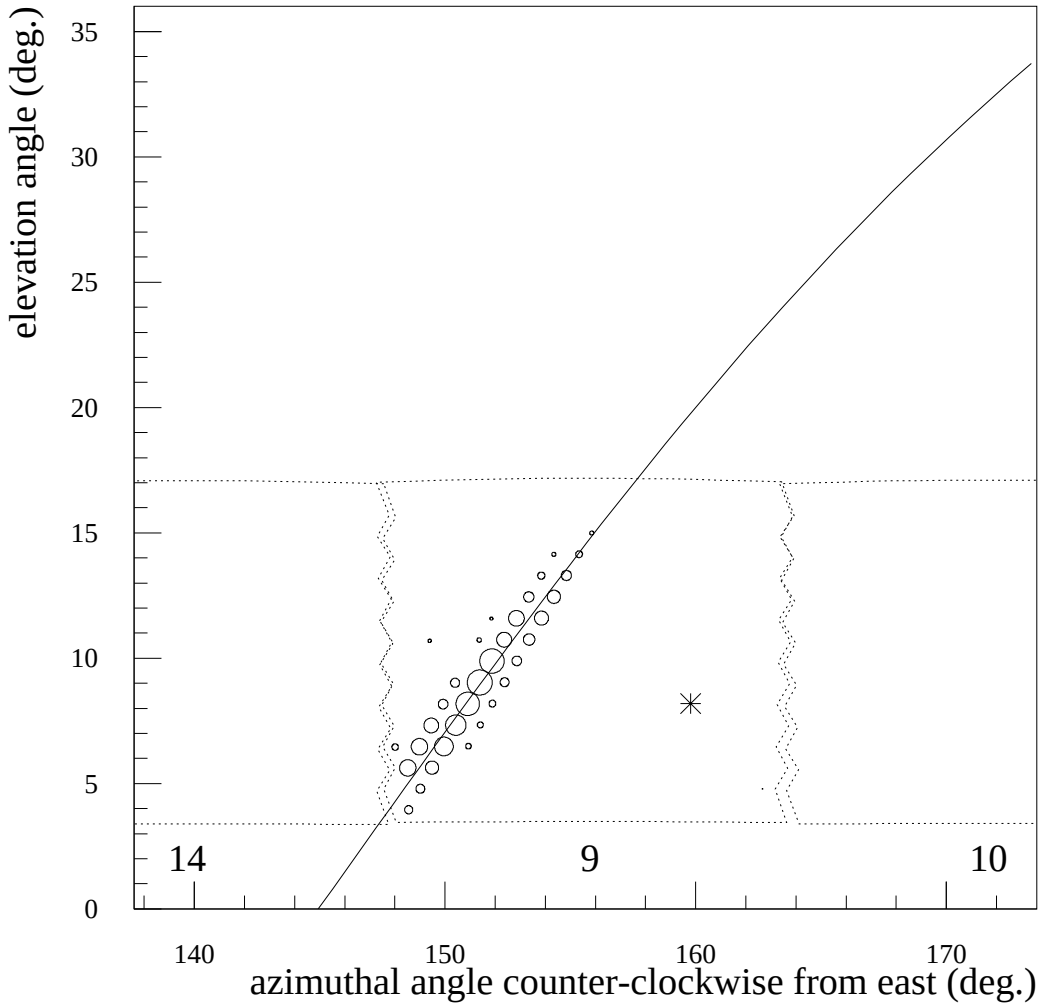

(b) HiRes1 event display.

Figure 4.62. continued.

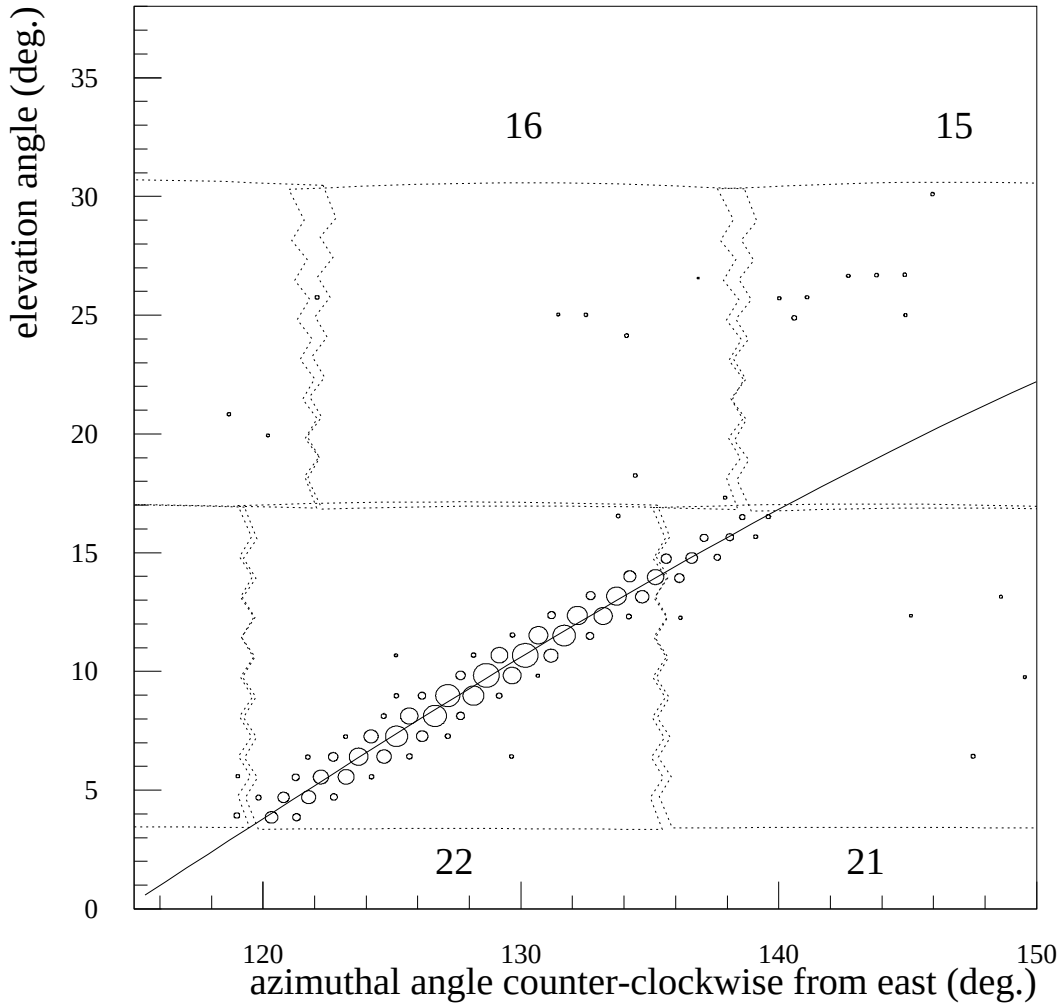

(c) HiRes2 event display.

Figure 4.62. continued.

5. Choose a largest $\Delta\chi_i^2(x_i;\boldsymbol{\alpha})_{\max}$. Find all experimental data points with $\Delta\chi_i^2(x_i;\boldsymbol{\alpha}) > \Delta\chi_i^2(x_i;\boldsymbol{\alpha})_{\max}$ and cut them.

6. Perform a standard χ^2 minimization using only the data points accepted in step 5.

7. Renormalize the $\chi^2 = \sum_i \Delta\chi_i^2(x_i;\boldsymbol{\alpha})$ result from step 6. This is done to correct for the data points that we cut from the experimental data distribution.

8. If the renormalized χ^2 is not acceptable, go back to step 5, using a smaller $\Delta\chi_i^2(x_i;\boldsymbol{\alpha})_{\max}$ to cut more outliers.

9. From the accepted χ^2 of the truncated data set compute the covariance matrix and correlation matrix.

It should be noted that the Λ_0^2 minimization gives the same $\chi^2 = \sum_i \Delta\chi_i^2$ as a standard χ^2 fit [18], so the χ^2 calculated in step 2 is the same as for a standard minimization.

The adaptive sieve algorithm gains its strength as a fitting algorithm by assuming that real data is better approximated by a distribution with long tails (i.e., not normally distributed) as opposed to a normal distribution (see Figure 4.63). The tails are manifested as outliers in real data that are distributed far from the true distribution of data points that are collected under ideal conditions with a perfectly operating measuring apparatus. For the HiRes experiment, profile measurements depend on the proper operation and accurate calibration of approximately 16000 photomultiplier tubes, 63 mirrors, all associated electronics, and good weather conditions. For example, outliers in a shower profile may be caused by a dead tube, an incorrectly calibrated tube or a shower viewed on the edge of a mirror which can cause a bin flux measurement to jump.

To understand how the adaptive sieve is derived, we examine the method of maximum likelihood and apply it to a normally distributed data sample and to a Lorentzian distributed sample. It will be seen that for a Gaussian distributed data set, the influence of large outliers is greater than for a Lorentzian distributed set.

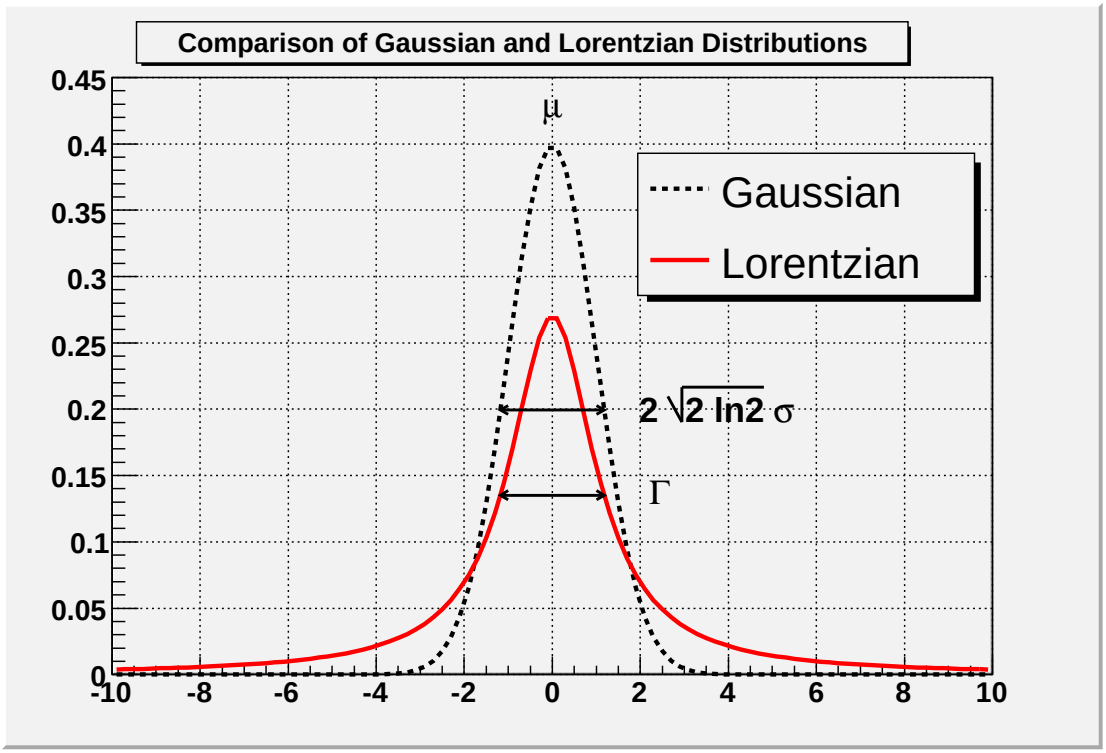

Figure 4.63. Comparison of normalized Gaussian and Lorentzian distributions with the same FWHM = 2.355. σ of the Gaussian distribution is chosen here to be 1 and Γ of the Lorentzian is chosen to be 2.355. The long tails of the Lorentzian distribution is assumed to better approximate the distribution of real data and is therefore used as the basis of a robust statistical estimator for the adaptive sieve algorithm. Here the Lorentzian is described by $(1/\pi)(\Gamma/2)/((x - x_o) + \Gamma^2/4)$, where Γ is the FWHM of the Lorentzian distribution and x_0 is the mean, chosen here to be 0.

Given an experimental set of i measured data points, the probability density of the ith measurement is P_i. If there are a total of N measurements then the probability of the entire data set in the interval Δy can be expressed as

$$\mathcal{P} = \prod_{i=1}^{N} P_i \Delta y \tag{4.57}$$

So $\mathcal{P}$ is the joint probability of measuring the experimental value y in the range from y to $y + \Delta y$. For data which is described by a normal distribution

$$P_i = \frac{1}{\sqrt{2\pi\sigma_i^2}} \exp\left(-\frac{1}{2}\left[\frac{y_i - y(x_i;\boldsymbol{\alpha})}{\sigma_i}\right]^2\right) \tag{4.58}$$

$$= \frac{1}{\sqrt{2\pi\sigma_i^2}} \exp\left(-\frac{1}{2}\Delta\chi_i^2(x_i;\boldsymbol{\alpha})\right) \tag{4.59}$$

where y_i is the value of the ith experimental measurement at x_i, $y(x_i;\boldsymbol{\alpha})$ is the theoretical value from the model being measured, σ_i is the experimental uncertainty, and $\boldsymbol{\alpha} = \{\alpha_1, \ldots, \alpha_M\}$ is the M-dimensional vector of parameters that describe the model. In equation 4.59 we simplify 4.58 by replacing $((y_i - y(x_i;\boldsymbol{\alpha})/\sigma_i)^2$ with $\Delta\chi_i^2(x_i;\boldsymbol{\alpha})$.

Utilizing the method of maximum likelihood, we wish to determine the parameters $\boldsymbol{\alpha}$, which best describe the model being studied by maximizing the probability of equation 4.57. An equivalent approach is to minimize the negative logarithm of $\mathcal{P}$. If we again assume the data is normally distributed, substituting equation 4.59 into 4.57 and taking the negative logarithm gives us

$$-\ln\mathcal{P} = -\ln\left[\prod_{i=1}^{N} \frac{\Delta y}{\sqrt{2\pi\sigma_i^2}} \exp\left(-\frac{1}{2}\Delta\chi_i^2(x_i;\boldsymbol{\alpha})\right)\right] \tag{4.60}$$

$$= \sum_{i=i}^{N}\left(\frac{1}{2}\Delta\chi_i^2(x_i;\boldsymbol{\alpha}) + \ln\sigma_i\right) - N\ln\left(\frac{\Delta y}{\sqrt{2\pi}}\right) \tag{4.61}$$

Since N, Δy, and σ_i are independent of the parameters $\boldsymbol{\alpha}$, they can be dropped from the minimization procedure. Additionally because minimization is done by taking the derivative with respect to the parameters $\boldsymbol{\alpha}$ and equating the result to 0, we can drop the factor of 1/2 as well. We are then left with the task of minimizing the

function $\chi^2 \equiv \sum_i \Delta\chi_i^2$. It is seen that for normally distributed data, the definition of the standard χ^2 function naturally follows.

To minimize χ^2 we solve the set of M equations

$$\frac{\partial \chi^2}{\partial \alpha_j} = 0 \tag{4.62}$$

where $j = 1, \ldots, M$. For the normal distribution this becomes

$$\begin{aligned} \frac{\partial \chi^2}{\partial \alpha_j} &= \frac{\partial}{\partial \alpha_j} \sum_{i=1}^{N} \Delta\chi_i^2(x_i; \boldsymbol{\alpha}) & (4.63) \\ &= \frac{\partial}{\partial \alpha_j} \sum_{i=1}^{N} \left(\frac{y_i - y(x_i; \boldsymbol{\alpha})}{\sigma_i} \right)^2 & (4.64) \\ &= \sum_{i=1}^{N} 2 \left(\frac{y_i - y(x_i; \boldsymbol{\alpha})}{\sigma_i} \right) \left(-\frac{1}{\sigma_i} \frac{\partial y(x_i; \boldsymbol{\alpha})}{\partial \alpha_j} \right) & (4.65) \end{aligned}$$

Inserting equation 4.65 into equation 4.62 we find the task of minimizing the normal distribution to be solving the M equations

$$\sum_{i=1}^{N} \frac{1}{\sigma_i} \left(\frac{y_i - y(x_i; \boldsymbol{\alpha})}{\sigma_i} \right) \left(\frac{\partial y(x_i; \boldsymbol{\alpha})}{\partial \alpha_j} \right) = 0 \tag{4.66}$$

We can generalize the procedure by writing the maximum likelihood function (equation 4.57) as a function of $z \equiv (y - y_i(x_i; \boldsymbol{\alpha}))/\sigma_i$

$$\mathcal{P} = \prod_{i=1}^{N} \exp\left(-f(z)\right) \Delta y \tag{4.67}$$

where $f(z) = -\ln P_i$. Using this form, the task of minimization becomes to find those parameters $\boldsymbol{\alpha}$ which minimize $\sum_i f(z)$. If we define the *weight* function $w(z) \equiv \partial f(z)/\partial z$, it is seen that equation 4.62 can now be written in a more general form as

$$\sum_{i=1}^{N} \frac{1}{\sigma_i} w \left(\frac{y - y_i(x_i; \boldsymbol{\alpha})}{\sigma_i} \right) \frac{\partial y(x_i; \boldsymbol{\alpha})}{\partial \alpha_j} = 0 \tag{4.68}$$

Upon inspection of equation 4.66 it can be seen that $f(z) = (1/2)z^2$ and $w(z) = z$ for the normal distribution. It should also be noted that $z \equiv (y_i - y(x_i; \boldsymbol{\alpha}))/\sigma_i = \sqrt{\Delta\chi_i^2(x_i; \boldsymbol{\alpha})}$. For the normal distribution then we can rewrite equation 4.68 as

$$\sum_{i=1}^{N} \frac{1}{\sigma_i} \sqrt{\Delta\chi_i^2(x_i; \boldsymbol{\alpha})} \frac{\partial y(x_i; \boldsymbol{\alpha})}{\partial \alpha_j} = 0 \tag{4.69}$$

Note that for the normal distribution the weight function is directly proportional to the residual $\sqrt{\Delta\chi_i^2(x_i;\boldsymbol{\alpha})}$, which the is the normalized difference of the measured data point from the theoretical model. The further an outlier in the data lies away from the theoretical value, the greater influence this point has on the χ^2 fit, which can potentially sour the minimization procedure.

Now consider instead the Lorentzian (or Breit-Wigner) distribution as a model to describe the probability density function, given by

$$\mathcal{P}_L = \frac{\sqrt{\gamma}}{\pi}\frac{1}{1+\gamma z^2} \tag{4.70}$$

where γ is related to the width of the distribution. Writing equation 4.70 as a function of y_i, $y(x_i;\boldsymbol{\alpha})$, and σ_i

$$\begin{aligned}\mathcal{P}_L &= \frac{\sqrt{\gamma}}{\pi}\frac{1}{1+\gamma\left(\frac{y_i-y(x_i;\boldsymbol{\alpha})}{\sigma_i}\right)^2} &(4.71)\\ &= \frac{\sqrt{\gamma}}{\pi}\frac{1}{1+\gamma\Delta\chi_i^2(x_i;\boldsymbol{\alpha})} &(4.72)\end{aligned}$$

Using equation 4.68 where

$$\begin{aligned}f(z) &= -\ln\mathcal{P}_L &(4.73)\\ &= \ln(1+\gamma z^2) - \ln\left(\frac{\sqrt{\gamma}}{\pi}\right) &(4.74)\\ &= \ln(1+\gamma\Delta\chi_i^2(x_i;\boldsymbol{\alpha})) - \ln\left(\frac{\sqrt{\gamma}}{\pi}\right) &(4.75)\end{aligned}$$

and

$$\begin{aligned}w(z) &= \frac{\partial f(z)}{\partial z} &(4.76)\\ &= \frac{2\gamma z}{1+\gamma z^2} &(4.77)\\ &= \frac{2\gamma\sqrt{\Delta\chi_i^2(x_i;\boldsymbol{\alpha})}}{1+\gamma\Delta\chi_i^2(x_i;\boldsymbol{\alpha})} &(4.78)\end{aligned}$$

we can write the M equations to be solved as

$$\sum_{i=1}^{N}\left(\frac{1}{\sigma_i}\right)\left(\frac{\sqrt{\Delta\chi_i^2(x_i;\boldsymbol{\alpha})}}{1+\gamma\Delta\chi_i^2(x_i;\boldsymbol{\alpha})}\right)\left(\frac{\partial y(x_i;\boldsymbol{\alpha})}{\partial\alpha_j}\right) = 0 \tag{4.79}$$

Because the Lorentzian distribution has long tails unlike the normal distribution (Figure 4.63), we see that the influence of the weight function, $w(z)$, varies depending on whether an outlier is small or large. For small variation of a point

from the theoretical value (i.e., $\sqrt{\Delta\chi_i^2(x_i;\boldsymbol{\alpha})} \ll 1$), w increases proportionally to $\sqrt{\Delta\chi_i^2}$. But if the residual is large, the influence of the data point on the weight function decreases as $1/\sqrt{\Delta\chi_i^2}$. The power of the adaptive sieve algorithm is derived from this behavior by not allowing data points with large residuals to have undue influence over the fitting procedure.

The minimization task for the Lorentzian probability density function then can be defined as minimizing Λ_0^2 over the parameters $\boldsymbol{\alpha}$. We define Λ_0^2 as

$$\Lambda_0^2(\boldsymbol{x};\boldsymbol{\alpha}) \equiv \sum_{i=1}^{N} \ln\left[1+\gamma\Delta\chi_i^2(x_i;\boldsymbol{\alpha})\right] \tag{4.80}$$

Extensive testing of this fitting procedure using various theoretical distributions are examined in [18] and the best choice of γ is found to be 0.179. This value is chosen to best minimize the RMS parameter widths of the tested input data. It is also noted that the sum of $\Delta\chi_i^2$ in equation 4.80 gives the same total χ^2 as found using a standard χ^2 fitting procedure. This is an important point as it is used in step 2 of the adaptive sieve algorithm.

As an example of how the adaptive sieve algorithm works a sample linear function that has a large noise background was fitted using the sieve and without the sieve. Figure 4.64 shows the sample function $f(x) = mx + b$, with the chosen parameters $m = \pi$ and $b = e$. One hundred data points are uniformly chosen in x from $x = 0$ to $x = 100$. Each "data" point represents 10 measurements, each of which is normally distributed about the theoretical value with $\sigma = 1$. Fifty noise points are randomly distributed in x. A random y value is chosen as the central value and again 10 measurements are taken, normally distributed with $\sigma = 1$. Two fits are then performed, one with the adaptive sieve and one without. As the figure shows, if the adaptive sieve is not used to hunt for outliers from the parent distribution, the fit is badly skewed from the line of true data points. The fitted parameters are found to be $m = 2.029 \pm 0.002$ and $b = 60.382 \pm 0.144$. If the adaptive sieve is used, most noise points are cut and the fit agrees very well with the parent function. Using the sieve the fitted parameters are found to be $m = 3.143 \pm 0.003$ and $b = 2.648 \pm 0.181$. The figure marks those points cut by the

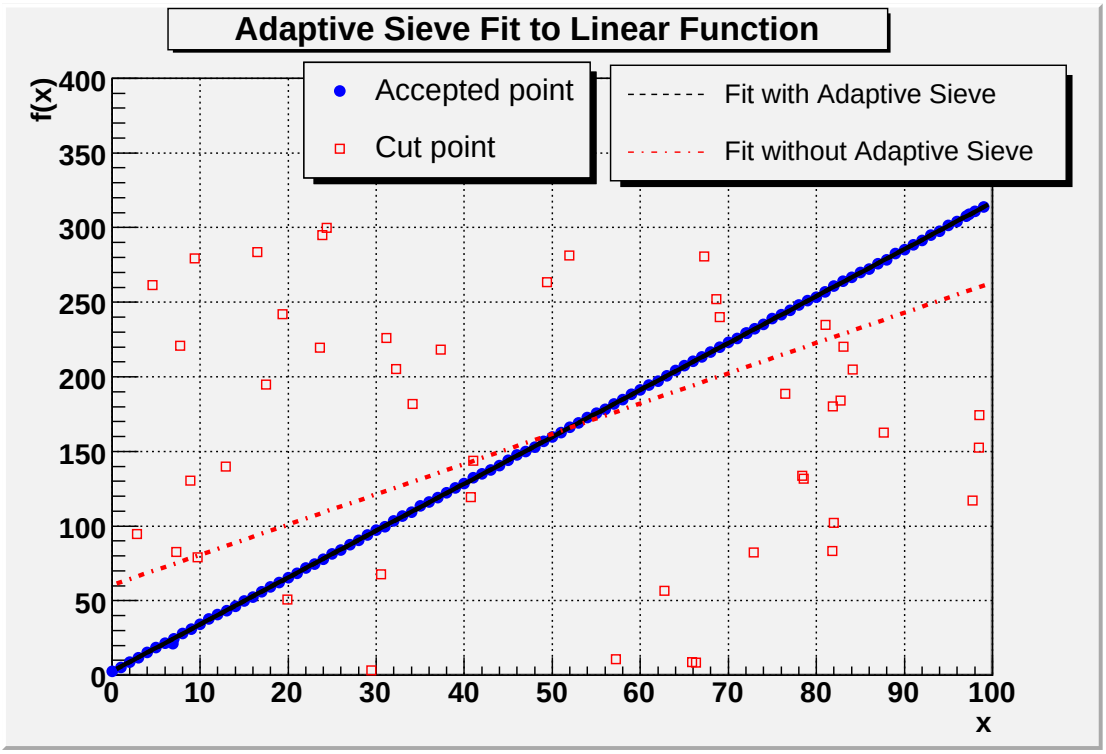

Figure 4.64. Fit to a linear function with a noise background. Each "signal" point is normally distributed around the parent function, $f(x) = mx + b$, where $m = \pi$ and $b = e$. The $(x,\ y)$ coordinate of the noise points are selected in a uniform random manner and then the y value is normally distributed about the point. The signal and data points are then fitted with and without using the adaptive sieve. The result of the fit using the adaptive sieve correctly cuts the noise points and returning a fit that very closely approximates the parent function. If the adaptive sieve is not used, the fit is contaminated by the noise.

sieve using squares and those not cut by circles. Note that all cut points are those that are clearly noise. Forty-seven of the fifty noise points were cut by the sieve for this sample distribution, all of which are part of the generated background noise. Those noise points that ended up very close to the parent function were accepted as data points, but did not significantly interfere with the fit. The sieve algorithm failed the initial Λ_0^2 fit, and then found an acceptable χ^2 after one iteration of the outlier removal loop with $\chi^2(x_i; m, b)_{\max} = 9$. More robust fitting examples and different distributions are tested in [18].

An example of how the adaptive sieve improves fitting results of showers is shown in Figure 4.65. The figure shows a Monte Carlo event using the SHWA global profile. This is a profile that incorporates the HiRes2 time binning observation of the shower with the HiRes1 angular binning observation. As can be seen the thrown shower profile and the profile obtained by fitting with the adaptive sieve agree very well. The thrown parameters are $x_{\max} = 723$ g/cm^2, $N_{\max} = 4.38 \times 10^9$ particles, and $\sigma_s = 0.223$. The parameters with the adaptive sieve fitting are found to be $x_{\max} = 739.18 \pm 19.24$ g/cm^2, $N_{\max} = (4.26 \pm 0.10) \times 10^9$ particles, and $\sigma_s = 0.23 \pm 0.01$. Without the adaptive sieve the parameters are $x_{\max} = 759.43 \pm 30.03$ g/cm^2, $N_{\max} = (3.81 \pm 0.09) \times 10^9$ particles, and $\sigma_s = 0.26 \pm 0.02$.

4.9 Weather Cuts

Selecting days with good weather is important. Nights with abnormally large aerosol components push our reconstruction into a realm of greater uncertainty. Cloudy skies can partially or entirely obscure a shower. Partially obscured showers can not be accurately reconstructed because the scattering and absorption of light in the cloud causes a loss of information about the shower development. Fully obscured showers show up as a artificial deficit in the spectrum since those weather conditions are not accounted for in the aperture calculation. Atmospheres with high aerosol content attenuate more light causing greater uncertainty in the profile and energy estimate of a shower.

Weather cuts are applied to the final pass5 data set. The zeroth order weather

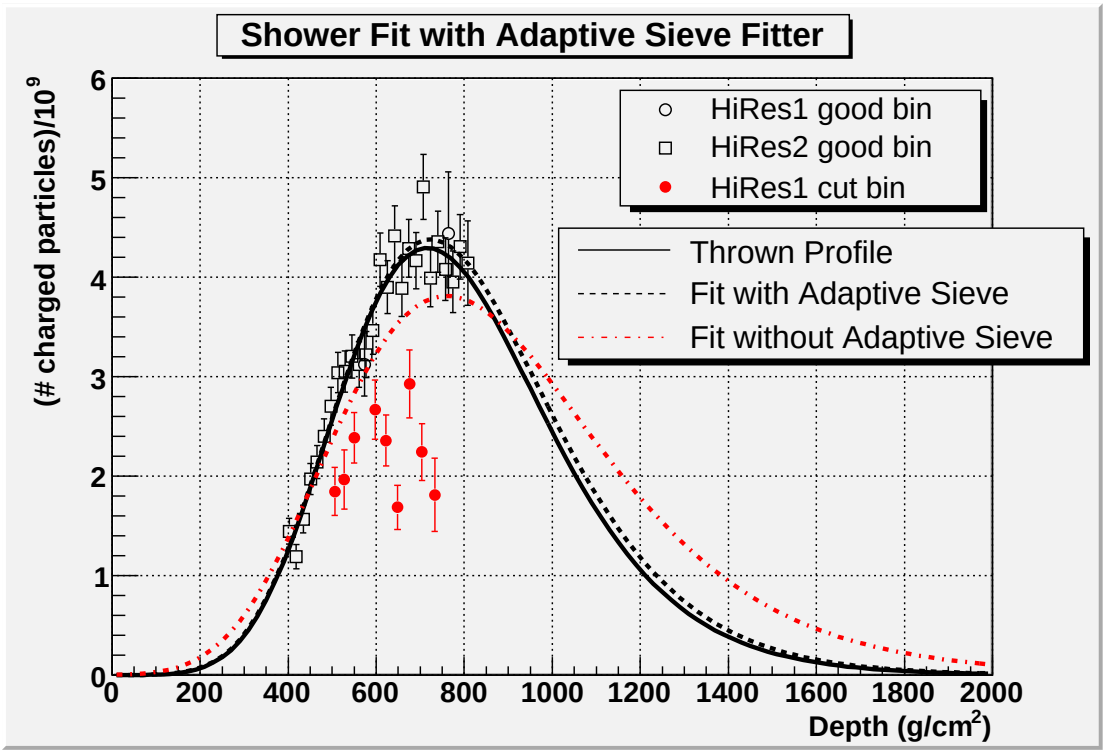

Figure 4.65. A fitted shower profile of a Monte Carlo event. This is a global fit which combines the HiRes1 and HiRes2 bins. The open circles are bins cut by the adaptive sieve algorithm and the open squares are accepted bins. When the adaptive sieve algorithm is used the fit closely approximates the thrown shower profile. When a simple χ^2 fit is done though, all the data points are used and the fit no longer returns the thrown profile.

cut is determined by seeing if the detector is running during a given period of time. Operators are instructed to not run during heavy overcast or during periods of inclement weather.

Periods of actual data collection are also cut by using the weather codes entered by the operators at HiRes1. Although it can be argued that this method is subjective, depending on an operator's judgement of weather conditions rather than an empirical measurement, this method is used in previously published results of the monocular spectrum (see [1]). In this way a consistent measurement of the stereo spectrum can be made with previous monocular results.

Good weather is determined by an analysis performed by Benjamin Stokes. The weather code of each HiRes1 data part is examined. If any of the horizon cloud digits are non-zero and the overhead digit is ≤ 2, then the data part is a good weather part [56]. This method is verified by examining event rates of good and bad parts. Bad parts are expected to have lower events rates because the sky is obscured in some part to the detector. Figure 4.66 shows the number of good weather stereo hours accumulated over the period of data collection studied in this work. Over 2500 hours of good weather stereo hours have been gathered during the 3460.08 hours of total stereo collection time (73 %). For comparison the HiRes1 monocular spectrum was calculated using 2800 hours of good weather data over ~ 3600 hours of operating time (78 %) covering the period between June 1997 and February 2003 [1].

As discussed in section 4.6.4, the Monte Carlo events are time scrambled to more realistically spread the event times to better reflect how data is collected. In this way, Monte Carlo events are also subjected to the weather cut. For nights in which some portion of the data is rejected by the weather cut, Monte Carlo events are time scrambled over the entire period of stereo data collection, including times which may be cut. The affect of the weather cut is thus considered in the aperture calculation.

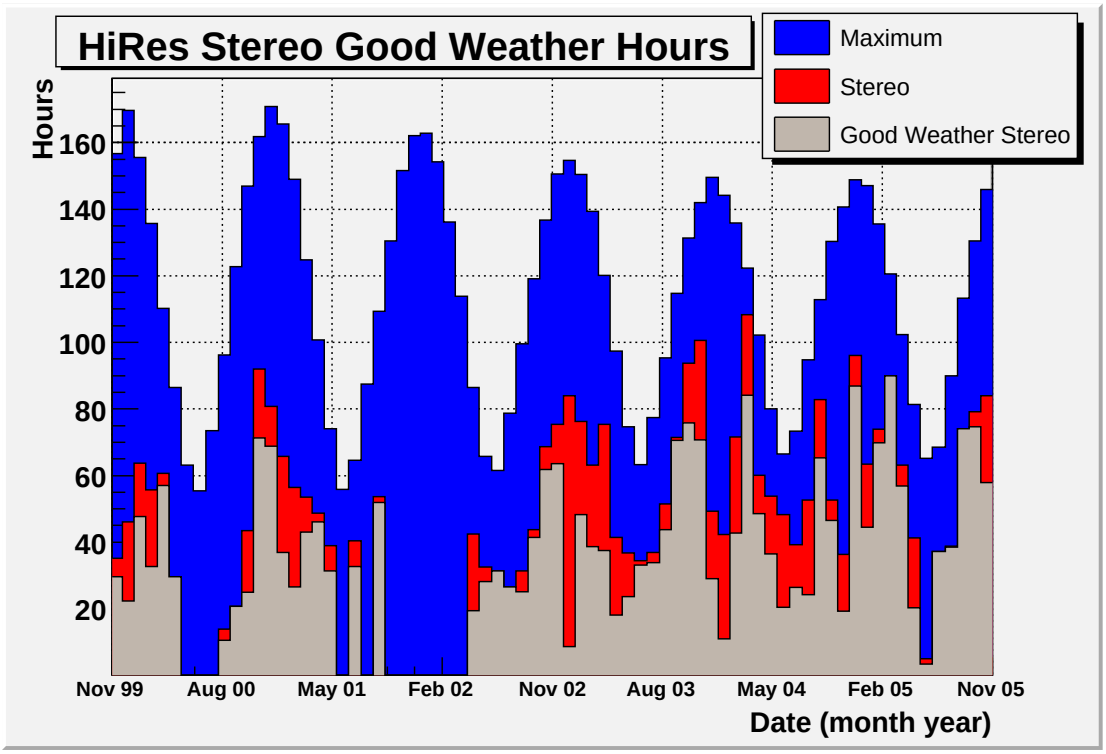

Figure 4.66. Good weather stereo hours at HiRes. Each bin is a single run. The period covered is from 1 December 1999 to 11 November 2005. The maximum possible stereo hours is 8507.29 hours, the actual stereo ontime is 3460.08 hours, and the good weather stereo ontime is 2591.87 hours.

CHAPTER 5

RESULTS

An analysis of stereo events used to determine the ultra high energy spectrum over the period covering 1 December 1999 to 11 November 2005 is discussed here. The validity of the reconstruction effort is tested by performing resolution studies of physics observables that characterize cosmic ray air showers and comparison of data to Monte Carlo. The aperture calculation is described and applied to the energy distribution of observed cosmic rays to determine the spectrum. A systematic uncertainty study and error analysis are performed. A discussion of concordance between observed events and the number expected above the GZK cutoff is also done.

5.1 Analysis Cuts

Analysis cuts applied to the pass5 events are simple and loose.

1. $18 < \log_{10}(E/\mathrm{eV}) < 21$.
2. $x_{\mathrm{low}} - 30\ \mathrm{g/cm^2} < x_{\mathrm{max}} < x_{\mathrm{high}} + 30\ \mathrm{g/cm^2}$.
3. $0.2 < \chi^2 < 3$.
4. $0.15 < \sigma_{\mathrm{s}} < 0.25$.
5. $500 < x_{\mathrm{max}} < 1200$.
6. $6 < \log_{10}(N_{\mathrm{max}}) < 12.5$.
7. Total Čerenkov light $< 40\,\%$ of total light in the track.
8. $P_{\mathrm{log}} > 2$ for both HiRes1 and HiRes2 track.
9. RMS deviation of on-plane tubes < 2 degrees.

Cut 1 restricts the energy lower bound to an energy acceptable for the detector's resolution and aperture sensitivity. x_{low} and x_{high} are the minimum and maximum

slant depths of the shower actually viewed by the detector. Cut 2 therefore requires that the shower $x_{\max}$ be *bracketed*, or be observed, by the detector. The additional 30 g/cm^2 allows some additional leeway in the determination of $x_{\max}$ within the reconstruction's ability to reconstruct $x_{\max}$ (i.e., $x_{\max}$ resolution). Cuts 3 through 6 restrict shower parameters to sensible limits. They are superfluous in this reconstruction since fitting limits given to the MINUIT fitter in SHWFIT restrict profiles to fall within this range of values. Cut 7 ensures that a shower profile is not corrupted with too much Čerenkov light. Cut 8 rejects noise events based on the pass2 $P_{\log}$ variable. Cut 9 eliminates "fat" tracks by looking at the RMS deviation of tubes that are considered part of the real shower (i.e., excluding noise tubes). If a track is too wide, it is too close to the detector and causes problems with saturating tubes. The shower profile can not be accurately reconstructed for this class of showers.

For each six different profile fits described in section 4.8.8.2, the above quantities are calculated. A simple selection algorithm then chooses which fit to use. The order in which profile fits are chosen as the one that best describes the shower is SHWA3, SHWB3, SHWA2, SHWB2, SHWB1, SHWA1. For a given event, if the SHWA3 shower profile passes the all cuts described above, then its data is selected to describe the shower. If the SHWA3 profile does not pass the cuts, then SHWB3 is selected. If SHWB3 does not pass the cuts then SHWA2 is selected and so on. For reconstruction of data and Monte Carlo the distribution of selected profiles is approximately 86.1 % SHWA3, 6.3 % SHWB3, 4.1 % SHWA2, 1.0 % SHWB2, 1.8 % SHWB1, and 0.8 % SHWA1.

5.2 Resolution Studies

Resolution studies are performed to verify that the analysis routines accurately reconstruct cosmic ray events. To know if this is being done, the true value of an observable must be known. In this analysis then resolution studies are performed on Monte Carlo simulated data. The true (or *thrown*) values of all important physics observables of interest are recorded. The events are subjected to the

same reconstruction routines as actual data, then the thrown and reconstructed information is compared.

Resolution plots are typically shown as the difference of the true value of a variable and the reconstructed value or estimator, normalized by the true value. The resolution can be formalized for an observable θ by

$$\delta(\hat{\theta};\theta) = \frac{\hat{\theta} - \theta}{\theta} \tag{5.1}$$

where θ is the true value and $\hat{\theta}$ is the reconstructed value. The value of δ is tested for many Monte Carlo events and plotted in a histogram. It is expected that this distribution be Gaussian with a mean of 0 for good reconstruction. The reconstruction resolution, $\mathcal{R}$, of the observable θ is the standard deviation of this distribution. If the mean of the distribution is not 0 then there may be systematic biases in the reconstruction that need to be investigated further. If the width of the distribution is very wide, then the resolution is considered poor. The determination of how large a resolution is acceptable is different for each experiment and each variable, and the desired accuracy of the measurement in question must be considered.

For the spectrum measurement, accurate reconstruction of the energy is important. A poor energy resolution means that there is a greater chance that events are reconstructed far away from the true value. Since we histogram the event distribution in energy bins, we want our energy resolution to be small enough that we have a small probability of reconstructing an event far from the true value and actually counting it as being seen in the wrong energy bin. Events in the energy distribution, aperture, and exposure are binned in histograms with bin width of 0.1 in units of $\log_{10}(\mathrm{eV})$. This bin width represents a 26 % increase in energy for each bin. So for acceptable reconstruction, the energy resolution must be less than 26 %.

Figure 5.1 shows the energy resolution of the reconstruction. The top figure shows the distribution of events thrown by the Monte Carlo and the distribution of reconstructed events. The bottom two figures show the resolution, $\mathcal{R}$. The figure on the right is plotted in a linear scale and the plot on the left is shown on a log scale to

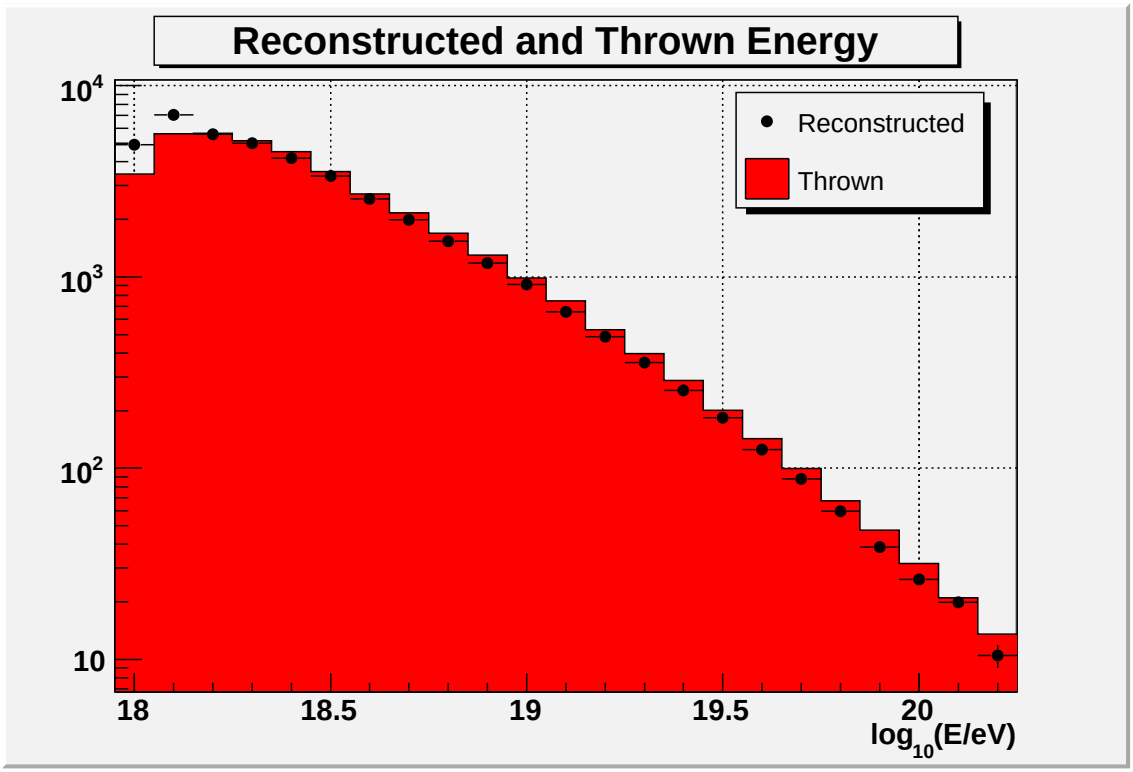

(a) Reconstructed and thrown energy

Figure 5.1. The HiRes stereo reconstruction energy resolution. The resolution is found by the fit to the distributions at the bottom of the page and is seen to be 13.5 %.

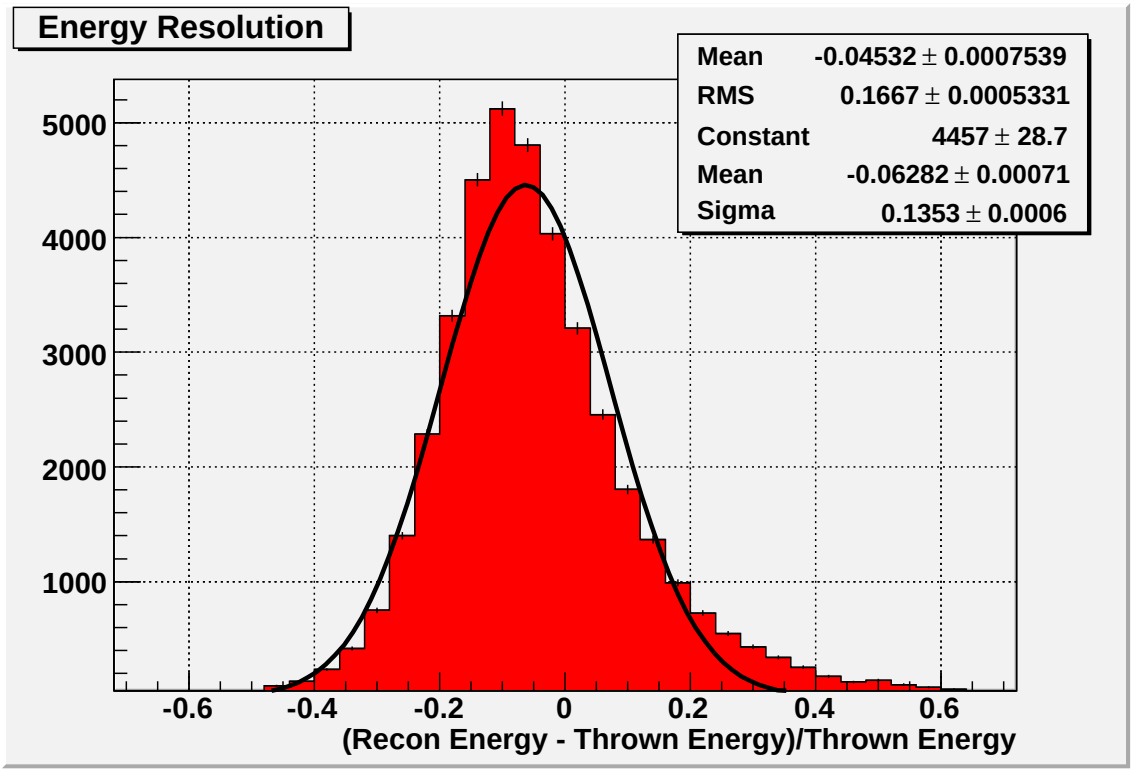

(b) Energy resolution (linear scale).

Figure 5.1. continued.

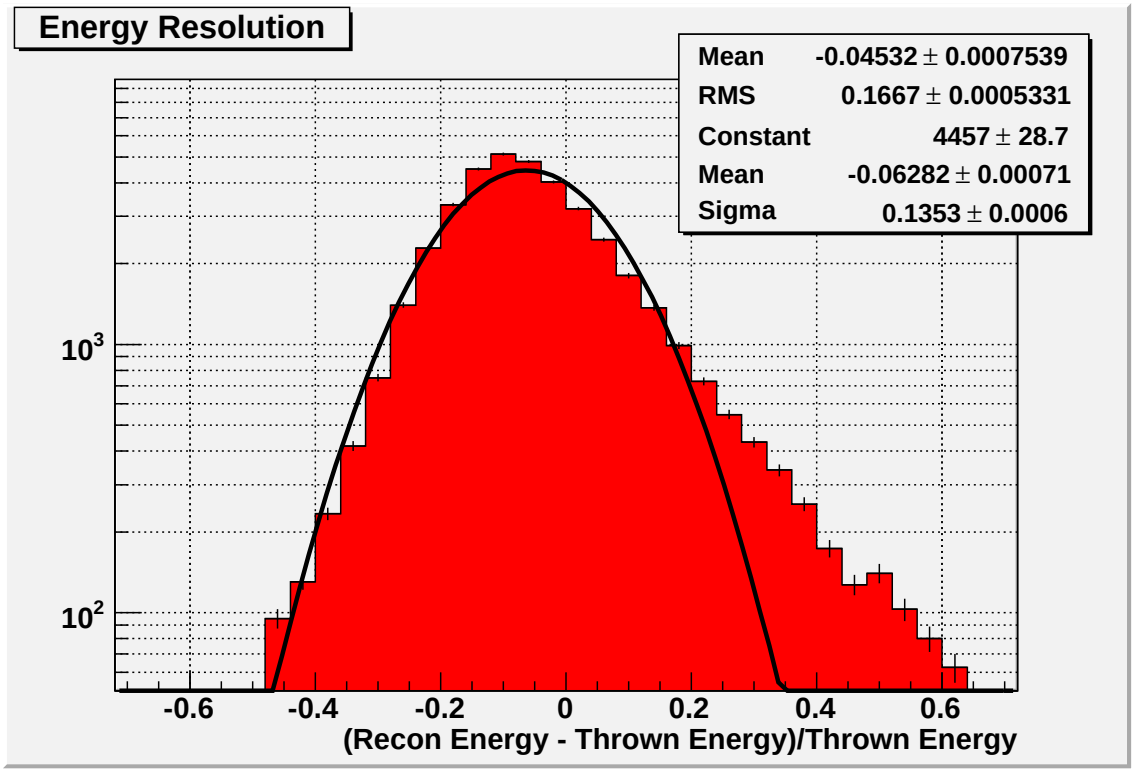

(c) Energy resolution (log plot).

Figure 5.1. continued.

better discriminate the tails. The resolution is shown by the fit to the distribution to be 13.5 %. Figure 5.2 is a plot of the energy resolution as a function of thrown energy. It can be seen here that the reconstruction energy resolution changes with energy. At energies below 10^{18} eV the resolution becomes unacceptable.

Figures 5.3 and 5.4 show the reconstructed and thrown distributions of the fitting parameters $N_{\max}$ and σ_s.

The $N_{\max}$ resolution is 11 % and the tails are small as seen between the close agreement of the RMS and the standard deviation of the resolution plot. The resolution of σ_s is seen to be 10 %.

The disagreement between thrown and reconstructed σ_s can partly be attributed to the profile constraint used in the shower fitting. If a profile fit is returned with the shower width beyond the physical limits expected for a real shower, *sigs* is fixed to the weighted average of the Monte Carlo thrown *sigs* distributions for proton and iron. The average is found to be $\sigma_s = 0.209$. This causes a peak in the reconstructed distribution at $\sigma_s = 0.209$ and a subsequent deficit in the remaining distribution. This peak in the reconstruction is seen in the top figure in Figure 5.4.

Figure 5.5 shows the $x_{\max}$ distributions and the reconstruction resolution. A systematic bias of -12 g/cm^2 can be seen in the resolution plots. The overall resolution overall energies is seen to be 37.8 g/cm^2.

Figure 5.6 shows the reconstructed energy and fitting parameters as a function of the value thrown by the Monte Carlo. The disagreement between thrown and reconstructed σ_s arises for real data showers where not all of the shower is seen. When fitting CORSIKA showers where most of the profile is available for fitting, the fitted σ_s agrees much better with the CORSIKA thrown σ_s. The reconstruction bias in $N_{\max}$ seen for low $N_{\max}$ occurs at low shower energies where showers are more difficult to reconstruct.

Figures 5.7 through 5.12 show the reconstruction resolution of the geometric observables that describe a shower. Figure 5.13 shows the distribution of reduced χ^2 for all reconstructed events. The distribution is peaked at $\chi^2 = 1$ which is the expected value.

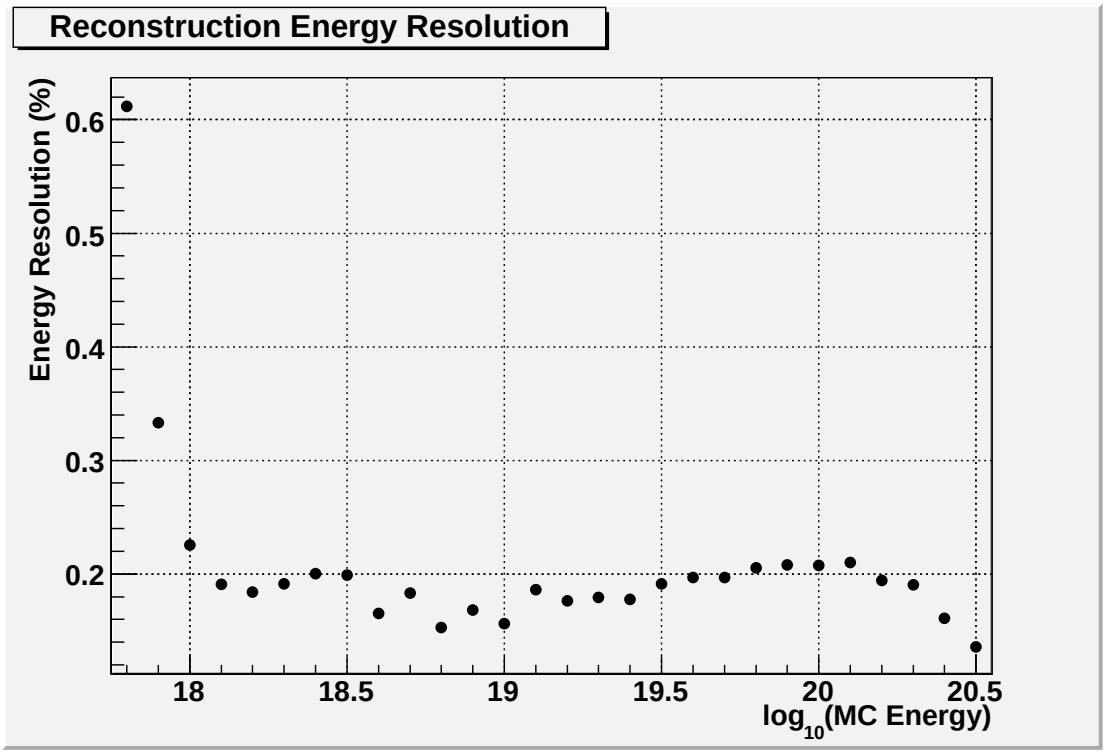

Figure 5.2. The reconstructed energy resolution as a function of Monte Carlo thrown energy. The RMS width of the energy resolution is shown for each bin.

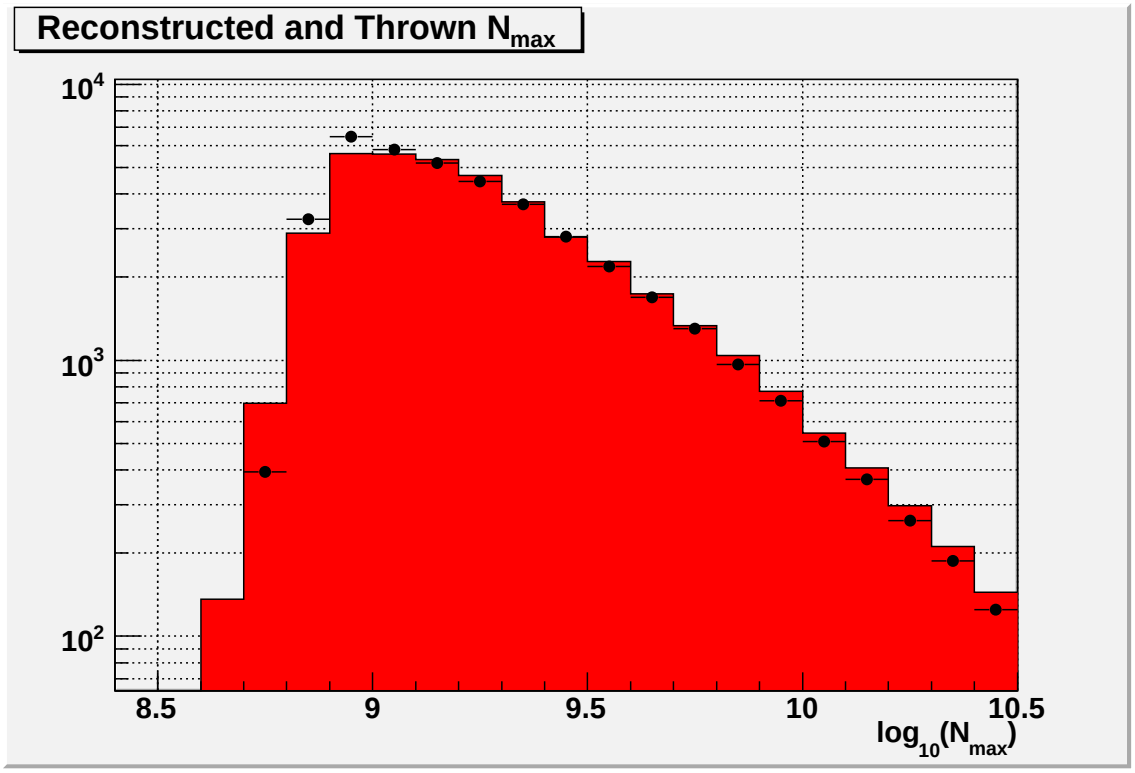

(a) Reconstructed and thrown $N_{\max}$

Figure 5.3. The HiRes stereo reconstruction $N_{\max}$ resolution. The resolution is found to be 11 %.

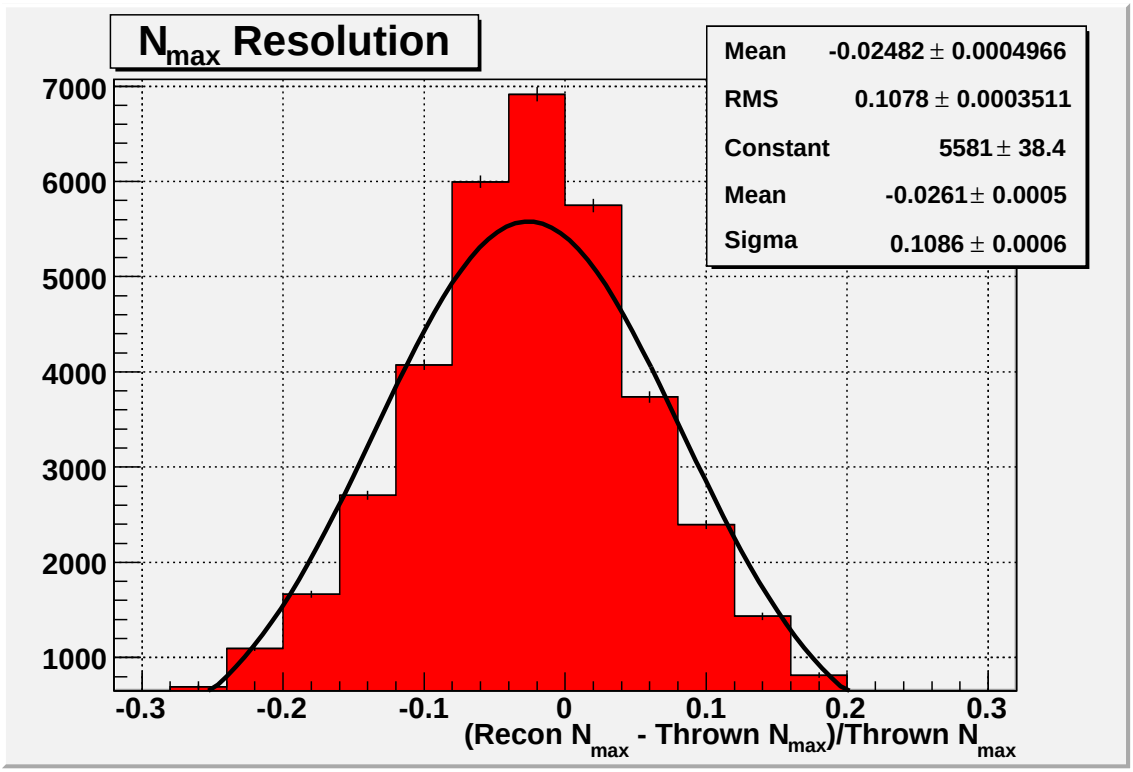

(b) $N_{\max}$ resolution (linear scale).

Figure 5.3. continued.

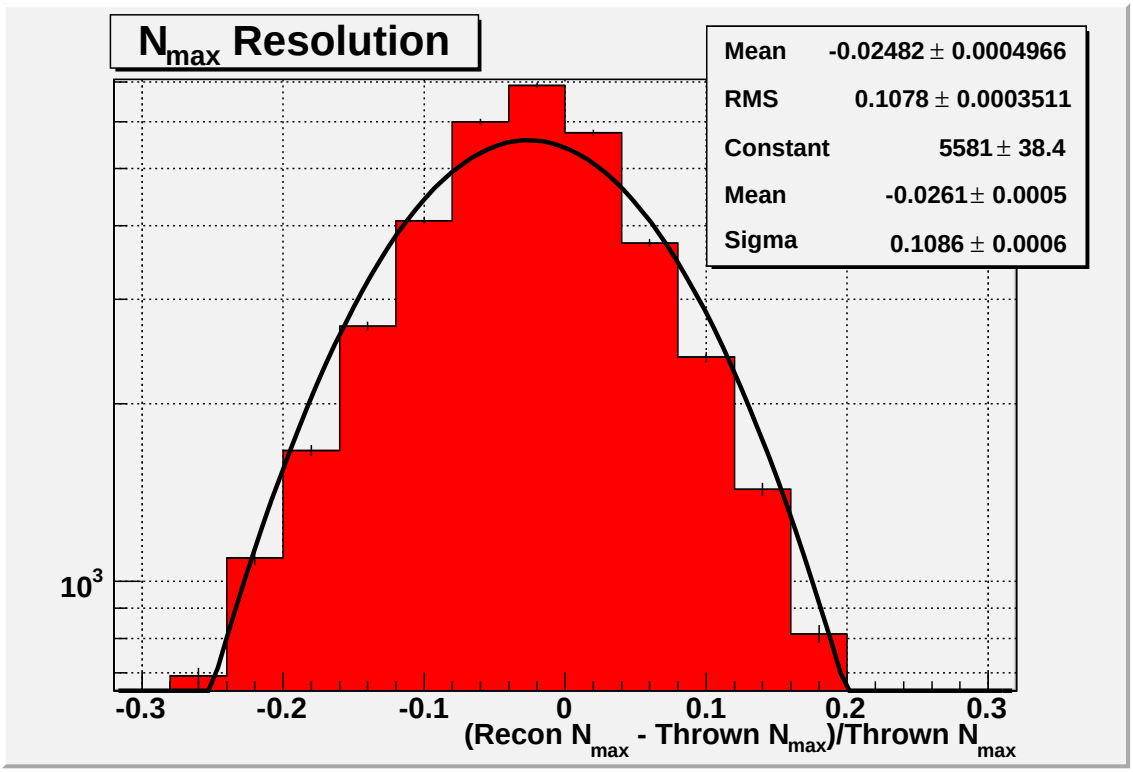

(c) $N_{\max}$ resolution (log scale).

Figure 5.3. continued.

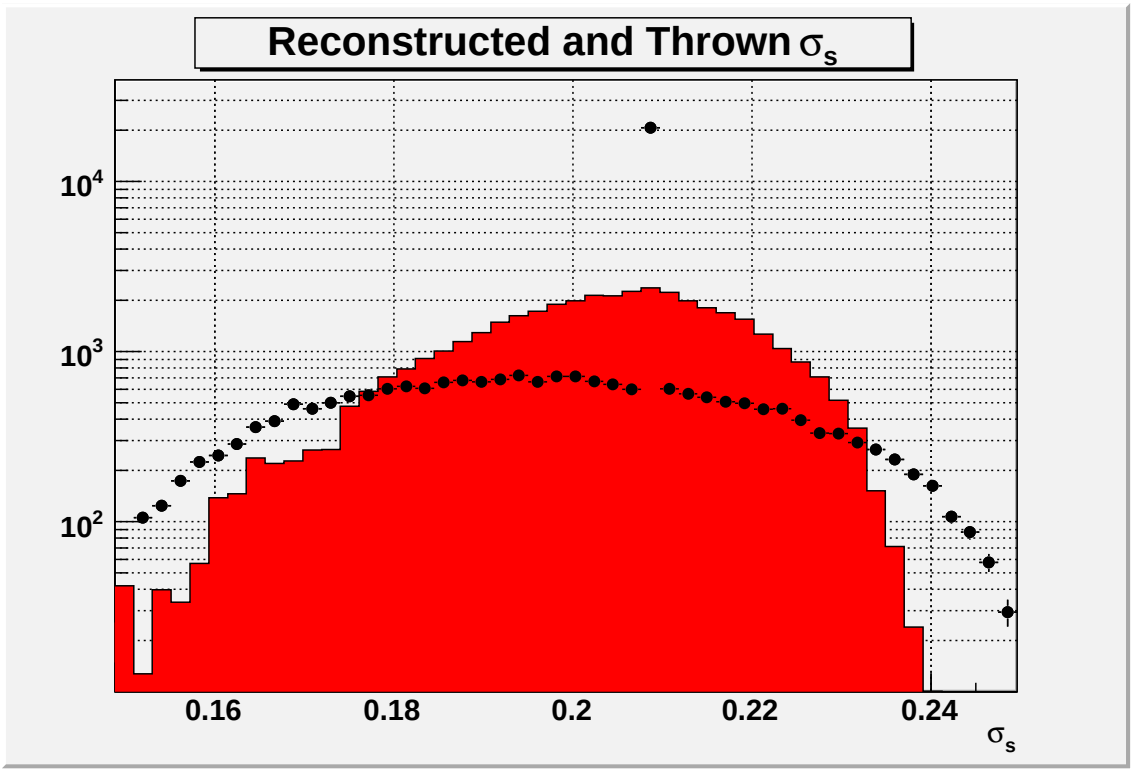

(a) Reconstructed and thrown σ_s

Figure 5.4. The HiRes stereo reconstruction σ_s resolution. The peak in the reconstructed σ_s is the result of the profile constraint applied to showers which have unrealistic σ_s during fitting. If σ_s is found to be unphysical during a fitting attempt it is fixed to the average value of 0.209 for all subsequent fitting attempts. The overall systematic shift is found to be only $-1.8\,\%$ and the resolution is $10.5\,\%$.

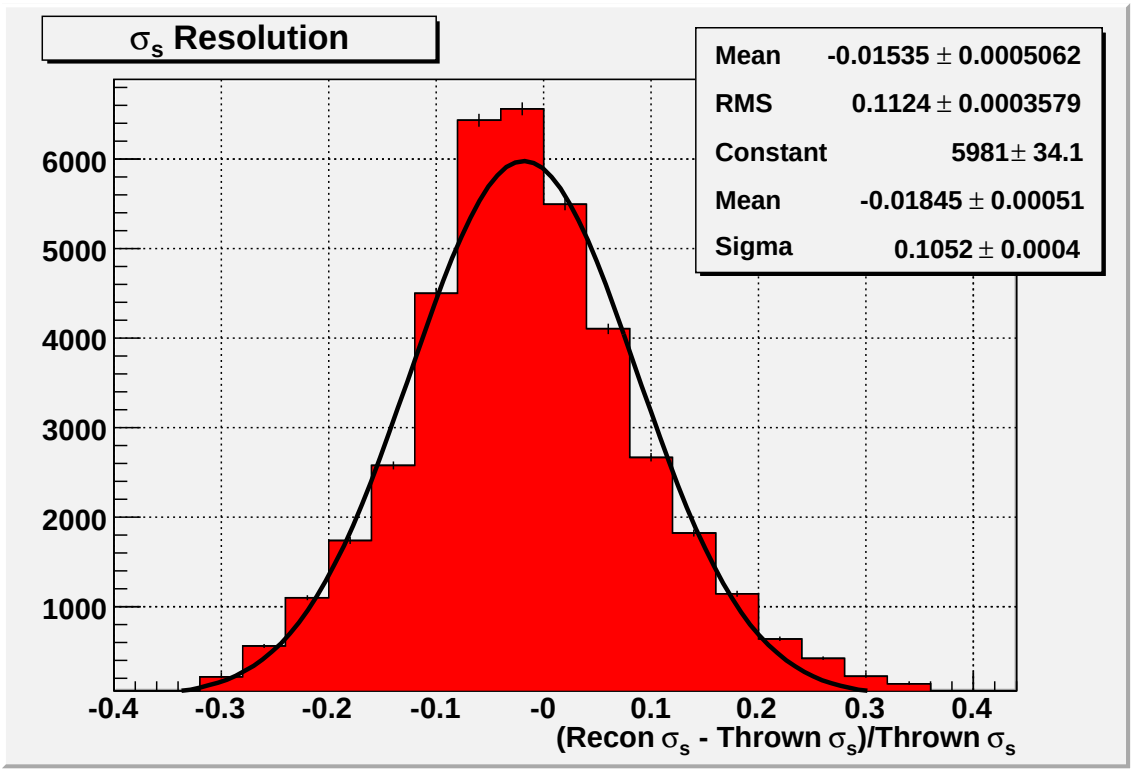

(b) σ_s resolution (linear scale).

Figure 5.4. continued.

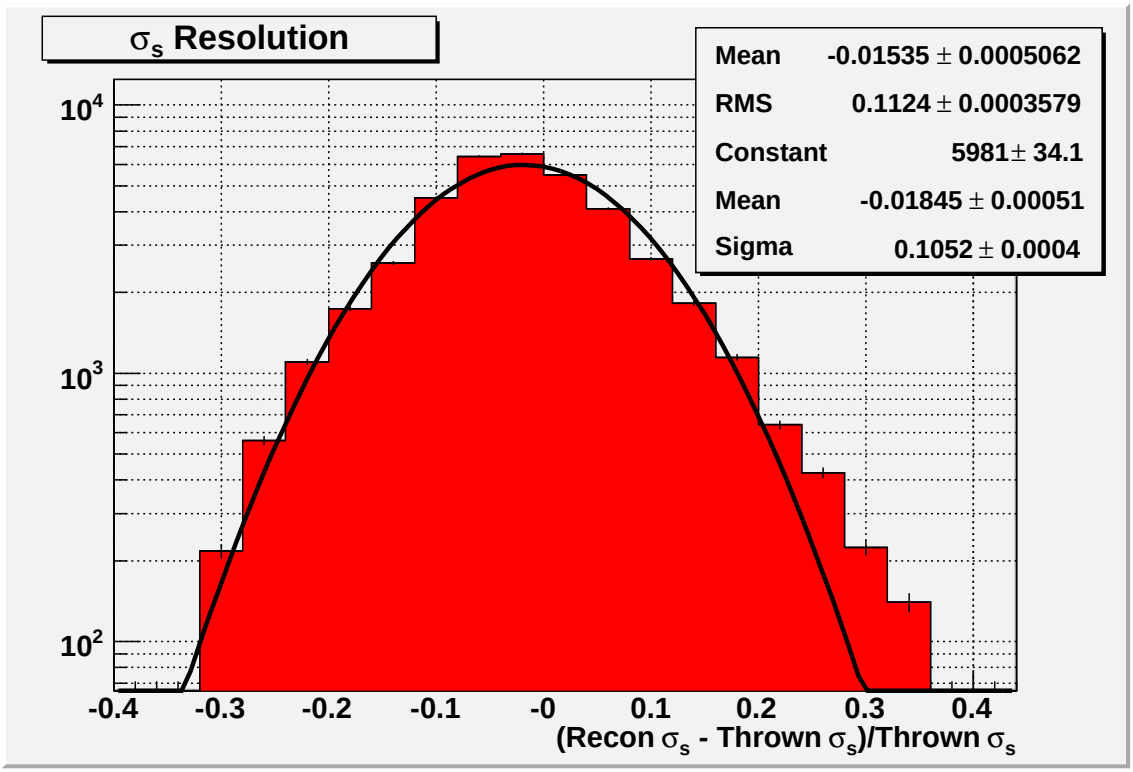

(c) σ_s resolution (log scale).

Figure 5.4. continued.

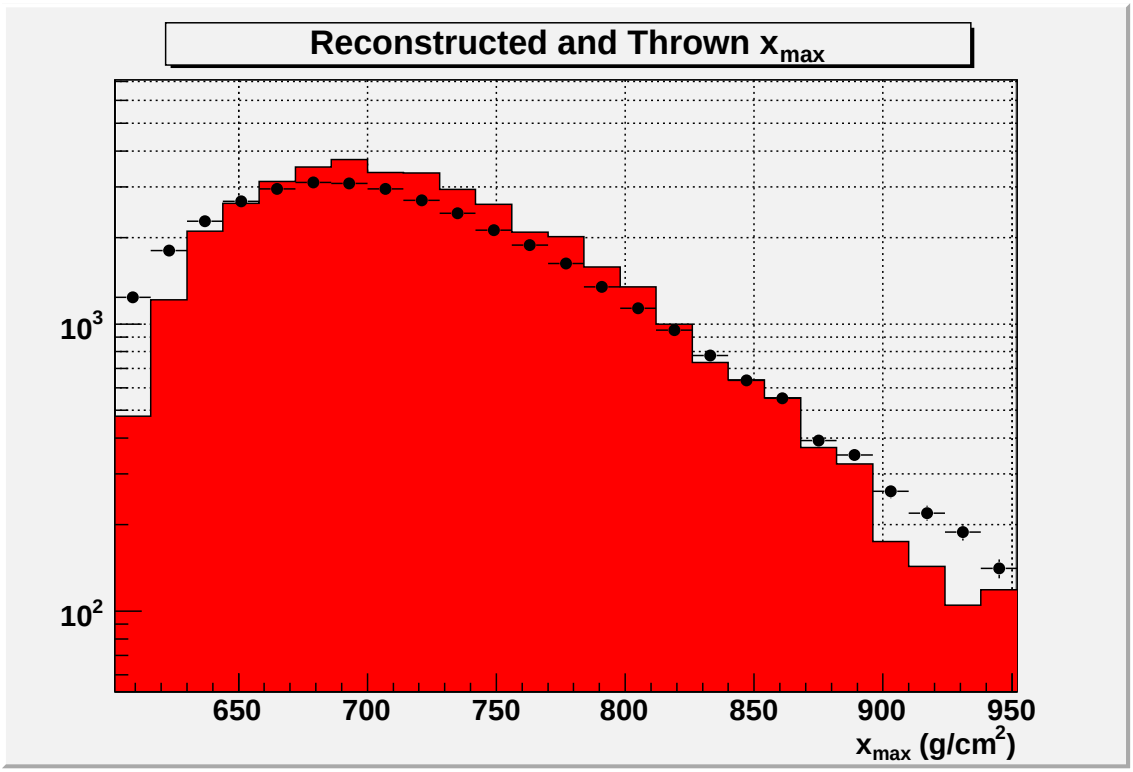

(a) Reconstructed and thrown $x_{\max}$.

Figure 5.5. The HiRes stereo reconstruction $x_{\max}$ resolution.

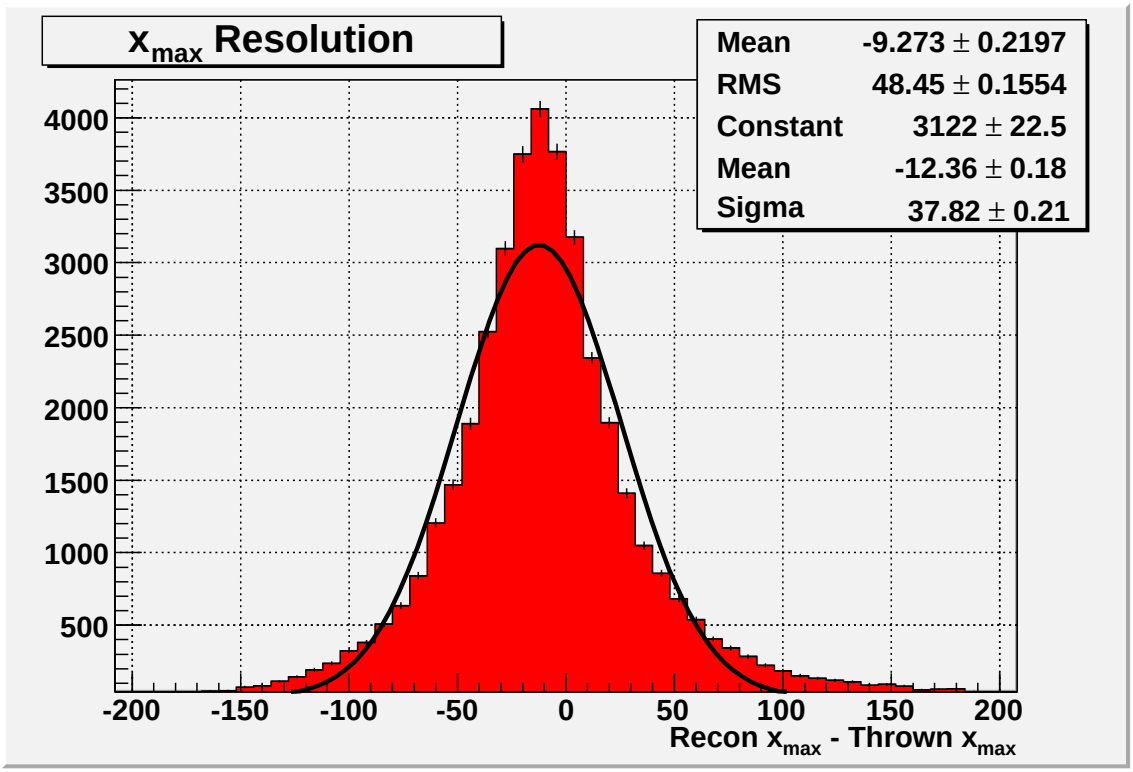

(b) $x_{\max}$ resolution (linear scale).

Figure 5.5. continued.

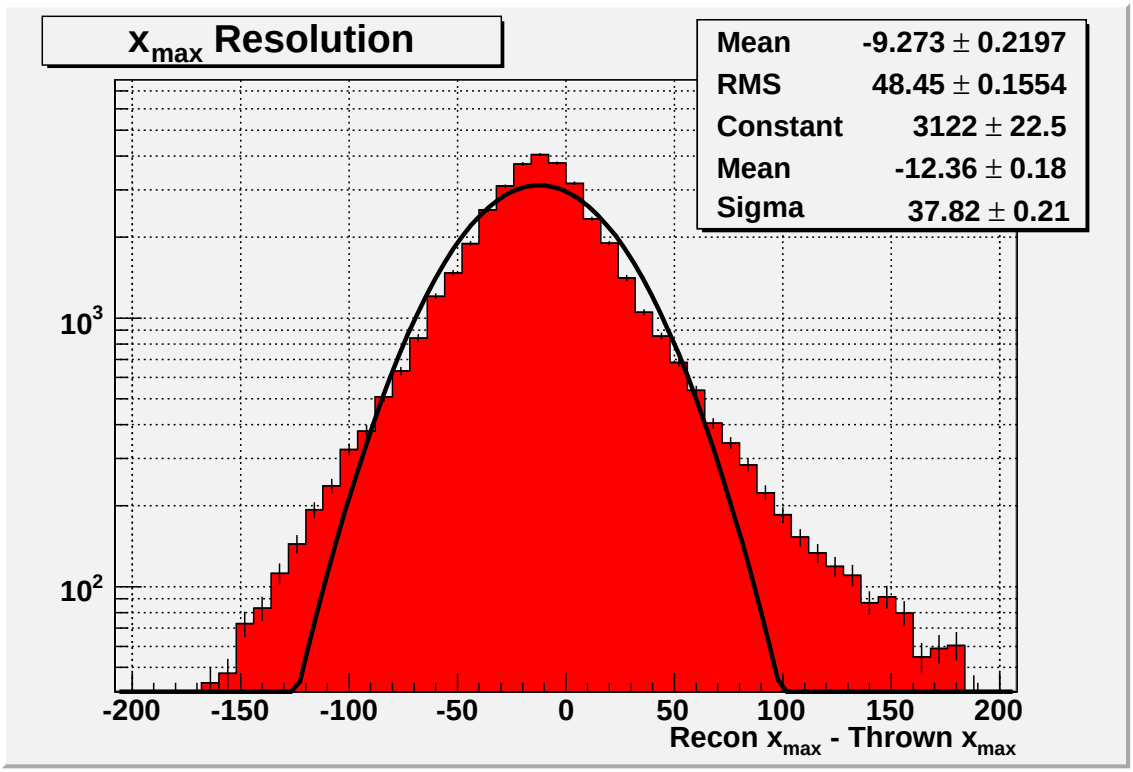

(c) $x_{\max}$ resolution (log scale).

Figure 5.5. continued

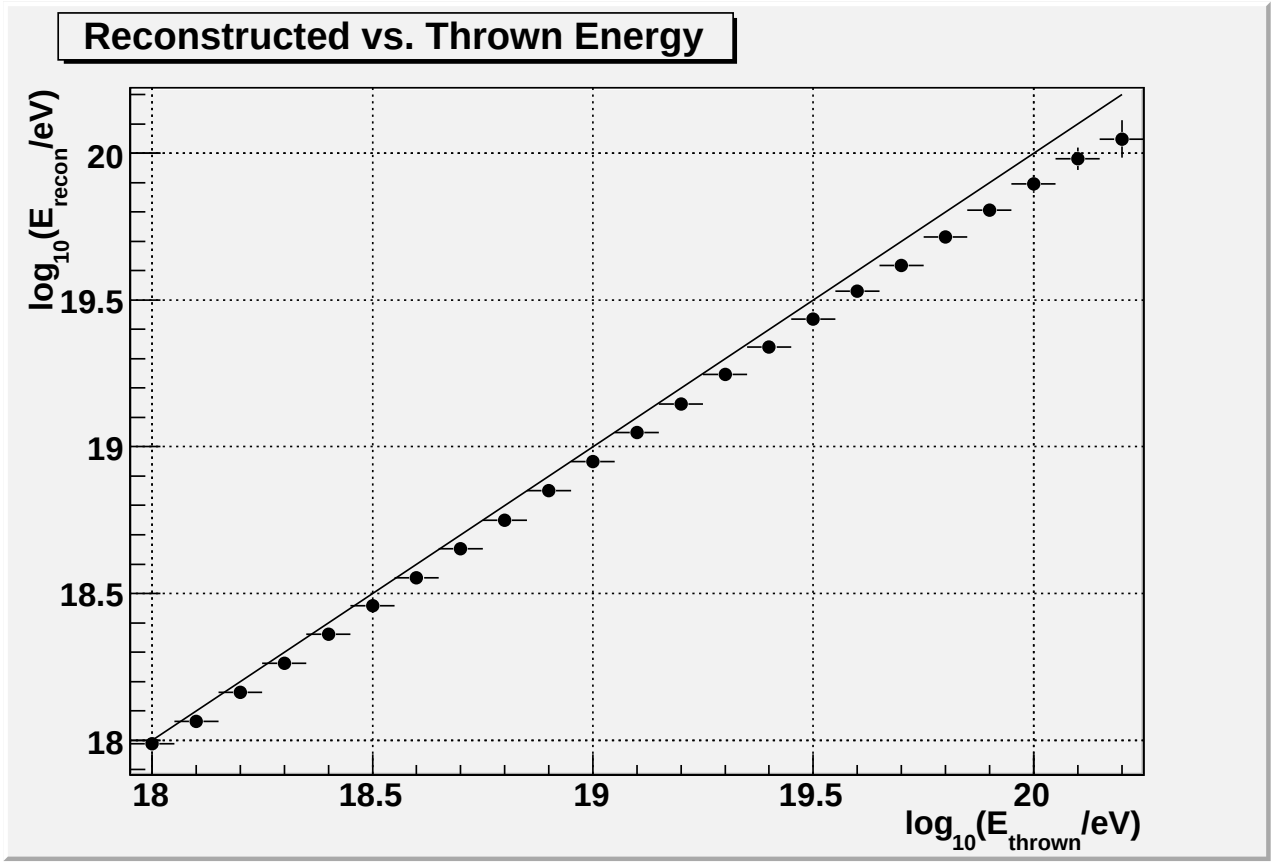

(a) Energy

Figure 5.6. Scatter plots of reconstructed versus thrown values of fitted parameters. The result of the scatter in energy reconstruction is shown as well. The line shown in each plot shows theoretical 1:1 correspondence expected.

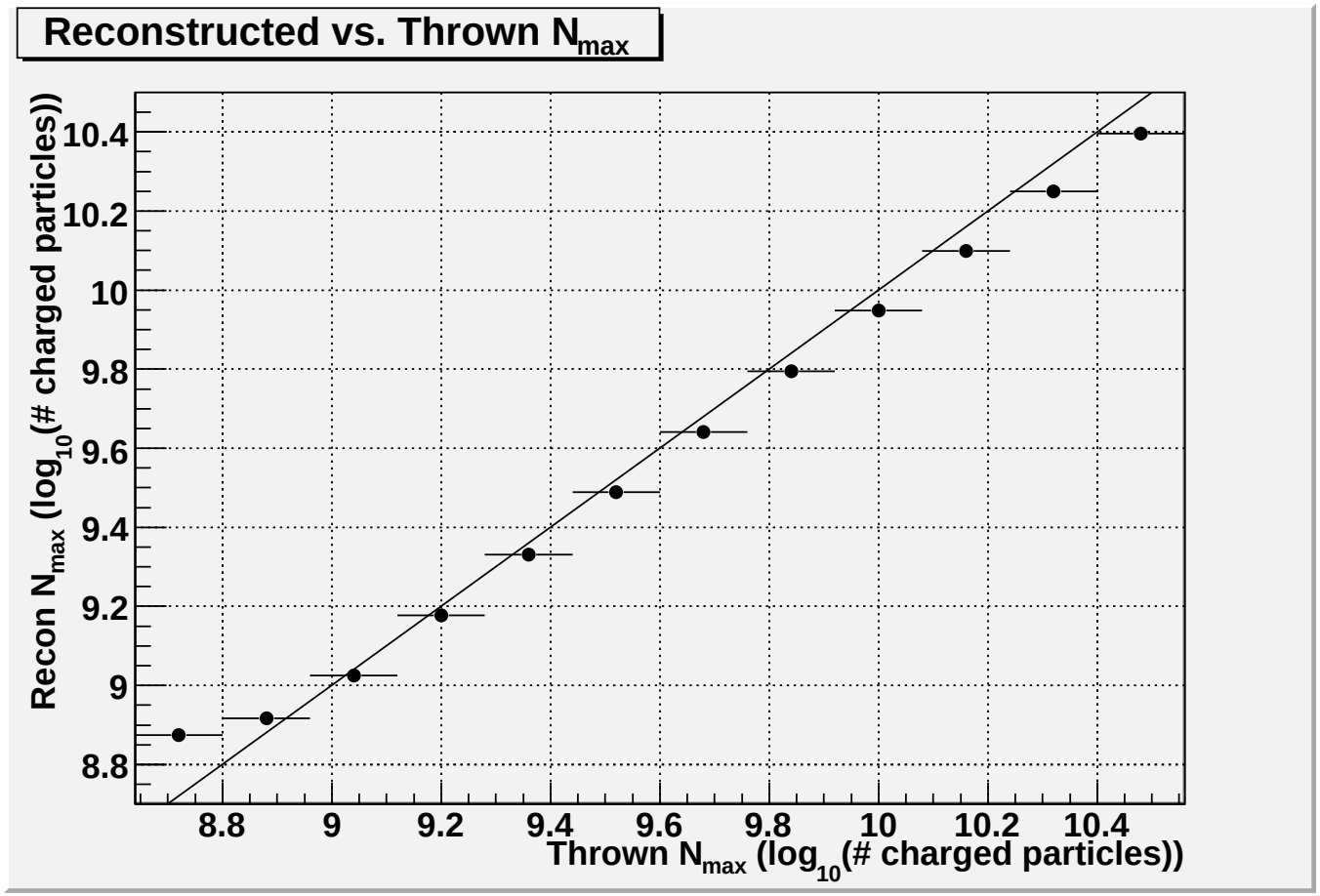

(b) $N_{\max}$

Figure 5.6. continued.

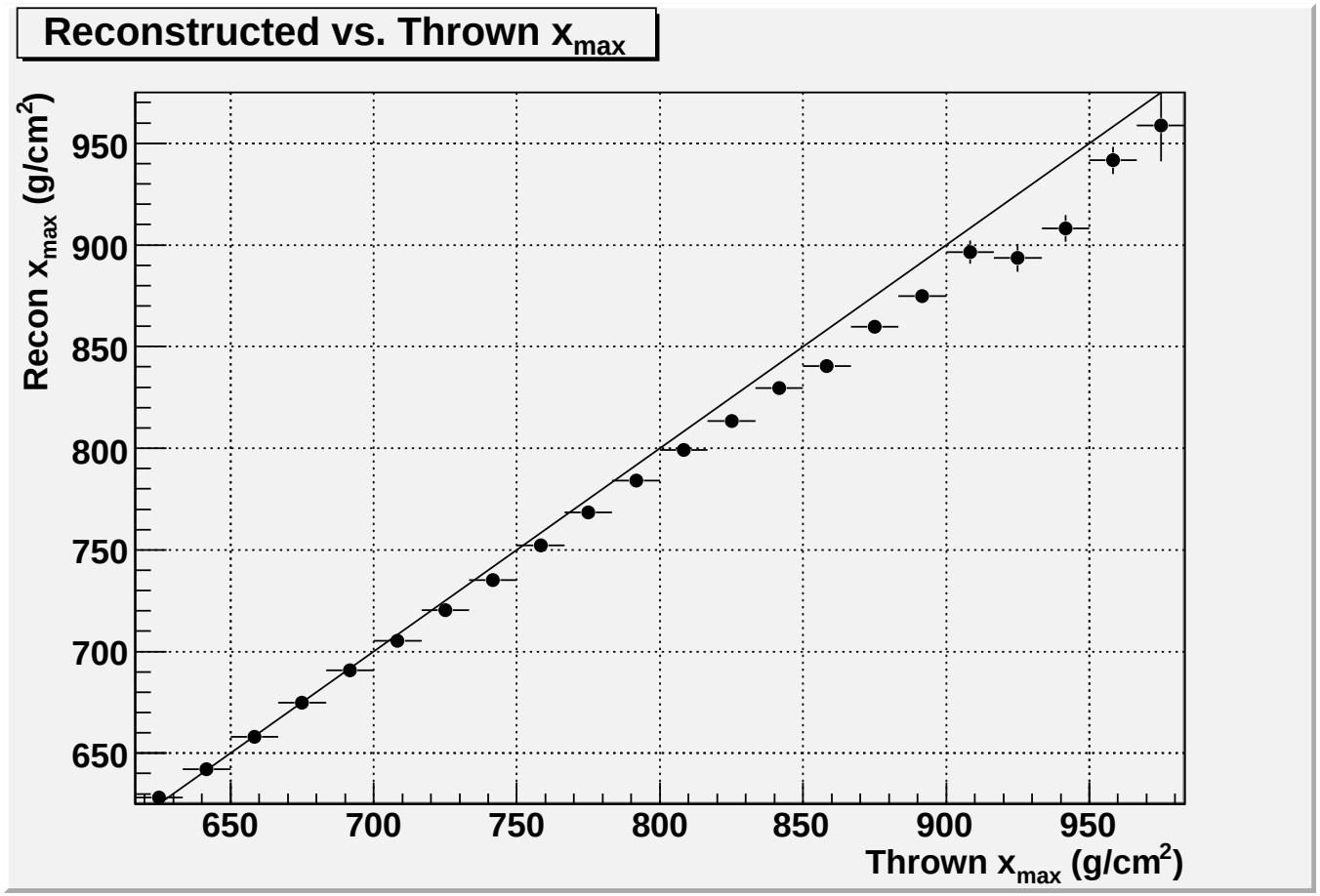

(c) $x_{\max}$

Figure 5.6. continued.

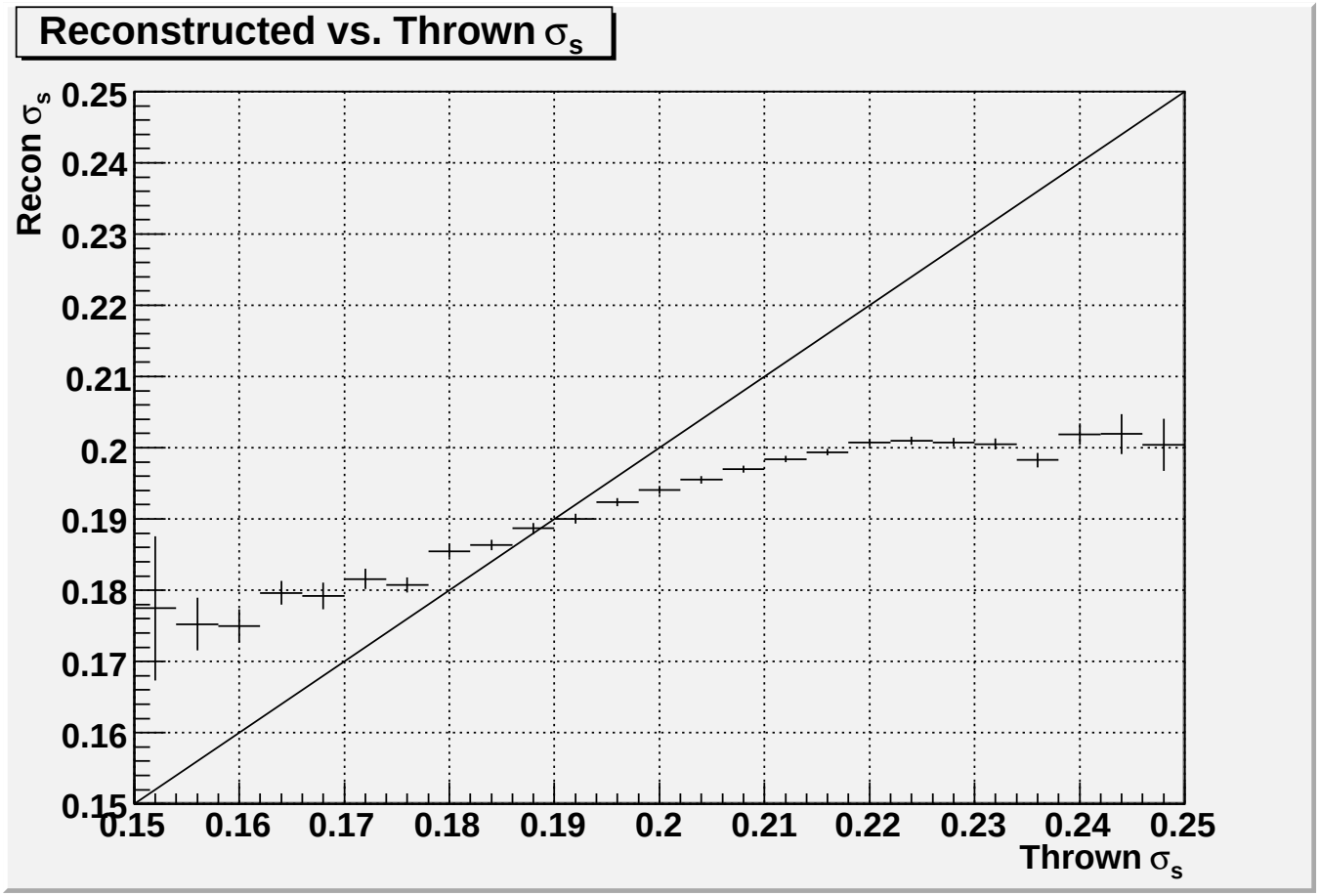

(d) σ_s

Figure 5.6. continued.

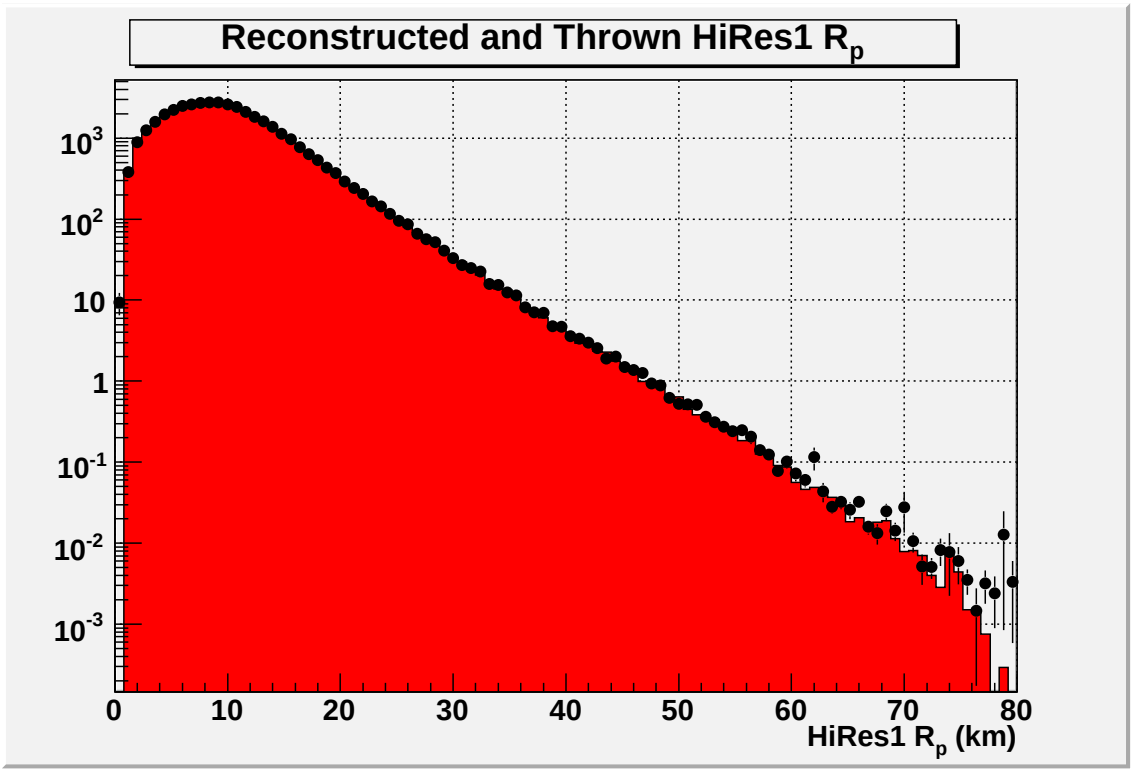

(a) Reconstructed and thrown HiRes1 $R_{\rm p}$

Figure 5.7. The HiRes1 $R_{\rm p}$ resolution.

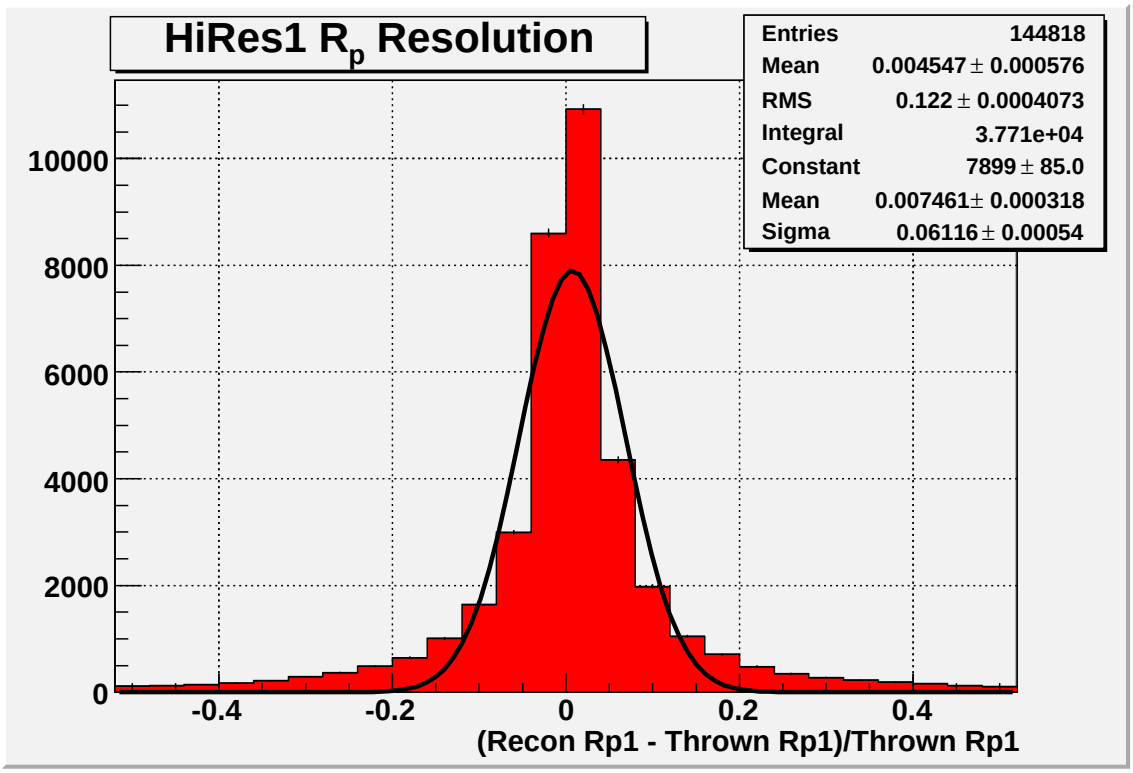

(b) HiRes1 $R_{\rm p}$ resolution (linear scale).

Figure 5.7. continued.

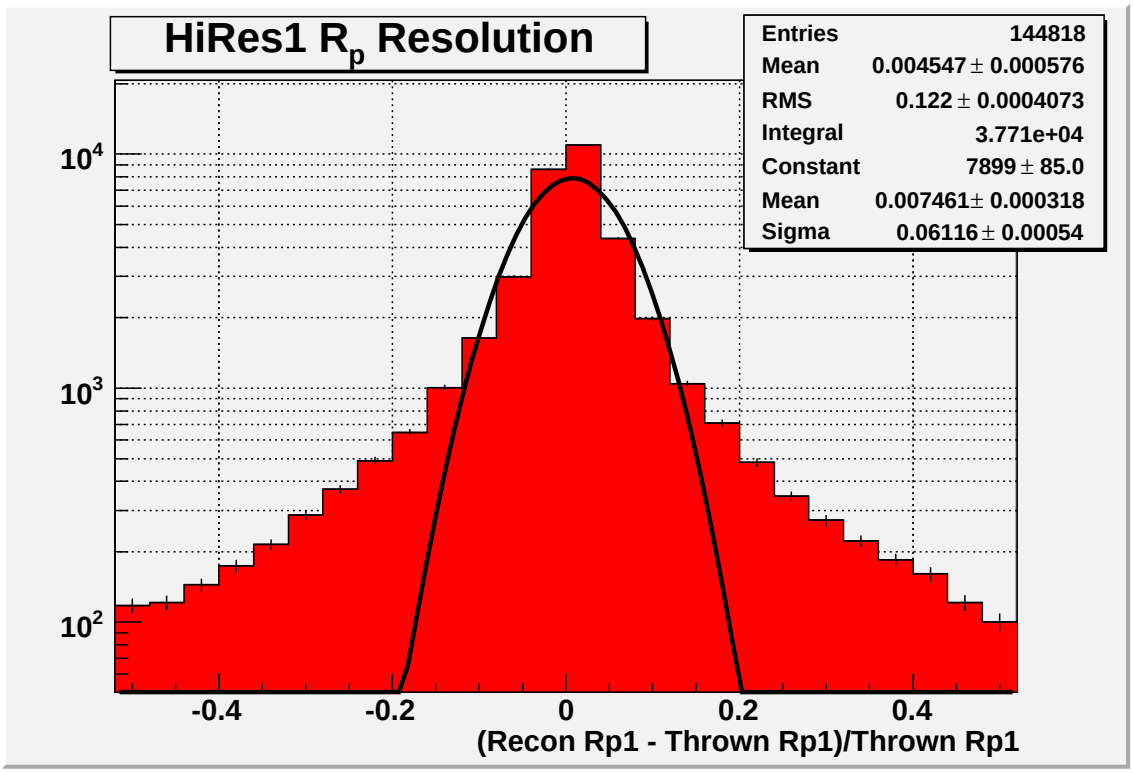

(c) HiRes1 $R_{\rm p}$ resolution (log scale).

Figure 5.7. continued.

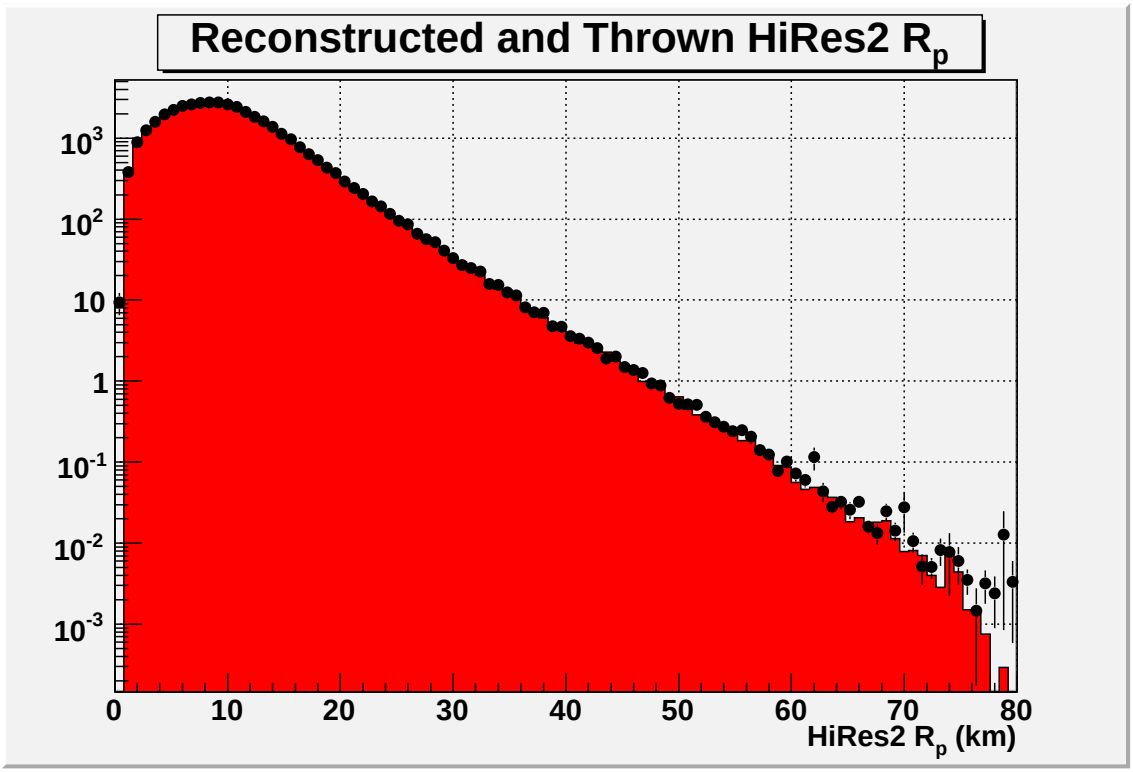

(a) Reconstructed and thrown HiRes2 $R_{\rm p}$.

Figure 5.8. The HiRes2 $R_{\rm p}$ resolution.

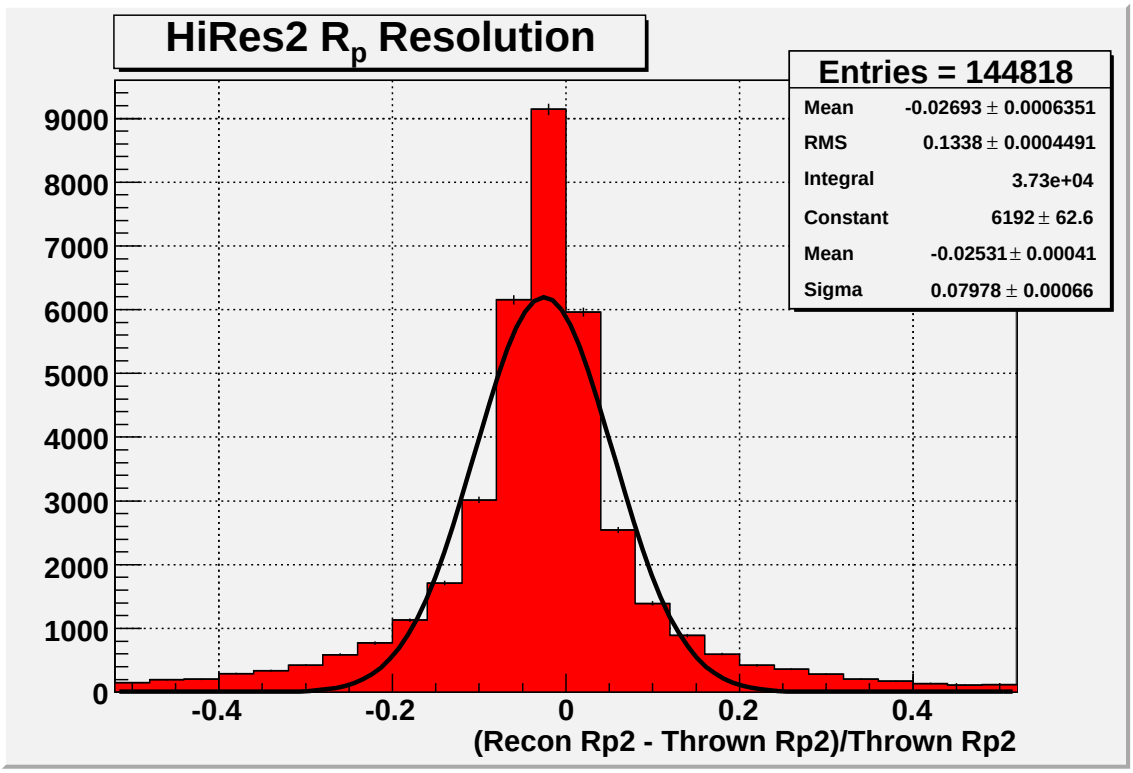

(b) HiRes2 $R_{\rm p}$ resolution (linear scale).

Figure 5.8. continued.

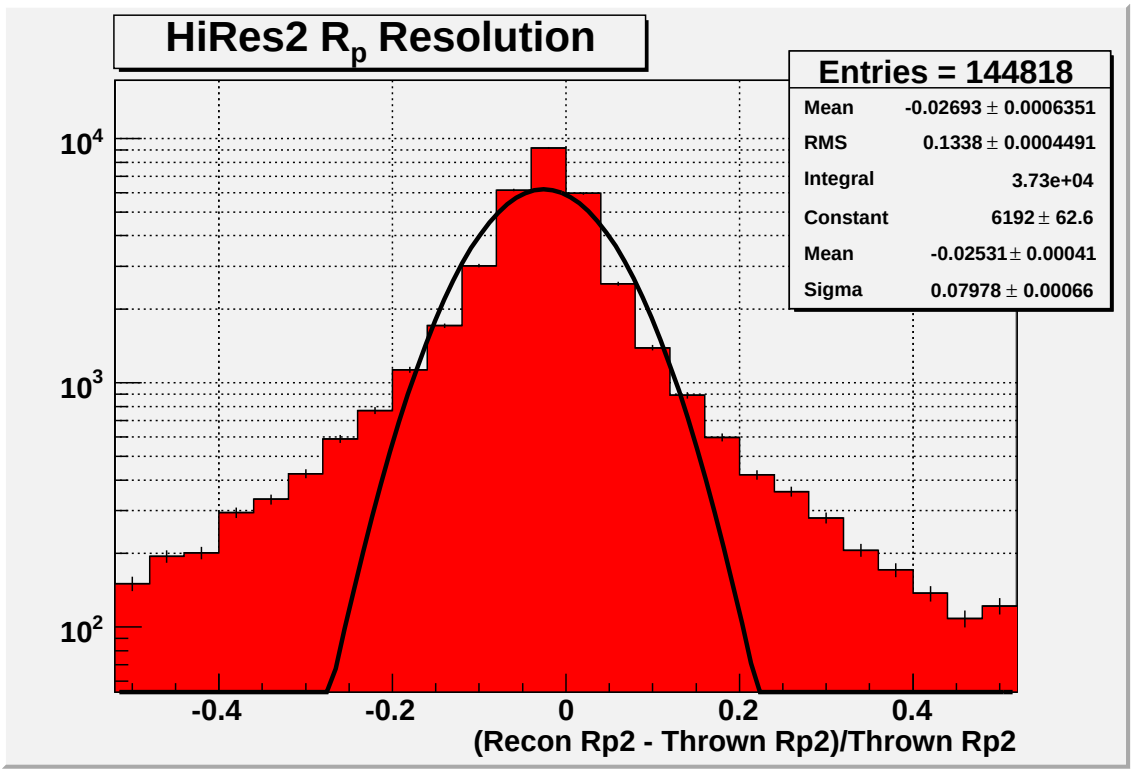

(c) HiRes2 $R_{\rm p}$ resolution (log scale).

Figure 5.8. continued.

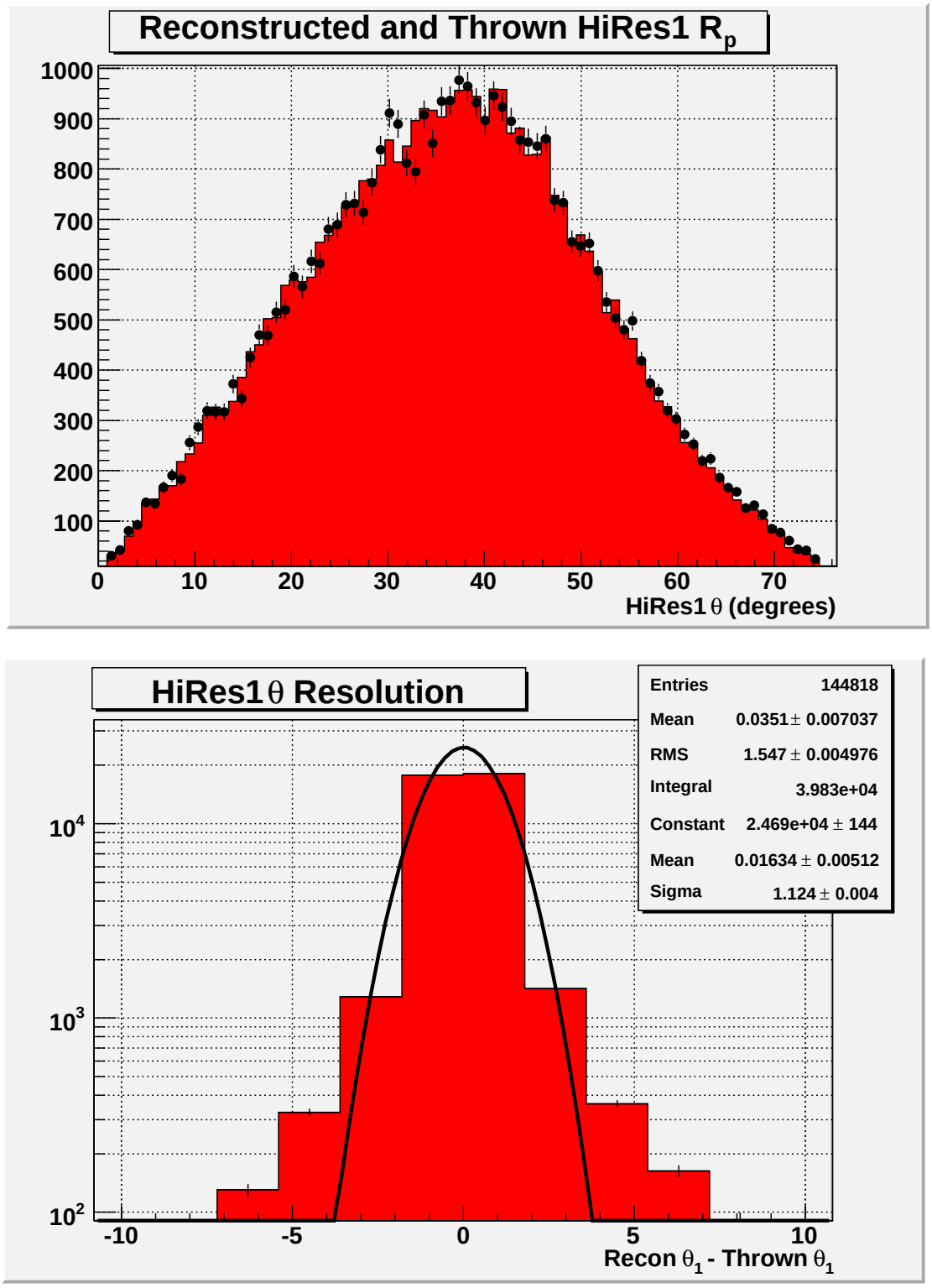

Figure 5.9. The HiRes1 θ angle resolution.

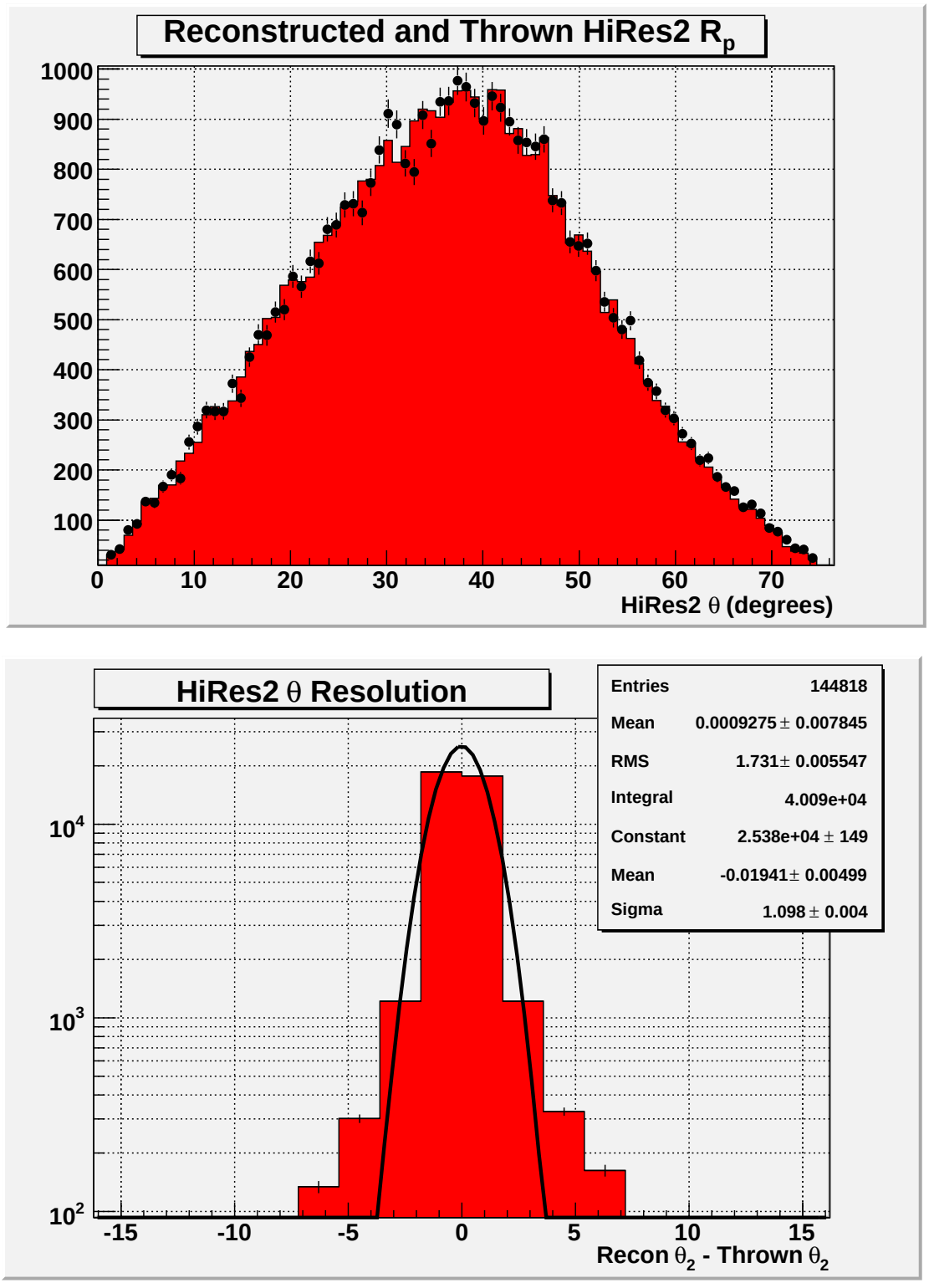

Figure 5.10. The HiRes2 θ angle resolution.

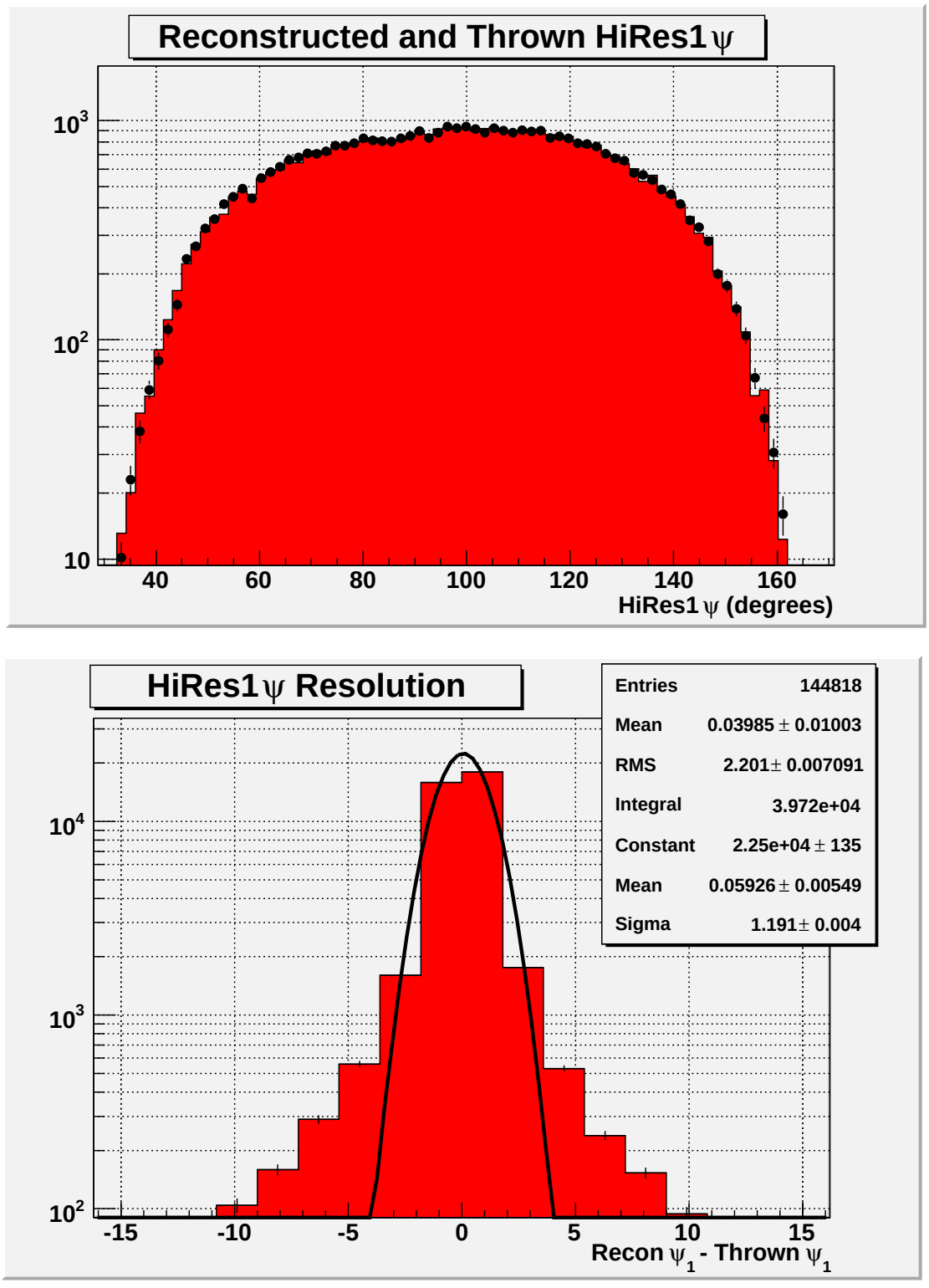

Figure 5.11. The HiRes1 ψ angle resolution.

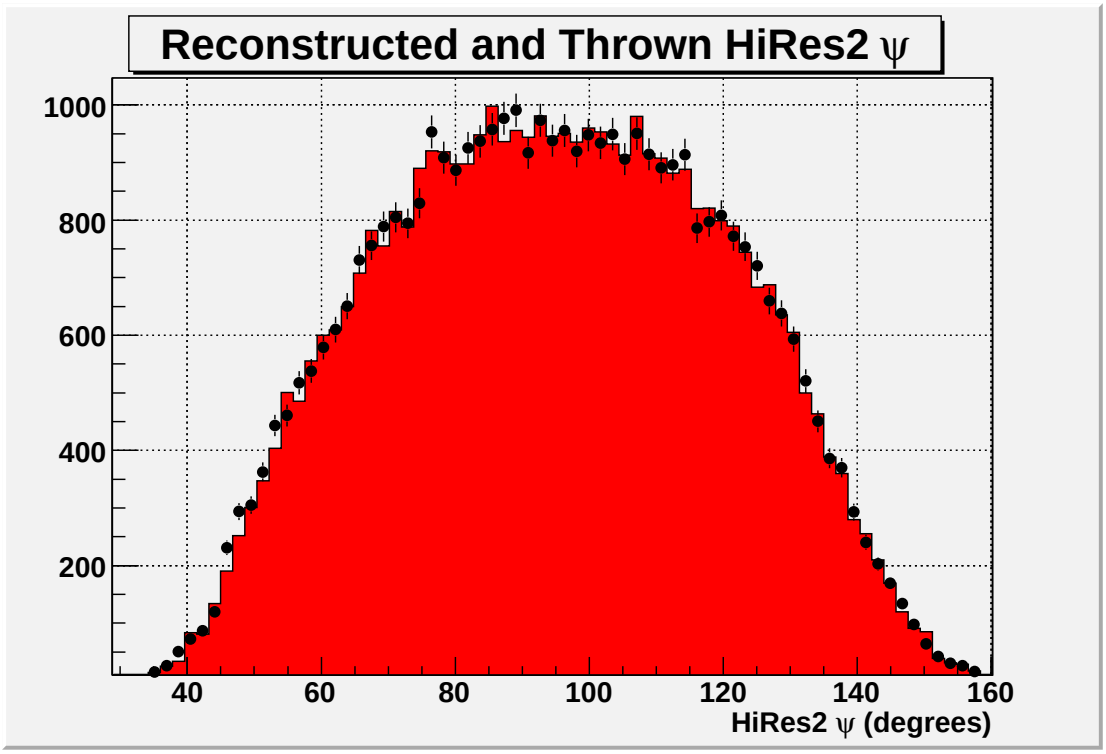

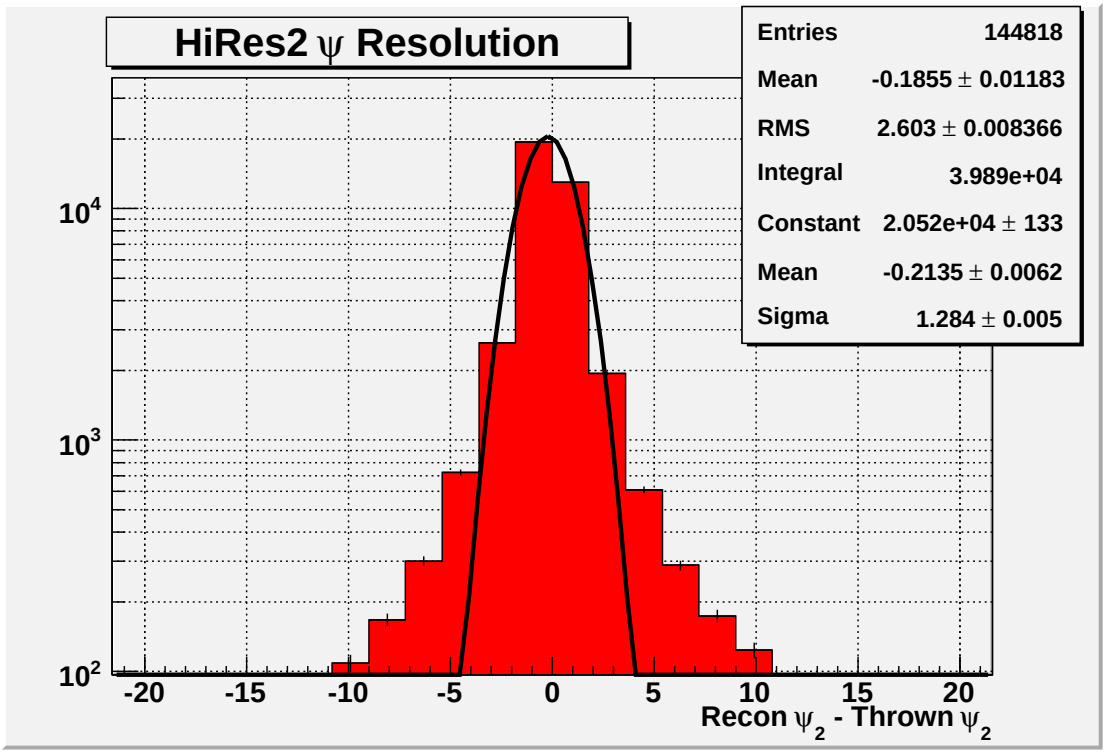

Figure 5.12. The HiRes2 ψ angle resolution.

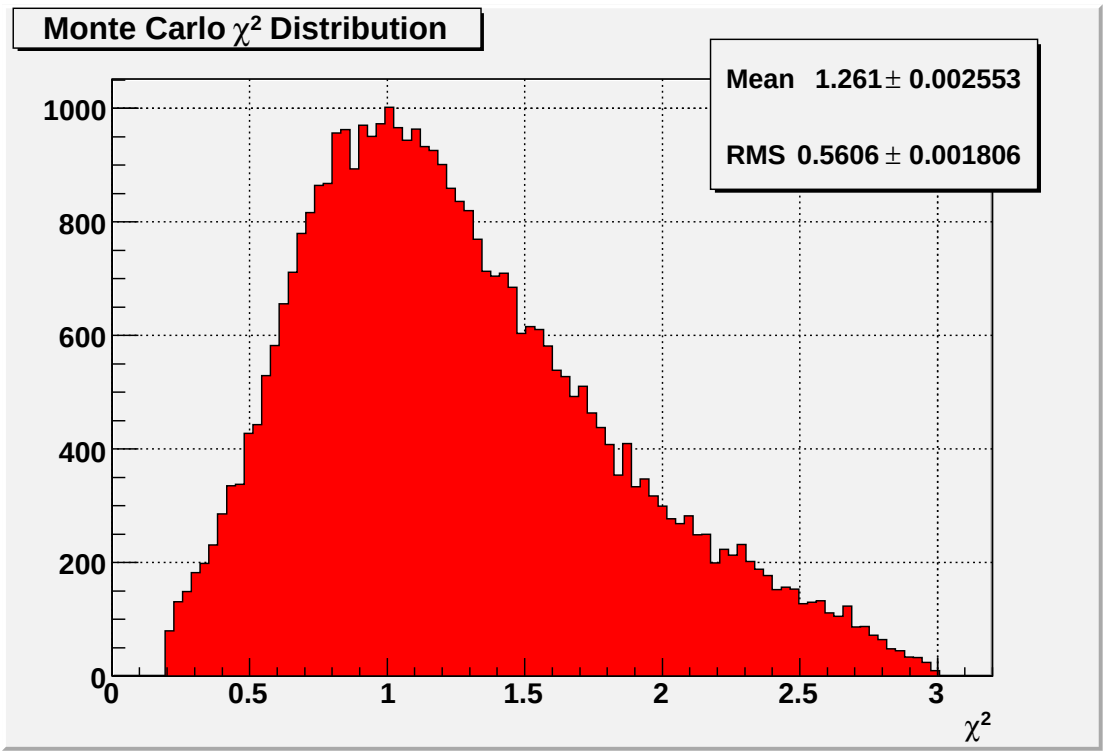

Figure 5.13. The χ^2 distribution of the Monte Carlo events.

5.3 Data/Monte Carlo Comparison

Comparison of the distribution of data to Monte Carlo is also important to ensuring that the detector is well understood. This is done by reconstructing both data and Monte Carlo using the same analysis routines and plotting them together. If the plots disagree then the Monte Carlo does not accurately simulate the detector and must be corrected. Accurate data/Monte Carlo comparison results also provide validation of the aperture calculation. Since the aperture can not be known *a priori* we rely heavily on an accurate simulation of the detector through the Monte Carlo. Data/Monte Carlo comparison is the test to determine how well the Monte Carlo simulates the conditions under which the detector operates, and therefore tells us that the aperture calculation is indeed the true aperture of the detector. Details of the aperture calculation are discussed in section 5.4.1. Figures 5.14 through 5.21 show the comparison between data and Monte Carlo for some of the important observables.

Figure 5.14 shows the comparison between the energy distribution of all reconstructed Monte Carlo events and the data. The ratio plot is not expected to be flat in this case since the Monte Carlo spectrum is a single index falling spectrum ($\propto E^{-3}$ upon reweighting above $10^{18.5}$ eV). The ratio plot shows similar features to the spectrum as discussed in section 5.4.2. Because $N_{\rm max}$ is proportional to the primary particle energy, the $N_{\rm max}$ data/Monte Carlo comparison shown in Figure 5.15 also shows similar features as the energy data/Monte Carlo comparison.

In Figure 5.16 the 12 g/cm^2 can be seen in the small shift between data and Monte Carlo $x_{\rm max}$. At very large $x_{\rm max}$, there are very few events. At the highest of energies the highest penetrating showers may actually have $x_{\rm max}$ in the ground. The high end of the $x_{\rm max}$ distribution may also contain these types of events, which are not well bracketed.

Data and Monte Carlo agree well for $\sigma_{\rm s}$ reconstruction. The profile constraint for failed shower fits (see section 5.2) is handled the same for both data and Monte Carlo in the reconstruction as evidenced by the peak in Figure 5.17. So even for cases of poor resolution in $\sigma_{\rm s}$, the stereo reconstruction is agreeing for both real

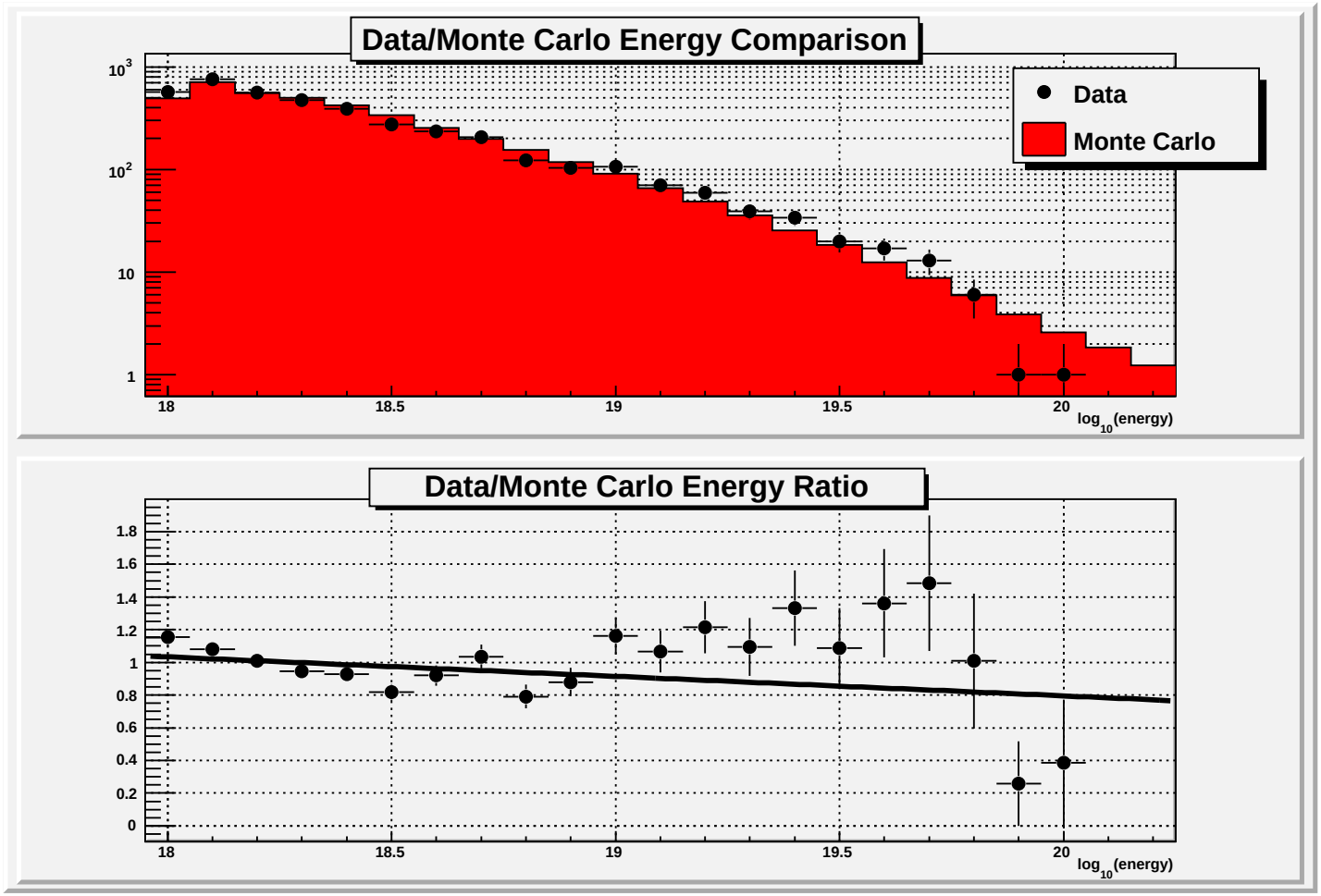

Figure 5.14. Data/Monte Carlo comparison of energy.

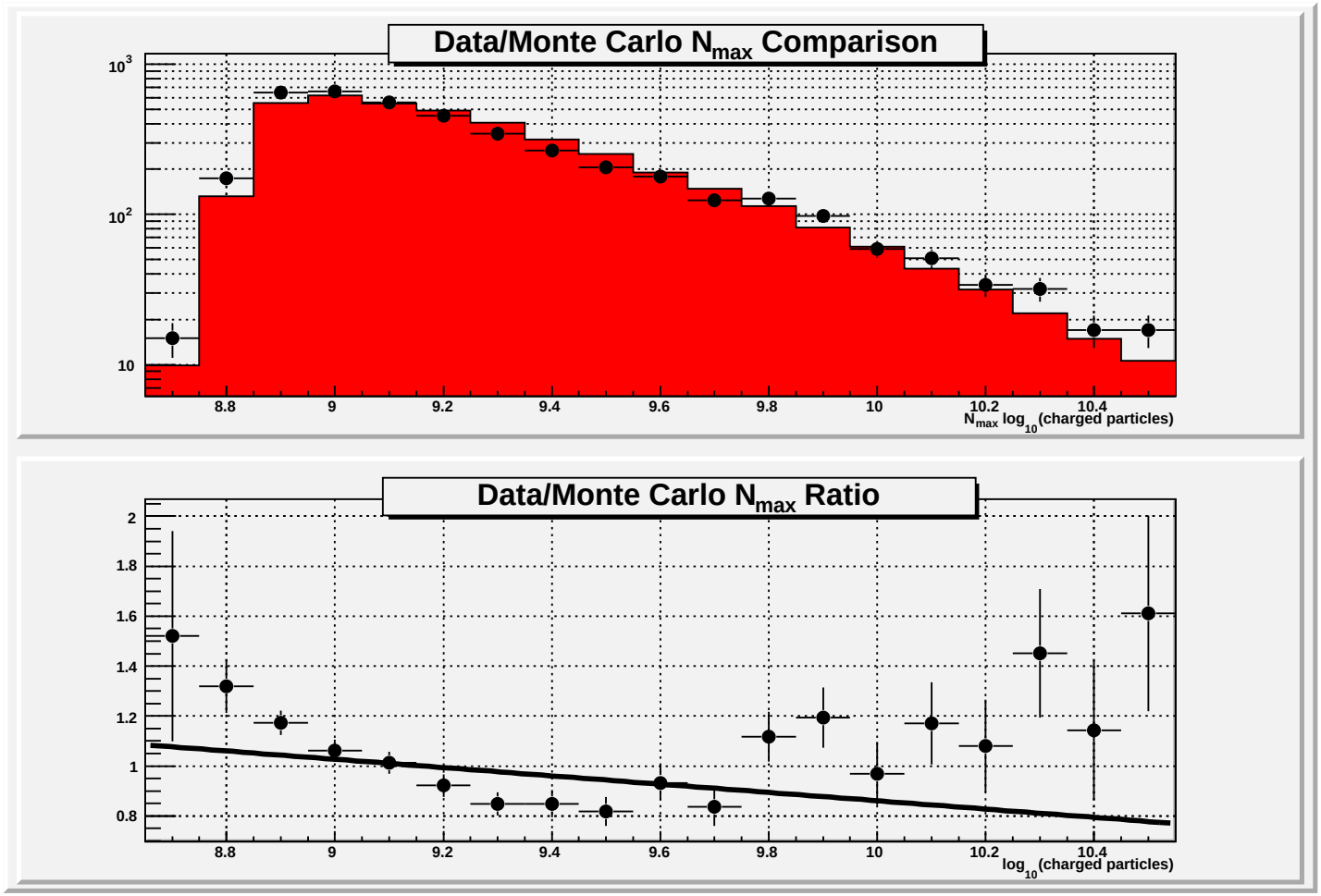

Figure 5.15. Data/Monte Carlo comparison of $N_{\max}$.

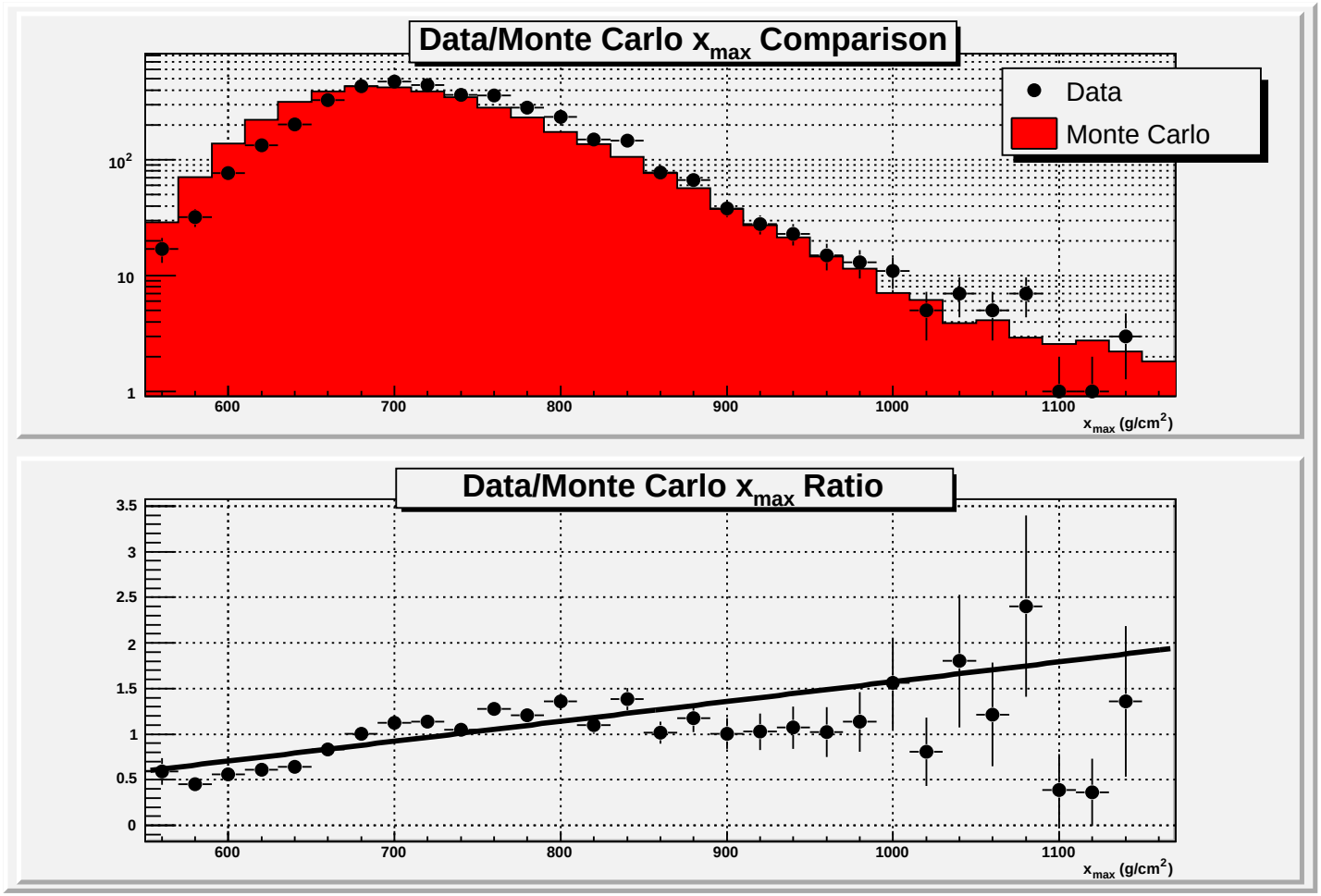

Figure 5.16. Data/Monte Carlo comparison of $x_{\max}$.

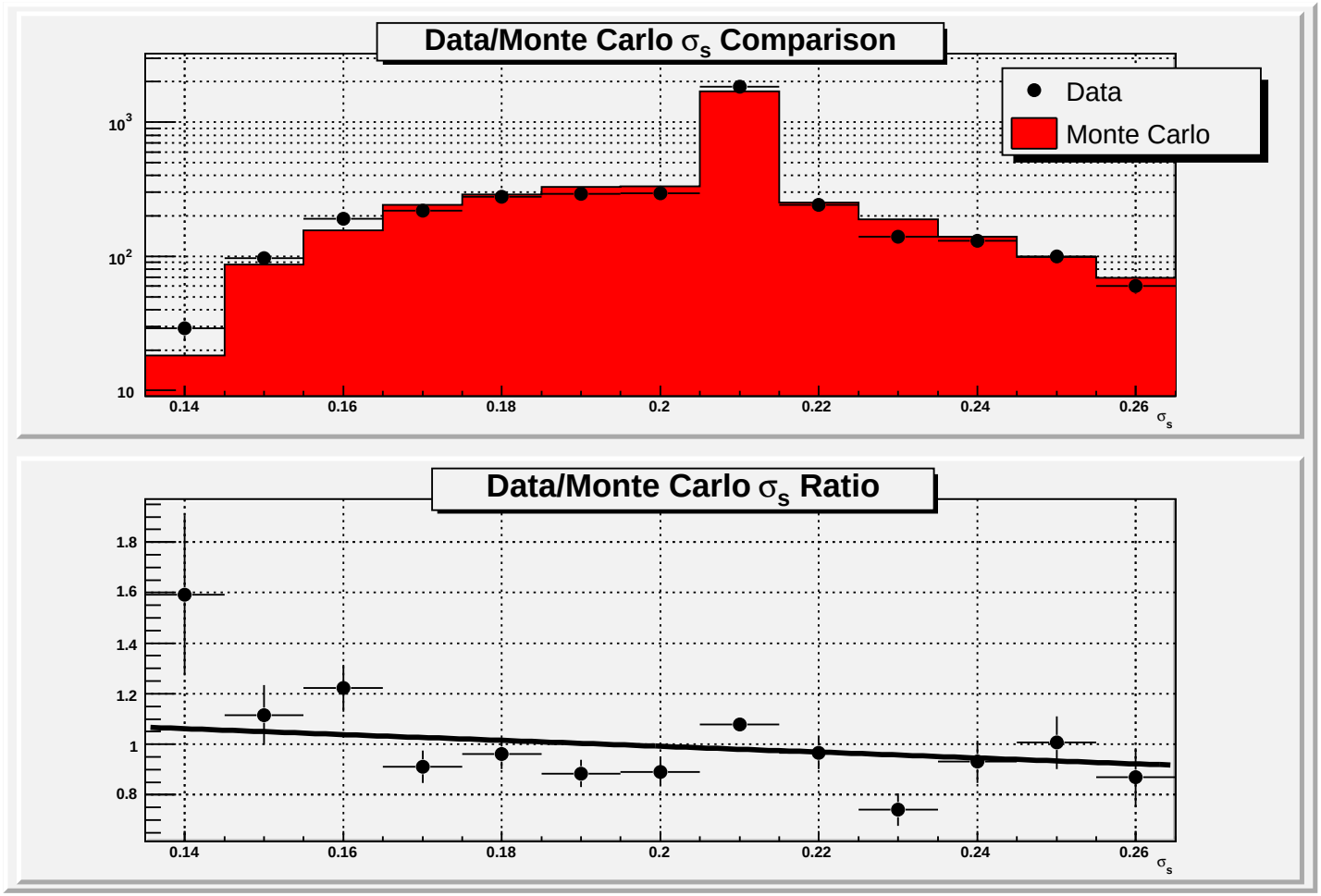

Figure 5.17. Data/Monte Carlo comparison of σ_s. The profile constraint peak is seen here. The effect of this constraint is consistent between data and Monte Carlo.

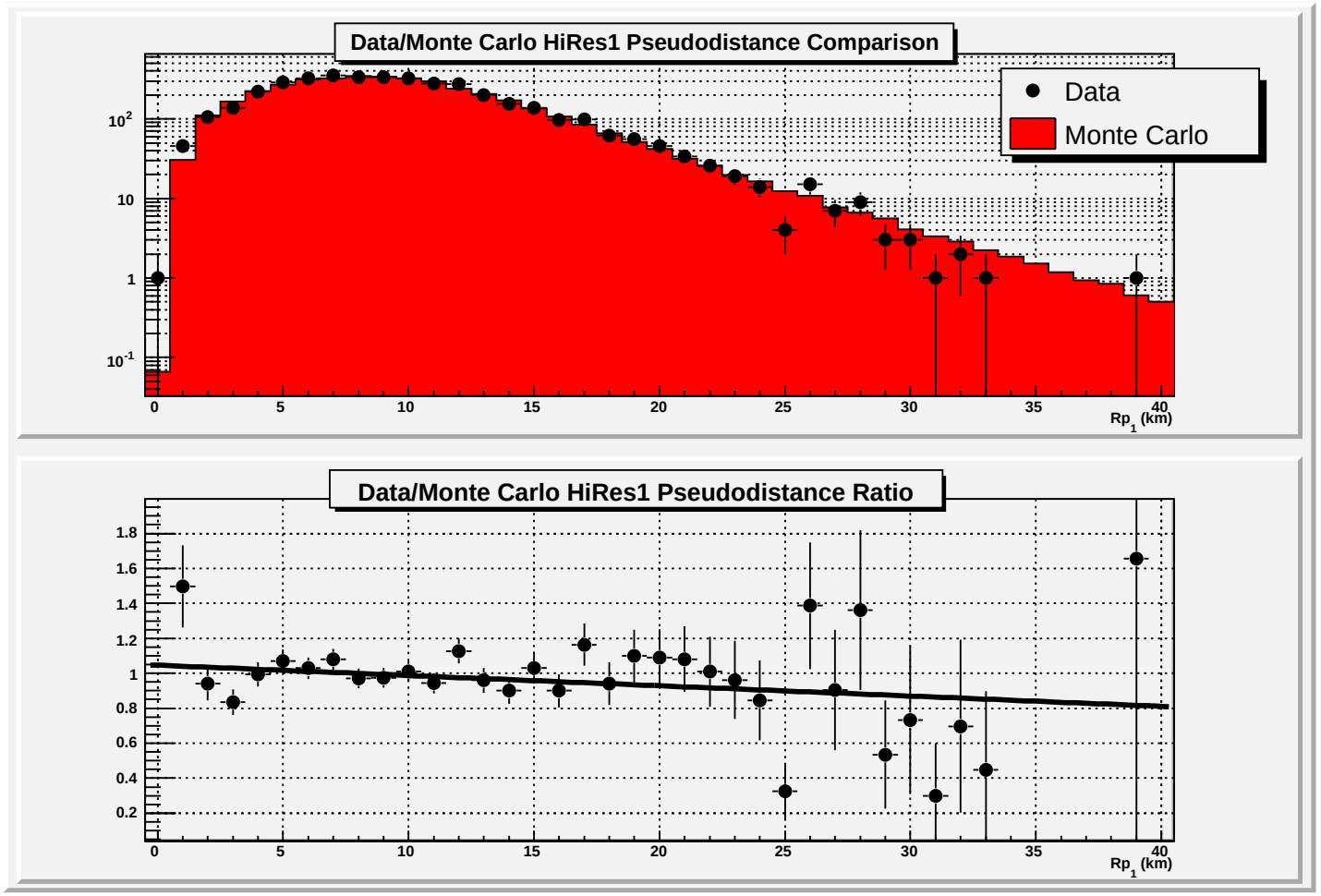

(a) HiRes1

Figure 5.18. Data/Monte Carlo comparison of HiRes1 and HiRes2 pseudodistance.

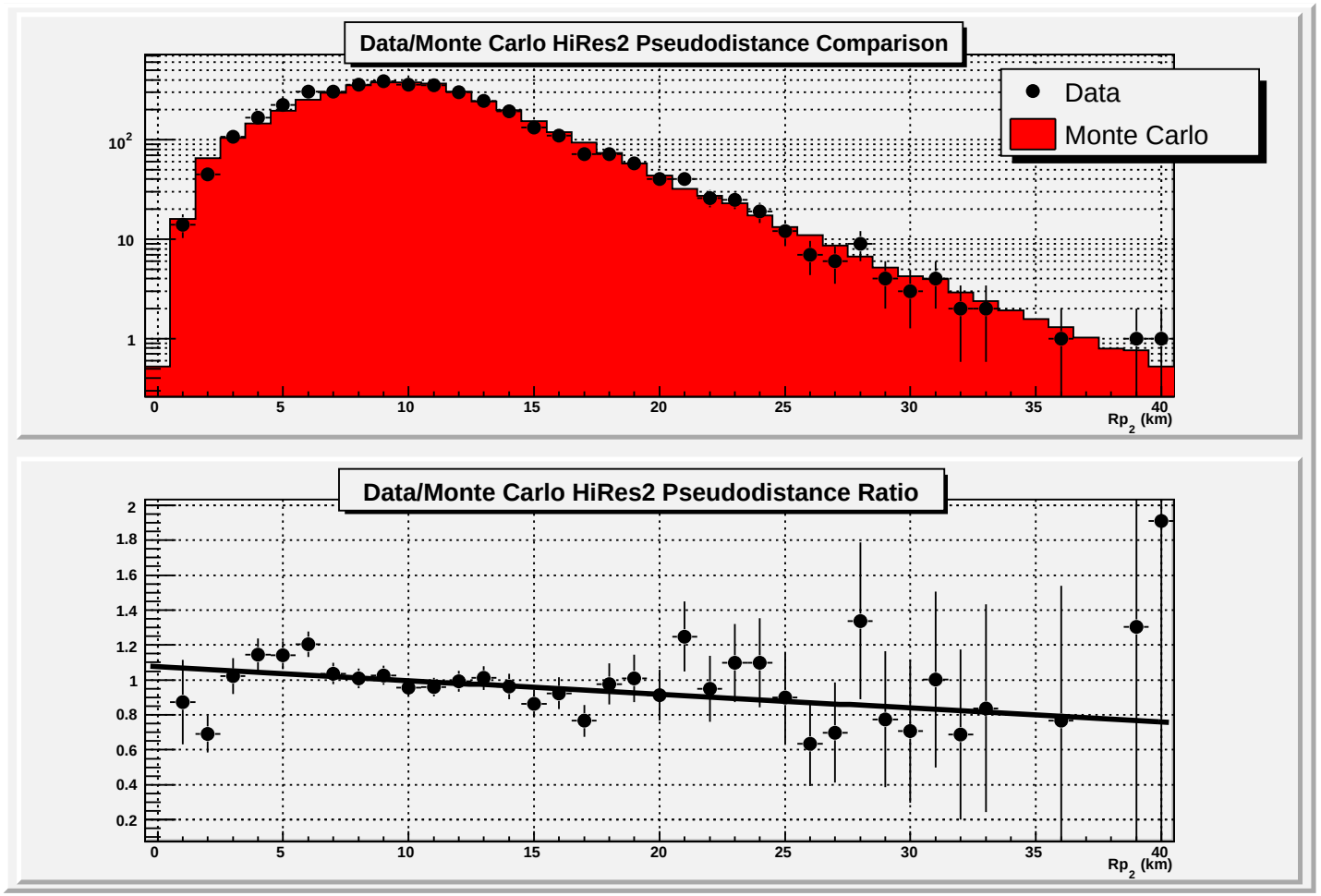

(b) HiRes2

Figure 5.18. continued.

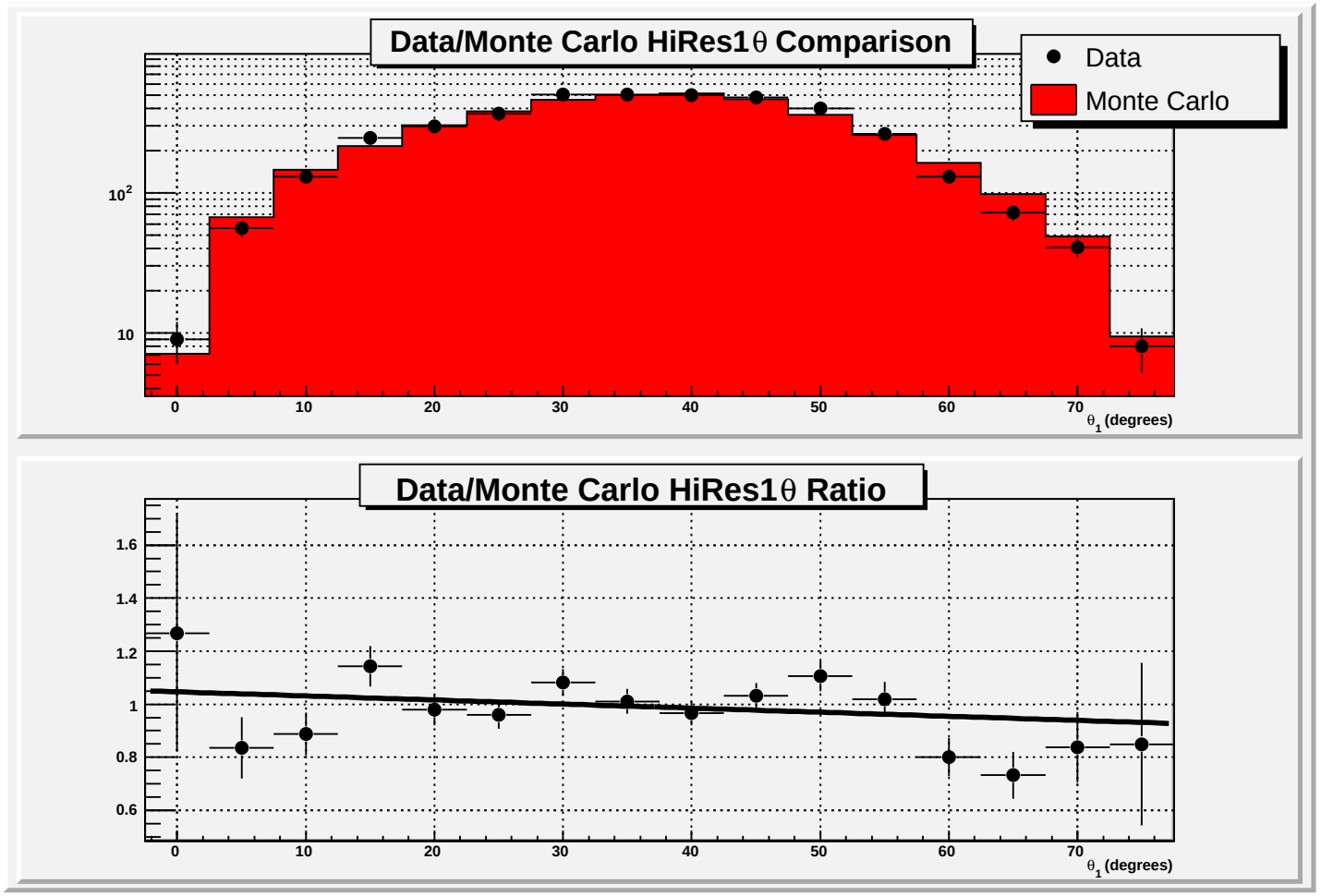

(a) HiRes1

Figure 5.19. Data/Monte Carlo comparison of HiRes1 and HiRes2 shower zenith angle.

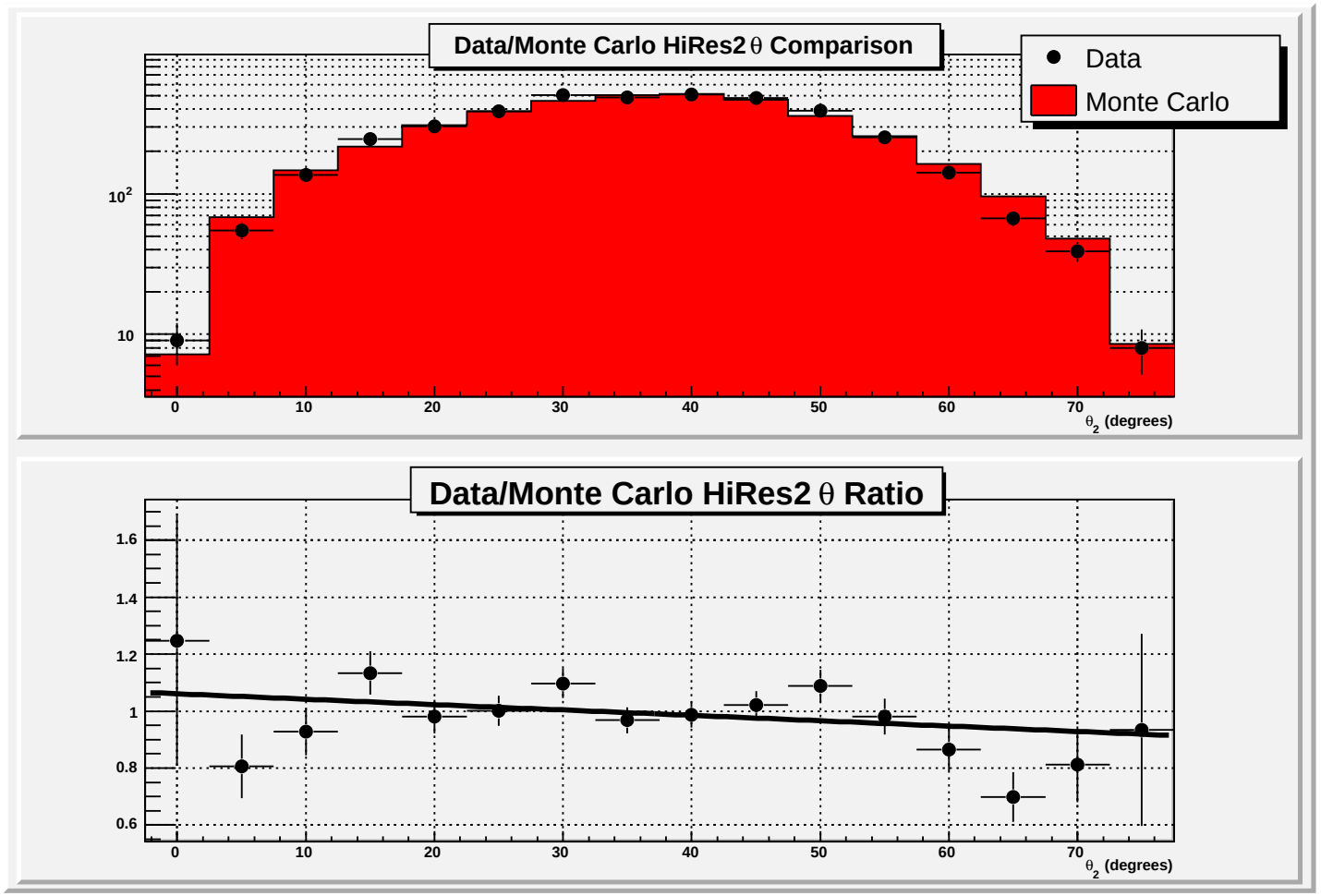

(b) HiRes2

Figure 5.19. continued.

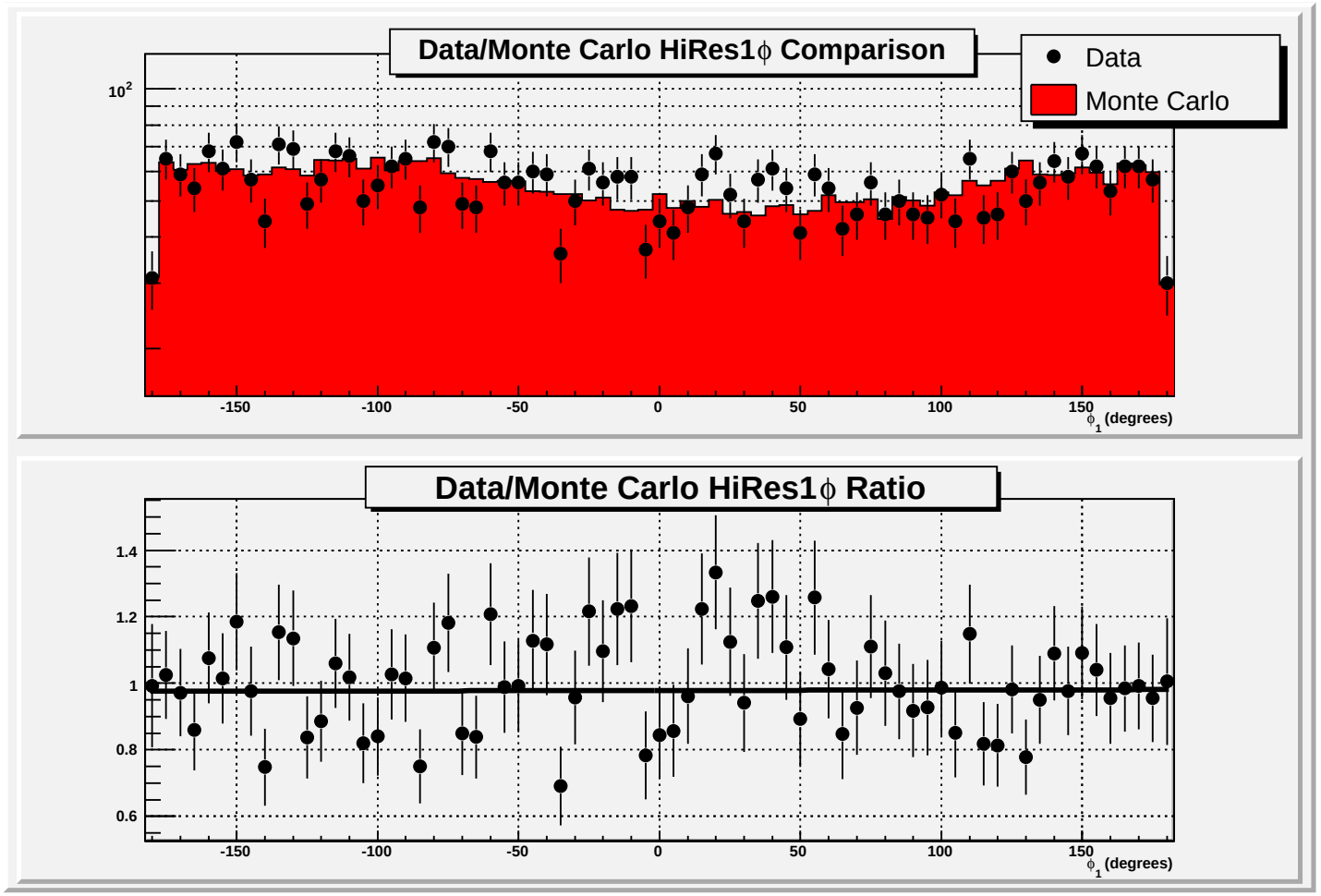

(a) HiRes1

Figure 5.20. Data/Monte Carlo comparison of HiRes1 and HiRes2 shower azimuth angle.

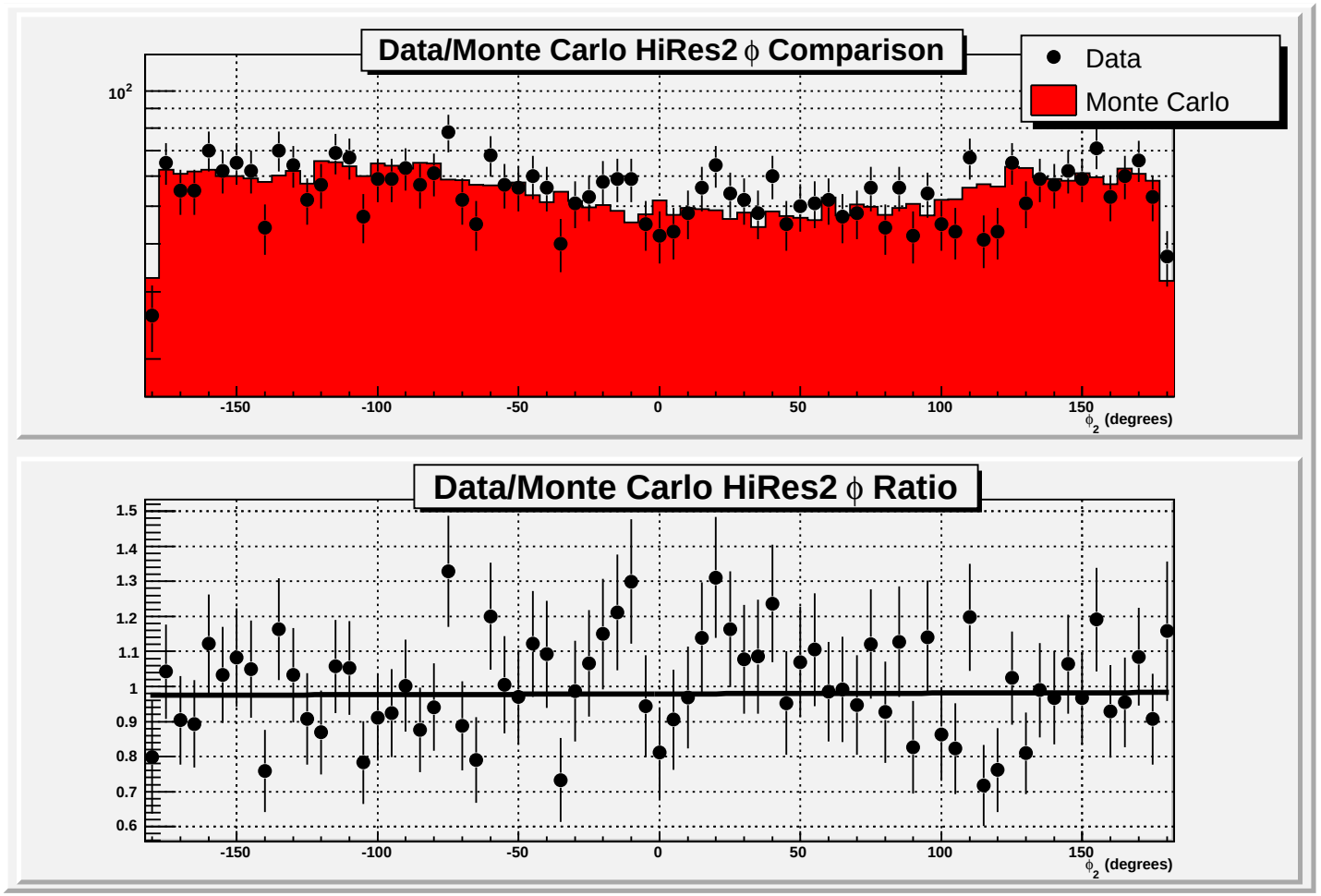

(b) HiRes2

Figure 5.20. continued.

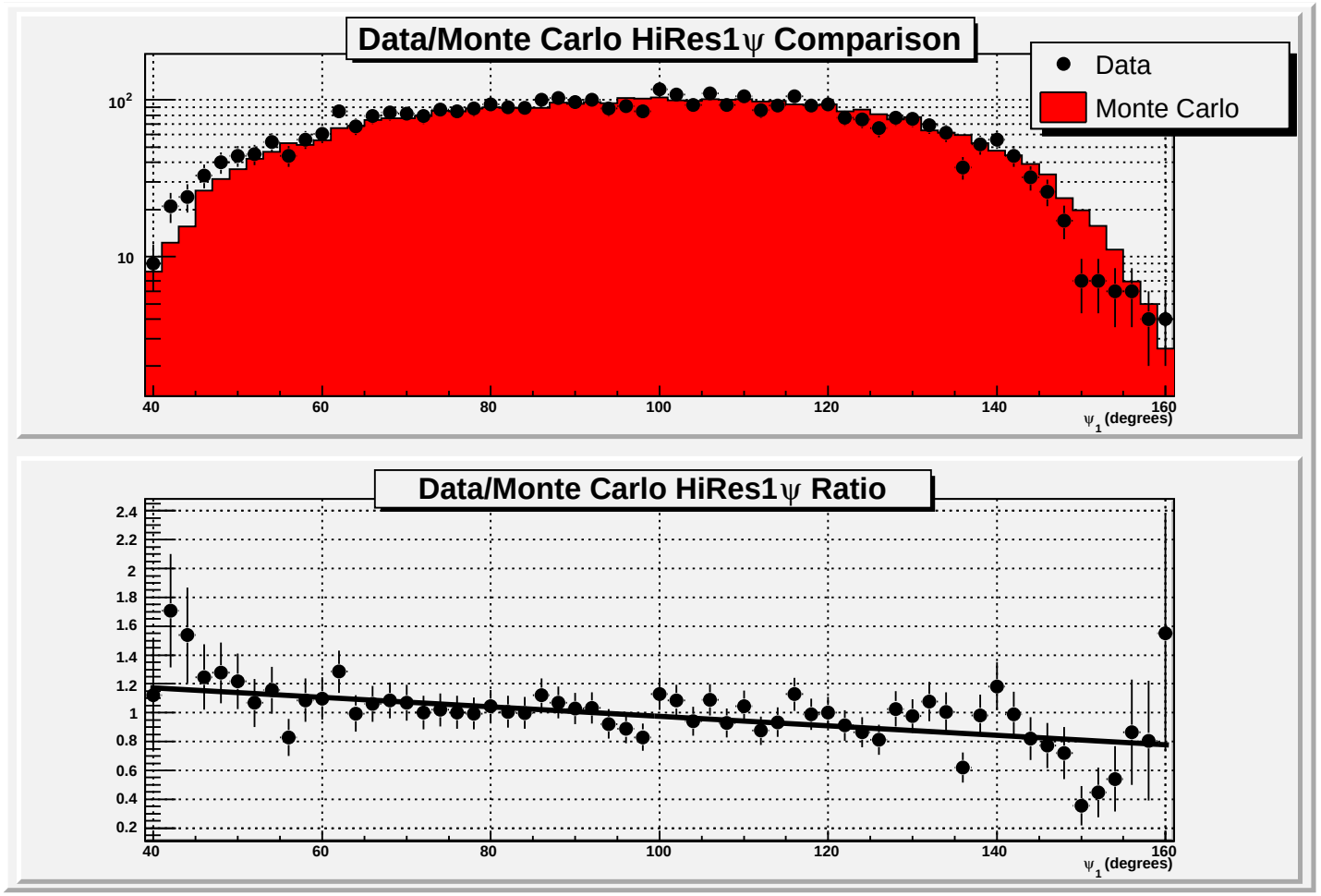

(a) HiRes1

Figure 5.21. Data/Monte Carlo comparison of HiRes1 and HiRes2 shower plane angle.

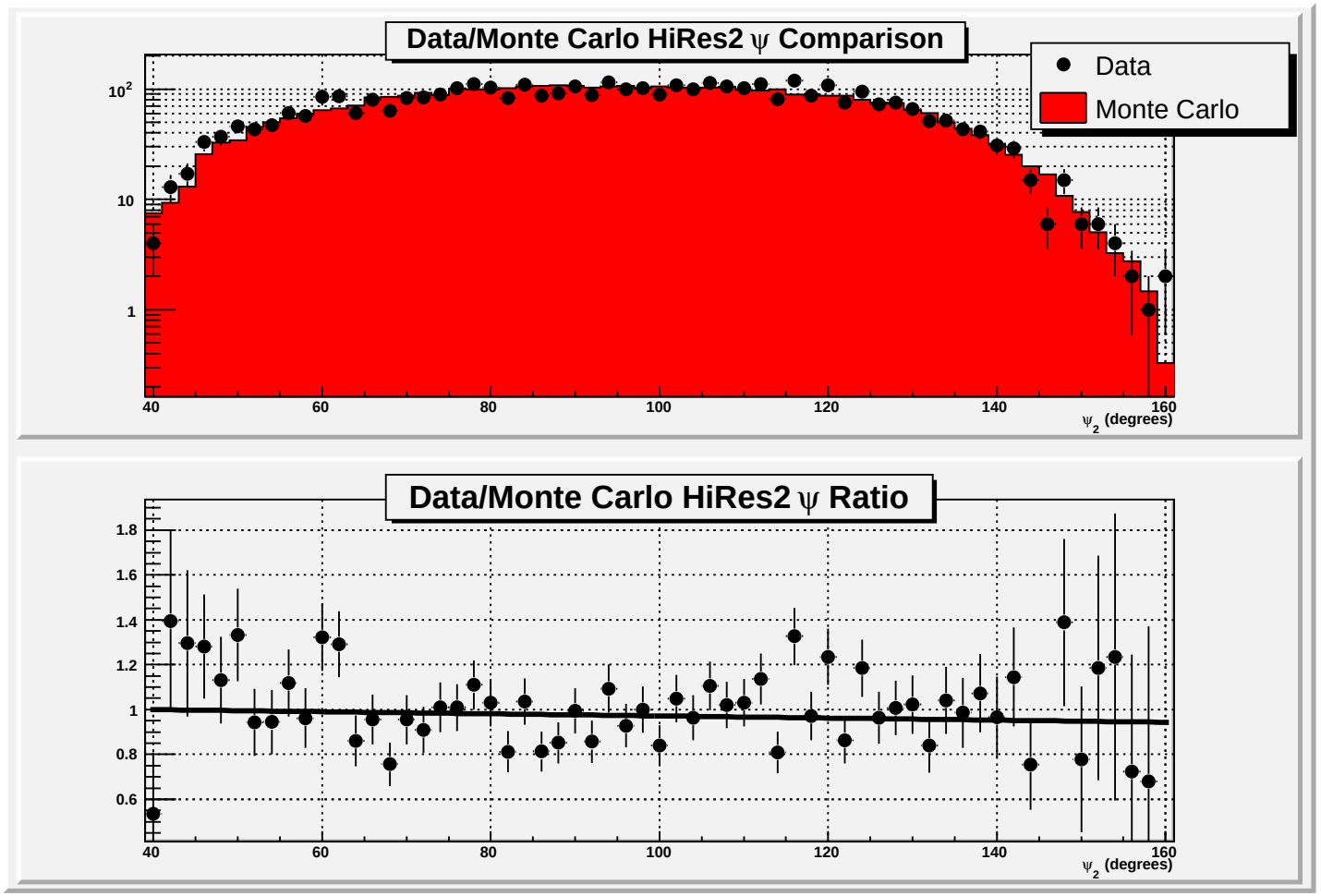

(b) HiRes2

Figure 5.21. continued.

and simulated data.

5.4 Spectrum

The differential energy flux is expressed as

$$J(E) = \frac{dN/dE}{A\Omega(E)\Delta t} \tag{5.2}$$

where dN is the number of cosmic ray primaries measured in the energy range dE, $A\Omega(E)$ is the energy dependent aperture, and Δt is the exposure time. The differential flux is therefore measured in units of length^{-2} time^{-1} solid angle^{-1} energy^{-1}. This flux measured over several different energies makes up the energy spectrum. In practice we bin our data into histograms to calculate the flux making equation 5.2 become

$$J(E) = \frac{\Delta N(E_i)/\Delta E_i}{\langle A\Omega(E_i)\rangle \Delta t} \tag{5.3}$$

where $\Delta N(E_i)$ is the number of events measured in energy bin E_i and $\langle A\Omega(E_i)\rangle$ is the aperture measured through Monte Carlo simulation.

Expression 5.3 for the flux can be derived by considering measuring the flux of particles over some surface S. Since particle number is a conserved quantity (or technically the primary cosmic ray in this case), the particle "current" flowing across a surface S can be calculated by the following relation

$$R \equiv \frac{dN}{dt} = \int_S \vec{\mathcal{J}}(E) \cdot d\vec{S} \tag{5.4}$$

where R is the rate at which particles cross surface S, $\vec{\mathcal{J}}(E)$ is the flux density measured in units of length^{-2} solid angle^{-1} time^{-1} and $d\vec{S}$ is the differential surface over which the flux is measured. If we assume that the flux density is isotropic and homogeneous we can pull $\mathcal{J}(E)$ out of the integral, and instead measure the angular and spatial dependence by using a simulation which measures the detector's efficiency by sampling in all directions and over some large area around the detector. We then have

$$R = \mathcal{J}(E) \int dA\, d\Omega\, \eta(E, r, \theta, \phi) \tag{5.5}$$

where we've introduced η which is the detector reconstruction efficiency. η is in general a function of energy, distance, and direction and is not known *a priori*.

Instead we calculate it using a Monte Carlo simulation of the detector by throwing cosmic ray primaries uniformly in all directions into the detector's field of view out to some very large distance. This allows us to find the average value of η in each energy bin. In this way we can express η as an explicit function of energy only and equation 5.5 becomes

$$R = \mathcal{J}(E)\langle\eta(E)\rangle A\Omega \tag{5.6}$$

$$= \mathcal{J}(E)\langle A\Omega(E)\rangle \tag{5.7}$$

where we have combined $\langle\eta(E)\rangle$ and $A\Omega$ in equation 5.6 into the average aperture as determined through simulation $\langle A\Omega(E)\rangle$ in equation 5.7. Since we are interested in the differential flux we can replace $\mathcal{J}(E)$ with $J(E)\,dE$ and since the rate of incoming cosmic ray primaries is assumed to be constant we replace R with $\Delta N/\Delta t$. We can then rewrite equation 5.7 as

$$\frac{\Delta N(E_i)}{\Delta t} = J(E_i)\Delta E_i\langle A\Omega(E_i)\rangle \tag{5.8}$$

where we now explicitly indicate that each quantity is measured in an energy bin E_i. Simple rearrangement gives us back equation 5.3. The factor of $\langle A\Omega(E)\rangle$ is called the instantaneous aperture, but it will be referred to as simply the aperture in this work. The product of $\langle A\Omega(E)\rangle\Delta t$ is called the detector exposure.

5.4.1 Aperture

The aperture is a measure of the detector's acceptance. It is dependent on energy of the cosmic ray primary, the distance from the detector and the direction it comes from. The energy dependence of the aperture is most problematic at low energies and care must be taken to not overextend the spectrum to regions where the aperture is not changing too rapidly with energy. Errors in the spectrum can be caused at low energy by this rapid change in spectrum due to reconstruction resolution. When events are moved into the wrong reconstructed energy bin the effect on the spectrum can be exacerbated by the rapid change in aperture between neighboring bins.

5.4.1.1 Aperture Theory

The aperture, denoted symbolically as $A\Omega$, is more accurately in our case written as shown in equation 5.3 as the average acceptance in an energy bin determined by Monte Carlo calculation. By throwing events uniformly over all directions and a very large area around the detector, we simulate an isotropic and homogeneous cosmic ray flux. We then determine the reconstruction efficiency in a given energy range over all directions and distances to calculate the aperture. Figure 5.22 shows how the aperture is determined using this method. The area $d\vec{A}$ over which the cosmic ray flux is measured is varied in all directions over all azimuthal (ϕ) and polar angles (θ) between 0 and $\pi/2$ (since we only look skyward).

The aperture in energy bin E_i is then expressed as

$$\langle A\Omega(E_i)\rangle = \int dA\, d\Omega\, \eta(E, r, \theta, \phi) \tag{5.9}$$

$$= \langle \eta(E_i)\rangle \left(\int_0^{2\pi} d\varphi \int_0^{\mathcal{R}_{\rm p}(E_i)} r dr\right)\left(\int_0^{2\pi} d\phi \int_0^{\pi/2} \sin(\theta) d\theta\right) \tag{5.10}$$

where φ is the azimuthal angle and r is the distance over the disk $d\vec{A}$ shown in Figure 5.22, and ϕ and θ are the directions over which $d\vec{A}$ is pointed. The integral over r is done out to $\mathcal{R}_{\rm p}(E_i)$ which is the maximum pseudodistance for energy E_i and is shown in Figure 4.25. Carrying out the integral in equation 5.10 we can write the aperture as

$$\langle A\Omega(E_i)\rangle = \langle \eta(E_i)\rangle 2\pi^2 \mathcal{R}_{\rm p}^2(E_i) \tag{5.11}$$

5.4.1.2 Aperture Calculation

The actual aperture calculation then is simply reduced to determining $\langle \eta(E_i)\rangle$. This is done by taking the ratio of all reconstructed events and thrown events or

$$\langle \eta(E_i)\rangle = \frac{N_{\rm recon}(E_i)}{N_{\rm thrown}(E_i)} \tag{5.12}$$

where $N_{\rm recon}(E_i)$ is the number of Monte Carlo events reconstructed in energy bin E_i and $N_{\rm thrown}(E_i)$ is the number of events thrown in the same energy bin. Note that the same cuts that are applied to the data analysis must also be applied to the reconstructed Monte Carlo events to get the proper aperture. Figure 5.23 shows the

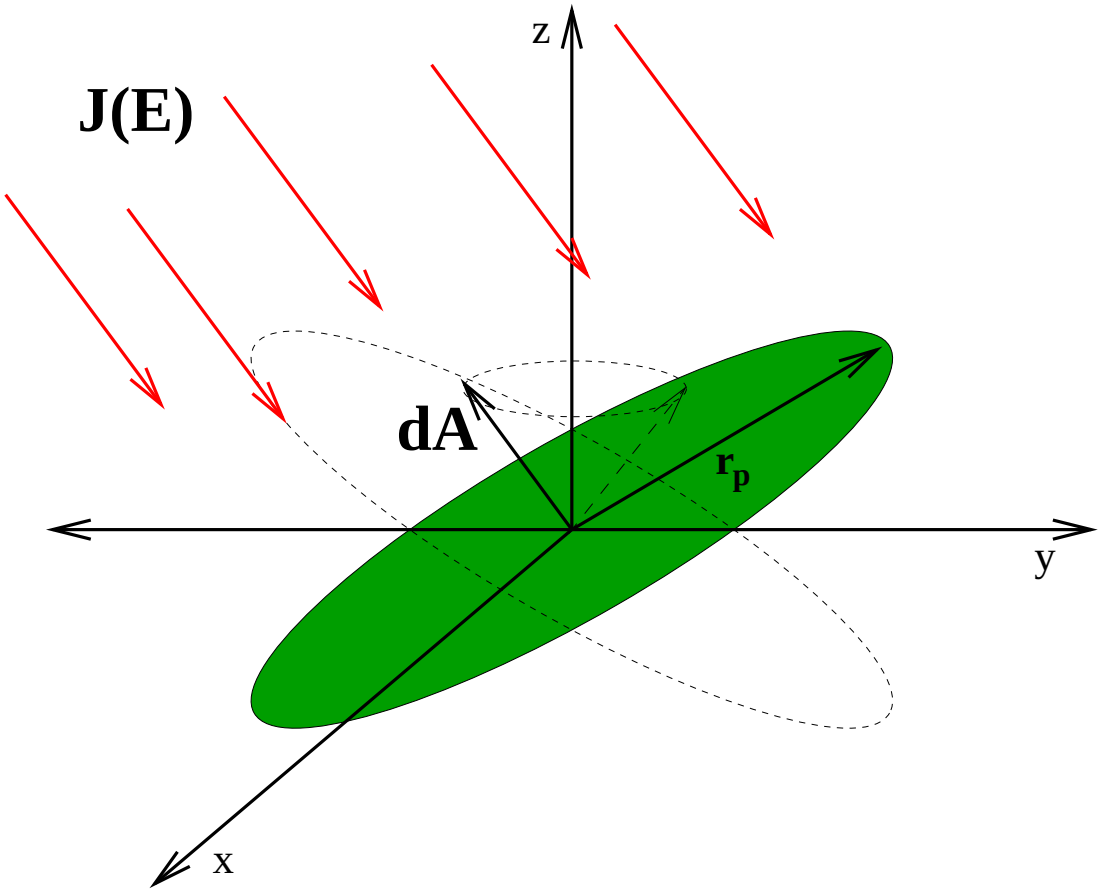

Figure 5.22. How the aperture is calculated for the HiRes detector. An isotropic and homogeneous flux is assumed and the efficiency of the detector in reconstructing events is measured over an area $d\vec{A}$. The efficiency is measured over all directions in 2π solid angle and over an area out to some maximum $R_{\rm p}$ which varies with energy.

Monte Carlo thrown and reconstructed events as well as the efficiency as calculated by equation 5.12. This aperture could also be referred to as the reconstruction aperture, since only events that are reconstructed and pass all cuts are included in $N_{\rm recon}$.

Another aperture, called the trigger aperture, can also be defined. Its calculated in a similar way to that shown in equation 5.12, except $N_{\rm recon}$ is replaced with the number of triggered events, $N_{\rm trig}$. This aperture is independent of cuts used in any analysis and shows the sensitivity of the detector to seeing events. The trigger efficiency is also shown in Figure 5.23.

Once the efficiency for each energy bin has been determined, the aperture is computed using equation 5.11. The result is shown in Figure 5.24.

Applying the ontime to the aperture calculation provides the detector exposure. Figure 4.66 shows the good weather stereo ontime used for the spectrum calculation. An additional correction is made for detector deadtime. Deadtime is time during which a mirror can not collect data because the mirror electronics are busy performing other tasks such as transferring event data to the DACQ. A malfunctioning mirror or artificial light sources may cause high trigger rates, therefore causing high deadtime, as the mirror attempts to process the data. Typically the deadtime for a mirror at HiRes1 is less than 1 % and about 4.5 % for HiRes2. Stereo deadtime is therefore dominated by the HiRes2 deadtime. The deadtime for a night is calculated by summing the total mirror deadtime seconds for all mirrors at a site and dividing by the total mirror seconds. For the exposure calculation, each night's ontime is reduced by the amount of deadtime that was accumulated. Figure 5.25 shows the distribution of stereo deadtime used for the exposure calculation.

The exposure is calculated by $\langle A\Omega(E)\rangle\Delta t$. Figure 5.26 shows the stereo exposure covering the period 1 December 1999 to 11 November 2005.

5.4.2 Spectrum Calculation

As equation 5.3 shows once the exposure is calculated one simply needs the energy distribution of events to compute the flux in each energy bin. Figure 5.27 shows the events distributed by energy bin used for the stereo spectrum. Because

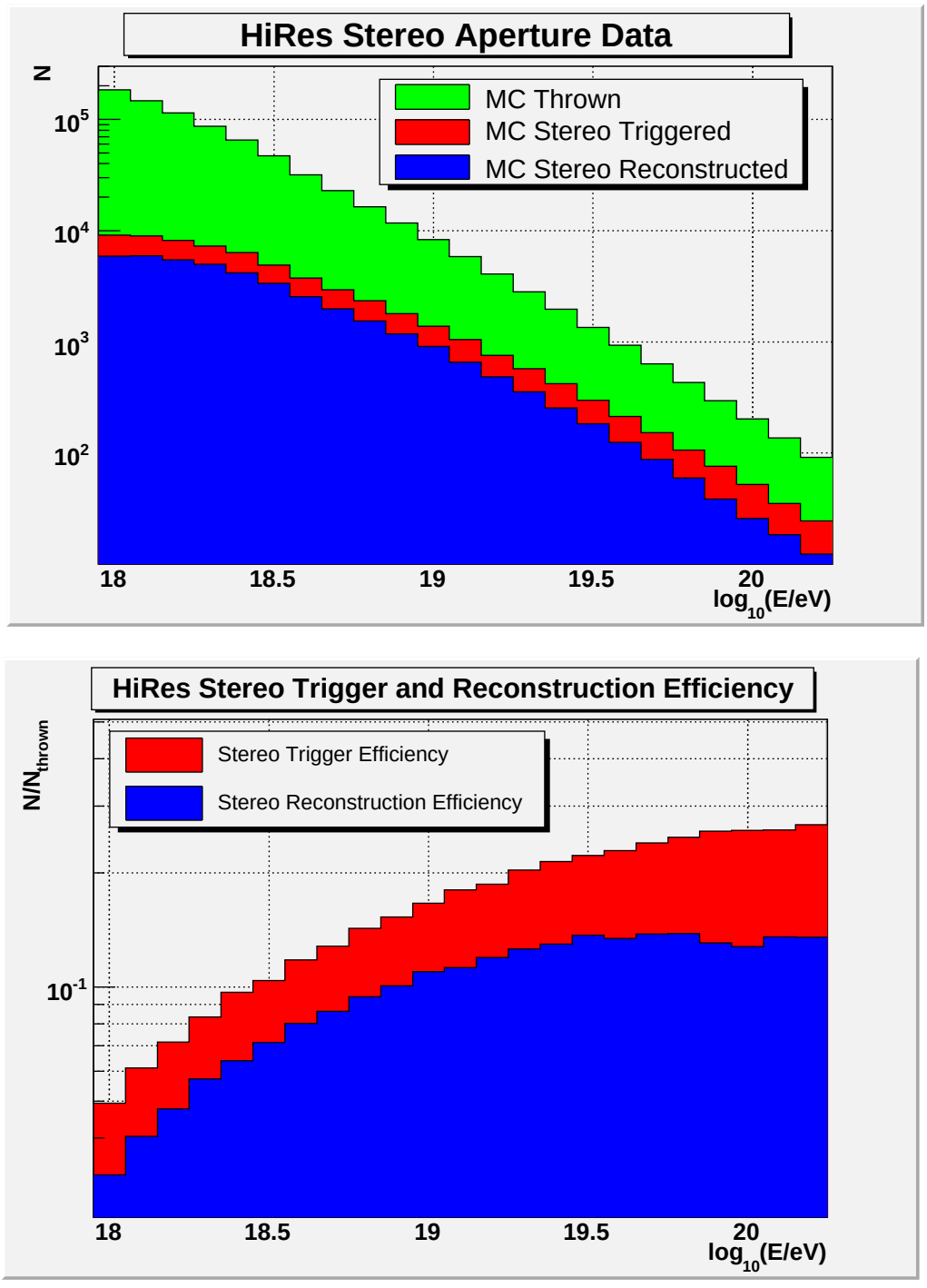

Figure 5.23. HiRes Monte Carlo thrown, triggered, and reconstructed event distributions. The efficiency is also shown. The fluctuations in reconstruction efficiency at the highest energies is statistical.

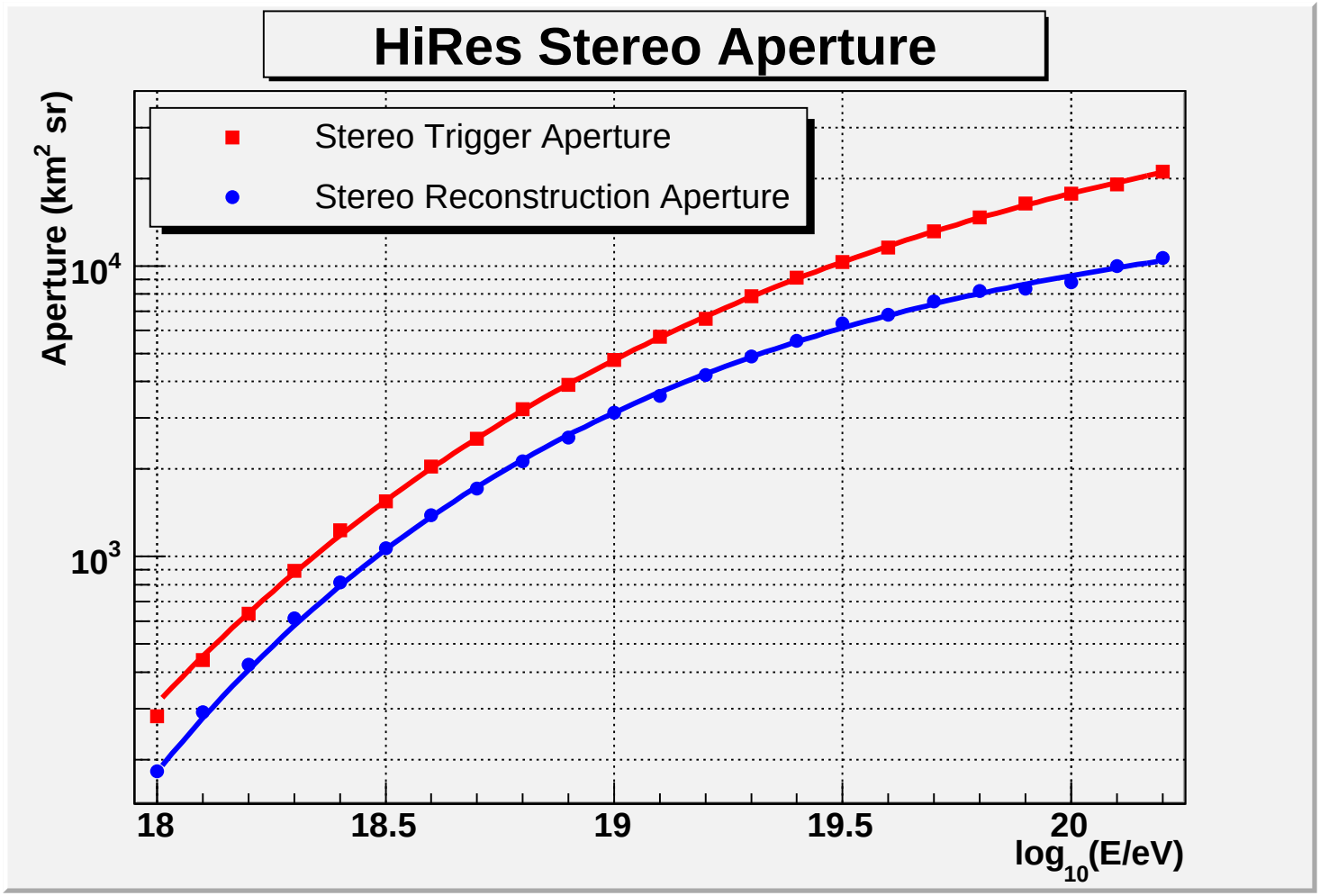

Figure 5.24. The HiRes stereo aperture. The trigger aperture and the reconstruction aperture are both shown.

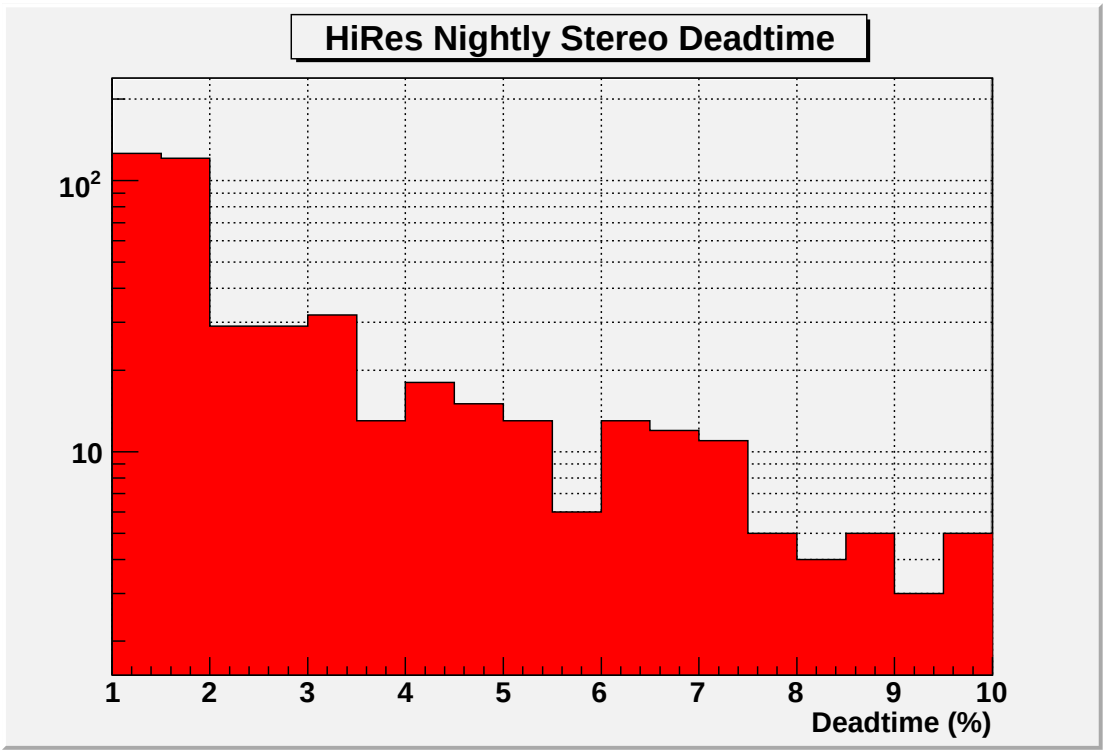

Figure 5.25. The distribution of deadtimes used in the exposure calculation. The avereage stereo deadtime is 4.5 %. The HiRes2 deadtime dominates the deadtime calculation.

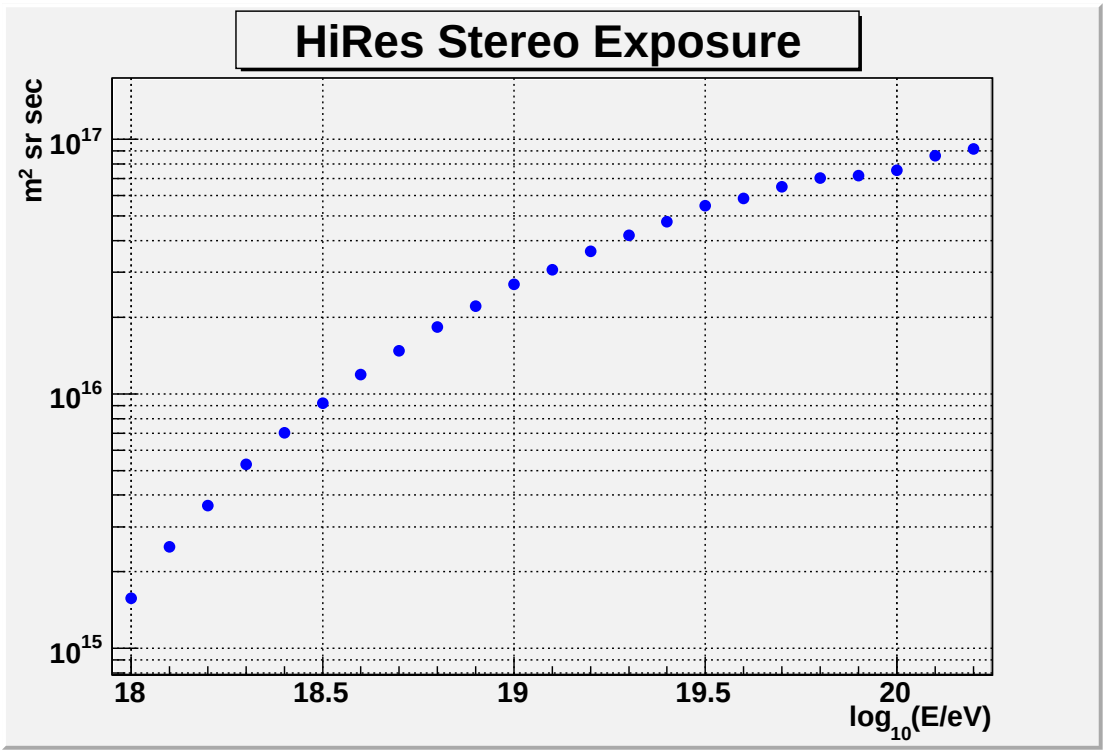

Figure 5.26. The stereo exposure for the HiRes detector over the period 1 December 1999 to 11 November 2005.

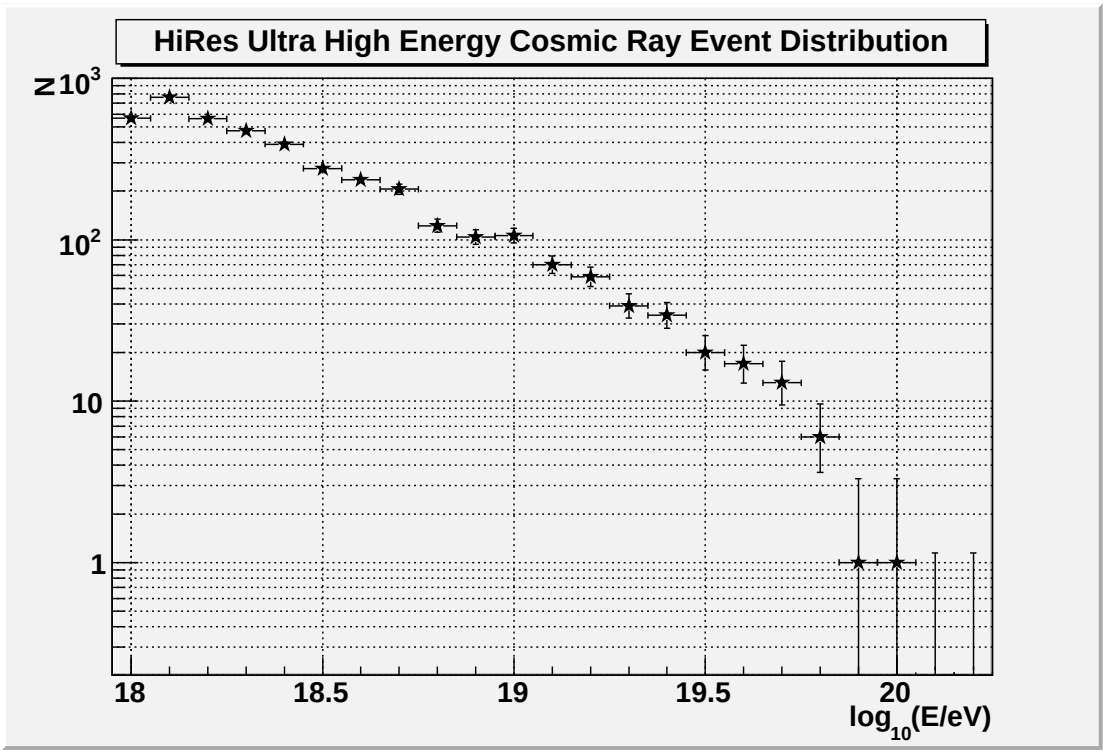

Figure 5.27. The energy distribution of ultra high energy cosmic rays. There are 4061 events in the event sample. The uncertainty shown in each bin is that for a Poisson distribution. Notice the rapid decline in events at around $10^{19.8}$ eV. Two empty bins are shown at $10^{20.1}$ and $10^{20.2}$. The error bars show the upper bound of the 68.3 % limit for no observed events.

we are filling the energy bins with a discrete variable, N the number of observed events, Poisson statistics apply. The uncertainty in each bin up to 10^{20} eV shows the 68.3 % central confidence interval for the number events contained in it. Two empty bins are also shown where no events were observed, but the upper limit of the one-sided confidence interval is shown. Since the detector has exposure in these bins, the significance of observing no events can be shown in this way.

Applying equation 5.3 to the data shown in Figures 5.26 and 5.27, the flux in each bin is calculated and shown in Figure 5.28.

Three maximum likelihood fits are performed on the spectrum to measure the spectral indices, normalization at 10^{18} eV, and energies where the spectral indices change, also called breakpoints. The first fit can be described by

$$J_1(E) \quad = bE^{-\gamma_1} \quad 1 \text{ EeV} \leq E \leq 158.5 \text{ EeV} \tag{5.13}$$

where b is the flux normalization at 1 EeV and γ_1 is the spectral index over the energy range 1 EeV to 158.5 EeV. This fit is called the 0 break point fit.

The 1 break point fit is a four parameter fit with a single constraint that the normalization of the two power laws match at the break point. It is described by

$$J_2(E) = \begin{cases} bE^{-\gamma_1} & 1 \text{ EeV} \leq E \leq E_1 \\ bE_1^{-(\gamma_1-\gamma_2)}E^{-\gamma_2} & E_1 \leq E \leq 158.5 \text{ EeV} \end{cases} \tag{5.14}$$

where E_1 is the break point, γ_1 is the spectral index from 1 EeV to E_1 and γ_2 is the spectral index from E_1 to 158.5 EeV.

The 2 break point fit is similar to the 1 break point fit, except there is a second energy at which the spectral index changes and is written as

$$J_3(E) = \begin{cases} bE^{-\gamma_1} & 1 \text{ EeV} \leq E \leq E_1 \\ bE_1^{-(\gamma_1-\gamma_2)}E^{-\gamma_2} & E_1 \leq E \leq E_2 \\ bE_1^{-(\gamma_1-\gamma_2)}E_2^{-(\gamma_2-\gamma_3)}E^{-\gamma_3} & E_2 \leq E \leq 158.5 \text{ EeV} \end{cases} \tag{5.15}$$

The constraint of matching normalizations at the break points is respected here as well making this a six parameter fit. All three fits are performed over the energy range 1 EeV (10^{18} eV) to 158.5 EeV ($10^{20.2}$ eV). Note that each fit has its own unique value for each fitting parameter. For example γ_1 of the 0 break point fit is not the same as γ_1 of the other fits.

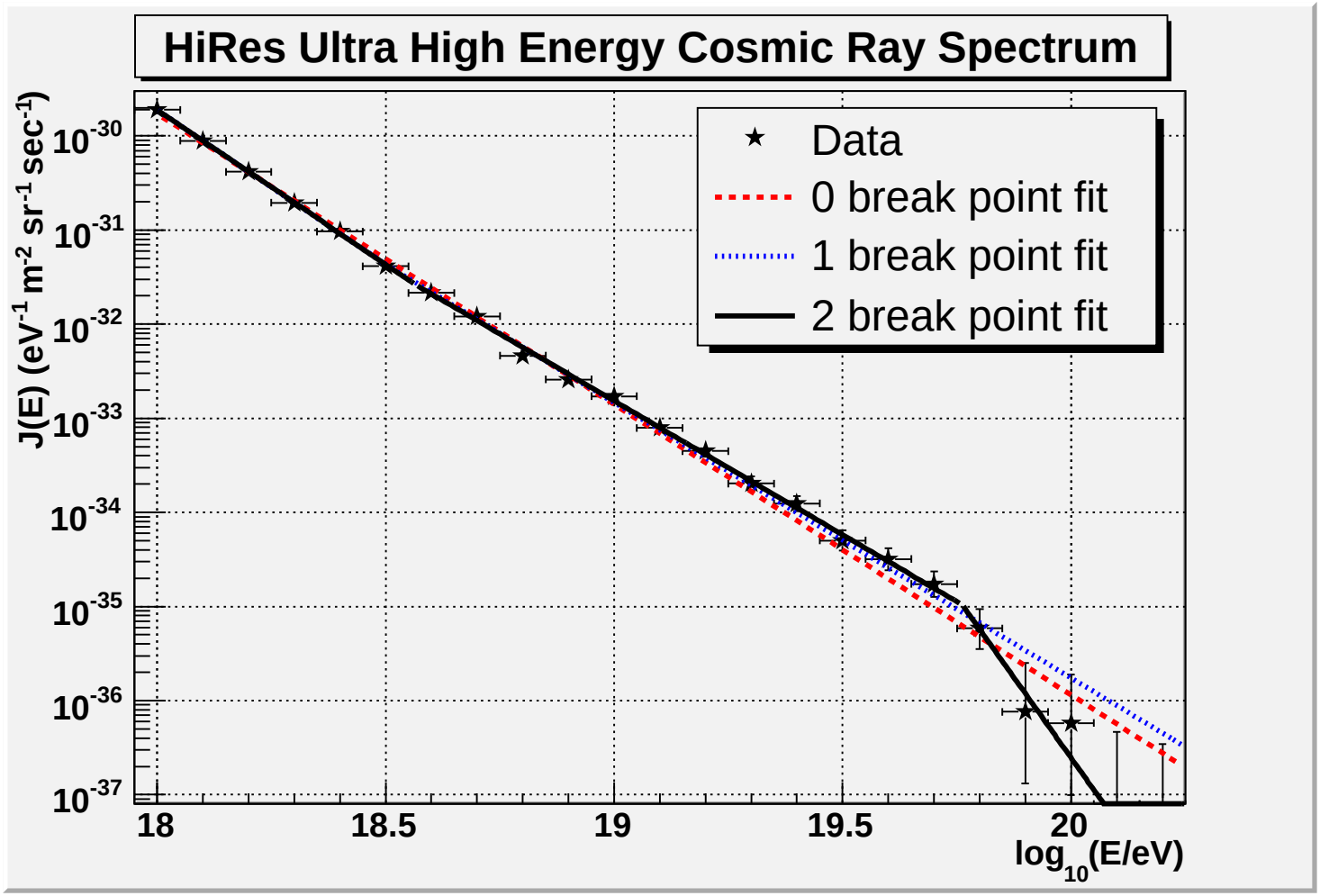

Figure 5.28. The HiRes ultra high energy spectrum. Several different fits to the data are also shown.

The results of each fit are

fit	b	γ_1	γ_2	γ_3	E_1	E_2
	$(10^{30}$ eV m sr s$)^{-1}$				$\log_{10}(E)$	$\log_{10}(E)$
J_1	1.73 ± 0.03	3.09 ± 0.01	-	-	-	-
J_2	1.91 ± 0.04	3.31 ± 0.03	2.91 ± 0.03	-	18.50 ± 0.05	-
J_3	1.91 ± 0.04	3.31 ± 0.03	2.84 ± 0.04	6.8 ± 1.5	18.55 ± 0.04	19.76 ± 0.04

The χ^2/DOF is 64.5/21 for J_1, 30.4/19 for J_2, and 15.3/17 for J_3. The p-values for these three fits are 1.8×10^{-7}, 0.05, and 0.57 respectively. The p-value measures the probability of getting a χ^2 greater than the one obtained if the experiment is repeated and the model is valid. The 2 break point fit with a p-value of 0.57 is the best fit to the data.

To better visualize the significance of the changing spectral indices, each energy bin of the spectrum plot can be weighted by E^3, creating an E^3J plot. For regions where the spectrum has a spectral index > 3, the flux will have a negative slope, and for regions where the spectral index is < 3, the flux will have a positive slope. The E^3J plot enhances these spectral features to make them easier to see. Figure 5.29 shows the E^3J plot made using the flux shown in Figure 5.28. Table 5.1 summarizes the spectrum in shown in Figures 5.28 and 5.29 in tabular form.

It can be seen in the figure that compared to the other fits the 2 break point fit best describes the data. The 2 break point fit identifies the features of the spectrum discussed in section 2.2.1. The ankle is located at 18.55 ± 0.04 $\log_{10}$(eV) and the GZK cutoff at 19.76 ± 0.04 $\log_{10}$(eV). As the figure indicates the spectrum falls sharply at this energy. The 1 break point fit places the ankle at about the same energy, 18.50 ± 0.05 $\log_{10}$(eV), but does not show the GZK cutoff. The significance of the sharp drop in the spectrum will be discussed further in section 5.6.

5.5 Systematics

Uncertainty in the reconstructed energy is dominated by several different components of the reconstruction process. The following are the most important contributors to assessing the systematic uncertainties: PMT calibration (10 %), fluorescence yield (6 %), missing energy correction (5 %), aerosol correction of atmospheric

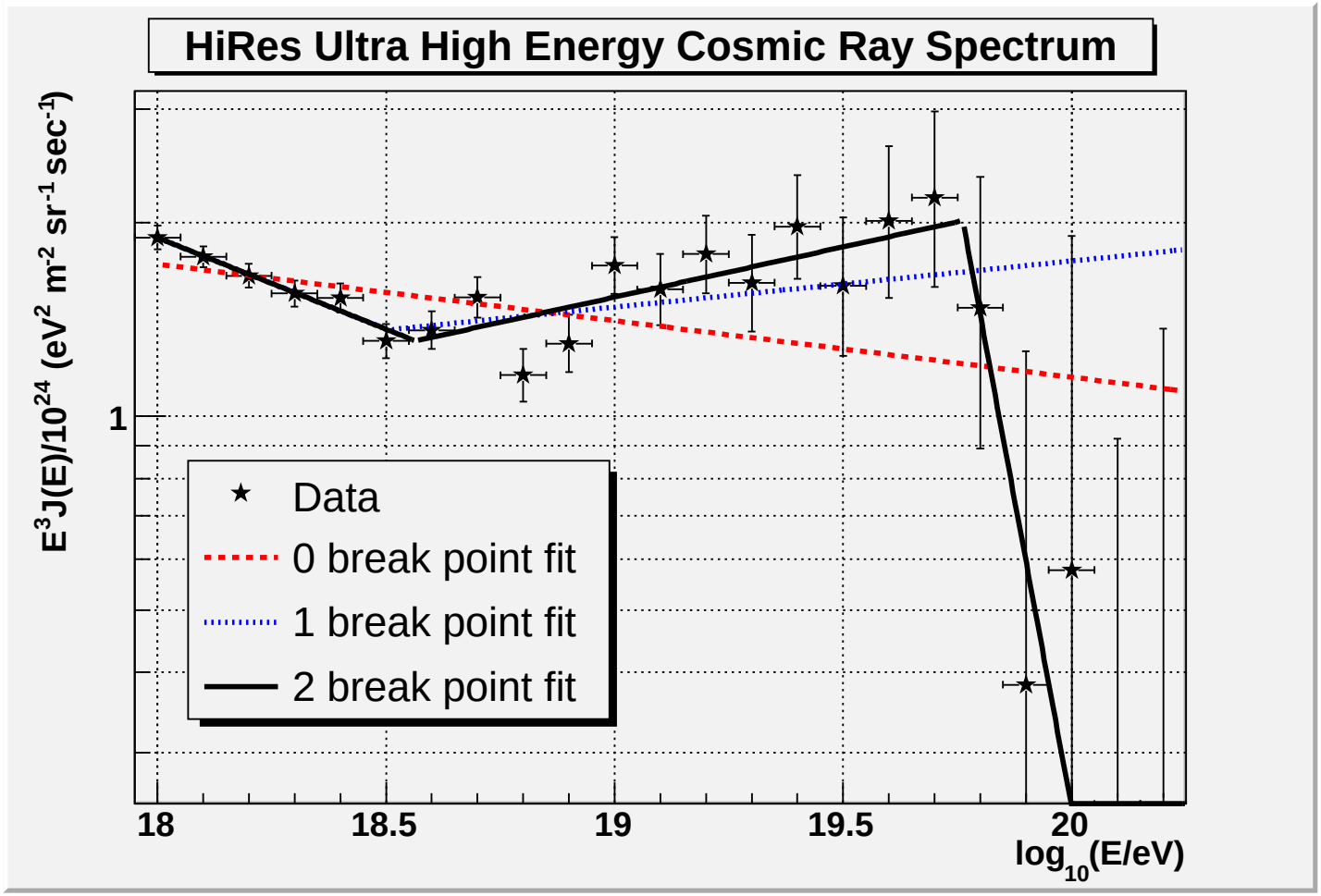

Figure 5.29. E^3J plot of the HiRes stereo spectrum. The different fits are shown as well. The 2 break point fit clearly identifies the suppression of the spectrum at the theorized energy of the GZK cutoff.

Table 5.1. Number of events, aperture, J, and E^3J for each $\log_{10}(E/\mathrm{eV})$ bin for the stereo spectrum. There are 4061 events with energies above 10^{18} eV.

$\log_{10}(E/\mathrm{eV})$	N	Aperture (km^2 sr)	Exposure (10^{16} m^2 s sr)	J (eV^{-1} m^{-2} sr^{-1} s^{-1})	$E^3J/10^{24}$ (eV^2 m^{-2} sr^{-1} s^{-1})
18.0	698	183	0.157	1.923×10^{-30}	1.923
18.1	648	291	0.250	8.910×10^{-31}	1.778
18.2	548	424	0.365	4.109×10^{-31}	1.636
18.3	469	614	0.528	1.929×10^{-31}	1.532
18.4	389	816	0.702	9.563×10^{-32}	1.516
18.5	276	1067	0.918	4.118×10^{-32}	1.302
18.6	235	1386	1.193	2.144×10^{-32}	1.353
18.7	206	1714	1.475	1.208×10^{-32}	1.521
18.8	122	2126	1.830	4.579×10^{-33}	1.150
18.9	104	2565	2.207	2.571×10^{-33}	1.289
19.0	106	3129	2.692	1.706×10^{-33}	1.706
19.1	70	3568	3.070	7.848×10^{-34}	1.566
19.2	59	4207	3.620	4.456×10^{-34}	1.774
19.3	39	4883	4.202	2.016×10^{-34}	1.601
19.4	34	5516	4.746	1.236×10^{-34}	1.959
19.5	20	6358	5.471	5.009×10^{-35}	1.584
19.6	17	6792	5.844	3.166×10^{-35}	1.998
19.7	13	7564	6.509	1.727×10^{-35}	2.174
19.8	6	8196	7.052	5.843×10^{-36}	1.468
19.9	1	8351	7.186	7.592×10^{-37}	0.380
20.0	1	8783	7.557	5.734×10^{-37}	0.573
20.1	0	9987	8.594		
20.2	0	10663	9.175		

transmission (5 %), and dE/dx (10 %) [3]. These errors arise from uncorrelated, independent processes and it is therefore appropriate to add them in quadrature to estimate the overall uncertainty on the energy scale. In this case we find that the total energy scale uncertainty is 17 %.

A study of the effect of a systematic shift in the energy of 17 % on the spectrum is therefore performed to understand the affect on the flux measurement. This is done by scaling all reconstructed energy measurements by ±17 % and observing its effect on the energy distribution of events. Both the aperture and spectrum analyses are subjected to this systematic energy shift. Figure 5.30 shows the effect of systematic errors on the E^3J plot of the spectrum.

The effect of a systematic energy shift on the 2 break point fit can be seen in Figure 5.31. The locations of the ankle and the GZK suppression vary, as well as the spectral indices. Using this information the systematic uncertainties of the spectrum can be stated. The location of the ankle is found to be at $18.55 \pm 0.04\ (\text{stat})^{+0.07}_{-0.02}\ (\text{sys})\ \log_{10}(\text{eV})$ and the GZK cutoff at $19.76 \pm 0.04\ (\text{stat})^{+0.01}_{-0.16}\ (\text{sys})\ \log_{10}(\text{eV})$. The spectral indices before the GZK suppression remain about the same, with $\gamma_1 = 3.31 \pm 0.03\ (\text{stat})^{+0.03}_{-0.06}\ (\text{sys})$ and $\gamma_2 = 2.84 \pm 0.04\ (\text{stat})^{+0.01}_{-0.02}\ (\text{sys})$. The spectral index is not as steep for the energy shifted spectra, so $\gamma_3 = 6.8 \pm 1.5\ (\text{stat})^{+0.0}_{-1.4}\ (\text{sys})$.

Because of the simultaneous shifting of the aperture and the energy distribution of events an unusual feature of the systematic uncertainties is seen. For example, the uncertainty in the ±17 % systematic energy shift in the ankle at $10^{18.55}$ eV is asymmetric because the shift in the aperture and the event distribution are moving in a way to move the ankle less when the energy scale is lowered by 17 % and move it more when the energy scale is increased by 17 %. This can be seen by examining Figure 5.30. The envelope of systematic uncertainties is pinched near $10^{18.55}$ eV and grows wider to either side. The change in the spectral shape also causes the spectral index above the GZK cutoff to be less steep than for the measured spectrum for the +17 % energy shift, so the upper systematic estimate for γ_3 is quoted as 0.0.

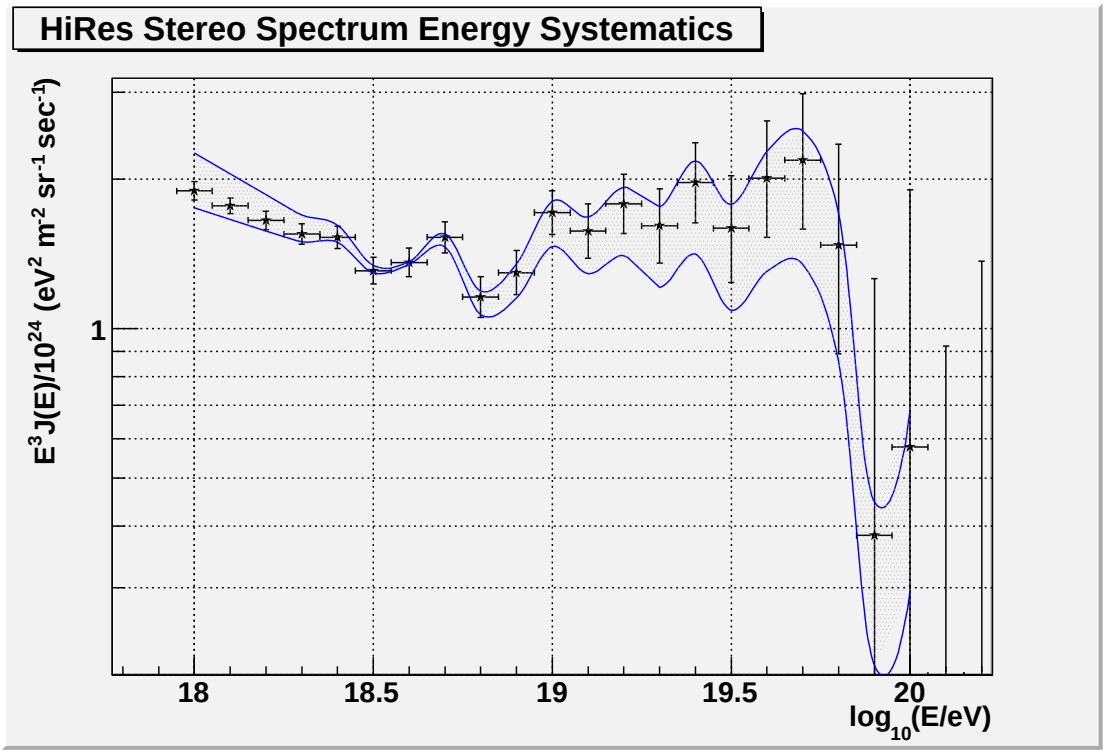

Figure 5.30. The HiRes stereo spectrum with 17 % energy systematic uncertainties indicated by the shaded region.

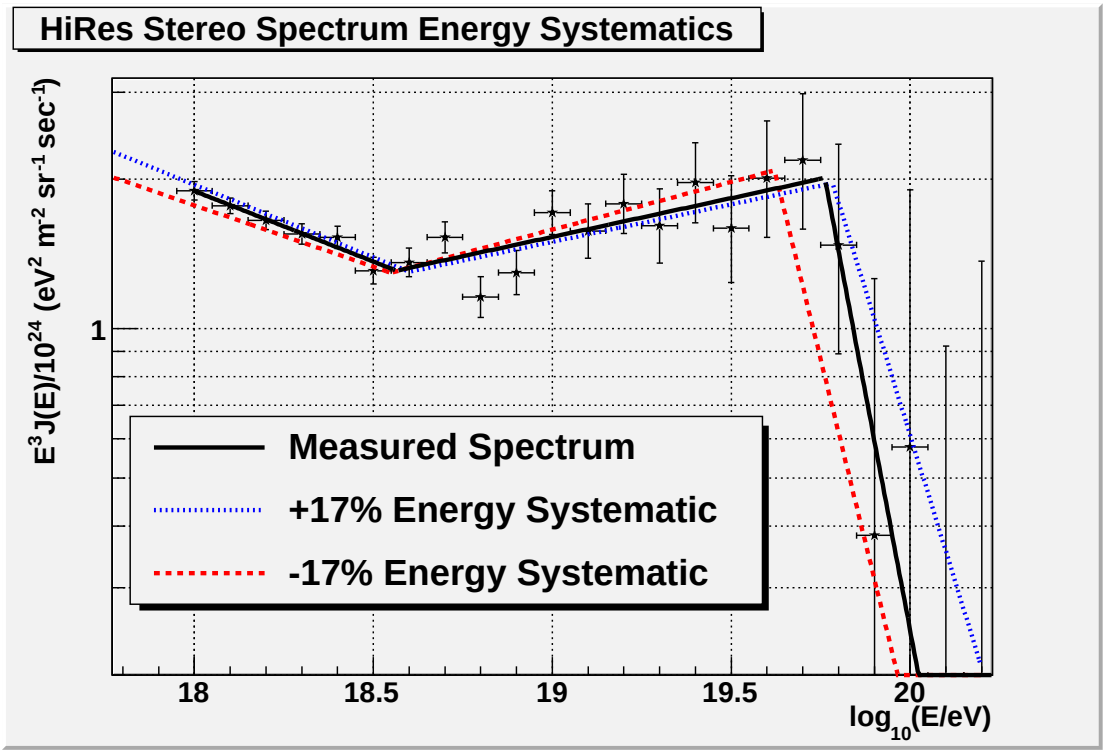

Figure 5.31. The effect of 17 % energy systematics on the 2 break point fits to the energy spectrum.

5.6 Super-GZK Analysis

The question of whether the GZK suppression has been observed can be answered by considering how many events should be seen above the theorized energy of the GZK limit and comparing that to the actual number of events observed. In practice this is done by taking the 2 break point fit and at the 2nd break point (i.e., the GZK limit) assuming the spectral index does not change, but instead remains the same. In other words, the fitted flux above the ankle is extrapolated with spectral index γ_2 out to some maximum energy above the GZK suppression. By applying the measured exposure of the detector to this theoretical flux, the number of expected events in an energy bin can be determined.

The location of the GZK suppression can be defined as the energy at which the predicted integral spectrum exceeds twice the number of events in the observed integral spectrum. The energy defined in this way is also referred to as $E_{1/2}$ by Berezinsky and Grigor'eva [12].

Figure 5.32 shows the predicted and observed integrated spectra. An examination of the ratio of the two spectra finds $E_{1/2}$ to lie at $10^{19.76}$ eV, the same energy as the second break point of the fitted spectrum.

The significance of the break can be measured by finding the number of expected events and the number of observed events in the integral spectra at $10^{19.76}$ eV. The number of predicted events is 24.69 and the number observed is 8. The Poisson probability for this deficit is 9×10^{-5}, which corresponds to 3.7 standard deviations.

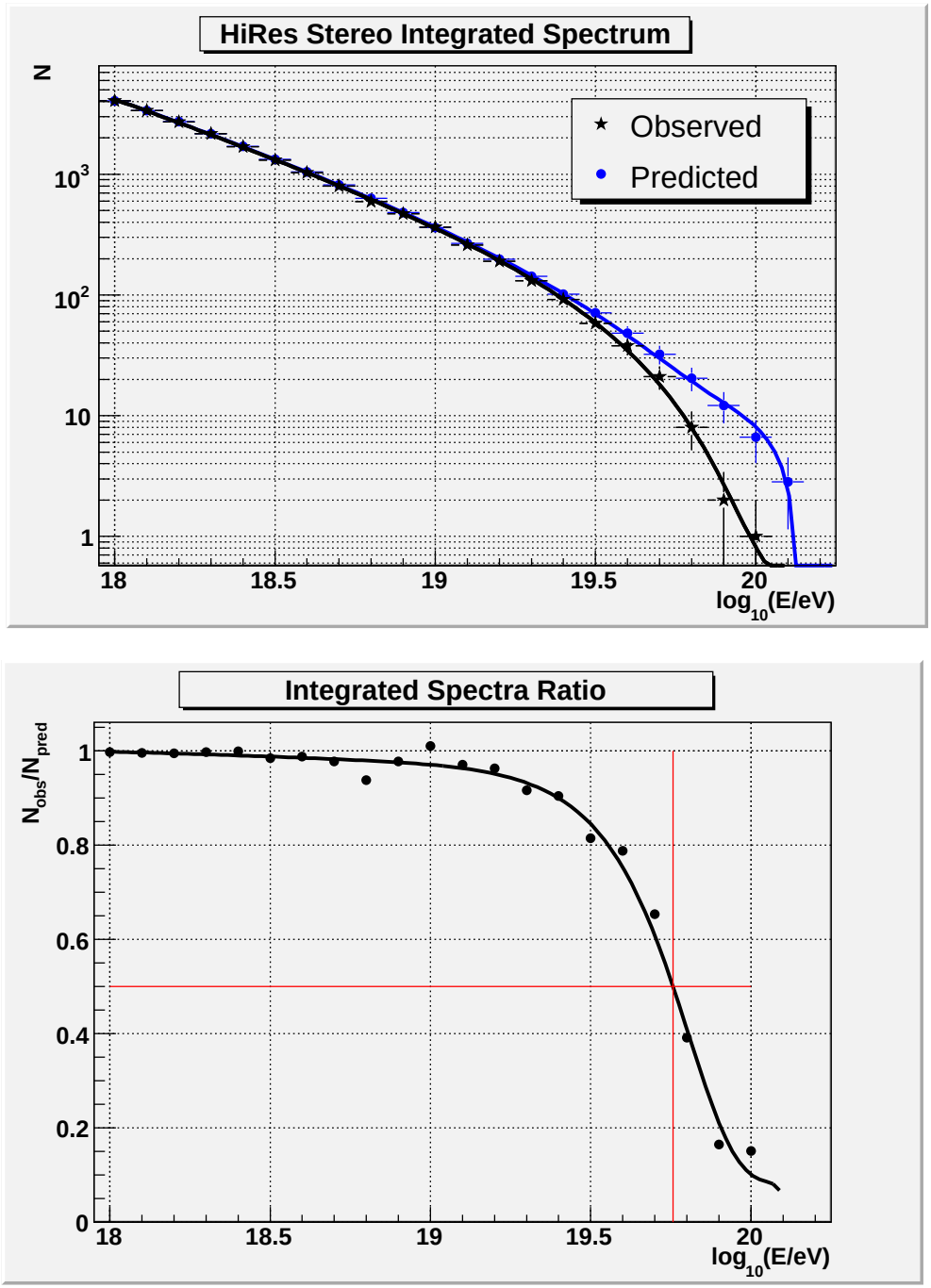

Figure 5.32. The HiRes stereo integrated spectrum. The observed points are the sum of observed events from the data for the current energy and above. The predicted points are the predicted number of events using the measured stereo exposure and the 2 break point fit, under that assumption that after the GZK suppression, the spectrum does not fall. The ratio of the integrated spectra used to find $E_{1/2}$. A fit to the ratio finds $E_{1/2}$ to lie at $10^{19.76}$ eV. The location of $E_{1/2}$ is marked on the figure.

CHAPTER 6

CONCLUSIONS

6.1 Experimental Conclusions

Approximately six years of stereo data have been collected and used in this measurement of the stereo spectrum. Over the six years of running, 2590 hours of good weather data have collected over 4000 stereo cosmic ray events with energies above 10^{18} eV.

Detailed Monte Carlo simulations providing approximately 10 times the statistics seen in the actual data provide the means for calculating the aperture and exposure of the detector. The energy dependent aperture is approximately 10,000 km^2 sr at 10^{20} eV. Comparison of the Monte Carlo distributions to those seen in data provide confidence that the aperture calculation is reliable and can be used to determine the energy spectrum.

A new reconstruction technique called the adaptive sieve has been implemented which attempts to fit real data that can be contaminated with spurious outliers which can degrade results of fitting.

The stereo spectrum measurement fits the data well under the assumption of changing spectral indices at two energies in the range measured, seeing similar features of the spectrum measured by other experiments and theorized by others. The ankle is found to be at 18.55 ± 0.04 (stat)$^{+0.07}_{-0.02}$ (sys) $\log_{10}$(eV) and the GZK suppression at 19.76 ± 0.04 (stat)$^{+0.01}_{-0.16}$ (sys) $\log_{10}$(eV). The spectral indices are also measured and found to be 3.31 ± 0.03 (stat)$^{+0.03}_{-0.06}$ (sys) below the ankle, 2.84 ± 0.04 (stat)$^{+0.01}_{-0.02}$ (sys) between the ankle and the GZK suppression, and 6.8 ± 1.5 (stat)$^{+0.0}_{-1.4}$ (sys) above the GZK suppression. The GZK suppression is observed with a significance of 3.7 standard deviations.

6.2 Suggestions For Improvement

There are several tasks that could be undertaken to improve the results of the experiment. Some of the most important improvements are described here.

The HiRes detector took stereo data up until 4 April 2006. These additional five months of data should be included in the stereo analysis for completeness, to improve statistics, and to increase the exposure to make a stronger statement on the observation of the GZK suppression. The calibration databases are only generated up to 11 November 2005. These databases need to be completed up until the end of stereo operations to fully complete the analysis.

After stereo operations ceased, on 18 May, 25 May, and 26 May 2006, a complete set of roving laser data was taken for all mirrors in both detectors. This last set of laser data needs to be analyzed and checked against the calibration databases for an absolute calibration of the detector, i.e., using the known energy of the laser and the response of the atmosphere, verify that the energy of the laser is correctly reconstructed by both detectors.

The monte carlo uses one constant pedestal value of 257.166 QDC counts for the electronics simulation of HiRes1 PMTs. The database of nightly pedestal readings needs to be incorporated into the monte carlo to more accurately simulate the response of HiRes1.

Some showers are too bright to be accurately measured by the detector. For a given energy shower, there is some minimum distance at which the fluorescence light saturates the detector electronics. When this happens the signal is "clipped" by the analog to digital converters and the shower can not be accurately fitted. HiRes2 high gain channels are particularly prone to this problem. HiRes2 electronics also have low gain channels with a wider dynamic range that can be used to correct for this problem. This saturation correction should be incorporated into this analysis to identify problem showers and to use the low gain channels to better reconstruct them.

The calculation of dE/dx assumes that the 11 % energy loss found in the missing energy of CORSIKA showers is due solely to the artificially imposed energy cut. A

study should be done to see where this energy is actually deposited and to make a correction to the CORSIKA derived dE/dx for energies below 100 keV.

The improved method of measuring mirror reflectivity using the reflectometer should be incorporated into the analysis. This work uses a simpler measurement of mirror reflectivity as described in section 3.1.3.1.

Improvement of the reconstruction of $x_{\max}$ and σ_{s}. The reconstruction routines are tuned for energy reconstruction, but a more accurate measure of $x_{\max}$ and σ_{s} would likely decrease the tails of the energy resolution function. This would further improve the spectrum measurement.

REFERENCES

[1] R. U. Abbasi et al., *Measurement of the Flux of Ultrahigh Energy Cosmic Rays from Monocular Observations by the High Resolution Fly's Eye Experiment*, Physical Review Letters, 92 (2004), pp. 151101–+.

[2] ——, *A Study of the Composition of Ultra-High-Energy Cosmic Rays Using the High-Resolution Fly's Eye*, ApJ, 622 (2005), pp. 910–926.

[3] ——, *First Observation of the Greisen-Zatsepin-Kuzmin Suppression*, Physical Review Letters, 100 (2008), pp. 101101–+.

[4] J. Abraham et al., *Correlation of the Highest-energy Cosmic Rays with the Positions of Nearby Active Galactic Nuclei*, Astroparticle Physics, 29 (2008), pp. 188–204.

[5] T. Z. Abu-Zayyad, *The Energy Sprectum of Ultra High Energy Cosmic Rays*, PhD thesis, University of Utah, Salt Lake City, UT, May 2000.

[6] T. Z. Abu-Zayyad et al., *Calibration and Stability Measurements of a FADC Based Data Acquisition System for the HiRes Fly's Eye Experiment*, in International Cosmic Ray Conference, International Cosmic Ray Conference, 1997, pp. 213–216. Prepared for the 25th International Cosmic Ray Conference (ICRC 1997), Durban, South Africa, 30 Jul - 6 Aug 1997.

[7] C. Amsler et al., *Review of Particle Physics*, Physics Letters, B667 (2008), p. 1.

[8] G. C. Archbold, *A Study of the Composition of Ultra High Energy Cosmic Rays Using the High Resolution Fly's Eye*, PhD thesis, University of Utah, Aug. 2002.

[9] P. Auger, P. Ehrenfest, R. Maze, J. Daudin, and R. A. Fréon, *Extensive Cosmic-Ray Showers*, Reviews of Modern Physics, 11 (1939), pp. 288–291.

[10] R. M. Baltrusaitis et al., *The Structure of EAS at $E > 0.1$ EeV*, in 19th International Cosmic Ray Conference, Conference Program, Sessions Vol. 7, Washington, D.C. 20546, Aug. 1985, Scientific and Technical Information Branch, National Aeronautics and Space Administration, pp. 159–162.

[11] K. V. Belov, *Proton-Air Inelastic Cross-Section at the Energies Above* 10^{18} *eV*, PhD thesis, University of Utah, Salt Lake City, UT, Aug. 2005.

[12] V. S. Berezinsky and S. I. Grigor'eva, *A Bump in the Ultra-high Energy Cosmic Ray Spectrum*, A&A, 199 (1988), pp. 1–12.

[13] M. J. Berger and S. M. Seltzer, *Tables of Energy Losses and Ranges of Electrons and Positrons. NASA SP-3012*, NASA Special Publication, 3012 (1964).

[14] X. Bertou, M. Boratav, and A. Letessier-Selvon, *Physics of Extremely High Energy Cosmic Rays.*, International Journal of Modern Physics A, 15 (2000), pp. 2181–2224.

[15] D. J. Bird et al., *Evidence for Correlated Changes in the Spectrum and Composition of Cosmic Rays at Extremely High Energies*, Physical Review Letters, 71 (1993), pp. 3401–3404.

[16] ——, *Detection of a Cosmic Ray with Measured Energy Well Beyond the Expected Spectral Cutoff Due to Cosmic Microwave Radiation*, ApJ, 441 (1995), pp. 144–150.

[17] ——, *Study of Broad-Scale Anisotropy of Cosmic-Ray Arrival Directions from* 2×10^{17} *to* 10^{20} *Electron Volts from Fly's Eye Data*, ApJ, 511 (1999), pp. 739–749.

[18] M. M. Block, *Sifting Data in the Real World*, Nuclear Instruments and Methods in Physics Research A, 556 (2006), pp. 308–324.

[19] J. Boyer, 10 %. email correspondence, Mar. 2005.

[20] J. H. Boyer, B. C. Knapp, E. J. Mannel, and M. Seman, *FADC-based DAQ for HiRes Fly's Eye*, Nuclear Instruments and Methods in Physics Research A, 482 (2002), pp. 457–474.

[21] A. N. Bunner, *Cosmic Ray Detection by Atmospheric Fluorescence*, PhD thesis, Cornell University, Ithica, N.Y., June 1964.

[22] *Radiation: Risks and Realities*, tech. rep., United States Environmental Protection Agency, May 2007.

[23] T. K. Gaisser and A. M. Hillas, *Reliability of the Method of Constant Intensity Cuts for Reconstructing the Average Development of Vertical Showers*, in International Cosmic Ray Conference, vol. 8 of International Cosmic Ray Conference, 1977, pp. 353–357.

[24] K. Greisen, *End to the Cosmic-Ray Spectrum?*, Physical Review Letters, 16 (1966), pp. 748–750.

[25] A. V. Gurevich and K. P. Zybin, *Runaway Breakdown and the Mysteries of Lightning*, Physics Today, 58 (2005), pp. 37–43.

[26] N. Hayashida et al., *The Anisotropy of Cosmic Ray Arrival Directions Around* 10^{18} *eV*, Astroparticle Physics, 10 (1999), pp. 303–311.

[27] D. Heck and J. Knapp, *Extensive Air Shower Simulation with CORSIKA: A User's Guide*, Institut für Kernphysik, Forschungszentrum Karlsruhe GmbH, Karlsruhe, Mar. 2001.

[28] D. Heck, J. Knapp, J. N. Capdevielle, G. Schatz, and T. Thouw, *CORSIKA: A Monte Carlo Code to Simulate Extensive Air Showers*. FZKA 6019, 1998.

[29] A. M. Hillas, *The Origin of Ultra-High-Energy Cosmic Rays*, ARA&A, 22 (1984), pp. 425–444.

[30] HIRES Collaboration, *A Steerable Laser System for Atmospheric Monitoring at the High Resolution Fly's Eye*, in International Cosmic Ray Conference, vol. 4 of International Cosmic Ray Conference, 1999, pp. 377 – 380.

[31] ——, *A Fiber-optic Based Calibration System for the HiRes Experiment*, in International Cosmic Ray Conference, vol. 2 of International Cosmic Ray Conference, 2001, pp. 623–626.

[32] ——, *Atmospheric Monitoring at HiRes Hardware Systems 2*, in International Cosmic Ray Conference, vol. 2 of International Cosmic Ray Conference, 2001, pp. 631–634.

[33] ——, *Cloud Monitoring at HiRes Detector using Infra-Red Sensors*, in International Cosmic Ray Conference, International Cosmic Ray Conference, 2007.

[34] E. J. Hopkins, *Radiosonde Observation (RAOB) Data Tabulation*, June 1996. `http://www.aos.wisc.edu/~hopkins/aos100/raobdoc.htm`.

[35] G. Hughes, *HiRes2 Trigger Epochs*. email correspondence, Jan. 2008.

[36] F. James, *Minuit: Function Minimization and Error Analysis: Reference Manual*, CERN, Geneva, Switzerland, Mar. 1994. CERN Program Library Long Writeup D506.

[37] B. F. Jones, J. N. Matthews, S. A. Moore, and S. B. Thomas, *Calibration and Stability of the High Resolution Fly's Eye Detector*, in International Cosmic Ray Conference, vol. 2 of International Cosmic Ray Conference, 2001, pp. 641–644. Prepared for 27th International Cosmic Ray Conference (ICRC 2001), Hamburg, Germany, 7-15 Aug 2001.

[38] F. Kakimoto, E. C. Loh, M. Nagano, H. Okuno, M. Teshima, and S. Ueno, *A Measurement of the Air Fluorescence Yield*, Nuclear Instruments and Methods in Physics Research A, 372 (1996), pp. 527–533.

[39] K. Kamata and J. Nishimura, *The Lateral and the Angular Structure Functions of Electron Showers*, Progress of Theoretical Physics Supplement, 6 (1958), pp. 93–155.

[40] J. Linsley, *Spectra, Anisotropies and Composition of Cosmic Rays Above 1000 GeV*, in 18th International Cosmic Ray Conference, Conference Program, Invited and Rapporteur Papers, Vol. 12, N. Durgaprasad, S. Ramadurai, P. V. Ramana Murthy, M. V. S. Rao, and K. Sivaprasad, eds., Homi Bhabha Rd., Colaba, Bombay, India, 400 005, Nov. 1983, Tata Institute of Fundamental Research, pp. 143–149.

[41] M. S. Longair, *High Energy Astrophysics. Vol.1: Particles, Photons and Their Detection*, High Energy Astrophysics, by Malcolm S. Longair, pp. 436. ISBN 0521387736. Cambridge, UK: Cambridge University Press, March 1992., Mar. 1992.

[42] *U.S. standard atmosphere, 1976*, tech. rep., National Aeronautics and Space Administration, Oct. 1976.

[43] National Institute of Standards and Technology, Physics Laboratory, *Description of the ESTAR database*. `http://physics.nist.gov/PhysRefData/Star/Text/method.html`.

[44] W. R. Nelson, H. Hirayama, and D. W. O. Rogers, *The EGS4 Code System*, Stanford Linear Accelerator Center, Stanford University, Stanford, California, 94305, Dec. 1985. SLAC-265.

[45] R. T. Pace, D. S. Riordan, A. G. K. Smith, and HIRES Collaboration, *Cloud Detection at the High Resolution Fly's Eye*, in International Cosmic Ray Conference, vol. 2 of International Cosmic Ray Conference, 2001, pp. 649–652.

[46] A. A. Penzias and R. W. Wilson, *A Measurement of Excess Antenna Temperature at 4080 Mc/s.*, ApJ, 142 (1965), pp. 419–421.

[47] K. Reil, *The Energy Sprectum of Ultra High Energy Cosmic Rays Measured by the High Resolution Fly's Eye Detectors*, PhD thesis, University of Utah, Mar. 2002.

[48] B. Rossi, *High-energy Particles*, Prentice-Hall, New York, 1952.

[49] M. Seman, *The Reconsruction of Light Transmission Through Atmosphere or The Reverse Monte Carlo of Laser Shots*. `http://www.nevis.columbia.edu/~hires/papers/atm_reconstruction.ps`, Sept. 2002.

[50] J. A. Simpson, *Elemental and Isotopic Composition of the Galactic Cosmic Rays*, Annual Review of Nuclear and Particle Science, 33 (1983), pp. 323–382.

[51] P. Sokolsky, *Introduction to Ultrahigh Energy Cosmic Ray Physics*, vol. 75 of Frontiers in Physics, Westview Press, Boulder, CO, 2004.

[52] C. Song, *Study of Ultra High Energy Cosmic Rays with the High Resolution Fly's Eye Prototype Detector*, PhD thesis, Columbia University, N.Y., N.Y., 2001.

[53] ——, *Longitudinal Profile of Extensive Air Showers*, Astroparticle Physics, 22 (2004), pp. 151–158.

[54] C. Song, Z. Cao, B. R. Dawson, B. E. Fick, P. Sokolsky, and X. Zhang, *Energy Estimation of UHE Cosmic Rays Using the Atmospheric Fluorescence Technique*, Astroparticle Physics, 14 (2000), pp. 7–13.

[55] F. W. Stecker, *Effect of Photomeson Production by the Universal Radiation Field on High-Energy Cosmic Rays*, Physical Review Letters, 21 (1968), pp. 1016–1018.

[56] B. T. Stokes, *Weather Cuts*. email correspondence, Jan. 2008.

[57] H. Svensmark, *The Antarctic Climate Anomaly and Galactic Cosmic Rays*, 2006.

[58] L. R. Wiencke et al., *Radio-controlled Xenon Flashers for Atmospheric Monitoring at the HiRes Cosmic Ray Observatory*, Nuclear Instruments and Methods in Physics Research A, 428 (1999), pp. 593–607.

[59] G. T. Zatsepin and V. A. Kuz'min, *Upper Limit of the Spectrum of Cosmic Rays*, ZhETF Pis'ma Redaktsiiu, 4 (1966), pp. 114–117.